Research Topics

Coastal environment in a changing world

Edited by
Javier Benavente, Mouncef Sedrati, Theocharis A. Plomaritis,
Amaia Ruiz de Alegría-Arzaburu and Effi Helmy Ariffin

Published in
Frontiers in Marine Science

ISSN 1664-8714
ISBN 978-2-8325-2598-2
DOI 10.3389/978-2-8325-2598-2

About Frontiers

Frontiers is more than just an open access publisher of scholarly articles: it is a pioneering approach to the world of academia, radically improving the way scholarly research is managed. The grand vision of Frontiers is a world where all people have an equal opportunity to seek, share and generate knowledge. Frontiers provides immediate and permanent online open access to all its publications, but this alone is not enough to realize our grand goals.

Frontiers journal series

The Frontiers journal series is a multi-tier and interdisciplinary set of open-access, online journals, promising a paradigm shift from the current review, selection and dissemination processes in academic publishing. All Frontiers journals are driven by researchers for researchers; therefore, they constitute a service to the scholarly community. At the same time, the *Frontiers journal series* operates on a revolutionary invention, the tiered publishing system, initially addressing specific communities of scholars, and gradually climbing up to broader public understanding, thus serving the interests of the lay society, too.

Dedication to quality

Each Frontiers article is a landmark of the highest quality, thanks to genuinely collaborative interactions between authors and review editors, who include some of the world's best academicians. Research must be certified by peers before entering a stream of knowledge that may eventually reach the public - and shape society; therefore, Frontiers only applies the most rigorous and unbiased reviews. Frontiers revolutionizes research publishing by freely delivering the most outstanding research, evaluated with no bias from both the academic and social point of view. By applying the most advanced information technologies, Frontiers is catapulting scholarly publishing into a new generation.

What are Frontiers Research Topics?

Frontiers Research Topics are very popular trademarks of the *Frontiers journals series*: they are collections of at least ten articles, all centered on a particular subject. With their unique mix of varied contributions from Original Research to Review Articles, Frontiers Research Topics unify the most influential researchers, the latest key findings and historical advances in a hot research area.

Find out more on how to host your own Frontiers Research Topic or contribute to one as an author by contacting the Frontiers editorial office: frontiersin.org/about/contact

Coastal environment in a changing world

Topic editors
Javier Benavente — University of Cádiz, Spain
Mouncef Sedrati — Université Bretagne Sud, France
Theocharis A. Plomaritis — University of Cadiz, Spain
Amaia Ruiz de Alegría-Arzaburu — Universidad Autónoma de Baja California, Mexico
Effi Helmy Ariffin — University of Malaysia Terengganu, Malaysia

Citation
Benavente, J., Sedrati, M., Plomaritis, T. A., de Alegría-Arzaburu, A. R., Ariffin, E. H., eds. (2023). *Coastal environment in a changing world*.
Lausanne: Frontiers Media SA. doi: 10.3389/978-2-8325-2598-2

Table of contents

frontiers | Frontiers in Marine Science

TYPE Editorial
PUBLISHED 17 May 2023
DOI 10.3389/fmars.2023.1213689

Editorial: Coastal environment in a changing world

J. Benavente[1]*, A. Ruiz de Alegría-Arzaburu[2], T. A. Plomaritis[3], M. Sedrati[4] and E. H. Ariffin[5,6]

[1]Faculty of Marine and Environmental Sciences, Earth Science Department, University of Cádiz, Puerto Real, Spain, [2]Universidad Autónoma de Baja California, Instituto de Investigaciones Oceanológicas, Ensenada, Mexico, [3]Faculty of Marine and Environmental Sciences, Applied Physic Department, University of Cádiz, Puerto Real, Spain, [4]Geo-Ocean, Univ Bretagne Sud, Univ Brest, CNRS, Ifremer, UMR6538, Vannes, France, [5]Institute of Oceanography and Environment, Universiti Malaysia Terengganu, Kuala Nerus, Terengganu, Malaysia, [6]Faculty of Maritime Studies, Universiti Malaysia Terengganu, Kuala Nerus, Terengganu, Malaysia

OPEN ACCESS

EDITED AND REVIEWED BY
Marta Marcos,
University of the Balearic Islands, Spain

*CORRESPONDENCE
J. Benavente
javier.benavente@uca.es

RECEIVED 28 April 2023
ACCEPTED 04 May 2023
PUBLISHED 17 May 2023

CITATION
Benavente J, Ruiz de Alegría-Arzaburu A, Plomaritis TA, Sedrati M and Ariffin EH (2023) Editorial: Coastal environment in a changing world.
Front. Mar. Sci. 10:1213689.
doi: 10.3389/fmars.2023.1213689

KEYWORDS

coastal evolution, coastal erosion, coastal risks, climate change, anthropogenic impact, coastal management, coastal adaptation

Editorial on the Research Topic
Coastal environment in a changing world

Coastal areas are among the most dynamic environments on Earth, affected by diverse continental and marine forcings, such as waves, tides, ocean currents, wind, and river discharges, interacting at different temporal and spatial scales. These areas also host 13% of the global urban population (McGranahan et al., 2007) and a large proportion of human activities, including industry, transport, tourism, and recreation. Overpopulation and an increase in intensive exploitation activities are currently disrupting the evolution of coasts worldwide and undermining their future resilience (Kombiadou et al., 2019). Moreover, the effects of climate change, associated with sea-level rise and changes in the magnitude and/or frequency of storms, may further contribute to altering the dynamics of these environments.

The aim of this Research Topic was to provide insights into some of the most prevalent processes that currently endanger our coasts and to assist in improving coastal management in the future. To achieve a comprehensive understanding of these problems, it is essential to conduct sustainable coastal monitoring activities and research that provide continuous information. This Research Topic consists of 10 papers that underscore the importance of addressing multiscale issues using a multidisciplinary approach that highlights crucial physical and environmental factors. The papers can be classified into four groups based on their themes.

Two of the contributions focus on the issues arising from ecosystem changes. Uribe-Martinez et al. address the growing problem of sargassum seaweed reaching tourist beaches. They provide valuable information that could assist the tourism industry and decision-makers in planning and prioritizing monitoring, collection, and restoration efforts. This would enable them to be prepared for unexpected arrivals of sargassum throughout the year, given the high variability of its distribution. On a different subject, Leichter et al. describe long-term patterns of giant kelp sea surface canopy area along with recent patterns of water column nitrate exposure inferred from temperature measurements at different sites on the southern California coast. They contribute to the understanding of the potential roles of seasonal and higher frequency nutrient dynamics for giant kelp persistence, under continuing ocean surface warming and an increasing frequency and intensity of marine heatwaves.

Coastal management is a topic that has also received attention due to the impact of climate change on coastal areas, with four articles addressing various management aspects. Fontán-Bouzas et al. emphasize the importance of identifying vulnerable sectors of beach-dune systems to support coastal management and propose an operational framework to construct a beach-dune system vulnerability map. In the same vein, Fernández-Montblanc et al. present a new methodology for assessing the risk to underwater cultural heritage sites in coastal areas due to wave-induced hazards. They provide a stepping stone toward a sustainable blue economy by ensuring the preservation of coastal environments and cultural heritage sites in the face of climate change. From a coastal development perspective, Saengsupavanich et al. examine the effectiveness of sand bypassing as a solution to jetty-induced coastal erosion in Thailand and identified the amount of sediment deposition that can inform sand bypassing budgets and implementation plans. Authorities build these coastal structures to protect the coast and improve living conditions. However, these structures can have significant environmental impacts, such as altering wave movement, seabed formation, and shoreline erosion. Therefore, it is crucial to understand and estimate sediment movement to ensure sustainable coastal management. Understanding littoral drift, the process by which natural forces move sediment along the shoreline, is essential for sustainable coastal development.

Tenebruso et al. discuss the significance of barrier islands and associated backbarrier environments in protecting populations and infrastructure from storm impacts and provide a morphodynamic model to describe their evolution. They also emphasize the need to understand the response of these environments to sea-level rise and anthropogenic effects to inform future management efforts. Additionally, two other contributions focus on wetlands and cohesive sediment processes at the microscale and mesoscale, respectively. Chen et al. (2022) examine erosion processes in cohesive sediments through the development of a new formula for the critical shear stress of the surface erosion of cohesive sediments, which are composed of fractal aggregates and based on the balance analysis of momentums acting on an aggregate in the bed surface. From a medium-term perspective, Jin et al. provide new insights into the dynamics of marshes through field observations from the central Jiang coast and numerical simulations, with the aim of improving predictions of the overall evolution of tidal flats. They contribute to the understanding of the morphological evolution of tidal flats in relation to the salt marsh edge and provide a formidable dataset for testing models of biomorphodynamics. Figure 1 summarizes the insights into coastal processes provided by this Research Topic and their relevance to coastal management practice. Hence, this Research Topic can be summarized by the notion that for any potential coastal management practice, the positive and negative impacts need to be considered in detail before implementation. To confirm these impacts, coastal management managers need to undertake a comprehensive study of the aerial imagery and simulate the impacts through a modeling approach.

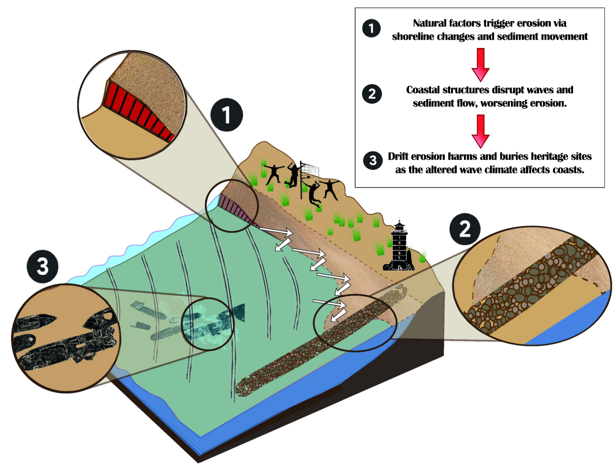

FIGURE 1
Insights into coastal processes provided by this Research Topic and their relevance to coastal management practice.

The final group comprises two contributions focusing on the use of satellite imagery to forecast future flood issues and anticipate changes in the coastline. Cisse et al. assess the vulnerability of the densely populated city of Saint Louis in Senegal to potential coastal flooding by combining satellite-derived data with sea-level observations and reanalyses. The results indicate an increased flood risk due primarily to rising sea levels, underscoring the urgent need for countermeasures to protect communities and infrastructure. The last paper by Ibaceta et al. proposes a new shoreline modeling approach that uses time-varying model parameters and tests it with multidecadal satellite-derived shorelines, thereby reducing the uncertainty associated with the misspecification of physical processes driving shoreline change.

Author contributions

All the authors have contributed to the review of the submitted articles as well as to the writing of this editorial. AEH has made the figure.

Funding

This special issue has been promoted within the project CRUNCJ (FEDER-UCA18-107062) founded by the European Union under the 2014-2020 ERDF Operational Programme and by the Department of Economi Transformation, Industry, Knowledge, and Universities of the Regional Government of Andalusia and the the project CRISIS (PID2019-109143RB-I00) funded by the Ministry of Science and Innovation and the European Union. AEH greatly supported on this research under the funding by the Malaysian Ministry of Education under the Fundamental Research Grants Scheme (FRGS) [FRGS/1/2022/WAB02/UMT/02/1].

Conflict of interest

Publisher's note

References

Kombiadou, K., Costas, S., Rita Carrasco, A., Plomaritis, T. A., Ferreira, O., and Matias, A. (2019). Bridging the gap between resilience and geomorphology of complex coastal systems. *Earth-Science Rev.* 198. doi: 10.1016/j.earscirev.2019.102934

McGranahan, G., Balk, D., and Anderson, B. (2007). The rising tide assessing the risks of climate change and human settlements in low elevation coastal zones. *Environ. Urban.* 19 (1), 17–37. doi: 10.1177/0956247807076960

Frontiers in Marine Science

ORIGINAL RESEARCH
published: 08 April 2022
doi: 10.3389/fmars.2022.861569

Wave Impact Analysis on a Beach-Dune System to Support Coastal Management and Nourishment Works: The Showcase of Mira, Portugal

Ángela Fontán-Bouzas[1,2], Umberto Andriolo[3], Paulo A. Silva[2] and Paulo Baptista[4]*

[1] Centro de Investigación Mariña, Universidade de Vigo, Geoma, Vigo, Spain, [2] CESAM & Department of Physics, University of Aveiro, Campus de Santiago, Aveiro, Portugal, [3] INESC Coimbra, Department of Electrical and Computer Engineering, University of Coimbra, Coimbra, Portugal, [4] CESAM & Department of Geosciences, University of Aveiro, Campus de Santiago, Aveiro, Portugal

OPEN ACCESS

Edited by:
Javier Benavente,
University of Cádiz, Spain

Reviewed by:
Rodolfo Silva,
National Autonomous University of Mexico, Mexico
Ana Vila-Concejo,
The University of Sydney, Australia

***Correspondence:**
Ángela Fontán-Bouzas
afontan@uvigo.es

Specialty section:
This article was submitted to Coastal Ocean Processes, a section of the journal Frontiers in Marine Science

Received: 24 January 2022
Accepted: 14 March 2022
Published: 08 April 2022

Citation:
Fontán-Bouzas Á, Andriolo U, Silva PA and Baptista P (2022) Wave Impact Analysis on a Beach-Dune System to Support Coastal Management and Nourishment Works: The Showcase of Mira, Portugal. Front. Mar. Sci. 9:861569. doi: 10.3389/fmars.2022.861569

At coasts, sandy beach-dune systems act as natural barriers to environmental forcing, preventing coastal flooding and protecting coastal communities. In the context of coastal studies, it is fundamental to identify beach-dune sectors exposed to wave impact to support coastal management and suggest soft engineering interventions. This work examines the morphodynamics of the Mira beach-dune system on the northern-central littoral of Portugal over the winter 2016-2017. Coupling topographic data with the estimation of wave runup and total water level (TWL) timeseries, we proposed an operational framework to spot the beach-dune system sectors most vulnerable to dune collision and overwash. The highest topographic variations occurred in the northern sector of the study area, where overwash events occurred due to low dune crest (DC) elevation. The dune toe (DT) was frequently collided by waves in the central sector, where the upper beach profile was the most variable during winter. Overall, wave collision and overwash events were registered not only during storms, but also during spring tides and mild wave conditions. Results highlight the importance of uploading the intertidal beach slope when computing the total water levels on wave-dominated mesotidal sandy beaches, and therefore, the need for a consistent monitoring program of the coastal zones. Findings of this work also supported the coastal management of beach-dune systems, where regional authorities need to restore dune ridges to prevent further overwash events and erosion. The presented framework can be applied to build a beach-dune system vulnerability map in response to wave forecast and predicted sea-level rise.

Keywords: coastal monitoring, coastal erosion, beach slope, beach-dune nourishment, wave run up

INTRODUCTION

The coastal zone is the highly dynamic interface between land, sea and atmosphere, important both in the environmental and socioeconomic contexts (e.g., Martínez et al., 2007). Currently, climate changes threaten most of the coastlines worldwide (e.g., Hinkel et al., 2013; Ranasinghe, 2016; Vousdoukas et al., 2020), and an erosional trend has been observed at about 30% worldwide in the last decade (Luijendijk et al., 2018; Mentaschi et al., 2018). The estimation of the vulnerability of coastal areas to erosion and hazard has received considerable attention. Most of works focused on the long-term prediction and evaluation of factors induced by climate changes, such as sea level rise (Alexandrakis and Poulos, 2014; Vousdoukas et al., 2018; Rocha et al., 2020; Sekovski et al., 2020) and storm occurrence (Beniston et al., 2007; Vousdoukas et al., 2016). However, it is of interest to assess the coastal vulnerability also in the short-term, since drastic changes may occur abruptly on the high dynamic coastal environment, and immediate mitigation measures may be needed. Among coastal features, sandy beach-dune systems occur along most global coastlines (Martínez et al., 2008). Beach-dune systems act as natural barriers to environmental forcing, prevent flooding of landward areas (Durán et al., 2016; Pagán et al., 2019) and islands (Matias et al., 2010; Timmons et al., 2010; Fontán-Bouzas et al., 2019; Matias et al., 2019; Blanco-Chao et al., 2020), and protect coastal communities (Ciavola et al., 2014). Tide, waves and wind dominate coastal processes, whereas beaches and dunes interact with a dynamic and delicate equilibrium. Beach configuration prevents the wave impact on dunes, while dunes play the role of sand reservoir for natural beach nourishment (Houser and Ellis, 2013; Jackson et al., 2019). Nevertheless, environmental forcing and human interventions (e.g. coastal structures) may affect this morphological equilibrium (Karunarathna et al., 2014; Castelle et al., 2015; Dissanayake et al., 2015; Flor-Blanco et al., 2021). Common morphodynamic analysis generally considers the spatial variation of proxy indicators such as coastline (Harley et al., 2014; Splinter et al., 2014; Angnuureng et al., 2017), beach width and volume (Phillips et al., 2017; Wiggins et al., 2019; Santos C. J. et al., 2020), along with beach profiles variability (Ludka et al., 2015; Turner et al., 2016; Eichentopf et al., 2020). However, the analysis of beach slope changes and wave hydrodynamics, coupled with geomorphological features such as dune toe and crest elevations, is crucial to understand morphodynamic processes (Del Río et al., 2012; Armaroli et al., 2013; Masselink and Van Heteren, 2014; Wernette et al., 2016), and to evaluate the wave impact on a beach-dune system (Sallenger, 2000; Vousdoukas et al., 2012; Masselink and Van Heteren, 2014; Castelle and Harley, 2020; Masselink, 2021). In particular, Sallenger (2000) proposed a scale of impact on a beach-dune system, based on four regimes: i) swash regime, when the maximum wave runup is confined to the foreshore; ii) collision regime, when waves impact the dune face, iii) overwash regime, when waves overtop the dune crest and iv) breaching and inundation regime. This work analyses the morphodynamics of the 2300 m long-shore Mira beach-dune system on the North Atlantic Portuguese coast during the winter 2016-2017. Beach and dune topographic surveys were performed by two conventional methods over five months on a fortnightly basis. We propose an operational framework that couples temporal and spatial morphological changes to total water level (TWL) dynamics on the foreshore i) to understand the influence of the beach profile configuration in preventing and/or determining wave impact on dunes and ii) to identify the dune sectors most vulnerable to wave collision and overwash regimes, following Sallenger (2000). This work provided a valid support to local authorities for the choice and implementation of soft engineering interventions, which were further adopted to restore the vulnerable sectors of the Mira beach dune ridge. This study also aims to shed light on the understanding of sedimentary deficit beach-dune systems including run-up processes to improve models and long-term predictions of their future evolution under a climate change scenario. The presented showcase can be implemented worldwide for improving coastal vulnerability assessment and support coastal management.

METHODS

Study Site and Topographic Surveys

Mira beach (Praia de Mira; 40°27’28.76”N, 8°48’10.74”W) is a sandy beach-dune system located on the western Portuguese coast facing the North Atlantic Ocean (**Figure 1**). The study area extends 2300 m long-shore with NNE-SSW orientation, limited

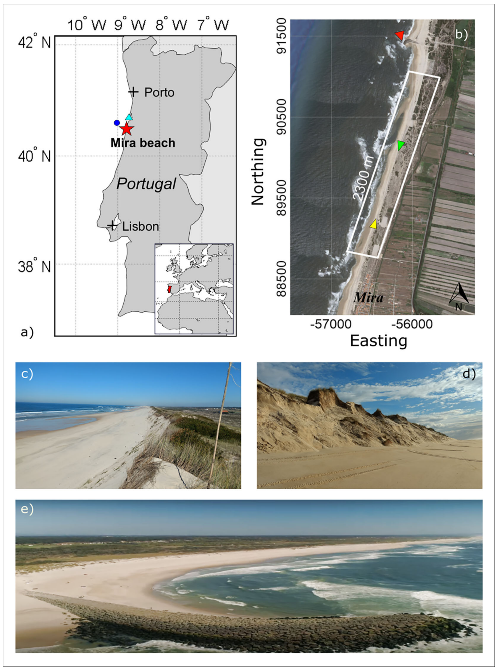

FIGURE 1 | Study site. **(A)** study site location (red star), SIMAR wave point (blue dot) and tidal gauge (cyan triangle); **(B)** map of Mira beach-dune system and study area (white rectangle). Yellow, green and red triangles indicate the location of pictures in **(C–E)**, respectively.

northward by a 200 m-long groin, and backed by a dune system with crest elevation varying between 5 and 16 m (**Figure 1**). The study site belongs to a sandy barrier eastward limited by the Aveiro lagoon. The dune system is the geomorphologic element that protects several socio-economic activities located eastward of these dunes. The beach is composed of medium-sized sand with relatively spatial uniformity (D50 ~ 0.4 mm) and supplied by a natural N-S littoral drift (Silva et al., 2009; Stronkhorst et al., 2018; Fernández-Fernández et al., 2019). Tides are semidiurnal and the tidal range oscillates between 2.8 m and 1.2 m for the spring and neaps tides, respectively (Antunes and Taborda, 2009; Baptista et al., 2014). Mira beach-dune system processes are dominated by the North Atlantic swell, with a mean annual significant wave height (H_s) of 2 m and wave periods between 7 s and 15 s mainly concentrated in the interval between W and NNW directions (Dodet et al., 2010; Oliveira et al., 2018). During winter seasons (from November to March), the mean Hs is approximate 3 m, and storm height can exceed 8 m (Silva et al., 2009). Previous multi-annual studies have observed that this littoral is subjected to coastline retreat between 5 and 8 $m/_{year}$ (Baptista et al., 2014 and Ponte Lira et al., 2016, respectively). This progressive long-term erosional trend, in which the frontal dunes have been progressively destroyed, under the action of winter waves, has been caused by the deficit in sediment supply from Douro River, which decreased from 1.5 million $m^3/_{year}$ to about 0.25 million $m^3/_{year}$ during the last decade (Coelho et al., 2009; Marinho et al., 2018). In this coastal stretch, beach erosion effects have been propagated southward due to sediment blockage by manmade structures (Costa and Coelho, 2013; Pereira and Coelho, 2013). The northern sector of the beach has been the more affected, largely induced by the groin built in 2003 (Baptista et al., 2014). During 2015, a nourishment was carried out on the northern Mira beach-dune system sector (Marinho et al., 2019).

A beach-dune morphology survey program was performed from October 2016 to February 2017 during the winter. A four-wheel motor quad (hereinafter ATV, **Figure 2B**), equipped with three high-grade Global Positioning System receivers and a laser distance sensor (INSHORE monitoring system - Baptista et al., 2011), was used to carry out three-dimensional beach topographic surveys. Subaerial beach area elevation (**Figure 2A**) was surveyed at a frequency of 1 s with vertical errors of 0.02–0.03 m and less than 0.01 horizontal errors (Baptista et al., 2011).

In the post-processing phase, for each survey dataset, using more than 5,000 topographic points, the collected points were spatially interpolated on a regular 1x1 m grid using the geostatistical Kriging method of Surfer Golden Software to obtain the digital elevation models (DEM) with 0.08–0.12 vertical (RMS) accuracy (**Figure 2C**). The whole dataset was homogenized, clipping each produced DEM to the same area extent. Besides the ATV surveys, one differential Global Positioning System (dGPS) receiver was used by an operator to obtain cross-shore transects elevation between the low tide limit and the backdune (**Figure 2B**). Transects were numbered from 1 to 6, starting from the northern sector of the beach (**Figure 2A**). The final topographic dataset comprised 18 DEMs (from the ATV surveys) and 72 beach-dune profiles, 12 for each of the six considered transects. On average, we produced three DEMs and collected two beach-dune profiles per month (**Figure 2D**). Yet, surveys were also performed before and after storms, to better describe the changes induced by the most energetic events. In addition topographical data collected by the COSMO programme (https://cosmo.apambiente.pt) was used to provide the morphological evolution and nourishment works effects after monitoring topographical dataset.

Morphodynamic Analysis

DEM dataset was used to retrieve the beach width (BW), the beach volume (BV) and the intertidal beach slope, while P1-P6 beach profiles were exploited to describe the dune characteristics. Moreover, a total amount of 230 transects were extracted from DEMs, with an offset of 10 m (**Figure 2C**). An *ad hoc* automated algorithm was developed to automatise the analysis.

The BW was considered as the subaerial beach horizontal distance between the location of shoreline (SL, 1 m) and the most landward points collected by the ATV, approximately coinciding with the dune toe (DT) location (**Figure 2C**). The BV was computed as the area underneath the BW, between the SL and DT elevation.

From the dGPS cross-shore transects P1-P6, the dune crest location (DC) was recognised as the point with the maximum elevation (**Figure 2C**). The location and elevation of DT were identified as the first point with local maximum concave curvature seaward the DC, found as the local minima of the beach profile first derivative (similarly to Diamantidou et al., 2020 and Gonçalves et al., 2020). For both DEMs and cross-shore transects, the intertidal beach slope was found as the average of the first derivative values considering the beach profile comprised between the SL (1 m) and 3 m elevations (Gonçalves et al., 2020).

Offshore wave conditions (**Figure 2D**) were obtained from the hindcast WAM numerical model at the SIMAR point 1044062 (40.50° N; 9.00° W) 10 km from the coast. The dataset, provided by the Spanish State port authority (http://www.puertos.es/, Pilar et al., 2008), was composed of hourly significant wave height (Hs), wave peak period (Tp), wave direction (Dir) for the period in analysis.

To complete the study of hydrodynamics, the time series of total water level (TWL) excursion on the beach slope was computed following Sallenger (2000) as:

$$TWL = \eta + R_{2\%}$$

Where η is the mean sea level, and $R_{2\%}$ is the wave runup. The mean sea level η was the hourly average of the tidal level (**Figure 2D**) measured by the Aveiro tidal gauge (**Figure 1**), which included both astronomical tide and storm surge.

The $R_{2\%}$ indicates the vertical swash extent exceeded by 2% on the beach. Many predictors have been developed over the past

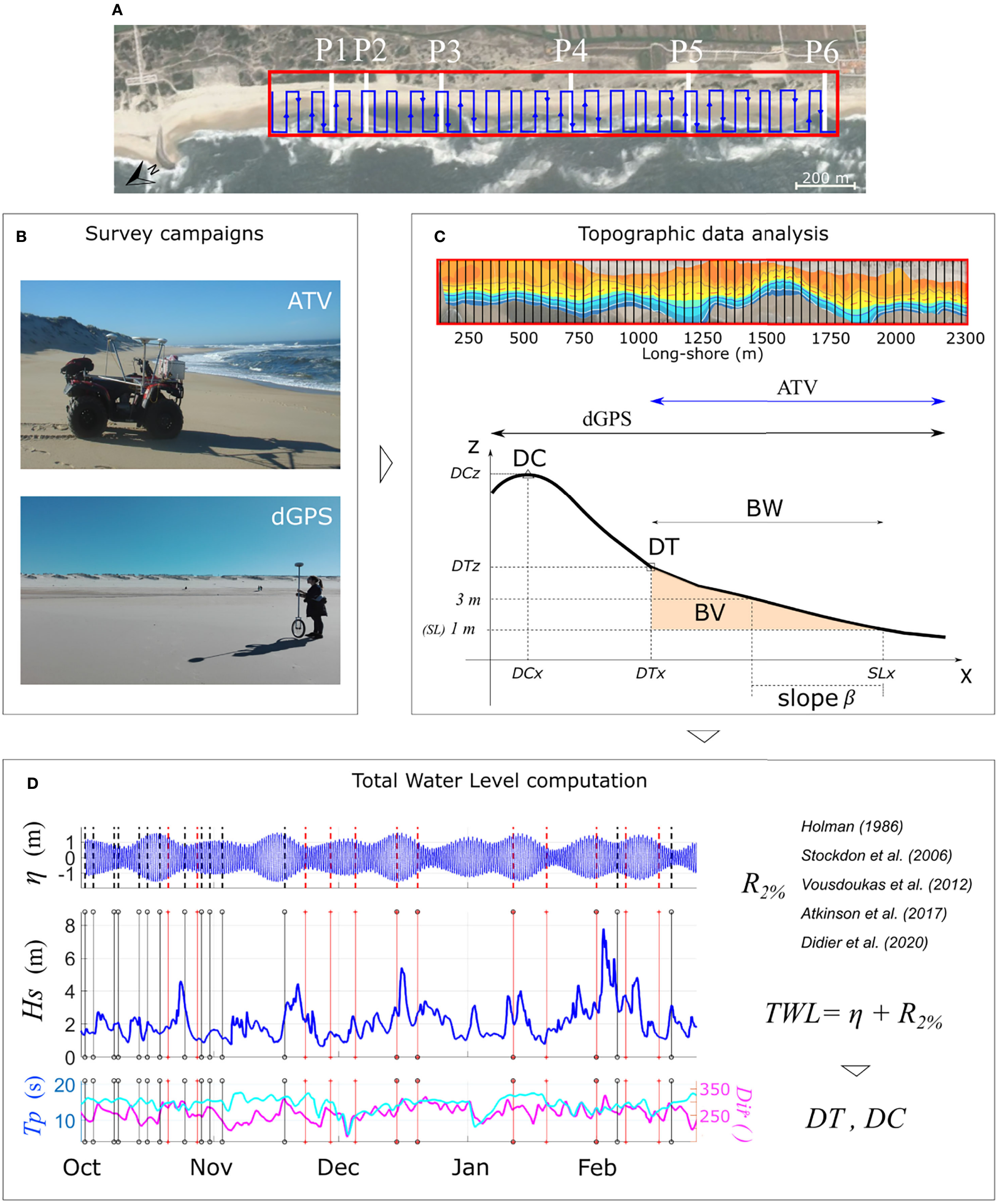

FIGURE 2 | Workflow and hydrodynamics. **(A)** Mira beach-dune system aerial photo and study area (red rectangle), with all-terrain vehicle (ATV) trajectories example (blue lines) on the subaerial beach, and locations of the six beach profiles (P1-P6, white lines) surveyed by the differential Global Positioning System (dGPS); **(B)** pictures of ATV (upper) and dGPS (lower) systems; **(C)** example of digital elevation model (DEM, upper) and series of transects (black lines) used to retrieve morphological indicators. Idealized beach profile (lower) with indicators used for the analysis:position of the shoreline (SLx), dune toe (DT), dune crest (DC), intertidal beach slope β (retrieved considering the profile sector between SL and 3 m elevation), beach width (BW) and beach volume (BV); **(D)** hydrodynamic data with tidal elevation (η), significant wave height (Hs), wave peak period (Tp) and wave direction (Dir). Black and red vertical lines indicate the dates of ATV and dGPS surveys, respectively. Wave runup and tidal elevation were combined to compute total water level (TWL) timeseries (right), eventually coupled to DC and DT elevations for evaluating beach-dune vulnerability.

decades based on field and laboratory experiments, generally parametrizing $R_{2\%}$ as a function of offshore wave conditions (H_S and wavelength L_S) and the intertidal beach slope β (Gomes da Silva et al., 2020 and references therein). For the computation of $R_{2\%}$, we considered five among the most common and recent formulas (**Table 1**) derived and from field measurements dataset collected by coastal video monitoring on sandy beaches, namely Holman (1986); Stockdon et al. (2006); Vousdoukas et al. (2012); Atkinson et al. (2017) and Didier et al. (2020). Besides being compiled over a wide range of hydrodynamic conditions and beach states, the considered formulas incorporate the wave setup component. Of note that for the computation of $R_{2\%}$, the intertidal beach slope β was updated for each profile measured over the monitored period.

The morphological parameters (BW and BV) were analysed to understand the long-shore beach topographical changes. The six beach transects and the respective dune characteristics (DT and DC), along with the intertidal beach slope, were used to verify the wave impact on the dune ridge, coupling the modelled TWL timeseries to the spatial information collected by the surveys. Finally, the beach slope over the long-shore, derived from DEM dataset, was used to compute the TWL excursion over the long-shore extent.

To characterise the wave impact on the beach-dune system, we adopted the Storm Impact Scale (SIS) presented by Sallenger (2000), which considered distinct impact regimes according to the relation between the TWL, the DT and DC heights. For example, in the collision regime the SIS=TWL/DC ranges between DT/DC and 1.

RESULTS

Beach-Dune Morphodynamics

Figure 3 shows the generated DEMs on a monthly basis, and the analysis of beach width (BW) and beach volume (BV) evolution.

The long-shore was characterised by the presence of beach mega-cusps, with long-shore embayments spacing between 500 m and 700 m, and horns protruding zones with an elevation of about 3 m (**Figure 3A**). The shortest BW and lowest BV values corresponded to the locations of the embayments. Over the winter, the mega-cusps gradually disappeared, resulting in more homogeneous BW and BV values over the long-shore. The standard deviation of the beach surface elevation (**Figure 3B**) revealed that the intertidal zone, which was considered to retrieve the beach slope (1-3 m), was the most variable, with the highest changes in the northern sector (about 1 m).

During the monitoring period, H_s varied between 0.6 and 7 m, with a mean value of 1.9 m, while T_p between 6 and 18 s, with a mean value of 12 s. These values are in agreement with the characteristic wave climate at the study site. The average BW (**Figure 3C**) increased from October (60 m) to November (80 m) and then decreased till the end of February (40 m). Overall, the subaerial beach surface diminished about 20% over the winter. The BV was most variable in the northern and central sectors, increasing till middle November, whereas it did not change significantly in the southern sector (**Figure 3D**). The BV was about 400.000 m3 at the start of winter, and decreased of about 27% with a constant trend in February.

Figure 4 shows the results of the 12 surveys of the six cross-shore transects P1-P6. From P1 to P4, the presence of beach berm determined the highest volume values, already observed in **Figure 3**, during the early winter months. Over the monitored period, the beach profile became smoother with a gentler slope. On P5 and P6, instead, the beach profiles did not change significantly. Overall, the DT elevation varied between 4 m (P2) and 6 m (P6), while the DC was between 5.5 m (P2) and 15.2 m (P6). The foredune slope differed among profiles, with the steepest gradient in the central part of the beach (from P3 to P5).

Figure 4 also shows the number of collisions calculated considering i) the TWL based on the five R2% formulas (**Table 1**), ii) the updated intertidal beach slope iii) the updated DT elevation, on a three-days basis. In the central part of the beach, P3 and P4 were less collided than the northern (P1 and P2) and southern (P5 and P6) profiles.

The analysis of TWL timeseries coupling morphologic features after Sallenger verify the foredune variability and scarped front dunes (P1, P3 on December, P4 Jan 2017 and P5 Oct 2016) and the signature of previous swash events up in the dune (P1 P4 Dec 2016, P5 Jan and Feb 2017). Regarding P2, **Figure 4** shows evidence of overwash events collected during the high-frequency field surveys. It was possible to verify the occurrence of overwash events during the storm event in the early February, with the presence of microliter on the foredune, and the observation of the typical overwash fan on the backdune (**Figure 5**).

The TWL estimated with the Stockdon et al. (2006) and Vousdoukas et al. (2012) formulations, did not indicate overwash events, suggesting that these formulations underestimated $R_{2\%}$. On the other hand, the ones computed

TABLE 1 | Wave runup $R_{2\%}$ formulas, based on offshore wave significant height (H_s), offshore wavelength (L_s), beach slope (β) and Iribarren number (ξ).

	Formula
Holman (1986)	$R_{2\%}=0.2\ Hs+0.83\ \xi$
Stockdon et al. (2006)	$R_{2\%} = 1.1(0.35\ \beta_f(H_0L_0)^{0.5} + [H_0L_0(0.563\ \beta_f^2 + 0.004)]^{0.5}/2)$
Vousdoukas et al. (2012) – *(7)*	$R_{2\%}=0.53\ \beta\ (HsLs)^{0.5} + 0.58\ \xi\ (Hs^3/Ls)^{0.5}+0.45$
Atkinson et al. (2017) – *M2*	$R_{2\%}=0.92\ \beta\ (HsLs)^{0.5} + 0.16\ Hs$
Didier et al. (2020) - *(14)*	$R_{2\%}=1.06\ [0.058(H_0L_0)^{0.5}+0.32(H_0L_0\beta)^{0.5}/2]$

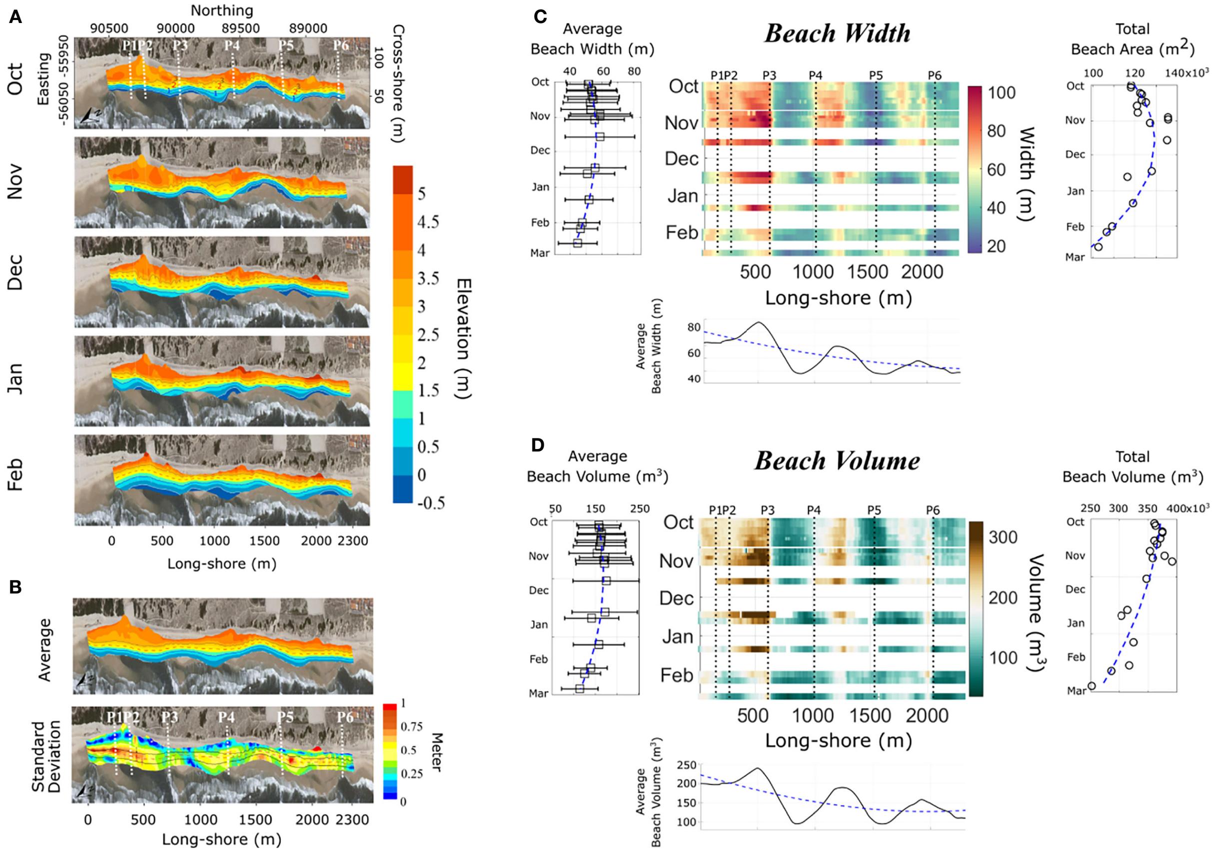

FIGURE 3 | Beach width and beach volume changes. **(A)** Digital elevation models (DEMs) of subaerial beach obtained by ATV surveys, on a monthly basis; **(B)** average (upper) and standard deviation (lower) values considering DEMs on a monthly basis. Common to a) and b), dashed orange line indicates the 2 m elevation contour, while solid black lines the contours of 1 m (seaward) and 3 m (landward) elevations; **(C)** beach width (BW) evolution over time and space (central panel), average BW over time (left), average BW over space (lower) and total beach area evolution over time (right); **(D)** beach volume (BV) evolution over time and space (central panel), average BV over time (left), average BV over space (lower) and total BV over time (right).

according to Didier et al. (2020) methodology predicted overwash during the December storm, which was not observed during the field inspection. Finally, Holman (1986) and Atkinson et al. (2017) $R_{2\%}$ formulations estimate a TWL in the overwash regime, which is in agreement with field observations (**Figure 5**)

Similar prediction accuracy was registered for P5. The dune retreat observed at the start of the monitoring period denotes a collision regime, with a TWL higher than the DT. This was correctly predicted by Holman (1986) and Atkinson et al. (2017) $R_{2\%}$ formulations. Instead, the formula from Didier et al. (2020) still overestimated the $R_{2\%}$, while Stockdon et al. (2006) and Vousdoukas et al. (2012) formulations slightly underestimated collision.

Overall, evidence collected in the field and the comparison among different $R_{2\%}$ formulas for TWL computations (**Figures 4**, **5**) confirmed the good performance of Holman (1986) and Atkinson et al. (2017) when applied in the field, as already pointed out by works specifically dedicated to evaluate the general accuracy of different $R_{2\%}$ predictions (e.g., Gomes da Silva et al., 2020). Given this, we further considered Atkinson et al. (2017) to describe TWL over the whole beach long-shore extent.

Wave Impact on Dunes

Using data obtained by the ATV for the whole long-shore extent, **Figures 6A** shows the intertidal beach slope variation, along with DT and DC average elevations. The beach slope varied between 0.05 and 0.12. In October, the average slope was about 0.1, with the highest long-shore variation, and decreased almost regularly over the monitored period. At the end of winter season, the intertidal beach slope was spatially more homogeneous, with an average value of 0.06 changing from reflective to dissipative beach state. Averaged-over-time beach slope was lowest in the central part, coinciding with the mega-cusp embayment, and generally higher on the northern and southern sectors. The minimum values of beach slope were lowest on the northern sector and linearly increased till the southern highest value. The highest points collected by the ATV coincided with the DT elevation retrieved by profiling surveys. Iribarren number (Battjes, 1988) had a median value of 0.95, with an

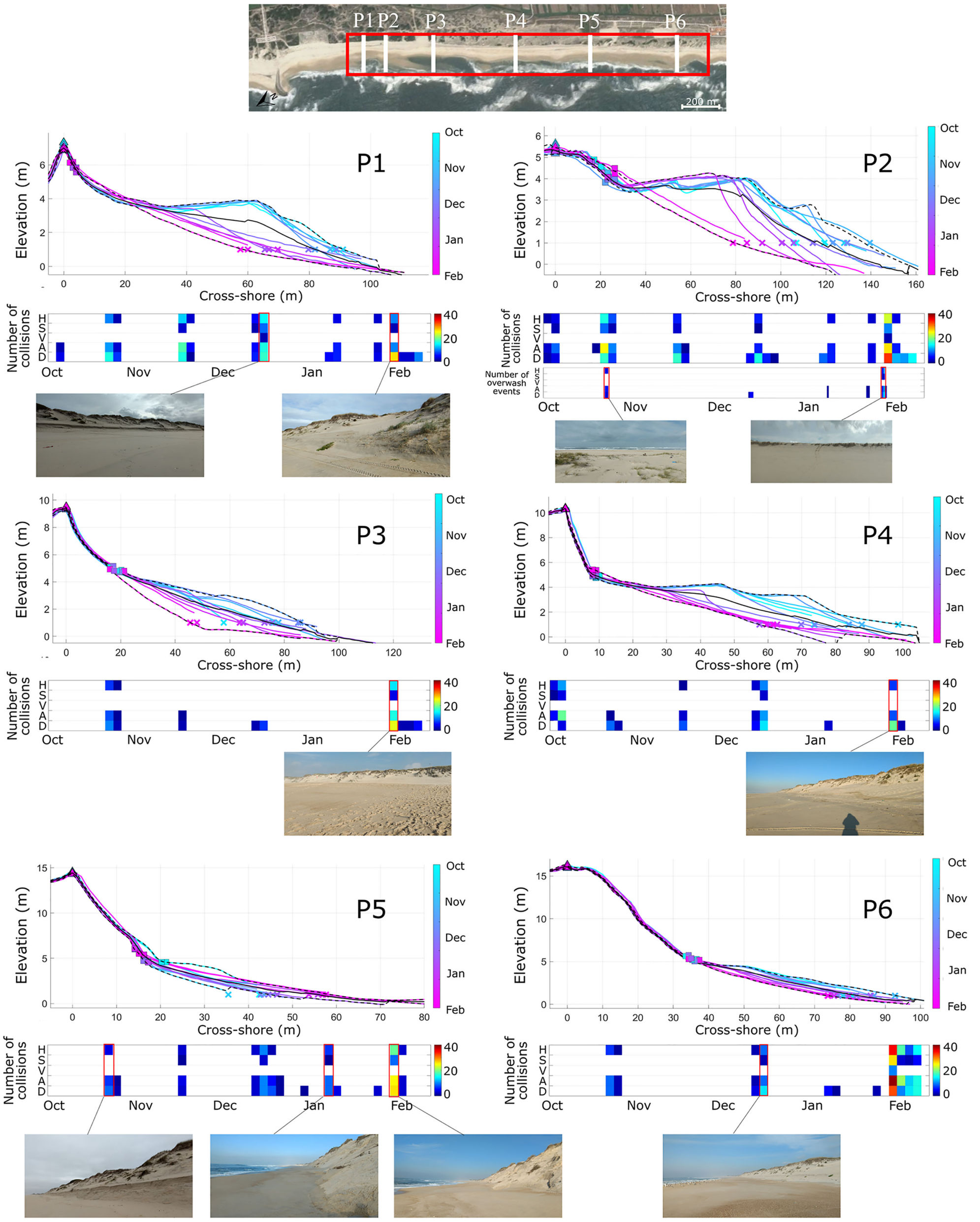

FIGURE 4 | Beach profiles changes and total water level (TWL) timeseries. Upper: beach transect location (white lines) within the study area (red rectangle). For each of the six profiles, colors refer to chronological order of surveys (see colorbar), while black line indicates the average profile. Squares and triangles indicate the dune toe (DT) and dune crest (DC), respectively, while crosses the shoreline (SL, 1 m). Below each profile plot, graph shows the number of DT collisions and overwash (registered only on P2) based on Sallenger (2000) method computed considering the five R2% formulas. Letters stand for the initials name of formulas, see **Table 1**).

interquartile between 0.2 and 2. However, it reached 3.5 during the most energetic events.

In **Figure 6B**, the TWL timeseries was coupled with the DT and DC elevations to characterize the wave impact regimes. Overall, waves collided the dune ridge for the whole long-shore extent, for a maximum period of 150 hours, corresponding to one and six days, respectively, over the monitored five months. Collision events were more numerous in the northern and southern sectors, corresponding to P2 and P5. In the central sector, where the mildest slope and lowest intertidal sector variation were observed over the winter, the dune was the less impacted.

As already observed in **Figure 4**, P2 was overwashed for a total period of 30 hours, and these events extend up to 250 m

FIGURE 5 | Observations on P2 and P5 dune-beach profiles of the maximum swash during the previous high tide. The limit between dry and wet sand shows the level reached by the total water level in this period (February 06, 2017).

south of P2, where the DC was lower than 7 m, and the highest volume change occurred (**Figure 3**).

Considering all collision and overwash events, **Figure 6** characterizes the TWL impacts normalized with the dune ridge (DC-DT) height, following Sallenger (2000). The mean values of SIS were lower than 0.2 for the whole long-shore extent, apart for the northern sector, where the ratio was higher than 0.3. The northern sector also registered the highest impact during the most energetic events, with overwash events (values >1) and dune collision up to 80% of the dune height. Between P3 and P4, the event of middle February also impacted the dune up to the 67%, however the impact was mitigated by dune vegetation. Overall, despite the high number of collision events in the southern sector, the normalize level of impact was lower than the 40%.

The mechanisms that controls the response of the dune and beach system at short and medium term (days, months) on high energetic coasts strongly depended on the collision and overwash events and morphological configuration.

DISCUSSION

Beach-Dune Morphodynamics

The high-frequency and high-resolution survey campaign was essential to monitor the short-term morphological variation of Mira beach. In particular, it was crucial updating beach slope changes for accurately describing total water level (TWL) excursion over space and time (**Figure 6**). On the one hand, the ATV provided a complete description of subaerial beach surfaces (**Figure 3**), whereas dGPS profiling only allowed to survey a limited number of transects with high long-shore offset. On the other hand, dGPS profiling allowed to describe wave collision and overwash on the dune compartment, along with corroborating the total water level (TWL) model (**Figure 4**). Winter 2016/17 was characterized by energetic waves and more significant events during 15th December with wave peak at Hs=4.5 m and 2nd February storm with wave heights above Hs=7.5 m, both with Tp more than 15 s. Wave directions occurred between 280-295°, concentrated on W to NNW directions. The morphological context of Mira as an open beach facing the Atlantic swell confers a uniformity on shoreline orientation. The sandy barrier extends in an NNE– SSW direction, with similar wave conditions in this coastal stretch from north to south. It was found that the northern sector of Mira beach was the most variable in terms of beach width (BW) and volume (BV), with the gradual beach berm formation and disappearing on the intertidal area (**Figure 3**). Although the BW was the longest here, the northern sector resulted in being the most vulnerable to wave impact and intrusion, with a high rate of dune collision (~150h), a considerable wave collision elevation relative to the dune height and, in some sectors overpassing the dune crest (DC). As previous works showed, no direct relationship between beach morphodynamics and dune erosion was found (Armaroli et al., 2013; Cohn et al., 2019). However, spatial variability in total water levels relative to antecedent beach and dune morphology can change wave collision % events and therefore exert a substantial control on dune evolution (e.g. Serafin et al., 2019). The largest variability and the major vulnerability of northern sector may be related to the presence of the groin at the northern limit of the beach (**Figure 1**). Groins influences the beach behaviour, causes downdrift erosion and generally affect the natural north-south littoral drift on the Portuguese coast (Rosa-Santos et al., 2009; Baptista et al., 2014).

The analysis showed that the DT was also impacted in the northern sector (between P1 and P3), where it was registered the highest variation of the upper beach profile (**Figures 3**, **4**), and the southern sector (P5, P6). However, the relative height of wave collision in the southern sector is lower than in the northern sector and small beach profile changes were observed. Where high dunes exist, the shoreline variation, and vertical elevation of beach-dune profiles remained more stable. In contrast, a clear sign of dune degradation was shown at northernmost (P1, P2). Given these, we emphasise that on a high-energy meso-tidal coast, the analysis of long-shore variation of shoreline, BW and BV, may not be sufficient to understand the complex interaction between hydrodynamic and morphology of a beach-dune system. We also showed that the local sea level elevation must be considered for an accurate evaluation of dune vulnerability since assuming the Hs exclusively as representative of storm impact may provide unsophisticated and incomplete analysis. As seen from TWL analysis, impacts on DT and overwash events occurred not only when the highest offshore wave height Hs was registered (8 m) but also during lower Hs (about 3 m) and spring tides (**Figure 6**).

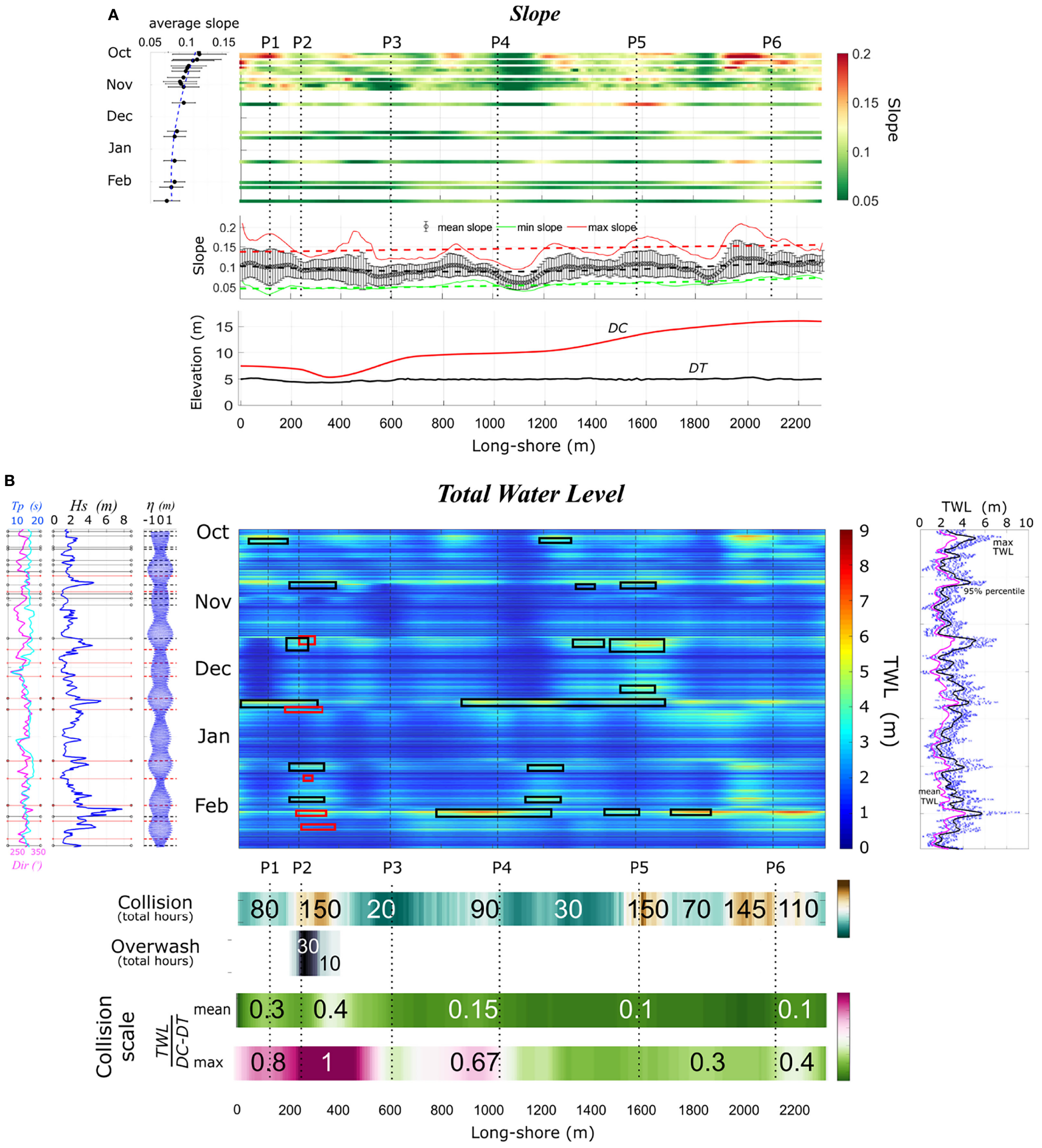

FIGURE 6 | Wave impact on dunes. **(A)** Beach slope change over time and space (central panel), average slope over time (left panel) and statistical values over the long-shore (minimum, maximum and average, middle panel). Lower graph shows the average dune toe (DT) and dune crest (DC) elevations; **(B)** total water level (TWL) timeseries over time and space (central panel). Black boxes indicate wave impact on DT, while red boxes overwash occurrence. Hydrodynamics (left panel), with peak period (Tp), significant wave height (Hs) and tide (η). Right panels show maximum values (blue crosses), 95% percentile (black line) and mean values (magenta line) of TWL. Lower panels show the total events of collisions and overwash (hour values), along with the average and maximum collision SIS of Sallenger (2000).

Total Water Level

Although the search for the most accurate $R_{2\%}$ prediction was beyond the scope of this study, the formula proposed by Atkinson et al. (2017) was chosen as the best representative for computing the TWL prediction at Mira beach (**Figure 6**). As this formula was built to fit a realistic range of conditions and different runup models (Atkinson et al., 2017), it has been proven to be best performing when compared with other formulas (e.g., Gomes da Silva et al., 2020), and already validated with field data on the Portuguese coast (Andriolo et al., 2020b; Gonçalves et al., 2020). Instead, we found that Stockdon et al. (2006) and Vousdoukas et al. (2012) underestimated the TWL, perhaps since they were parameterized considering gentler slope, milder Hs and lower wave steepness ranges (**Table 2**) than at our study site. Even though the Hs range for the parameterization of Holman (1986) and Atkinson et al. (2017) did not reach the Hs of 7 m registered during the monitored period at Mira beach, the estimation of $R_{2\%}$ was more accurate than Didier et al. (2020). The latest formula overestimated TWL at the open coast study site, likely due to the fact that it was parameterized considering sheltered beaches data, where the wave set up component plays a significant role in the total computation of $R_{2\%}$.

Beach-Dune Surveys

As already mentioned, the good assessment of TWL was prone to the beach slope update provided by the high-frequency monitoring program; therefore, the technique can be considered valuable also for future works. Nevertheless, field surveys required intense human effort and time spent in the field.

In recent years, remote sensing techniques, such as video monitoring (Holman and Stanley, 2007; Andriolo et al., 2019), unmanned aerial systems (Manfreda et al., 2018; Tmušić et al., 2020) and satellite images (McCarthy et al., 2017) have been shown to be suitable to support coastal studies (Splinter et al., 2018). However, remote sensing applications still have some limitations compared to conventional (high resolution) surveys. First, video monitoring technique may allow the estimation of beach profile slope with high frequency (Vousdoukas et al., 2011; Valentini et al., 2017; Andriolo et al., 2018), nearshore wave transformation (Andriolo, 2019), and wave breaking height (Andriolo et al., 2020c). Nevertheless, the quantitative use of video imagery is spatially constrained and dependent on the camera installation height, with an approximated ratio of 1/10 (10 m camera height allows to cover approximately 100 m with good spatial resolution). Second, satellite imagery has been used to retrieve the beach-dune morphology and beach slope (Almeida et al., 2019; Vos et al., 2020). Although satellites allow a comprehensive spatial coverage, the use of Pleiades images (Almeida et al., 2019) is still economically demanding. On the other hand, the accuracy of the beach slope estimation from freely-available Sentinel 2 (Vos et al., 2020) seems not be appropriate for the detailed wave runup modelling yet, as 10 x 10 m spatial resolution may be too low to retrieve the highly variable foreshore beach slope (**Figure 4**). Finally, the use of drones has been shown to be effective for a high-resolution survey of the subaerial beach (Trembanis et al., 2017; Duo et al., 2018; Pagán et al., 2019), coastal dunes (Laporte-Fauret et al., 2019; Taddia et al., 2020) and cliffs (Gómez-Gutiérrez and Gonçalves, 2020; Gonçalves et al., 2021) through the Structure-from-Motion technique. Drones also allow integrating different types of environmental observations to beach-dune topographical surveys, such as coastal cliffs (Gómez-Gutierrez and Gonçalves, 2020; Gonçalves et al., 2021), such as marine litter abundance (Andriolo et al., 2020a; Andriolo et al., 2020b; Gonçalves et al., 2020; Andriolo et al., 2021a; Andriolo et al., 2021b) and coastal dune vegetation census (Taddia et al., 2019; Laporte-Fauret et al., 2020). However, the SfM technique has been shown to be inadequate to retrieve the foreshore slope, as wet saturated sand can negatively affects the 3D reconstruction of the intertidal area (e.g., Brunier et al., 2016). Given the above-cited remote sensing techniques limitations, the use of conventional methods was optimal for the detailed description of beach slope variation all over the monitored 2300 m of Mira beach.

It is worth mentioning that the missing bathymetry data limited the morphodynamic analysis, since the nearshore bars location may also influence nearshore wave transformation on the barred coastal stretch of Mira beach (Rey and Bernardes, 2004), and be spatially related to wave impact on dunes (Cox et al., 2013; Castelle et al., 2015; Gomes da Silva et al., 2020). Conventional vessel-based bathymetric measurements are complex tasks to perform with the required frequency, in particular on high-energy coasts (Fontán et al., 2012). Therefore, the depth-inversion method from satellites (Pacheco et al., 2015; Bergsma et al., 2019a; Pereira et al., 2019), coastal video stations (Holman et al., 2013; Abessolo Ondoa et al., 2016; Simarro et al., 2019; Thuan et al., 2019; Santos D. et al., 2020) and unmanned aerial systems (e.g., Bergsma et al., 2019b; Hashimoto et al., 2021) imagery may be useful to retrieve nearshore bottom configuration in future works.

It must be highlighted that the study site is situated in a sensitive ecosystem adjacent to the Aveiro lagoon, with vast areas with farms and road axis. Therefore, it is mandatory to preserve the socio-economic activities. Local authorities and decision-makers must be well documented to make the best choices in a cost-benefit approach (Elko et al., 2016). The work results here provided valuable information to achieve this goal. In fact, following this work within a local adaptive project for dune management, Regional authorities (Polis Litoral Ria de Aveiro) restored the dune ridge of Mira beach, placing natural sand (260.000 m^3) prior the winter 2017-2018 (**Figure 7**) aiming to improve shoreline stability and reduction of the vulnerability to coastal overwash/flooding (Pinto et al., 2020).

Analysing the topographical data collected by the COSMO programme (https://cosmo.apambiente.pt) in summer 2018

TABLE 2 | Wave runup R2% formulas considered in this work, with the range of conditions tested in the field [from Gomes da Silva et al. (2020)].

	Ho	Tp	Beach slope	Iribarren ξ	Wave steepness Hs/Ls
Holman (1986)	*0.4 – 4 m*	*6 s– 16 s*	*0.07 – 0.2*	-	-
Stockdon et al. (2006)	*0.7 - 2.5 m*	-	*0.01 - 0.16*	-	*0.0008 – 0.03*
Vousdoukas et al. (2012)	*0.14 – 3.6 m*	*2.7 s – 16.5 s*	*0.04 – 0.15*	*0.3 – 2.9*	-
Atkinson et al. (2017) – ***M2***	***0 – 5 m***	***6 s- 15 s***	***0 – 0.2***	***-***	***0 – 0.14***
Didier et al. (2020) *(14)*	-	-	-	*0.3 – 2.5*	-
This work	***0.7 – 7.5 m***	***6 s– 18 s***	***0.02 – 0.21***	***0.10 - 4***	***0.002 – 0.05***

Bold highlights the values considered for setting the formula adopted in this works (Atkinson et al. 2017, M2), and parameters of the study site.

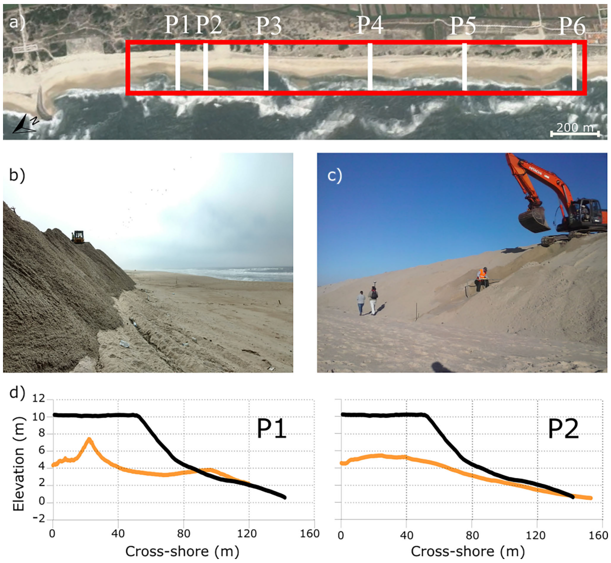

FIGURE 7 | Nourishment along Mira dune ridge. (A) Satellite image of the study area (red rectangle)and beach-dune profiles location (white lines); (B,C) pictures taken during dune nourishment operations at P1 and P2 (November 13, 2017); (D) beach-dune profiles prior (orange lines) and after (black lines) nourishment works.

(**Figure 7**), we verified that the intervention on the Mira dune ridge was efficient to decrease the beach-dune system vulnerability. On P1 and P2, the DC height was re-established at 11 m (**Figure 7**), an elevation sufficient to prevent overwash events and thus dune erosion. Further monitoring of the Mira beach-dune system evolution will be necessary to support future coastal management (Silva et al., 2020; Mendes et al., 2021; Pinto et al., 2022) and dune vulnerability maps to wave forecast and predicted sea level rise (e.g., Vousdoukas et al., 2012; Mickey et al., 2018; Cunha et al., 2021). Besides this, research works point towards a significant increase in overwash frequency and magnitude by 2055 and further aggravation by 2100, particularly at the central part of a barrier (Ferreira et al., 2021). Thus, nature-based (soft) solutions, such as dune-beach nourishment, is regarded as the most viable mitigation and adaptation action, which have been implemented with success along the Portugal coast during the last decades (Teixeira, 2016; Pinto et al., 2020; Pinto et al., 2022).

CONCLUSIONS

This work examined the wave impact on the 2300 m long-shore Mira beach-dune system on the Portuguese coast over the winter 2016-2017. A high-frequency field survey campaign collected beach topographic data, which were coupled to the description of total water level (TWL) dynamic. The analysis focused on evaluating the beach-dune vulnerability to the wave impact, identifying i) the locations where TWL reached the dune toe (DT) causing sand removal and ii) the locations where overwash of the dune crest (DC) occurred.

The northernmost long-shore 500 m extent was the most vulnerable to overwash events, and in general the most variable in terms of beach width (BW) and volume (BV), likely due to the influence of cross-shore coastal structure that limits the beach northward. Collision of DT was more significant in the northern and central part of the beach, where it was registered the most significant variation of the upper beach profile over the winter. Instead, DT collision was mildest in the southern sector, where beach profiles did not change significantly and dunes were the tallest and best preserved. The analysis underlined that the total water level excursion on the foreshore must be taken in account for an accurate evaluation of dune vulnerability, since impacts on DT and overwash occurred not only during storm events, but also during spring tides and mild wave conditions.

Results highlight the importance of uploading the intertidal beach slope when computing the total water levels on wave-dominated mesotidal sandy beaches. A consistent monitoring program of the hydrodynamic drivers (e.g., waves and wind) and morphological parameters (e.g., topo-bathymetry) which determine both the sediment transport and waves impact on foredune is vital for a better knowledge of the state of the coastal zone environment regarding erosion and accretion and management decision-making.

This work supported the coastal management of Mira beach-dune system, where regional authorities nourished and restored the northern dune ridge to prevent further overwash events and erosion. The presented framework can be applied to build a beach-dune system vulnerability map in response to forecasted and predicting sea level rise, upon a detailed development of a morphodynamic model for describing the beach slope variation.

DATA AVAILABILITY STATEMENT

The raw data supporting the conclusions of this article will be made available by the authors, without undue reservation.

ETHICS STATEMENT

Written informed consent was obtained from the individual(s) for the publication of any potentially identifiable images or data included in this article.

AUTHOR CONTRIBUTIONS

AF-B: Conceptualization, Methodology, Software, Formal Analysis, Investigation, Data curation, Validation, Writing-Original draft preparation, Writing – Review and Editing, Visualization, Funding acquisition. UA: Conceptualization, Methodology, Software, Formal Analysis, Investigation, Data curation, Validation, Writing- Original draft preparation, Writing – Review and Editing, Visualization. PS: Investigation, Data curation, Writing – Review and Editing, Funding acquisition. PB: Investigation, Data curation, Writing – Review & Editing, Funding acquisition. All authors contributed to the article and approved the submitted version.

FUNDING

AF-B is supported by a Post-Doc Fellowship (ED481D2019/028) awarded by Xunta de Galicia (Spain). We acknowledge financial support to GEOMA-XM2 ED431C2019/27 Xunta de Galicia grant and CESAM by FCT/MCTES (UIDP/50017/2020+UIDB/ 50017/ 2020+ LA/P/0094/2020), through national funds. UA was supported by the Portuguese Foundation for Science and Technology (FCT) and by the European Regional Development Fund (FEDER) through COMPETE 2020 - Operational Program for Competitiveness and Internationalization (POCI) in the framework of UIDB/00308/ 2020 and the research project UAS4Litter (PTDC/EAM-REM/30324/2017).

ACKNOWLEDGMENTS

The authors wish to gratefully thank Javier Alcántara-Carrió, Sandra Fernández-Fernández, Caroline Costa Ferreira, Laura López Olmedilla and Laura Teresa Nobre Tubarão for fruitful discussions and their fundamental help and support during fieldwork. We are also grateful to Rita Nolasco for the tide data computed for the Aveiro tidal gauge.

REFERENCES

Abessolo Ondoa G., Almar R., Kestenare E., Bahini A., Houngue G.-H., Jouanno J., et al. (2016). Potential of Video Cameras in Assessing Event and Seasonal Coastline Behaviour: Grand Popo, Benin (Gulf of Guinea). *J. Coast. Res.* 75, 442–446. doi: 10.2112/SI75-089.1

Alexandrakis G., Poulos S. E. (2014). An Holistic Approach to Beach Erosion Vulnerability Assessment. *Sci. Rep.* 4, 6078. doi: 10.1038/srep06078

Almeida L. P., Almar R., Bergsma E. W. J., Berthier E., Baptista P., Garel E., et al. (2019). Deriving High Spatial-Resolution Coastal Topography From Sub-Meter Satellite Stereo Imagery. *Remote Sens.* 11, 590. doi: 10.3390/rs11050590

Andriolo U. (2019). Nearshore Wave Transformation Domains From Video Imagery. *J. Mar. Sci. Eng.* 7, 186. doi: 10.3390/jmse7060186

Andriolo U., Almeida L. P., Almar R. (2018). Coupling Terrestrial LiDAR and Video Imagery to Perform 3D Intertidal Beach Topography. *Coast. Eng.* 140, 232–239. doi: 10.1016/j.coastaleng.2018.07.009

Andriolo U., Gonçalves G., Bessa F., Sobral P. (2020a). Mapping Marine Litter on Coastal Dunes With Unmanned Aerial Systems: A Showcase on the Atlantic Coast. *Sci. Total Environ.* 736. doi: 10.1016/j.scitotenv.2020.139632

Andriolo U., Gonçalves G., Rangel-Buitrago N., Paterni M., Bessa F., Gonçalves L. M. S., et al. (2021a). Drones for Litter Mapping: An Inter-Operator Concordance Test in Marking Beached Items on Aerial Images. *Mar. Pollut. Bull.* 169, 112542. doi: 10.1016/j.marpolbul.2021.112542

Andriolo U., Gonçalves G., Sobral P., Bessa F. (2021b). Spatial and Size Distribution of Macro-Litter on Coastal Dunes From Drone Images: A Case Study on the Atlantic Coast. *Mar. Pollut. Bull.* 169, 112490. doi: 10.1016/j.marpolbul.2021.112490

Andriolo U., Gonçalves G., Sobral P., Fontán-Bouzas Á., Bessa F. (2020b). Beach-Dune Morphodynamics and Marine Macro-Litter Abundance: An Integrated Approach With Unmanned Aerial System. *Sci. Total Environ.* 749, 141474. doi: 10.1016/j.scitotenv.2020.141474

Andriolo U., Mendes D., Taborda R. (2020c). Breaking Wave Height Estimation From Timex Images: Two Methods for Coastal Video Monitoring Systems. *Remote Sens.* 12, 204. doi: 10.3390/rs12020204

Andriolo U., Sánchez-García E., Taborda R. (2019). Operational Use of Surfcam Online Streaming Images for Coastal Morphodynamic Studies. *Remote Sens.* 11, 78. doi: 10.3390/rs11010078

Angnuureng D. B., Almar R., Senechal N., Castelle B., Addo K. A., Marieu V., et al. (2017). Shoreline Resilience to Individual Storms and Storm Clusters on a Meso-Macrotidal Barred Beach. *Geomorphology* 290, 265–276. doi: 10.1016/j.geomorph.2017.04.007

Antunes C., Taborda R. (2009). Sea Level at Cascais Tide Gauge: Data, Analysis and Results. *J. Coast. Res.* 2009, 218–222.

Armaroli C., Grottoli E., Harley M. D., Ciavola P. (2013). Beach Morphodynamics and Types of Foredune Erosion Generated by Storms Along the Emilia-Romagna Coastline, Italy. *Geomorphology* 199, 22–35. doi: 10.1016/j.geomorph.2013.04.034

Atkinson A. L., Power H. E., Moura T., Hammond T., Callaghan D. P., Baldock T. E. (2017). Assessment of Runup Predictions by Empirical Models on non-Truncated Beaches on the South-East Australian Coast. *Coast. Eng.* 119, 15–31. doi: 10.1016/j.coastaleng.2016.10.001

Baptista P., Coelho C., Pereira C., Bernardes C., Veloso-Gomes F. (2014). Beach Morphology and Shoreline Evolution: Monitoring and Modelling Medium-Term Responses (Portuguese NW Coast Study Site). *Coast. Eng.* 84, 23–37. doi: 10.1016/j.coastaleng.2013.11.002

Baptista P., Cunha T. R., Matias A., Gama C., Bernardes C., Ferreira Ó. (2011). New Land-Based Method for Surveying Sandy Shores and Extracting DEMs: The INSHORE System. *Environ. Monit. Assess.* 182, 243–257. doi: 10.1007/s10661-011-1873-5

Battjes J. A. (1988). Surf-Zone Dynamics. *Annu. Rev. Fluid Mech.* 20, 257–291. doi: 10.1146/annurev.fl.20.010188.001353

Beniston M., Stephenson D. B., Christensen O. B., Ferro C. A. T., Frei C., Goyette S., et al. (2007). Future Extreme Events in European Climate: An Exploration of Regional Climate Model Projections. *Clim. Change.* 81, 71–95. doi: 10.1007/s10584-006-9226-z

Bergsma E. W. J., Almar R., Maisongrande P. (2019a). Radon-Augmented Sentinel-2 Satellite Imagery to Derive Wave-Patterns and Regional Bathymetry. *Remote Sens.* 11 (16), 1918. doi: 10.3390/rs11161918

Bergsma E. W. J., Almar R., Melo de Almeida L. P., Sall M. (2019b). On the Operational Use of UAVs for Video-Derived Bathymetry. *Coast. Eng.* 152, 103527. doi: 10.1016/j.coastaleng.2019.103527

Blanco-Chao R., Cajade-Pascual D., Costa-Casais M. (2020). Rotation, Sedimentary Deficit and Erosion of a Trailing Spit Inside Ria of Arousa (NW Spain). *Sci. Total Environ.* 749, 141480. doi: 10.1016/j.scitotenv.2020.141480

Brunier G., Fleury J., Anthony E. J., Gardel A., Dussouillez P. (2016). Close-Range Airborne Structure-From-Motion Photogrammetry for High-Resolution Beach Morphometric Surveys: Examples From an Embayed Rotating Beach. *Geomorphology* 261, 76–88. doi: 10.1016/j.geomorph.2016.02.025

Castelle B., Harley M. (2020). Extreme Events: Impact and Recovery, in: Sandy Beach Morphodynamics. *Elsevier* pp, 533–556. doi: 10.1016/b978-0-08-102927-5.00022-9

Castelle B., Marieu V., Bujan S., Splinter K. D., Robinet A., Sénéchal N., et al. (2015). Impact of the Winter 2013-2014 Series of Severe Western Europe Storms on a Double-Barred Sandy Coast: Beach and Dune Erosion and Megacusp Embayments. *Geomorphology* 238, 135–148. doi: 10.1016/j.geomorph.2015.03.006

Ciavola P., Ferreira O., Van Dongeren A., Van Thiel de Vries J., Armaroli C., Harley M. (2014). Prediction of Storm Impacts on Beach and Dune Systems. *Hydrometeorol. Hazards Interfacing Sci. Policy* 9781118629, 227–252. doi: 10.1002/9781118629567.ch3d

Coelho C., Silva R., Veloso-gomes F., Taveira-pinto F. (2009). Potential Effects of Climate Change on Northwest Portuguese Coastal Zones. *ICES J. Marine Sci.* 66 (7), 1497–1507. doi: 10.1093/icesjms/fsp132

Cohn N., Ruggiero P., García-Medina G., Anderson D., Serafin K. A., Biel R. (2019). Environmental and Morphologic Controls on Wave-Induced Dune Response. *Geomorphology* 329, 108–128. doi: 10.1016/J.GEOMORPH.2018.12.023

Costa S., Coelho C. (2013). Northwest Coast of Portugal – Past Behavior and Future Coastal Defense Options. *J. Coast. Res.* 65, 921–926. doi: 10.2112/si65-156.1

Cox N., Dunkin L. M., Irish J. L. (2013). An Empirical Model for Infragravity Swash on Barred Beaches. *Coast. Eng.* 81, 44–50. doi: 10.1016/j.coastaleng.2013.06.008

Cunha J., Cardona F. S., Bio A., Ramos S. (2021). Importance of Protection Service Against Erosion and Storm Events Provided by Coastal Ecosystems Under Climate Change Scenarios. *Front. Mar. Sci.* 8. doi: 10.3389/fmars.2021.726145

Del Río L., Plomaritis T. A., Benavente J., Valladares M., Ribera P. (2012). Establishing Storm Thresholds for the Spanish Gulf of Cádiz Coast. *Geomorphology* 143–144, 13–23. doi: 10.1016/j.geomorph.2011.04.048

Diamantidou E., Santinelli G., Giardino A., Stronkhorst J., De Vries S. (2020). An Automatic Procedure for Dune Foot Position Detection: Application to the Dutch Coast. *J. Coast. Res.* 36, 668–675. doi: 10.2112/JCOASTRES-D-19-00056.1

Didier D., Caulet C., Bandet M., Bernatchez P., Dumont D., Augereau E., et al. (2020). Wave Runup Parameterization for Sandy, Gravel and Platform Beaches in a Fetch-Limited, Large Estuarine System. *Cont. Shelf Res.* 192, 104024. doi: 10.1016/J.CSR.2019.104024

Dissanayake P., Brown J., Wisse P., Karunarathna H. (2015). Effects of Storm Clustering on Beach/Dune Evolution. *Mar. Geol.* 370, 63–75. doi: 10.1016/j.margeo.2015.10.010

Dodet G., Bertin X., Taborda R. (2010). Wave Climate Variability in the North-East Atlantic Ocean Over the Last Six Decades. *Ocean Model.* 31, 120–131. doi: 10.1016/j.ocemod.2009.10.010

Duo E., Chris Trembanis A., Dohner S., Grottoli E., Ciavola P. (2018). Local-Scale Post-Event Assessments With GPS and UAV-Based Quick-Response Surveys: A Pilot Case From the Emilia-Romagna (Italy) Coast. *Nat. Hazards Earth Syst. Sci.* 18, 2969–2989. doi: 10.5194/nhess-18-2969-2018

Durán R., Guillén J., Ruiz A., Jiménez J. A., Sagristà E. (2016). Morphological Changes, Beach Inundation and Overwash Caused by an Extreme Storm on a Low-Lying Embayed Beach Bounded by a Dune System (NW Mediterranean). *Geomorphology* 274, 129–142. doi: 10.1016/j.geomorph.2016.09.012

Eichentopf S., Alsina J. M., Christou M., Kuriyama Y. (2020). Storm Sequencing and Beach Profile Variability at Hasaki , Japan. *Mar. Geol.* 424, 106153. doi: 10.1016/j.margeo.2020.106153

Elko N., Brodie K., Stockdon H., Nordstrom K., Houser C., McKenna K., et al. (2016). Dune Management Challenges on Developed Coasts. *Shore Beach* 84, 15.

Fernández-Fernández S., Ferreira C. C., Silva P. A., Baptista P., Romão S., Fontán-Bouzas Á., et al. (2019). Assessment of Dredging Scenarios for a Tidal Inlet in a High-Energy Coast. *J. Mar. Sci. Eng.* 7 (11), 395. doi: 10.3390/jmse7110395

Ferreira Ó., Kupfer S., Costas S. (2021). Implications of Sea-Level Rise for Overwash Enhancement at South Portugal. *Nat. Hazards*. 109, 2221–2239. doi: 10.1007/s11069-021-04917-0

Flor-Blanco G., Alcántara-Carrió J., Jackson D. W. T., Flor G., Flores-Soriano C. (2021). Coastal Erosion in NW Spain: Recent Patterns Under Extreme Storm Wave Events. *Geomorphology* 387, 107767. doi: 10.1016/j.geomorph.2021.107767

Fontán A., Alcántara-Carrió J., Correa I. D. (2012). Combined Beach - Inner Shelf Erosion in Short and Medium Term (Maspalomas, Canary Islands). *Geol. Acta.* 10, 4111–426. doi: 10.1344/105.000001756

Fontán-Bouzas Á., Alcántara-Carrió J., Albarracín S., Baptista P., Silva P. A., Portz L., et al. (2019). Multiannual Shore Morphodynamics of a Cuspate Foreland: Maspalomas (Gran Canaria, Canary Islands). *J. Mar. Sci. Eng.* 7 (11), 416. doi: 10.3390/jmse7110416

Gomes da Silva P., Coco G., Garnier R., Klein A. H. F. (2020). On the Prediction of Runup, Setup and Swash on Beaches. *Earth-Science Rev.* 204, 103148. doi: 10.1016/j.earscirev.2020.103148

Gómez-Gutiérrez Á., Gonçalves G. R. (2020). Surveying Coastal Cliffs Using Two UAV Platforms (Multi-Rotor and Fixed- Wing) and Three Different Approaches for the Estimation of Volumetric Changes. *Int. J. Remote Sens.* 0, 1–33. doi: 10.1080/01431161.2020.1752950

Gonçalves G., Andriolo U., Pinto L., Bessa F. (2020). Mapping Marine Litter Using UAS on a Beach-Dune System: A Multidisciplinary Approach. *Sci. Total Environ.* 706, 135742. doi: 10.1016/j.scitotenv.2019.135742

Gonçalves G., Gonçalves D., Gómez-gutiérrez Á., Andriolo U., Pérez-alvárez J. A. (2021). 3d Reconstruction of Coastal Cliffs From Fixed-Wing and Multi-Rotor Uas: Impact of Sfm-Mvs Processing Parameters, Image Redundancy and Acquisition Geometry. *Remote Sens.* 13 (6), 1222. doi: 10.3390/rs13061222

Harley M. D., Andriolo U., Armaroli C., Ciavola P. (2014). Shoreline Rotation and Response to Nourishment of a Gravel Embayed Beach Using a Low-Cost Video Monitoring Technique: San Michele-Sassi Neri, Central Italy. *J. Coast. Conserv.* 18, 551–565. doi: 10.1007/s11852-013-0292-x

Hashimoto K., Shimozono T., Matsuba Y., Okabe T. (2021). Unmanned Aerial Vehicle Depth Inversion to Monitor River-Mouth Bar Dynamics. *Remote Sens.* 13 (3), 412. doi: 10.3390/rs13030412

Hinkel J., Nicholls R. J., Tol R. S. J., Wang Z. B., Hamilton J. M., Boot G., et al. (2013). A Global Analysis of Erosion of Sandy Beaches and Sea-Level Rise: An Application of DIVA. *Glob. Planet. Change*. 111, 150–158. doi: 10.1016/j.gloplacha.2013.09.002

Holman R. A. (1986). Extreme Value Statistics for Wave Run-Up on a Natural Beach. *Coast. Eng.* 9 (6), 527–544. doi: 10.1016/0378-3839(86)90002-5

Holman R., Plant N., Holland T. (2013). CBathy: A Robust Algorithm for Estimating Nearshore Bathymetry. *J. Geophys. Res. Ocean.* 118, 2595–2609. doi: 10.1002/jgrc.20199

Holman R. A., Stanley J. (2007). The History and Technical Capabilities of Argus. *Coast. Eng.* 54, 477–491. doi: 10.1016/j.coastaleng.2007.01.003

Houser C., Ellis J. (2013). *Beach and Dune Interaction, in: Treatise on Geomorphology*. (San Diego: Elsevier Inc.), 267–288. doi: 10.1016/B978-0-12-374739-6.00283-9

Jackson D. W. T., Costas S., Guisado-Pintado E. (2019). Large-Scale Transgressive Coastal Dune Behaviour in Europe During the Little Ice Age. *Glob. Planet. Change* 175, 82–91. doi: 10.1016/j.gloplacha.2019.02.003

Karunarathna H., Pender D., Ranasinghe R., Short A. D., Reeve D. E. (2014). The Effects of Storm Clustering on Beach Profile Variability. *Mar. Geol.* 348, 103–112. doi: 10.1016/j.margeo.2013.12.007

Laporte-Fauret Q., Lubac B., Castelle B., Michalet R., Marieu V., Bombrun L., et al. (2020). Classification of Atlantic Coastal Sand Dune Vegetation Using in Situ, UAV, and Airborne Hyperspectral Data. *Remote Sens.* 12 (14), 2222. doi: 10.3390/rs12142222

Laporte-Fauret Q., Marieu V., Castelle B., Michalet R., Bujan S., Rosebery D. (2019). Low-Cost UAV for High-Resolution and Large-Scale Coastal Dune Change Monitoring Using Photogrammetry. *J. Mar. Sci. Eng.* 7 (3), 63. doi: 10.3390/jmse7030063

Ludka B. C., Guza R. T., O'Reilly W. C., Yates M. L. (2015). Field Evidence of Beach Profile Evolution Toward Equilibrium. *J. Geophys. Res. Ocean.* 120 (11), 7574–7597. doi: 10.1002/2015JC010893

Luijendijk A., Hagenaars G., Ranasinghe R., Baart F., Donchyts G., Aarninkhof S. (2018). The State of the World's Beaches. *Sci. Rep.* 8, 1–11. doi: 10.1038/s41598-018-24630-6

Manfreda S., Mccabe M. F., Miller P., Lucas R., Pajuelo V. M., Mallinis G., et al. (2018). Use of Unmanned Aerial Systems for Environmental Monitoring. *Remote Sens.* 10 (4), 641. doi: 10.3390/rs10040641

Marinho B., Coelho C., Hanson H., Tussupova K. (2019). Coastal Management in Portugal: Practices for Reflection and Learning. *Ocean Coast. Manage.* 181, 104874. doi: 10.1016/j.ocecoaman.2019.104874

Marinho B., Coelho C., Larson M., Hanson H. (2018). Short- and Long-Term Responses of Nourishments: Barra-Vagueira Coastal Stretch, Portugal. J. *Coast. Conserv.* 22, 475–489. doi: 10.1007/s11852-017-0533-5

Martínez M. L., Intralawan A., Vázquez G., Pérez-Maqueo O., Sutton P., Landgrave R. (2007). The Coasts of Our World: Ecological, Economic and Social Importance. *Ecol. Econ*. 63 (2–3), 254–272. doi: 10.1016/j.ecolecon.2006.10.022

Martínez M. L., Psuty N. P., Lubke R. A. (2008). A Perspective on Coastal Dunes. *Ecolog. Studies* 171. doi: 10.1007/978-3-540-74002-5_1

Masselink G. (2021). Sandy Beach Morphodynamics. *J. Coast. Res.* 37 (2), 456–457. doi: 10.2112/jcoastres-d-20a-00008.1

Masselink G., Van Heteren S. (2014). Response of Wave-Dominated and Mixed-Energy Barriers to Storms. *Mar. Geol.* 352, 321–347. doi: 10.1016/j.margeo.2013.11.004

Matias A., Ferreira Ó., Vila-Concejo A., Morris B., Dias J. A. (2010). Short-Term Morphodynamics of non-Storm Overwash. *Mar. Geol.* 274, 69–84. doi: 10.1016/j.margeo.2010.03.006

Matias A., Rita Carrasco A., Loureiro C., Masselink G., Andriolo U., McCall R., et al. (2019). Field Measurements and Hydrodynamic Modelling to Evaluate the Importance of Factors Controlling Overwash. *Coast. Eng.* 152, 103523. doi: 10.1016/j.coastaleng.2019.103523

McCarthy M. J., Colna K. E., El-Mezayen M. M., Laureano-Rosario A. E., Méndez-Lázaro P., Otis D. B., et al. (2017). Satellite Remote Sensing for Coastal Management: A Review of Successful Applications. *Environ. Manage.* 60 (2), 323–339. doi: 10.1007/s00267-017-0880-x

Mendes D., Pais-Barbosa J., Baptista P., Silva P. A., Bernardes C., Pinto C. (2021). Beach Response to a Shoreface Nourishment (Aveiro, Portugal). *J. Mar. Sci. Eng.* 9, 1112. doi: 10.3390/jmse9101112

Mentaschi L., Vousdoukas M. I., Pekel J. F., Voukouvalas E., Feyen L. (2018). Global Long-Term Observations of Coastal Erosion and Accretion. *Sci. Rep.* 8, 12876. doi: 10.1038/s41598-018-30904-w

Mickey R., Long J., Dalyander P. S., Plant N., Thompson D. (2018). A Framework for Modeling Scenario-Based Barrier Island Storm Impacts. *Coast. Eng.* 138, 98–112. doi: 10.1016/J.COASTALENG.2018.04.012

Oliveira T. C. A., Neves M. G., Fidalgo R., Esteves R. (2018). Variability of Wave Parameters and Hmax/Hs Relationship Under Storm Conditions Offshore the Portuguese Continental Coast. *Ocean Eng.* 153, 10–22. doi: 10.1016/j.oceaneng.2018.01.080

Pacheco A., Horta J., Loureiro C., Ferreira (2015). Retrieval of Nearshore Bathymetry From Landsat 8 Images: A Tool for Coastal Monitoring in Shallow Waters. *Remote Sens. Environ.* 159, 102–116. doi: 10.1016/j.rse.2014.12.004

Pagán J. I., Bañón L., López I., Bañón C., Aragonés L. (2019). Monitoring the Dune-Beach System of Guardamar Del Segura (Spain) Using UAV, SfM and GIS Techniques. *Sci. Total Environ.* 687, 1034–1045. doi: 10.1016/j.scitotenv.2019.06.186

Pereira P., Baptista P., Cunha T., Silva P. A., Romão S., Lafon V. (2019). Estimation of the Nearshore Bathymetry From High Temporal Resolution Sentinel-1a C-Band SAR Data - A Case Study. *Remote Sens. Environ.* 223 (15), 166–178. doi: 10.1016/j.rse.2019.01.003

Pereira C., Coelho C. (2013). Mapping Erosion Risk Under Different Scenarios of Climate Change for Aveiro Coast, Portugal. *Nat. Hazards* 69, 1033–1050. doi: 10.1007/s11069-013-0748-1

Phillips M. S., Blenkinsopp C. E., Splinter K. D., Harley M. D., Turner I. L., Cox R. J. (2017). "High-Frequency Observations of Berm Recovery Using a Continuous Scanning Lidar," in *Australas. Coasts Ports 2017 Conf.* (Cairns, Australia: Australasian Coasts and Ports Conference).

Pilar P., Soares C. G., Carretero J. C. (2008). 44-Year Wave Hindcast for the North East Atlantic European Coast. *Coast. Eng.* 55 (11), 861–871. doi: 10.1016/j.coastaleng.2008.02.027

Pinto C. A., Silveira T. M., Teixeira S. B. (2020). Beach Nourishment Practice in Mainland Portugal, (1950–2017): Overview and Retrospective. *Ocean Coast. Manage.* 192, 105211. doi: 10.1016/j.ocecoaman.2020.105211

Pinto C. A., Taborda R., Andrade C., Baptista P., Silva P. A. (2022). Morphological Development and Behaviour of a Shoreface Nourishment in the Portuguese Western Coast. *J. Mar. Sci. Eng.* 10 (2), 146. doi: 10.3390/jmse10020146

Ponte Lira C., Silva A. N., Taborda R., De Andrade C. F. (2016). Coastline Evolution of Portuguese Low-Lying Sandy Coast in the Last 50 Years: An Integrated Approach. *Earth Syst. Sci. Data* 8, 265–278. doi: 10.5194/essd-8-265-2016

Ranasinghe R. (2016). Assessing Climate Change Impacts on Open Sandy Coasts: A Review. *Earth-Science Rev.* 160, 320–332. doi: 10.1016/j.earscirev.2016.07.011

Rey S., Bernardes C. (2004). Short-Term Morphodynamics of Intertidal Bars The Case of Areão Beach (Aveiro, Northwest Portugal). *J. Coast. Res.* 2006, 588–593.

Rocha C., Antunes C., Catita C. (2020). Coastal Vulnerability Assessment Due to Sea Level Rise: The Case Study of the Atlantic Coast of Mainland Portugal. *Water (Switzerland)* 12, 1–24. doi: 10.3390/w12020360

Rosa-Santos P., Veloso-Gomes F., Taveira-Pinto F., Silva R., Pais-Barbosa P. (2009). Evolution of Coastal Works in Portugal and Their Interference With Local Morphodynamics. *J. Coast. Res.* 2009, 757–761.

Sallenger J. (2000). Storm Impact Scale for Barrier Islands. *J. Coast. Res.* 16, 890–895.

Santos D., Abreu T., Silva P. A., Baptista P. (2020). Estimation of Coastal Bathymetry Using Wavelets. *J. Mar. Sci. Eng.* 8, 1–16. doi: 10.3390/jmse8100772

Santos C. J., Andriolo U., Ferreira J. C. (2020). Shoreline Response to a Sandy Nourishment in a Wave-Dominated Coast Using Video Monitoring. *Water (Switzerland)* 12, 1–15. doi: 10.3390/W12061632

Sekovski I., Del Río L., Armaroli C. (2020). Development of a Coastal Vulnerability Index Using Analytical Hierarchy Process and Application to Ravenna Province (Italy). *Ocean Coast. Manage.* 183, 104982. doi: 10.1016/j.ocecoaman.2019.104982

Serafin K. A., Cohn N., Anderson D., García-Medina G., Ruggiero P., Biel R. (2019). Environmental and Morphologic Controls on Wave-Induced Dune Response. *Geomorphology* 329, 108–128. doi: 10.1016/j.geomorph.2018.12.023

Silva R., Baptista P., Veloso-Gomes F., Coelho C., Taveira-Pinto F. (2009). Sediment Grain Size Variation on a Coastal Stretch Facing the North Atlantic (NW Portugal). *J. Coast. Res. I*, 762–766.

Silva R., Martínez M. L., van Tussenbroek B. I., Guzmán-rodríguez L. O., Mendoza E., López-portillo J. (2020). A Framework to Manage Coastal Squeeze. *Sustain.* 12, 1–21. doi: 10.3390/su122410610

Simarro G., Calvete D., Luque P., Orfila A., Ribas F. (2019). UBathy: A New Approach for Bathymetric Inversion From Video Imagery. *Remote Sens.* 11 (23), 2722. doi: 10.3390/rs11232722

Splinter K. D., Harley M. D., Turner I. L. (2018). Remote Sensing is Changing Our View of the Coast: Insights From 40 Years of Monitoring at Narrabeen-Collaroy, Australias. *Remote Sens.* 10 (11), 1744. doi: 10.3390/rs10111744

Splinter K. D., Turner I. L., Davidson M. A., Barnard P., Castelle B., Oltman-shay J. (2014). Journal of Geophysical Research: Earth Surface A Generalized Equilibrium Model for Predicting Daily to Interannual Shoreline Response. *J. Geophys. Res. Earth Surf.*, 1936–1958. doi: 10.1002/2014JF003106.Received

Stockdon H. F., Holman R. A., Howd P. A., Sallenger A. H. (2006). Empirical Parameterization of Setup, Swash, and Runup. *Coast. Eng.* 53, 573–588. doi: 10.1016/j.coastaleng.2005.12.005

Stronkhorst J., Huisman B., Giardino A., Santinelli G., Santos F. D. (2018). Sand Nourishment Strategies to Mitigate Coastal Erosion and Sea Level Rise at the Coasts of Holland (The Netherlands) and Aveiro (Portugal) in the 21st Century. *Ocean Coast. Manage.* 156, 266–276. doi: 10.1016/j.ocecoaman.2017.11.017

Taddia Y., Corbau C., Zambello E., Pellegrinelli A. (2019). UAVs for Structure-From-Motion Coastal Monitoring: A Case Study to Assess the Evolution of Embryo Dunes Over a Two-Year Time Frame in the Po River Delta, Italy. *Sensors (Switzerland)* 19 (7), 1717. doi: 10.3390/s19071717

Taddia Y., Stecchi F., Pellegrinelli A. (2020). Coastal Mapping Using DJI Phantom 4 RTK in Post-Processing Kinematic Mode. *Drones* 4, 9. doi: 10.3390/drones4020009

Teixeira S. B. (2016). A Alimentaçao Artificial Como Medida De Redução do Risco Em Praias Suportadas Por Arribas Rochosas Na Costa do Barlavento (Algarve, Portugal). *J. Integr. Coast Zone Manag/rev Gestão Costeira Integr.* 16 (3), 327–342.

Thuan D. H., Almar R., Marchesiello P., Viet N. T. (2019). Video Sensing of Nearshore Bathymetry Evolution With Error Estimate. *J. Mar. Sci. Eng.* 7, 233. doi: 10.3390/jmse7070233

Timmons E. A., Rodriguez A. B., Mattheus C. R., DeWitt R. (2010). Transition of a Regressive to a Transgressive Barrier Island Due to Back-Barrier Erosion, Increased Storminess, and Low Sediment Supply: Bogue Banks, North Carolina, USA. *Mar. Geol.* 278, 100–114. doi: 10.1016/j.margeo.2010.09.006

Tmušić G., Manfreda S., Aasen H., James M. R., Gonçalves G., Ben-Dor E., et al. (2020). Current Practices in UAS-Based Environmental Monitoring. *Remote Sens.* 12 (6), 1001. doi: 10.3390/rs12061001

Trembanis A., Duo E., Dohner S., Grottoli E., Ciavola P. (2017). Quick Response Assessment of the Impact of an Extreme Storm Combining Aerial Drone and RTK GPS. *Nat. Hazards Earth Syst. Sci. Discuss.*, 1–30. doi: 10.5194/nhess-2017-337

Turner I. L., Harley M. D., Short A. D., Simmons J. A., Bracs M. A., Phillips M. S., et al. (2016). A Multi-Decade Dataset of Monthly Beach Profile Surveys and Inshore Wave Forcing at Narrabeen, Australia. *Sci. Data* 3, 1–13. doi: 10.1038/sdata.2016.24

Valentini N., Saponieri A., Damiani L. (2017). A New Video Monitoring System in Support of Coastal Zone Management at Apulia Region, Italy. *Ocean Coast. Manage.* 142, 122–135. doi: 10.1016/j.ocecoaman.2017.03.032

Vos K., Harley M. D., Splinter K. D., Walker A., Turner I. L. (2020). Beach Slopes From Satellite-Derived Shorelines. *Geophys. Res. Lett.* 47, e2020GL088365. doi: 10.1029/2020GL088365

Vousdoukas M. I., Ferreira P. M., Almeida L. P., Dodet G., Psaros F., Andriolo U., et al. (2011). Performance of Intertidal Topography Video Monitoring of a

Meso-Tidal Reflective Beach in South Portugal. *Ocean Dyn.* 61, 1521–1540. doi: 10.1007/s10236-011-0440-5

Vousdoukas M. I., Mentaschi L., Voukouvalas E., Verlaan M., Jevrejeva S., Jackson L. P., et al. (2018). Global Probabilistic Projections of Extreme Sea Levels Show Intensification of Coastal Flood Hazard. *Nat. Commun.* 9, 2360. doi: 10.1038/s41467-018-04692-w

Vousdoukas M. I., Ranasinghe R., Mentaschi L., Plomaritis T. A., Athanasiou P., Luijendijk A., et al. (2020). Sandy Coastlines Under Threat of Erosion. *Nat. Clim. Change* 10, 260–263. doi: 10.1038/s41558-020-0697-0

Vousdoukas M. I., Voukouvalas E., Annunziato A., Giardino A., Feyen L. (2016). Projections of Extreme Storm Surge Levels Along Europe. *Clim. Dyn.* 47, 3171–3190. doi: 10.1007/s00382-016-3019-5

Vousdoukas M. I., Wziatek D., Almeida L. P. (2012). Coastal Vulnerability Assessment Based on Video Wave Run-Up Observations at a Mesotidal, Steep-Sloped Beach. *Ocean Dyn.* 62, 123–137. doi: 10.1007/s10236-011-0480-x

Wernette P., Houser C., Bishop M. P. (2016). An Automated Approach for Extracting Barrier Island Morphology From Digital Elevation Models. *Geomorphology* 262, 1–7. doi: 10.1016/j.geomorph.2016.02.024

Wiggins M., Scott T., Masselink G., Russell P., McCarroll R. J. (2019). Coastal Embayment Rotation: Response to Extreme Events and Climate Control, Using Full Embayment Surveys. *Geomorphology* 327, 385–403. doi: 10.1016/J.GEOMORPH.2018.11.014

Conflict of Interest: The authors declare that the research was conducted in the absence of any commercial or financial relationships that could be construed as a potential conflict of interest.

frontiers | Frontiers in Marine Science

TYPE Original Research
PUBLISHED 02 August 2022
DOI 10.3389/fmars.2022.970592

EDITED BY
Effi Helmy Ariffin,
University of Malaysia Terengganu,
Malaysia

REVIEWED BY
Amila Ratnayake,
Uva Wellassa University, Sri Lanka
Umakanta Pradhan,
National Centre for Coastal Research,
India
Mohamad Hidayat Jamal,
Universiti Teknologi Malaysia, Malaysia

*CORRESPONDENCE
Cherdvong Saengsupavanich
cherdvong.saengsupavanich@hotmail.com;
cherdvong.sa@ku.th

SPECIALTY SECTION
This article was submitted to
Coastal Ocean Processes,
a section of the journal
Frontiers in Marine Science

RECEIVED 16 June 2022
ACCEPTED 11 July 2022
PUBLISHED 02 August 2022

CITATION
Saengsupavanich C, Yun LS, Lee LH and Sanitwong-Na-Ayutthaya S (2022) Intertidal intercepted sediment at jetties along the Gulf of Thailand. *Front. Mar. Sci.* 9:970592.
doi: 10.3389/fmars.2022.970592

Intertidal intercepted sediment at jetties along the Gulf of Thailand

Cherdvong Saengsupavanich[1]*, Lee Shin Yun[1], Lee Hin Lee[2] and Sarinya Sanitwong-Na-Ayutthaya[1]

[1]Faculty of International Maritime Studies, Kasetsart University, Chonburi, Thailand, [2]National Hydraulic Research Institute of Malaysia, Ministry of Environment and Water, Seri Kembangan, Selangor, Malaysia

Sand bypassing is one of the promising solutions to rectify jetty-induced coastal erosion. Estimating alongshore sediment transport rate and understanding hydrodynamic conditions at a jetty are crucial for successful downdrift erosion management. This research investigated three major jetties in Thailand (Cha Am jetty, Krai jetty, and Na Saton jetty) that protrude across the surf zone and completely intercept alongshore sediment transport. Sub-aerial and inter-tidal field surveys by Real Time Kinematic (RTK) technique were undertaken in 2019 and 2020. The collected data was processed and overlaid to calculate the amount of sediment deposition at the updrift jetty. Numerical simulations using MIKE21 SW and MIKE21 HD were carried out in order to understand how waves and water currents interacted with the jetties. From the results, we found that the Cha Am jetty trapped approximately 38,187 cu.m/yr of the alongshore sediment. While the Krai jetty intercepted approximately 34,170 cu.m/yr of the alongshore drift, and approximately 65,951 cu.m/yr of longshore sediment transport was blocked by the Na Saton jetty. Such estimated amounts of deposited sediment are the quantities that should be bypassed at each jetty. Budgets and implementation plans for sand bypassing can be prepared. Decision makers can decide how to manage updrift deposition and downdrift erosion.

KEYWORDS
coastal erosion, beach survey, sediment deposition, beach management, coastal engineering

Introduction

Coastal zone is dynamic (Ariffin et al., 2018). Wind, waves, tides, and currents are major forcings that influence sediment transport (King et al., 2019; Fan et al., 2019). When waves break, they create longshore current within surf zone (United States Army Corps of Engineers, 1984; Lim et al., 2018). The effect of tidal currents is added to wave-generated currents, mobilizing sediment. Sediment transport, in turn, affects coastal geomorphology

(Ariffin et al., 2019; Selamat et al., 2019; Saengsupavanich, 2020). Fan et al. (2019) found that swells induce intensified sediment resuspension and a flood-ebb symmetry of suspended sediment concentration. Net horizontal sediment fluxes are significantly increased in the presence of strong waves. Significant amounts of suspended sediments can be taken away from shoreline, implying the occurrence of coastal erosion. Sediment movement also varies seasonally, depending on incoming wave and water current characteristics, as well as monsoons (Amalan et al., 2018; Ratnayake et al., 2018; Ismail et al., 2020; Shetty and Jayappa, 2020; Zulfakar et al., 2021). Based on the theory of sediment budget (Kamphuis, 2010), coastal erosion can occur when the quantity of incoming sediment is less than the quantity of sediment leaving a certain coastal cell. Understanding and being able to estimate the net quantity of sediment transport is, therefore, one of the key requirements that lead to sustainable coastal management (Ariffin et al., 2020; Fortunato et al., 2021).

Many structures are constructed in coastal zones to protect the coast and to enhance the quality of living (Saengsupavanich, 2013; Oyegbile and Oyegbile, 2017; Saengsupavanich, 2017; Ariffin et al., 2020; Zulfakar et al., 2020). Jetties are one of the most encountered coastal structures. They help maintain safe navigation in and out of inlets. They also help fishermen, who are vulnerable to climate change (Muhammad et al., 2016), in terms of convenient catch transportations, while mitigating inland flooding. However, one of the critical environmental impacts of jetties is significant shoreline change. Ghashemizadeh and Tajziehchi (2013) and Rangel-Buitrago et al. (2015) showed that jetty construction influenced wave propagation, seabed evolution, and shoreline deposition as well as erosion. The sediment deposition associated with jetties is one of the key topics for sustainable coastal zone management. Previous studies have reported significant beach accretion on the updrift side in response to jetty constructions (Hapke et al., 2013; Garel et al., 2015; Wang et al., 2022). Salleh and Nadzir (2020) showed that flow velocity and current direction around a jetty significantly affected the deposition of coastal sediments. In the United States, Hein et al. (2019) presented that the northwards diffracted/refracted waves induced sediment accretion proximal to the south of the jetty and delivered the sediment across the jetty to an adjacent area. Silva et al. (2021) reported that the immediate updrift shoreline at the Tweed River, Australia, responded rapidly (from the first few months to two-three years) to the introduction of coastal management structures, while the extension of those impacts further updrift along the beach was gradual and took decades. In Europe, Žilinskas et al. (2020) showed that a sediment accretion occurred in a nearshore zone after completing a jetty. In Iran, Azarmsa et al. (2009) evidently showed the increased sedimentation, reduction in significant wave height, and flushing rate after a jetty construction at the Kiashahr lagoon. Anh et al. (2021) investigated the erosion-deposition process along a jetty in Vietnam and found that there was 56,442 m^3 of deposited sediment during the northeast monsoon, which was ten times higher than the amount occurring in the southwest monsoon.

While a jetty creates an updrift coastline deposition, the downdrift shoreline is eroded (Bruun, 1995; Saengsupavanich, 2019; Ariffin et al., 2020). Installing more coastal protection structures, such as revetments or breakwaters, along the downdrift eroded shoreline cannot solve such a problem, rather the erosion will be migrated further downdrift (Nassar et al., 2018; Ariffin et al., 2020; Zulkafar et al., 2020). One of the possible solutions to downdrift erosion is sand-bypassing (Garel et al., 2014; Garel et al., 2015; Nassar et al., 2018), which involves moving the sand deposited at the updrift side to the downdrift zone. In Palm Beach County Florida, South Lake Worth Inlet (Boynton Beach Inlet) is a man-made inlet cut in 1927; a sand transfer plant was installed in 1937 to solve the problematic accretion and erosion (Zurmuhlen, 1957; Witmer et al., 2018). Boswood and Murray (2001) listed 53 different bypassing stations from around the world, including Oceanside Harbor, USA, with a pumping rate of 75,000–190,000 m^3/year, and Channel Islands, USA, with an average pumping rate of 1,000,000 m^3/year. Another example is the fixed system at the Tweed River Entrance in Australia where pumps located within and offshore of the entrance channel achieved a maximum daily rate of over 12,000 m^3 (Dyson et al., 2002). The Indian River inlet, USA, constructed in 1940, experienced downdrift horizontal shoreline erosion between 10 and 60 m during the pre-bypassing period, but accreted 10–20 m during the bypassing period (Keshtpoor et al., 2013). The quantity of the sand being bypassed must be determined correctly, otherwise it will not solve the problem, and may create other issues. If the sediment is bypassed less than what it should be, downdrift erosion will still occur. On the other hand, if too much sediment is bypassed, the erosion will take place along the updrift shoreline instead. Overdredging may destabilize nearby coastal structures or induce slope instability and sliding because the counter-weight is taken away, as mentioned in many geotechnical engineering investigations (Murthy, 2003). Thus, accurately determining the quantity of sediment that needs to be bypassed is of utmost importance. Additionally, where to place the bypassed sediment on the downdrift shoreline must be clearly understood. For instance, when the bypassed sediment is blocked by any structure, it will be trapped, and less sediment will be supplied to another area (Ariffin et al., 2020).

Estimating deposited sediment at a jetty can be carried out by empirical calculation, numerical simulation, and field measurement. The empirical formula has been proposed by many researchers, such as Bayram et al. (2007) and Kamphuis (1991). Numerical simulation can be undertaken using many commercially available software packages such as MIKE21 or LITPACK (developed by Danish Hydraulics Institute) (Nassar et al., 2018; Rautenbach and Theron, 2018) or CMS (developed by US Army Corps of Engineers) (Wang and

Beck, 2012). Although the implementations of both empirical equations and numerical simulations are useful, coastal engineers are well aware that there are many unknown parameters, as well as a lot of related calibration procedures, in such calculations that can lead to inaccurate results. On the other hand, the field measurements have been applied. Bergillos et al. (2017) applied topographic measurements over 36 days to compare them with numerical models predicting cross-shore distribution of alongshore sediment transport. Each topographic survey was performed under low tide conditions and the observations were referenced to the mean low water spring level. Masselink et al. (2016) collected subaerial beach morphological data by using RTK-GPS and total station to estimate the beach volume above the mean sea level along the Atlantic coast of Europe. Their surveys were then used to estimate storm impacts on beaches. Nevertheless, there is no previous publication about quantifying sediment deposition at jetties in Thailand. This study is the first one of its kind to estimate intertidal intercepted sediment quantity at jetties in Thailand. To determine net longshore sediment transport and to identify the volume of sediment that should be bypassed at certain jetties in Thailand, this study applies field surveys to determine the net alongshore sediment transport. Numerical simulations are carried out to help understand wave and water current around the jetties. This research will greatly help Thai coastal managers and the Thai government to solve jetty-induced downdrift erosion by appropriately estimating the required amount of sediment that should be bypassed.

Study locations and methodology

Study areas

This research focused on net alongshore sediment transport at three major jetties in Thailand, being Cha Am jetty, Krai jetty, and Na Saton jetty (Figure 1; Table 1). All of them extend across the surf zone, completely intercepting alongshore sediment transport. Each jetty has created severe downdrift coastal erosion. A responsible governmental department attempted to mitigate the downdrift erosion by constructing detached breakwaters at both the Krai jetty and the Na Saton jetty, while private property owners at the Cha Am jetty built a revetment along the downdrift shoreline. Such approaches did not solve the problems, but postponed erosion further downdrift. Historical coastline change analysis showed that each jetty simultaneously created updrift deposition and downdrift erosion. At the Cha Am jetty (Figures 2A, B), the accretion rate at the updrift jetty was greater than 4 m/yr, while the downdrift erosion occurring at the endpoint of the seawalls constructed by the private property owners was more severe than 1.5 m/yr. At the Krai jetty, the updrift jetty intercepted the alongshore sediment, inducing coastline deposition at a rate greater than 4 m/yr. Although the Marine Department attempted to solve the downdrift erosion by installing fourteen detached breakwaters, erosion still occurred further downdrift at a rate greater than 2 m/yr (Figures 2C, D). Similarly, the Na Saton jetty created updrift deposition with a rate of roughly 4.5 m/yr (Figures 2E, F). However, downdrift erosion was small because the Marine Department had constructed a series of detached breakwaters along the 7-km downdrift shoreline (Saengsupavanich, 2012).

The jetties in this study are located along the east side of southern Thailand (Figure 1). They are exposed to seasonal storms during the northeast monsoon (November to February). Long-term tidal statistics near each jetty were collected from the Royal Thai Navy and the Marine Department (Table 2). To determine an appropriate time and scope for field surveys, information about wave climate at the jetties was indispensable. For each jetty, JONSWAP method (Kamphuis, 2010) was applied with data from the nearest wind station of the Thai Meteorological Department.

After calibrating the wave hindcasting calculation, the authors found that dominant waves at the Krai jetty were from the east. The annual calm period (having a significant wave height of less than 0.5 m or Beaufort scale level 3) was approximately 89% (Figure 3). Big waves with wave height greater than 4 m (Beaufort scale level 6) are from the east. When considering coastal alignment, it could be concluded that net alongshore sediment transport at this location was from the southeast to the northwest. Coastal deposition was expected to occur along the south side of the Krai jetty. Therefore, the field survey to determine the net alongshore sediment transport was carried out along the south side of the jetty. For the Na Saton jetty, the same approach was undertaken, because the annual wave characteristics, as well as the shoreline alignments, of the Krai jetty and the Na Saton jetty are very similar. At the Cha Am jetty, JONSWAP calculation showed that dominant waves with height greater than 2 m (Beaufort scale level 5) were from the south-southeast (SSE). The annual calm period (having a significant wave height of less than 0.5 m or Beaufort scale level 3) was approximately 91.4% (Figure 3). Therefore, sediment accretion was expected to occur along the south side of the Cha Am jetty, thus, the location of the field survey.

Survey methods

Time for the surveys was determined from the monsoon period (November to February). Direction of alongshore sediment transport depends on season. The basic theory of pre- and post-storm beach morphology suggests that the coast is likely to be eroded during storms when big waves are present (in this study, the stormy months are between November to February). Some sediment deposited at the updrift jetty will be carried offshore and will again return to the beach berm during the calm period (March to October). In the meantime, the calm waves that obliquely approach the shoreline will carry new sediment to deposit more at the updrift jetty. Thus, the suitable time for the

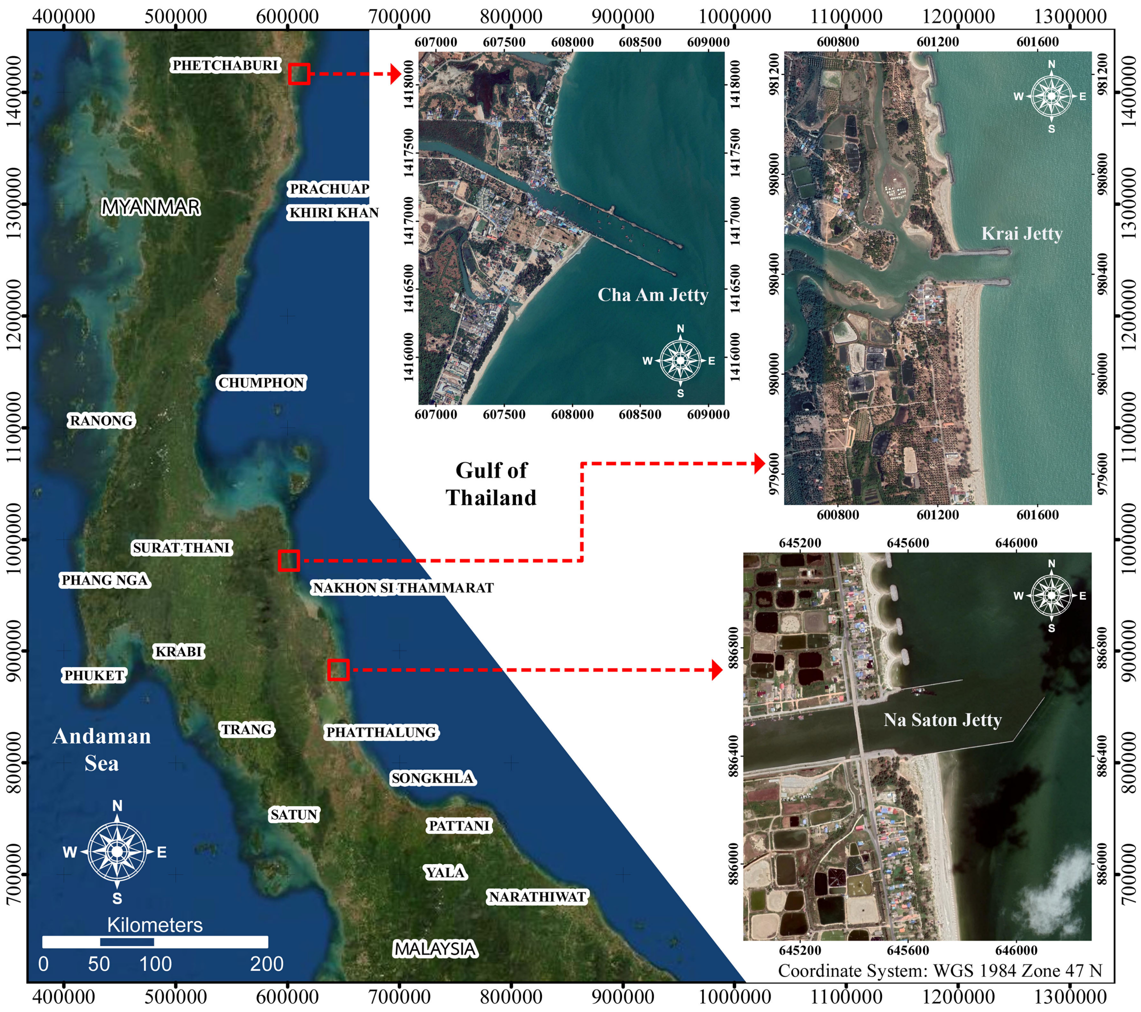

FIGURE 1
Jetties in this study.

survey along the south side of the jetties (Cha Am jetty, Krai jetty, and Na Saton jetty) was prior to the stormy season. The authors chose to conduct field surveys in August 2019, September 2019, August 2020, and September 2020.

The field investigations measured coastal elevation by Real Time Kinematic (RTK) technique. Benchmark descriptions can be found in Table 3. The coastal level along 2-km shoreline south from each jetty was surveyed, with each beach profile being

TABLE 1 General information about the jetties in this study.

Jetty name	Approximate length(m)	Easting (m)	Northing (m)	Year of construction	Shoreline configuration (°)	Jetty impacts
Cha Am jetty	1,000	608350	1417000	Prior to 1985	132.66	Coastal deposition has occurred along the south shoreline, while erosion has occurred along the north shoreline.
Krai jetty	250	602780	972450	Prior to 2013	89.58	Sediment transport is obstructed. The south shoreline has been deposited, while the north shoreline has been eroded.
Na Saton jetty	550	645800	886410	Prior to 2014	82.85	Erosion has taken place along the north shoreline of the jetty. Sediment has accumulated at the south jetty.

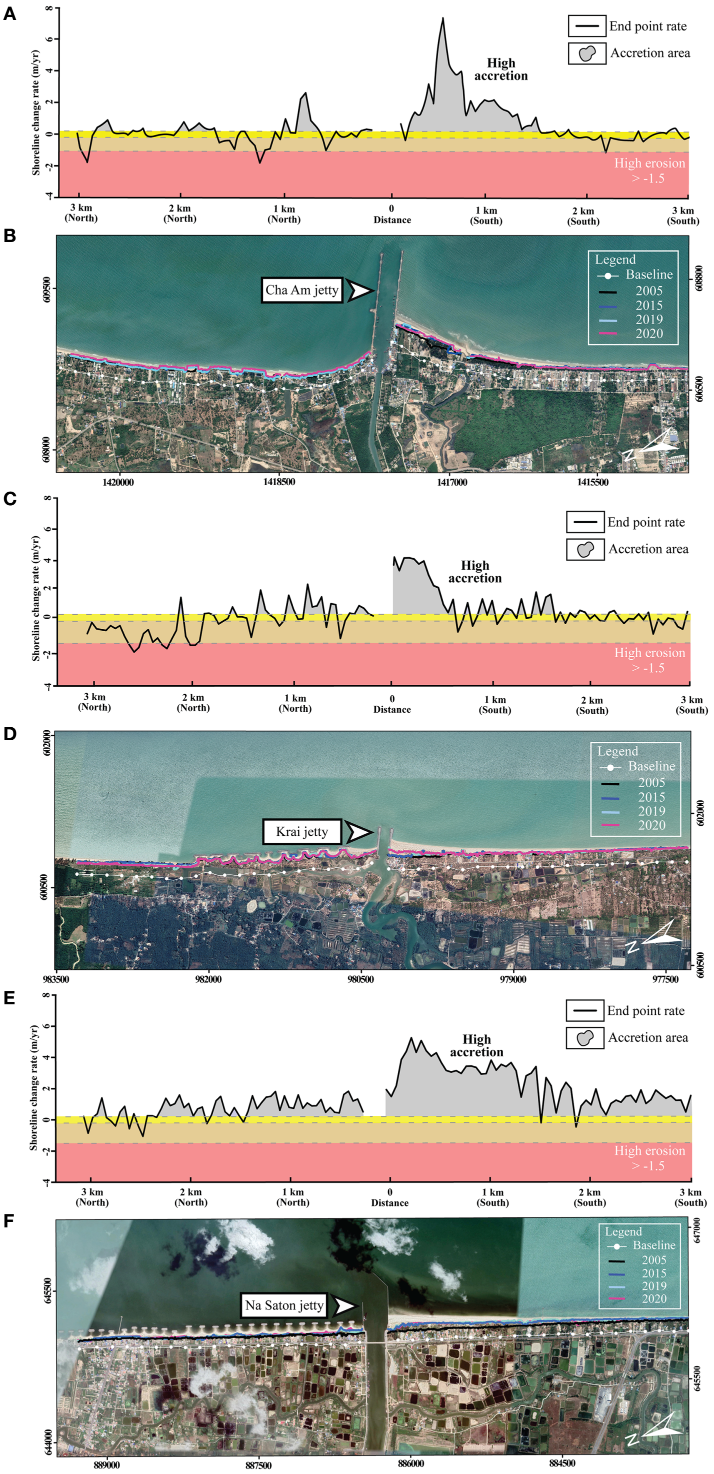

FIGURE 2
Updrift deposition and downdrift erosion at the jetties in this study. **(A)** Shoreline change rate at the Cha Am jetty, **(B)** historical coastline near the Cha Am jetty, **(C)** Shoreline change rate at the Krai jetty, **(D)** historical coastline near the Krai jetty, **(E)** Shoreline change rate at the Na Saton jetty, **(F)** historical coastline near the Na Saton jetty.

TABLE 2 Long-term tidal statistics at stations near each jetty.

	MHWS	MHWN	Local MSL	MLWN	MLWS
Cha Am jetty	+0.90	+0.70	+0.11	-0.54	-0.82
Krai jetty	+0.41	+0.31	-0.08	-0.40	-0.46
Na Saton jetty	+0.34	+0.280	-0.03	-0.30	-0.35

spaced 25 m apart. In order to cover the sub-aerial and intertidal zones, the uppermost point of each beach profile was set at a beach dune foot, while the lowermost point was set at an elevation of -0.5 m from national mean sea level (MSL). The number of the RTK survey points at each jetty can be found in Table 4. Although net alongshore sediment transport should be measured from the beach dune down to the closure depth, in order to achieve the perfect result, no echo-sounding was undertaken because of self-supported financial limitations. This study focuses on the sub-aerial and intertidal sediment deposition at the updrift jetties, not in the surf zone. Such deposition would be a potential source of the sediment that might be bypassed. This survey scope, which measures only the sub-aerial and the intertidal beach profiles, has been applied by many researchers to quantify sediment volume (Masselink et al., 2016; Bergillos et al., 2017).

Analysis of field data

After acquiring relevant field data, the authors created a bathymetric map of each survey by AutoCAD 3D software package, using a bilinear interpolation technique. The ArcGIS software package was then applied afterwards to overlay the maps of each month at each jetty (August 2019 versus August 2020, and September 2019 versus September 2020). The results revealed how much of the sediment was deposited along the surveyed coastal strips. Volumetric change of the sediment was then calculated from multiplying the difference in vertical beach elevation with the horizontal area. Since finer sediment may bypass the jetty tip, leaving coarser sediment trapped at the updrift jetty, the amount of the deposited sediment at the updrift jetty should be the amount of the required sediment to be manually bypassed.

Numerical modelling

The two-dimensional MIKE 21 Spectral Wave (SW) and Flexible Mesh Hydrodynamic Module (FM-HD) model packages, developed by the Danish Hydraulic Institute, were implemented to study the 2-dimension significant wave field and free-surface flow respectively. A flexible mesh was used to simulate the hydrodynamic model, as it was suitable for irregular boundaries and to determine

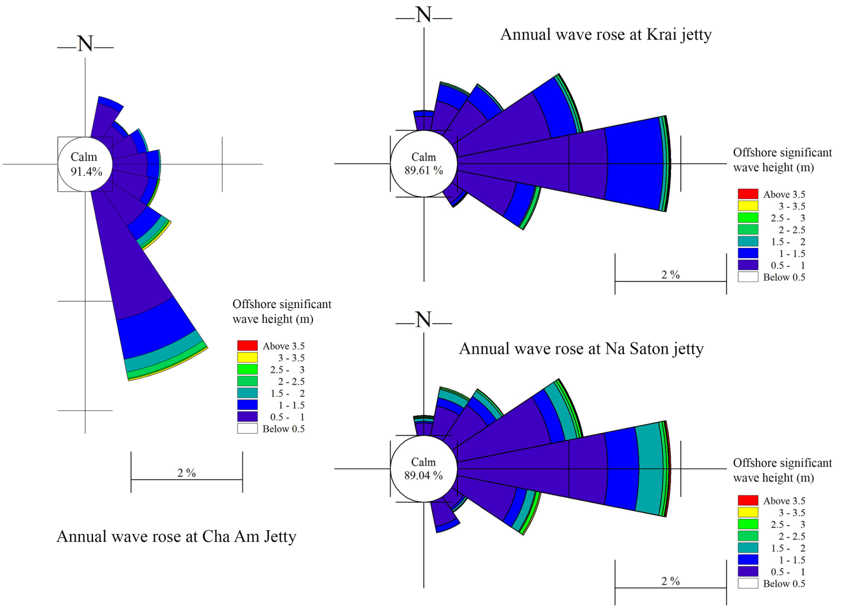

FIGURE 3
Annual wave rose at the jetties in this study.

TABLE 3 Benchmark descriptions at the jetties in this study.

	Cha Am jetty	Krai jetty	Na Saton jetty
Benchmark 1			
Easting (m)	608,115.212	601,475.487	645,676.890
Northing (m)	1,416,902.331	980,373.753	886,413.232
Elevation	+3.269	+3.862	+2.500
Benchmark 2			
Easting (m)	607,104.923	601,219.068	645,824.293
Northing (m)	1,415,434.736	980,349.384	884,860.520
Elevation	+3.408	+2.490	+2.762

the wave and current parameters in coastal areas. The model domain, covering the whole southern South China Sea and the Gulf of Thailand, had two open boundaries; the north boundary started from east of Vietnam to west of the Philippines, while the south boundary started from south of Johor to west of Kalimantan. General Bathymetric Chart of the Oceans (GEBCO) and MIKE C-Map were utilized for better water depth coverage in offshore and coastal waters. The data was processed by a pre-processing tool called Mesh Generator in MIKE ZERO to prepare the bathymetry. The unstructured mesh had a medium resolution of 3 km in the southern South China Sea region and a fine resolution of 1 km in Thailand's coastal waters, including the jetty locations.

The numerical simulations started from November 2018 to December 2019. They were spun up by the six-hourly wind and wave data retrieved from the Era-Interim European Centre for Medium-Range Weather Forecast (ECMWF), with a spatial resolution of 0.125° x 0.125°. Afterward, a model validation was performed by comparing the simulation outputs with field data measured by an Acoustic Doppler Current Profiler-Acoustic Wave and Currents (ADCP-AWAC) at the nearshore area in Terengganu, Malaysia (5°26'33.936" N, 103°9'37.548" E) for three months with every 10-min interval. The root-mean-square-error was found to be 0.17 for significant wave height and 0.13 for current speed, which were considered acceptable, referring to Ariffin et al. (2016) (0.28), Shariful et al. (2020) (0.18), and Zulfakar et al. (2021) (0.15).

Results

Intertidal intercepted sediment at Cha Am jetty

This research found that sediment accumulated at the updrift Cha Am jetty, as expected. Most deposition occurred on the beach berm. The increase of beach elevation was +0.80 to + 1.0 m in some areas, and the increase decreased further away from the jetty (Figure 4). On the other hand, the elevation in a further offshore area did not change much. Beach erosion was also found near a creek outlet, probably because of creek discharge. Multiplying the changes in the coastal elevation with the area and summing them up revealed a volumetric change of the intertidal intercepted sediment at the updrift jetty. It was found that the Cha Am jetty trapped approximately 38,187 cu.m/yr (Table 5).

The seasonal pattern of waves at the Cha Am jetty changes during the southwest (SW) and northeast (NE) monsoons (Figure 5). During the SW monsoon (May to October), predominant waves come from the southeast (SE) direction, transporting sediment northwards. They are not severe, having wave heights of less than 0.50 m (Figure 5A). However, the waves are stronger during February to April (the transitional period), also coming from the SE direction, carrying the sediment northwards. On the other hand, while the waves around the Cha Am jetty during the NE monsoon (November to January) are not aggressive, they come from the NE direction, moving the sediment southwards (Figure 5B). Since the Cha Am jetty is located near the bottom of the Gulf of Thailand, a NE fetch distance is not long enough to generate high waves. Therefore, at the Cha Am jetty, the waves during February to October move the sediment northwards, while the waves during November to January carry the sediment southwards. Moreover, alongshore water current is greatly affected by the Cha Am jetty (Figures 5C, D). The water current flows northwards during flood tides, and vice versa. Current speed is normally less than 0.3 m/s. The water current in the shallow zone near the jetty flows very slowly, while the current speed at the tips is much higher. The Cha Am jetty

TABLE 4 Number of survey points at the updrift jetties in this study.

Number of survey points	Cha Am jetty	Krai jetty	Na Saton jetty
August 2019 (points)	1,647	678	634
September 2019 (points)	1,386	886	1,142
August 2020 (points)	1,067	735	1,069
September 2020 (points)	1,203	858	1,049

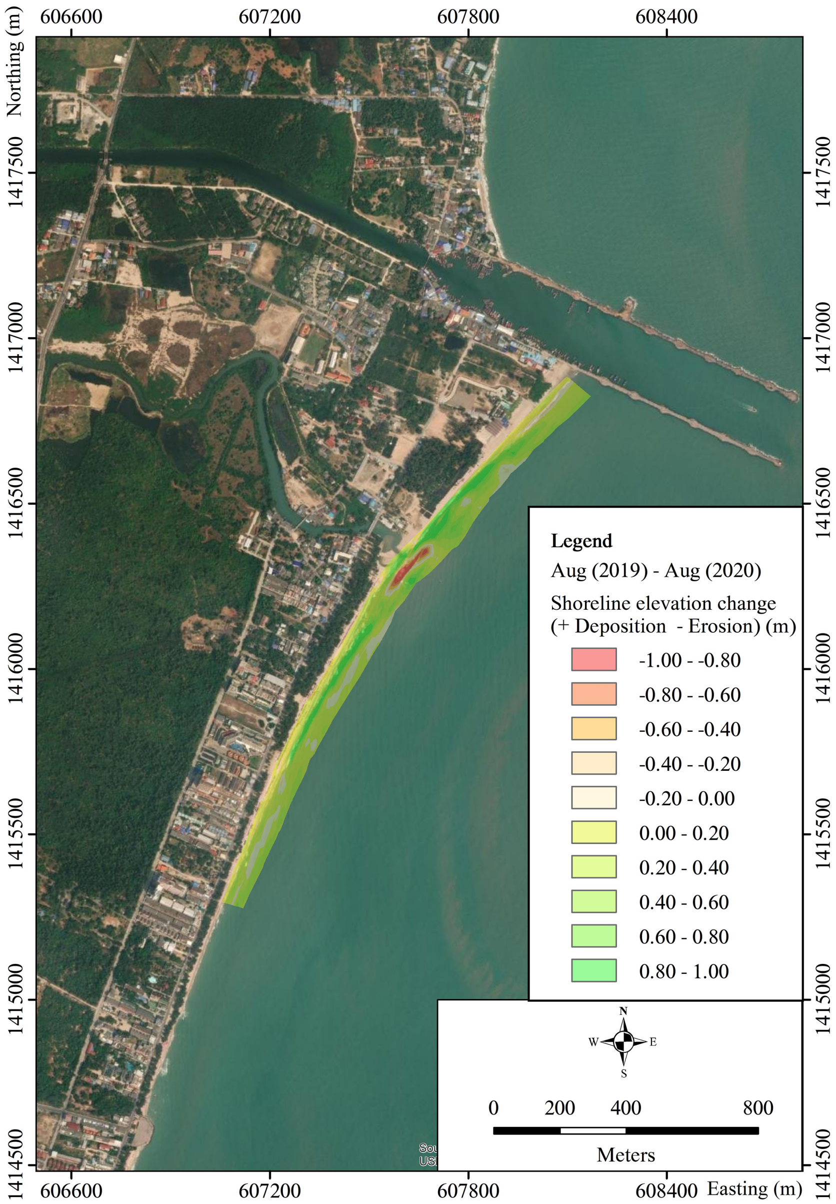

FIGURE 4
Differences in coastal elevation at the updrift Cha Am jetty (August 2019 versus August 2020).

clearly changes the waves and the water currents, thus resulting in alongshore sediment transport.

Intertidal intercepted sediment at Krai jetty

As anticipated, the updrift coastal strip at the Krai jetty experienced noticeable deposition. Most sediment accumulation took place within 1 km south from the jetty. Further down south, the coastal elevation did not exhibit much change (Figure 6). Multiplying the differences of the coastal elevation with the areas and adding them together showed a volumetric change of the intertidal deposited sediment at the updrift jetty. As a result, it was found that the Krai jetty intercepted approximately 34,170 cu.m/yr of the alongshore sediment (Table 5). Such an amount of the intertidal intercepted sediment was the quantity that should be bypassed to the downdrift shoreline.

Figure 7 reveals that the Krai jetty influences nearshore wave regime and water current pattern, resulting in the altered alongshore sediment transport. During the SW monsoon (May to October), waves at the Krai jetty are calm. They mainly come

TABLE 5 Volumetric changes at the updrift jetties in this study.

	Cha Am jetty	Krai jetty	Na Saton jetty
August 2019 versus August 2020 (Cu.m.)	45,211.8	33,236.3	75,463.3
September 2019 versus September 2020 (Cu.m.)	31,163.0	35,103.8	56,438.8
Average (Cu.m.)	38,187.4	34,170.1	65,951.1

from the SE direction, moving sediment northwards (Figure 7A). The Krai jetty is also under the influence of the NE monsoon (November to January), when large waves approach the shoreline from the NE (Figure 7B), transporting the sediment southwards. During the transitional period (February to April), the waves come from the east, but with a smaller wave height. Therefore, at the Krai jetty, the waves during February to October transport the sediment northwards. On the other hand, the waves during November to January carry the sediment southwards. Moreover, water current around the Krai jetty is greatly deviated (Figures 7C, D). The water current flows northwards during flood tide, and vice versa. Current speed varies with a normal maximum value of less than 0.3 m/s. The water current flows very slowly around the downdrift detached breakwaters, while the offshore current

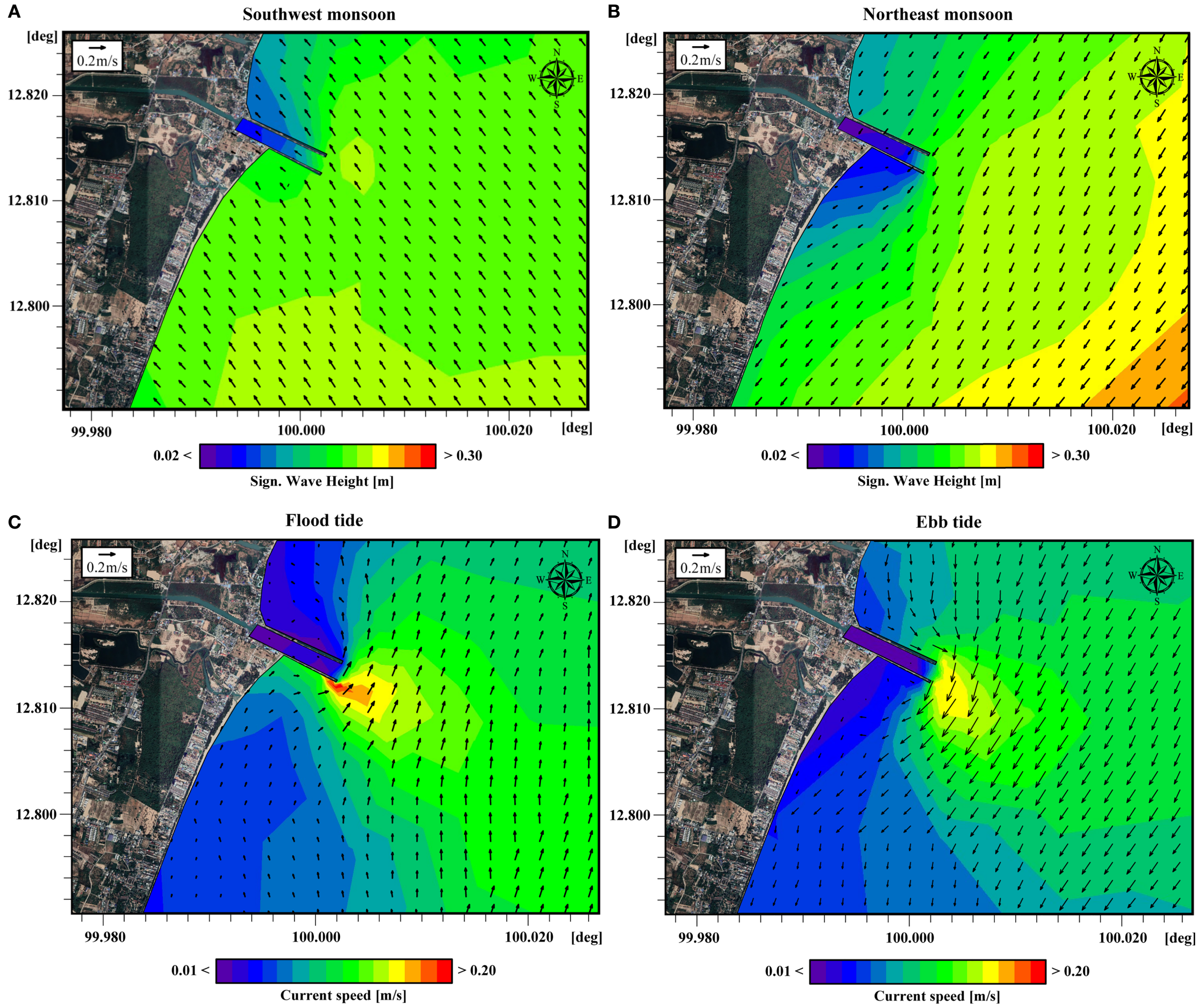

FIGURE 5
Results of MIKE 21 SW and HD at the Cha Am jetty **(A)** significant wave height and direction (arrows) during the southwest monsoon, **(B)** significant wave height and direction (arrows) during the northeast monsoon, **(C)** current speed and direction (arrows) during flood tide, **(D)** current speed and direction (arrows) during ebb tide.

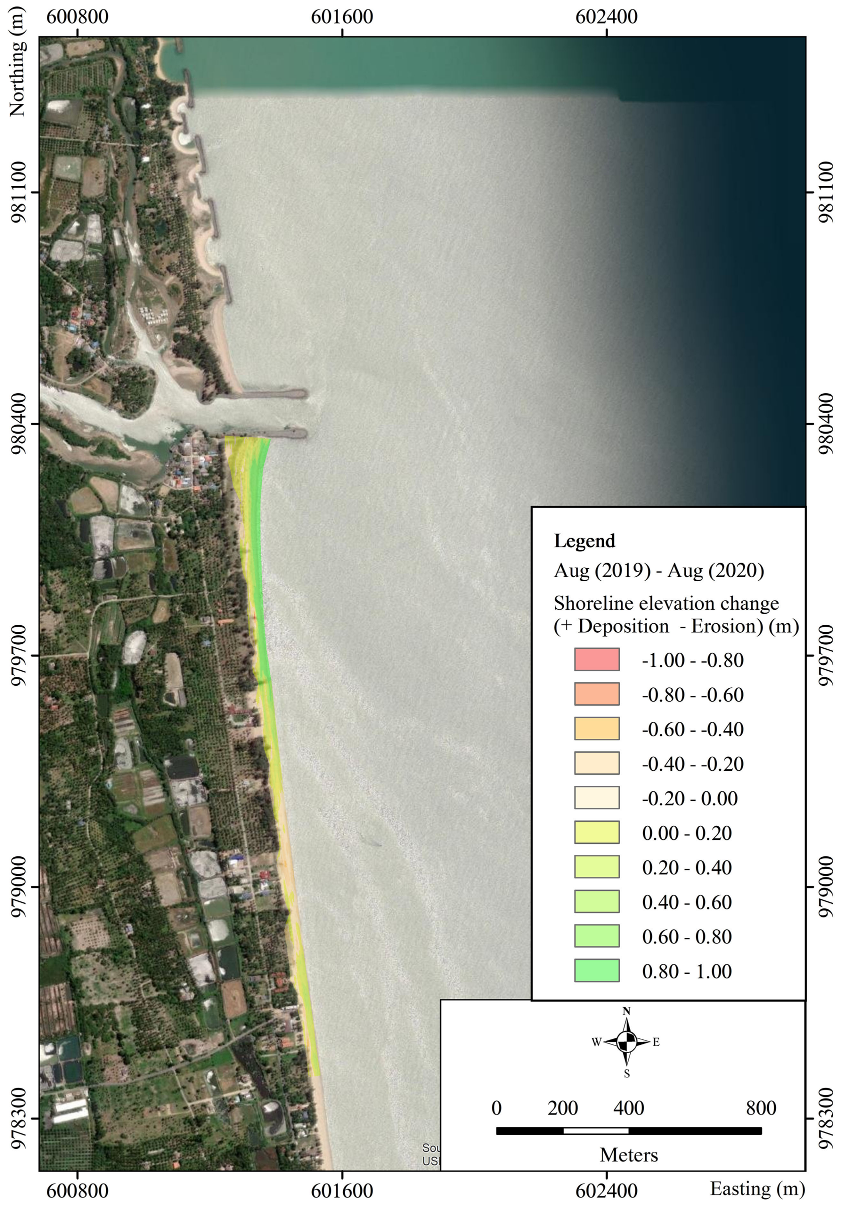

FIGURE 6
Differences in coastal elevation at the updrift Krai jetty (August 2019 versus August 2020).

speed is faster. The Krai jetty evidently has an impact on coastal hydrodynamics, resulting in altered alongshore sediment deposition.

Intertidal intercepted sediment at Na Saton jetty

The intertidal sediment accumulation rate at the Na Saton jetty was estimated by the same approach applied to the previous jetties. It was found that approximately 65,951 cu.m of longshore sediment transport was blocked by the Na Saton jetty annually (Table 5). The increase of beach elevation was +0.80 to + 1.0 m at some locations, and the accretion decreased further away from the jetty. The apparent deposition occurred within 1 km south from the updrift jetty (Figure 8). The alongshore sediment transport rate at the Na Saton jetty was larger than those of the other jetties in this study because the wave climate at the Na Saton jetty was more intense.

Wave and water current characteristics at the Na Saton jetty are somehow analogous to those of the Krai jetty because their coastline orientations are similar. During the SW monsoon (May

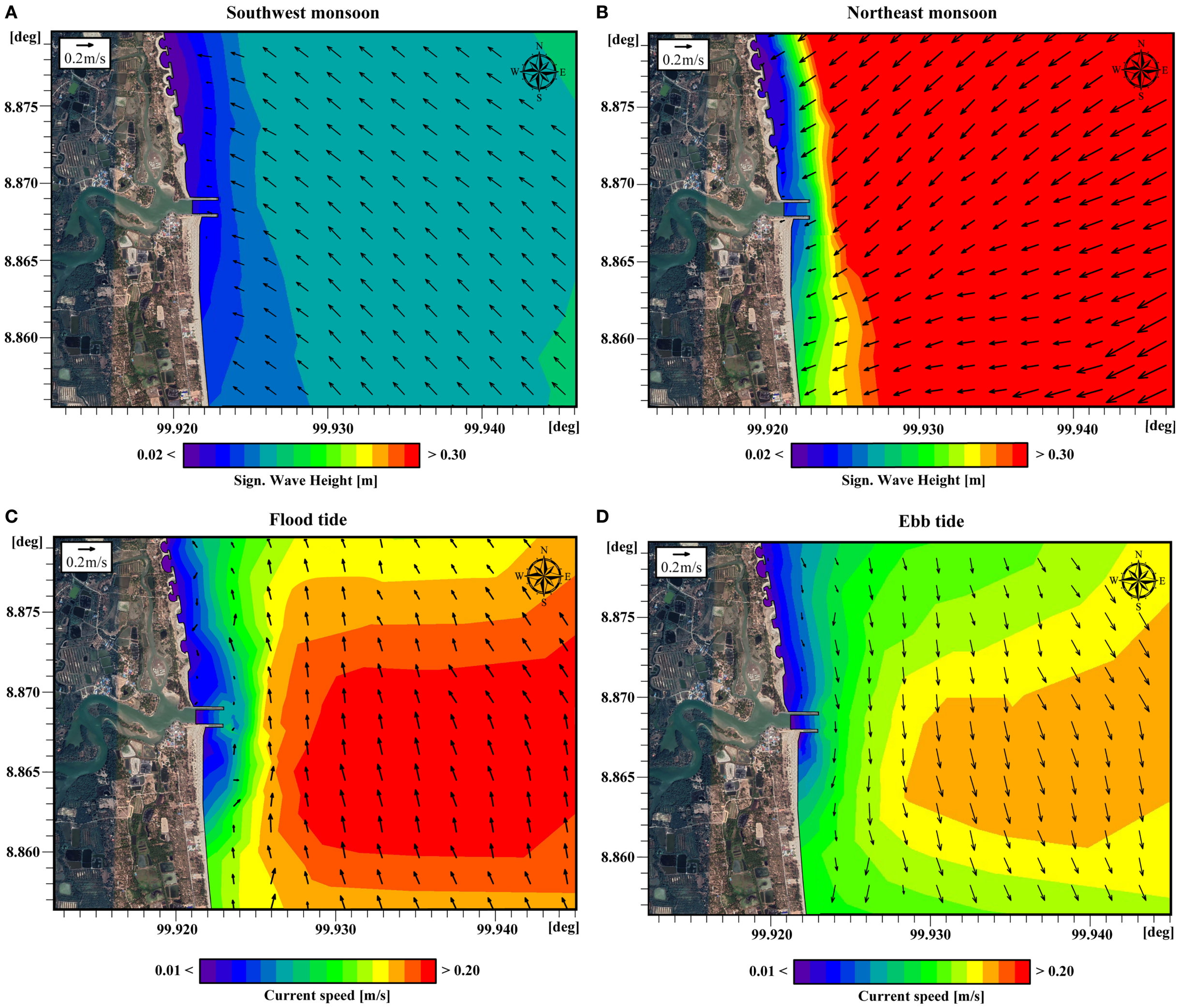

FIGURE 7
Results of MIKE 21 SW and HD at the Krai jetty **(A)** significant wave height and direction (arrows) during the southwest monsoon, **(B)** significant wave height and direction (arrows) during the northeast monsoon, **(C)** current speed and direction (arrows) during flood, **(D)** current speed and direction (arrows) during ebb tide.

to October), mild waves are predominantly from the SE direction, carrying the sediment northwards (Figure 9A). Big waves, happening during the NE monsoon (November to January), approaching the shoreline from the NE (Figure 9B), move the sediment southwards. During the transitional period (February to April), the waves come from the east, but with lesser magnitude. Therefore, at the Na Saton jetty, the waves during February to October bring the sediment northwards, while the waves during November to January carry the sediment southwards. Similar to other jetties in this study, the Na Saton jetty alters water current characteristics. The water current flows northwards during flood tide (Figure 9C), and vice versa (Figure 9D). The maximum current speed is less than 0.3 m/s. The nearshore water current direction is deviated by the jetty's tip. The Na Saton jetty clearly changes coastal hydrodynamics, inducing a change in sediment transport.

Discussion

Beach morphology and sediment volumetric change exhibit a seasonal variation (Yaacob et al., 2018). Alongshore sediment transport rate varies from location to location, depending on wave climate (wave height, wave period, and wave direction), sediment characteristics, and coastline alignment (Gunasinghe et al., 2021; Weerasingha and Ratnayake, 2022). Estimating the alongshore sediment transport quantity allows coastal managers to mitigate negative externalities generated by coastal structures

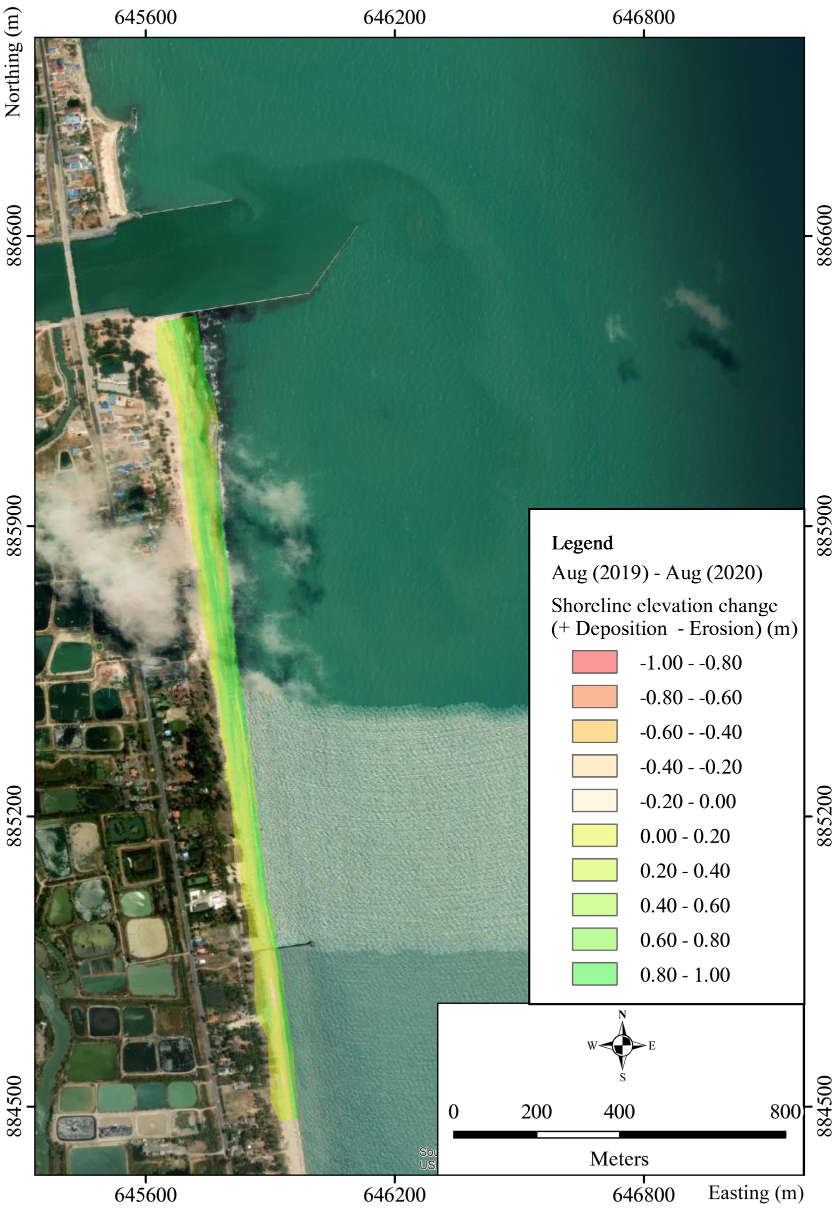

FIGURE 8
Differences in coastal elevation at the updrift Na Saton Jetty (August 2019 versus August 2020).

that obstruct longshore sediment movement. Influences of wave propagation and water current pattern should be understood since they can create different shoreline adjustments between coastal structures (Adamo et al., 2014; Ratnayake et al., 2019).

Jetties are one of the most encountered coastal structures. They help maintain safe navigation in and out of inlets. However, one of the critical environmental impacts of jetties is significant shoreline change. An updrift coastline will be deposited, while the downdrift shoreline will be eroded. Numerical simulations at three jetties in this study indicated that the net sediment transport moves northwards while the longshore water current flows northwards and southwards along the shore, depending on flood or ebb tides. The beach sediment is transported and accumulated on the jetty's updrift side as the jetty blocks the sediment movement. The jetty breaks the sediment budget equilibrium. Figure 10 illustrates how a jetty, waves, currents, and a beach interact. Swash and backwash promote sediment accretion at the updrift jetty. In this study, waves during February to October transport the sediment northwards (Figure 10A), while the waves during November to January carry the sediment southwards (Figure 10B). While wave direction changes seasonally, the water current direction changes daily. If the wave and the tidal current are in the same direction, a greater

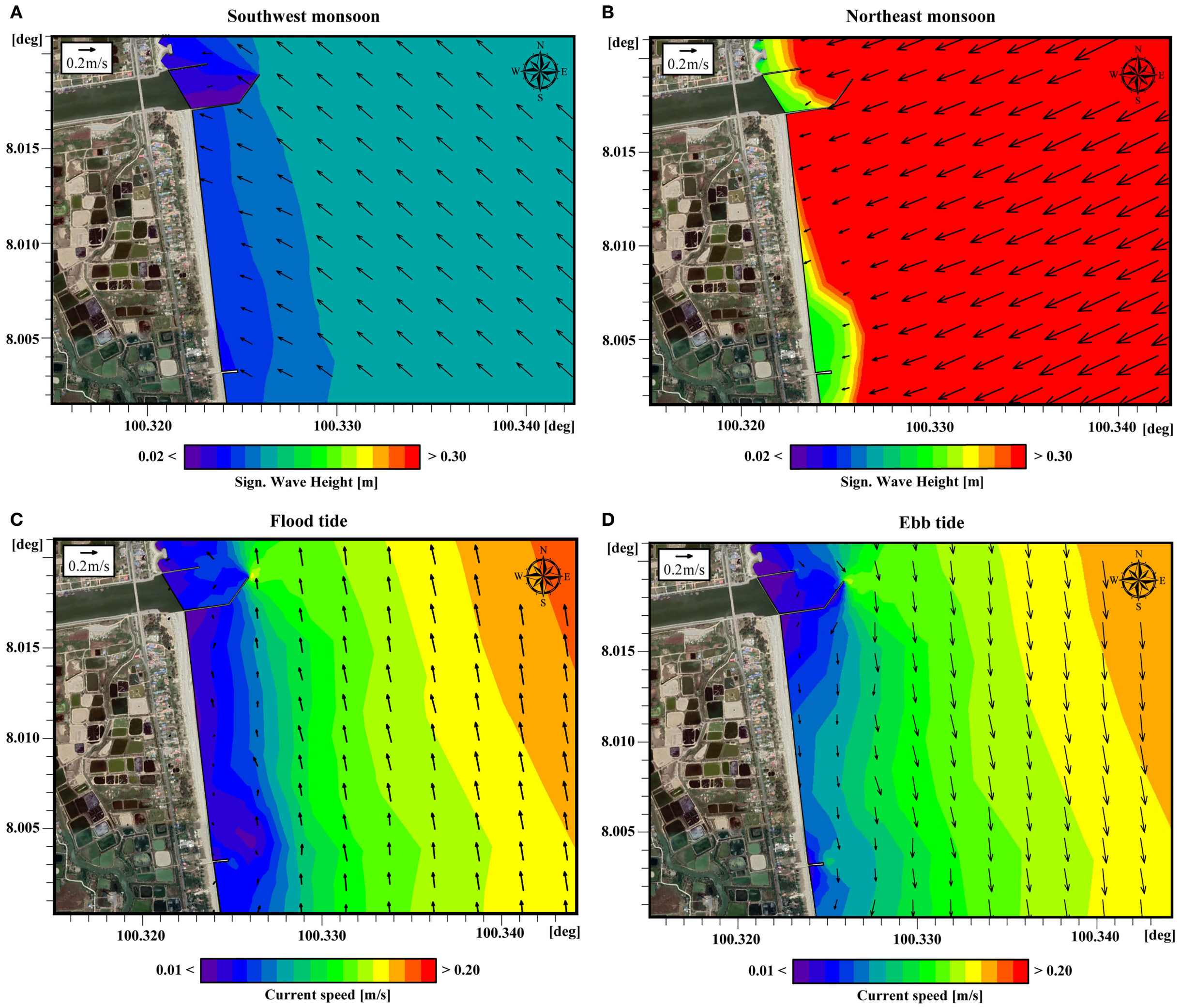

FIGURE 9
Results of MIKE 21 SW and HD at Na Saton jetty **(A)** significant wave height and direction (arrows) during the southwest monsoon, **(B)** significant wave height and direction (arrows) during the northeast monsoon, **(C)** current speed and direction (arrows) during flood tide, **(D)** current speed and direction (arrows) during ebb tide.

amount of the sediment will be transported. The same interaction was found by Ismail et al. (2020) and Shariful et al. (2020). Ariffin et al. (2020), who undertook a study in Malaysia, where the coastline is influenced by northeast monsoon like the jetties in this study, found that most of the deposition of sediment occurred near coastal protection structures.

Bypassing the sediment deposited at the updrift jetty can be one of the good solutions to solve downdrift coastal erosion (Garel et al., 2014, 2015; Franklin et al., 2021). Downdrift erosion can extend 8 to 10 times the length of the protrusion of a coastal structure (Kudale, 2010). However, how much of the sediment should be bypassed must be correctly estimated because it affects budget planning. This study is the first one in Thailand that estimates the sub-aerial and intertidal sediment deposition at jetties. Although there have been a few publications that have dealt with coastal erosion and protection in Thailand, none of them has elicited the amount of sediment that was intercepted by those coastal structures. This research found that the sub-aerial and intertidal sediment deposition at the Cha Am jetty was approximately 38,187 cu.m/yr, the rate at the Krai jetty was approximately 34,170 cu.m/yr, and 65,951 cu.m/yr at the Na Saton jetty. Nevertheless, the sediment transport rate estimated by this study might be less than the actual quantity, because the surveys were not expanded to cover the closure depth. The authors realized that there was a fraction of the alongshore sediment transport within the surf zone. Such sediment was

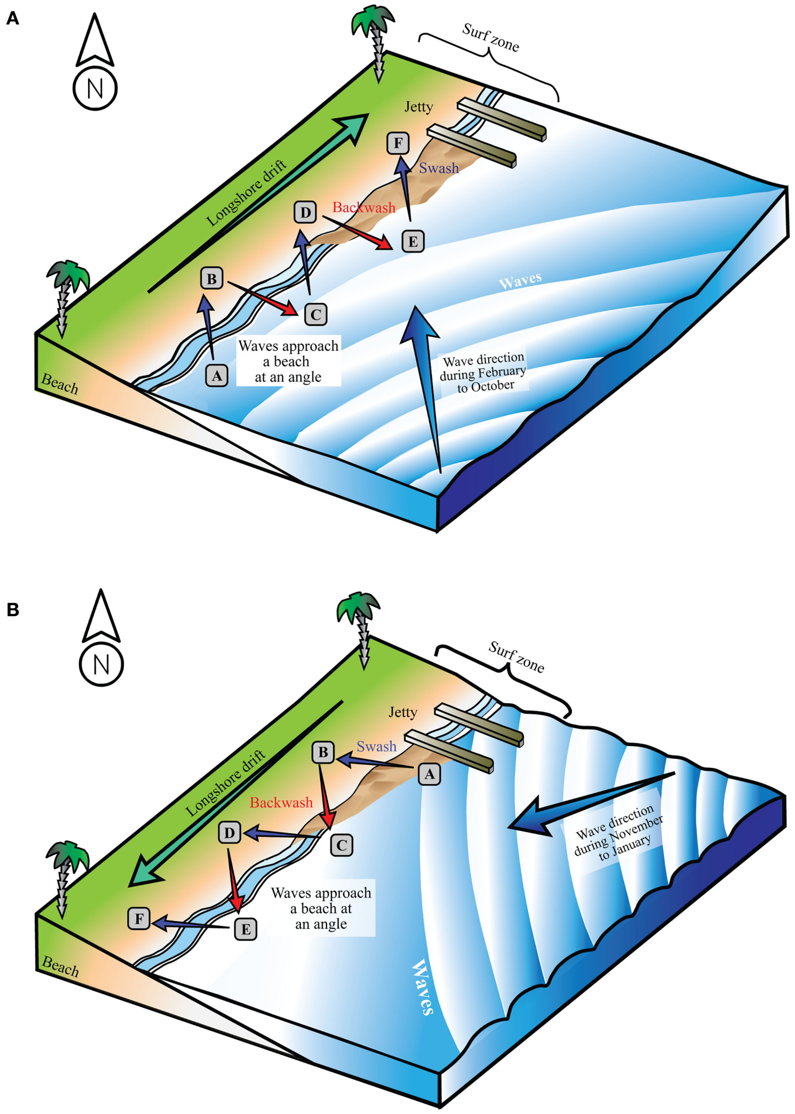

FIGURE 10
Interactions of a jetty, waves, currents, and beach morphology **(A)** during the southwest monsoon, waves transport sediment from A to F (northwards), creating accretion at the updrift jetty, **(B)** during the northeast monsoon, the waves carry the sediment away from the jetty from A to F (southwards).

carried by the longshore current and would accumulate at the updrift jetty. It would be washed ashore during calm periods (especially during the southwest monsoon) and deposited on the beach berm, as was concluded by a similar study in Sri Lanka (Ratnayake et al., 2018).

Bypassing sub-aerial and intertidal intercepted sediment can be a useful and an easy-to-implement approach to mitigate downdrift erosion, because it does not involve any advanced construction machinery. It can be seen from the literature that constructing coastal protection structures, such as revetments and offshore breakwaters, cannot solve the problem but rather move the erosion further downdrift (Kamphuis, 2010; Anfuso et al., 2012; Saengsupavanich, 2019). The construction costs of such coastal protection structures are not cheap. In Thailand, protecting a 1-km of shoreline with a revetment may cost approximately 2.2 million USD. Detached breakwaters may cost a little more, depending on their configurations such as gap width, crest height, and breakwater slope. The design lifetime of these coastal protection structures in Thailand is usually 50 years (Saengsupavanich, 2017). The overall construction cost will depend on how many kilometers of downdrift shoreline must be protected. Such approaches may induce more coastal erosion further downdrift, and more revetments/breakwaters will be kept going. On the other hand, bypassing sediment will not require any additional structural installation. In Thailand, the cost of sand excavation and dumping by an excavator is roughly 1 USD/cu.m, and 2 USD/cu.m by a dredger. The transportation cost varies, depending on the distance from the borrow to the dump sites. If the land-based sand bypassing (by excavators, trucks, and lorries) is implemented at the Na Saton jetty, it would cost at approximately 2 USD/cu.m or about 131,902 USD/yr, or a total of 6.6 million USD in 50 years. Decision makers can now weigh the benefits against the disadvantages before selecting which approach is more appropriate and sustainable.

Implementing sediment bypassing is not easy in reality. Many limitations may emerge (Beck & Wang, 2019; Saengsupavanich, 2020). Firstly, sediment bypassing is a continuous activity that needs continual budget allocation. Each year, Thailand must ration the national revenue, and there is no guarantee that sand bypassing will be given priority. Secondly, deposited sediment may be under the authority of different Subdistrict Administration Organizations (the smallest local government unit taking care of a group of villages) (SAOs). Moving the sediment from one SAO to another SAO can create social resistance, as has already happened in Thailand. The deposited beach at the updrift jetty is usually used as a recreational area. Bypassing the deposited sediment will inevitably destroy the wide beach, and deteriorate the updrift beach's utilization.

Conclusion

Estimating sub-aerial and intertidal sediment deposition is necessary to mitigate downdrift coastal erosion caused by jetties. Along the southern coast of Thailand, there are a few jetties that have created severe downdrift erosion, particularly the Cha Am jetty, the Krai jetty, and the Na Saton jetty. At every jetty, understanding the governing hydrodynamic interaction and accurately determining the quantities of sediment that should be bypassed influence a successful solution of the downdrift erosion. The magnitude of the sub-aerial and intertidal sediment that should be bypassed, estimated by this study, was in the range of 34,170 to 65,951 cu.m/yr. Budget planning and implementation preparations can be set up. Decision makers can choose between 1) a one-off solution, such as constructing revetments/offshore breakwaters to solve erosion occurring adjacent to downdrift jetties, which may induce more erosion further downdrift, or 2) bypassing the sediment once in a few years without having to install any coastal protection structures. Each option has different shortcomings that need to be addressed before downdrift coastal protection can be achieved.

Data availability statement

The raw data supporting the conclusions of this article will be made available by the corresponding author, without undue reservation, to any qualified researcher upon request.

Author contributions

CS conceived and planned the research, including the main ideas and theoretical background, led the survey teams, analyzed the field data, undertook numerical simulations, and wrote the manuscript. LY prepared the figures and helped conduct the numerical modeling. LL commented on the design of the research. SS-N-A assisted in the field survey and took part in analyzing the field data. All authors provided critical feedback and helped shape the research, analysis, and manuscript.

Funding

This research did not receive any specific grant from funding agencies in the public, commercial, or not-for-profit sectors. CS provided full financial support of field surveys, and partly paid the article processing fee. Kasetsart University greatly supported the article processing fee. SS-N-A partly supported the article processing fee.

Acknowledgments

The authors would like to express their heartfelt appreciation to the anonymous reviewers for their meticulous work and thoughtful suggestions, which have significantly improved this paper.

Conflict of interest

The authors declare that the research was conducted in the absence of any commercial or financial relationships that could be construed as a potential conflict of interest.

Publisher's note

References

Adamo, F., De Capua, C., Filianoti, P., Lanzolla, A. M. L., and Morello, R. (2014). A coastal erosion model to predict shoreline changes. *Measurement* 47 (1), 734–740. doi: 10.1016/j.measurement.2013.09.048

Amalan, K., Ratnayake, A. S., Ratnayake, N. P., Weththasinghe, S. M., Dushyantha, N., Lakmali, N., et al (2018). Influence of nearshore sediment dynamics on the distribution of heavy mineral placer deposits in Sri Lanka. *Environ. Earth Sci.* 77, 737. doi: 10.1007/s12665-018-7914-4

Anfuso, G., Martínez-del-Pozo, J. Á., and Rangel-Buitrago, N. (2012). "Bad practice in erosion management: The southern Sicily case study," in *Pitfalls of shoreline stabilization*. Eds. J. A. G. Cooper and O. Pilkey (Netherland: Springer), 215–233. doi: 10.1007/978-94-007-4123-2

Anh, V. T., Trung, P. B., Nguyen, K. A., Liou, Y. A., and Phan, M. T. (2021). Human impacts on estuarine erosion-deposition in southern central Vietnam: Observation and hydrodynamic simulation. *Sustainability* 13 (15), 8303. doi: 10.3390/su13158303

Ariffin, E. H., Mathew, M. J., Yaacob, R., Akhir, M. F., Shaari, H., Zulfakar, M. S. Z., et al (2018). Beach morphodynamic classification in different monsoon seasons at terengganu beaches, Malaysia. *J. Sustain. Sci. Manage.* 13 (5), 65–74.

Ariffin, E. H., Sedrati, M., Akhir, M. F., Yaacob, R., and Husain, M. L. (2016). Open sandy beach morphology and morphodynamic as response to seasonal monsoon in Kuala terengganu, Malaysia. *J. Coast. Res.* 75 (10075), 1032–1036. doi: 10.2112/SI75-207.1

Ariffin, E. H., Sedrati, M., Daud, N. R., Mathew, M. J., Akhir, M. F., Awang, N. A., et al (2019). "Shoreline evolution under the influence of oceanographic and monsoon dynamics: The case of terengganu, Malaysia," in *Coastal zone management*. Eds. M. Ramkumar, R. A. James, D. Menier and Kumaraswamy, (Netherland: Elsevier), 113–130. doi: 10.1016/B978-0-12-814350-6.00005-7

Ariffin, E. H., Zulfakar, M. S. Z., Redzuan, N. S., Mathew, M. J., Akhir, M. F., Baharim, N. B., et al (2020). Evaluating the effects of beach nourishment on littoral morphodynamics at Kuala nerus, terengganu (Malaysia). *J. Sustain. Sci. Manage.* 15 (5), 29–42. doi: 10.46754/jssm.2020.07.005

Azarmsa, S. A., Esmaeili, M., and Khaniki, A. K. (2009). Impacts of jetty construction on the wave heights off the kiashahr lagoon. *Aquat. Ecosyst. Health Manage.* 12 (4), 358–363. doi: 10.1080/14634980903354726

Bayram, A., Larson, M., and Hanson, H. (2007). A new formula for the total longshore sediment transport rate. *Coast. Eng.* 54 (9), 700–710. doi: 10.1016/j.coastaleng.2007.04.001

Beck, T. M., and Wang, P. (2019). Morphodynamics of barrier-inlet systems in the context of regional sediment management, with case studies from west-central Florida, USA. *Ocean Coast. Manage.* 177, 31–51. doi: 10.1016/j.ocecoaman.2019.04.022

Bergillos, R. J., Masselink, M., and Ortega-Sanchez, M. (2017). Coupling cross-shore and longshore sediment transport to model storm response along a mixed sand-gravel coast under varying wave directions. *Coast. Eng.* 129, 93–104. doi: 10.1016/j.coastaleng.2017.09.009

Boswood, P. K., and Murray, R. J. (2001) *World-wide sand bypassing systems: Data report* (Queensland, Australia). Available at: https://repository.tudelft.nl/islandora/object/uuid%3Af05038b9-3e0d-4d95-be99-f2266600e1fe (Accessed 19 October 2021).

Bruun, P. (1995). The development of downdrift erosion. *J. Coast. Res.* 11, 1242–1257.

Dyson, A., Lawson, S., Victory, S., Boswood, P., Mahon, B., Trucchi, L., et al (2002). "Tweed River entrance sand bypassing project post commissioning coastal behaviour," in *Paper presented at proceedings of the 28th international conference on coastal engineering. American society of civil engineers* (Cardiff, Wales, UK: World Scientific).

Fan, R., Wei, H., Zhao, L., Zhao, W., Jiang, C., and Nie, H. (2019). Identify the impacts of waves and tides to coastal suspended sediment concentration based on high-frequency acoustic observations. *Mar. Geol.* 408, 154–164. doi: 10.1016/j.margeo.2018.12.005

Fortunato, A. B., Freire, P., Mengual, B., Bertin, X., Pinto, C., Martins, K., et al (2021). Sediment dynamics and morphological evolution in the tagus estuary inlet. *Mar. Geol.* 440, 106590. doi: 10.1016/j.margeo.2021.106590

Franklin, G. L., Medellín, G., Appendini, C. M., Gómez, J. A., Torres-Freyermuth, A., González, J. L., et al (2021). Impact of port development on the northern Yucatan peninsula coastline. *Reg. Stud. Mar. Sci.* 45, 101835. doi: 10.1016/j.rsma.2021.101835

Garel, E., Sousa, C., and Ferreira, O. (2015). Sand bypass and updrift beach evolution after jetty construction at an ebb-tidal delta. *Estuar. Coast. Shelf Sci.* 167, 4–13. doi: 10.1016/j.ecss.2015.05.044

Garel, E., Sousa, C., Ferreira, O., and Morales, J. A. (2014). Decadal morphological response of an ebb-tidal delta and downdrift beach to artificial breaching and inlet stabilisation. *Geomorphology* 216, 13–25. doi: 10.1016/j.geomorph.2014.03.031

Ghashemizadeh, N., and Tajziehchi, M. (2013). Impact of long jetty on shoreline evaluation (Case study: Eastern coast of Bandar abbas). *J. Basic Appl. Sci. Res.* 3 (3), 1256–1266.

Gunasinghe, G. P., Ruhunage, L., Ratnayake, N. P., Ratnayake, A. S., Samaradivakara, G. V. I., and Jayaratne, R. (2021). Influence of manmade effects on geomorphology, bathymetry and coastal dynamics in a monsoon-affected river outlet in southwest coast of Sri Lanka. *Environ. Earth Sci.* 80, 238. doi: 10.1007/s12665-021-09555-0

Hapke, C. J., Kratzmann, M. G., and Himmelstoss, E. A. (2013). Geomorphic and human influence on large-scale coastal change. *Geomorphology* 199, 160–170. doi: 10.1016/j.geomorph.2012.11.02

Hein, C. J., Fallon, A. R., Rosen, P., Hoagland, P., Georgiou, I. Y., FitzGerald, D. M., et al (2019). Shoreline dynamics along a developed river mouth barrier island: Multi-decadal cycles of erosion and event-driven mitigation. *Front. Earth Sci.* 7. doi: 10.3389/feart.2019.00103

Ismail, N. I., Ariffin, E. H., Yaacob, R., Lokman, M. H., and Baharim, N. B. (2020). The impact of seasonal monsoons on the morphology of beaches protected by barrier islands in setiu, terengganu, Malaysia. *J. Sustain. Sci. Manage.* 15 (4), 1–10. doi: 10.46754/jssm.2020.06.012

Kamphuis, J. W. (1991). Alongshore sediment transport rate. *J. Waterw. Port Coast. Ocean Eng.* 117 (6), 624–640. doi: 10.1061/(ASCE)0733-950X(1991)117:6(624

Kamphuis, J. W. (2010). *Introduction to coastal engineering and management* (Singapore: World Scientific), 472 p.

Keshtpoor, M., Puleo, J. A., Gebert, J., and Plant, N. G. (2013). Beach response to a fixed sand bypassing system. *Coast. Eng.* 73, 28–42. doi: 10.1016/j.coastaleng.2012.09.006

King, E. V., Conley, D. C., Masselink, G., Leonardi, N., McCarroll, R. J., and Scott, T. (2019). The impact of waves and tides on residual sand transport on a sediment-poor, energetic, and macrotidal continental shelf. *J. Geophys. Res.: Oceans* 124 (7), 4974–5002. doi: 10.1029/2018JC014861

Kudale, M. D. (2010). Impact of port development on the coastline and the need for protection. *Indian J. Geo-Mar. Sci.* 39 (4), 597–604.

Lim, H. S., Kim, M., Do, J., Kim, S., Lee, H. J., and Kim, D. H. (2018). Variability of wave-induced current analyzed with intensive field measurements in the coastal waters of anmok. *J. Coast. Res.* 85, 686–690. doi: 10.2112/SI85-138.1

Masselink, G., Castelle, B., Scott, T., Dodet, G., Suanez, S., Jackson, D., et al (2016). Extreme wave activity during 2013/2014 winter and morphological impacts along the Atlantic coast of Europe. *Geophys. Res. Lett.* 43, 2135–2143. doi: 10.1002/2015GL067492

Muhammad, M., Idris, K., Ariffin, E. H., Shaffril, H. A. M., Samah, B. A., and Suandi, T. (2016). The impact of climate change on small-scale fishermen in Malaysia. *Soc. Sci. (Pakistan)* 11 (13), 3352–3356. doi: 10.3923/sscience.2016.3352.3356

Murthy, V. N. S. (2003). *Geotechnical engineering: Principles and practices of soil mechanics and foundation engineering* (New York: Marcel Dekker), 1029 p.

Nassar, K., Mahmod, W. E., Masria, A., Fath, H., and Nadaoka, K. (2018). Numerical simulation of shoreline responses in the vicinity of the western artificial inlet of the bardawil lagoon, Sinai peninsula, Egypt. *Appl. Ocean Res.* 74, 87–101. doi: 10.1016/j.apor.2018.02.015

Oyegbile, B. O., and Oyegbile, B. A. (2017). Applications of geosynthetic membranes in soil stabilization and coastal defence structures. *Int. J. Sustain. Built Environ.* 6, 636–662. doi: 10.1016/j.ijsbe.2017.04.001

Rangel-Buitrago, N. G., Anfuso, G., and Williams, A. T. (2015). Coastal erosion along the Caribbean coast of Colombia: Magnitudes, causes and management. *Ocean Coast. Manage.* 114, 129–144. doi: 10.1016/j.ocecoaman.2015.06.024

Ratnayake, N. P., Ratnayake, A. S., Azoor, R. M., Weththasinghe, S. M., Seneviratne, I. D. J., Senarathne, N., et al (2019). Erosion processes driven by monsoon events after a beach nourishment and breakwater construction at uswetakeiyawa beach, Sri Lanka. *SN Appl. Sci.* 1, 52. doi: 10.1007/s42452-018-0050-7

Ratnayake, N. P., Ratnayake, A. S., Keegle, P. V., Mallawa Arachchi, M. A. K. M., and Premasiri, H. M. R. (2018). An analysis of beach profile changes subsequent to the Colombo harbor expansion project, Sri Lanka. *Environ. Earth Sci.* 77, 24. doi: 10.1007/s12665-018-7234-8

Rautenbach, C., and Theron, A. K. (2018). Study of the Durban bight shoreline evolution under schematised climate change and sand–bypassing scenarios. *J. South Afr. Inst. Civ. Eng.* 60 (4), 2–15. doi: 10.17159/2309-8775/2018/v60n4a1

Saengsupavanich, C. (2012). Unwelcome environmental impact assessment for coastal protection along a 7-km shoreline in southern Thailand. *Ocean Coast. Manage.* 61, 20–29. doi: 10.1016/j.ocecoaman.2012.02.008

Saengsupavanich, C. (2013). Detached breakwaters: Communities' preferences for sustainable coastal protection. *J. Environ. Manage.* 115, 106–113. doi: 10.1016/j.jenvman.2012.11.029

Saengsupavanich, C. (2017). Coastal revetment design process in Thailand. *WIT Trans. Built Environ.* 170, 33–44. doi: 10.1016/j.jenvman.2012.11.029

Saengsupavanich, C. (2019). Willingness to restore jetty-created erosion at a famous tourism beach. *Ocean Coast. Manage.* 178, 104817. doi: 10.1016/j.ocecoaman.2019.104817

Saengsupavanich, C. (2020). Deconstructing a jetty to rectify the downdrift erosion. *J. Sustain. Sci. Manage.* 15 (2), 79–88.

Salleh, A. M., and Nadzir, N. (2020). Study of sediment deposition at tanjung laboh due to jetty structural. *IOP Conference Series: Earth and Environmental Science.* 498, 1, 012016. doi: 10.1088/1755-1315/498/1/012016. IOP Publishing.

Selamat, N. S., Maulud, K. N., Mohd, F. A., Rahman, A. A. A., Zainal, M. K., Wahid, M. A. A., et al (2019). Multi method analysis for identifying the shoreline erosion during northeast monsoon season. *J. Sustain. Sci. Manage.* 14 (3), 43–54.

Shariful, F., Sedrati, M., Ariffin, E. H., Shubri, S. M., and Akhir, M. F. (2020). Impact of 2019 tropical storm (Pabuk) on beach morphology, terengganu coast (Malaysia). *J. Coast. Res.* 95 (Special Issue), 346–350. doi: 10.2112/SI95-067.1

Shetty, A., and Jayappa, K. S. (2020). Seasonal variation in longshore sediment transport rate and its impact on sediment budget along the wave-dominated karnataka coast, India. *J. Earth Syst. Sci.* 129, 234. doi: 10.1007/s12040-020-01504-y

Silva, A. P., Vieira da Silva, G., Strauss, D., Murray, T., and Tomlinson, R. (2021). Updrift morphological impacts of a coastal protection strategy. how far and for how long? *Mar. Geol.* 441, 106625. doi: 10.1016/j.margeo.2021.106625

United States Army Corps of Engineers (1984). *Shore protection manual* (Washington: Coastal Engineering Research Center), 652 p.

Wang, P., and Beck, T. M. (2012). Morphodynamics of an anthropogenically altered dual-inlet system: John's pass and blind pass, west-central Florida, USA. *Mar. Geol.* 291–294, 162–175. doi: 10.1016/j.margeo.2011.06.001

Wang, Y. H., Wang, Y. H., Deng, A. J., Feng, H. C., Wang, D. W., and Guo, C. S. (2022). Emerging downdrift erosion by twin long-range jetties on an open mesotidal muddy coast, China. *J. Mar. Sci. Eng.* 10 (5), 570. doi: 10.3390/jmse10050570

Weerasingha, W. A. D. B., and Ratnayake, A. S. (2022). Coastal landform changes on the east coast of Sri Lanka using remote sensing and geographic information system (GIS) techniques. *Remote Sens. Appl.: Soc. Environ.* 26, 100763. doi: 10.1016/j.rsase.2022.100763

Witmer, A. D., Ammons, A. W., Bell, A. C., and Rowe, J. B. (2018). Anthropogenic transport of macrofauna through a sand transfer plant. *Ocean Coast. Manage.* 155, 1–7. doi: 10.1016/j.ocecoaman.2018.01.026

Yaacob, R., Shaari, H., Sapon, N., Ahmad, M. F., Arifin, E. H., Zakariya, R., et al (2018). Annual changes of beach profile and nearshore sediment distribution off dungun-Kemaman,Terengganu, Malaysia. *J. Teknol.* 80 (5), 57–66.

Žilinskas, G., Janušaitė, R., Jarmalavičius, D., and Pupienis, D (2020). The impact of Klaipėda Port entrance channel dredging on the dynamics of coastal zone, Lithuania. *Oceanologia.* 62 (4), 489–500. doi: 10.1016/j.oceano.2020.08.002

Zulfakar, M. S. Z., Akhir, M. F., Ariffin, E. H., Awang, N. A., Yaakob, M. A. M., and Muslim, A. M. (2020). The effect of coastal protections on the shoreline evolution at Kuala nerus, terengganu (Malaysia). *J. Sustain. Sci. Manage.* 15 (3), 71–85.

Zulfakar, M. S. Z., Ariffin, E. H., Akhir, M. F., and Awang, N. A. (2021). Variation of seasonal monsoon wave-driven circulation pattern in the lee of groyne in Kuala nerus beach. *IOP Conf. Ser.: Earth Environ. Sci.* 698 (1), 012042. doi: 10.1088/1755-1315/698/1/012042

Zurmuhlen, F. H. (1957). The sand transfer plant at Lake Worth Inlet. *Coastal Engineering Proceedings* 1 (6), 25. doi: 10.9753/icce.v6.25

frontiers | Frontiers in Marine Science

TYPE Original Research
PUBLISHED 02 September 2022
DOI 10.3389/fmars.2022.920339

Check for updates

OPEN ACCESS

EDITED BY
Mouncef Sedrati,
Université Bretagne Sud,
France

REVIEWED BY
Leonel Pereira,
University of Coimbra, Portugal
Luci Pereira,
Federal University of Pará, Brazil

*CORRESPONDENCE
Rodolfo Silva
rsilvac@iingen.unam.mx
Valeria Chávez
vchavezc@iingen.unam.mx

SPECIALTY SECTION
This article was submitted to
Coastal Ocean Processes,
a section of the journal
Frontiers in Marine Science

RECEIVED 14 April 2022
ACCEPTED 04 August 2022
PUBLISHED 02 September 2022

CITATION
Uribe-Martínez A, Berriel-Bueno D, Chávez V, Cuevas E, Almeida KL, Fontes JVH, van Tussenbroek BI, Mariño-Tapia I, Liceaga-Correa MA, Ojeda E, Castañeda-Ramírez DG and Silva R (2022) Multiscale distribution patterns of pelagic rafts of sargasso (*Sargassum* spp.) in the Mexican Caribbean (2014–2020).
Front. Mar. Sci. 9:920339.
doi: 10.3389/fmars.2022.920339

Multiscale distribution patterns of pelagic rafts of sargasso (*Sargassum* spp.) in the Mexican Caribbean (2014–2020)

Abigail Uribe-Martínez[1], Diana Berriel-Bueno[2], Valeria Chávez[3]*, Eduardo Cuevas[4], Karla L. Almeida[3], Jassiel V. H. Fontes[5], Brigitta I. van Tussenbroek[6], Ismael Mariño-Tapia[7], Maria de los Ángeles Liceaga-Correa[2], Elena Ojeda[8], D. Gerardo Castañeda-Ramírez[9] and Rodolfo Silva[3]*

[1]Harte Research Institute Furgason Fellow, Mérida, Mexico, [2]Departamento Recursos del Mar, Centro de Investigación y de Estudios Avanzados del Instituto Politécnico Nacional, Unidad Mérida, Mérida, Mexico, [3]Instituto de Ingeniería, Universidad Nacional Autónoma de México, Mexico City, Mexico, [4]Consejo Nacional de Ciencia y Tecnología, Universidad Autónoma del Carmen, Ciudad del Carmen, Mexico, [5]Departamento de Engenharia Naval, Escola Superior de Tecnologia, Universidade do Estado do Amazonas, Manaus, Brazil, [6]Unidad Académica de Sistemas Arrecifales - Puerto Morelos, Instituto de Ciencias del Mar y Limnología, Universidad Nacional Autónoma de México, Puerto Morelos, Mexico, [7]Escuela Nacional de Estudios Superiores, Universidad Nacional Autónoma de México, Mérida, Mexico, [8]Laboratoire de Morphodynamique Continentale et Côtière (M2C), Normandie Université, Caen, France, [9]Gerencia Corporativa Ambiental, Moon Palace Resort, Cancún, Mexico

As the biomass of pelagic *Sargassum* spp. increased across the North Atlantic equatorial recirculation region from 2011 onwards, massive rafts of sargasso appeared in the Western Caribbean in 2015, 2018, 2019, and 2020. These events raised concerns regarding their negative consequences on the environment, local income, and human wellbeing. As adequate monitoring and analysis tools are needed for designing in-water and on-beach control strategies to reduce potential negative impacts, more robust and spatially explicit information is needed in order to improve sargasso management and focus restoration efforts. In this paper, we offer a spatiotemporal multiscale description of sargasso distribution and dynamics for 2014–2020 in the Mexican Caribbean: (1) for the entire region (millions of km^2); (2) at the local scale (thousands of km^2) evaluating the dynamics inside the reef lagoon at Puerto Morelos, Mexico; and finally, (3) specific beach observations (hundreds of km^2) derived from data on beach cleaning volumes. Fifteen areas in the Mexican Caribbean, with different sargasso dispersions and on-shore accumulations, were evaluated. The areas around Tulum, Solidaridad, and Puerto Morelos have the most extreme and most frequent episodes but also exhibited the greatest seasonal variability. Extreme sargasso presence can occur in the Western Caribbean in any season, albeit with increasing coverage and recurrence in the summer. Images from a coastal video monitoring station at Puerto Morelos showed that massive sargasso beaching was associated with low energy conditions ($Hs<$ 0.25 m, wind speed<4 m/s, neap tide), while non-accumulation of sargasso on the beach occurred under high energy conditions (*Hs* >0.4 *m*, wind speed = 8 m/s, spring tide). Time-series analyses of sargasso beaching showed different periods of historic maximum sargasso coverage over July–October 2018 and others in January–February 2019. Wind and wave regimes influenced sargasso in distinct ways, depending on the coastal section, probably related to coastline morphology, oceanic regime, or the extent of the continental platform. This work presents the longest systematic time series (2014-2020) of high resolution satellite detected sargasso in Mexico. Spatial and temporal patterns are proposed as fundamental steps for managing sargasso accumulations.

KEYWORDS

satellite detection, numerical model, beach cast, surface drift, Quintana Roo

Introduction

The study of the holopelagic *Sargassum* species (*S. natans* and *S. fluitans*, Phylum Ochrophyta, Class Phaeophyceae; referred to as sargasso from hereon) in the NW Atlantic dates back to the 1830s, with the discovery of the Sargasso Sea (Butler et al., 1983). Sargasso is the only seaweed that passes its complete life cycle drifting on the ocean surface. It has elongated, highly ramified thalli, up to 0.5 m in length, with numerous blades and vesicles, that allow the thalli to float either singly, or in floating, entangled masses (rafts) that can extend up to several km at sea (see Supplementary Material 1).

The size and spatial configuration of sargasso aggregations (rafts) depend on its growth but also on the spatiotemporal dynamics of oceanic and atmospheric forces, such as wind, wave, and surface marine currents (Butler et al., 1983; Brooks et al., 2018; Putman et al., 2020; Marsh et al., 2021; Skliris et al., 2022). In the Western Caribbean, close to the Yucatan Channel, sargasso rafts are shaped like cyclonic and anticyclonic gyres, drops, compact mats, linear formations, or raft aggregations caused by Langmuir circulation (several short, parallel lines of sargasso arranged perpendicular to the shore, moving in the same direction as the wind), their size varying from centimeters to kilometers, the former found mainly as string lines and spirals (Guzmán-Ramírez et al., 2020). In the north-central Gulf of Mexico, Powers et al. (2013) reported different types of aggregations of sargasso: scattered clumps when the winds were high, small and mesoscale convergence lines, and larger circular-like rafts that may persist for several weeks or even months while drifting in the ocean. These pelagic rafts of sargasso have key ecological roles, serving as a refuge for marine life, hosting species such as sea turtles, fish (of which several are commercially important), invertebrates, and birds, which use the sargasso ecosystem as a refuge, feeding ground, nursery, and breeding habitat, either permanently or temporarily (Pendleton et al., 2014).

Unusually large concentrations of sargasso in the tropical Atlantic near the Equator and SW Caribbean Sea were reported for the first time in 2011 (Smetacek and Zingone, 2013). Since then, several studies have reported a sustained increase in the biomass of pelagic sargasso in this region (Hu et al., 2016; Xing et al., 2017; Wang et al., 2018) (Figure 1). Schell et al. (2015) estimated that the concentration of sargasso in the Western Atlantic in 2014 was approximately 10 times greater than that of 2011 and 300 times higher than that of previous decades. In 2016 and 2017, the sargasso coverage decreased, but in 2018 and 2019 it rose again (Wang et al., 2019). In 2020 and 2021, the volume of sargasso cover was moderate to high in the Caribbean (Marsh et al., 2021). The peak sargasso year in the Caribbean Sea and central Western Atlantic was 2018, with the highest biomass in June, the rafts covering almost 3,000 km^2 in the area bounded by 8°–23°N and 89°–58° W (Wang et al., 2019). Wang et al. (2019) named this new area of sargasso concentration, extending from Equatorial Africa to the Gulf of Mexico, the Great Atlantic Sargasso Belt (Figure 1A).

According to Cuevas et al. (Cuevas et al., 2018), the first massive arrival of sargasso in the Mexican Caribbean, recorded with satellite imagery, began in late 2014, reaching a first peak in September 2015. In 2015, an average of ~2,360 m^3 of sargasso was removed per kilometre of coastline in the north, between Cancun and Puerto Morelos (Rodríguez-Martínez et al., 2016) (Figure 1B). After a decrease in 2016 and 2017, the influx of sargasso resumed in February 2018 and continued until September 2019 (Chávez et al., 2020; Rodriguez-Martínez et al., 2022). Even though those are the last published time series, it is known that large amounts of sargasso were collected in 2020 and 2021.

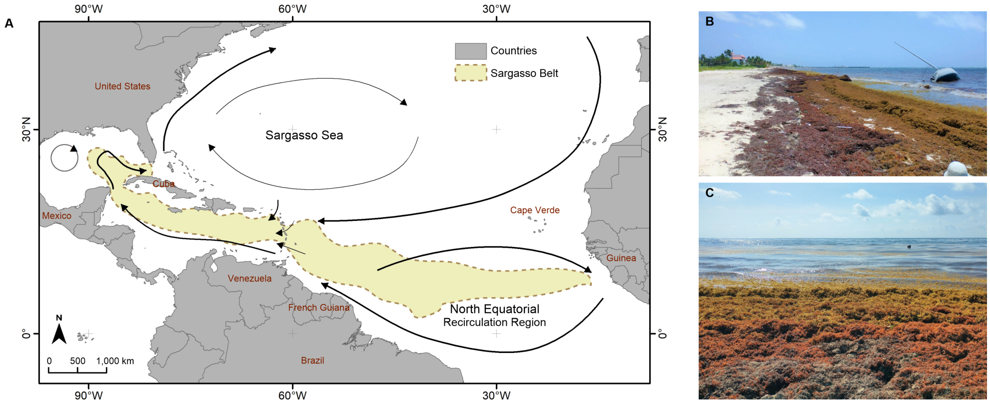

FIGURE 1
(A) Schematic representation of the main ocean current patterns and areas of sargasso accumulation in the Atlantic Ocean. (The Great Atlantic Sargasso Belt; July 2011–2018 configuration; made by the authors, using information from Wang et al. (2019). **(B, C)** Accumulation of beach-cast sargasso at Puerto Morelos, Mexican Caribbean (June 2021, Photographs by Laura Ribas).

Sargasso concentrations (abundance and distribution) in the tropical Atlantic vary greatly both seasonally and interannually. Johns et al. (2020) offered a concise, plausible theory regarding the seasonality of this phenomenon in the Atlantic, suggesting that the new sargasso aggregations recirculate in the North Equatorial Recirculation Region (NERR) and that in early spring (March–April) some masses move south, causing a summer bloom in the Caribbean. Once released from the NERR and transported towards the northern coast of South America, the sargasso flows through the Caribbean and the Gulf of Mexico (Putman et al., 2018). However, it is more difficult to understand the large interannual variations in the abundance of the sargasso aggregations, as these occur at different spatial and temporal scales, under distinct environmental forces. Skliris et al. (2022) recently suggested that in 2015 and 2018, the years with the highest sargasso bloom, the Intertropical Convergence Zone (ITZ), an area of maximal trade wind convergence and sargasso accumulation, shifted southward, thereby enriching the seawater with nutrients flowing from the Amazon, and equatorial upwelling in this zone stimulated the growth of sargasso. The easterly trade winds also transport Sahara dust into the tropical Atlantic, possibly fertilizing seaweeds in the Great Atlantic Sargasso belt, although the importance of this fertilization is still unknown (supplements Wang et al., 2019).

Gower et al. (2013) suggested that the sudden increase in the sargasso masses may have been the result of the water discharging from the Amazon containing more fertilizers in the runoff from agricultural lands in the interior.

However, Jouanno et al. (2021) showed that there was no significant increase in riverine influence in areas where sargasso proliferated. On the other hand, Johns et al. (2020) have proposed that increased winds, created by an anomaly in the North Atlantic Oscillation in 2010, may have transported large masses of sargasso from the Sargasso Sea into the NERR. Wang et al. (2019) and Johns et al. (2020) suggested a regime change in the NERR, together with changes in the Canaries upwelling, or discharges from the Amazon, resulting in recurrent blooms of sargasso and promoting the spatial pattern known as the Great Atlantic Sargasso Belt (Figure 1). The sargasso aggregation showed enhanced growth thanks to nutrients entrained in the upper water column (Johns et al., 2020).

Part of the pelagic sargasso at sea is destined to arrive on Caribbean shores, causing diverse negative impacts on coastal ecosystems (Silva et al., 2016; van Tussenbroek et al., 2017; Chávez et al., 2020; Bartlett and Elmer, 2021; Maurer et al., 2021; Rodríguez-Muñoz et al., 2021), local and regional economics (Solarin et al., 2014; Milledge and Harvey, 2016), and human health (Devault et al., 2021). The impacts include aesthetics (of the previously pristine white beaches), additional organic matter input, light attenuation, anoxia, and leaching (van Tussenbroek et al., 2017; Chávez et al., 2020). The consequences are mortality of near-shore benthos, including seagrass and coral (Silva et al., 2016), beach erosion (van Tussenbroek et al., 2017; Silva et al., 2020), the modification of sediment structure (Maurer, 2019), changes in the trophic relationships (Cabanillas-Terán et al., 2019), respiratory and skin health issues in humans (Resiere et al., 2018), and economic losses for the tourist industry. Although the latter has not been fully assessed, losses are estimated to be substantial as the beaches lost their attractiveness due to the unsightly accumulations of sargasso (Langin, 2018). In Mexico, enormous human and financial resources have been invested in preventing the sargasso reaching the coast, or in removing it from the beaches; most of these efforts have been insufficient due to the huge volumes involved.

Understanding the spatial movement patterns of sargasso in the open sea, as related to oceanographic conditions, is needed. This knowledge should be a part of the toolbox of decision makers and stakeholders, to help them when implementing mitigation strategies and embarking upon restoration actions (Casas-Beltrán et al., 2020). Coastal and marine management requires a comprehensive, integral perspective and feasible environmental frameworks (El Mahrad et al., 2020; Silva et al., 2020; Guimarais et al., 2021; Silva et al., 2021). Remote sensing has been shown to be a key piece of any timely detection tool, furthering the understanding of patterns of sargasso circulation and accumulation (Wang and Hu, 2017; Brooks et al., 2018; Berline et al., 2020; Johns et al., 2020; Putman et al., 2020; Wang and Hu, 2021). While sargasso rafts can be detected during oceanographic expeditions or using advanced unmanned vehicles (Butler et al., 1983; Lapointe, 1995; Huffard et al., 2014), high-resolution imagery from free satellite sensing inputs is essential for systematic long-term and regional coverage if we are to understand the ocean-scale dynamics behind the movements of sargasso (Hu et al., 2015; Wang and Hu, 2017; Xing et al., 2017 Supplementary Material 2).

Remote sensing techniques can help in establishing early warning systems that are strategic tools for emergency planning. They also provide long-term data series with high-resolution delimitation of the sargasso rafts, necessary for a comprehensive management plan. A spatially explicit time-series analysis can contribute to regionalization and prioritization criteria that can be incorporated in integral marine spatial planning schemes (Ogden, 2010; Shucksmith et al., 2014; Domínguez-Tejo et al., 2016). Remote sensing images are essentially input for influx trend assessment and to understand the regional and local dynamics of sargasso that can respond to distinct atmospheric and ocean forcing variables. In addition to understanding sargasso circulation in the Central Atlantic basin, regional and local knowledge of the spatiotemporal dynamics is necessary for appropriate decision making, preparedness, and adaptive management (López-Miranda et al., 2021; Oxenford et al., 2021). Information on the spatial and temporal patterns of Sargasso would allow more appropriate monitoring, and in-sea and on-shore recollection efforts, as well as promote protection and restoration initiatives in the areas most affected, or areas considered to be of special social, economic, or ecological value.

In this study, we aim to fill knowledge gaps on the distribution patterns of sargasso at regional and local scales in the Mexican Caribbean and to describe the oceanographic and atmospheric features associated with the spatial and temporal patterns of massive influxes of sargasso, through a multiple-spatial- and temporal-scale approach. The underlying premises are that the spatiotemporal patterns of sargasso distribution, beaching, and accumulation are locally and regionally driven by atmospheric (wind) and oceanographic (tides, wave power) conditions operating at different spatial scales. These drive the sargasso dynamics onshore and offshore and the intra- and interannual variability of sargasso flux which are the result of similar variance in patterns of the driving forces.

We adopted different spatial and temporal scales to appraise sargasso distribution: (a) a regional evaluation (Mexican Caribbean) using high-resolution remotely sensed imagery; (b) a local-scale evaluation in the Puerto Morelos reef lagoon; (c) a beach-scale evaluation considering wrack collection (usually mostly sargasso) from two beach sections at Puerto Morelos, Quintana Roo, Mexico; and (d) a time-specific comparison of detected sargasso rafts captured by both means (satellite and aerial platform).

Materials and methods

Through a multi-scale analysis, we described and documented the spatiotemporal distribution patterns of the sargasso rafts in the Mexican Caribbean at various scales, from detection of sargasso at sea with satellite imagery to modelling its movements inside a reef lagoon (Puerto Morelos) (Figure 2). Our aim was to provide a comprehensive overview of the spatiotemporal patterns of the sargasso at regional, local, and micro scales in the northern Mexican Caribbean.

Study area

The Mexican Caribbean, on the east side of the Yucatan Peninsula (see Figure 3), is a biodiverse area with key ecosystems, such as coral reefs, seagrass meadows, calcareous sandy beaches, complex dune vegetation, mangroves, and submarine springs from one of the most intricate subterraneous aquifers in the world (Guimarais et al., 2021).

The region has a tropical climate, with two seasons (winter and summer) reflected in distinct wind patterns and air temperatures. Winter conditions occur approximately from November to April, with mean monthly air temperatures of 24°C–25°C, although the diurnal minima can fall briefly during the passage of cold fronts, known as “Nortes”. Northeastern winds prevail from October to February, while northerly and southeasterly winds occur following the passage of cold fronts. In summer, easterly trade winds predominate with speeds of 3–9 m s^{-1}. The maximum air temperature is in August, with a monthly average of 29°C, raising to above 33.5°C (Coronado et al., 2007). Sea surface temperatures are between 25°C and 31°C (SAMMO, 2015). Measurements at buoy 42056 (NDBC-NOAA), in the Caribbean basin, at a water depth of 4,446 m, show that swell propagates from the Caribbean Sea (SSE direction), driven by the dominant winds, with an average significant wave height (H_s) of 0.8 m and a relatively short dominant wave period (T_p) of 6–8 s in summer (Coronado et al., 2007; Mariño-Tapia et al., 2011). As for the wave patterns, in winter, higher-energy waves (H_s >1.75 m) occur as a consequence of the

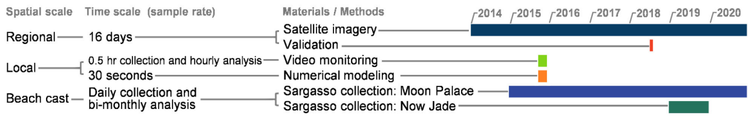

FIGURE 2
Timeline of the multi-scale analyses conducted into sargasso patterns.

passage of cold fronts. In summer, H_s is typically small (H_s<0.3 m) but can reach 7 m during a hurricane event.

The region has a microtidal regime, with semidiurnal oscillations averaging 0.40 m. The Yucatan Current has a strong influence in the region. Its direction varies from northeastward to northwestward from south of Cozumel Island and along the western side of Yucatan Channel into the Gulf of Mexico, where it becomes the Loop Current. From April to November, there are more intense currents, up to 2 m s^{-1}, with a decrease in its intensity of 0.9 m s^{-1} during winter. The average velocity is 1.5 m s^{-1} near the surface (Coronado et al., 2007; Athié et al., 2011).

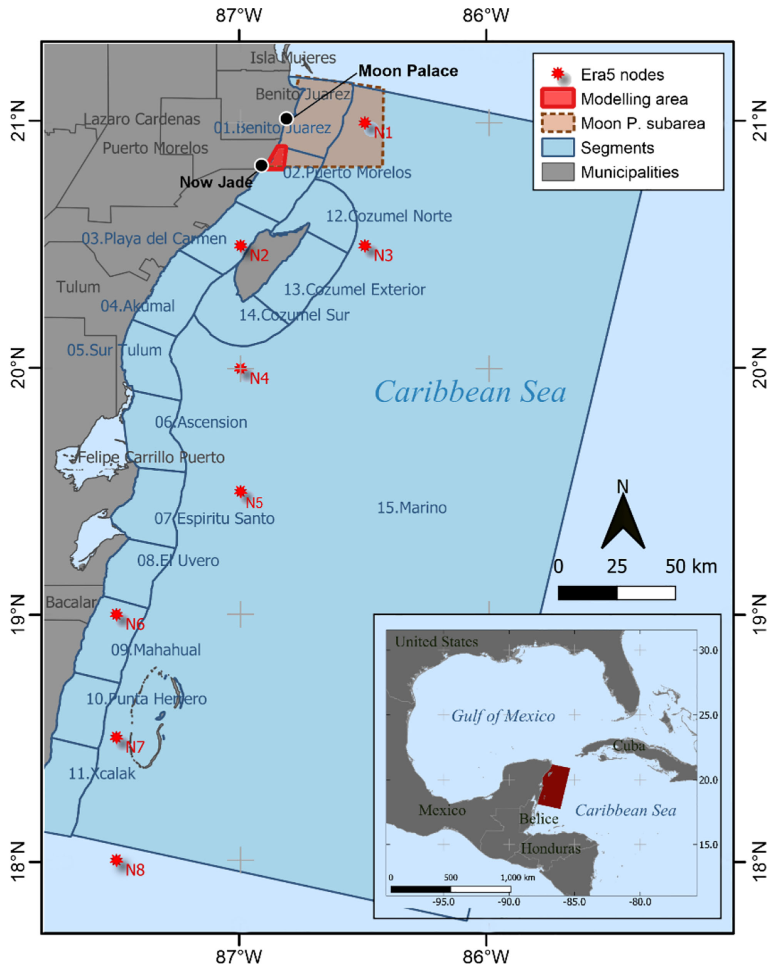

FIGURE 3
Study area within the Caribbean region. The solid blue lines delimit the 15 coastal segments (see 2.2). The bright-red polygon shows the area of the local-scale analysis, where circulation modelling was conducted (see 2.4); the black dots show locations for the beach-scale analysis, where time-series analyses of wrack were obtained (see 2.5); the red stars are the nodes for the oceanographic analysis (see 2.3); and the area shaded brown is in front of the Moon Palace Hotel, where sargasso detected was compared with beach-cast sargasso (see 2.5).

Puerto Morelos is a small coastal town, in the north of the Mexican Caribbean (Figure 3). The National Park of Puerto Morelos Reef has a well-developed fringing reef that delimits a 0.4–3-km-wide reef lagoon. Dense seagrass meadows cover the bottom of the reef lagoon, which are habitat for local and regional key species (McHenry et al., 2021). The reef has two main openings: in the north, a reef discontinuity gives an entrance 300 m wide and 6 m deep, and in the south there is a navigational channel 400 m wide and 8 m deep (Coronado et al, 2007). Inside the lagoon, under normal conditions, the average H_s is 0.3 m. Circulation conditions in reef lagoons normally consist of a surface wave-induced flow, entering the lagoon over the shallow reef flat, with strong flows exiting through both channels. The wave-induced flow in the reef lagoon is modulated by a low-frequency sea-level change related to a geostrophic response to the variability of the Yucatan Current, with less influence of tides and direct wind on the sea surface (Coronado et al., 2007). Odériz et al. (2020) mentions that the physical components and dynamics of this lagoon have been extensively studied over several years. The average current speed is ~0.10 m/s with a predominantly northward direction and little tidal influence. In the northern and southern inlets, the mean current speed is ~0.20 m/s, reaching maximum values of ~1 m/s (Coronado et al., 2007; Mariño-Tapia et al., 2011; Torres-Freyermuth et al., 2012).

Regional scale using satellite imagery

The Operational Land Imager (OLI) sensor launched with Landsat 8 mission has proven to be reliable in detecting sargasso, with high spatial resolution, and this imagery is freely available, making it a very good option for long-term sargasso detection (Wang and Hu, 2021). We used Landsat 8 OLI imagery to compile a time series (2014–2020) of sargasso distribution at the regional scale for the Mexican Caribbean (Hu et al., 2016; Cuevas et al., 2018; Hardy et al., 2018; Chávez et al., 2020; Uribe-Martínez et al., 2020). The imagery has a spatial resolution of 30 m and a systematic revisiting time of 16 days.

The satellite detection covers 7 years (January 2014 to December 2020), including observations before the first anomalous high sargasso influx in this region. A total of 432 Landsat 8 OLI images were processed, using the semi-automated multi-index classification of Cuevas et al. (2018), for detection of pixels with and without sargasso. This approach uses the normalized difference vegetation index (NDVI), atmospherically resistant vegetation index (ARVI), soil-adjusted vegetation index (SAVI), enhanced vegetation index (EVI), and floating algae index (FAI)), plus band 2 Blue (0.452–0.512 µm) and band 5 near infrared (NIR) (0.851–0.879 µm).

The preprocessing of the images was done using the open-source software QGIS (QGIS-Association, 2021) starting with atmospheric correction, using the Semi-Automatic Classification Plugin (Congedo, 2021). The land was masked using the Global Administrative Areas as reference (https://gadm.org/), and finally, the clouds were masked using the codified quality assessment bands (BQA). Training polygons were drawn using the following categories: sargasso, clouds, shadows, saturated bright sea, and open sea, on a false-colour composition (red = NIR, green = blue; blue = coastal blue/violet). These datasets were used in a supervised classification process with the random forest algorithm.

The quantification of detected sargasso in each Landsat image was standardized to the effective analysis area in the images, excluding the cloud cover. The area was divided into 2-km-diameter hexagons in a lattice that covered the complete swath of Landsat 8 OLI paths (approximately 150 km). There are about two monthly observations, so the satellite sargasso detection per month was averaged for subsequent analysis. Based on the sargasso coverage detected by satellite for 2014–2020 per hexagon, we were able to:

(i) Build a time-series plot and boxplots indicating sargasso coverage in the sea each month

(ii) Perform an autocorrelation analysis through an autocovariance function, to evaluate possible correlations between detected sargasso during a certain month with sargasso coverage in following months, i.e., to assess different time lags of association

(iii) Sum all detected coverage along the time series per hexagon and create a cumulative sargasso cover map

(iv) Classify cumulative sargasso cover in four coverage categories: low, moderate, high, and very high, based on the Jenks ranking method that maximizes the variability between categories and minimizes the variability within delimited areas (North, 2009)

(v) Create a sargasso recurrence map, i.e., the number of times that a sargasso raft occurred in each hexagon, and classify these recurrence values (see iv)

(vi) Classify the spatial patterns of the sargasso, based on both cumulative sargasso cover and recurrence categorizations, to spatially identify areas from no sargasso to extreme sargasso cover (Table 1). This analysis was done for the entire period and per season.

The sea off the Mexican Caribbean coastline was divided into 15 segments (≈30 km long and 20 km wide), based on the influx patterns of sargasso on the shore (Chávez et al., 2020; Uribe-Martínez et al., 2020) (Figure 3). For each segment, we estimated the cumulative sargasso coverage area and recurrence based on the proportion of the hexagons intersected by the polygonal segments. This analysis was made for the entire period and per season. A non-parametric variance test (Kruskal–Wallis) was

TABLE 1 Classification criteria of sargasso presence, based on the cumulative sargasso area and recurrence from 2014 to 2020.

Cumulative area classification (min–max km^2)	Recurrence classification (min–max number of images)	Spatial pattern classification	Description
No Sargasso	No sargasso	0. No sargasso	No sargasso detected
Low (1-10)	Low (1-3)	1. Low	Little presence of sargasso, infrequent
Low (1-10)	Moderate (4-7)	2. Moderate	Some presence, when cumulative area and frequency are a combination of low and moderate
Low (1-10)	Moderate (4-7)		
Moderate (10-20)	Low (1-3)		
Moderate (10-20)	Moderate (4-7)		
Low (1-10)	High (8-14)	3. Frequent	Repeated presence of sargasso, with low to moderate cover
Moderate (10-20)	High (8-14)		
Moderate (10-20)	High (8-14)		
High (20-40)	Low (1-3)	4. Intense episodes	Few episodes, with high or very high cover
High (20-40)	Moderate (4-7)		
Very high (>40)	Low (1-3)		
Very high (>40)	Moderate (4-7)		
High (20-40)	High (8-14)	5. Frequent and intense	High recurrence and cumulative area is high or very high
High (20-40)	Very high (>14)		
Very high (>40)	High (8-14)		
Very high (>40)	Very high (>14)	6. Extreme	Very high recurrence and cover

performed to evaluate the significance of possible differences between the regions.

Putman et al. (2020) and Rutten et al. (2021) explained the influence of waves, wind, and tides on the sargasso dynamics close to shore and governing its beach casting; we described graphically the mean oceanographic conditions (wind and wave power). To do this, daily mean wave, wind power, and direction were obtained for eight sampling nodes along the Mexican Caribbean coast (N1: 21°N 86.5°W; N2: 20.5°N 87°W; N3: 20.5°N 86.5°W; N4: 20°N 87°W; N5: 19.5°N 87°W; N6: 19°N 87.5°W; N7: 18.5°N 87.5°W and N8: 18°N 87.5°W; Figure 3) from ERA5 climate reanalysis (https://climate.copernicus.eu/climate-reanalysis) using marine climate data for 2018 and 2019.

Cross-validation of satellite detected sargasso

Pelagic sargasso is constantly moving on the ocean surface and changing its form as winds and waves force sargasso, giving very difficult conditions for a typical cross-validation assessment.

In order to validate the location and form of a sargasso raft, it is necessary to fly over an area known to be covered by a Landsat 8 scene, to find a sargasso raft at the same time that the satellite will acquire the image, so the location and the form of the raft is not significantly altered. It is also crucial that there is no cloud between the raft and the satellite at the time the image is acquired.

Therefore, a flight was planned, at a maximum height of about 300 m, to coincide with the passing of the Landsat 8 OLI satellite on 13 July 2018. Sargasso rafts in the northern Mexican Caribbean were photographed from the air at around 11:00 a.m. (CST) corresponding with the approximate time of passage of the satellite, and the geographic coordinates of the raft photos were recorded. We built a multi-index composite (FAI, NDVI, SAVI) of the Landsat 8 OLI satellite image for that day, following Cuevas et al. (2018), and visually validated the presumed sargasso aggregations in the satellite product with the aerial photographs. To complement the verification using Landsat 8 OLI in sargasso detection at different spatial scales and methods, we overlaid the areas of detected sargasso using MODIS (Wang and Hu, 2016) and Landsat 8 imagery (Cuevas et al., 2018).

For this comparison, we selected some clear cases that had occurred on a date when the two images had the least possible time difference (~2 h). The georeferenced images were added to the software QGIS for image compositions. Both detection approaches were based on the “red-edge” spectral feature of the sargasso, and the MODIS image were processed based on thresholds of the alternative floating algae index (AFAI) (Wang and Hu, 2016).

Local beached sargasso dynamics

The possible relationship between the wrack beaching and near-shore oceanographic features were evaluated at the Puerto Morelos reef lagoon, in the north of the Mexican Caribbean (Figure 4A, see also Figure 3). The daily accumulation of sargasso was estimated using data from a coastal video monitoring station located at the Reef Systems Academic Unit (*Unidad Académica de Sistemas Arrecifales*, UASA) of the

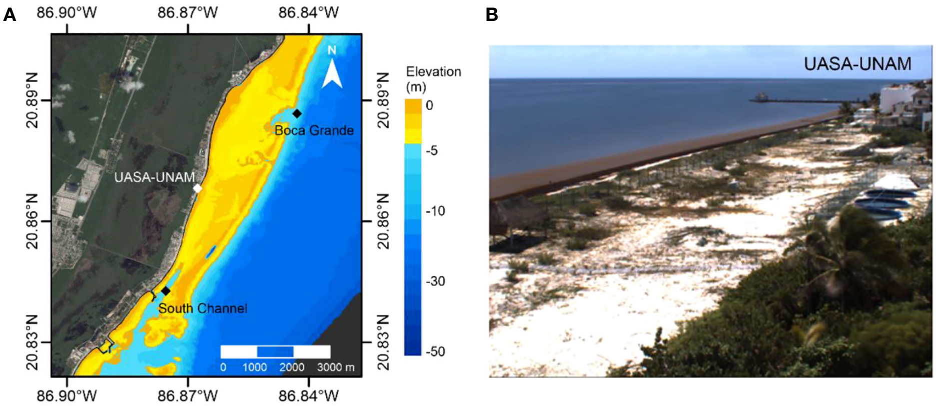

FIGURE 4
(A) Puerto Morelos reef lagoon, adapted from Parra et al. (2015). This map also shows the domain of the numerical model (see Figure 3). **(B)** Targeted beach section of ~210 m, of the fixed video monitoring.

National Autonomous University of Mexico (*Universidad Nacional Autónoma de México*, UNAM) (Figure 4B). Image analysis techniques were used to evaluate the cover of beached plant material (mainly sargasso). This information was integrated in datasets to evaluate the arrival and departure of sargasso and wind, waves, or tides.

Time average images (timex) were calculated with video images that were captured at 3.75 frames per second, for 10 min, every 0.5 h, from September to December 2015. The sargasso coverage was calculated on the beach section of approximately 210 × 21 m. Detection of sargasso on the beach was performed using segmentation techniques and the optimal thresholding methodology (Otsu, 1979). The analysis was systematized through a series of routines to process the images, where the colour scale of the area was transformed from RGB (red–green–blue) to HSV (hue–saturation–value), to improve detection and better solve colour variations of the sargasso caused by daylight changes and the degradation of the algae. The segmentation of the area covered by sargasso was done by optimal thresholding, and the sargasso coverage polygons were estimated and transformed to geographic coordinates using georeferenced control points following Simarro et al. (2017) and Rutten et al. (2021), showing that this kind of analysis provides a very valuable insight on the dynamics (arrival and separation) of onshore sargasso.

The correlation between sargasso cover with wind, wave, and tidal data was evaluated using daily average offshore wind and offshore wave power calculated from ERA5 data for Puerto Morelos (N1: 21°N 86.5°W). The direction corresponds to where the waves and wind come from and is relative to the geographic location of the north pole. The local wind and tide data were obtained at a frequency of 60 s from the records of the Meteorological and Oceanographic Academic Service (*Servicio Académico de Monitoreo Meteorológico y Oceanográfico*, SAMMO) of UNAM in Puerto Morelos. Finally, the offshore significant wave height (Hs_{off}) was taken from NOAA buoy 42056 (19°55′6″N, 84°56′18″W) in the Yucatan Basin. To estimate the significant wave height inside the lagoon, Hs_{lag}, the following transfer function was used.

$$Hs_{lag} = \sqrt{Hs_{off}/10} \tag{1}$$

To link the video-derived observations with the forcing variables responsible for sargasso movement, a numerical model was implemented (see map in Figure 4A). The sargasso dynamics inside the reef lagoon were simulated by reducing the process to two basic stages: “inflow” and “outflow.” The Delft3D model was implemented in 2D mode with a grid resolution of 50 m, which was forced with the observations of wind, tides and waves obtained from the measured conditions described above. The model was able to reproduce the general circulation of the lagoon, as reported in Coronado et al. (2007).

Sargasso inflow into the model domain was simulated using the “discharges” feature of the hydrodynamic module of Delft3D-FLOW. This works like a dye, with a given concentration and discharge rate that spreads through the modelling area at a specific time, following the hydrodynamics resulting from the flow–wave coupling. Every “sargasso discharge” had a concentration of 84 kg/m^3 and a constant discharge rate of 0.01 m^3/s for a simulation period of 7 days. This concentration gave a visualization of the dispersion.

From inspection of the video-derived sargasso coverage and the measured met-ocean data, the “inflow” scenario was implemented with mild winds of 3.5 m/s, and low-energy wave conditions, Hs_{off} = 0.3 m, Tp = 6 s, from the dominant direction (SE, 135° according to the Nautical convention). The “separation” scenario consisted of exacerbated hydrodynamic conditions with Hs_{off} = 1.0 m, Tp = 10 s, and a direction of 135°.

In this scenario, two conditions were considered, one assuming a continuous inflow of sargasso from offshore (4 additional days of the simulation, 11 days in total) and the second with sargasso inflow for only the first days of the simulation, assuming a subsequent absence of offshore sargasso.

Beach cast dynamics

Since 2015, when the first massive sargasso beach casting occurred, many owners of land on the beach front have undertaken beach cleaning actions. A few have kept a systematic log of the volume of sargasso collected every day or, at least, the accumulated monthly volumes. These data have given us key temporal patterns at a very fine spatial resolution, at the local scale (<10 km), and are considered a direct sample of the proportion of casted sargasso.

Two hotels in Puerto Morelos, Now Jade and Moon Palace, contributed data on collected vegetation volumes from their beach cleaning for a combined distance of 3 km, for 2015 to 2020. The main aim of the beach cleaning in front of resorts is to have a comfortable, visually attractive, and smell-free beach. Therefore, the beached sargasso on the Moon Palace property is collected, mostly mechanically, and a detailed composition of the collected matter is not possible. Nevertheless, the log books of the collected sargasso include a qualitative indicator of what was the dominant material (seagrass or sargasso), so it contributes to the interpretation of the long-term sargasso beaching in this locality.

The time-series analysis of these data was done bimonthly, to standardize both data sources and make them comparable to satellite detected sargasso cover in time steps. We identified the spatiotemporal coincidences and divergences between the patterns of satellite-detected sargasso inside a 20-km in-water strip and the sargasso collected on the beach at Puerto Morelos, similar to Trinanes et al. (2021). The oceanic and atmospheric conditions were taken into account to analyse the temporal patterns. This comparison gives a better understanding of the association between the sargasso detected in the open sea and the coasting volumes, and volumes collected on the beach, in order to establish an indicative reference for sargasso influxes in the context of regional-scale systematic detection.

Results

Structured spatiotemporal patterns at different spatial and temporal scales were seen in the sargasso influx occurring along the Mexican Caribbean.

Regional-scale, high-resolution satellite detections

This systematic time series of medium-to-high spatial-resolution satellite detected sargasso coverage data from 2014 to 2020 for the Western Caribbean Sea. The observations start a year before the massive sargasso arrivals became recurrent, setting a baseline. The minimum coverage values were recorded from July to November of 2014, from March 2016 to December 2017, and then from October 2019 to May 2020. The highest sargasso coverage at sea was detected from the summer of 2018 to May 2019. In 2019, three peaks were detected: in January, April, and August, with minimum values in the period October 2019 to May 2020, close to zero, which meant 140 times less satellite detected sargasso than in the previous year. For 2020, there was a very clear summer peak (June–August), slightly more than half that of the historical maximum (≈160 km^2) (Figure 5A).

Even though the maximum medians occur in summer (Figure 5B), there is great variability throughout the year, meaning that medium to high sargasso coverage is possible in any month. This was the case for the sargasso peaks detected in December 2018 and January 2019, which were almost as high as the peak of September 2018. Excluding the summer months, April has the most variability in sargasso coverage, as it usually has low sargasso volumes, but in 2018 and 2019 there were large areas covered by the algae. Variability was also high in January and February, the former to a lesser degree but with the highest median of both.

Autocorrelation analysis through the autocovariance function shows that the coverage of sargasso in 1 month is significantly correlated with the sargasso in lags of 1 to 4 months (coefficient > 0.2; p< 0.05), with lag = 4 higher than the although the correlation of lag = 4 is higher than the second and third lags (Supplementary 3; Figure 1).

The accumulated sargasso coverage varied significantly between regions in the Mexican Caribbean (H = 36.04, N = 24, p = 0.0001). The near-shore segments tended to have higher sargasso coverage and recurrence than areas offshore. The segments in the north and centre, 04 (Akumal), 02 (Puerto Morelos), and 03 (Playa del Carmen), had the highest cumulative sargasso coverage during the analysis period (Figure 6C). In these segments, some hexagons had over 40-km^2 coverage.

Based on the categories of cumulative sargasso coverage (Figure 6C; Table 1) segment 04, central-northern Tulum and southern Solidaridad municipalities, had the largest proportion of very high and high cumulative areas, totalling almost 75%, with 25% of the area having moderate and low accumulated coverage (Figure 6A). In segments 02 and 03, about 50% of the area had very high and high sargasso coverage.

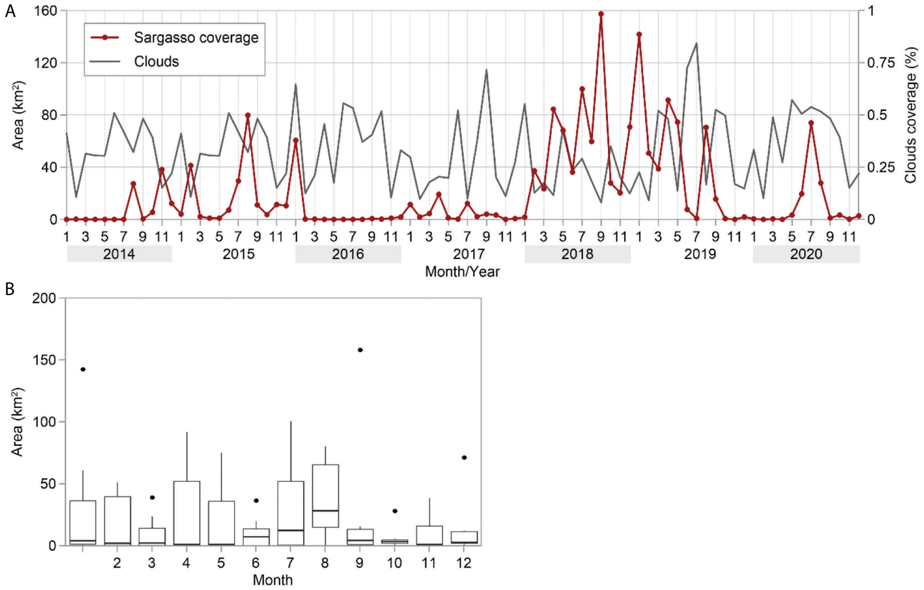

FIGURE 5
(A) Coverage of satellite-detected sargasso in the Mexican Caribbean, 2014 2020, and cloud coverage. **(B)** Area covered by sargasso each month. Rectangles represent the first and third quartiles, the middle line represents the median, the upper whisker represents maximum values, and black dots are outliers.

The lowest cumulative sargasso coverages per segment were recorded in the south of the study area (segments 08, 10, and 11), with less than 25% of area covered with very high and high cumulative sargasso coverage, although segment 09 (Mahahual) had very high accumulations in more areas than in the adjacent segments. It is important to notice that this study did not cover all of the in-water area of segments 9–11, so their values may be underestimated. However, different patterns are not expected, as only a very small part was not accounted for (Figures 6A, B).

Most of the segments have an area of high cumulative coverage, less than 10 km from shore. There were a few exceptions, such as at the entrance to the Cozumel channel, where a strip of areas with more than 40 km^2 of accumulated sargasso was detected, but this was the only segment where the whole polygon had a high cumulative coverage (Figure 6A) and the only one to have a strip of over 20 km of high coverage. Segment 01 (Benito Juarez) also has a different spatial pattern, with large amounts of sargasso in a shore-divergent strip and a small amount of accumulated sargasso on the north shore.

Sargasso was detected in at least 8 months (10% of the time series) on almost all of the coast, with >17% recurrence (14 months) in the area in front of Puerto Morelos and Tulum (segments 02 and 04), as well as part of the Felipe Carrillo Puerto coast (segments 06 and 07) (Figure 6D; Table 1). Almost 75% of the segments were covered by the classes high and very high recurrence (Figure 6D). Nevertheless, in segments 02 (Puerto Morelos) and 06 (Ascension) very high recurrences were recorded, as in segment 04 (≈45% of very high–high categories). The segment with the least cumulative sargasso coverage and recurrence was segment 11, followed by its northern neighbour, segment 10, although the underestimation here must be considered (Figure 6D).

In the open sea, high cumulative sargasso coverages were recorded along disperse and intricate sargasso streams (Figure 6A), where recurrence values were mostly less than 7 (months), although north of Cozumel island in the central eastern area, the sargasso was found more frequently (Figure 6B). In the central eastern area, the sargasso was more frequent (four to seven times, i.e., 5% to 8% of the time) than the southwest and in the north of segment 15 (Marine area) (Figures 6B, D). It is also important to notice that high recurrence values were recorded (8—over 14 times) north of Cozumel island, similar to those in the coastal fringe.

Combining the accumulated coverage and recurrence values of sargasso (Table 1; Figure 7), segments with frequent and high coverages of sargasso are found, mainly segments 01 to 06. Off Puerto Morelos (the north of segment 02 and south of segment 01), and in the inlet of Ascension Bay (06, Ascension), these extreme sargasso patterns have a well-defined spatial configuration (Supplementary 3; Figure 2). Classification also showed areas with frequent, intense events, particularly in segment 04 (Akumal).

The seasonal dynamics of sargasso coverage in the coastal segments, with maxima in the summer, are influenced by the dominant winds, ≤0.2 kW/m^2 (≤6.9 m/s), coming from the east/

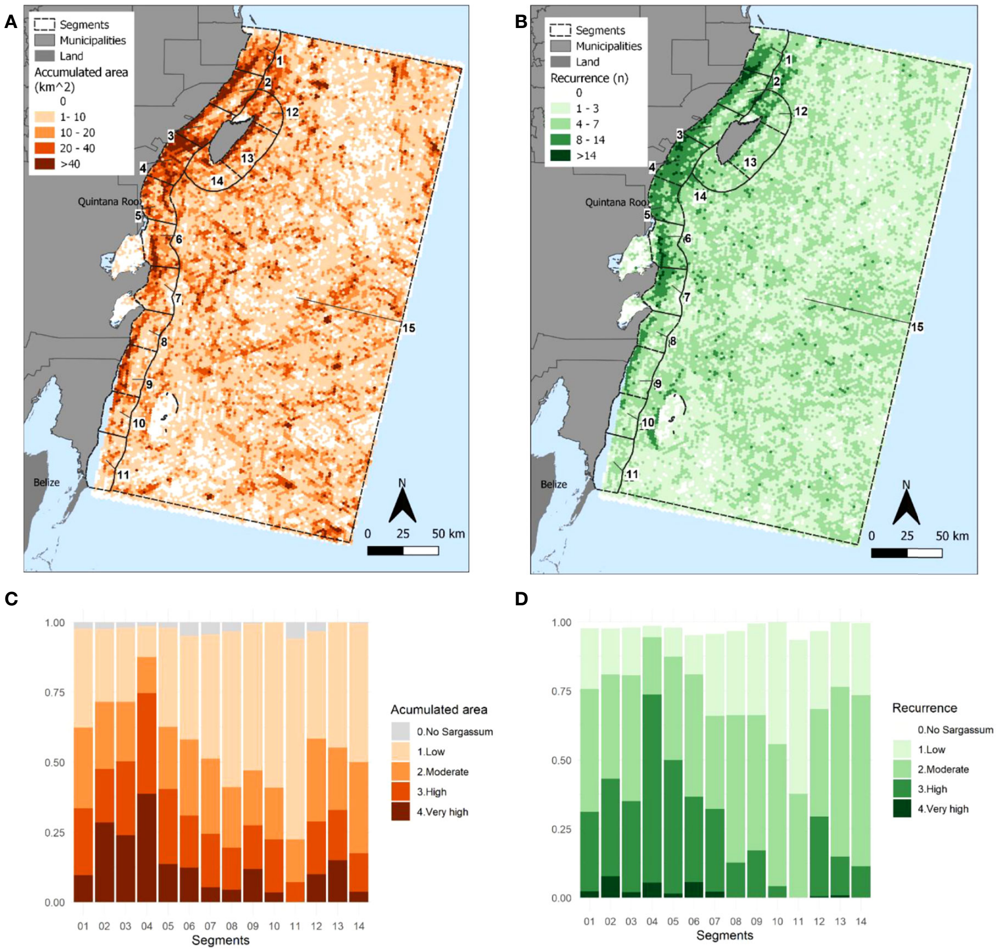

FIGURE 6
Sargasso coverage (2014–2020) off the Mexican Caribbean coast; the numbered areas are coastal segments ≈30 km long. **(A)** Accumulated area, **(B)** recurrence, **(C)** categories of accumulated area of sargasso in the coastal segments, and **(D)** categories recurrence of sargasso per coastal segment.

east–southeast (67.5°–112.5°) and which are stronger in the south (nodes 5–8) (Figure 7C). In spring, frequent and intense events were also quite common, as high as summer values in segment 04 (Akumal) (Supplementary 3; Figure 3). The strong influence of more powerful winds >0.2–0.4 kW/m^2 (>6.9–8.7 m/s) from east/southeast–east (90°–135°) was also observed in spring.

In winter (Figure 7B), sargasso was seen less frequently and with lower coverage in most of the segments, with only a few areas in the extreme category (very high recurrence and coverage), south of Tulum (segments 5–7), where similar or even larger areas had more frequent and intense sargasso coverage than in summer. Areas without sargasso were observed in segments 01–04 and 12–14, increasing from ≈25% of the area in summer, to more than 50% in the winter, including areas very close to the shore, a change that occurred to a lesser degree in segments 05–08. This can be explained by the high variability in wind direction in winter, from 67.5° to 135°, with prevailing wind power of 0.2–0.4 kW/m^2, commonly reaching >0.4–0.6 kW/m^2 and even >0.6–0.8 kW/m^2 (Figure 7D).

There were intense episodes (Table 1), however, all along the coastline. The spatial pattern of these intense episodes differs from those of the summer, in the open sea mainly but also around Cozumel Island (segments 12–14), Puerto Morelos, and Solidaridad.

Cross-validation of satellite-detected sargasso and beached sargasso

On 13 July 2018, from 9 a.m. to 12 p.m. (local time), we flew over an area covered by the Landsat scene path 018, row 045, spanning the satellite acquisition time of around 11 a.m. We took over 800 geolocalized photographs of sargasso rafts, from the Cancun to the open sea. A subset of well-consolidated sargasso rafts that were observed from the plane at approximately 11 a.m., in a cloud-free area, was chosen to

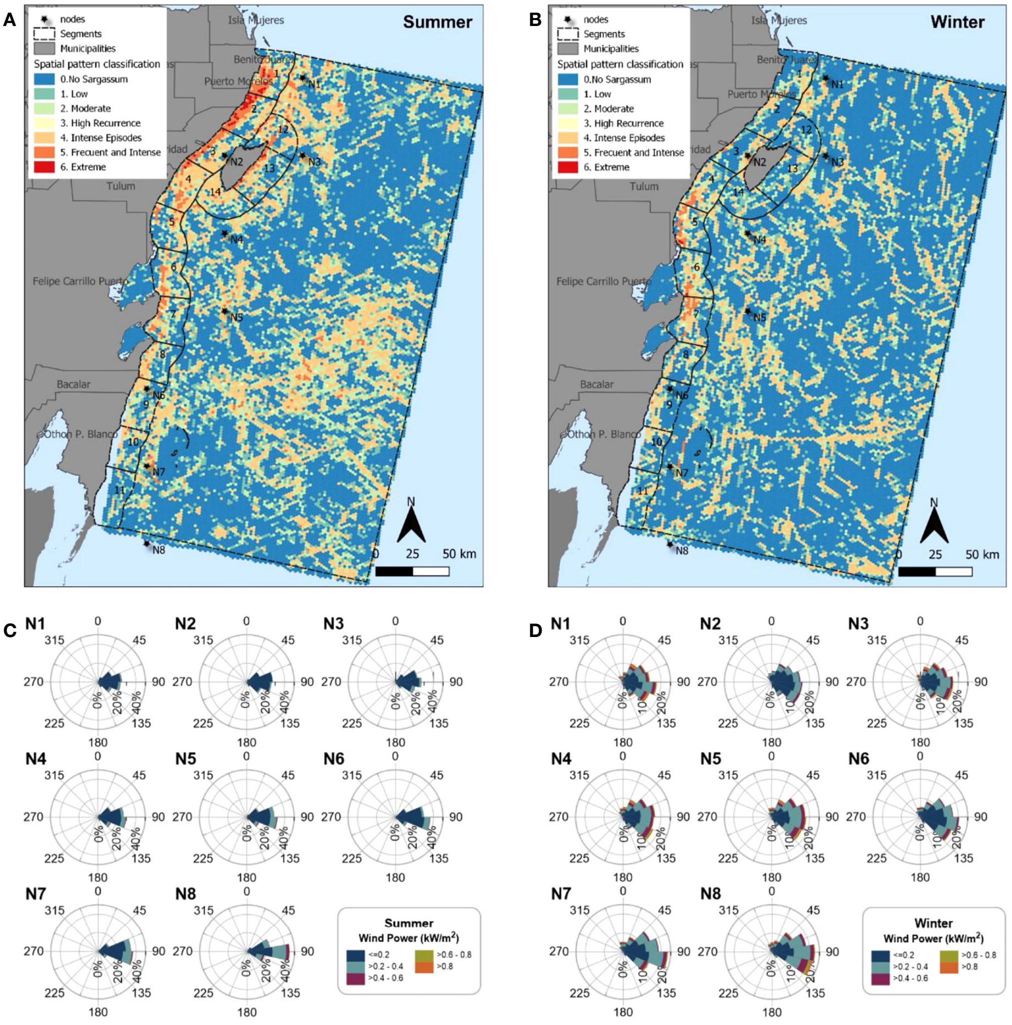

FIGURE 7

Spatial sargasso pattern classifications for **(A)** summer and **(B)** winter. The black stars show the nodes where climate data were recorded. Wind power charts for 2014–2021 in **(C)** summer and **(D)** winter.

compare with the sargasso multi-index of this site. The selected rafts were positively detected in the satellite image (Figure 8), and the spectral features of the objects detected as sargasso in the Landsat 8 images were radiometrically similar to the sargasso rafts photographed from the plane. The third largest area of sargasso detected in this study (Figure 5A), and one of the largest sargasso volumes collected from the beach (see Section 3.3), coincided with the date of the aerial observations.

Local beached sargasso dynamics-video images

Analysis of 1,019 images of the 210-m beach section, September to December 2015, showed that the largest accumulation of beach-cast vegetation (mostly sargasso) along the beach (area ~4,200 m^2) was in September, covering an area of ≈1,600 m^2 (Figure 9). This area subsequently decreased, to less than 400 m^2, by late October.

Although the amount of beach wrack varied daily, a pattern between the oceanographic parameters and wrack coverage was observed in this period (Figure 10). When there was over 500-m^2 wrack coverage on the beach for more than 3 days, the average wind speed was<4 m/s, Hs_{lag} ≤0.3 m, and tidal range ≤0.25 m, conditions favourable to arrival. This occurred eight times in the study period (red boxes in Figure 10), with September being the month with most wrack coverage. These low-energy conditions, with gentle winds, low *Hs*, and neap tides, are typical summer conditions in the region; this is the season when the massive arrivals of sargasso have occurred most often in the last 5 years.

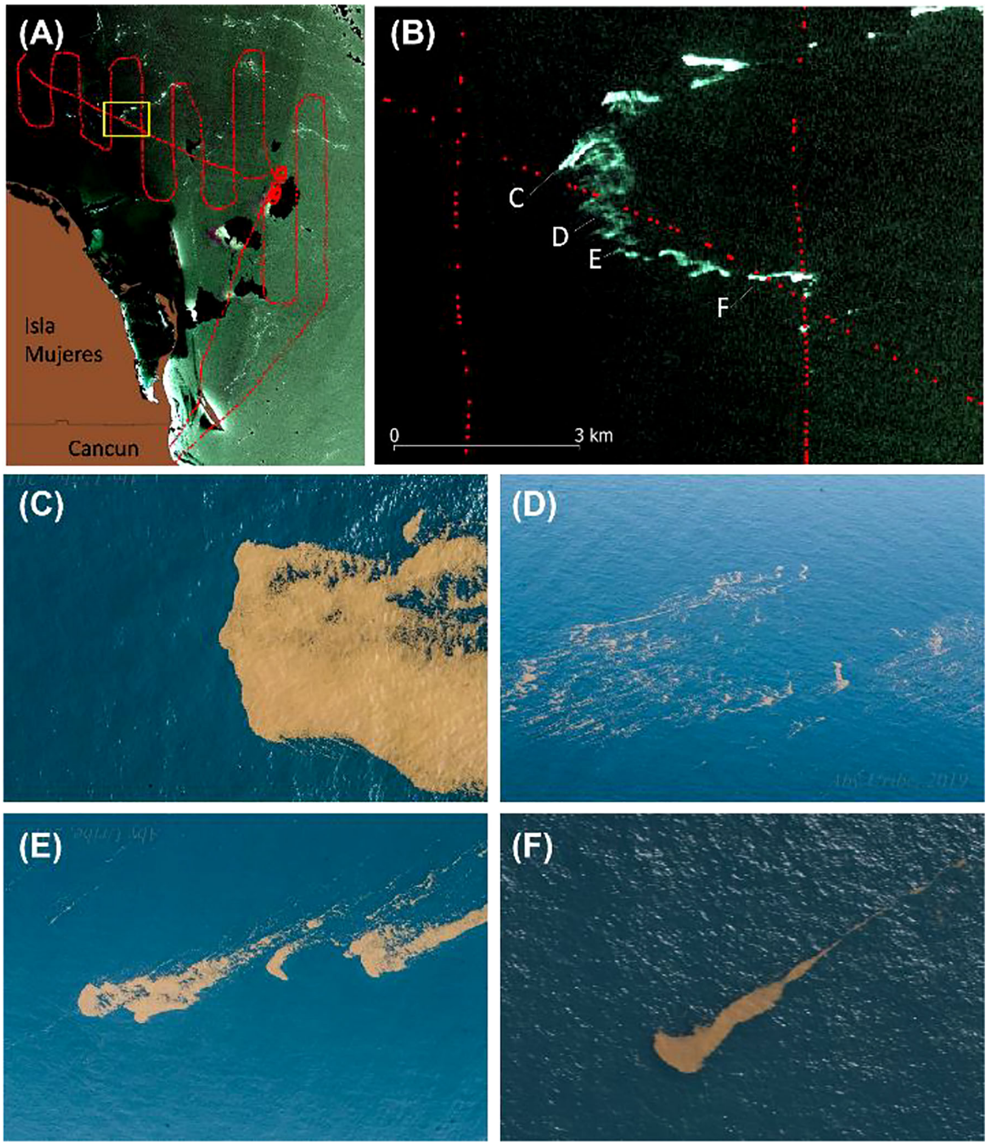

FIGURE 8
(A) A multi-index composite of a Landsat 8 OLI satellite image and aerial photographs of the same sargasso rafts, from 13 July 2018. **(B)** Close-up of the area observed at the time of the image acquisition (11:06 a.m.). Red dots show the photograph locations, and the white to light green shows the sargasso multi-index detection; **(C–F)**, aerial photographs of sargasso rafts photographed at approximately the time the satellite passed overhead.

Wrack event separation (natural removal), shown by green boxes in Figure 10, was seen when wrack coverage was less than 160 m^2 for 2 or 3 consecutive days and was related to high-energy conditions—wind speeds over 10 m/s and $Hs_{lag} > 0.4$ m in the reef lagoon. These high-intensity sporadic events activate the circulation in the reef lagoon, reducing the residence time of the wrack and favouring its movement towards the open sea. The resuspension of beached wrack is induced by spring tides and waves, which create a wide swash zone where the wrack is pushed offshore into the reef lagoon, and its eventual exit.

These results were partly confirmed by hydrodynamic modelling. The arrival scenario (Figure 11A) of low-energy winds and waves showed cross-reef (onshore) transport of the dye through the reef tops, with a maximum velocity of 0.01 m/s. Two major pathways were observed, in the north and south of the lagoon, and the interaction caused great accumulations in the central part of the lagoon. In this scenario, by day 2 of the simulation, there are inflows from both offshore sources. Day 3 shows the lagoon partially covered with sargasso, and by day 7 the lagoon is completely covered (see Figure 11A). Even though

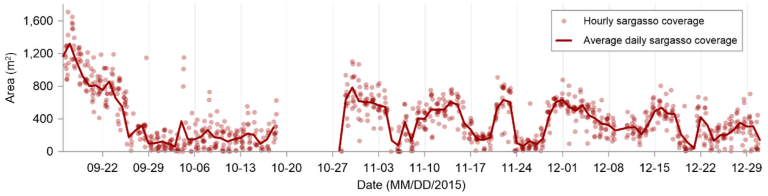

FIGURE 9
Time series of the coverage of beach-cast vegetation (mostly sargasso) for the beach section studied, at Puerto Morelos, September–December, 2015. There are no data in mid-October due to camera failure.

it is known that sargasso arrives as patches or strands, the discharge feature does not permit modification of the shape of the discharge (dye) as it spreads through the area. Therefore, as an approximation of the dynamics of sargasso inside the lagoon, it was assumed that the lagoon was fully covered with the algae.

On the other hand, in the separation scenario, with more dynamic hydrodynamic conditions, the main outflow is through the main discontinuities of the reef (mouths), to the south and northeast of the lagoon. Figure 11B shows the first separation scenario: 4 days of inflow and then a stop. On day 1, the lagoon is fully covered, especially in the north and centre (light green). Then, also on day 1, the outflow starts through the reef openings (southern and northeast regions). On day 2, the north is completely free of dye, and there is only a minor accumulation in the south. Finally, on day 3, the lagoon outflow is complete, sargasso-free, showing that the high-energy conditions can clear the lagoon of sargasso.

However, this is not always the case: sometimes the sargasso arrivals are constant and accumulation continues, mainly in the north and in zones of flow convergence, despite high-energy conditions. Figure 11C shows that on day 1 of the second separation scenario, with high-energy conditions and a constant inflow, sargasso rafts occurred throughout the reef lagoon. On day 2, an outflow of sargasso through the mouths is observed. The northern region seems to clear, but by day 5 of the simulation, sargasso rafts are present everywhere again, until the end of the simulation. On day 10, only the central region was clear and there were two main concentrations of sargasso, in the north and south of the lagoon.

The simulations only give an approximation of the dynamics of drifting wrack (sargasso) within the lagoon, since the dye concentrations do not behave in exactly the same way as the sargasso rafts, although it helps to understand the potential cover of the algae and its dispersion.

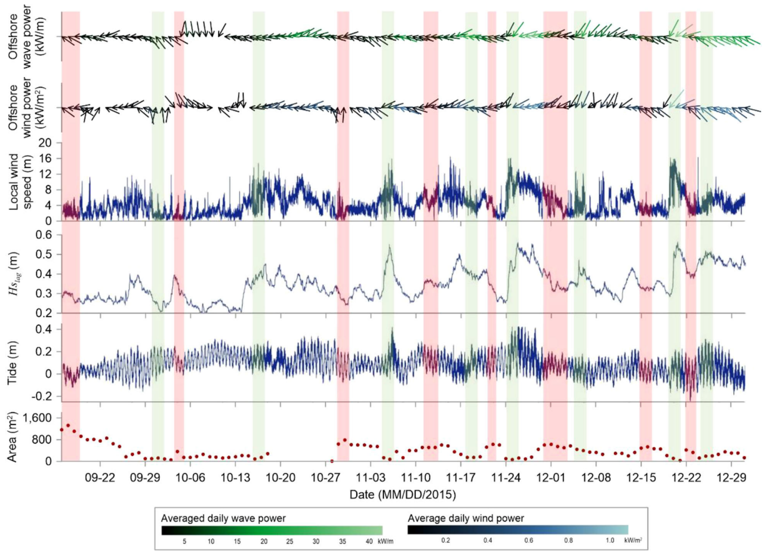

FIGURE 10
Time series of oceanographic variables and wrack coverage for the beach at Puerto Morelos, September–December, 2015. The red boxes show arrival events, and the green boxes separation events.

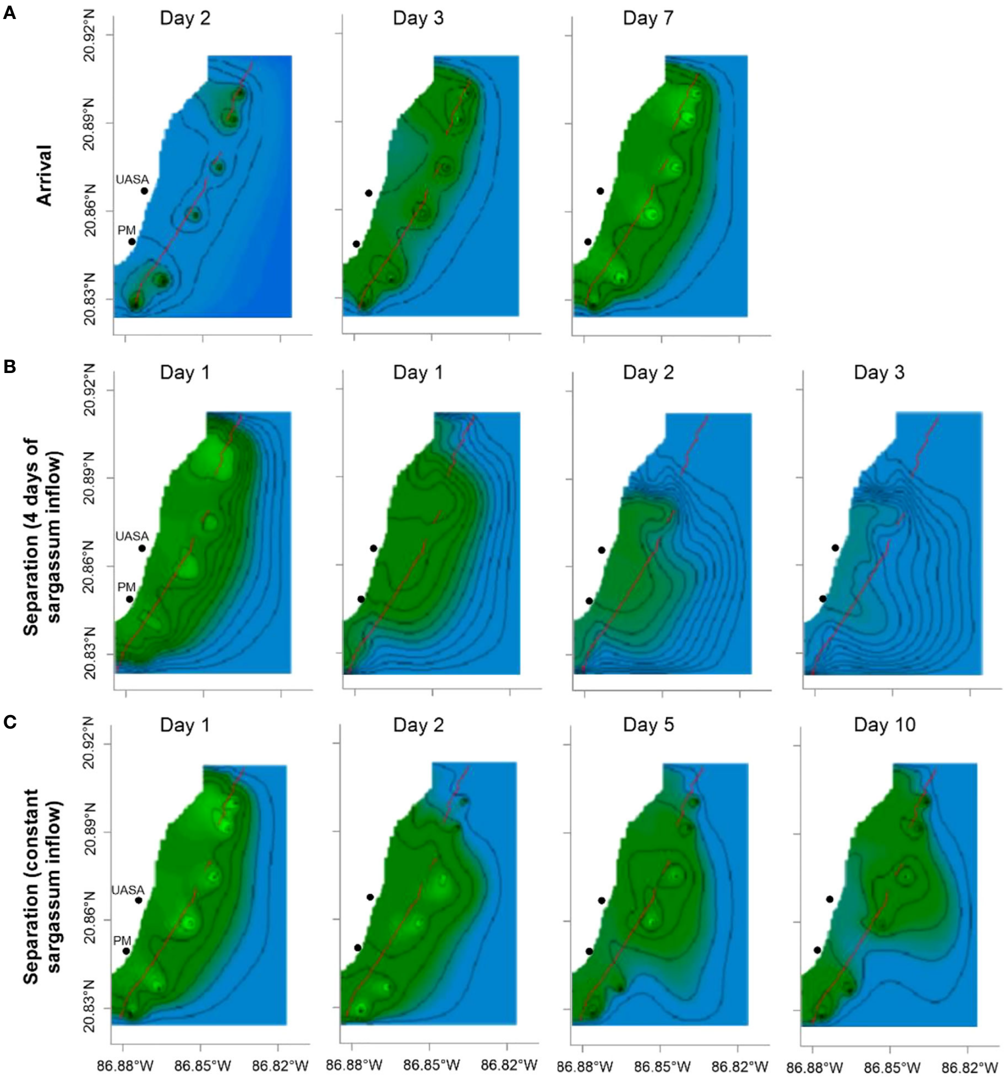

FIGURE 11
Concentrations of drifting rafts obtained by numerical modelling of the arrival and separation of sargasso in Puerto Morelos. Lighter (darker) green shows larger (lower) sargasso concentrations. **(A)**. Arrival scenario;**(B)** Separation scenario for 4 days of sargasso inflow. **(C)** Separation scenario with a constant inflow of sargasso. The black dots in all the panels show the location of the UASA-UNAM (top) and the town of Puerto Morelos (bottom). The red line indicates the position of the reef crest.

Beach cast dynamics

In 2019, when data were available for the beaches at both Moon Palace and Now Jade, the dynamics of the beach-cast wrack had the same pattern at both sites. The largest amounts of beach-cast wrack were collected in May and June, >10,000–>20,000 m^3/km from the Moon Palace Beach (Figure 12A). Another peak in beach cast occurred in May–June 2018, although the volume was lower (<10,000 m^3/km) (Figure 12A). Although there were marked differences showing a knowledge gap in the offshore–inshore transition (Figure 12B), the satellite-detected sargasso observed in the subarea and the beach-cast wrack at Moon Palace episodically showed similar temporal patterns throughout the period.

The beach-cast wrack at Moon Palace is mostly a combination of seagrasses with sargasso (i.e., sargasso being less abundant), followed by a mix of sargasso and seagrasses (Supplementary 3; Figure 4). A cast of pure sargasso occurs mainly in summer but also in January and to a lesser degree in December, then the influxes start in April, when a mainly sargasso collection was recorded, coinciding with the peaks in the satellite detections (see section 3.1).

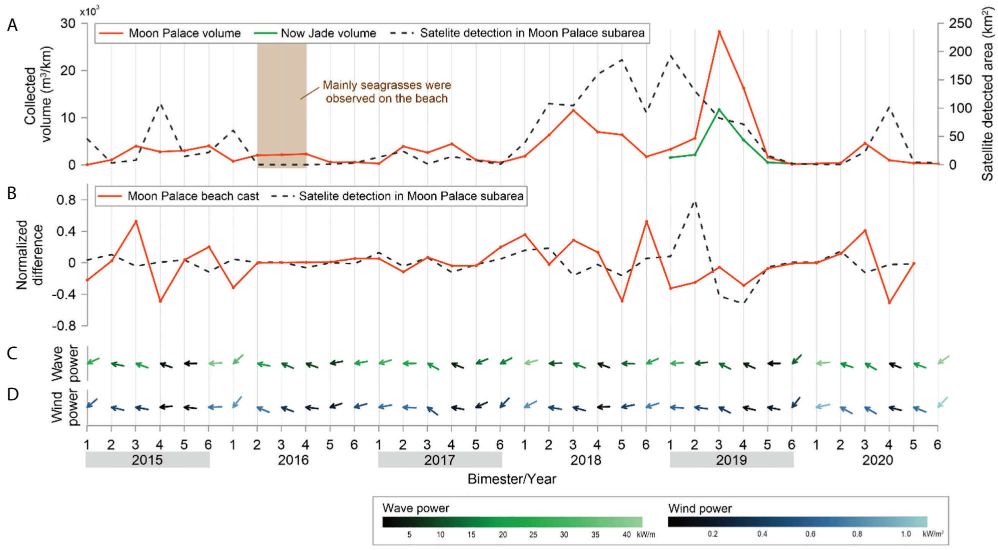

FIGURE 12
Bimonthly analysis of the beach-cast vegetation and sargasso quantification from satellite detection. **(A)** The collected wrack from the beaches at Moon Palace and Now Jade, and the satellite-detected sargasso rafts in the area adjacent to the Moon Palace (for location see Figure 3). **(B)** instantaneous normalized difference ($t_2 - t_1$) of sargasso quantification from satellite detection and data on Moon Palace collection; **(C)** bimonthly mean wave power; **(D)** bimonthly mean wind power. Both **(C, D)** were calculated for the nearest ERA5 node (N1: 21.0°N, 86.5°W) (for location see Figure 3).

For March to July 2017, discrepancies between the wrack collected from the beach and the satellite detected sargasso were observed, which may be attributable to differences in wrack composition. Logbook records indicate that in these months most wrack was seagrass. The largest discrepancies were found for the time of the highest sargasso fluxes, September–October 2018 and May–August 2019.

Discussion

While there are numerous published works on ocean-scale monitoring and forecasting sargasso spread and dynamics (Brooks et al., 2018; Putman et al., 2018; Wang et al., 2019; Trinanes et al., 2021; Wang and Hu, 2021), local and regional patterns in countries affected by sargasso in the Caribbean is limited, when such information is key for management and decision making. This is the longest (2014–2020) systematic time series of medium-to-high spatial-resolution satellite-detected sargasso coverage data for the Western Caribbean Sea to be published.

Satellite-detected sargasso is the most effective and efficient strategy for long-term monitoring (Marsh et al., 2021; Wang and Hu, 2021). There is still room for improvement in this strategy, as with any methodological approach, but as it is standardized and systematic, the spatiotemporal patterns give a robust background and a tool for decision making, management, and ecological restoration. As the ocean hydrodynamics are a key driver of sargasso distribution and dynamics (Brooks et al., 2018; Putman et al., 2020), knowledge of local and regional hydrodynamics is essential. By combining analysis of satellite images at the regional scale, with local observations on sargasso beaching, and hydrodynamic modelling, we increased our understanding of the dynamics and potential drivers of the beaching of sargasso biomass. It is also important to be able to recognise knowledge gaps in the understanding of variability closer to the coast, where the transition from oceanic to coastal dynamics occurs.

The present study offers spatial and seasonal patterns of sargasso coverage, together with wave and wind climates, to give a general panorama of the phenomenon, where atmospheric and oceanographic conditions drive sargasso distribution and beaching in different ways, depending on the spatial and temporal observation scales, as well as the location of the observations. This study did not reveal any particular area of aggregation of sargasso in open waters, although some complex shapes of cumulative coverage were detected, presumably underlining the paths of the dominant ocean currents. The spatial recurrence patterns of sargasso distribution in the open sea show no major recurrent areas, maybe because of the highly dynamic oceanic conditions. The highest cumulative sargasso coverage and the highest recurrence rates occur on the coast, mainly in the centre and north of the Mexican Caribbean. How the maritime climate drives the sargasso influx onto the beaches is still patchy, however, and is the subject of several local-scale oceanographic works.

There are several studies on the hydrodynamics of the Yucatan Current (Ochoa et al., 2001; Candela et al., 2002; Candela et al., 2003; Ochoa et al., 2005; Cetina et al., 2006), but the maritime climate at the local scale has been little studied. Carrillo et al. (2015) studied the coastal circulation off the Mesoamerican Barrier Reef System, including the Mexican Caribbean, and described the influence of the Cayman Current on the Yucatan and other local currents. This depends on the latitude where the former encounters the Mexican Caribbean continental shelf.

The Cozumel island splits the Yucatan Current into two, while its western shore lies in the highly dynamic Ascencion-Cozumel Coastal Eddy (Carrillo et al., 2015) and the eastern shore has oceanic regimes more similar to the Yucatan Current, with stronger and more focused flows (Chávez et al., 2003; Ochoa et al., 2005; Athié et al., 2011; Alcérreca-Huerta et al., 2019) that induce on each side of the island a specific sargasso spatial configuration. In the present work, the area south of the Cozumel island was seen to have the highest cumulative satellite-detected sargasso coverage at sea (Figures 6A, B), presumably because of the slowing in the speed of the current in this area. North of Cozumel, where the Yucatan Current is fully developed (current speeds of approximately 1 m/s), sargasso is transported by more steady currents, inducing differences in the accumulations on the east and west shores of Cozumel.

Sargasso can be found in the Western Caribbean in all months, with increased coverage and recurrence in the summer, when the impact on the coasts was severe, mainly in the north of Quintana Roo (van Tussenbroek et al., 2017; Casas-Beltrán et al., 2020; Chávez et al., 2020; Rodríguez-Muñoz et al., 2021). Despite this clear seasonal pattern, intense episodes are seen all along the coast in fall and winter, except on the western side of the Cozumel Channel. The numerical modelling of the Puerto Morelos lagoon showed that sargasso cast is more likely to occur in summer due to lower wave energy, while in winter there are stronger energy pulses with higher magnitudes and a northeastern wind direction. Onshore sargasso dynamics had already been described before for Puerto Morelos by Garcia-Sanchez et al. (2020) and Rutten et al. (2021) who reported similar interannual variability in the influx to that reported in this work, although over shorter observation periods. Rutten et al. (2021) reported that the greatest sargasso beachings were in 2018 and 2019 and that 2016 was a mild year; this pattern is mostly consistent with the sargasso coverage time series reported, although in 2020 offshore sargasso coverages are comparable to those of 2019 (Figure 5).

The higher onshore accumulation of sargasso biomass in the summer months can be explained by various factors. In summer (July–September), the greatest and most frequent sargasso coverage occurs offshore, coinciding with onshore beaching events. The greatest sargasso coverages close to shore were found in calm maritime conditions (≤0.2-kW/m^2 winds), with the dominant winds coming from east/east–southeast (Rutten et al., 2021; this study). However, when oceanographic conditions are more variable, there are notable differences between sargasso available at sea and the wrack cast. The smallest sargasso coverage and beaching events in winter are related with the most variable wind direction recorded, as well as the most powerful winds and waves in the region (Figures 12C, D). These rough atmospheric and maritime conditions could break up the sargasso rafts and put them below the detectable threshold for Landsat 8 OLI imagery, as Wang and Hu (2021) suggested, and a northward offshore transport could also be the cause of the low observation of sargasso in the coastal area.

Beaching events were associated with low-energy conditions (H_s< 0.25 m, wind speed<4m/s, neap tide), and separation events occurred during high-energy conditions (H_s > 0.4 m, wind speed = 8 m/s, spring tide), with a great accumulation in the middle of the lagoon at Puerto Morelos during arrival events. During separation events, the main outflow of sargasso is the main opening in the reef, to the centre and south of the lagoon. A considerable sargasso biomass remain in the lagoon, if the rafts continue to arrive, and only when the wrack input ceases the energetic hydrodynamic conditions flush out the wrack from the lagoon, over a period of days. However, flushing during higher-energy events also pushes part of the wrack up to the beach dune or drives it partially offshore where it settles on the lagoon floor, especially when it is already in a partially decomposed state (Rutten et al., 2021).

The greatest sargasso coverage has tended to be in the northern Mexican Caribbean, an area of major tourism. Some places here, such as Cancun, depend on tourism almost entirely for their income and local employment (World Travel and Tourism Council, https://wttc.org/Research/Economic-Impact/Cities); management of the sargasso influx is vital if tourists are to keep visiting. While evidence shows a decrease in profits over vacation periods of -3% to -8%, there was a general increase in revenue (0.4%–2.3%) in the region, prior to COVID-19, suggesting that the negative impact had not been devastating until then. Maybe the sargasso was not a relevant factor in touristic demand or perhaps management strategies to contain the phenomena have been successful locally (Espinosa and Li-Ng, 2020).

The information provided here can be used by the tourism industry and decision makers to plan and prioritize their monitoring, recollecting, and restoration efforts and also to allow them to be prepared for anomalous arrivals of sargasso at any time in the year, correcting strict assumptions regarding temporal or other patterns, due to the high variability of the sargasso distribution in the Western Caribbean.

Final remarks

In the present work, the spatial and temporal patterns of sargasso coverage at different scales were studied, together with wave and wind climates, to give a general panorama of the phenomenon, where such atmospheric and oceanographic conditions drive sargasso distribution and beaching in different ways. These findings reinforce the need for ongoing work in accurately detecting sargasso, using freely available satellite data (Cuevas et al., 2018). These data were used in this work not just as a monitoring system, but to better understanding the situation, as a fundamental step in managing sargasso accumulations, nearshore and onshore. The on-site planning and operation of sargasso deflection, collection, and management are complex tasks that depend on a multifactorial context that must respond to changes in the atmospheric and oceanographic conditions.

The spatiotemporal patterns presented in this study contribute to understand sargasso dynamics. They offer additional robust reference information for the recent acquis in regional knowledge that is providing the basis for public policy makers tasked with developing technical guidelines for the crises caused by the sargasso influxes in the Mexican Caribbean.

Even though seasonal and spatial patterns were noted, high variability was observed in them. The flow of sargasso from the open sea towards the shore, and then onto the beaches, is due to complex interactions between the amount and location of the sargasso accumulations with oceanic and atmospheric conditions at different scales. Caution is therefore needed in decision making because, under certain conditions, substantial on- and offshore sargasso accumulations can be found in almost any season of the year in this region. *In situ* monitoring combined with numerical modelling should be carried out at different spatial scales; numerical assumptions can better address if field data are available, so as to understand more fully sargasso dynamics. Further fine-scale modelling is still needed for the area, in order to forecast accurately, in a resolution at hundreds of metres. Then, local authorities and other interested parties can formulate beach cleaning plans and other management actions more confidently.

Not only should building integral guidelines for sargasso management contain biological, ecological, and physical information, but also the integral analyses must include operative capabilities of the on-site operators, including harbour location, vessels' autonomy, and collecting capacity, length, and type of the different barriers, among other operative criteria. Only by integrally analysing all these multiple factors will we reach a complete system capable of emitting direct recommendations in terms of sargasso contention, collection, and management, and this more complete analysis spaces the scope of this study.

Finally, linking the dynamics of beach-cast wrack to sargasso raft coverage in the sea using satellite images showed that peak events in both generally coincide, but not always, because the wrack may consist of other material, such as seagrass. It is important to target research and management efforts to effectively count the volume of beach-cast sargasso, so that this can be more directly associated with the rafts detected at sea. Beached sargasso datasets should also be gattered systematically in other areas of the region.

The recent sargasso phenomenon has attracted the attention of the scientific community. However, the economic resources invested in research to fully understand this complex phenomenon are scarce. If we are to have more effective and efficient management of the sargasso on- and offshore, a more concerted effort must be made to monitor/record and make data public in the Caribbean region.

Data availability statement

The raw data supporting the conclusions of this article will be made available by the authors, without undue reservation.

Author contributions

Conceptualization, AU-M, VC, EC, IM-T, BT, and RS. Methodology, AU-M, DB-B, VC, EC, ML-C, IM-T, and EO. Software, AU-M, DB-B, VC, and EC. Validation, AU-M and DB-B. Formal analysis, AU-M, DB-B, VC, EC, and IM-T. Investigation, AU-M, DB-B, VC, KA, JH, EC, and BT. Resources, AU-M, DB-B, VC, EC, IM-T, ML-C, DC-R, and VC. Data curation, AU-M, DB-B, VC, and EC. Writing—original draft preparation, AU-M, DB-B, VC, KA, JH, and EC. Writing—review and editing, AU-M, DB-B, VC, KA, JH, EC, ML-C, IM-T, BT, EO, DC-R, and RS. Visualization, AU-M, DB-B, VC, and EC. Supervision, VC and RS. Project administration, AU-M, EC, CE, IM-T, and RS. Funding acquisition, AU-M, EC, ML-C, VC, IM-T, and RS. All authors contributed to the manuscript revision and read and approved the submitted version.

Funding

This research was partially funded by the Mexican Centre for Ocean Energy Innovation (CEMIE-Océano, Centro Mexicano de Innovación en Energía del Océano) CONACYT-SENER

Sustentabilidad Energética project: FSE-2014-06-249795. This research has been also partially funded by CONACyT - SENER - Hydrocarbon Fund (project 201441) as a contribution of the Gulf of Mexico Research Consortium (CIGoM). CONACYT and Universidad Nacional Autónoma de México provided financial support through projects INFR-2014-01-225561 and Proyectos Internos Instituto de Ingeniería 5341 'Implementación de estación de video monitoreo para la obtención de indicadores de vulnerabilidad a la erosión'.

Acknowledgments

We want to thank Sandra Gallegos and Jorge Trujillo for the coordination of the detection team at the Spatial Ecology and Movement Lab. We acknowledge Gonzalo Uriel Martín Ruiz and Juan Alberto Gómez Liera for technical support with the video monitoring system installation. Thanks are given to the Servicio Académico de Monitoreo Meteorológico y Oceanográfico (SAMMO) of the Academic Unit of Reef Systems Puerto Morelos (UASAPM) of the ICML of UNAM, and Edgar Escalante Mancera, Miguel Ángel Gómez Reali, and Maria Guadalupe Barba Santos, for sharing environmental information. Finally, special thanks are given to the Furgason Fellowship Program which partially supported this research.

Conflict of interest

DC-R works at the Hotelera Palace Resorts, S.A.P.I de C.V., from which sargasso collection data were used in this study.

The remaining authors declare that the research was conducted in the absence of any commercial or financial relationships that could be construed as a potential conflict of interest.

Publisher's note

Supplementary material

The Supplementary Material for this article can be found online at: https://www.frontiersin.org/articles/10.3389/fmars.2022.920339/full#supplementary-material

References

Alcérreca-Huerta, J. C., Encarnacion, J. I., Ordoñez-Sánchez, S., Callejas-Jiménez, M., Gallegos Diez Barroso, G., Allmark, M., et al. (2019). Energy yield assessment from ocean currents in the insular shelf of cozumel island. *J. Mar. Sci. Eng.* 7 (5), 147. doi: 10.3390/jmse7050147

Athié, G., Candela, J., Sheinbaum, J., Badanf, A., and Ochoa, J. (2011). Yucatan Current variability through the cozumel and Yucatan channels. *Cienc. Marinas* 37 (4a), 471–492.doi: 10.7773/cm.v37i4A.1794

Bartlett, D., and Elmer, F. (2021). The impact of sargassum inundations on the Turks and Caicos islands. *Phycology* 1 (2), 83–104. doi: 10.3390/phycology1020007

Berline, L., Ody, A., Jouanno, J., Chevalier, C., André, J.-M., Thibaut, T., et al. (2020). Hindcasting the 2017 dispersal of sargassum algae in the tropical north Atlantic. *Mar. pollut. Bull.* 158, 111431. doi: 10.1016/j.marpolbul.2020.111431

Brooks, M. T., Coles, V. J., Hood, R. R., and Gower, J. F. R. (2018). Factors controlling the seasonal distribution of pelagic sargassum. *Mar. Ecol. Prog. Ser.* 599, 1–18. doi: 10.3354/meps12646

Butler, J. N., Morris, B. F., Cadwallader, J., and Stoner, A. W. (1983). "Studies of sargassum and the sargassum community," in *Bermuda Biological station*, vol. 22. (St. George, Bermuda:Special Publication), 259.

Cabanillas-Terán, N., Hernández-Arana, H. A., Ruiz-Zárate, M.-Á., Vega-Zepeda, A., and Sanchez-Gonzalez, A. (2019). Sargassum blooms in the Caribbean alter the trophic structure of the sea urchin diadema antillarum. *PeerJ* 7, e7589. doi: 10.7717/peerj.7589

Candela, J., Sheinbaum, J., Ochoa, J., Badan, A., and Leben, R. (2002). The potential vorticity flux through the Yucatan channel and the loop current in the gulf of Mexico. *Geophysical Res. Lett.* 29 (22), 16–11-16-14. doi: 10.1029/2002GL015587

Candela, J., Tanahara, S., Crepon, M., Barnier, B., and Sheinbaum, J. (2003). Yucatan Channel flow: Observations versus CLIPPER ATL6 and MERCATOR PAM models. *J. Geophysical Research: Oceans* 108 (C12), 15/1–15/24. doi: 10.1029/2003JC001961

Carrillo, L., Johns, E., Smith, R., Lamkin, J., and Largier, J. (2015). Pathways and hydrography in the mesoamerican barrier reef system part 1: Circulation. *Continental Shelf Res.* 109, 164–176. doi: 10.1016/j.csr.2015.09.014

Casas-Beltrán, D. A., Gallaher, C. M., Hernandez Yac, E., Febles Moreno, K., Voglesonger, K., Leal-Bautista, R. M., et al. (2020). Seaweed invasion! temporal changes in beach conditions lead to increasing cenote usage and contamination in the Riviera Maya. *Sustainability* 12 (6), 1–24. doi: 10.3390/su12062474

Cetina, P., Candela, J., Sheinbaum, J., Ochoa, J., and Badan, A. (2006). Circulation along the Mexican Caribbean coast. *J. Geophysical Research: Oceans* 111 (C8), 1–19. doi: 10.1029/2005JC003056

Chávez, G., Candela, J., and Ochoa, J. (2003). Subinertial flows and transports in cozumel channel. *J. Geophysical Research: Oceans* 108 (C2), 1–11. doi: 10.1029/2002JC001456

Chávez, V., Uribe-Martínez, A., Cuevas, E., Rodríguez-Martínez, R. E., van Tussenbroek, B. I., Francisco, V., et al. (2020). Massive influx of pelagic sargassum spp. on the coasts of the Mexican Caribbean 2014–2020: Challenges and opportunities. *Water* 12 (10), 1–24. doi: 10.3390/w12102908

Congedo, L. (2021). Semi-automatic classification plugin: A Python tool for the download and processing of remote sensing images in QGIS. *J. Open Source Software* 6 (64), 3172. doi: 10.21105/joss.03172

Coronado, C., Candela, J., Iglesias-Prieto, R., Sheinbaum, J., López, M., and Ocampo-Torres, F. J. (2007). On the circulation in the Puerto morelos fringing reef lagoon. *Coral Reefs* 26 (1), 149–163. doi: 10.1007/s00338-006-0175-9

Cuevas, E., Uribe-Martínez, A., and Liceaga-Correa, M.D.L.Á. (2018). A satellite remote-sensing multi-index approach to discriminate pelagic sargassum in the waters of the Yucatan peninsula, Mexico. *Int. J. Remote Sens.* 39 (11), 3608–3627. doi: 10.1080/01431161.2018.1447162

Devault, D. A., Modestin, E., Cottereau, V., Vedie, F., Stiger-Pouvreau, V., Pierre, R., et al. (2021). The silent spring of sargassum. *Environ. Sci. pollut. Res.* 28 (13), 15580–15583. doi: 10.1007/s11356-020-12216-7

Domínguez-Tejo, E., Metternicht, G., Johnston, E., and Hedge, L. (2016). Marine spatial planning advancing the ecosystem-based approach to coastal zone management: A review. *Mar. Policy* 72, 115–130. doi: 10.1016/j.marpol.2016.06.023

El Mahrad, B., Newton, A., Icely, J. D., Kacimi, I., Abalansa, S., and Snoussi, M. (2020). Contribution of remote sensing technologies to a holistic coastal and marine environmental management framework: A review. *Remote Sens.* 12 (14), 1–47. doi: 10.3390/rs12142313

Espinosa, L. A., and Li-Ng, J. J. (2020). El Riesgo del sargazo para la economía y turismo de quintana roo y méxico. *BBVA Res.* 20 (2), 1–35

García-Sánchez, M., Graham, C., Vera, E., Escalante-Mancera, E., Alvarez-Filip, L., and Tussenbroek, B. (2020). Temporal changes in the composition and biomass of beached pelagic Sargassum species in the Mexican Caribbean. *Aquatic Botany* 167 (103275). doi: /10.1016/j.aquabot.2020.103275

Gower, J., Young, E., and King, S. (2013). Satellite images suggest a new sargassum source region in 2011. *Remote Sens. Lett.* 4 (8), 764–773. doi: 10.1080/2150704X.2013.796433

Guimarais, M., Zúñiga-Ríos, A., Cruz-Ramírez, C. J., Chávez, V., Odériz, I., van Tussenbroek, B. I., et al. (2021). The conservational state of coastal ecosystems on the Mexican Caribbean coast: Environmental guidelines for their management. *Sustainability* 13 (5), 1–24. doi: 10.3390/su13052738

Guzmán-Ramírez, A. A., Uribe-Martínez, A., García-Castro, C., and Cuevas, E. (2020). "Caracterización espacial de figuras de sargazo pelágico formadas por El viento en El canal de yucatán," in *Abstract book of the 5th conference on aquatic resources of the gulf of Mexico and Caribbean sea. ciudad del Carmen, Mexico, November 27th – 29th* (Ciudad Del Carmen, Mexico: Universidad Autónoma Del Carmen-CONACYT).

Hardy, R. F., Hu, C., Witherington, B., Lapointe, B., Meylan, A., Peebles, E., et al. (2018). Characterizing a Sea turtle developmental habitat using landsat observations of surface-pelagic drift communities in the Eastern gulf of Mexico. *IEEE J. Selected Topics Appl. Earth Observations Remote Sens.* 11, 3646–3659. doi: 10.1109/JSTARS.2018.2863194

Hu, C., Feng, L., Hardy, R. F., and Hochberg, E. J. (2015). Spectral and spatial requirements of remote measurements of pelagic sargassum macroalgae. *Remote Sens. Environ.* 167, 229–246. doi: 10.1016/j.rse.2015.05.022

Huffard, C. L., von Thun, S., Sherman, A. D., Sealey, K., and Smith, K. L. (2014). Pelagic sargassum community change over a 40-year period: temporal and spatial variability. *Mar. Biol.* 161 (12), 2735–2751. doi: 10.1007/s00227-014-2539-y

Hu, C., Hardy, R., Ruder, E., Geggel, A., Feng, L., Powers, S., et al. (2016). Sargassum coverage in the northeastern gulf of Mexico during 2010 from landsat and airborne observations: Implications for the deepwater horizon oil spill impact assessment. *Mar. pollut. Bull.* 107 (1), 15–21. doi: 10.1016/j.marpolbul.2016.04.045

Johns, E. M., Lumpkin, R., Putman, N. F., Smith, R. H., Muller-Karger, F. E., T. Rueda-Roa, D., et al. (2020). The establishment of a pelagic sargassum population in the tropical Atlantic: Biological consequences of a basin-scale long distance dispersal event. *Prog. Oceanography* 182, 102269. doi: 10.1016/j.pocean.2020.102269

Jouanno, J., Moquet, J.-S., Berline, L., Radenac, M.-H., Santini, W., Changeux, T., et al. (2021). Evolution of the riverine nutrient export to the tropical Atlantic over the last 15 years: is there a link with sargassum proliferation? *Environ. Res. Lett.* 16 (3), 034042. doi: 10.1088/1748-9326/abe11a

Langin, K. (2018). Seaweed masses assault Caribbean islands. *Science* 360 (6394), 1157. doi: 10.1126/science.360.6394.1157

Lapointe, B. E. (1995). A comparison of nutrient-limited productivity in sargassum natans from neritic vs. oceanic waters of the western north Atlantic ocean. *Limnology Oceanography* 40 (3), 625–633. doi: 10.4319/lo.1995.40.3.0625

López-Miranda, J. L., Celis, L. B., Estévez, M., Chávez, V., Van Tussenbroek, B. I., Uribe-Martínez, A., et al. (2021). Commercial potential of pelagic sargassum spp. in Mexico. *Front. Mar. Science.* 8, 768470. doi: 10.3389/fmars.2021.7684

Mariño-Tapia, I., Silva-Casarín, C., Enriquez-Ortiz, E., Mendoza-Baldwin, E., Escalante-Mancera, F., and Ruiz-Rentería, F (2011). Wave transformation and wave-driven circulation on natural reefs under extreme hurricane conditions. *Coast. Eng. Proc.* 1 (32), 1–9. doi: 10.9753/icce.v32.waves.28

Marsh, R., Addo, K. A., Jayson-Quashigah, P.-N., Oxenford, H. A., Maxam, A., Anderson, R., et al. (2021). Seasonal predictions of holopelagic sargassum across the tropical Atlantic accounting for uncertainty in drivers and processes: The SARTRAC ensemble forecast system. *Front. Mar. Sci.* 8. doi: 10.3389/fmars.2021.722524

Maurer, A. S. (2019). Impacts of the Caribbean sargassum influx on Sea turtle nesting ecology. *In Proc. Proc. 71st Gulf Caribbean Fisheries Institute* 71, 327–329.

Maurer, A. S., Stapleton, S. P., Layman, C. A., and Burford Reiskind, M. O. (2021). The Atlantic sargassum invasion impedes beach access for nesting sea turtles. *Climate Change Ecol.* 2, 100034. doi: 10.1016/j.ecochg.2021.100034

McHenry, J., Rassweiler, A., Hernan, G., Uejio, C. K., Pau, S., Dubel, A. K., et al. (2021). Modelling the biodiversity enhancement value of seagrass beds. *Diversity Distributions* 27 (11), 2036–2049. doi: 10.1111/ddi.13379

Milledge, J. J., and Harvey, P. J. (2016). Golden tides: Problem or golden opportunity? the valorisation of sargassum from beach inundations. *J. Mar. Sci. Eng.* 4 (3), 1–19. doi: 10.3390/jmse4030060

North, M. A. (2009). "A method for implementing a statistically significant number of data classes in the jenks algorithm," in *2009 sixth international conference on fuzzy systems and knowledge discovery* (Tianjin, China: IEEE), 35–38.

Ochoa, J., Candela, J., Badan, A., and Sheinbaum, J. (2005). A geostrophic fluctuations in cozumel channel. *J. Geophysical Research: Oceans* 110 (C2), 1–16. doi: 10.1029/2004JC002408

Ochoa, J., Sheinbaum, J., Badan, A., Candela, J., and Wilson, D. (2001). Geostrophy *via* potential vorticity inversion in the Yucatan channel. *J. Mar. Res.* 59 (5), 725–747. doi: 10.1357/002224001762674917

Odériz, I., Gómez, I., Ventura, Y., Díaz, V., Escalante, A., Gómez, D. T., et al. (2020). Understanding drivers of connectivity and resilience under tropical cyclones in coastal ecosystems at Puerto morelos, Mexico. *J. Coast. Res.* 95 (sp1), 128–132. doi: 10.2112/SI95-025.1

Ogden, J. C. (2010). Marine spatial planning (MSP): a first step to ecosystem-based management (EBM) in the wider Caribbean. *Rev. Biol. Trop.* 58 Suppl 3, 71–79.

Otsu, N. (1979). A threshold selection method from Gray-level histograms. *IEEE Trans. Systems Man Cybernetics* 9 (1), 62–66. doi: 10.1109/TSMC.1979.4310076

Oxenford, H. A., Cox, S.-A., van Tussenbroek, B. I., and Desrochers, A. (2021). Challenges of turning the sargassum crisis into gold: Current constraints and implications for the Caribbean. *Phycology* 1 (1), 27–48. doi: 10.3390/phycology1010003

Parra, S. M., Valle-Levinson, A., Mariño-Tapia, I., and Enriquez, C. (2015). Salt intrusion at a submarine spring in a fringing reef lagoon. *J. Geophysical Research: Oceans* 120 (4), 2736–2750. doi: 10.1002/2014JC010459

Pendleton, L., Krowicki, F., Strosser, P., and Hallett-Murdoch, J. (2014) *The Sargasso Sea - a vital ecosystem of global importance [Online*. Available at: https://clmeplus.org/app/uploads/2020/03/Sargasso-Sea-Infographic-Valuation.jpg (Accessed July 9, 2021).

Powers, S. P., Hernandez, F. J., Condon, R. H., Drymon, J. M., and Free, C. M. (2013). Novel pathways for injury from offshore oil spills: Direct, sublethal and indirect effects of the deepwater horizon oil spill on pelagic sargassum communities. *PloS One* 8 (9), e74802. doi: 10.1371/journal.pone.0074802

Putman, N. F., Goni, G. J., Gramer, L. J., Hu, C., Johns, E. M., Trinanes, J., et al. (2018). Simulating transport pathways of pelagic sargassum from the equatorial Atlantic into the Caribbean Sea. *Prog. Oceanography* 165, 205–214. doi: 10.1016/j.pocean.2018.06.009

Putman, N. F., Lumpkin, R., Olascoaga, M. J., Trinanes, J., and Goni, G. J. (2020). Improving transport predictions of pelagic sargassum. *J. Exp. Mar. Biol. Ecol.* 529, 151398. doi: 10.1016/j.jembe.2020.151398

QGIS-Association (2021). Available at: http://www.qgis.org (Accessed January 6, 2021).

Resiere, D., Valentino, R., Nevière, R., Banydeen, R., Gueye, P., Florentin, J., et al. (2018). Sargassum seaweed on Caribbean islands: an international public health concern. *Lancet* 392 (10165), 2691. doi: 10.1016/s0140-6736(18)32777-6

Rodríguez-Martínez, R. E., van Tussenbroek, B., and Jordán-Dahlgren, E. (2016). Afluencia masiva de sargazo pelágico a la costa del caribe mexicano, (2014–2015). *Florecimientos Algales Nocivos en México. Ensenada: CICESE* 352, 352–365.

Rodríguez-Muñoz, R., Muñiz-Castillo, A. I., Euán-Avila, J. I., Hernández-Núñez, H., Valdés-Lozano, D. S., Collí-Dulá, R. C., et al. (2021). Assessing temporal dynamics on pelagic sargassum influx and its relationship with water quality parameters in the Mexican Caribbean. *Regional Stud. Mar. Sci.* 48, 102005. doi: 10.1016/j.rsma.2021.102005

Rodríguez-Martínez, R.E., Jordán-Dahlgren, E., and Hu, C. (2022). Spatiotemporal variability of pelagic Sargassum landings on the northern Mexican Caribbean. *Remote Sensing Applications: Society and Environment* 27 (100767), 2352–9385. doi: 10.1016/j.rsase.2022.100767

Rutten, J., Arriaga, J., Montoya, L. D., Mariño-Tapia, I. J., Escalante-Mancera, E., Mendoza, E. T., et al. (2021). Beaching and natural removal dynamics of pelagic sargassum in a fringing-reef lagoon. *J. Geophysical Research: Oceans* 126 (11), e2021JC017636. doi: 10.1029/2021JC017636

SAMMO (2015) *"Universidad nacional autónoma de méxico, instituto de ciencias del mar y limnología, servicio académico de monitoreo meteorológico y oceanográfico, Puerto morelos q. roo méxico*. Available at: http://www.sammo.icmyl.unam.mx.

Schell, J. M., Goodwin, D. S., and Siuda, A. N. S. (2015). Recent sargassum inundation events in the Caribbean shipboard observations reveal dominance of a previously rare form. *Oceanography* 28 (3), 8–11. doi: 10.5670/oceanog.2015.70

Shucksmith, R., Gray, L., Kelly, C., and Tweddle, J. F. (2014). Regional marine spatial planning – the data collection and mapping process. *Mar. Policy* 50, 1–9. doi: 10.1016/j.marpol.2014.05.012

Silva, R., Martínez, M. L., van Tussenbroek, B. I., Guzmán-Rodríguez, L. O., Mendoza, E., and López-Portillo, J. (2020). A framework to manage coastal squeeze. *Sustainability* 12 (24), 1–20. doi: 10.3390/su122410610

Silva, R., Mendoza, E., Mariño-Tapia, I., Martínez, M. L., and Escalante, E. (2016). An artificial reef improves coastal protection and provides a base for coral recovery. *J. Coast. Res.* 75 (10075), 467–471. doi: 10.2112/SI75-094.1

Silva, R., Oumeraci, H., Martínez, M. L., Chávez, V., Lithgow, D., van Tussenbroek, B. I., et al. (2021). Ten commandments for sustainable, safe, and W/Healthy sandy coasts facing global change. *Front. Mar. Sci.* 8 (126). doi: 10.3389/fmars.2021.616321

Simarro, G., Ribas, F., Álvarez, A., Guillén, J., Chic, Ó., and Orfila, A. (2017). ULISES: An open source code for extrinsic calibrations and planview generations in coastal video monitoring systems. *J. Coast. Res.* 33 (5), 1217–1227. doi: 10.2112/JCOASTRES-D-16-00022.1

Skliris, N., Marsh, R., Appeaning Addo, K., and Oxenford, H. (2022). Physical drivers of pelagic sargassum bloom interannual variability in the central West Atlantic over 2010–2020. *Ocean Dynamics* 72 (6), 383–404. doi: 10.1007/s10236-022-01511-1

Smetacek, V., and Zingone, A. (2013). Green and golden seaweed tides on the rise. *Nature* 504 (7478), 84–88. doi: 10.1038/nature12860

Solarin, B., Bolaji, D., Fakayode, O., and Akinnigbagbe, R. (2014). Impacts of an invasive seaweed sargassum hystrix var. fluitans (borgesen 1914) on the fisheries and other economic implications for the nigerian coastal waters. *IOSR J. Agric. Veterinary Sci.* 7 (7), 1–6. doi: 10.9790/2380-07710106

Torres-Freyermuth, A., Mariño-Tapia, C., Coronado, P., Salles, G., Medellín, A., Pedrozo-Acuña, R., et al. (2012). Wave-induced extreme water levels in the Puerto morelos fringing reef lagoon. *Natural Hazards Earth System Sci.* 12, 3765–3773. doi: 10.5194/nhess-12-3765-2012

Trinanes, J., Putman, N., Goni, G., Hu, C., and Wang, M. (2021). Monitoring pelagic sargassum inundation potential for coastal communities. *J. Operational Oceanography* 1, 1–12. doi: 10.1080/1755876X.2021.1902682

Uribe-Martínez, A., Guzmán-Ramírez, A., Arreguín-Sánchez, F., and Cuevas, E. (2020). "El Sargazo en el caribe mexicano, revisión de una historia impensable," in *Gobernanza y manejo de las costas y mares ante la incertidumbre*. Eds. E. Rivera-Arriaga, I. Azuz-Adeath, O. D. Cervantes Rosas, A. Espinoza-Tenorio, R. Silva Casarín, A. Ortega-Rubio, et al, (Campeche, Mexico: Universidad Autónoma de Campeche, RICOMAR) 743–768.

van Tussenbroek, B. I., Hernández Arana, H. A., Rodríguez-Martínez, R. E., Espinoza-Avalos, J., Canizales-Flores, H. M., González-Godoy, C. E., et al. (2017). Severe impacts of brown tides caused by sargassum spp. on near-shore Caribbean seagrass communities. *Mar. pollut. Bull.* 122 (1), 272–281. doi: 10.1016/j.marpolbul.2017.06.057

Wang, M., and Hu, C. (2016). Mapping and quantifying sargassum distribution and coverage in the central West Atlantic using MODIS observations. *Remote Sens. Environ.* 183, 350–367. doi: 10.1016/j.rse.2016.04.019

Wang, M., and Hu, C. (2017). Predicting sargassum blooms in the Caribbean Sea from MODIS observations. *Geophysical Res. Lett.* 44 (7), 3265–3273. doi: 10.1002/2017GL072932

Wang, M., and Hu, C. (2021). Satellite remote sensing of pelagic sargassum macroalgae: The power of high resolution and deep learning. *Remote Sens. Environ.* 264, 112631. doi: 10.1016/j.rse.2021.112631

Wang, M., Hu, C., Barnes, B. B., Mitchum, G., Lapointe, B., and Montoya, J. P. (2019). The great Atlantic sargassum belt. *Science* 365 (6448), 83. doi: 10.1126/science.aaw7912

Wang, M., Hu, C., Cannizzaro, J., English, D., Han, X., Naar, D., et al. (2018). Remote sensing of sargassum biomass, nutrients, and pigments. *Geophysical Res. Lett.* 45 (22), 12,359–312,367. doi: 10.1029/2018GL078858

Xing, Q., Guo, R., Wu, L., An, D., Cong, M., Qin, S., et al. (2017). High-resolution satellite observations of a new hazard of golden tides caused by floating sargassum in winter in the yellow Sea. *IEEE Geosci. Remote Sens. Lett.* 14 (10), 1815–1819. doi: 10.1109/LGRS.2017.2737079

Frontiers in Marine Science

TYPE Original Research
PUBLISHED 12 September 2022
DOI 10.3389/fmars.2022.988240

Medium-term observations of salt marsh morphodynamics

Chuang Jin[1,2], Zheng Gong[1,2]*, Lei Shi[3], Kun Zhao[1,2], Rafael O. Tinoco[4], Jorge E. San Juan[5], Liang Geng[1,2] and Giovanni Coco[6]

[1]State Key Laboratory of Hydrology-Water Resources and Hydraulic Engineering, Hohai University, Nanjing, China, [2]Jiangsu Key Laboratory of Coast Ocean Resources Development and Environment Security, Hohai University, Nanjing, China, [3]Zhejiang Institute of Hydraulic and Estuary (Zhejiang Institute of Marine Planning and Design), Hangzhou, China, [4]Department of Civil and Environmental Engineering, University of Illinois at Urbana-Champaign, Urbana, IL, United States, [5]Department of Civil, Environmental and Geo-Engineering, University of Minnesota Twin Cities, Minneapolis, MN, United States, [6]School of Environment, Faculty of Science, University of Auckland, Auckland, New Zealand

OPEN ACCESS

EDITED BY
Javier Benavente,
University of Cádiz, Spain

REVIEWED BY
Charlie Emma Louise Thompson,
University of Southampton,
United Kingdom
Gerardo M. Perillo,
CONICET Instituto Argentino de
Oceanografía (IADO), Argentina

*CORRESPONDENCE
Zheng Gong
gongzheng@hhu.edu.cn

SPECIALTY SECTION
This article was submitted to
Coastal Ocean Processes,
a section of the journal
Frontiers in Marine Science

RECEIVED 07 July 2022
ACCEPTED 24 August 2022
PUBLISHED 12 September 2022

CITATION
Jin C, Gong Z, Shi L, Zhao K,
Tinoco RO, San Juan JE, Geng L and
Coco G (2022) Medium-term
observations of salt marsh
morphodynamics.
Front. Mar. Sci. 9:988240.
doi: 10.3389/fmars.2022.988240

Salt marshes play a key role in attenuating wave energy and promoting sedimentation necessary to potentially adapt to sea level rise. The changes in the soil surface elevation, as a result of spatially and temporally varied sedimentation pattern, affect the hydrodynamics, marsh edge extension and so the sedimentation rate. Little attention has yet been paid to the medium-term sedim\entation under the influence of marsh extension. To fill this gap, we performed a 6-year (from 2012 to 2018) field observation to obtain the soil surface elevation of the cross-shore tidal flats in the center Jiangsu Coast (China). The salt marsh edge is extracted from remote sensing images using NVDI technique, which allows us to quantify the seaward extension of salt marshes. Results highlight that soil surface elevation in the salt marsh region varies spatially and temporally as a function of marsh topography, inundation frequency and distance to the salt marsh edge. The sedimentation rate reduces linearly shoreward as a result of increasing soil surface elevation in the marsh region. At the transition of salt marshes and bare flats, the sedimentation rate follows a parabolic relationship with the increase in distance to the salt marsh edge but decreases linearly at the more landward sites. The maximum sedimentation rate is initially located around the mean high-water level and moves towards the edge of the salt marsh as a result of marsh extension and increasing soil surface elevation. Our field observations reveal these medium-term marsh dynamics and provide a unique dataset for development, testing and validation of numerical simulations to enhance predictions of the overall evolution of tidal flats.

KEYWORDS

salt marsh, tidal flat, morphodynamics, sedimentation rate, field observations

1 Introduction

Tidal flats are the transition region of sea and land. They are important geomorphological and ecological systems providing habitat for aquatic species (van Eerden et al., 2005; Friedrichs, 2011), preventing coastal inundation (Möller et al., 2014), and protecting against sea level rise (Krauss et al., 2010; Webb et al., 2013; Kirwan et al., 2016). The morphology of tidal flats is continuously modulated by the interactions between hydrodynamics (e.g., tidal currents, waves, storm events), sediment supply, global climate change (i.e. storm events and sea level rise), and biological factors (e.g., salt marshes, biofilms) (Le Hir et al., 2000; D'Alpaos et al., 2007; Green and Coco, 2007; Kirwan et al., 2010; Friedrichs, 2011; Fagherazzi et al., 2012; Chen et al., 2019; Zhao et al., 2021; Jin et al., 2022). Salt marshes in front of coastal infrastructure provide important ecological services in attenuating wave and current energy, trapping sediment and accelerating sedimentation (Temmerman et al., 2003; van de Koppel et al., 2005; Anderson and Smith, 2014; Gong et al., 2017). Sedimentation in salt marshes, in turn, facilitates the further growth and extension of salt marshes, forming the so-called "biogeomorphic feedback loop" (Wang and Temmerman, 2013; Bouma et al., 2016; Schwarz et al., 2018). Increasing attention has been paid to field investigations, which focus either on the limit of the salt marsh edge controlled by a dynamic retreat behavior (Marani et al., 2011; Bendoni et al., 2016; Zhao et al., 2022) or on the survival of salt marshes under the threat of sea level (Mudd et al., 2004; Fagherazzi et al., 2012; Wang and Temmerman, 2013; Möller et al., 2014; Rogers et al., 2014; Lovelock et al., 2015; Bouma et al., 2016; Swales et al., 2016; Brückner et al., 2019). Short-term (e.g., days, months, <1 year) field work has been widely performed to investigate the hydrodynamics or the morphodynamic response to forcing conditions on tidal flats (e.g., Fan, 2010; Shi et al., 2014; Zhang et al., 2021). The impact of the seaward growth of salt marshes is usually ignored. In terms of the long-term (e.g., >10 years) morphological evolution of tidal flats, the marsh dynamics (e.g., seaward growth, sediment trapping) exert a large impact on the sedimentation and the morphological evolution in the marsh region. However, the long-term morphological evolution is usually studied using numerical simulation rather than field observations. Field investigations on sedimentation patterns over a medium-term to long-term timescale are scarce, and the association with the constant seaward extension of salt marshes remain unclear.

Past studies have revealed important features of the dynamics of salt marshes: (1) Salt marshes dampen velocities, enhance turbulence and promote sedimentation through their leaf, stem, and root networks (Nepf, 2012; Tinoco and Coco, 2018; Yang and Nepf, 2018; San Juan et al., 2019; Tinoco et al., 2020). (2) Laboratory experiments show that salt marshes can cause up to 60% of wave height reduction (Möller et al., 2014). (3) The stem and leaves capture and settle suspended sediment effectively, exceeding 70% of the overall amount of sedimentation under dense salt marsh and rapid flow (Mudd et al., 2010; Chen et al., 2018). (4) The density of stems partly determines the sedimentation rate (Gleason et al., 1979). (5) Salt marsh roots also contribute to sedimentation by enhancing the soil strength and preventing erosion. Therefore, salt marshes are an important factor in promoting sedimentation and affecting the marsh topography.

The presence of salt marshes causes large temporal and spatial variability in sedimentation in the upper-intertidal flats. This has been studied through field observations and bio-geomorphological numerical simulations (Temmerman et al., 2003; Temmerman et al., 2005; Bouma et al., 2007; D'Alpaos et al., 2007; Fagherazzi et al., 2012; Zhou et al., 2016; Brückner et al., 2019; Geng et al., 2021). Existing field investigations have shown continuous and seasonal sedimentation associated with inundation frequency in the marsh region (Gong et al., 2017; Willemsen et al., 2018). The largest bed level change occurs in the spring and summer seasons (March to May and June to August). Numerical simulations have compared the sedimentation with and without the coverage of salt marshes (D'Alpaos et al., 2007). Without the cover of salt marshes, the sedimentation rate displays a linear relationship from the marsh edge to the landside. The increasing distance from the marsh edge corresponds to the decreasing sedimentation rate. With the presence of *Spartina alterniflora*, the accretion rate is high at the elevation of Mean Sea Level (MSL) and decreases progressively with the increase in the marsh elevation. The lowest limit of the vegetation is set at the MSL in the numerical model. The maximum sedimentation appears in the vicinity of the salt marsh edge owing to the rapid reduction of the suspended sediment concentration in this region (D'Alpaos et al., 2007). Field observations also found a similar increase in the sedimentation rate (*SR*) near the edge (Willemsen et al., 2018). However, medium to long term field observations in the marsh region are still scarce. To better understand the morphodynamics of tidal flats, the sedimentation rate along the cross-shore profile and the impact factors need further investigations.

The soil surface elevation and inundation frequency are known to affect the sedimentation pattern. The sedimentation rate increases exponentially with the inundation period, while an increase in the soil surface elevation corresponds to a decreased sedimentation rate (Pethick, 1981; French, 1993; Allen, 1994; Cahoon et al., 1995). No direct link has been found between waves and bed level change in the marsh region (Willemsen et al., 2018). Marsh sedimentation alters the hydrodynamics (e.g., water level and inundation frequency) and feedbacks to the following sedimentation rate and marsh edge extension. Once the hydrodynamics (e.g., water depth or inundation frequency) and disturbance period allow the survival of salt marshes (Bouma et al., 2016), salt marshes will establish and the border extends seaward (D'Alpaos et al., 2007; Hu et al., 2011; Zhou et al., 2016; Brückner et al., 2019; Geng et al., 2021). It has been pointed out that when the *Spartina* colonizes seaward, the overall accretion rate increases (D'Alpaos et al., 2007). The distance to the marsh edge can also affect the sedimentation. However, the influence of salt marsh extension on sedimentation rate has not been well considered.

Researchers have focused on the establishment and extension of salt marshes as a function of hydrodynamics (Morris et al., 2002; Mudd et al., 2004; D'Alpaos et al., 2007; Hughes et al., 2012; Balke et al., 2016). According to a long record of plant productivity in an estuary, Morris et al. (2002) proposed a linear relationship between plant biomass and marsh topography. The biomass is highly related to the marsh properties (e.g., the plant density). Spatially, the increase in the soil surface elevation results in a linear decrease in biomass. Later, Morris (2006) suggested a parabolic relationship between the soil surface elevation and biomass. With the increase in the water depth in the seaward direction, the biomass first increases until reaching a maximum value, and then drops as it goes farther in the seaward direction. The lowest border of the salt marsh survival has also been widely studied. Researches in different locations have indicated that the lowest border could be located at the Mean Low Water Level (MLWL), Mean Sea Level (MSL, D'Alpaos et al., 2007), or at a certain elevation below the Mean High Water Level (MHWL), e.g., 20 - 40 cm and 50 - 60 cm below MHWL suggested by Bakker et al. (2002) and Morris et al. (2002), respectively. Mckee and Patrick (1988) found the lowest elevation of *Spartina alterniflora* is relative to MLWL and increases with the tidal range. Wang and Temmerman (2013) analyzed remote sensing images and noted rapid shifts of tidal flats from bare to vegetated states once a threshold of a certain elevation (0.5 m below MHWL) is exceeded. Rather than relative elevation and inundation duration, inundation frequency is suggested to better determine the marsh edge than inundation duration (Balke et al., 2016; van Belzen et al., 2017). Moreover, van de Koppel et al. (2005) further highlight the importance of slope at the marsh edge through a theoretical and empirical study. The sedimentation promotes the salt marsh growth, and the salt marsh stops growing when a steep slope at the salt marsh edge is reached. However, there is still no agreement on the lowest limit of the salt marsh edge.

Overall, a large number of studies have focused on the morphological evolution of tidal flats considering the effects of salt marshes through numerical simulations, but the sedimentation related to the seaward extension of salt marshes is less investigated through field observations. The objective of this study is to investigate the impact of the seaward extension of salt marshes on the morphological evolution of tidal flats. We performed medium-term field observations (6 years) on the soil surface elevation in the cross-shore profile of the tidal flats and extracted the marsh edge from remote sensing images. We then evaluated the sedimentation characteristics in association with the marsh elevation and the distance to the marsh edge. This manuscript is structured as follows. In section 2 we introduce the methodology of the topography measurement and marsh edge extraction. In section 3, we describe the variation of the sedimentation and the marsh edge. The results are discussed in section 4, followed by conclusions provided in section 5.

2 Methodology

2.1 Field observations

We performed monthly field observations of the soil surface elevation (*SSE*) at the south tidal flat of Chuandong Estuary in the center of Jiangsu coast (China) from 2012 to 2018 (Figure 1). This region is the most rapidly propagating mudflat on the Jiangsu coast. The width of the tidal flat is about 2-6 km and the slope is 0.1% to 0.3%. As it is affected by a combination of the counterclockwise rotary tidal wave and progressive tidal waves, the tide is irregular, and semi-diurnal, with an average tidal range of 3.68 m. The maximum current velocity ranges from 0.5 m/s to 1 m/s, and there is a weak component of the longshore current according to a previous field study (Zhang et al., 2016). The flood duration is shorter than the ebb duration with a ratio of 0.73. The velocity during the flood tide is larger than that during the ebb tide. Waves tend to be small with the maximum significant wave height of 1.0 m in winter and 0.5 m in summer. The MHWL is 2.19 m and the MLWL is -1.87 m (Figure 1C). The substrate consists of a mixture of clay, silt, and sand (Gong et al., 2017). The grain size becomes coarser from the upper intertidal flats to the lower intertidal flats, but the occasional storm events can bring the coarse sand to the upper intertidal flats. We collected the bedload samples at sites S3 and S7 in January 2021 and analysed the grain size distribution using MasterSizer3000. The median grain size (d_{50}) is 15.2μm at site S3 while 69.8μm at site S7. From the sea dyke to the lower intertidal flat, the cross-shore profile can be divided into four distinctive zones: (1) grass flats (freshwater or brackish water wetland), (2) *Suaeda salsa* and *Spartina alterniflora* salt marshes, (3) muddy flats, and (4) silt or sand flat (Jin et al., 2018).

Nine benchmarks (S1-S9) were set up on the cross-shore profile from the upper to the lower intertidal flat in July 2012 (Figure 1A). At the beginning of field observations, sites S1-S4 are located in the salt marsh region and sites S5-S9 are on the bare flat (Figure 1B). Site S5 is located at the edge of the salt marsh surrounded by low-height salt marshes (Figure 1C). During our field survey, severe erosion occurred around some benchmarks in the lower intertidal flat. Therefore, four more sites were added (SG6, SG7, SG8 and SG89).

The soil surface elevation is calculated from the measurements using a Rod Surface Elevation Table (Rod-SET),

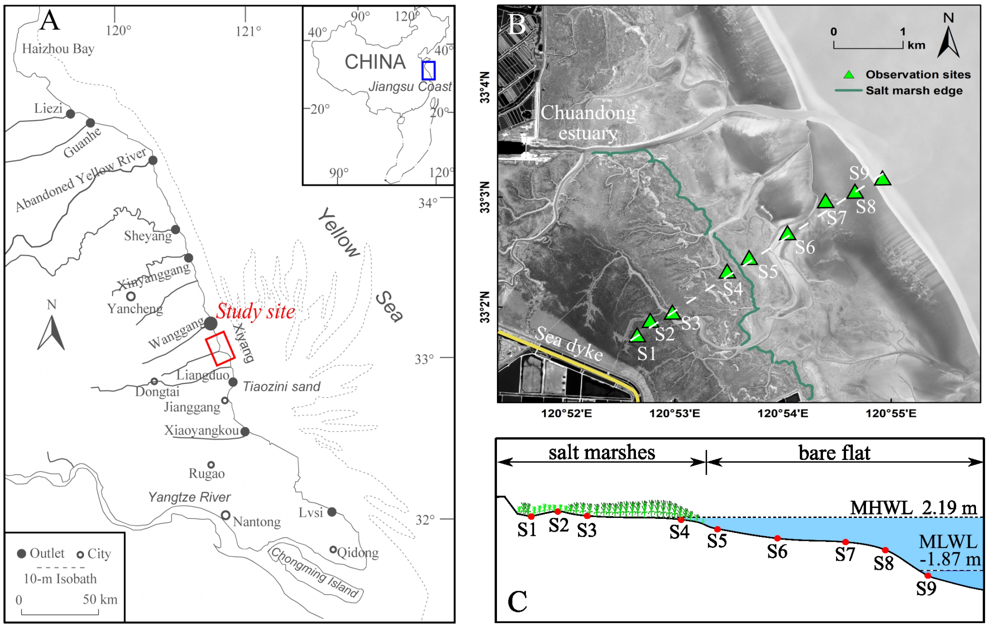

FIGURE 1
Observation sites, Jiangsu coast, China. **(A)** Map of the study site. **(B)** Location of observation sites S1-S9 from the upper to lower intertidal flat. Image is taken in 2013. **(C)** Cross-shore profile in 2012.

an instrument originally developed by Cahoon et al. (2002). This instrument measures the distance from the top of the benchmark to the soil surface (see Figure 2B). The changes in distance from the top of the benchmark to the soil surface indicate the variation of the soil surface elevation. The absolute elevation at the top of the benchmark is measured and re-evaluated using Real-Time Kinematic GPS (RTK-GPS) every half a year to assess any subsidence of the benchmark. We then obtain the absolute elevation by subtracting the distance from the benchmark to the soil surface from the absolute elevation at the top of the benchmark. Readers are referred to Gong et al. (2017) for more detailed settings of benchmarks and components of the Rod-SET instrument.

The tide level is predicted using a dataset from the nearest tidal level station (Zhang et al., 2016; Gong et al., 2017). The inundation duration is quantified by counting the inundation hours within a month. The inundation frequency (f) is defined as the proportion of the submerged time in a month. The sedimentation rate (SR) is calculated as the difference of the soil surface elevation in two adjacent months.

2.2 Assessment of the salt marsh edge

The salt marsh edge is extracted from the remote sensing images obtained by Landsat series satellites. Image quality and tide level are considered when choosing the images. Only images with cloud cover less than 10% and salt marshes not submerged are selected. We selected images taken in October each year from 2012 to 2018 since they coincide with the time of our field observations. To extract the edge of salt marshes, we further calculated the Normalized Difference Vegetation Index (NDVI). The location where a significant change in NDVI occurs is defined as the marsh edge. The obtained location is then visually validated in the remote sensing images. As it is shown in Figure 2, the edge of salt marshes advances seaward from 2013 to 2017. The observation site S5 is fully covered by salt marshes since 2014.

3 Results

We focus on the morphological evolution of salt marshes (S2-S5) and the variation of the soil surface elevation in association with the inundation frequency, topography, and salt marsh extension. Site S1 is close to the sea dyke and is less affected by tidal currents compared to rainfall and longshore currents. Sites S6-S9 are on the bare flat, where the morphological evolution is dominated by tide currents and storm events. The sedimentation and erosion, however, are less relevant to the salt marsh growth on the bare flat.

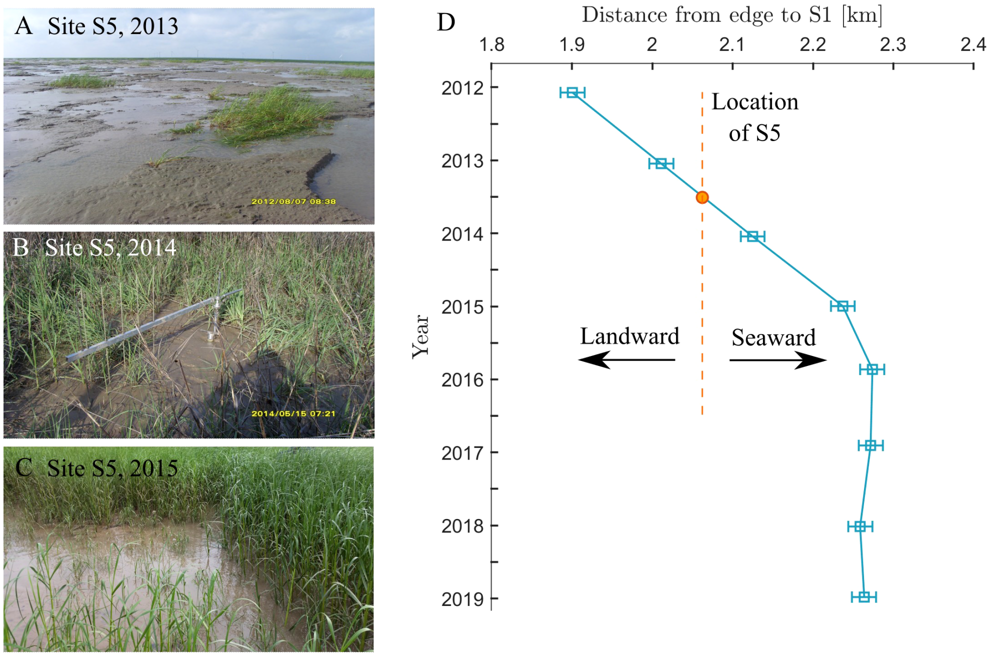

FIGURE 2
Photos taken at the observation site S5 in **(A)** 2013, **(B)** 2014, **(C)** 2015, and **(D)** the location of salt marsh edge as a function of time. The resolution of the remote sensing image (30 m) is shown by the errorbar.

3.1 Soil surface elevation

Site S2 locates at the highest elevation of the cross-shore profile. It can only be submerged during high tide between June and November. The overall inundation frequency is extremely low (<0.05 of the overall time in a month, Figure 3B). The maximum variation in the soil surface elevation is 5 cm throughout the period of observations (Figure 3A). This is attributed to the high soil surface elevation and the resultant low inundation frequency. Although the suspended sediment transported to this site is significantly reduced, the change of the soil surface elevation still correlates with inundation frequency (Figures 3A, B). In particular, the soil surface elevation increases slightly with the inundation frequency period from June to November. Low inundation frequency also means less hydrodynamic interaction with the bed at S2. It may allow substrate accretion from the build-up of the local generated organic matter within the salt marsh. On the other hand, there is a time lag between the increase in the soil surface elevation and the inundation frequency. For example, the inundation frequency at this site (S2) increases from September 2014 to October 2014, followed by a drop from October 2014 to November 2014, but the soil surface elevation increases from October 2014 to November 2014, and later decreases subsequently. Our previous measurements have indicated that the variation of the soil surface elevation is alternatively controlled by the consolidation of the subsurface soil and surface sedimentation (Gong et al., 2017). When the inundation frequency is low, the subsurface soil consolidates, and the elevation reduces slightly. During months with increasing inundation frequency, there is suspended sediment transported to this site. The increase in the soil surface elevation is thus explained by surface sedimentation.

The variation of the soil surface elevation near MHWL is strongly associated with the inundation frequency and salt marsh propagation, and it displays a strong seasonal characteristic. Sites S3 and S4 are located around the MHWL (Figure 1). These two sites are about 1 km and 500 m from the salt marsh edge and covered by the densest salt marshes in the cross-shore profile. In general, the soil surface elevation keeps rising during the period of observations, and the seasonal variation is evident (Figure 3C). The inundation frequency increases from April to November, which corresponds to the increase in the soil surface elevation. During months with decreasing/low inundation frequency, little change in the soil surface elevation is observed (Figure 3D). With the continuous increasing soil surface elevation, the inundation frequency drops correspondingly, which in turn results in the decline in the sedimentation rate. In 2018, both sites reach an elevation that minimizes inundation and so morphological change. The sedimentation rate drops by an order of magnitude, from 0.1-0.2 m/y in 2013 to 0.02-0.04 m/y in 2018 (Figure 4A). This is due to the feedback between the soil surface elevation and inundation frequency (Temmerman et al., 2005; Fagherazzi et al., 2012). High inundation frequency induces large sedimentation in salt marshes. The increase in the soil surface elevation in turn reduces the inundation frequency. Therefore, the sedimentation rate decreases.

Sedimentation rates at Site S3 to S4 are highly related to inundation frequency (Figure 4B). We calculate the mean inundation frequency and monthly sedimentation rate from June to November at sites S3 to S4. Clearly, a larger inundation frequency corresponds to a higher sedimentation rate, and the best fitting of these dots is described by a linear function ($SR = 0.31f - 0.007$, $R^2 = 0.84$, $p = 0.00005$) can be obtained from the curve fitting. The inundation frequency at S2 is not sensitive to the variation of inundation frequency due to the high elevation and low sedimentation rate (~mm), while the

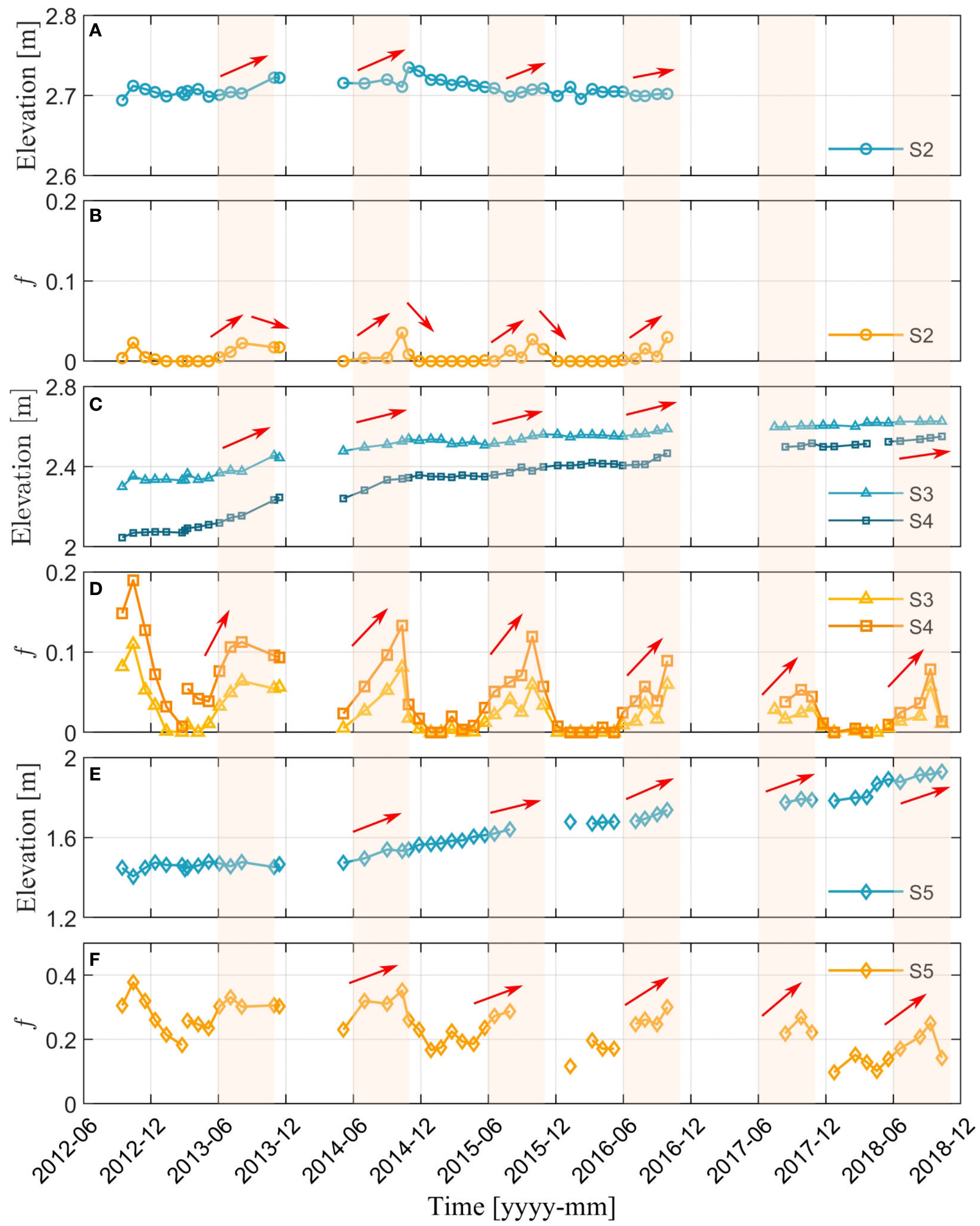

FIGURE 3
Variation of the soil surface elevation at sites **(A)** S2, **(C)** S3 and S4, **(E)** S5, and **(B, D, F)** their corresponding inundation frequency. Light yellow shades highlight the months June to November with the increase in the inundation frequency. Red arrows highlight the increasing trend of the soil surface elevation and inundation frequency.

sedimentation rate at Site S3 and S4 has a strong relation to changes in the inundation frequency.

Site S5 was located at the salt marsh edge at the beginning of our field campaign in 2012 (Figure 1). Although its inundation frequency is higher than S3 and S4 due to the lower elevation at this site (Figure 3E), the magnitude of the variation in the soil surface elevation is rather low compared to S3 and S4 since the site is not fully covered by salt marshes (only patches of salt marshes can be found, see pictures in Figure 2). The sedimentation and erosion are almost in balance at this site and there is no evident seasonal variation as in sites S3 and S4. After this site is gradually covered by salt marshes (Figure 2), the soil surface elevation increases by nearly 40 cm from 2014 to 2018 (Figure 3F), with noticeable seasonal variation after 2014. The soil surface elevation is nearly constant before June, while it increases from June to November.

The morphological elevation of the cross-shore profile from 2012 to 2018 is shown in Figure 5. The overall amount of sedimentation increases from S2 to S4 (~0 m to 0.44 m from 2012 to 2018) and then drops from S4 to the marsh edge (See inset of Figure 5). The maximum deposition region occurs around S4, which is about the elevation of MHWL. With the increase in the soil surface elevation, the slope between S3 and S4 reduces. S5 is initially located at the deposition-erosion balance point before 2014 when the nearby flats are not fully colonized by salt marshes. Once S5 is covered by marshes, the deposition-erosion balance point moves gradually seaward direction due to sedimentation but does not change as much as the marsh edge (Figure 5). The bare flat experienced significant erosion during the 6-year field observations. Together with the rapid sedimentation near the marsh edge, the bed slope at the marsh edge (S5 to S6) increases significantly from 0.001 to 0.003. The most severe erosion (about 1.5m) occurs at the lower intertidal flat which can be attributed to the storm events. Site S7 was entirely eroded, and it has not recovered during the past 6 years.

3.2 The soil surface elevation, salt marsh extension and sedimentation rate

Using remote sensing, we obtained the salt marsh edge and calculated the distance from the salt marsh edge to site S1 in the cross-shore profile (Figure 2). Note that our field measurements cover the time scale from the rapid growth to the relatively steady stage of the salt marsh with minimum seaward growth. From 2012 to 2016, the salt marsh expands and propagates rapidly seaward with an average rate of 92 m/y. The salt marsh edge reached site S5 in 2014. After, the salt marsh extension slows down and displays a slight retreat. The turning point of the salt marsh extension occurs at the end of 2015, which coincides with the major change in the sedimentation rate (Figure 4A). The variation trend of the sedimentation rate changed abruptly at sites S3, S4 and S5 in 2015. The final distance from the salt marsh edge to site S1 is about 2.26 km.

In order to evaluate the amount of sedimentation as a function of distance to the salt marsh edge, we considered the soil surface elevation and the edge of the salt marsh in 2012 as the baseline and displayed the relative soil surface elevation at sites S2-S5 in Figure 6. Since the magnitude of the surface sedimentation/erosion is much higher than the subsurface consolidation/expansion at sites S3-S5, we simply consider the changes in the soil surface elevation as the amount of sedimentation. In 2013, the relative soil surface elevation of sites S2 and S5 is lower than S3 and S4. The maximum amount

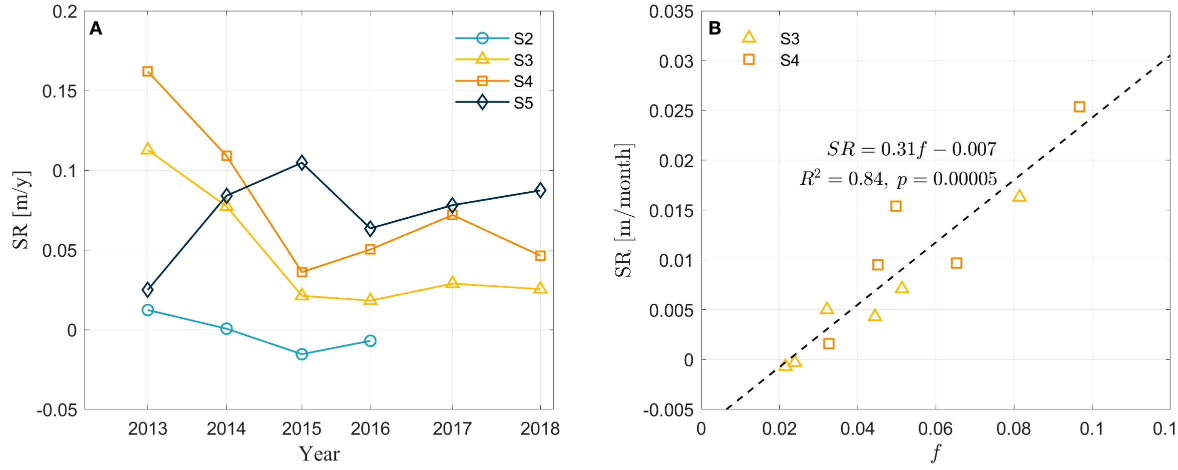

FIGURE 4
(A) Sedimentation rate at S2 to S5 as a function of time. **(B)** The relationship between sedimentation rate and averaged inundation frequency from June to Nov at sites S2 to S4.

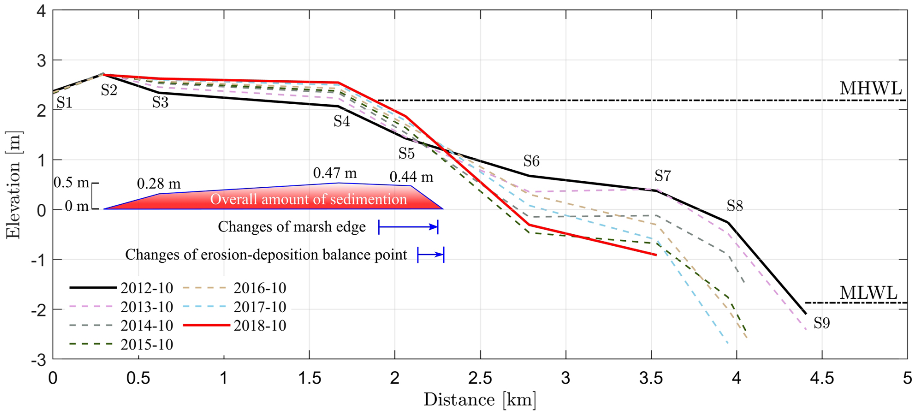

FIGURE 5
Variation of the cross-shore profile from 2012 to 2018. The shade highlights the changes of the salt marsh edge from 2012 to 2018. The changes of marsh edge and the erosion-deposition balance point is highlighted with the blue arrows.

of sedimentation occurs at about 0.8 km from the edge of the salt marsh. With the extension of the salt marsh edge, the soil surface elevation at sites S3-S5 increases. The most rapid deposition position moves to 0.64 km from the salt marsh edge (Figure 6). Overall, the accumulated sedimentation displays a parabolic relationship with the distance to the salt marsh edge which is consistent with the simulation results of D'Alpaos et al. (2007).

The annual sedimentation rate is calculated and quantified as a function of the relative soil surface elevation (relative to the MHWL) (Figure 7A). The overall sedimentation rate displays a parabolic relationship with the soil surface elevation. The maximum sedimentation rate appears near the MHWL (zero on the x-axis, Figure 7A). When only the sites above the MHWL (>0 on the x-axis) are considered, the sedimentation rate follows an exponential relation, which is partly consistent with Temmerman et al. (2003). the sedimentation rate reduces to 0 gradually, with the increase in the soil surface elevation. Figure 7B displays the sedimentation rate as a function of distance to the salt marsh edge. At sites S3 and S4, which are around the MHWL, the sedimentation rate decreases linearly with the propagation of the salt marsh. At the salt marsh edge (site S5), the sedimentation rate first increases and then drops due to the marsh extension following a parabolic relationship. Since S5 locates at the marsh edge and the sedimentation rate is dynamic, here we further plot the normalized *SR* as a function of non-dimensionalized distance to the marsh edge for sites S2 to S4. *SR* is normalized by the soil surface elevation (Figure 7C). The distance to the marsh edge is non-dimensionalized by the distance to the marsh edge in 2018 when the salt marsh edge does not expand seaward any further. We note that the dataset congregates indicating that the *SR* is correlated to both the soil surface elevation and the distance to the marsh edge. With the further extension of the salt marsh edge, Dis/Dis_{end} is close to 1. In the meantime, the sedimentation rate reduces but soil surface elevation increases faster, which finally results in the reduction in the normalized *SR*. Compared to S3 and S4, S5 is more unstable at the marsh edge experiencing an increase to decrease in the sedimentation rate (Figure 7B). The rapid increase in soil surface elevation causes the normalized *SR* slightly lower than S3 and S4. Overall, a linear fitting well describes the relationship between the normalized *SR* and the non-dimensionalized distance to the marsh edge. This result might provide a comparison for future observations and numerical simulation of marsh dynamics.

4 Discussions

Our field observations focused on the morphological evolution of the cross-shore tidal flats and quantified sedimentation rate as a function of the soil surface elevation and the distance to the salt marsh edge.

4.1 Morphological evolution of salt marshes

The morphological evolution of the central Jiangsu coast is mostly controlled by tide inundation, which can be considered as a representative of the tidal forcing (Gong et al., 2017). From June to November, the mean tidal level and inundation frequency increased. High inundation frequency indicates stronger tidal flows and larger suspended sediment

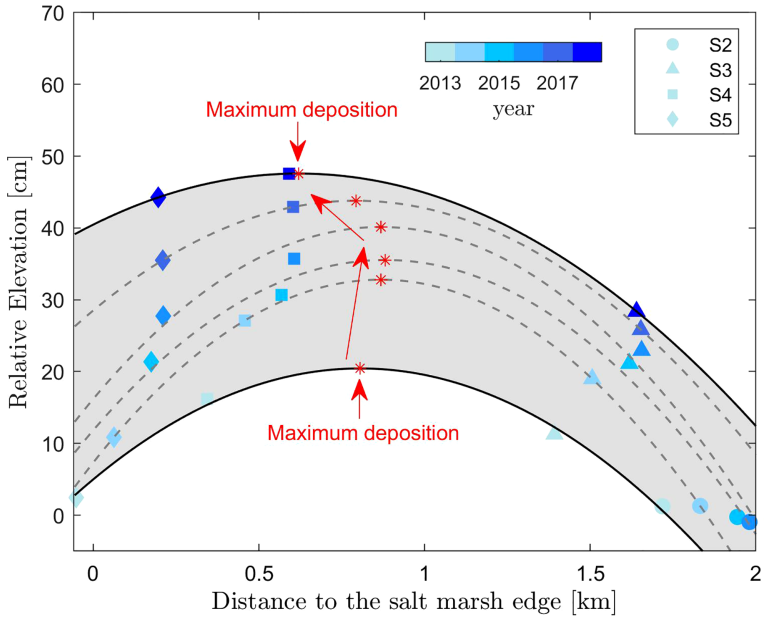

FIGURE 6
The relative soil surface elevation as a function of distance to the salt marsh edge. The shade highlights the changes in the soil surface elevation from 2012 to 2018 at sites S2-S5. The soil surface elevation is relative to that in 2012. Dashed lines and solid lines show the parabolic fitting of all the relative elevations in each year. Red stars highlight the maximum deposition position in each year and the variation trend is highlighted by red arrows.

concentration transported landward (Fan, 2010). Due to the progressive tidal wave, there is slack at the flood tide which allows sediment to deposit. In the meantime, the strong ability of salt marshes in attenuating wave energy and trapping sediment prevents the further suspension and seaward transport of the settled sediment (Temmerman et al., 2005; Mudd et al., 2010). Therefore, the soil surface elevation increases with inundation frequency. During the remaining months, the soil surface elevation varies slightly due to the low inundation frequency and suspended sediment transported to the salt marsh. This seasonal variation in the salt marsh has also been reported in other estuaries, e.g., meso- to macro-tidal Scheldt estuary (e.g., Temmerman et al., 2003) and Nanhui Mudflat (Fan, 2010). Our study further reveals the variation of the soil surface elevation at the edge of the salt marsh, which has been rarely investigated. When the observation site at the edge is not covered by salt marshes, there is less reduction in the flow velocity, and no significant sedimentation occurs in this region. Such tidal flats are affected by occasional wind-wave action, resulting in the occasional erosion. This could explain the erosion-deposition balance at the salt marsh edge when salt marshes are not present. Additionally, tidal flow-vegetation interactions at the edge of vegetated coastal areas create high turbulent zones that pick up more sediments around the fringe (Norris et al., 2017). When salt marshes are present, strong attenuation of forcing conditions causes rapid sedimentation near the salt marsh edge.

Our field data indicate that the sedimentation rate is a function of the soil surface elevation and the distance to the salt marsh edge. The sedimentation rate above the MHWL follows an exponential relationship. This result is consistent with Temmerman et al. (2003), who reported that the sedimentation rate declines exponentially with the increase of the distance from the salt marsh edge or the marsh soil surface elevation, but slightly different from Cahoon et al. (2011), who obtained that sedimentation rate reduces linearly as the increase in the relative site elevation through 6 years field investigations. However, when we further consider the sedimentation rate at the salt marsh edge, the sedimentation rate follows a parabolic relationship with the soil surface elevation. This can be explained by the development stage of the salt marsh. Before 2015, the salt marsh keeps propagating in the seaward direction. The salt marsh at the edge is sparse and characterized by low height. The density of salt marsh first increases and then drops in the landward direction. It has been previously reported that the local sedimentation rate is a function of the density of salt marsh (Gleason et al., 1979). Therefore, the sedimentation rate is low and unstable at the marsh edge, while it is higher in the more landward direction. When the edge site (S5) is covered by salt marshes, the soil surface elevation increases with a low sedimentation rate. With the further extension of salt marshes, the sedimentation rate increases, but is still not as large as sites

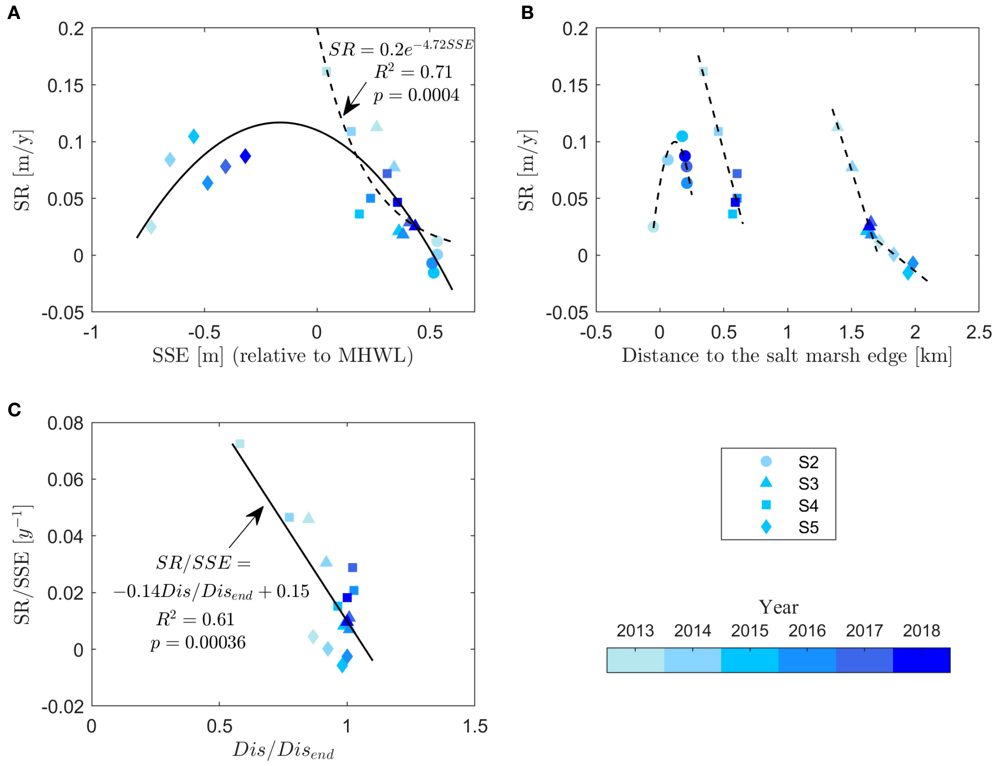

FIGURE 7
The yearly sedimentation rate as a function of **(A)** the relative soil surface elevation and **(B)** the distance from the salt marsh edge. **(C)** The normalized sedimentation rate by the soil surface elevation (*SSE*) as a function of the non-dimensionalized distance to the marsh edge (*Dis*) by the distance to the marsh edge in the year 2018 (Dis_{end}).

around MHWL (Figure 7A). The identified parabolic relationship is generally consistent with the numerical results of D'Alpaos et al. (2007) demonstrating a sharp increase and then gradually drops of the sedimentation rate from the elevation of MWL to MHWL when the salt marsh is dominated by *Spartina alterniflora*. Since there are no dense observation sites set up near the marsh edge, we are unable to detect a more detailed sedimentation pattern at the very edge region. Our study reports a gentler variation of the sedimentation rate in early stages (before 2015) when salt marshes keep propagating seaward (Figure 6). However, after the edge of the salt marsh reaches a steady status (after 2015), the maximum deposition position shift rapidly towards the marsh edge. This should be explained by the density of the salt marshes at the edge. After reaching the steady status, the low-height and low-density salt marshes could be slowly destroyed leaving the high and dense salt marshes at the edge. In this case, the mean velocity reduces more significantly and more sediment is settled down near the edge. Therefore, the maximum deposition point could shift towards the marsh edge, but more investigation on the marsh density is needed.

4.2 On the limit of the salt marsh growth

Our field observations also reveal the limit of the growth of salt marshes. As it is shown in Figure 2, salt marshes stop propagation in 2015 at this cross-shore tidal flat profile. The final location of the salt marsh edge is 2.27 m from Site S1 where the soil surface elevation is 1.3 m, which is 0.8 m below the MHWL. This is greater than that reported by Morris et al. (2002) that the lowest limit is located at 0.5 - 0.6 m below the MHWL which could be attributed to the larger tidal range. The lowest limit of the marsh edge increases with the tidal range (Mckee and Patrick, 1988). The inundation frequency is 0.32 in 2016 when salt marshes stop further extending in the offshore direction. This is close to values reported by van Belzen et al. (2017) indicating that the maximum inundation frequency for salt marsh recovery is around 40%. Besides the water depth and the inundation frequency which limit the extension of salt marshes, here we further assume that the slope at the salt marsh edge might also be an important parameter affecting the salt marsh growth. With the increase in the soil surface elevation of site S5, the slope at the salt marsh edge increases gradually from 0.001 to 0.003 (Figure 5). When the slope reaches a certain threshold, it will be difficult for the salt marsh seedlings to survive and establish in the seaward direction. Hence the salt marsh cannot propagate any longer.

Previous studies have reported two different types of relationship, parabolic and linear, between the water depth and the biomass. In this study, we did not quantify the biomass, but the density of salt marshes is linearly related to the biomass. According to our field observations, we noted the salt marsh is sparse at the edge before reaching a steady status with minimum changes in the marsh edge, which indicates low biomass at the salt marsh edge with a large water depth. Visually, the density of salt marshes increases and then decreases in the landward direction, indicating that the biomass seemingly follows a parabolic relationship. However, after the salt marsh reaches a steady status, it stops propagating seaward. The sparse salt marsh at the edge is exposed to strong tidal currents and occasional wave conditions and they may not survive or further extend in the offshore direction. This will potentially cause the retreat of the salt marsh, leaving a high and dense salt marsh at the edge. In this situation, the biomass might follow a linear relationship. Overall, our study implies that both models well describe the salt marsh dynamic, but at different developing stages.

4.3 Implications for morphodynamic modelling

We have demonstrated a medium-term temporal and spatial variation of the sedimentation in the marsh region using field observations, which is rarely investigated. Our results further revealed that the sedimentation rate is associated with hydrodynamics, distance to the marsh edge and the soil surface elevation. The outcomes of the relationship between sedimentation rate with the soil surface elevation and the distance to the marsh edge can provide a potential function for large-scale numerical simulations, which might lead to a better prediction of the evolution of tidal flats considering the influence of marsh extension.

The morphological evolution of the tidal flat is an extremely complicated process, and more field observations are imperative to understand the underlying mechanism of sedimentation in the salt marsh region. Even though the adaption to sea level rise can make salt marshes reach equilibrium in the vertical direction (Kirwan et al., 2010), they are inherently unstable in the horizontal direction due to the marsh edge retreat (Feagin et al., 2009; Francalanci et al., 2013; Bendoni et al., 2016; Zhao et al., 2022), leading to a dynamic behavior of marsh border retreat and vegetation colonization. As a result, the feedback between the soil surface elevation, salt marsh expansion, lateral marsh edge retreat and hydrodynamics should be all taken into account. Further investigations are needed to better understand salt marsh dynamics providing robust predictions of the morphological evolution of tidal flats.

5 Conclusions

We performed medium-term field observations of salt marsh elevations in the central part of the Jiang coast (China) and extracted the marsh edge from remote sensing images. Our field observations cover a period of rapid marsh extension until they reach a steady status with a minimum change in the location of the salt marsh edge. The salt marsh edge moved 400 m from 2012 to 2014 in the seaward direction and stopped propagating afterwards. The marsh elevation increases constantly, and the slope becomes steeper at the marsh edge. The soil surface elevation consistently increases with the inundation frequency from June to November. The monthly sedimentation rate is linearly related to the mean inundation frequency. The sedimentation rate changes abruptly in 2015 because of the growth stage of salt marshes. Overall, the spatial sedimentation rate is a function of the distance to the marsh edge and the marsh topography. The sedimentation rate displays a parabolic relationship with the surface topography with the maximum sedimentation rate occurring around MHWL. Meanwhile, the sedimentation rate decreases with the distance to the marsh edge. This study adds to the understanding of the morphological evolution of tidal flats in relation to the salt marsh edge and provides a formidable dataset to test models of biomorphodynamics.

Data availability statement

The original contributions presented in the study are included in the article/Supplementary Material. Further inquiries can be directed to the corresponding author.

Author contributions

CJ: Data visualization, Manuscript writing, Funding support. ZG: Review, Editing, Project administration, Funding support. LS: Field observations, Image processing, Data analysis. KZ: Review and Editing. ROT: Review and editing. JSJ: Review and Editing. LG: Review and Editing. GC: Review and Editing. All authors contributed to the article and approved the submitted version.

Funding

This work is funded by China Postdoctoral Science Foundation (No. 2022M711020) and National Nature Science Foundation (No. 51925905)

Acknowledgments

The authors thank Charlie Emma Louise Thompson and Gerardo M. Perillo for their comments. Chuang Jin acknowledges Huan Li, Qian Zhang, JunCheng Hang and Beibei Xu for contributing to the field observations. Chuang Jin is supported by the funding of China Postdoctoral Science Foundation. Zheng Gong acknowledges the funding of National Nature Science Foundation for the support of field observation work.

Conflict of interest

The authors declare that the research was conducted in the absence of any commercial or financial relationships that could be construed as a potential conflict of interest.

Publisher's note

References

Allen, J. R. L. (1994). A continuity-based sedimentological model for temperate-zone tidal salt marshes. *J. Geol. Soc Lond.* 151, 41–49. doi: 10.1144/gsjgs.151.1.0041

Anderson, M. E., and Smith, J. M. (2014). Wave attenuation by flexible, idealized salt marsh vegetation. *Coast. Eng.* 83, 82–92. doi: 10.1016/j.coastaleng.2013.10.004

Bakker, J. P., Esselink, P., Dijkema, K. S., Van Duin, W. E., and De Jong, D. J. (2002). "Restoration of salt marshes in the Netherlands," in *Ecological restoration ofAquatic and semi-aquatic ecosystems in the Netherlands (NW Europe)*. Eds. P. H. Nienhuis and R. D. Gulati (Dordrecht: Springer Netherlands), 29–51.

Balke, T., Stock, M., Jensen, K., Bouma, T. J., and Kleyer, M. (2016). A global analysis of the seaward salt marsh extent: The importance of tidal range. *Water Resour. Res.* 52 (5), 3775–3786. doi: 10.1002/2015WR018318

Bendoni, M., Mel, R., Solari, L., Lanzoni, S., Francalanci, S., and Oumeraci, H. (2016). Insights into lateral marsh retreat mechanism through localized field measurements. *Water Resour. Res.* 52 (2), 1446–1464. doi: 10.1002/2015WR017966

Bouma, T. J., van Belzen, J., Balke, T., van Dalen, J., Klaassen, P., Hartog, A. M., et al. (2016). Short-term mudflat dynamics drive long-term cyclic salt marsh dynamics. *Limnol. Oceanogr.* 61 (6), 2261–2275. doi: 10.1002/lno.10374

Bouma, T. J., van Duren, L., Temmerman, S., Claverie, T., Blanco- Garcia, A., Ysebaert, T., et al. (2007). Spatial flow and sedimentation patterns within patches of epibenthic structures: Combining field, flume and modelling experiments. *Cont. Shelf Res.* 27, 1020–1045. doi: 10.1016/j.csr.2005.12.019

Brückner, M. Z. M., Schwarz, C., van Dijk, W. M., van Oorschot, M., Douma, H., and Kleinhans, M. G. (2019). Salt marsh establishment and eco-engineering effects in dynamic estuaries determined by species growth and mortality. *J. Geophys. Res.: Earth Surf.* 124 (12), 2962–2986. doi: 10.1029/2019JF005092

Cahoon, D. R., Lynch, J. C., Hensel, P. F., Boumans, R., Perez, B. C., Segura, B., et al. (2002). High-precision measurements of sediment elevation: I. recent improvements to the sediment-erosion table. *J. Sediment. Res.* 72 (5), 730–733. doi: 10.1306/020702720730

Cahoon, D. R., Reed, D. J., and Day, J. W. (1995). Estimating shallow subsidence in microtidal salt marshes of the southeastern united states: Kaye and barghoorn revisited. *Mar. Geol.* 128 (1–2), 1–9. doi: 10.1016/0025-3227(95)00087-F

Cahoon, D. R., White, D. A., and Lynch, J. C. (2011). Sediment infilling and wetland formation dynamics in an active crevasse splay of the Mississippi river delta. *Geomorphology* 131 (3–4), 57–68. doi: 10.1016/j.geomorph.2010.12.002

Chen, Y., Li, Y., Thompson, C., Wang, X., Cai, T., and Chang, Y. (2018). Differential sediment trapping abilities of mangrove and saltmarsh vegetation in a subtropical estuary. *Geomorphology* 318, 270–282. doi: 10.1016/j.geomorph.2018.06.018

Chen, X., Zhang, C., Paterson, D. M., Townend, I. H., Jin, C., Zhou, Z., et al. (2019). The effect of cyclic variation of shear stress on non-cohesive sediment stabilization by microbial biofilms: the role of 'biofilm precursors.'. *Earth Surf. Process. Land.* 44 (7), 1471–1481. doi: 10.1002/esp.4573

D'Alpaos, A., Lanzoni, S., Marani, M., and Rinaldo, A. (2007). Landscape evolution in tidal embayments: Modeling the interplay of erosion, sedimentation, and vegetation dynamics. *J. Geophys. Res.* 112, F01008. doi: 10.1029/2006JF000537

Fagherazzi, S., Kirwan, M. L., Mudd, S. M., Guntenspergen, G. R., Temmerman, S., Rybczyk, J. M., et al. (2012). Numerical models of salt marsh evolution: Ecological, geormorphic, and climatic factors. *Rev. Geophys.* 50 (2011), 1–28. doi: 10.1029/2011RG000359.1.INTRODUCTION

Fan, D. (2010). "Open-coast tidal flats," in *Principles of tidal sedimentology*. Eds. R. A. Davis and R. W. Dalrymple (Dordrecht: Springer Netherlands), 187–229. doi: 10.1007/978-94-007-0123-6_9

Feagin, R. A., Lozada-Bernard, S. M., Ravens, T. M., Möller, I., Yeager, K. M., and Baird, A. H. (2009). Does vegetation prevent wave erosion of salt marsh edges? *Proc. Natl. Acad. Sci.* 106 (25), 10109–10113. doi: 10.1073/pnas.0901297106

Francalanci, S., Bendoni, M., Rinaldi, M., and Solari, L. (2013). Ecomorphodynamic evolution of salt marshes: Experimental observations of bank retreat processes. *Geomorphology* 195 (Supplement C), 53–65. doi: 10.1016/j.geomorph.2013.04.026

French, J. R. (1993). Numerical-simulation of vertical marsh growth and adjustment to accelerated Sea-level rise, north Norfolk, UK, earth surf. *Process. Land.* 18, 63–81. doi: 10.1002/esp.3290180105

Friedrichs, C. T. (2011). Tidal flat morphodunamics: a synthesis. *Earth Syst. Environ. Sci.* 3, 137–170. doi: 10.1016/j.nano.2009.07.003

Geng, L., D'Alpaos, A., Sgarabotto, A., Gong, Z., and Lanzoni, S. (2021). Intertwined eco-morphodynamic evolution of salt marshes and emerging tidal channel networks. *Water Resour. Res.* 57, e2021WR030840. doi: 10.1029/2021WR030840

Gleason, M. L., Elmer, D. A., Pien, N. C., and Fisher, J. S. (1979). Effects of stem density upon sediment retention by salt marsh cord grass, spartina alterniflora loisel. *Estuar.* 2, 271–273. doi: 10.2307/1351574

Gong, Z., Jin, C., Zhang, C., Zhou, Z., Zhang, Q., and Li, H. (2017). Temporal and spatial morphological variations along a cross-shore intertidal profile, jiangsu, China. *Cont. Shelf Res.* 144, 1–9. doi: 10.1016/j.csr.2017.06.009

Green, M. O., and Coco, G. (2007). Sediment transport on an estuarine intertidal flat: Measurements and conceptual model of waves, rainfall and exchanges with a tidal creek. *Estuar. Coast. Shelf Sci.* 72 (4), 553–569. doi: 10.1016/j.ecss.2006.11.006

Hughes, A. L. H., Wilson, A. M., and Morris, J. T. (2012). Hydrologic variability in a salt marsh: Assessing the links between drought and acute marsh dieback. *Estuar. Coast. Shelf Sci.* 111, 95–106. doi: 10.1016/j.ecss.2012.06.016

Hu, Z., Stive, M. J. F., Zitman, T. J., Ye, Q. H., Wang, Z. B., Luijendijk, A., et al. (2011). "Interaction between hydrodynamics and salt marsh dynamics: An example from jiangsu coast," in *2011 Proceedings of the 6th International Conference*. 1079–1087. doi: 10.1142/9789814366489_0128

Jin, C., Coco, G., Tinoco, R. O., Ranjan, P., Gong, Z., Dutta, S., et al. (2022). High-resolution Large eddy simulations of vortex dynamics over ripple defects under oscillatory flow. *J. Geophys. Res.: Earth Surf.* 127 (3), 1–24. doi: 10.1029/2021jf006328

Jin, C., Gong, Z., Geng, L., Zhao, K., Xu, B., and Coco, G. (2018). Observations of surface and subsurface processes on a saltmarsh in the central jiangsu coast (China). *J. Coast. Res.* 85 (85), 296–300. doi: 10.2112/SI85-060.1

Kirwan, M. L., Guntenspergen, G. R., D'Alpaos, A., Morris, J. T., Mudd, S. M., and Temmerman, S. (2010). Limits on the adaptability of coastal marshes to rising sea level. *Geophys. Res. Lett.* 37 (23). doi: 10.1029/2010GL045489

Kirwan, M. L., Temmerman, S., Skeehan, E. E., Guntenspergen, G. R., and Fagherazzi, S. (2016). Overestimation of marsh vulnerability to sea level rise. *Nat. Climate Change* 6 (3), 253–260. doi: 10.1038/nclimate2909

Krauss, K. W., Cahoon, D. R., Allen, J. A., Ewel, K. C., Lynch, J. C., and Cormier, N. (2010). Surface elevation change and susceptibility of different mangrove zones to Sea-level rise on pacific high islands of Micronesia. *Ecosystems* 13 (1), 129–143. doi: 10.1007/s10021-009-9307-8

Le Hir, P., Roberts, W., Cazaillet, O., Christie, M., Bassoullet, P., and Bacher, C. (2000). Characterization of intertidal flat hydrodynamics. *Cont. Shelf Res.* 20 (12–13), 1433–1459. doi: 10.1016/S0278-4343(00)00031-5

Lovelock, C. E., Adame, M. F., Bennion, V., Hayes, M., Reef, R., Santini, N., et al. (2015). Sea Level and turbidity controls on mangrove soil surface elevation change. *Estuarine, coastal and shelf science*. 153, 1–9. doi: 10.1016/j.ecss.2014.11.026

Marani, M., D'Alpaos, A., Lanzoni, S., and Santalucia, M. (2011). Understanding and predicting wave erosion of marsh edges. *Geophys. Res. Lett.* 38 (21), L21401. doi: 10.1029/2011gl048995

Mckee, K. L., and Patrick, W. H. (1988). The relationship of smooth cordgrass (Spartina alterniflora) to tidal datums: A review. *Estuaries* 11 (3), 143–151. doi: 10.2307/1351966

Möller, I., Kudella, M., Rupprecht, F., Spencer, T., Paul, M., Van Wesenbeeck, B. K., et al. (2014). Wave attenuation over coastal salt marshes under storm surge conditions. *Nat. Geosci.* 7 (10), 727–731. doi: 10.1038/NGEO2251

Morris, J. T. (2006). Competition among marsh macrophytes by means of geomorphological displacement in the intertidal zone. *Estuar. Coast. Shelf Sci.* 69 (3–4), 395–402. doi: 10.1016/j.ecss.2006.05.025

Morris, J. T., Sundareshwar, P. V., Nietch, C. T., Kjerfve, B., and Cahoon, D. R. (2002). Responses of coastal wetlands to rising sea level. *Ecol.* 83, 2869.e2877. doi: 10.1890/0012-9658(2002)083[2869:ROCWTR]2.0.CO;2

Mudd, S. M., D'Alpaos, A., and Morris, J. T. (2010). How does vegetation affect sedimentation on tidal marshes? investigating particle capture and hydrodynamic controls on biologically mediated sedimentation. *J. Geophys. Res.: Earth Surf.* 115 (F3), F03029. doi: 10.1029/2009JF001566

Mudd, S. M., Fagherazzi, S., Morris, J. T., and Furbish, D. J. (2004). Flow, sedimentation, and biomass production on a vegetated salt marsh in South Carolina: Toward a predictive model of marsh morphologic and ecologic evolution, in *The Ecogeomorphology of Tidal Marshes, Coastal Estuarine Stud.*, vol. 59, edited by S. Fagherazzi, M. Marani and L. K. Blum, pp. 165–188, AGU, Washington, D. C.

Nepf, H. (2012). Flow and transport in regions with aquatic vegetation. *Annu. Rev. Fluid Mech.* 44, 123–142. doi: 10.1146/annurev-fluid-120710-101048

Norris, B. K., Mullarney, J. C., Bryan, K. R., and Henderson, S. M. (2017). The effect of pneumatophore density on turbulence: a field study in a sonneratia-dominated mangrove forest, Vietnam. *Cont. Shelf Res.* 147, 114–127. doi: 10.1016/j.csr.2017.06.002

Pethick, J. S. (1981). Long-term accretion rates on tidal marshes. journal of. *Sediment. Petrol.* 61, 571.e577. doi: 10.1306/212F7CDE-2B24-11D7-8648000102C1865D

Rogers, K., Saintilan, N., and Woodroffe, C. D. (2014). Surface elevation change and vegetation distribution dynamics in a subtropical coastal wetland: Implications for coastal wetland response to climate change. *Estuar. Coast. Shelf Sci.* 149 (0), 46–56. doi: 10.1016/j.ecss.2014.07.009

San Juan, J. E., Veliz Carrillo, G., and Tinoco, R. O. (2019). Experimental observations of 3D flow alterations by vegetation under oscillatory flows. *Environ. Fluid Mech.* 19 (6), 1497–1525. doi: 10.1007/s10652-019-09672-2

Schwarz, C., Gourgue, O., van Belzen, J., Zhu, Z., Bouma, T. J., van de Koppel, J., et al. (2018). Self-organization of a biogeomorphic landscape controlled by plant life-history traits. *Nat. Geosci.* 11 (9), 672–677. doi: 10.1038/s41561-018-0180-y

Shi, B. W., Yang, S. L., Wang, Y. P., Yu, Q., and Li, M. L. (2014). Intratidal erosion and deposition rates inferred from field observations of hydrodynamic and sedimentary processes: A case study of a mudflat–saltmarsh transition at the Yangtze delta front. *Cont. Shelf Res.* 90, 109–116. doi: 10.1016/j.csr.2014.01.019

Swales, A., Denys, P., Pickett, V. I., and Lovelock, C. E. (2016). Evaluating deep subsidence in a rapidly-accreting mangrove forest using GPS monitoring of surface-elevation benchmarks and sedimentary records. *Mar. Geol.* 380, 205–218. doi: 10.1016/j.margeo.2016.04.015

Temmerman, S., Bouma, T. J., Govers, G., Wang, Z. B., De Vries, M. B., and Herman, P. M. J. (2005). Impact of vegetation on flow routing and sedimentation patterns: Three-dimensional modeling for a tidal marsh. *J. Geophys. Res.: Earth Surf.* 110 (4), 1–18. doi: 10.1029/2005JF000301

Temmerman, S., Govers, G., Wartel, S., and Meire, P. (2003). Spatial and temporal factors controlling short-term sedimentation in a salt and freshwater tidal marsh, scheldt estuary, Belgium, SW Netherlands. *Earth Surf. Process. Land.* 28 (7), 739–755. doi: 10.1002/esp.495

Tinoco, R. O., and Coco, G. (2018). Turbulence as the main driver of resuspension in oscillatory flow through vegetation. *J. Geophys. Res.: Earth Surf.* 123 (5), 981–904. doi: 10.1002/2017JF004504

Tinoco, R. O., San Juan, J. E., and Mullarney, J. C. (2020). Simplification bias: lessons from laboratory and field experiments on flow through aquatic vegetation. *Earth Surf. Process. Land.* 45 (1), 121–143. doi: 10.1002/esp.4743

van Belzen, J., van de Koppel, J., Kirwan, M. L., van der Wal, D., Herman, P. M. J., Dakos, V., et al. (2017). Vegetation recovery in tidal marshes reveals critical slowing down under increased inundation. *Nat. Commun.* 8 (1), 15811. doi: 10.1038/ncomms15811

van de Koppel, J., van der Wal, D., Bakker, J. P., and Herman, P. M. J. (2005). Self-organization and vegetation collapse in salt marsh ecosystems. *Am. Nat.* 165 (1), 1–12. doi: 10.1086/426602

van Eerden, M. R., Drent, R. H., Stahl, J., and Bakker, J. P. (2005). Connecting seas: Western palaearctic continental flyway for water birds in the perspective of changing land use and climate. *Global Change Biol.* 11 (6), 894–908. doi: 10.1111/j.1365-2486.2005.00940.x

Wang, C., and Temmerman, S. (2013). Does biogeomorphic feedback lead to abrupt shifts between alternative landscape states?: an empirical study on intertidal flats and marshes. *J. Geophys. Res.: Earth Surf.* 118 (1), 229–240. doi: 10.1029/2012JF002474

Webb, E. L., Friess, D. A., Krauss, K. W., Cahoon, D. R., Guntenspergen, G. R., and Phelps, J. (2013). A global standard for monitoring coastal wetland vulnerability to accelerated sea-level rise. *Nat. Climate Change* 3 (5), 458–465. doi: 10.1038/nclimate1756

Willemsen, P., Borsje, B., Hulscher, S., van der Wal, D., Zhu, Z., Oteman, B., et al. (2018). Quantifying bed level change at the transition of tidal flat and salt marsh: Can we understand the lateral location of the marsh edge? *J. Geophys. Res.: Earth Surf.* 23, 2509–2524. doi: 10.1029/2018JF004742

Yang, J., and Nepf, H. (2018). A turbulence-based bed-load transport model for bare and vegetated channels. *Geophys. Res. Lett.* 45,10, 428–10,436. doi: 10.1029/2018GL079319

Zhang, Q., Gong, Z., Zhang, C., Lacy, J., Jaffe, B., Xu, B., et al. (2021). The role of surges during periods of very shallow water on sediment transport over tidal flats. *Front. Mar. Sci.* 8. doi: 10.3389/fmars.2021.599799

Zhang, Q., Gong, Z., Zhang, C. K., Townend, I., Jin, C., and Li, H. (2016). Velocity and sediment surge: What do we see at times of very shallow water on intertidal mudflats? *Cont. Shelf Res.* 113, 10–20. doi: 10.1016/j.csr.2015.12.003

Zhao, K., Coco, G., Gong, Z., Darby, S. E., Lanzoni, S., Xu, F., et al. (2022). A review on bank retreat: Mechanisms, observations, and modeling. *Rev. Geophys.* 60, e2021RG000761. doi: 10.1029/2021RG000761

Zhao, K., Lanzoni, S., Gong, Z., and Coco, G. (2021). A numerical model of bank collapse and river meandering. *Geophys. Res. Lett.* 48, e2021GL093516. doi: 10.1029/2021GL093516

Zhou, Z., Ye, Q., and Coco, G. (2016). A one-dimensional biomorphodynamic model of tidal flats: Sediment sorting, marsh distribution, and carbon accumulation under sea level rise. *Adv. Water Res.* 93, 288–302. doi: 10.1016/j.advwatres.2015.10.011

frontiers | Frontiers in Marine Science

TYPE Original Research
PUBLISHED 15 September 2022
DOI 10.3389/fmars.2022.847985

OPEN ACCESS

EDITED BY
Mouncef Sedrati,
UniversitéBretagne Sud,
France

REVIEWED BY
Peter M.J. Herman,
Delft University of Technology,
Netherlands
Liqin Zuo,
Nanjing Hydraulic Research Institute,
China

*CORRESPONDENCE
Chi Zhang
zhangchi@hhu.edu.cn

SPECIALTY SECTION
This article was submitted to
Coastal Ocean Processes,
a section of the journal
Frontiers in Marine Science

RECEIVED 03 January 2022
ACCEPTED 23 August 2022
PUBLISHED 15 September 2022

CITATION
Chen D, Zheng J, Zhang C, Guan D,
Li Y and Huang H (2022) Threshold of
surface erosion of cohesive sediments.
Front. Mar. Sci. 9:847985.
doi: 10.3389/fmars.2022.847985

Threshold of surface erosion of cohesive sediments

Dake Chen[1,2], Jinhai Zheng[3], Chi Zhang[2,3]*, Dawei Guan[3], Yuan Li[2,3] and Huiming Huang[3]

[1]Nanjing Hydraulic Research Institute, Nanjing, China, [2]State Key Laboratory of Hydrology-Water Resources and Hydraulic Engineering, Nanjing, China, [3]College of Harbour, Coastal and Offshore Engineering, Hohai University, Nanjing, China

Cohesive sediment is ubiquitous in aquatic systems, which often forms fractal aggregates due to cohesive and adhesive forces between particles and is generally eroded as aggregates at low bed shear stresses. The erosion of aggregates plays a significant role in cohesive sediment dynamics. However, the effects of fractal bed aggregation on the erosion threshold of sediment have not been well understood. The incipient motion condition of cohesive sediment is investigated, in which particle aggregation is taken into account by employing the fractal theory and the van der Waals force between particles. A formula for the critical shear stress for surface erosion of cohesive sediments composed of fractal aggregates is developed based on the balance analysis of momentums acting on an aggregate in the bed surface. The developed formula has been successfully applied to different kinds of cohesive sediment. The fractal dimension is found as a function of the solid volume fraction and the diameter of primary particles. The contribution rate of the effective weight of aggregate to the erosion threshold of cohesive sediment is quantified.

KEYWORDS

erosion threshold, critical shear stress, surface erosion, cohesive sediment, sediment transport, fractal aggregates, coastal erosion

Introduction

Cohesive sediments are composed primarily of clay- and silt-sized particles usually mixed with organic matters, microorganisms, etc. They are ubiquitous in aquatic systems and have significant ecological functions, including habitats for benthic organisms, stores for organic carbon, and sites of biogeochemical cycling (Grabowski et al., 2011). Therefore, the transport of cohesive sediments plays an essential role in water quality, aquatic ecosystem, and morphological evolution (Hua et al., 2019; Yuan et al., 2021). Erosion of the sedimentary bed is one of the controlling processes of sediment dynamics (Winterwerp et al., 2012; Li et al., 2021; Li, Zhang, Dai, et al., 2022). It has been attracting numerous interests and studied extensively.

The erodibility of bed sediment is usually measured by an erosion threshold and an erosion rate (Forsberg et al., 2018; Li et al., 2022). The erosion threshold describes the critical hydrodynamic condition that initiates sediment erosion, while the erosion rate specifies the mass of sediment eroded per unit time once the threshold is exceeded. The erosion rate is often a function of the erosion threshold (Mehta et al., 1989; Sanford & Maa, 2001). Therefore, accurately determining the erosion threshold is one of the most crucially important steps in modeling the erosion process of cohesive sediments and solving those erosion-related problems.

There are mainly two approaches to the threshold of cohesive sediments. One adopts an empirical method, which relates the erosion threshold of cohesive sediments to their physicomechanical properties, usually based on experimental results. Relations have been proposed between the critical shear stress or critical velocity and dry (wet) bulk density (Owen, 1970; Thorn & Parsons, 1980; Ockenden & Delo, 1988; Amos et al., 2004; Xu et al., 2015), total water content (Jacobs et al., 2011), water content of the mud matrix (Dickhudt et al., 2011); solid volume fraction (Kusuda et al., 1984), solid/void volume ratio (Wu et al., 2017), plasticity index (Smerdon & Beasley, 1959; Jacobs et al., 2011), yield stress (Zhang & Yu, 2017; Zhang et al., 2017), etc. Some have been widely used, e.g., Smerdon and Beasley (1959) and Wu et al. (2017). The other approach attempts to quantify the cohesive force between particles and study the erosion threshold of cohesive sediment by analyzing the balance between hydrodynamic forces that cause erosion and the forces within the sediment that resist it. Several formulae for the critical shear stress or velocity have been developed by this approach. A few threshold curves have been also proposed for cohesive sediment based on those formulae, which are similar to the Shields curve but sort according to the consolidation degree. Detailed introductions of this approach and the formulae for the critical shear stress and critical velocity based on this approach have been given by Chen et al. (2018).

According to current studies, cohesive sediment usually forms aggregates due to cohesive and adhesive forces between particles. Field and laboratory observations have indicated that cohesive sediment in unidirectional flow is generally eroded aggregate-by-aggregate at low bed shear stresses and in form of large chunks of sediment masses being removed from the bed at high bed shear stresses (Thomsen & Gust, 2000; Amos et al., 2003; Sharif, 2003; Righetti & Lucarelli, 2007; Grabowski et al., 2011; Forsberg et al., 2018; Perkey et al., 2020). The former mode of erosion is referred to as surface erosion or aggregate erosion, and the latter is called mass erosion or bulk erosion (Winterwerp & Van Kesteren, 2004; Mehta, 2014).

Experimental studies have verified that the eroded aggregates from the bed surface are an important component of the flocs typically observed in water bodies in aquatic systems (Righetti & Lucarelli, 2007; Forsberg et al., 2018). The eroded aggregates can transport in suspension or bedload on the order of tens of meters to many kilometers under the right conditions (Schieber et al., 2010; Perkey et al., 2020). Therefore, erosion of bed aggregates plays a significant role in cohesive sediment dynamics as it affects not only the water-bed boundary but also the subsequent transport and settling of the eroded materials (McAnally & Mehta, 2000; McAnally & Mehta, 2002; Amos et al., 2003; Chang et al., 2006; Forsberg et al., 2018). The characteristics of erosion, transport and settling of bed aggregates are considerably different from that of the fine particles composing the aggregates (Amos et al., 2003; Roberts et al., 2003; Forsberg et al., 2018; Perkey et al., 2020). This could significantly alter the fate of fine sediments in the aquatic systems and further influence the geomorphology and aquatic ecosystem. However, the examination of the erosion and transport processes for bed aggregates remains largely unknown, which limits the progress of elaborate simulation of cohesive sediment transport processes.

Besides, the strength resisting erosion in cohesive sediment has been believed principally coming from the cohesive and adhesive forces, and the effective gravity of cohesive sediment is often considered negligible (Yang & Wang, 1995; Righetti & Lucarelli, 2007; Debnath & Chaudhuri, 2010; Chen et al., 2021). However, for aggregate erosion of cohesive sediment, how much the effective gravity contributes to the erosion threshold has been a mystery, and no one has quantified it.

The present study investigates the erosion threshold of cohesive sediment composed of fractal aggregates in which fractal bed aggregation is taken into account. The fractal theory is employed to describe the sediment aggregates, and the van der Waals attraction is introduced to quantify the cohesive force. The contribution of the effective weight of aggregate to the erosion threshold of cohesive sediment is quantified. The theoretical consideration, formula application, and discussion are described in the following sections.

Theoretical consideration

Fractal aggregates of cohesive sediment

Fine-grained cohesive particles often form complex structures called aggregates due to cohesive and adhesive forces among the sediment. Such aggregates are of much larger size and smaller density than that of primary particles. Krone (1963, 1986) and Partheniades (1965) were the pioneers of studying the structure of cohesive sediment aggregates. They found the primary particles of cohesive sediment form small aggregates and the small aggregates join together to form large aggregates, which would further combine to form larger aggregates, etc. Krone introduced the order of aggregation concept to describe the structure of aggregates and showed experimentally that aggregate density, yield strength, and viscosity depend on the order of aggregation. The findings of the two pioneers and many subsequent studies have suggested the structure of cohesive sediment aggregates can be often approximately described in terms of self-similarity (Kranenburg, 1994; Chen & Eisma, 1995; Winterwerp, 1998).

The fractal theory initially proposed by Mandelbrot (1967, 1975) provides a useful mathematical framework for describing those structures of self-similarity. According to the fractal theory, the number of primary particles in an aggregate is related to its size and the fractal dimension:

$$N_p = \left(\frac{d_a}{d_p}\right)^F \tag{1}$$

where N_p is the number of primary particles in the aggregate; d_a is the aggregate size; d_p is the diameter of the primary particles; and F is the fractal dimension characterizing the space-filling ability of the aggregates (Logan & Kilps, 1995; Serra & Casamitjana, 1998). The value of F varies from 1 to 3, with F=1 meaning linear self-similarity; F=2 meaning area self-similarity; and F=3 meaning volumetric self-similarity. Aggregates with a low fractal dimension close to 1 are tenuous and stringy. The pure coalescence of particles is of a fractal dimension F equaling 3 (Kranenburg, 1994). Suspended macroflocs in the estuary and coastal environments usually have a fractal dimension around 2 (Khelifa & Hill, 2006; Son & Hsu, 2009; Fall et al., 2021).

Following the fractal theory, the effective density of an aggregate is given as a function of the size of the aggregate, the size and density of the primary particles (Kranenburg, 1994):

$$\frac{\rho_a - \rho}{\rho_s - \rho} = \left(\frac{d_a}{d_p}\right)^{F-3} \tag{2}$$

where ρ_a is the density of the aggregate; ρ_s and ρ are the densities of primary particles and water, respectively.

By analyzing the conservation of mass of a captured bed, the average density of aggregates could be estimated by:

$$\rho_a \varphi_a = \rho_s \varphi_s + \rho(\varphi_a - \varphi_s) \tag{3}$$

where φ_s is the volume fraction of primary particles in the bed (i.e., the solid volume fraction or the solid volumetric concentration) and φ_a is the volume fraction of aggregates in the bed (i.e., the volumetric concentration of aggregates). Considering equations (2) and (3), the representative aggregate size of a cohesive bed is given by:

$$\left(\frac{d_a}{d_p}\right)^{F-3} = \frac{\varphi_s}{\varphi_a} \tag{4}$$

Cohesion force

Interparticle attraction is the defining characteristic of cohesive sediment. There are two principal forms of attraction, cohesion and adhesion, which are essential to the discussion of erodibility. According to the definition by Israelachvili (1985), cohesion describes attraction between chemically similar particles, while adhesion is used to describe the attraction between particles of dissimilar media. In terms of soil and sediment erosion research, cohesion usually refers to the bonding between fine-grained particles by electrochemical forces, and adhesion refers to the binding of sediment components by an additional inter-particle substance, such as organic polymers or iron oxides, *via* cation bridging or polymerization (Grabowski et al., 2011). In this study, we particularly focus on cohesive force between particles induced by electrochemical actions. The adhesive force due to the presence of additional media, e.g., organic matters and biofilms, is not taken into account.

Deriagin and Malkin (1950) confirmed the existence of cohesive forces between quartz particles by the experiment of cross-quartz fibers. They found the cohesive force between two particles scales with the particle diameter. After Deriagin and Malkin, numerous researchers found that the cohesive force not only scales with particle diameter but also is enhanced by the increasing compactness degree of sediment. Researchers including Tang (1963); Yang and Wang (1995); Li et al. (1995); Dou (2000); Zuo et al. (2017); Chen et al. (2018), etc., used a power function of the ratio of the dry bulk density of cohesive sediment to its stable dry bulk density (i.e., the dry bulk density of the sediment when it gets fully consolidated) to reflect the effect of the compactness of sediment. However, this method has two defects, limiting the application of the formulae for the erosion threshold based on those empirical functions for the cohesive force. One defect is although the stable dry bulk density is clear in the physical meaning, it is difficult to determine its value in practice accurately. A minor mistake of the stable dry bulk density would induce a massive error in the erosion threshold. The second defect is according to those studies mentioned above, the exponent of the power function seems not a constant but varies between 2 and 10.

The van der Waals attraction has been believed to be the fundamental source of cohesion caused by electrochemical actions (Han, 1982; Lick et al., 2004; Righetti & Lucarelli, 2007; Ternat et al., 2008). The van der Waals forces are intermolecular forces arising from the instantaneous dipole-induced dipole interactions among adjacent apolar atoms and molecules. Independently but similarly, Han (1982) and Israelachvili (1985) proposed the expression for the van der Waals force between two spherical particles by integrating the van der Waals forces between molecules in the two particles:

$$f_c = \frac{A_h}{24} d_p \frac{1}{l_\Delta^2} \tag{5}$$

where d_p is the diameter of cohesive particles; l_Δ is the separation distance between the two particles (i.e., the smallest distance between the surfaces of the particles); A_h is the Hamaker constant which reflects the strength of the van der Waals force.

Some researchers also considered the additional water pressure induced by the overlapping of the bound water layers as a fake cohesive force (Dou, 1962; Han, 1982; Dou, 2000; Zhang, 2012; Zuo et al., 2017). The fine-grained particles usually carry a negative electric charge on their surfaces. The electric charge on a particle surface attracts the surrounding water molecules to form a so-called bound water layer coating the particle. The bound water does not transmit hydrostatic pressure. Therefore, when two bound water layers overlap, the water pressure would induce an additional force acting on the overlapping area. This kind of additional force has been verified by the experiment with cross-quartz fibers (Dou, 1962; Dou, 2000). However, the relative magnitude between the additional force and the cohesive force induced by electrochemical actions has not been quantified. Besides, most of the existing erosion tests of cohesive sediments were conducted in small-depth water flumes. Therefore, the additional force induced by water pressure is not taken into account in this study.

Back to the van der Waals force between particles, studies have shown it is a short-range force with the effective acting range typically around 0.1 μm, being on the same order of magnitude as the thickness of the bound water layer (Han, 1982; Chien & Wan, 1999; Mehta, 2014; Hoath, 2016). Han (1982) pointed out that the van der Waals force is negligible when the separation distance between the two particles is beyond twice the thickness of the bound water layer. Accordingly, the van der Waals force is only significant between two contacted particles with the bound water layer overlapping. The average separation distance between contacted particles decreases with the increasing compactness degree of cohesive sediment, with the average van der Waals forces between contacted particles increasing with the increasing compactness degree. However, it is difficult to determine the average separation distance between two contacted particles accurately. This makes it impossible to apply Eq. (5) in cohesive sediment directly.

Although the average separation distance between two contacted particles is difficult to determine, the average separation distance between neighboring particles could be obtained. From a geometrical consideration, the average center-to-center distance between neighboring particles, s, in cohesive sediment could be computed by (Yang & Wang, 1995; Chauchat et al., 2013):

$$\frac{d_p^3}{s^3} = \varphi_s \tag{6}$$

According to Eq. (6), the average separation distance between neighboring particles is given by $s - d_p = d_p(\varphi_s^{-1/3} - 1)$, showing its value decreases with increasing compactness degree of cohesive sediment. Considering the solid volume fraction is in the range of 0.05 - 0.35 (a typical range for cohesive sediment), the average separation distance between neighboring particles, $(s - d_p)$, is on the same order of magnitude as the particle diameter, far beyond the effective acting range of the van der Waals force. This means the van der Waals force is not always effective between neighboring particles, which is expectable as not all the neighboring particles are contacted with each other because of the structure of aggregates, especially in a newly deposited sediment.

According to the above analysis, the dimensionless average separation distance between two contacted particles, l_Δ/δ (where δ is the thickness of the bound water layer), and the dimensionless average separation distance between neighboring particles, $(s - d_p)/d_p = \varphi_s^{-1/3} - 1$, are two measures of the compactness degree of sediment. As a first approximation, the two dimensionless average separation distances are assumed proportional:

$$\frac{l_\Delta}{\delta} = \eta \frac{s - d_p}{d_p} \tag{7}$$

where η is a coefficient. By substituting Eqs. (6) and (7) into Eq. (5), the average van der Waals force between two contacted particles in cohesive sediment is obtained:

$$f_c = \frac{A_h}{24\eta^2\delta^2} d_p \left(\varphi_s^{-1/3} - 1\right)^{-2} \tag{8}$$

Analysis of incipient motion of aggregates

Consider a horizontal cohesive sediment bed exposed to unidirectional flow and an aggregate located at the water-bed interface as presented in Figure 1. The stability of the aggregate depends on the balance of the hydrodynamic forces (i.e., the drag and lift forces of the overlying flow) and the erosion-resisting forces (i.e., the submerged weight of the aggregate and the cohesive forces). The aggregate is assumed a rigid body to possess a physically recognizable identity considering the entrainment of aggregates into flow is usually completed instantaneously. The movement initiation of aggregates usually comes from a rotation around a pivot. The momentum balance for the critical condition of the incipient motion of the aggregate leads to the following equation:

$$F_d k_1 d_a + F_l k_2 d_a = G_a k_3 d_a + F_c k_4 d_a \tag{9}$$

where F_d and F_l are the drag and lift forces, respectively; G_a is the submerged weight of the aggregate; F_c is the resultant of the cohesive forces acting on the aggregate; $k_1 d_a$,$k_2 d_a$, $k_3 d_a$ and $k_4 d_a$ are the moment arms of the drag force F_d , lift force F_l , submerged weight G_a , and resultant cohesive force F_c , respectively, with k_1 , k_2 , k_3 and k_4 being the proportionality coefficients.

The drag and lift forces acting on the aggregate are given by $F_d = C_d \rho u_*^2 \alpha_1 d_a^2$ and $F_l = C_l \rho u_*^2 \alpha_1 d_a^2$, respectively (Torfs et al.,

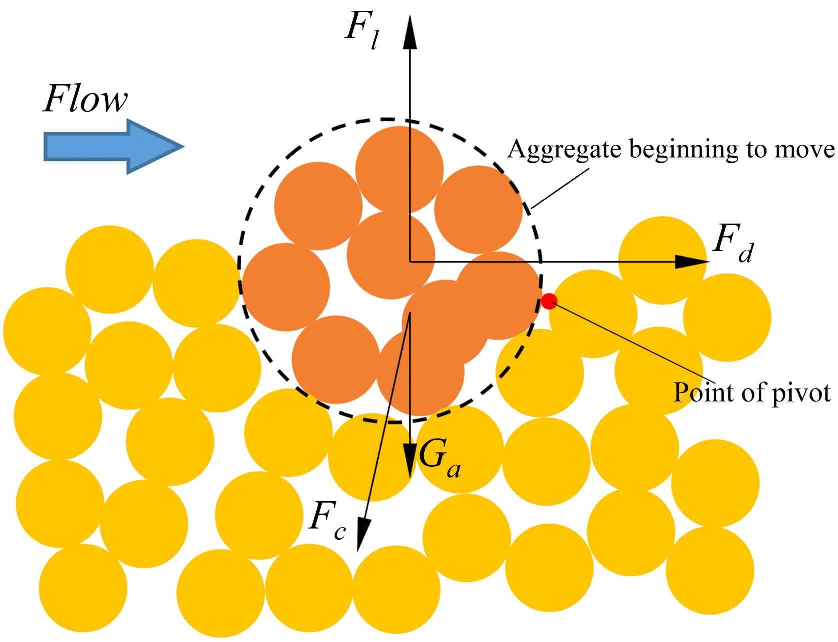

FIGURE 1
Aggregate at the water-sediment interface and force balance.

2000; Righetti & Lucarelli, 2007; Vollmer & Kleinhans, 2007), where C_d and C_l are drag and lift coefficients, respectively; ρ is the density of water; u_* is the shear velocity and α_1 is the area shape factor of the aggregate.

The submerged weight of the aggregate is given by $G_a=\alpha_2(\rho_a-\rho)gd_a^3$, where α_2 is a volumetric shape coefficient of the aggregate and g is the gravitational acceleration.

The resultant F_c could be obtained by integrating the van der Waals forces between the particles in the surface of the aggregate and those particles surrounding the aggregate: $F_c=k_5nc_nf_c$, where f_c is the van der Waals force between two contacted particles; n is the number of cohesive particles in the buried surface of the aggregate; c_n is the coordination number, i.e. the average number of the contacted particles of a cohesive particle; and k_5 is a coefficient.

The coordination number c_n is dependent on the solid volume fraction. According to the study of Meissner et al. (1964), c_n can be calculated by:

$$c_n = 2\exp(2.4\varphi_s) \tag{10}$$

The number of cohesive particles in the buried surface of the aggregate, n, could be computed by: $n=(1-\eta_\Delta)\pi d_a^2 N_{pa}$, where $(1-\eta_\Delta)\pi d_a^2$ denotes the buried surface area of the aggregate with η_Δ being the relative protruding fractal height of the aggregate (i.e., the ratio of the protruding fractal height to the diameter of the aggregate); and N_{pa} is the number of cohesive particles per unit area of the aggregate surface. It is assumed that the number of cohesive particles per unit area of the aggregate surface is proportional to the number of cohesive particles per unit area of the bed surface (N_{pb}):

$$N_{pa} = k_6 N_{pb} \tag{11}$$

where k_6 is a coefficient. N_{pb} could be estimated by:

$$1 \cdot N_{pb} \cdot \frac{\pi}{6} d_p^3 = 1 \cdot s \cdot \varphi_s \tag{12}$$

where 1 denotes a unit area of the bed surface and $\frac{\pi}{6} d_p^3$ denotes the volume of the primary particle. Considering Eqs. (11) and (12), n is given by $n=6(1-\eta_\Delta)k_6\varphi_s^{2/3}(d_a/d_p)^2$. Further considering Eqs. (10) and (8), the resultant cohesive force F_c is obtained:

$$F_c = \frac{A_h(1-\eta_\Delta)k_5k_6}{2\eta^2\delta^2}\frac{1}{d_p}d_a^2\varphi_s^{2/3}\left(\varphi_s^{-1/3}-1\right)^{-2}\exp(2.4\varphi_s) \tag{13}$$

Substituting the expressions for F_d, F_l, G_a and F_c into Eq. (9) and considering $u_* = \sqrt{\tau_b/\rho}$ in which τ_b is the bed shear stress, the critical shear stress for surface erosion of cohesive sediment, τ_{cr}, is given by:

$$\tau_{cr} = \frac{\alpha_2 k_3}{\alpha_1(k_1C_d+k_2C_l)}[(\rho_a-\rho)gd_a + \frac{A_h(1-\eta_\Delta)k_4k_5k_6}{2\alpha_2k_3\eta^2\delta^2}\frac{1}{d_p}\varphi_s^{2/3}\left(\varphi_s^{-1/3}-1\right)^{-2}\exp(2.4\varphi_s)] \tag{14}$$

Eq. (14) shows the erosion threshold of cohesive sediment comes from two parts respectively contributed by the effective gravity of the aggregate [corresponding to the first term in the square brackets in Eq. (14)] and the cohesive strength of the sediment (corresponding to the second term). If ignoring the cohesive forces acting on the aggregate, Eq. (14) would be reduced to:

$$\tau_{cr}=\frac{\alpha_2 k_3}{\alpha_1(k_1C_d+k_2C_l)}(\rho_a-\rho)gd_a \tag{15}$$

Eq. (15) denotes the critical shear stress of a cohesionless particle of a density of ρ_a and a diameter of d_a . This yields

$$\theta_{cr0}\left(d_{a\star}\right)=\frac{\alpha_2 k_3}{\alpha_1(k_1C_d+k_2C_l)} \tag{16}$$

where $\theta_{cr0}(d_{a^*})$ is the critical Shields parameter of noncohesive sediment of a dimensionless diameter d_{a^*} , which is defined as $d_{a^*}=d_a[(\rho_a/\rho\text{-}1)g/\upsilon^2]^{1/3}$ with υ being the kinematic viscosity of water. Considering Eqs. (3) and (4), d_{a^*} could be calculated by:

$$d_{a\star}=d_{p\star}\left(\frac{\varphi_s}{\varphi_a}\right)^{\frac{F}{3(F-3)}} \tag{17}$$

where d_{p^*} is the dimensionless particle diameter, defined as $d_{p^*}=d_p[(\rho_s/\rho\text{-}1)g/\upsilon^2]^{1/3}$. $\theta_{cr0}(d_{a^*})$ could be calculated by the Shields diagram or the formula of Soulsby and Whitehouse (1997).

Substituting Eq. (16) into Eq. (14), the critical shear stress for surface erosion of cohesive sediment is obtained:

$$\tau_{cr}=\theta_{cr0}\left(d_{a\star}\right)\left[(\rho_a-\rho)gd_a+C\frac{1}{d_p}\varphi_s^{2/3}\left(\varphi_s^{-1/3}-1\right)^{-2}\exp(2.4\varphi_s)\right] \tag{18}$$

where $C=0.5A_h(1-\eta_\Delta)k_4k_5k_6{\alpha_2}^{-1}{k_3}^{-1}\eta^{-2}\delta^{-2}$. The dimensionless form of Eq. (18) is given by:

$$\theta_{cr}=\theta_{cr0}\left(d_{a\star}\right)\left[\left(\frac{\varphi_s}{\varphi_a}\right)^{\frac{F-2}{F-3}}+C\frac{1}{(\rho_s-\rho)gd_p}\frac{1}{d_p}\varphi_s^{2/3}\left(\varphi_s^{-1/3}-1\right)^{-2}\exp(2.4\varphi_s)\right] \tag{19}$$

where θ_{cr} is the critical Shields parameter, $\theta_{cr}=\tau_{cr}/[(\rho_s-\rho)gd_p]$.

Eq. (19) is the formula we developed for predicting the threshold of surface erosion of cohesive sediment in which particle aggregation has been taken into account. Eq. (19) shows the critical Shields parameter of a cohesive sediment bed is a function of the diameter of the primary particles, the volume fraction of solid and the volume fraction of aggregates.

The volume fraction of aggregates φ_a of suspended cohesive sediment in a water body is usually lower than 1.0 (Winterwerp, 2002). However, when a cohesive sediment bed is formed from the deposition of flocs, the structure of the sediment changes from that of a high concentration of suspended sediment in the water to a flocculated matrix with a space-filling network (Kranenburg, 1994; Whitehouse, 2000; Winterwerp & Van Kesteren, 2004). Therefore, for cohesive sediment beds, φ_a=1.0 . However, we prefer to keep φ_a in Eq. (19) as keeping it in the formula makes the formula consistent with the existing theory for noncohesive sediments. For noncohesive sediment that is eroded particle-by-particle, the primary particles could be treated the same as the aggregates here. For such condition, the aggregate volume fraction equals the solid volume fraction, i.e. $\varphi_a=\varphi_s$, and Eq. (19) is therefore changed into:

$$\theta_{cr}=\theta_{cr0}\left(d_{p\star}\right)\left[1+C\frac{1}{(\rho_s-\rho)gd_p}\frac{1}{d_p}\varphi_s^{2/3}\left(\varphi_s^{-1/3}-1\right)^{-2}\exp(2.4\varphi_s)\right] \tag{20}$$

If ignoring the cohesion between particles, i.e., ignoring the second term in the square brackets, Eq. (20) is simplified to the general formula for the critical Shields parameter of noncohesive sediment: $\theta_{cr}=\theta_{cr0}(d_{p^*})$. In fact, the second term in the square brackets in Eq. (20) tends to vanish with the increase of the particle diameter as it is inversely proportional to the square of the particle diameter provided a low value of *C*. This makes that Eq. (20) also applies for coarse-grained noncohesive sediment. The values of *C* will be discussed in a later section.

There are two coefficients in Eq. (19): *F* and *C* . The fractal dimension *F* is a fundamental parameter of the aggregate structure, whose value reflects the space-filling ability of the aggregates. Structures with a high fractal dimension are usually compact and dense, whereas those with a low fractal dimension are more open. As the aggregate structure is formed by primary particles mainly characterized by the particle diameter, and changes during the consolidation process of the sediment, the fractal dimension of cohesive sediment is supposed to be a function of the particle diameter and the consolidation degree. Measurements of the fractal dimension of macroflocs of cohesive sediment in the water column reveal values from about 1.6 to 2.4, with a median value of 2 (Dyer & Manning, 1999; Khelifa & Hill, 2006; Son & Hsu, 2009; Fall et al., 2021). The fractal dimension of cohesive bed is often reported in the range of 2.0 to 2.8 (Kranenburg, 1994; Winterwerp & Van Kesteren, 2004; Sharif & Atkinson, 2012). Hasmy et al. (1997) reported a type of transition into a gelation stage takes place when the solid volume fraction exceeds the gel point resulting in a high value of the fractal dimension larger than 2.0. Therefore, the fractal dimension of cohesive sediment beds is considered between 2 and 3 in this study. The coefficient *C* mainly reflects the cohesive strength of the sediment. Currently, determination of its value is unavailable as coefficients involved in the expression for *C*, e.g., A_h , η , and δ , are usually unknown. The fractal dimension *F* and the coefficient *C* are treated as empirical coefficients that will be determined by the measured erosion thresholds of sediments.

In some research areas and practices, the bulk density is the more common variable than the solid volume fraction. By assuming the average dry and wet bulk densities of aggregates to be the same as the dry and wet bulk densities of the bed, respectively, the solid volume fraction has the following relations with the dry and wet bulk densities of a cohesive bed according to Eq. (3):

$$\varphi_s = \frac{\rho_b - \rho}{\rho_s - \rho} = \frac{\rho_d}{\rho_s} \tag{21}$$

where ρ_b is the wet bulk density and ρ_d is the dry bulk density. Equivalent forms of Eq. (19) which express the Shields parameter of cohesive sediment as a function of the wet or dry bulk density of sediment are given below:

$$\theta_{cr} = \theta_{cr0}\left(d_{a\star}\right)\left[\begin{array}{l}\left(\frac{\rho_b-\rho}{\rho_s-\rho}\right)^{\frac{F-2}{F-3}}+ \\ C\frac{1}{(\rho_s-\rho)gd_p}\frac{1}{d_p}\left(\frac{\rho_b-\rho}{\rho_s-\rho}\right)^{2/3}\left[\left(\frac{\rho_b-\rho}{\rho_s-\rho}\right)^{-1/3}-1\right]^{-2}\exp\left(2.4\frac{\rho_b-\rho}{\rho_s-\rho}\right)\end{array}\right] \tag{22}$$

$$\theta_{cr} = \theta_{cr0}\left(d_{a\star}\right)\left[\begin{array}{l}\left(\frac{\rho_d}{\rho_s}\right)^{\frac{F-2}{F-3}}+ \\ C\frac{1}{(\rho_s-\rho)gd_p}\frac{1}{d_p}\left(\frac{\rho_d}{\rho_s}\right)^{2/3}\left[\left(\frac{\rho_d}{\rho_s}\right)^{-1/3}-1\right]^{-2}\exp\left(2.4\frac{\rho_d}{\rho_s}\right)\end{array}\right] \tag{23}$$

where

$$d_{a\star} = d_{p\star}\left(\frac{\rho_b - \rho}{\rho_s - \rho}\right)^{\frac{F}{3(F-3)}} = d_{p\star}\left(\frac{\rho_d}{\rho_s}\right)^{\frac{F}{3(F-3)}}$$

Formula application

In this section, the developed formula for the threshold for surface erosion of cohesive sediment, i.e., Eq. (19), is applied to a series of experimental data with two approaches. One is treating the fractal dimension F as a constant and the other is regarding the fractal dimension F as a function of the diameter of primary particles and the compactness degree of sediment. The two approaches are employed to seek a complete solution to predicting the threshold of surface erosion of cohesive sediment.

Experimental data of different cohesive sediments are collected from previous studies. Those sediments include three groups of kaolinite, two groups of quartz, nine groups of lake and pond mud, and nine groups of coastal mud. In each of the collected experiments, the sediments prepared of different bulk densities were tested and the critical shear stresses of those sediments are measured. The adequacy of the experimental data has been carefully checked. The synopsis of the collected experimental data and data sources are presented in Table 1. It is noted that quartz also exhibits significant cohesion when the particle size is small enough despite that quartz is one of the common minerals in noncohesive sediment. According to Roberts et al. (1998) and Roberts et al. (2003), the sediment consisting of quartz particles behaves in a cohesive manner when the particle diameter is smaller than 40 microns and is eroded as aggregates when the particle diameter is smaller than 19 microns.

The fractal dimension *F* being constant

Figures 2–4 show the applications of Eq. (19) in kaolinite, quartz, lake and pond mud and coastal mud with the fractal dimension F being treated as a constant in each application. The best-match values of F and C are used in each application, which are obtained by performing the nonlinear regressions. The figures show although constant values of F are used, the calculated critical Shields parameters agree well with the measured values. This would be because the contribution rate of the effective weight of aggregates to the erosion threshold is relatively low for most of the sediments (i.e., the first term in the square brackets in Eq. (19) is much lower than the second term). Therefore, Eq. (19) could match the data well when a suitable value of C is provided. The contribution rate of the effective weight of aggregates to the erosion threshold of cohesive sediment will be further analyzed in a later section after the function for F is formulated.

The obtained fractal dimension F and coefficient C are listed in Table 2. As shown in Table 2, the obtained fractal dimension F varies between 2.0 to 2.76, with an average value being 2.36 and a standard deviation being 0.25. The covariance between the obtained fractal dimension F and the obtained coefficient C is nearly zero, which shows there are not any clear relations between the two variables. It is emphasized here that although Eq. (19) could reproduce the critical Shields parameters provided a constant F and C, the obtained values of F and C cannot reflect the property of the sediment aggregates accurately as F is insufficiently constrained in this approach.

The fractal dimension *F* being a function

The fractal dimension of an aggregate with a diameter closer to the size of the primary particles should approach the value of 3, which applies to coalescence of particles. By reference to Khelifa and Hill (2006) and Maggi et al. (2007), the following power law would present the reasonable approximation for F:

$$F = 3\left(\frac{d_a}{d_p}\right)^{\beta} \tag{24}$$

where β is a coefficient. Maggi et al. (2007) found Eq. (24) matches well with the floc size for flocculated kaolinite minerals in their experiments when β is taken a value of -0.1. Khelifa and Hill (2006) considered β is a function of the primary particle diameter of flocs. They proposed two models for the settling velocity and effective density of flocs under this consideration, which reproduce well the experimental data. By reference to

TABLE 1 Summary of collected experimental data of and data sources.

Kind of sediment	Sediment	Median diameter (mm)	Solid volume fraction	Critical shear stress (Pa)	Data source
Kaolinite	Kaolinite (Group 1)	0.006	0.06 ~ 0.23	0.29 ~ 1.69	Sharif (2003)
	Kaolinite (Group 2)	0.006	0.15 ~ 0.23	0.34 ~ 1.06	
	Kaolinite (Group 3)	0.0065	0.10 ~ 0.27	0.13 ~1.46	Otsubo and Muraoka (1988)
Quartz	Quartz (5.7 µm)	0.0057	0.41 ~ 0.53	0.22 ~ 1.33	Roberts et al. (1998)
	Quartz (14.8 µm)	0.0148	0.41 ~ 0.59	0.08 ~ 0.61	
Lake and pond mud	Kasumi Lake mud	0.0207	0.06 ~ 0.11	0.12 ~ 1.18	Otsubo and Muraoka (1988)
	Kasumigaura Lake mud	0.0277	0.03 ~ 0.06	0.07 ~ 0.65	
	Teganuma Pond mud	0.0256	0.05 ~ 0.10	0.19 ~ 1.43	
	Ushikunuma Pond mud	0.0173	0.06 ~ 0.10	0.16 ~ 0.88	
	Hinuma Lake mud	0.0118	0.05 ~ 0.08	0.20 ~ 0.78	
	Yunoko Lake mud	0.0165	0.04 ~ 0.07	0.15 ~ 0.94	
	Suwako Lake mud	0.011	0.05 ~ 0.07	0.31 ~ 0.75	
	Harunako Lake mud	0.0345	0.05 ~ 0.07	0.12 ~ 0.65	
	Inbanuma Lake mud	0.0154	0.07 ~ 0.08	0.24 ~ 0.45	
Coastal mud	Chikugo Estuary mud	0.0073	0.03 ~ 0.11	0.02 ~ 0.18	Kusuda et al. (1984)
	Tianjin New Port mud (Location 1)	0.0053	0.05 ~ 0.36	0.02 ~ 3.40	Hong and Xu (1991)
	Tianjin New Port mud (Location 2)	0.004	0.04 ~ 0.13	0.01 ~ 0.31	Dou (2000)
	Lianyungang Port mud	0.004	0.07 ~ 0.23	0.12 ~ 2.39	Huang (1989)
	Lianyungang Waterway mud	0.00512	0.09 ~ 0.23	0.08 ~ 1.34	Yang et al. (2018)
	Hangzhou Bay mud	0.0104	0.15 ~ 0.24	0.19 ~ 0.55	Yang & Wang (1995)
	Zhejiang Coastal Mud (Location 1)	0.0041	0.14 ~ 0.20	0.29 ~ 0.76	Li et al. (1995)
	Zhejiang Coastal Mud (Location 2)	0.0054	0.16 ~ 0.21	0.31 ~ 0.73	
	Huangmaohai Estuary mud	0.007	0.06 ~ 0.33	0.03 ~ 4.19	Xu et al. (2015)

Khelifa and Hill (2006), we also assume that the value of β is a function of the primary particle diameter of cohesive sediment beds in this study. As the critical shear stresses of the sediments prepared of the same primary particles and different bulk densities are measured in each collected experiment, the value of β will be constant in each dataset.

Substituting Eq. (4) into Eq. (24), the fractal dimension F of aggregates of cohesive sediment can be computed by:

$$\frac{F}{3} = \left(\frac{\varphi_s}{\varphi_a}\right)^{\frac{\beta}{F-3}} \tag{25}$$

Eq. (19) is then applied to the experimental data of kaolinite, quartz, lake and pond mud and coastal mud with the fractal dimension F being calculated by Eq. (25). The applications are shown in Figures 2-4, which show good agreements between the calculated and measured values. The best-match values of β and C for each dataset are used in the applications, which are obtained by the nonlinear regressions. They are also listed in Table 2 along with the ranges of the fractal dimension calculated by Eq. (25).

Discussion

Function for the fractal dimension

As presented in Table 2, the fractal dimension of cohesive sediment aggregates predicted by Eq. (25) is in the range of 2.01 to 2.80, being consistent with the reported ranges in cohesive beds by Kranenburg (1994); Sharif and Atkinson (2012) and Xu et al. (2014). The value of β is in the range of -0.02 to -0.14, being also consistent with the study of Maggi et al. (2007), in which a value of -0.1 was reported for flocculated kaolinite minerals. Figure 5 shows the obtained values of β decreases with increasing primary particle diameter and could be predicted by a linear function:

$$\beta = -\frac{d_p}{d_{pr}} - 0.02 \tag{26}$$

where d_{pr} is a reference primary particle diameter, d_{pr}=0.000290 m. Since here, Eqs. (19), (25) & (26) constitute a

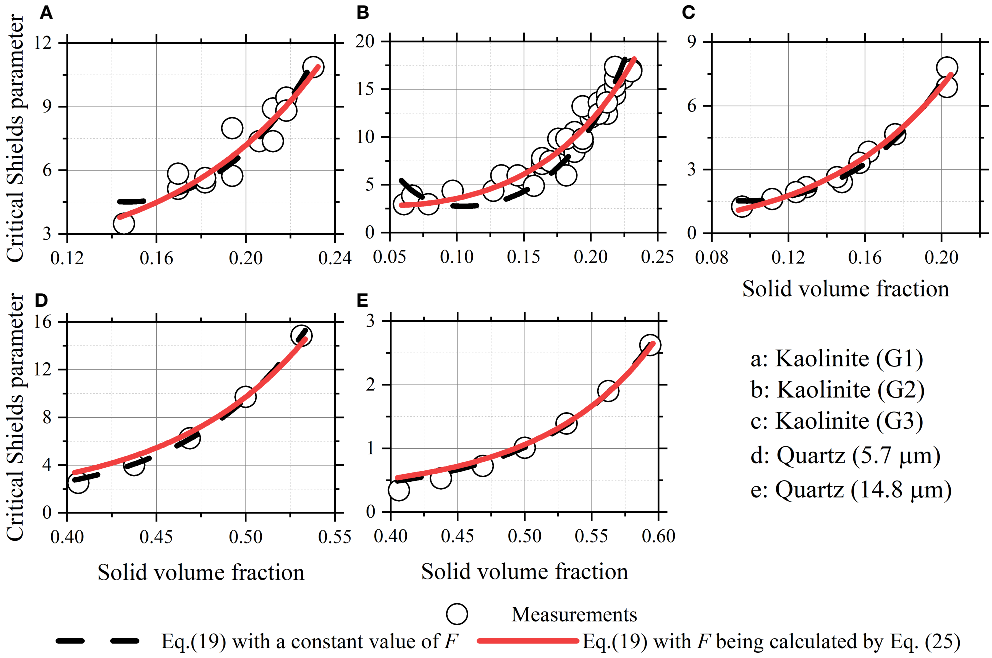

FIGURE 2
Applications of the developed formula in kaolinite and quartz.

complete solution to predicting the threshold of surface erosion of cohesive sediment.

Figure 6 shows the fractal dimension calculated by Eqs. (25) & (26) varying with the solid volume fraction and the primary particle diameter. It shows the fractal dimension increases with increasing solid volume fraction for sediments of the same primary particle diameter, and decreases with increasing primary particle diameter for sediments of the same solid volume fraction. The aggregate structure in the sediment of a high solid volume fraction is usually tightly packed, leading to a high value of the fractal dimension. The effect of the solid volume fraction on the fractal dimension has also been observed by other researchers, e.g., Sharif and Atkinson (2012), who reported that the fractal dimension of a cohesive sediment bed increases with increasing consolidation time. This effect is also consistent with the observations of suspended flocs in water bodies and colloids. Aubert and Cannell (1986) reported the fractal dimension of silica aggregates increases from 1.75 to 2.05 with the increase of silica concentration. Monte Carlo studies showed the rather compact clusters formed in the DLCA range exhibit the fractal dimension ranging between 1.8 ($\varphi_s \rightarrow 0$) and 2.5 ($\varphi_s \approx 0.5$), significantly larger than the typically reported values, of about 1.8 (Lazzari et al., 2016). The increase in the fractal dimension is ascribed to cluster collisions occurring close to the cluster centers rather than at their tips. Bowers et al. (2017) reported that the lowest mean value of the fractal dimension of marine flocs is observed off the west coast of Scotland, a region of relatively clearwater, and the highest values of the fractal dimension are observed in areas of fast tidal currents and high turbidity.

The finding of the fractal dimension decreasing with increasing particle diameter has seldom been reported in cohesive sediment research. It is consistent with a recent study on colloidal aggregation conducted by Wu et al. (2013). By analyses of a significant amount of data involving colloidal suspension of various types (e.g., polystyrene, silica, hematite) and performing adhoc experiments with differently sized polystyrene particles, they found the value of the fractal dimension decreases significantly as the primary particle size increases. Currently, there is an absence of a theoretical explanation for the effect of the particle diameter. Lazzari et al. (2016) suggested that small dipolar interactions could be at the root of the effect.

Cohesion coefficient C

The coefficient C denotes the cohesion strength of cohesive sediment, whose value is related to the Hamaker constant, the thickness of the bound water layer, the volumetric shape coefficient of the aggregates, the microstructure of aggregates in the bed surface, etc. Since the Hamaker constant and the thickness of the double water layer are usually a function of both the sediment material and the intervening medium, the

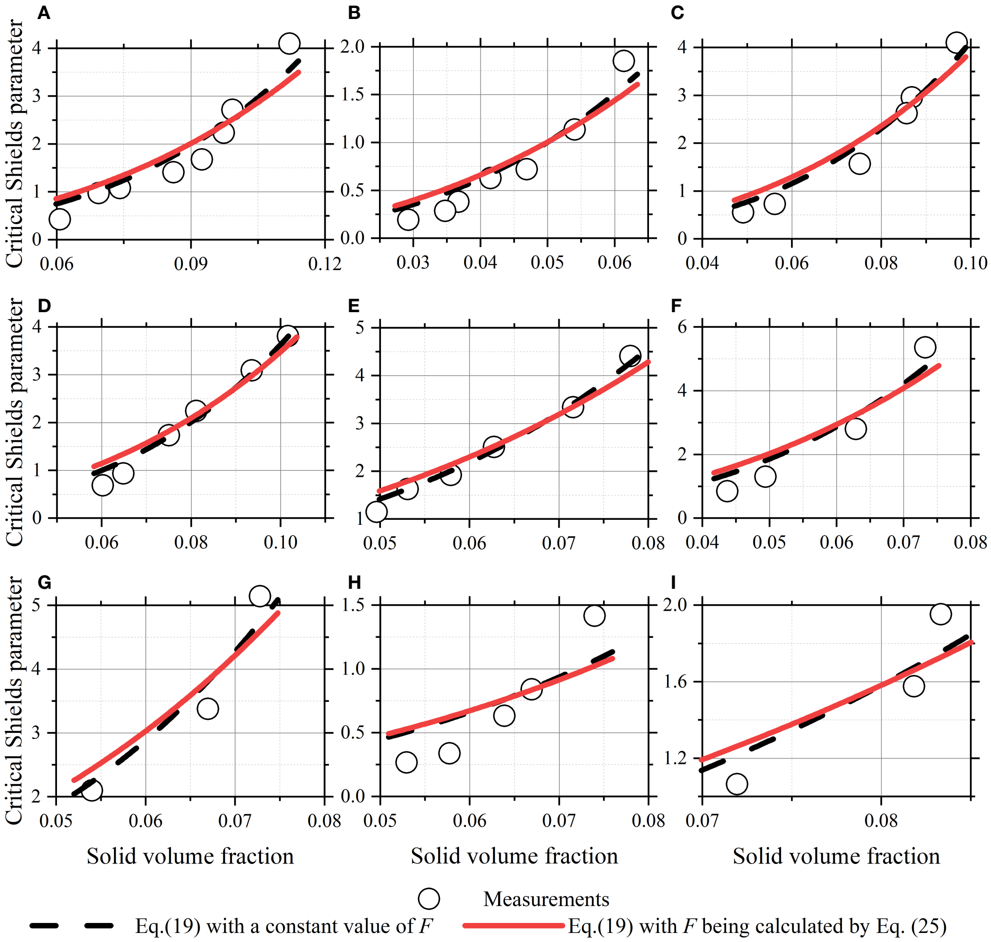

FIGURE 3
Applications of the developed formula in lake and pond mud. **(A)** Kasumi Lake mud; **(B)** Kasumigaura Lake mud; **(C)** Teganuma Pond mud; **(D)** Ushikunuma Pond mud; **(E)** Hinuma Lake mud; **(F)** Yunoko Lake mud; **(G)** Suwako Lake mud; **(H)** Harunako Lake mud; **(I)** Inbanuma Lake mud.

coefficient *C* would be affected by the mineral composition of particles, the shape and roughness of the particles, the sort and concentration of cations in pore waters, the pH value and temperature of the pore water, etc. As those data were often missing in research on the erosion of cohesive sediment, the relationship between the value of *C* and those affecters is unavailable.

As the mineral composition of sediment, the particle shape, and the pore water environment often vary from site to site, the value of *C* is supposed to be site- or sediment- specific. This property makes it futile to develop a universal formula with constant parameters for all sediments. A database of the value of *C* corresponding to the kind (or site) of sediment, like Table 2, would be necessary and valuable for practical applications.

As presented in Table 2, the value of *C* is generally on the order of magnitude of 10^{-6} to 10^{-3} J m^{-2}. Specifically, the value of *C* is the range of 7.44×10^{-5} ~ 19.04×10^{-5} J m^{-2} for kaolinite; 1.02×10^{-6} ~ 2.28×10^{-6} J m^{-2} for quartz; 0.80×10^{-3} ~ 3.93×10^{-3} J m^{-2} for lake and pond mud; and 1.93×10^{-5} ~ 12.97×10^{-5} J m^{-2} for coastal mud. The value of *C* for coastal mud is near to that of kaolinite. This may be because kaolinite is one of the common clay minerals of coastal mud. The value of *C* for quartz is one or two magnitudes lower than the value of *C* for kaolinite, which is consistent with the general recognition: kaolinite, as one of the common clay minerals, is much more cohesive than quartz, as one of the common minerals in noncohesive sediments. The value of *C* for the lake and pond mud is one or two magnitudes higher than the values of *C* for kaolinite and coastal mud. The reason may lie in that the lake and pond muds used in the experiments contain 11 ~ 19% organic matters that greatly enhance the adhesion of mud. Since adhesion is not considered in this study, the adhesive force brought by organic matter is regarded as part of the cohesive force, leading to a high value of *C* for the lake and pond mud.

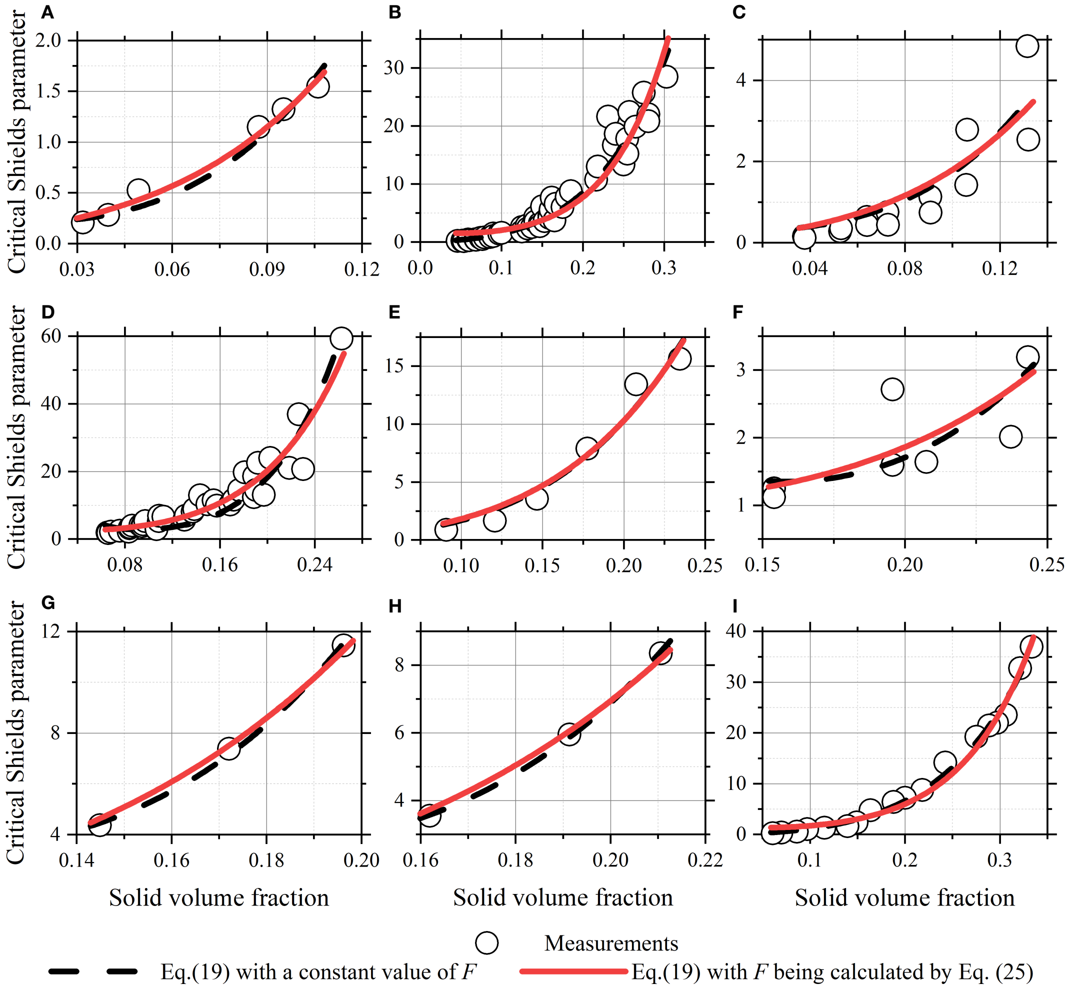

FIGURE 4
Applications of the developed formula in coastal mud. **(A)** Chikugo Estuary mud; **(B)** Tianjin New Port mud; **(C)** Tianjin New Port Waterway mud; **(D)** Lianyungang Port mud (L1); **(E)** Lianyungang Port mud (L2); **(F)** Hangzhou Bay mud; **(G)** Zhejiang coastal mud (L1); **(H)** Zhejiang coastal mud (L2); **(I)** Huangmaohai Estuary mud.

Although the coefficient C is site- and sediment- specific, one expects a guideline or reference value of C, with which Eq. (19) can give a reasonable estimate of critical shear stress of a certain kind of cohesive sediment. The guideline value, 9.12×10^{-5} J m^{-2}, is suggested for pure kaolinite; 1.05×10^{-6} J m^{-2} for pure quartz; 1.60×10^{-3} J m^{-2} for natural mud of 11 ~ 19% organic matters; 6.49×10^{-5} J m^{-2} for natural mud with almost no organic matter. These guideline values are respectively obtained based on the experimental data of kaolinite, quartz, lake and pond mud, and coastal mud by the following approach. For each kind of sediment, the value of C is allowed to increase step by step from 1.00×10^{-7} J m^{-2} to 1.00×10^{-2} J m^{-2} with an increment of each step 1.00×10^{-7} J m^{-2}. For each step, Eq. (19) is applied to the sediments and the logarithmic root-mean-square error of the predicted critical shear stress is calculated. The logarithmic root-mean-square error, defined as $\log E_{rms} = \sqrt{\sum_{i=1}^{N}\{\log[(\tau_{cr,c,i}+1)/(\tau_{cr,m,i}+1)]\}^2/N}$, is used as an indicator to evaluate the performance of Eq. (19) as the measured erosion threshold varies in several orders of magnitude. The fractal dimension in Eq. (19) is calculated by Eqs. (25) & (26). The guideline value of C is gained when the logarithmic root-mean-square error reaches its minimum value.

The comparisons of Eq. (19) with the experimental data of kaolinite, quartz, lake and pond mud, and coastal mud are shown in Figure 7. In the calculations of Eq. (19), the guideline values of C are used and the fractal dimension F is computed by Eqs. (25) & (26). As shown in the figure, Eq. (19) can give acceptable predictions when the guideline values of C are used and the fractal dimension is calculated by Eqs. (25) & (26).

TABLE 2 Application results of the developed formula in different cohesive sediments.

Kind of sediment	Sediment	F being a constant		F being a function		
		F	C	β	C	F
Kaolinite	Kaolinite (G1)	2.67	10.47	-0.02	19.04	2.58 ~ 2.69
	Kaolinite (G2)	2.62	13.00	-0.02	11.06	2.65 ~ 2.70
	Kaolinite (G3)	2.59	8.16	-0.04	7.44	2.49 ~ 2.58
Quartz	Quartz (5.7 µm)	2.76	0.17	-0.02	0.23	2.77 ~ 2.80
	Quartz (14.8 µm)	2.55	0.07	-0.06	0.10	2.66 ~ 2.71
Lake and pond mud	Kasumi Lake mud	2.24	144.93	-0.09	151.60	2.19 ~ 2.28
	Kasumigaura Lake mud	2.02	369.17	-0.12	393.19	1.97 ~ 2.08
	Teganuma Pond mud	2.15	329.32	-0.10	357.23	2.11 ~ 2.21
	Ushikunuma Pond mud	2.22	114.20	-0.09	129.70	2.21 ~ 2.28
	Hinuma Lake mud	2.26	121.33	-0.07	130.10	2.24 ~ 2.29
	Yunoko Lake mud	2.21	226.50	-0.08	242.12	2.19 ~ 2.25
	Suwako Lake mud	2.29	131.24	-0.07	134.69	2.27 ~ 2.31
	Harunako Lake mud	2.02	296.78	-0.14	305.83	2.01 ~ 2.06
	Inbanuma Lake mud	2.25	78.72	-0.08	80.40	2.24 ~ 2.26
Coastal mud	Chikugo Estuary mud	2.34	6.68	-0.05	9.83	2.32 ~ 2.44
	Tianjin New Port mud (L1)	2.00	1.69	-0.03	8.43	2.54 ~ 2.71
	Tianjin New Port mud (L2)	2.61	1.81	-0.06	1.93	2.27 ~ 2.42
	Lianyungang Port mud	2.63	7.18	-0.02	12.97	2.58 ~ 2.70
	Lianyungang Waterway mud	2.64	2.10	-0.10	2.80	2.23 ~ 2.39
	Hangzhou Bay mud	2.63	6.43	-0.03	7.03	2.62 ~ 2.67
	Zhejiang Coastal Mud (L1)	2.00	6.31	-0.03	4.58	2.57 ~ 2.60
	Zhejiang Coastal Mud (L2)	2.12	6.58	-0.04	4.82	2.56 ~ 2.59
	Huangmaohai Estuary mud	2.38	2.51	-0.03	11.92	2.58 ~ 2.69

C is in 10^{-5} J m^{-2}.

Although some guideline or reference values of *C* are given here, it is emphasized that these values can be optimized when Eq. (19) is applied to a specific site. The accurate value of *C* for a specific site can be obtained by applying Eq. (19) to a sediment sample of known critical shear stress collected in the site.

Effects of particle aggregation

Figure 8 shows the predicted diameter of aggregates and the average number of primary particles in an aggregate varying with the particle diameter and the solid volume fraction. The predicted diameter of aggregates is calculated by Eq. (4) and the average number of primary particles in an aggregate is calculated by Eq. (1), with the fractal dimension *F* being computed by Eqs. (25) & (26). The figure shows both the predicted aggregate diameter and the average number of primary particles in an aggregate decrease with increasing solid volume fraction, which indicates reshuffling of particles occurs during the consolidation process of cohesive sediment. The predicted aggregate diameter behaves with the primary particle diameter in a relatively complicated manner. For a relatively high value of solid volume fraction, the predicted aggregate diameter increases monotonously with increasing primary particle diameter. While for a relatively low value of solid volume fraction, the predicted aggregate diameter increases with the primary particle diameter first, but decreases with increasing primary particle diameter at the diameter around 0.01 mm, and then converts to increase again.

The predicted diameter of aggregates is mainly on the order of magnitude of tens of microns to hundreds of microns for cohesive sediment of a solid volume fraction in the range of 0.05 ~ 0.35 (a typical range for cohesive sediment). The range of the predicted diameter of aggregates is consistent with the observations of the surface erosion of cohesive fractal aggregates by Thomsen and Gust (2000); Righetti and Lucarelli (2007) and Forsberg et al. (2018). However, some researchers observed the eroded aggregates from cohesive bed surfaces could be up to 2 ~ 4 mm, e.g., Amos et al. (2003); Sharif (2003); Mostafa et al. (2008). This would be because the aggregates are usually of a broad size distribution range, which has been observed by Thomsen and Gust (2000); Righetti and Lucarelli (2007) and Forsberg et al. (2018). While the diameter of aggregates calculated by Eq. (4) is only the average diameter.

Eq. (19) suggests the erosion threshold of cohesive sediment comes from two parts, respectively contributed by the

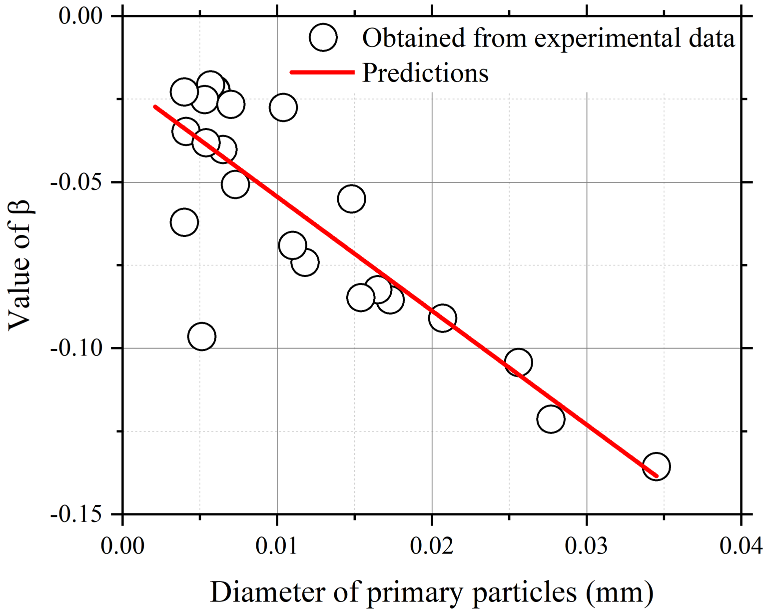

FIGURE 5
The value of β varying with the diameter of primary particles.

submerged weight of the aggregate (which corresponds to the product of $\theta_{cr0}(d_{a^*})$ and the first term in the square brackets) and the cohesive strength (corresponding to the product of $\theta_{cr0}(d_{a^*})$ and the second term). The contribution rate of the submerged aggregate weight to the erosion threshold equals the ratio of the first term in the square brackets in Eq. (19) to the sum of the first term and the second term. Figure 9 shows the critical Shields parameter of cohesive sediment and the contribution rate of the

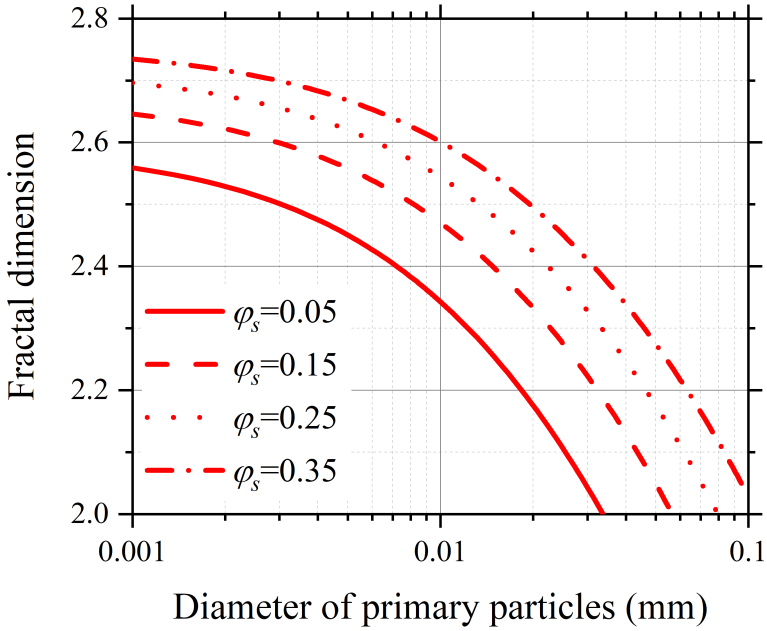

FIGURE 6
The fractal dimension varying with the diameter of primary particles and the solid volume fraction.

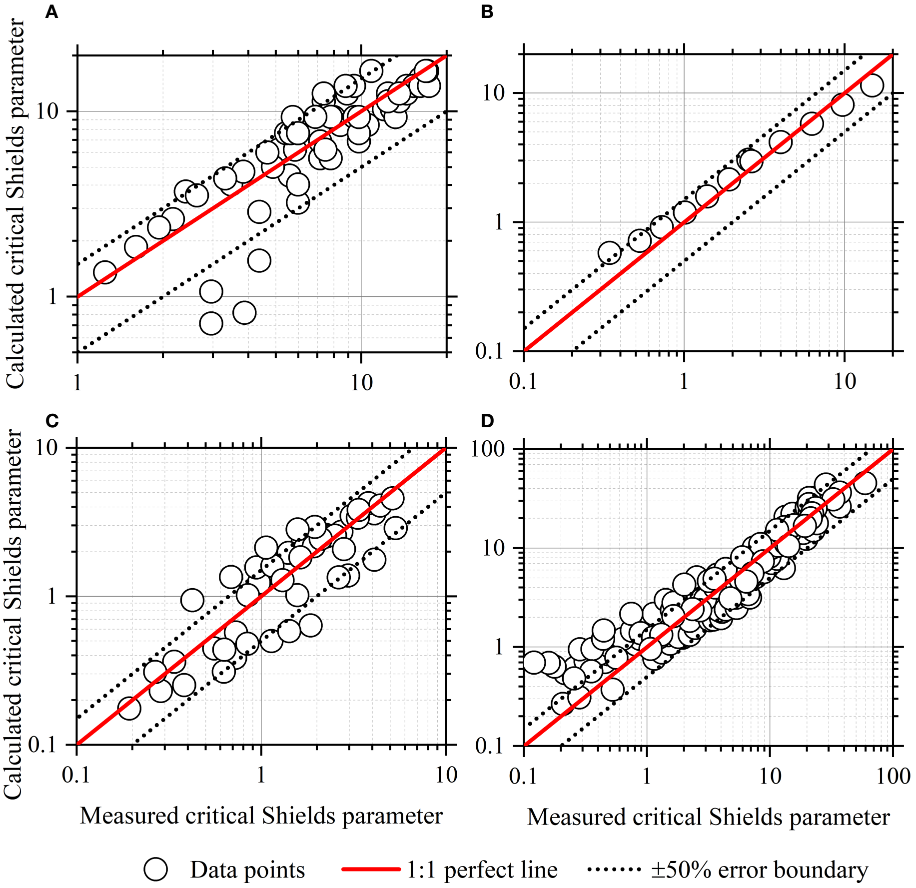

FIGURE 7
The calculated versus measured critical Shields parameters in the datasets of **(A)** kaolinite, **(B)** quartz, **(C)** lake and pond mud and **(D)** coastal mud.

submerged aggregate weight varying with the particle diameter and the solid volume fraction. In the calculations, the coefficient C is taken the guideline value for natural mud of no organic matter, i.e., 6.49×10^{-5} J m^{-2}. The threshold band and the mean threshold curve for noncohesive sediment are also plotted in the figure. The upper and lower boundaries of the threshold band are calculated by the formulae of Paphitis (2001). The mean threshold curve is calculated by the formula of Soulsby and Whitehouse (1997). As shown in Figure 9, the calculated critical Shields parameter increases with increasing solid volume fraction for the same particle diameter and decreases with increasing particle diameter for the same solid volume fraction. It is found that for those sediments of large particle diameters and low solid volume fractions, the calculated critical Shields parameters could be lower than the threshold values of noncohesive sediments. In fact, this would not happen in practical circumstances as a sediment bed consisting of relatively large particles is only formed with enough high solid volume fraction. From this point of view, the applicable range for Eq. (19) in natural mud of no organic matter is given by:

$$\varphi_s > \left(d_p/d_{p0}\right)^{0.15} - 0.45 \tag{27}$$

where d_{p0} is a reference diameter, being 0.001 m.

As shown in Figure 9, the contribution rate of the effective weight of aggregate decreases with increasing solid volume fraction for the same particle diameter and increases with increasing particle diameter for the same solid volume fraction. It is found that the contribution rate of the effective weight of aggregate is sufficiently low to be negligible for the sediment of relatively small particle diameter and high solid volume fraction, e.g., the contribution rate is approximately 0.6 ~ 2.1% for the sediment of the particle diameter 0.004 mm and the solid volume fraction in the range of 0.25-0.35. However, for those sediments of relatively large particle diameters and low solid volume fractions, the contribution rate of the effective weight of aggregate could be high that cannot be ignored. For example, for the sediment of the particle diameter 0.02 mm with the solid volume fraction in the range of 0.10~ 0.15, the contribution rate of the effective weight is between 33 and 53%.

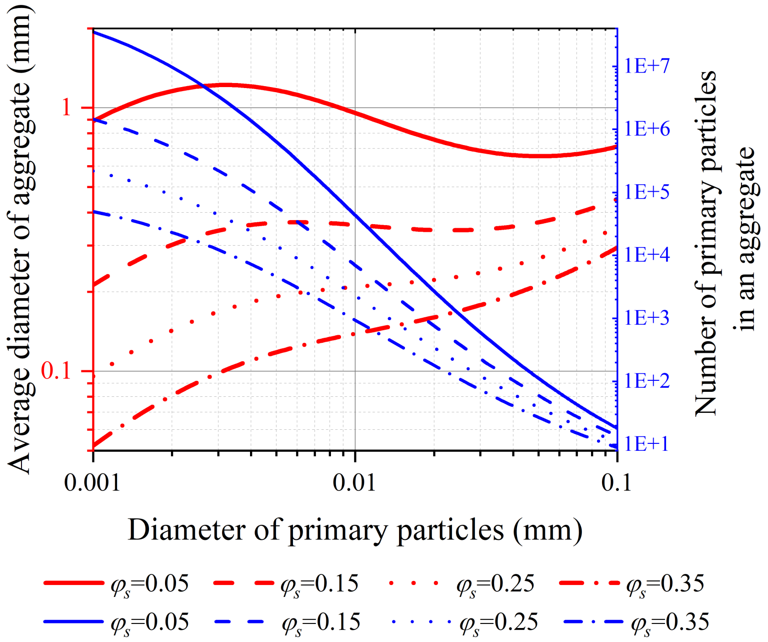

FIGURE 8
The predicted aggregate diameter and the average number of primary particles in an aggregate varying with the primary particle diameter and the solid volume fraction.

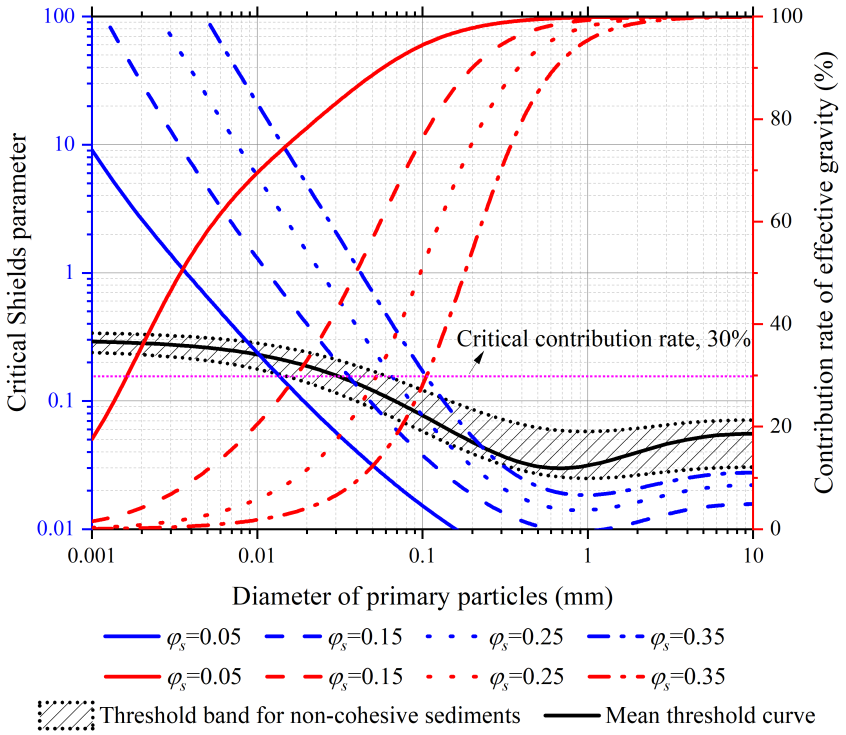

FIGURE 9
The critical Shields parameter and contribution rate of effective gravity of aggregate versus diameter of primary particles and solid volume fraction.

Here a critical contribution rate is further proposed, being 30%, below which the contribution rate of the effective gravity of cohesive sediment to the erosion threshold is considered negligible, while beyond which the contribution rate of the effective gravity is significant that should be taken into account. According to the calculations of Eq. (19), for natural mud of no organic matter, the contribution rate of the effective gravity of cohesive sediment is higher than the critical contribution rate when

$$\varphi_s \le \left(d_p/d_{p0}\right)^{0.47} \tag{28}$$

While for the sediments of $\varphi_s>(d_p/d_{p0})^{0.47}$, the contribution rate of the effective gravity of sediment is lower than the critical contribution rate. For those sediments, Eq. (19) can be simplified to the following form:

$$\theta_{cr} = A\frac{1}{(\rho_s-\rho)gd_p}\frac{1}{d_p}\varphi_s^{2/3}\left(\varphi_s^{-1/3}-1\right)^{-2}\exp(2.4\varphi_s) \tag{29}$$

where $A=\theta_{cr0}(d_{a*})C$. The value of $\theta_{cr0}(d_{a*})$ varies in a narrow range for the sediments of $\varphi_s>(d_p/d_{p0})^{0.47}$ .Therefore, the value of A could be approximately constant.

Eq. (29) shows the critical Shields parameter approaches zero with the increase of the particle diameter provided a low value of A as it is inversely proportional to the square of the particle diameter. Since the critical Shields parameter of non-cohesive sediment, i.e., $\theta_{cr}=\theta_{cr0}(d_{p*})$, is generally far lower than the critical Shields parameter of the cohesive sediment for fine particles, Eq. (29) is further revised into the following form to make it applicable for both cohesive sediment and non-cohesive sediment:

$$\begin{aligned}\theta_{cr} &= \theta_{cr0}\left(d_{p*}\right)\\ &\quad + A\frac{1}{(\rho_s-\rho)gd_p}\frac{1}{d_p}\varphi_s^{2/3}\left(\varphi_s^{-1/3}-1\right)^{-2}\exp(2.4\varphi_s)\end{aligned} \tag{30}$$

According to the collected experimental data, the guideline or reference values of A obtained by the same approach of the reference values of C are given as: 5.24×10^{-6} J m^{-2} for kaolinite; 1.00×10^{-7} J m^{-2} for quartz and noncohesive sediments; 6.54×10^{-5} J m^{-2} for natural mud of 11 ~ 19% organic matters; and 3.71×10^{-6} J m^{-2} for natural mud of no organic matter. Figure 10 shows the comparison of Eq. (30) and the measured critical Shields parameters of those sediments of solid volume fractions higher than $(d_p/d_{p0})^{0.47}$ in the series of coastal mud. The agreement is generally good.

Figure 11 shows the critical Shields parameter predicted by Eq. (30) varying with the particle diameter and the solid volume fraction for $A = 1.00\times10^{-7}$ J m^{-2}. The critical Shields parameters of quartz of different particle diameters measured by Roberts et al. (1998) are also plotted in the figure. It shows that Eq. (30) could reproduce well the critical Shields parameter of both fine

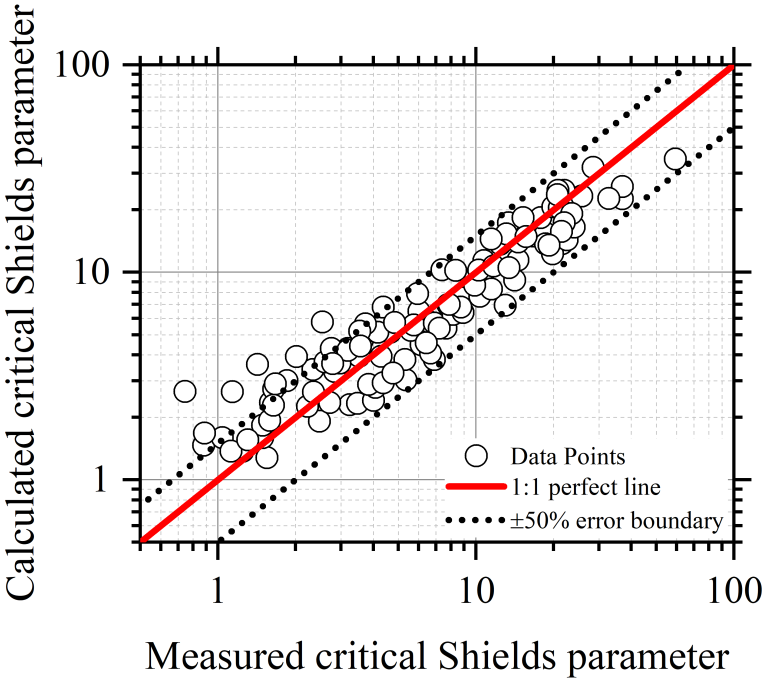

FIGURE 10
Comparison of the calculated critical Shields parameters by Eq. (30) and measured critical Shields parameters for sediments of the contribution rate of effective gravity lower than 30% in the datasets of coastal mud.

cohesive quartz and coarse non-cohesive quartz, demonstrating the capacity of Eq. (30). It is emphasized here that *A* in Eq. (30) is an empirical coefficient. Its value not only reflects the cohesion strength of cohesive sediment but also covers part of the effect of particle aggregation and accounts for part of the compensation of the neglected aggregate weight. Compared with Eqs. (19), (25) & (26), Eq. (30) is simpler that could be used where the characteristics of aggregate erosion are not necessary to be considered. While Eqs. (19), (25) & (26) provide a complete solution to the threshold of surface erosion of cohesive sediment, in which the fractal bed aggregation is appropriately taken into account.

Conclusion

The threshold of surface erosion of cohesive sediments composed of fractal aggregates is investigated in this study. The fractal theory is employed to describe the size and density of cohesive sediment aggregates and the van der Waals force is introduced to quantify the cohesive force between particles. A formula for the critical shear stress for erosion of cohesive sediment aggregates is obtained by analyzing the momentum balance of an aggregate at the bed surface under the critical condition of initial motion. It is expressed as a function of the diameter of primary particles and the solid volume fraction, and has two coefficients: the fractal dimension *F* and the cohesion coefficient *C*.

The developed formula, i.e., Eq. (19), has been successfully applied to three groups of kaolinite, two groups of quartz, nine groups of lake and pond mud, and nine groups of coastal mud with two approaches. One is treating the fractal dimension *F* as a constant and the other is regarding the fractal dimension *F* as a function of the diameter of primary particles and the compactness degree of sediment. The first approach is not recommended as the fractal dimension *F* is insufficiently constrained to give any meaningful value. Formulae [i.e., Eqs. (25) & (26)] are developed for predicting the fractal dimension *F* based on the application results of the developed formula. The two formulae for predicting *F* constitute a complete solution to the threshold of surface erosion of cohesive sediment along with Eq. (19).

The cohesion coefficient *C* denotes the cohesion strength of sediment, with its value usually being site- or sediment- specific. Guideline or reference values of *C* are given based on the collected experimental data.

According to the function for the fractal dimension and the fractal theory, the average diameter of aggregates is mainly on the order of magnitude of hundreds of microns. The contribution rate of the submerged aggregate weight could be high and cannot be ignored for the sediments of relatively large particle diameters and low solid volume fractions. While for the

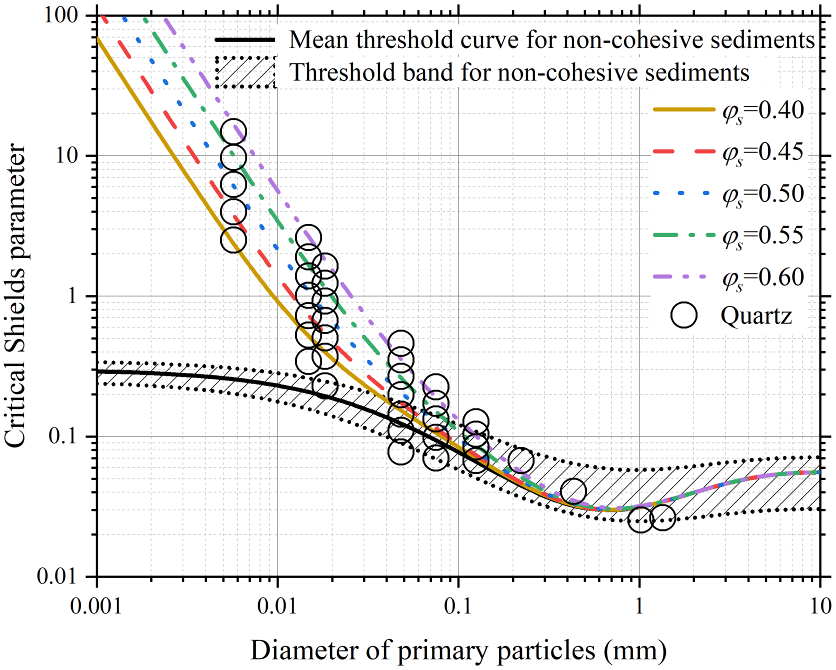

FIGURE 11
The critical Shields parameter predicted by Eq. (30) varying with the diameter of primary particles and solid volume fraction and being compared with the critical Shields parameters of quartz of different particle diameters measured by Roberts et al. (1998).

sediments of relatively small particle diameter and high solid volume fraction, the contribution rate of the submerged aggregate weight is sufficiently low that could be negligible. For those sediments, the developed formula could further be simplified into a simple formula with only one coefficient.

Notation

A = coefficient (J m^{-2})
A_h = Hamaker constant (J)
C = coefficient (J m^{-2})
C_d, C_l= drag and lift coefficients (-)
C_n = coordination number (-)
d_a = aggregate diameter (m)
d_p = diameter of primary particles (m)
d_{pr} = reference particle diameter (m)
d_{p0} = reference particle diameter (m)
d_{a*} = dimensionless diameter of aggregates (-)
d_{p*} = dimensionless diameter of primary particles (-)
E_r = relative error (-)
F = fractal dimension (-)
F_c = resultant cohesive force (kg m s^{-2})
F_d = drag force (kg m s^{-2})
F_l = lift force (kg m s^{-2})
f_c = van der Waals force (kg m s^{-2})
G_a = submerged weight of the aggregate (kg m s^{-2})
g = gravitational acceleration (m s^{-2})
K_1, K_2, K_3, K_4, K_5, K_6, = coefficients (-)
$/_{\Delta}$ = separation distance between two particles (m)
log E_{rms} = logarithmic root-mean-square error (-)
N = total number of the data (-)
n = number of particles in the buried surface of the aggregate (-)
N_p = number of primary particles in the aggregate of a diameter d_a (-)
N_{pa}= number of cohesive particles per unit area of the aggregate surface (-)
N_{pb} = number of cohesive particles per unit area of the bed surface (-)
s = average center-to-center distance between neighboring particles (m)
u_* = shear velocity (m s^{-1})
α_1 = area shape factor of aggregate (-)
α_2 = volumetric shape coefficient of aggregate (-)
β = coefficient (-)
δ = thickness of the water film coating particles (m)
η = coefficient (-)
η_Δ = relative protruding height of an aggregate (-)
Θ_{cr0} = critical Shields parameter of noncohesive sediment (-)
υ = kinematic viscosity of water (m^2 s)
ρ = density of water (kg m^{-3})
ρ_a = density of aggregate (kg m^{-3})
ρ_b = bulk density of sediment (kg m^{-3})
ρ_s = density of primary particles (kg m^{-3})
τ_b = bed shear stress (Pa)
τ_{cr} = critical shear stress (Pa)
$\tau_{cr,c}$ = calculated critical shear stress (Pa)
$\tau_{cr,m}$ = measured critical shear stress (Pa)
φ_a = volume fraction of aggregates (-)
φ_s = volume fraction of primary particles (-)

Data availability statement

The original contributions presented in the study are included in the article/supplementary material. Further inquiries can be directed to the corresponding author.

Author contributions

DC and CZ contributed to the conception of the study, the theory development, and manuscript preparation. JZ and DG contributed significantly to constructive discussions. YL and HH contributed to the analysis of the data for the work. All authors contributed to the article and approved the submitted version.

Funding

This work was supported by the National Natural Science Foundation of China [52101310]; the National Natural Science Foundation of China [51879096, 51979096]; the Major International (Regional) Joint Research Project of National Natural Science Foundation of China [51920105013] and the Key Project of NSFC-Shangdong Joint Research Funding POW3C [U1906230].

Conflict of interest

The authors declare that the research was conducted in the absence of any commercial or financial relationships that could be construed as a potential conflict of interest.

Publisher's note

References

Amos, C., Bergamasco, A., Umgiesser, G., Cappucci, S., Cloutier, D., DeNat, L., et al. (2004). The stability of tidal flats in Venice lagoon–the results of *in-situ* measurements using two benthic, annular flumes. *J. Mar. Syst.* 51 (1), 211–241. doi: 10.1016/j.jmarsys.2004.05.013

Amos, C. L., Droppo, I. G., Gomez, E. A., and Murphy, T. P. (2003). The stability of a remediated bed in Hamilton harbour, lake Ontario, Canada. *Sedimentology* 50 (1), 149–168. doi: 10.1046/j.1365-3091.2003.00542.x

Aubert, C., and Cannell, D. S. (1986). Restructuring of colloidal silica aggregates. *Phys. Rev. Lett.* 56 (7), 738. doi: 10.1103/PhysRevLett.56.738

Bowers, D., McKee, D., Jago, C., and Nimmo-Smith, W. (2017). The area-to-mass ratio and fractal dimension of marine flocs. *Estuarine Coast. Shelf Sci.* 189, 224–234. doi: 10.1016/j.ecss.2017.03.026

Chang, T. S., Joerdel, O., Flemming, B. W., and Bartholomä, A. (2006). The role of particle aggregation/disaggregation in muddy sediment dynamics and seasonal sediment turnover in a back-barrier tidal basin, East Frisian wadden Sea, southern north Sea. *Mar. Geology* 235 (1-4), 49–61. doi: 10.1016/j.margeo.2006.10.004

Chauchat, J., Guillou, S., Pham Van Bang, D., and Dan Nguyen, K. (2013). Modelling sedimentation–consolidation in the framework of a one-dimensional two-phase flow model. *J. Hydraulic Res.* 51 (3), 293–305. doi: 10.1080/00221686.2013.768798

Chen, S., and Eisma, D. (1995). Fractal geometry of *in situ* flocs in the estuarine and coastal environments. *Netherlands J. Sea Res.* 33 (2), 173–182. doi: 10.1016/0077-7579(95)90004-7

Chen, D., Wang, Y., Melville, B., Huang, H., and Zhang, W. (2018). Unified formula for critical shear stress for erosion of sand, mud, and sand-mud mixtures. *J. Hydraulic Eng.* 144 (8), 04018046. doi: 10.1061/(Asce)Hy.1943-7900.0001489

Chen, D., Zheng, J., Zhang, C., Guan, D., Li, Y., and Wang, Y. (2021). Critical shear stress for erosion of sand-mud mixtures and pure mud [Original research]. *Front. Mar. Sci.* 8 (1502). doi: 10.3389/fmars.2021.713039

Chien, N., and Wan, Z. (1999). *Mechanics of sediment transport*. Ed. J. S. McNown (Reston, VA: ASCE Press). Trans.; ASCEOriginal in Chinese published by China Science Press, Beijing. ed. doi: 10.1061/9780784404003

Debnath, K., and Chaudhuri, S. (2010). Cohesive sediment erosion threshold: A review. *ISH J. Hydraulic Eng.* 16 (1), 36–56. doi: 10.1080/09715010.2010.10514987

Deriagin, B. I., and Malkin, A. D. (1950). Cohesive forces between quartz fibers in water environments. *Colloid J.* 12 (6), 431–447. (in Russian)

Dickhudt, P. J., Friedrichs, C. T., and Sanford, L. P. (2011). Mud matrix solids fraction and bed erodibility in the York river estuary, USA, and other muddy environments. *Continental Shelf Res.* 31 (10, Supplement), S3–S13. doi: 10.1016/j.csr.2010.02.008

Dou, G. (1962). Theory for incipient motion of sediment. *Scientia Sin.* 11 (7), 999–1032. (in Russian)

Dou, G. (2000). Incipient motion of sediment under currents. *China Ocean Eng.* 14 (4), 391–406.

Dyer, K., and Manning, A. (1999). Observation of the size, settling velocity and effective density of flocs, and their fractal dimensions. *J. Sea Res.* 41 (1-2), 87–95. doi: 10.1016/S1385-1101(98)00036-7

Fall, K. A., Friedrichs, C. T., Massey, G. M., Bowers, D. G., and Smith, S. J. (2021). The importance of organic content to fractal floc properties in estuarine surface. *Waters: Insights From Video LISST Pump Sampling* 126 (1), e2020JC016787. doi: 10.1029/2020JC016787

Forsberg, P. L., Skinnebach, K. H., Becker, M., Ernstsen, V. B., Kroon, A., and Andersen, T. J. (2018). The influence of aggregation on cohesive sediment erosion and settling. *Continent. Shelf Res.* 171, 52–62. doi: 10.1016/j.csr.2018.10.005

Grabowski, R. C., Ppo, I. G., and Wharton, G. (2011). Erodibility of cohesive sediment: The importance of sediment properties. *Earth-Science Rev.* 105 (3), 101–120. doi: 10.1016/j.earscirev.2011.01.008

Han, Q. (1982). Characteristics of incipient sediment motion and incipient velocity. *J. Sediment Res.* 2, 11–26. (in Chinese).

Hasmy, A., Anglaret, É., Thouy, R., and Jullien, R. (1997). Fluctuating bond aggregation: a numerical simulation of neutrally-reacted silica gels. *J. Physique I* 7 (3), 521–542. doi: 10.1051/jp1:1997173

Hoath, S. D. (2016). *Fundamentals of inkjet printing: the science of inkjet and droplets.* Weingeim, Germany: Wiley-VCH.

Hong, R., and Xu, S. (1991). Experimental study on incipient of mud in a fluid. *J. Tianjin. Univ.*(S2), 79–85. (in Chinese).

Hua, X., Huang, H., Wang, Y., Lan, Y., Zhao, K., and Chen, D. (2019). Abnormal ETM in the North Passage of the Changjiang River Estuary: Observations in the wet and dry seasons of 2016. *Estuarine Coast. Shelf Sci.* 227, 12. doi: 10.1016/j.ecss.2019.106334

Huang, J. (1989). An experimental study of the scouring and settling properties of cohesive sediment. *Ocean Eng.* 7(1), 61–70. (in Chinese).

Israelachvili, J. (1985). *Intermolecular and surface forces* (London: Academic Press).

Jacobs, W., Le Hir, P., Van Kesteren, W., and Cann, P. (2011). Erosion threshold of sand-mud mixtures. *Continental Shelf Res.* 31 (10), 514–525. doi: 10.1016/j.csr.2010.05.012

Khelifa, A., and Hill, P. S. (2006). Models for effective density and settling velocity of flocs. *J. Hydraulic Res.* 44 (3), 390–401. doi: 10.1080/00221686.2006.9521690

Kranenburg, C. (1994). The fractal structure of cohesive sediment aggregates. *Estuarine Coast. Shelf Sci.* 39 (5), 451–460. doi: 10.1006/ecss.1994.1075

Krone, R. B. (1963). *A study of rheologic properties of estuarial sediments (Technical bulletin no. 7).* (California Univ Berkeley Sanitary Engineering Research Lab. Vicksburg, MS).

Krone, R. B. (1986). "The significance of aggregate properties to transport processes," in *Estuarine cohesive sediment dynamics*, Tampa, Florida: Springer 1986, 66–84.

Kusuda, T., Umita, T., Koga, K., Futawatari, T., and Awaya, Y. (1984). Erosional process of cohesive sediments. *Water Sci. Technol.* 17 (6-7), 891–901.

Lazzari, S., Nicoud, L., Jaquet, B., Lattuada, M., and Morbidelli, M. (2016). Fractal-like structures in colloid science. *Adv. colloid Interface Sci.* 235, 1–13. doi: 10.1016/j.cis.2016.05.002

Lick, W., Jin, L., and Gailani, J. (2004). Initiation of movement of quartz particles. *J. Hydraulic Eng.* 130 (8), 755–761. doi: 10.1061/(ASCE)0733-9429(2004)130:8(755)

Li, H., Yuan, M., and Zhang, X. (1995). Study on critical motion and erosion of cohesive sediment. *J. Waterway Harbor* 3), 20–26. (in Chinese).

Li, Y., Zhang, C., Chen, D., Zheng, J., Sun, J., and Wang, P. (2021). Barred beach profile equilibrium investigated with a process-based numerical model. *Continent. Shelf Res.* 222, 104432. doi: 10.1016/j.csr.2021.104432

Li, Y., Zhang, C., Dai, W., Chen, D., Sui, T., Xie, M., and Chen, S. (2022). Laboratory investigation on morphology response of submerged artificial sandbar and its impact on beach evolution under storm wave condition. *Mar. Geo.* 443, 106668. doi: 10.1016/j.margeo.2021.106668

Logan, B. E., and Kilps, J. R. (1995). Fractal dimensions of aggregates formed in different fluid mechanical environments. *Water Res.* 29 (2), 443–453. doi: 10.1016/0043-1354(94)00186-B

Maggi, F., Mietta, F., and Winterwerp, J. (2007). Effect of variable fractal dimension on the floc size distribution of suspended cohesive sediment. *J. Hydrology* 343 (1-2), 43–55. doi: 10.1016/j.jhydrol.2007.05.035

Mandelbrot, B. (1967). How long is the coast of Britain? statistical self-similarity and fractional dimension. *Science* 156 (3775), 636–638.

Mandelbrot, B. (1975). *Fractal: Form, chance and dimension*. Flammarian, Paris

McAnally, W. H., and Mehta, A. J. (2000). Aggregation rate of fine sediment. *J. Hydraulic Eng.* 126 (12), 883–892. doi: 10.1061/(ASCE)0733-9429(2000)126:12(883)

McAnally, W. H., and Mehta, A. J. (2002). Significance of aggregation of fine sediment particles in their deposition. *Estuarine Coast. Shelf Sci.* 54 (4), 643–653. doi: 10.1006/ecss.2001.0847

Mehta, A. J. (2014). *An introduction to hydraulics of fine sediment transport*. (Vol. 38) Hackensack: World Scientific Publishing Company.

Mehta, A. J., Hayter, E. J., Parker, W. R., Krone, R. B., and Teeter, A. M. (1989). Cohesive sediment transport. I: Process description. *J. Hydraulic Eng.* 115 (8), 1076–1093.

Meissner, H., Michaels, A., Kaiser, R.Development (1964). Crushing strength of zinc oxide agglomerates. *Ind. Eng. Chem. Process Design* 3 (3), 202–205. doi: 10.1021/i260011a003

Mostafa, T. S., Imran, J., Chaudhry, M. H., and Kahn, I. B. (2008). Erosion resistance of cohesive soils. *J. Hydraulic Res.* 46 (6), 777–787. doi: 10.1080/00221686.2008.9521922

Ockenden, M., and Delo, E. (1988). *Consolidation and erosion of estuarine mud and sand mixtures-an experimental study (Report no SR 149).* H. R. Limited. Wallingford (UK).

Otsubo, K., and Muraoka, K. (1988). Critical shear stress of cohesive bottom sediments. *J. Hydraul. Eng.* 114 (10), 1241–1256.

Owen, M. (1970). *A detailed study of the settling velocities of an estuary mud (INT 78).* Ed. H. R. Station (Wallingford, HK).

Paphitis, D. (2001). Sediment movement under unidirectional flows: an assessment of empirical threshold curves. *Coast. Eng.* 43 (3), 227–245. doi: 10.1016/S0378-3839(01)00015-1

Partheniades, E. (1965). Erosion and deposition of cohesive soils. *J. Hydraulics Division* 91 (1), 105–139. doi: 10.1061/JYCEAJ.0001165

Perkey, D. W., Smith, S. J., Fall, K. A., Massey, G. M., Friedrichs, C. T., and Hicks, E. M. (2020). Impacts of muddy bed aggregates on sediment transport and management in the tidal James river, VA. *J. Waterway Port Coastal Ocean Eng.* 146, 5, 04020028. doi: 10.1061/(ASCE)WW.1943-5460.0000578

Righetti, M., and Lucarelli, C. (2007). May the shields theory be extended to cohesive and adhesive benthic sediments? *J. Geophysical Research: Oceans* 112, C05039. doi: 10.1029/2006JC003669

Roberts, J., Jepsen, R., Gotthard, D., and Lick, W. (1998). Effects of particle size and bulk density on erosion of quartz particles. *J. Hydraulic Eng.* 124 (12), 1261–1267. doi: 10.1061/(ASCE)0733-9429(1998)124:12(1261)

Roberts, J. D., Jepsen, R. A., and James, S. C. (2003). Measurements of sediment erosion and transport with the adjustable shear stress erosion and transport flume. *J. Hydraulic Eng.* 129 (11), 862–871. doi: 10.1061/(ASCE)0733-9429(2003)129:11(862)

Sanford, L. P., and Maa, J. P.-Y. (2001). A unified erosion formulation for fine sediments. *Mar. Geology* 179 (1), 9–23. doi: 10.1016/S0025-3227(01)00201-8

Schieber, J., Southard, J. B., and Schimmelmann, A.J.J.o. (2010). Lenticular shale fabrics resulting from intermittent erosion of water-rich muds–interpreting the rock record in the light of recent flume experiments *J. Sediment. Res.* 80, 1, 119–128. doi: 10.2110/jsr.2010.005

Serra, T., and Casamitjana, X. (1998). Structure of the aggregates during the process of aggregation and breakup under a shear flow. *J. colloid Interface Sci.* 206 (2), 505–511. doi: 10.1006/jcis.1998.5714

Sharif, A. R. (2003). *Critical shear stress and erosion of cohesive soils* (Buffalo, New York: State University of New York at Buffalo). PhD thesis.

Sharif, A. R., and Atkinson, J. F. (2012). Model for surface erosion of cohesive soils. *J. Hydraulic Eng.* 138 (7), 581–590. doi: 10.1061/(ASCE)HY.1943-7900.0000551

Smerdon, E. T., and Beasley, R. P. (1959). *Tractive force theory applied to stability of open channels in cohesive soils* (University of Missouri, College of Agriculture, Agricultural Experiment Station. Columbia, MO). Research Bulletin No. 715.

Son, M., and Hsu, T.-J. (2009). The effect of variable yield strength and variable fractal dimension on flocculation of cohesive sediment. *Water Res.* 43 (14), 3582–3592. doi: 10.1016/j.watres.2009.05.016

Soulsby, R., and Whitehouse, R. (1997). "Threshold of sediment motion in coastal environments pacific coasts and ports' 97," in *Proceedings of the 13th Australasian Coastal and Ocean Engineering Conference and the 6th Australasian Port and Harbour Conference*, Christchurch, New Zealand.

Tang, C. (1963). Law of sediment threshold. *J. Hydraulic Eng.* 2, 1–12. (in Chinese).

Ternat, F., Boyer, P., Anselmet, F., and Amielh, M. (2008). Erosion threshold of saturated natural cohesive sediments: Modeling and experiments. *Water Resour. Res.* 44 (11), W11434. doi: 10.1029/2007WR006537

Thomsen, L., and Gust, G. (2000). Sediment erosion thresholds and characteristics of resuspended aggregates on the western European continental margin. *Deep Sea Res. Part I: Oceanographic Res. Papers* 47 (10), 1881–1897. doi: 10.1016/S0967-0637(00)00003-0

Thorn, M., and Parsons, J. (1980). "Erosion of cohesive sediments in estuaries: an engineering guide," in *Proc. of the 3rd Int. Symp. on Dredging Technol*, BHRA, Cranfield, UK.

Torfs, H., Jiang, J., and Mehta, A. (2000). Assessment of the erodibility of fine/coarse sediment mixtures. *Proc. Mar. Sci.* 3, 109–123. doi: 10.1016/S1568-2692(00)80116-3

Vollmer, S., and Kleinhans, M. G. (2007). Predicting incipient motion, including the effect of turbulent pressure fluctuations in the bed. *Water Resour. Res.* 43 (5), W05410. doi: 10.1029/2006WR004919

Whitehouse, R. (2000). *Dynamics of estuarine muds: A manual for practical applications*. Thomas Telford, London

Winterwerp, J. C. (1998). A simple model for turbulence induced flocculation of cohesive sediment. *J. Hydraulic Res.* 36 (3), 309–326. doi: 10.1080/00221689809498621

Winterwerp, J. (2002). On the flocculation and settling velocity of estuarine mud. *Continental Shelf Res.* 22 (9), 1339–1360. doi: 10.1016/S0278-4343(02)00010-9

Winterwerp, J. C., and Van Kesteren, W. G. (2004). *Introduction to the physics of cohesive sediment dynamics in the marine environment.* Vol. Vol. 56) (Amsterdam: Elsevier).

Winterwerp, J., Kesteren, W., Prooijen, B., and and Jacobs, W. (2012). A conceptual framework for shear flow–induced erosion of soft cohesive sediment beds. *J. Geophys. Res. Ocean* 117 (C10), C10020. doi: 10.1029/2012JC008072

Wu, H., Lattuada, M., and Morbidelli, M. (2013). Dependence of fractal dimension of DLCA clusters on size of primary particles. *Adv. colloid Interface Sci.* 195, 41–49. doi: 10.1016/j.cis.2013.04.001

Wu, W., Perera, C., Smith, J., and Sanchez, A. (2017). Critical shear stress for erosion of sand and mud mixtures. *J. Hydraulic Res.* 56 (1), 1–15. doi: 10.1080/00221686.2017.1300195

Xu, D., Bai, Y., Ji, C., and Williams, J. (2015). Experimental study of the density influence on the incipient motion and erosion modes of muds in unidirectional flows: the case of huangmaohai estuary. *Ocean Dynamics* 65 (2), 187–201. doi: 10.1007/s10236-014-0803-9

Xu, Y., Jiang, H., Chu, F., and Liu, C. (2014). Fractal model for surface erosion of cohesive sediments. *Fractals* 22 (03), 1440006. doi: 10.1142/S0218348X14400064

Yang, M., and Wang, G. (1995). The incipient motion formulas for cohesive fine sediments. *J. Basic Sci. Eng.* 3 (1), 99–109. (in Chinese)

Yang, B., Luo, Y., Jeng, D., Feng, J., and Huhe, A. (2018). Experimental studies on initiation of current-induced movement of mud. *Applied Ocean Res.* 80, 220–227. doi: 10.1016/j.apor.2018.09.006.

Yuan, S., Tang, H., Li, K., Xu, L., Xiao, Y., Gualtieri, C., et al (2021). Hydrodynamics, sediment transport and morphological features at the confluence between the Yangtze River and the Poyang Lake. *Water Resource. Res.* 57 (3), e2020WR028284. doi: 10.1029/2020WR028284.

Zhang, H. (2012). A unified formula for incipient velocity of sediment. *J. Hydraulic Eng.* 43 (12), 1387–1396. (in Chinese).

Zhang, M., and Yu, G. (2017). Critical conditions of incipient motion of cohesive sediments. *Water Resour. Res.* 53 (9), 7798–7815. doi: 10.1002/2017WR021066

Zhang, M., Yu, G., La Rovere, A., and Ranzi, R. (2017). Erodibility of fluidized cohesive sediments in unidirectional open flows. *Ocean Eng.* 130, 523–530. doi: 10.1016/j.oceaneng.2016.12.021

Zuo, L., Roelvink, D., Lu, Y., and Li, S. (2017). On incipient motion of silt-sand under combined action of waves and currents. *Appl. Ocean Res.* 69, 116–125. doi: 10.1016/j.apor.2017.10.005

frontiers | Frontiers in Marine Science

TYPE Original Research
PUBLISHED 21 October 2022
DOI 10.3389/fmars.2022.958573

OPEN ACCESS

EDITED BY
Javier Benavente,
University of Cádiz, Spain

REVIEWED BY
Carlos Loureiro,
University of Stirling, United Kingdom
Eli Lazarus,
University of Southampton,
United Kingdom
Duncan FitzGerald,
Boston University, United States

*CORRESPONDENCE
Jorge Lorenzo-Trueba
lorenzotruej@montclair.edu

SPECIALTY SECTION
This article was submitted to
Coastal Ocean Processes,
a section of the journal
Frontiers in Marine Science

RECEIVED 31 May 2022
ACCEPTED 26 September 2022
PUBLISHED 21 October 2022

CITATION
Tenebruso C, Nichols-O'Neill S,
Lorenzo-Trueba J, Ciarletta DJ and
Miselis JL (2022) Undeveloped and
developed phases in the centennial
evolution of a barrier-marsh-lagoon
system: The case of Long Beach
Island, New Jersey.
Front. Mar. Sci. 9:958573.
doi: 10.3389/fmars.2022.958573

Undeveloped and developed phases in the centennial evolution of a barrier-marsh-lagoon system: The case of Long Beach Island, New Jersey

Christopher Tenebruso[1], Shane Nichols-O'Neill[1], Jorge Lorenzo-Trueba[1*], Daniel J. Ciarletta[2] and Jennifer L. Miselis[2]

[1]Department of Earth and Environmental Studies, Montclair State University, Montclair, NJ, United States, [2]U.S. Geological Survey, St. Petersburg Coastal and Marine Science Center, St. Petersburg, FL, United States

Barrier islands and their associated backbarrier environments protect mainland population centers and infrastructure from storm impacts, support biodiversity, and provide long-term carbon storage, among other ecosystem services. Despite their socio-economic and ecological importance, the response of coupled barrier-marsh-lagoon environments to sea-level rise is poorly understood. Undeveloped barrier-marsh-lagoon systems typically respond to sea-level rise through the process of landward migration, driven by storm overwash and landward mainland marsh expansion. Such response, however, can be affected by human development and engineering activities such as lagoon dredging and shoreline stabilization. To better understand the difference in the response between developed and undeveloped barrier-marsh-lagoon environments to sea-level rise, we perform a local morphologic analysis that describes the evolution of Long Beach Island (LBI), New Jersey, over the last 182 years. We find that between 1840 and 1934 the LBI system experienced landward migration of all five boundaries, including 171 meters of shoreline retreat. Between the 1920s and 1950s, however, there was a significant shift in system behavior that coincided with the onset of groin construction, which was enhanced by beach nourishment and lagoon dredging practices. From 1934 to 2022 the LBI system experienced ~22 meters of shoreline progradation and a rapid decline in marsh platform extent. Additionally, we extend a morphodynamic model to describe the evolution of the system in terms of five geomorphic boundaries: the ocean shoreline and backbarrier-marsh interface, the seaward and landward lagoon-marsh boundaries, and the landward limit of the inland marsh. We couple this numerical modeling effort with the map analysis during the undeveloped phase of LBI evolution, between 1840 and 1934. Despite its simplicity, the modeling framework can describe the average cross-shore evolution of the barrier-marsh-lagoon system during this period without accounting for human landscape modifications, supporting the premise that natural processes were the key drivers of morphological change. Overall, these results suggest that anthropogenic effects have played a major role in the evolution of LBI over the past century by altering overwash fluxes and marsh-lagoon geometry; this is likely the case for other barrier-marsh-lagoon environments around the world.

KEYWORDS

barrier island, marsh, lagoon, overwash processes, coastal development, beach nourishment, hold the line

Introduction

Barrier islands and their associated backbarrier environments, including salt marsh, lagoon, bay, and tidal flat environments, front 10–13% of the world's coastlines; this percentage is even higher in the United States, which has the greatest length of barrier shoreline and the largest number of barriers of any country in the world (Stutz and Pilkey, 2011). These barrier-marsh-lagoon systems commonly serve as buffer zones between the coastal ocean and mainland development, protecting investments in infrastructure, human population centers, and agricultural lands from the impacts of storm surge and wave energy during storm events (Gedan et al., 2011; Ferreira et al., 2014; Anarde et al., 2018; Passeri et al., 2018; Kopp et al., 2019). In addition to coastal protection, barrier-marsh-lagoon environments also support diverse ecologic communities (Boesch and Turner, 1984; Erwin, 1996; Day et al., 2008), and provide long-term carbon storage (Mcleod et al., 2011; Kirwan and Mudd, 2012; Theuerkauf and Rodriguez, 2017), recreation, and tourism (Barbier et al., 2011).

Notwithstanding recent improvements in understanding the response of barrier islands to anthropogenic effects (Stutz and Pilkey, 2005; Werner and Mcnamara, 2007; McNamara and Werner, 2008a; McNamara and Werner, 2008b; Roberts and Wang, 2012; Hapke et al., 2013; Lazarus and Goldstein, 2019; Lazarus et al., 2021), the interplay between natural processes and human development over decadal to centennial time scales remains poorly quantified. Simultaneous with the increase in human influence on the coasts, the rate of sea-level rise has accelerated from 1.4 mm/year throughout most of the twentieth century to 3.6 mm/year between 2006–2015 (IPCC, 2014; Kopp et al., 2019), which in the absence of coastal engineering can lead to an increase in the rate of barrier island retreat (Deaton et al., 2017; Odezulu et al., 2017). Rapid sea-level rise can also result in drastic changes in the backbarrier environment, including lagoon deepening and lateral expansion, with the associated squeeze of the marsh platforms (Mariotti and Fagherazzi, 2013; Kirwan et al., 2016; Miselis and Lorenzo-Trueba, 2017; Fagherazzi et al., 2020; Zhang et al., 2020). The rate of overwash sedimentation can be influenced by nearshore and foreshore influences (Houser et al., 2008), as well as changes in backbarrier geometry, which can enhance the ocean-lagoon tidal exchange and increase the rate of barrier landward migration (Walters et al., 2014; Lorenzo-Trueba and Mariotti, 2017; FitzGerald et al., 2018; Lauzon et al., 2018; Reeves et al., 2020). Many coastal communities have decided to limit these effects by investing in either soft (i.e. beach nourishment) or hard (i.e. groins, revetments) engineering structures (Kolodin et al., 2021; Janoff, 2021; Janoff et al., 2020). Additionally, morphological changes in backbarrier environments have been often counteracted with engineering efforts such as hardening of marsh shorelines to prevent marsh-edge erosion, removal of embankments in previously reclaimed saltmarsh land, opening dikes, (re)creating or deepening tidal channels, or vegetating intertidal dredge disposal areas (Weinstein et al., 2001; Teal and Weishar, 2005; Wolters et al., 2005; Hein et al., 2021). It is unclear, however, what the relative effect of these anthropogenic changes is on the evolution of barrier-marsh-lagoon systems over decadal to centennial time scales.

To address this, here we study and quantify the geomorphic change contrast between the undeveloped and developed phases of Long Beach Island (LBI), New Jersey over the past two centuries. Specifically, we analyze historical maps and images that describe the evolution of LBI between 1840 and 2022 and separate it into undeveloped and developed phases. We then couple the undeveloped phase with a numerical model for barrier-marsh-lagoon evolution. LBI (Figure 1) is an ideal location to study the role of anthropogenic effects on barrier-marsh-lagoon evolution as it transitioned from an undeveloped outpost for hunters and fishers to a populated and developed region that hosts an additional 100,000 inhabitants seasonally over the last ~180 years (Lloyd, 2005).

Physical setting and morphology

LBI is a ~34 km long barrier island located on the southern half of the New Jersey coastline, separated from adjacent barriers by Barnegat Inlet and Little Egg Inlet, and from the mainland by Barnegat Bay, Manahawkin Bay, and Little Egg Harbor

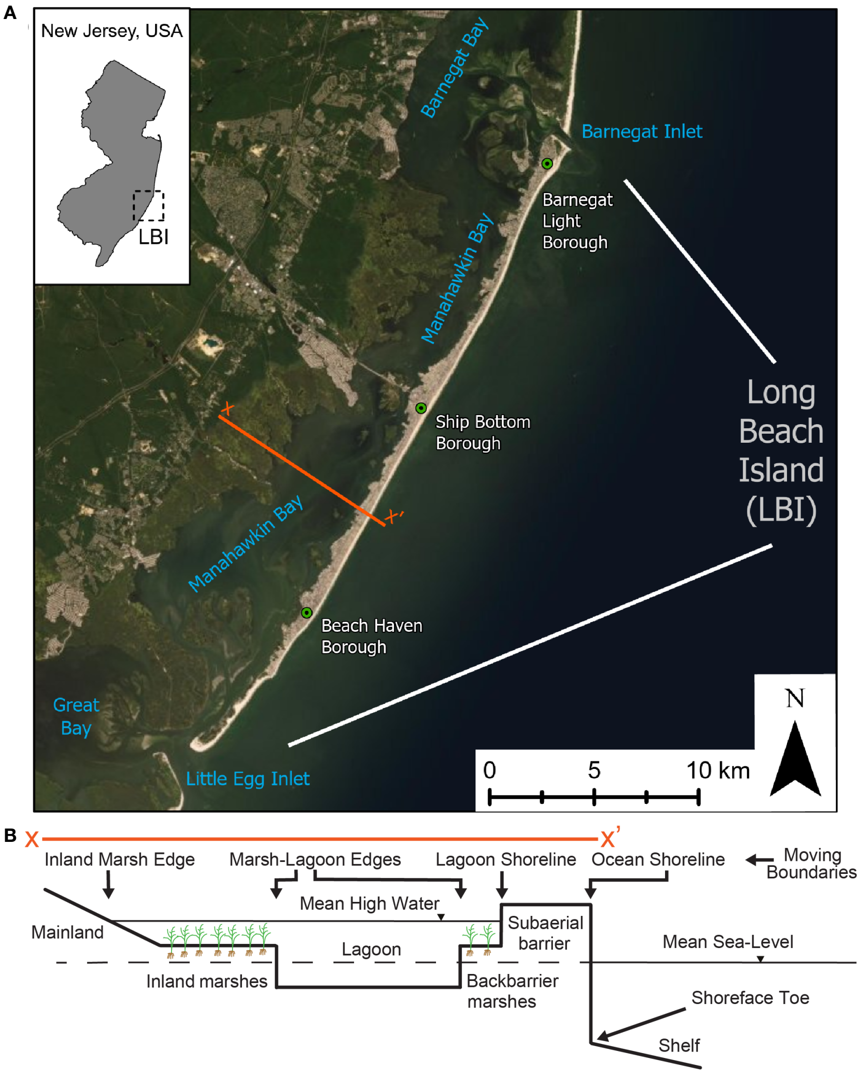

FIGURE 1
(A) Regional setting: Long Beach Island New Jersey. **(B)** Idealized cross-shore geometry of the barrier-marsh-lagoon system, including the key geomorphic moving boundaries. Base map image is the property of Esri and is used herein under license. Copyright © 2022 Esri and its licensors. All rights reserved.

(Figure 1A). LBI is generally characterized as a mixed-energy, semidiurnal micro-tidal barrier with a neap range of 0.9 m, a spring range of 1.5 m, and southward alongshore sediment transport (Cialone and Thompson, 2000; McBride et al., 2013). From an idealized cross-section of a barrier-marsh-lagoon system such as LBI (Figure 1B), we typically see different ecogeomorphic environments such as the subaqueous shoreface, the subaerial portion of the barrier, and the backbarrier region, which can be separated into backbarrier marsh, lagoon, and inland marsh habitats. The boundaries between these environments are generally visible on maps and represent fundamental transitions in terms of sediment transport, plant growth, and organic sediment accumulation. From ocean to the mainland, we find the ocean shoreline, associated with the transition from subaqueous shoreface to the subaerial barrier, the backbarrier-marsh interface, where the sandy subaerial barrier converts into organic-rich backbarrier marsh, the seaward and landward lagoon-marsh boundaries, and the mainland limit of the inland marsh (Figure 1B). The trajectories of these boundaries describe the morphological evolution of the system over decadal to millennial time scales (Lorenzo-Trueba and Ashton, 2014; Lorenzo-Trueba and Mariotti, 2017), and can be used to describe the long-term geomorphic and stratigraphic evolution of the barrier-marsh-lagoon system (Ciarletta et al., 2019a; Ciarletta et al., 2019b; Ciarletta et al., 2019c; Shawler et al., 2021).

The geological setting on which LBI has developed comprises channel and baymouth deposits dating back to the Pleistocene and slopes gently upward from offshore towards the mainland (Uptegrove et al., 2012). Overlying layers contain bay/estuarine deposits and then barrier/shoal deposits (where the barrier is currently located) of Holocene age, indicative of a landward retreating barrier system. However, based on historical imagery, we know that this landward migration has stalled over the past few decades. To better understand the circumstances leading to this behavioral shift, we analyze different historical records in the next section.

Phases of LBI evolution: From undeveloped to fully developed

In this section, we use historical maps from National Oceanic and Atmospheric Administration (NOAA), images from the U.S. Army Corps of Engineers, and records from state departments (New Jersey Department of State, 1906; United States Bureau of the Census, 1912; New Jersey State Data Center, 2001) to quantify changes in morphology, population, and human development at LBI over the past two centuries. We georeference NOAA T-sheets and nautical charts from 1840, 1879, 1934, 1957 and 2022 to quantify the magnitude of change of each geomorphic boundary in the system (Figure 2). Boundary positions for the ocean shoreline, the backbarrier-marsh interface, the seaward and landward lagoon-marsh interfaces, and the marsh-mainland boundary were identified for each year (Supplementary Figures 1, 2). We then compute the cross-shore location for each by averaging over the length of the island. Additionally, we determine changes in the areal extent of the primary environments, including the marsh platforms (Figure 2C). We note that publicly available GIS datasets for this period, including those from Smith and Terrano, 2017, do not account for backbarrier and inland marsh areas. Thus, the dataset that we provide for the years 1840, 1879, 1934, 1957, and 2022, is novel as it spans both the barrier and its backbarrier environment, digitizing inland and

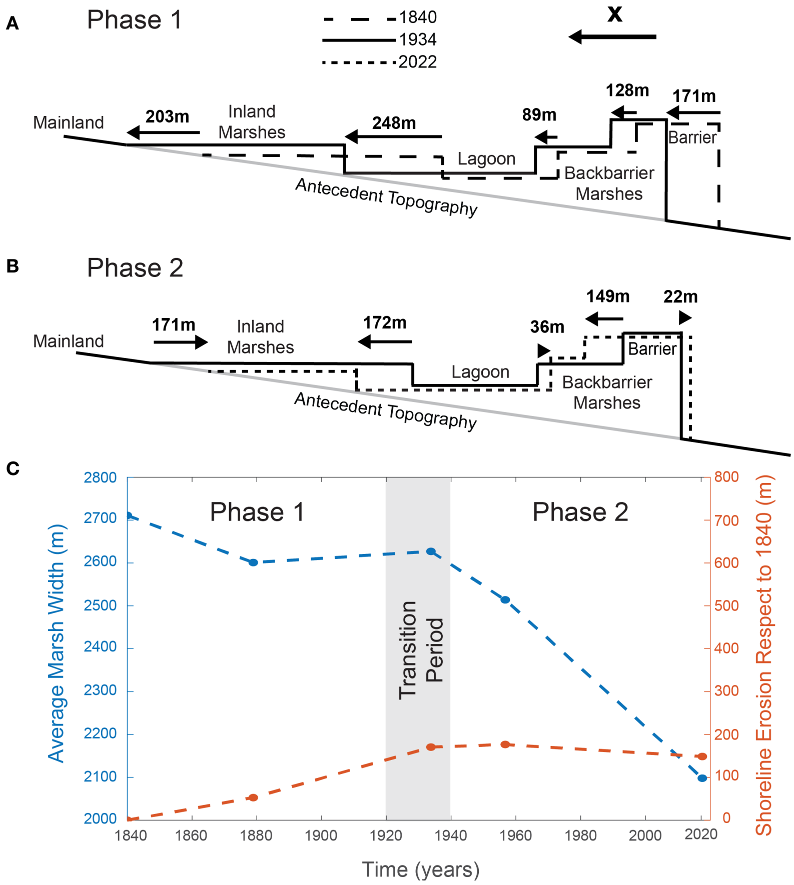

FIGURE 2
Long Beach Island cross-shore evolution between **(A)** 1840 and 1934, and **(B)** 1934 and 2022. **(C)** Average marsh width and ocean shoreline location respect to 1840 over time.

backbarrier marsh areas, along with ocean and bay shorelines (Supplementary Figure 3). We also use historical images from 1920, 1944, 1962 of three communities in LBI: Beach Haven, Barnegat Light, and Ship Bottom (Figures 1A) to illustrate the morphological transition the island underwent over this time period (Figure 3). All historical images, maps, and GIS files used in this analysis are included in a Zotero database described in the Supplementary Information.

The construction of the first tended lighthouse at LBI in 1834, a railroad connecting the island to the mainland in 1886, and the establishment of Beach Haven in 1872 and Barnegat Light in 1878 did not prevent LBI from maintaining an overall landward migration. We find evidence of this dynamic and associated morphological change in NOAA T-sheets and nautical charts from the 1800s and early 1900s (Figure 2A). In the late 1920s and early 1930s, the population of Beach Haven, Barnegat Light, and Ship Bottom was on the order of a few hundred people each (Supplementary Figure 4), and coastal protection measures such as wooden jetties were implemented for the first time at a few locations during this time period (U.S. Army Corps of Engineers, 1999; Lloyd, 2005). Given the limited effect of development and coastal engineering, LBI continued to undergo substantial morphological changes between 1920 and 1944, including the expansion of backbarrier marshes into the lagoon (Figure 3). After 1944, this trend changed with increased levels of development and coastal engineering, including the onset of beach nourishment activities in 1954 (Trembanis et al., 1999; U.S. Army Corps of Engineers, 1999; Valverde et al., 1999), the opening of a four-lane highway in 1956 to replace a railroad and a 1914 wooden bridge, and LBI population doubling between the 1944 and 1970 (Supplementary Figure 3). With coastal engineering and development accelerating and spanning a larger portion of the island, morphological changes between 1944 and 1962 were substantially reduced compared to the previous period, between 1920 and 1944 (Figure 3).

Based on this temporal variation in morphological change (Figure 2) and human development (Supplementary Figure 3) between 1920 and 1944, we separate the evolution of LBI into two phases: a largely undeveloped phase 1 between 1840 and 1934, and a developed phase 2 between 1934 and 2022. We selected 1934 as a breakpoint that corresponds to the 1920 to 1944 period that separates phases 1 and 2 based on the availability of NOAA T-sheets and nautical charts; the purpose of this selection, however, is just to mark a significant change in morphological behavior. During phase 1 all geomorphic boundaries migrate landwards, including a 171 m retreat of the ocean shoreline, an 89 m migration of backbarrier marshes into the lagoon, and a 203 m migration of inland marshes into the mainland (Figure 3A). Backbarrier marshes contract as barrier-island migration outpaces their expansion into the lagoon. Similarly, marsh erosion in the lagoon drives inland marsh loss despite their expansion towards the mainland. Overall, the marsh platform area is reduced by 4% during phase 1. Phase 2 is characterized by the reversal of the dynamics in phase 1, with seaward growth of the ocean shoreline, erosion of the marsh platforms on both sides of the lagoon, and marsh loss to development on both the backbarrier and the mainland environments (Figure 3B). The overall marsh loss during phase 2 is ~20% (Figure 3C), a significant increase with respect to phase 1.

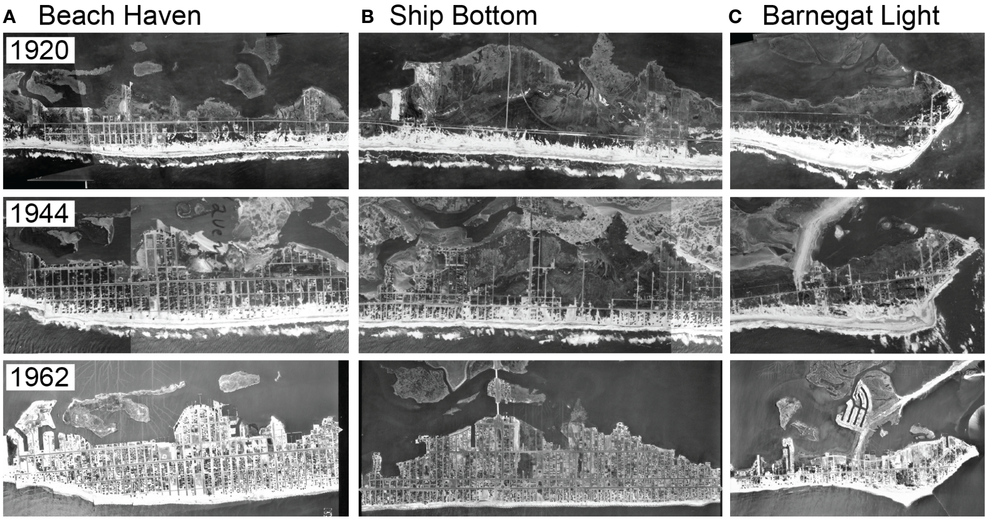

FIGURE 3
Historical images that demonstrate the transition from undeveloped to developed barrier-marsh lagoon system between 1920 and 1962 of three coastal towns in LBI: **(A)** Beach Haven, **(B)** Ship Bottom, and **(C)** Barnegat Light. Aerial photographs from archives of Beach Erosion Board (BEB), United States Army Corps of Engineers (USACE). Original prints digitized by USACE Engineer Research and Development Center for use by coastal managers and researchers. See https://rsm.usace.army.mil/shore/index.php.

The migration of all the different geomorphic boundaries during phase 1 is the result of a complex interaction between physical and biological processes, whereas in phase 2 anthropogenic effects dominate. To quantify such complex interplay during phase 1, we present a numerical modeling framework that describes the rates of migration of each boundary as a function of the leading physical and biological processes. A key aspect of this modeling framework is the treatment of the geomorphic moving boundaries as internal boundaries, whose location must be defined as part of the numerical solution to the overall morphodynamic problem (Swenson et al., 2000; Lorenzo-Trueba et al., 2009; Lorenzo-Trueba et al., 2013; Lorenzo-Trueba and Mariotti, 2017; Anderson et al., 2019; Ciarletta et al., 2019a).

Barrier-marsh-lagoon numerical model for the undeveloped phase

Our starting point is a morphodynamic model for cross-shore barrier-marsh-lagoon evolution recently developed by Lorenzo-Trueba and Mariotti (2017) (Figures 1A, 4A). With this modeling framework, we account for the dynamics of the ocean shoreline, driven by overwash processes, and the expansion/contraction of the marsh and lagoon environments in terms of wave energy and sedimentation processes in the lagoon. Unlike Lorenzo-Trueba and Mariotti (2017), the model introduced here does not account for changes in shoreface geometry or vertical dynamics of the marsh-lagoon environment. In this way, we characterize the geometry of the system with the average barrier width W and height H, shoreface depth D_T, lagoon depth respect to mean high water (MHW) z_L, lagoon width b_L, marsh platform depth respect to MHW z_m, backbarrier marsh width m_b, and inland marsh width m_i (Figure 4B). Below, we describe the dynamic changes of this idealized geometry as a function of key processes that operate on the barrier and marsh-lagoon domains.

Barrier dynamics

Given the idealized geometry included in Figure 4, we can describe the evolution of the barrier in terms of the ocean

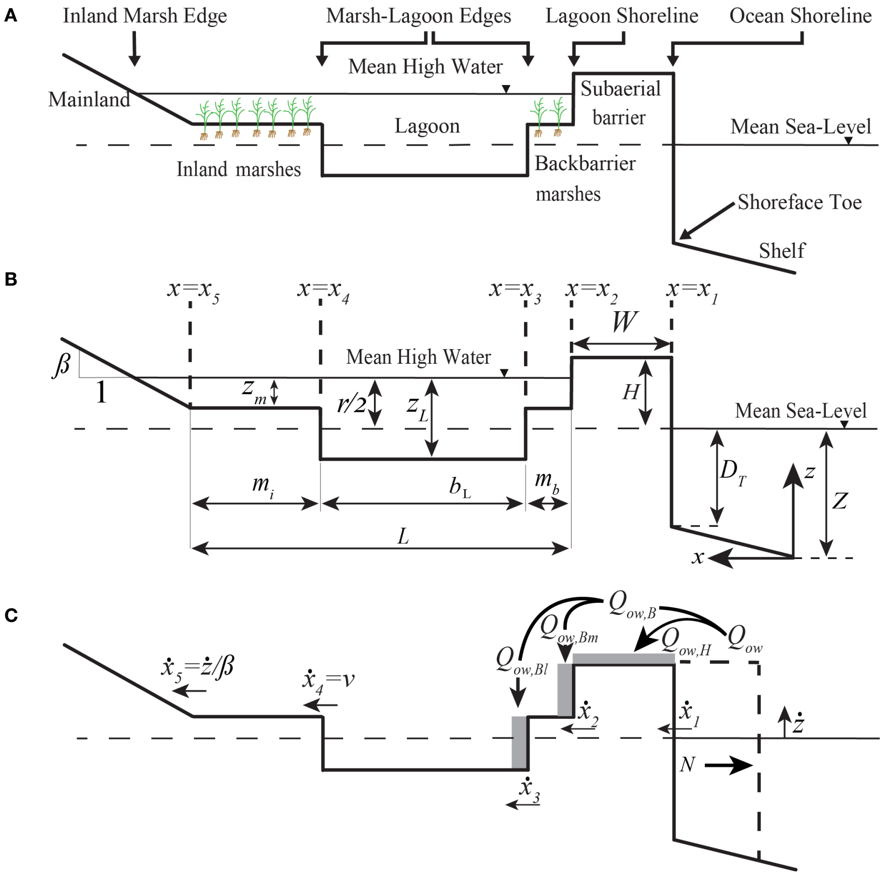

FIGURE 4
Cross-shore barrier-marsh-lagoon model set up, including **(A)** the different geomorphic domains and their moving boundaries, **(B)** state variables, and **(C)** the key processes that drive the evolution of the moving boundaries.

shoreline x_1 and the backbarrier-marsh interface x_2 locations. We express the rate of migration of the ocean shoreline (i.e., $\dot{x}_1 = dx_1/dt$) as a function of the total sediment flux from the front to the top and back of the island Q_{ow}, and the net sediment loss at the shoreface *via* alongshore sediment transport E (Figure 4C), as follows:

$$\dot{x}_1 = \frac{Q_{ow}}{H + D_T} - E \tag{1}$$

In an undeveloped barrier island, natural processes such as storm overwash and aeolian processes drive landward migration of the backbarrier-marsh interface during storms and growth of the subaerial volume of the barrier during fair weather. Thus, to first order we compute Q_{ow} as follows:

$$Q_{ow} = Q_{ow,B} + Q_{ow,H} \tag{2}$$

where $Q_{ow,H}$ and $Q_{ow,B}$ are the top-barrier and backbarrier overwash components (Figure 4C). Given the limited information on barrier height dynamics in LBI while it was undeveloped during the 1800's and early 1900's, we assume that barrier height keeps pace with the rate of sea-level rise $\dot{z}$ (i.e., $Q_{ow,H} = W{\cdot}\dot{z}$). Additionally, following Lorenzo-Trueba and Ashton, 2014, we compute $Q_{ow,B}$ in terms of the maximum overwash flux $Q_{ow,max}$, its associated maximum deficit volume $V_{d,max}$, and the backbarrier deficit volume $V_{d,B}$, i.e.,

$$Q_{ow,B} = Q_{ow,max} \frac{V_{d,B}}{V_{d,\max}} \tag{3}$$

We partition the backbarrier flux into a barrier-marsh edge flux $Q_{ow,Bm}$ and a marsh-lagoon edge flux $Q_{ow,Bl}$ (i.e., $Q_{ow,B} = Q_{ow,Bm}+Q_{ow,Bl}$; see Figure 4C), and define the backbarrier deficit volume $V_{d,B}$ as (Lorenzo-Trueba and Mariotti, 2017):

$$V_{d,B} = max[0, (W_e - W)(H + \varphi(z_m - r/2) + (1 - \varphi)(z_L - r/2))] \tag{4}$$

where W_e is the critical barrier width (first defined by Leatherman, 1979) beyond which the deficit volume and therefore the backbarrier overwash flux is equal to zero (i.e., $Q_{ow,B} = 0$). Similarly, we define the partitioning coefficient $\phi = min\ (1,m_b/m_{bc})$ in terms of the critical width of the backbarrier marsh platform mb mbc m_{bc} and compute the backbarrier fluxes as follows:

$$Q_{ow,Bm} = \phi \cdot Q_{ow,B} \tag{5}$$

$$Q_{ow,Bl} = (1 - \phi) \cdot Q_{ow,B} \tag{6}$$

As stated in equations (5) and (6), when the backbarrier marsh width is greater than its critical value (i.e., $m_b > m_{bc}$), overwash sediment does not reach the backbarrier marsh-lagoon edge (i.e., $Q_{ow,Bl} = 0$). In contrast, when the backbarrier marsh completely erodes away (i.e., $m_b = 0$), the backbarrier flux only contributes to the landward migration of the backbarrier-marsh interface (i.e., $Q_{ow,Bm} = 0$), and therefore we recover the formulation introduced by Lorenzo-Trueba and Ashton, 2014. In intermediate cases, when $m_{bc} > m_b > 0$, the backbarrier overwash is partitioned between the barrier and the backbarrier marsh platform. In this way, we can describe the rate of migration of the backbarrier-marsh interface $\dot{x}_2 = dx_2/dt$ as follows:

$$\dot{x}_2 = \frac{Q_{ow,Bm}}{H + z_m - r/2} \tag{7}$$

where r is the tidal range. Thus, as captured by equations (5), (6), and (7), the rate of backbarrier-marsh interface migration is a function of marsh-lagoon geometry.

Marsh-lagoon dynamics

The geometry of the backbarrier environment can be described by the width of the marsh platforms m_b and m_i the lagoon width b_L (Figure 4B), which can in turn be expressed in terms of the locations of the seaward and landward lagoon-marsh boundaries x_3 and x_4, and the upland limit of mainland marsh x_5 as follows:

$$m_b = x_2 - x_3 \tag{8}$$

$$m_i = x_4 - x_5 \tag{9}$$

$$b_L = L - m_b - m_i - (x_2 - x_{20}) \tag{10}$$

where x_{20} is the initial location of the backbarrier-marsh interface (i.e., $x_2(t = 0) = x_{20}$), and $L(t)$ is the backbarrier cross-shore width. We define L as a function of the change in sea level and the mainland slope $ß$ as follows:

$$L = L_0 + \frac{Z - Z_0}{\beta} \tag{11}$$

where Z is sea level, Z_0 is the initial sea level (i.e., $Z_0 = Z\ (t{=}0)$), and L_0 is the initial basin length (i.e., $L_0 = L\ (t = 0)$). Given the range of physical and biological feedbacks that allow marshes to keep up vertically with sea-level rise (Kirwan and Megonigal, 2013), we assume to first order that marsh-lagoon lateral changes dominate backbarrier dynamics (Mariotti and Fagherazzi, 2013). We can therefore fully describe the dynamics of the backbarrier environment as a function of the backbarrier marsh $\dot{m}_b = dm_b/dt$ and the inland marsh $\dot{m}_i = dm_i/dt$ width change rates. Such changes are driven by the rates of barrier migration $\dot{x}_2$, backbarrier mash expansion into the lagoon $\dot{x}_3 = Q_{ow,Bl}/(z_L\text{-}z_m)\text{-}\nu$, marsh-lagoon edge progradation $\dot{x}_4 = \nu$, and mainland marsh expansion $\dot{x}_5 = \dot{z}/ß$ (Lorenzo-Trueba and Mariotti, 2017), which leads to the following state equations:

$$\dot{m}_b = \frac{Q_{ow,Bl}}{z_L - z_m} - \nu - \dot{x}_2 \tag{12}$$

$$\dot{m}_i = \frac{\dot{z}}{\beta} - v \tag{13}$$

We calculate v as a balance between erosion driven by lagoon waves and progradation due to lagoon sedimentation (Mariotti and Fagherazzi, 2013). The rate of progradation is computed in terms of a reference suspended sediment concentration in the lagoon C_r, the settling velocity of suspended sediments at the marsh-lagoon edge w_s, a shape factor that represents the geometry of the marsh-lagoon edge k_a, and the average sediment bulk density ρ. The rate of erosion is defined based on the wave power density at the marsh-lagoon edge W_p, an erodability coefficient k_e, and the marsh boundary cliff face height z_L-z_m, i.e.,

$$v = \frac{k_e W_P}{z_L - z_m} - \frac{k_a w_s C_r}{\rho} \tag{14}$$

We define the wave power density as $W_P = 1/16\gamma c_g H_s^2$ (Marani et al., 2011; Mariotti and Fagherazzi, 2013), where γ is the specific weight of water, H_s is the significant wave height, and c_g is the group velocity, computed using the wave period T. We use basic formulations to determine the significant wave height and wave period T as a function of the average wind speed u, and the lagoon width, i.e., $H_s = 3.63 \cdot 10^{-4} \cdot u^{1.23} \cdot b_L^{0.5}$ (Komar, 1998), and $T = 6.238{\cdot}10^{-2}{\cdot}(u{\cdot}b_L)^{1/3}$ (U.S. Army Corps of Engineers, 1984).

Numerical solution

The evolution of the coupled barrier-marsh-lagoon-marsh system is fully determined by the rates of change of the ocean shoreline $\dot{x}_1$ and the backbarrier-marsh interface $\dot{x}_2$, described in equations (1) and (7), and the rates of back-barrier $\dot{m}_b$ and inland $\dot{m}_i$ marsh width change, described by equations (10) and (11). To examine system behavior, we numerically solve equations (1) to (14) using a simple Euler scheme. All the variables and input parameters involved in the calculation are included in Supplementary Tables 1, 3, and the initial barrier-marsh-lagoon geometry is included in Supplementary Table 2.

A process-based perspective on LBI's evolution

In this section we use the numerical model and our analysis of historical maps and images to describe the evolution of LBI during phase 1, with the geometry of the barrier-marsh-lagoon system in 1840 as our initial condition (Supplementary Table 2). Furthermore, we extend the map analysis from section 3 to include supplementary data points; in addition to 1840, 1879, 1934, 1957 and 2022 (see Figure 3 and Supplementary Figure 4), we georeference and analyze nautical charts from 1983, 1993, 2007, and 2012 to better constrain the last few decades of phase 2. We then analyze and contrast the process-based context provided by the numerical model during the phase 1 evolution with our map analysis of LBI during phases 1 and 2.

Parameter estimation

We include a full list of the input parameters of the model in Supplementary Table 3. We define the majority of the parameter values based on the historical image analysis from section 3, Google Earth to estimate mainland slope or additional constraints from the literature. Additionally, we estimate those parameters that are not well constrained over centennial time scales (Supplementary Table 4) by minimizing the differences in moving boundary positions between the model and the map analysis of the barrier-marsh-lagoon phase 1 evolution. We compute this difference in terms of the root mean square error ϵ, which we define as follows:

$$\epsilon = \sum_{j=1}^{m} \sqrt{\sum_{i=1}^{n} \left(\frac{\Delta x_i}{x_i}\right)^2} \tag{15}$$

where $\Delta x_i/x_i$ is the normalized boundary movement difference between the model and observations, $i = 1,2,\ldots n$ is a counter to specify each geomorphic moving boundary, with $n = 5$ (Figures 1B, 4B), and $j = 1,2,\ldots m$ is a counter to describe the points in time used for comparison, with $m = 5$ (i.e., 1840, 1879, and 1934). Note that we normalize the boundary movements to avoid giving a higher weight to those that undergo larger displacements. We compute ϵ for a wide parameter space (Supplementary Table 4) and select the combination of parameter values associated with the total minimum error. The selected values are sensitive to neither the resolution nor the boundary limits employed for each parameter and fall within the range of values reported in the literature (Supplementary Table 4). We use these parameter values to produce the results presented below.

Undeveloped phase: Observations-model coupling

We first present the evolution of each geomorphic boundary of the system during phase 1 as described by field observations constrained by data points in 1840, 1879, and 1934 (Figure 5, open circles). We find that the ocean shoreline eroded on average at ~2m/y during phase 1, with an increase in this rate to ~3m/y after 1879 (Figure 5A). The backbarrier-marsh interface migrated seaward initially due to backbarrier marsh migration onto the barrier island (Supplementary Figure 5); this trend was followed by landward migration at ~3m/y after 1879 (Figure 5B). The lagoon-backbarrier marsh boundary also reversed its direction of migration during phase 1, with mild marsh erosion initially and followed by lagoonward expansion at

2-3m/y (Figure 5C). In contrast, erosion of the inland marshes on the lagoon side was maintained during phase 1 at 2-3m/y (Figure 5D), whereas the mainland boundary remained stable on average before 1879 and then expanded landward at 3-4m/y (Figure 5E). The initial stability of the mainland-inland marsh boundary location was due to a balance between natural landward expansion and marsh conversion to agricultural fields (Supplementary Figure 6).

Using the numerical model (Figure 5, solid and dashed lines), we can provide a process-based explanation of the dynamics captured by field observations. During the initial portion of phase 1, the barrier was too wide for overwash fluxes to reach the backbarrier environment (Figure 5F). Without this sediment source and natural disturbance, the backbarrier-marsh interface was relatively stable (Figure 5B), and the marsh edges eroded at similar rates on both sides of the lagoon (Figures 5C, 5D). As the ocean shoreline retreated (Figure 5A) and the barrier narrowed below a critical value (Figure 5F), overwash fluxes activated and drove landward migration of the backbarrier-marsh interface (Figure 5B), as well as backbarrier marsh expansion into the lagoon (Figure 5C). Although inland marshes eroded on the lagoon side, they also migrated up the mainland slope (Figure 5E) and approximately maintained their aerial extent during phase 1 (Supplementary Figure 1). Although our model does not account for the conversion of marshes to agricultural land, the average rate of inland marsh expansion towards land matched the ratio between sea-level rate and the average mainland slope (i.e. $\dot{z}/\beta$) as described in equation (13) and depicted in Figure 4C.

In Figure 5, we also include an example of the sensitivity of the results to changes in the input parameter values. We find that the higher the $Q_{ow,max}$ value, the faster the migration of the ocean shoreline, backbarrier-marsh interface, and lagoon-backbarrier marsh boundary towards land after the barrier width threshold condition is met (i.e., $W<W_\epsilon$). Despite the change in the magnitude of the migration rates, the system's dynamics are qualitatively the same under the different $Q_{ow,max}$ scenarios. Similarly, when we change the values of other key input parameters (i.e., $k_\epsilon, W_\epsilon, m_{bc}$, and E, in Supplementary Figures S5–S7), the migration rates and the timing at which the width threshold condition is met can vary. Still, the direction of migration of all geomorphic boundaries is the same under the full range of explored input parameter values.

Developed phase observations

As expected from an undeveloped barrier-marsh-lagoon system responding to sea-level rise, all boundaries migrate landwards during phase 1. In contrast, during phase 2 the

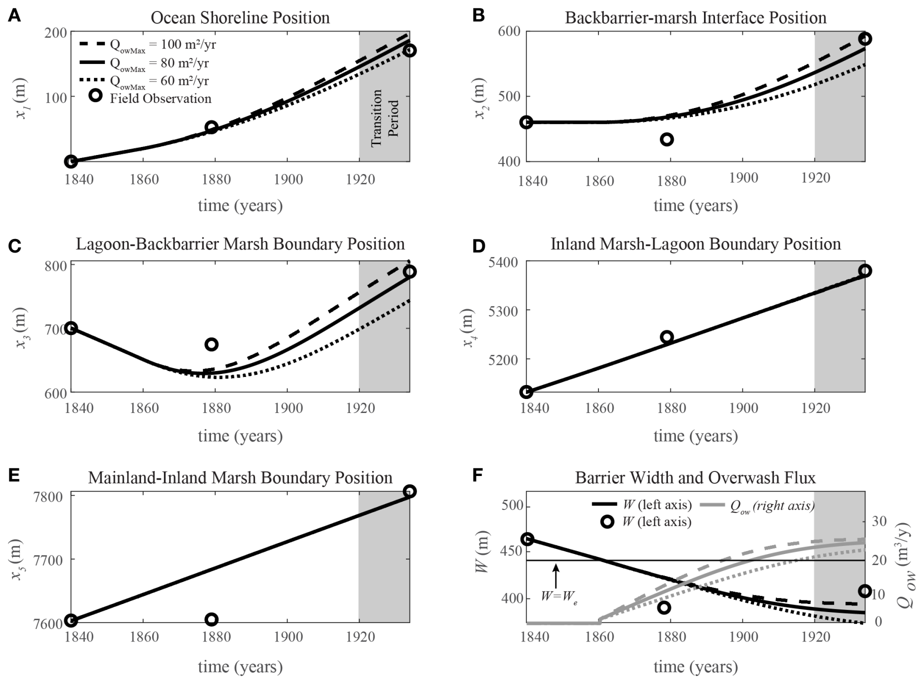

FIGURE 5
Evolution of the geomorphic moving boundaries (panels **A–E**) with landward directed migration assumed to be positive, and overwash fluxes and barrier width (panel **F**), during phase 1. Sensitivity of barrier-influenced geomorphic boundaries to variations in maximum overwash are indicated for rates of 60, 80, and 100 m^2/yr. See Figure 4B for a schematic of model geometry that includes the boundaries being tracked, x_1 to x_5. The input parameter values are included in Supplementary Table 3.

dynamics of the barrier and the backbarrier environment were decoupled due to human development, with an associated reversal in the migration direction of most geomorphic boundaries. The ocean shoreline transitioned from a landward migration rate of above 1m/y during phase 1 to less than 0.5m/y during the first half of phase 2, and a complete reversal during the last two decades of phase 2 with substantial seaward growth (Figure 6A). Although there is some natural variability, this shift in the rate and direction of migration of the ocean shoreline can be explained by the exponential increase in beach nourishment volumes that took place in New Jersey during phase 2 (Figure 6B). Such excess sand added to the coastline helped counteract the long-term geomorphic signal of storm events such as Ash Wednesday in 1962 or Hurricane Sandy in 2012 in Figure 6B. Additionally, the quick expansion of residential/commercial infrastructure at LBI significantly reduced the overwash reaching the backbarrier environment, which led to rapid wave-driven erosion of backbarrier marshes during the first couple of decades of phase 2 (Figure 6D). Soon after 1957, however, housing and infrastructure occupied the majority of barrier and backbarrier marsh environments (Figure 2). Under such a level of development, the separation between the barrier and backbarrier marshes fades (Figures 2, 6C), and the lagoon-backbarrier marsh boundary location remained fixed until present (Figure 6D). While inland marsh erosion on the lagoon side continued at a similar pace as in phase 1, human structures such as roads, seawalls, dikes, and revetments prevented the expansion of marshes on the mainland (Figure 6F and Supplementary Figure 2). Moreover, large portions of the inland marsh were lost to development during phase 2 (Supplementary Figure 2).

Discussion

Barrier island and backbarrier evolution are generally treated separately; however, our spatial analysis demonstrates that all key geomorphic boundaries of the barrier-marsh-lagoon system migrate towards land during the LBI undeveloped phase (i.e., phase 1). Such behavior suggests important relationships exist between LBI and its associated backbarrier environment during this period. We further explore these relationships by integrating the spatial analysis with a process-based numerical model and find that the cross-shore evolution of LBI in phase 1 can be to a large extent explained by natural processes. That is, with the exception of the mainland-inland marsh boundary between 1840 and 1879, which was partially affected by an expansion of agricultural practices (Supplementary Figure 6), the rate of migration of all boundaries can be quantified by the processes included in the model and with a set of parameter values that are within the range reported

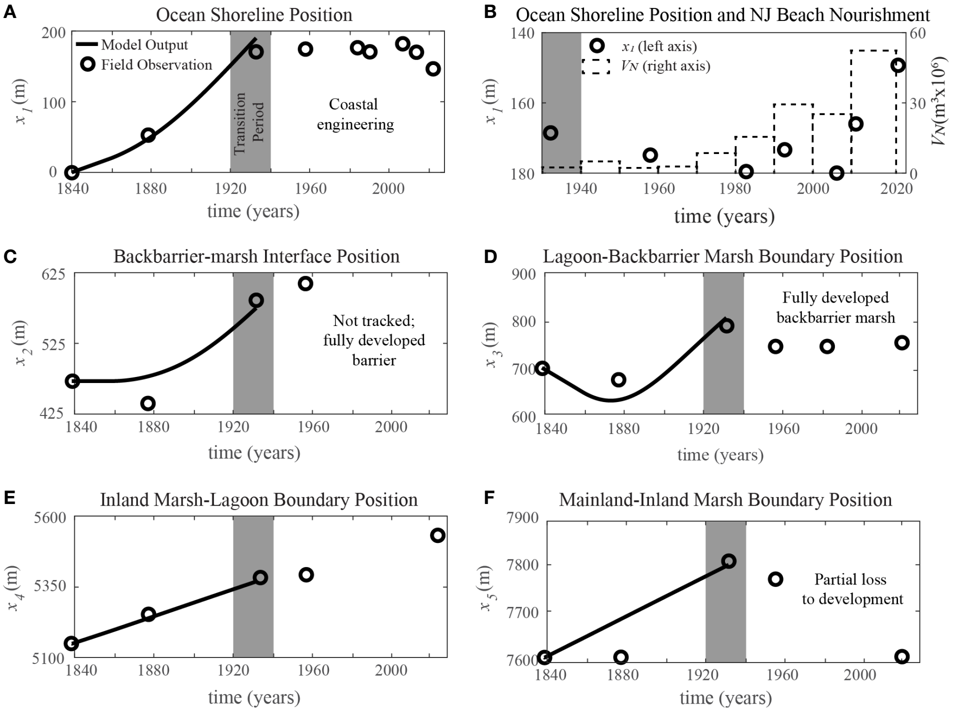

FIGURE 6
Evolution of the geomorphic moving boundaries **(A–F)** during phases 1 and 2. See Figure 4B for a schematic of model geometry that includes the boundaries being tracked, x_1 to x_5. The input parameter values are included in Supplementary Table 3. Ocean shoreline position compared to decadal Long Beach Island beach nourishment volume (V_N) **(B)**.

in the literature (see Supplementary Tables S3, S4). Moreover, the mechanics of the numerical model used to describe the dynamics of these boundaries are consistent with several recent studies on different barrier islands along the U.S. East and Gulf Coasts (e.g., Walters et al., 2014; Rogers et al., 2015; Walters and Kirwan, 2016, and Bernier et al., 2021). For instance, barrier width can exert a primary control over the magnitude of overwash fluxes (Figure 5F), which not only drive barrier landward migration (Figure 5B) but also are an important sediment source for backbarrier marshes (Figure 5C), allowing lower rates of erosion in comparison to isolated marshes (Figures 5D). Additionally, despite the role of marsh conversion that partially affected the migration of the mainland-inland marsh boundary, we find that the ratio between the rate of sea-level rise and mainland slope is a first-order control of the average response of this boundary (Figure 5E); in other words, the steeper the mainland slope, the lower the rate of inland marsh upland migration as discussed by Kirwan et al., 2016, Fagherazzi et al., 2019, and others.

Although the integration between the geomorphological analysis and the numerical model provides a novel process-based understanding of the evolution of LBI during phase 1, we do not account for the impacts of event-scale processes (e.g., individual storms) or alongshore variability on the morphological response of the coupled system. We focus on decadal to centennial timescales, which are consistent with the resolution of our field observations, and use conceptual relationships between barrier geometry and overwash fluxes instead of laboratory-validated sediment transport formulations from engineering approaches (e.g., Roelvink et al., 2009; Lin et al., 2010, Lin et al., 2014; Orton et al., 2015). In particular, in our current version of the numerical model, we assume the existence of an average ‘characteristic’ event that merges the effects of storms and recovery periods and drives the long-term geomorphic evolution of the barrier in conjunction with sea-level rise and backbarrier processes. In future work, however, we plan to integrate individual storm events and account for the effect of changes in the frequency and intensity of storms and recovery periods. We will then assess if this updated version of the model offers improvements over the storm-integrated approach presented here. Additionally, we neglect the alongshore variability captured by our map analysis to focus on the average cross-shore evolution; future efforts aim to integrate a more detailed analysis of the historical maps, records, and images we have collected with recent modeling efforts that account for the plan view evolution of the barrier (Ashton and Lorenzo-Trueba, 2018; Nienhuis and Lorenzo-Trueba, 2019a; Nienhuis and Lorenzo-Trueba, 2019b).

The current model version does not incorporate land-use changes and human development, which would be required to model the migration of the geomorphic boundaries in phase 2. For instance, the reversal in the direction of migration of the mainland-marsh boundary between phase 1 and phase 2 (Figure 6F) cannot be explained by the ratio between sea-level rise rate and mainland slope as the model suggests; a seaward migration of this boundary requires a loss of inland marshes to development (Supplementary Figure 2). Similarly, the migration reversal of the ocean shoreline (Figure 6A) cannot be explained without accounting for beach nourishment volumes at LBI or from updrift locations (Figure 6B). Soon after the beginning of phase 2, the backbarrier-marsh interface disappears and the lagoon-backbarrier marsh remains stagnant, as development occupies the subaerial portion of LBI and the backbarrier marsh platform (Figures 2, 6C). Highlighting this stark contrast in landscape change between the undeveloped and developed phases of LBI is the focus of this manuscript; in future work, we aim to extend the moving-boundary framework to account for human development, land-use changes, and different coastal protection strategies.

Implications for coastal management

Overall, our analysis of the undeveloped phase of LBI evolution supports previous work that indicates that barrier-marsh-lagoon systems can be analyzed using a variety of moving boundaries to predict their response to global climate change. This statement is most applicable when human development is absent and barrier systems are allowed to evolve naturally and can freely roll over and migrate landward in response to sea-level rise (Figure 7A). Such an approach has been taken by The Nature Conservancy along much of the Virginia Eastern Shore coast since the 1970s. The opposite approach is to “hold the line” (Figure 7B) with either the placement of sand fill on the beach or the construction of hard infrastructures, such as groins, jetties, dikes, seawalls, or revetments (Titus et al., 1991; Valverde et al., 1999; Hapke et al., 2013; Kolodin et al., 2021). The U.S. Army Corps of Engineers has followed this approach by engineering a significant portion of the U.S. coast, including LBI after the 1930s (Figure 6), using a combination of hard infrastructure and localized beach replenishment, allowing economic benefits for coastal living and tourism to continue to be realized.

The two approaches illustrated in Figure 7 do not cover the full range of coastal responses and management decisions we see today or will likely see in the future (Janoff et al., 2020; Janoff, 2021; Kolodin et al., 2021). First, the “no action” management plan adopted in Virginia (Figure 6A) can lead to a substantial loss of marsh platforms due to the squeezing of the backbarrier environment (Deaton et al., 2017). Such rapid loss of valuable ecosystem services may make this approach unlikely to become widely implemented. On the other hand, it is unclear whether coastal communities will be able or willing to continue to cover the costs associated with holding the line as sea-level rise accelerates (IPCC, 2014; Kopp et al., 2019), large storms potentially become more frequent (Emanuel, 2005; Emanuel, 2013; Kirshen et al., 2020), and the cost of sand for nourishment practices increases (McNamara et al., 2011). We

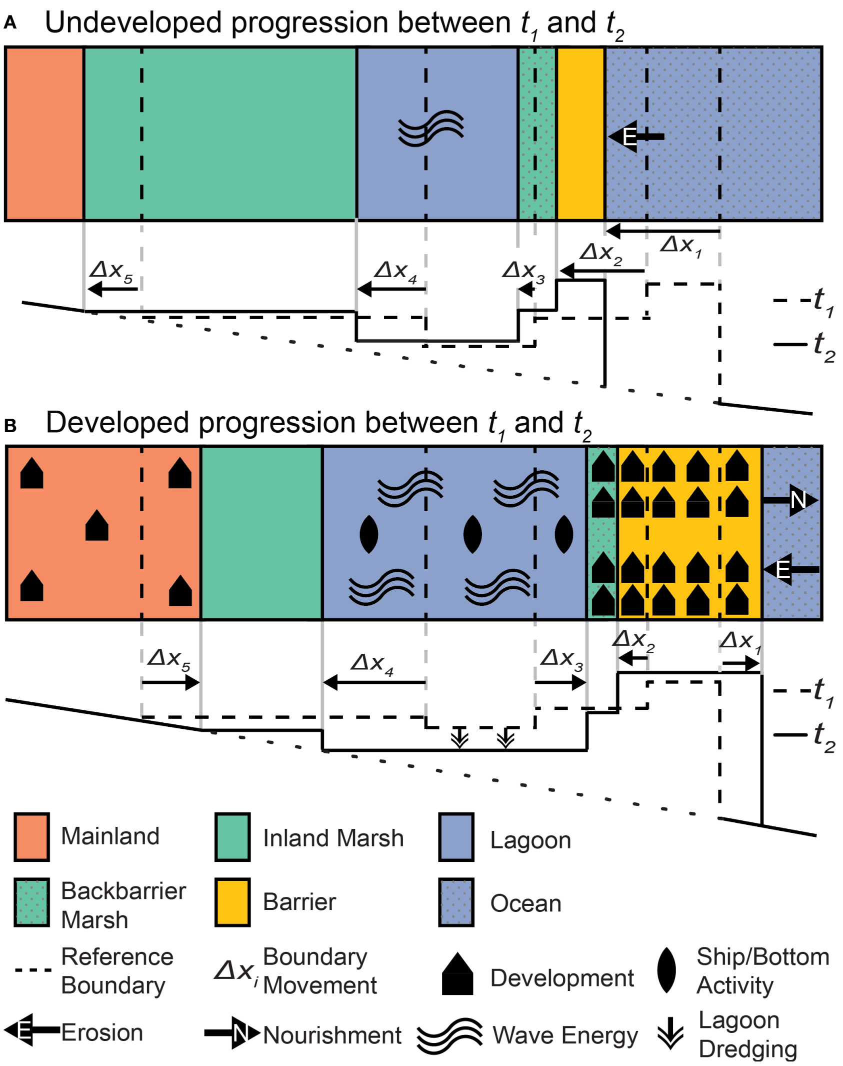

FIGURE 7
Conceptual illustrations depicting the evolution of **(A)** an undeveloped and **(B)** a fully developed barrier-marsh-lagoon system.

can therefore envision a third management option that balances the costs and benefits of barrier stabilization and ecosystem services by recognizing the interconnected nature of barriers and their backing marshes and lagoons (Miselis et al., 2021) but retreats at a lower rate than the undeveloped scenario. Relatively little is known about the mechanisms of such an approach, and efforts such as the one presented here can contribute to obtaining the required quantitative understanding for practical implementation.

Conclusions

Linking the evolution of barrier island and backbarrier environments through biogeomorphic feedback under a geomorphic moving-boundary framework represents an innovative approach for coastal management and scientific study; yet, our approaches remain largely untested with specific field locations over decadal to centennial time scales. Here, we test whether these concepts indeed govern the integrated evolution of barrier systems by analyzing the 180-year evolution of LBI using a moving-boundary approach. The first step of our approach is to map the location of five geomorphic boundaries over time: the ocean and bay shorelines, the marsh-lagoon boundaries on the landward and seaward sides of the lagoon, and the mainland-marsh boundary. This map analysis demonstrates that LBI transitioned from an undeveloped and coupled barrier-marsh-lagoon system with all its geomorphic boundaries moving landwards to a second phase in which anthropogenic effects overwhelmed the expected morphological natural response, with the ocean shoreline migrating seaward, the absence of overwash fluxes reaching the backbarrier environment, and a faster rate of marsh loss. For the second step of our approach, we integrate our map analysis with a numerical model of barrier-marsh-lagoon evolution; this effort demonstrates that the cross-shore dynamics of LBI during the undeveloped phase can be solely explained by the natural processes accounted by the numerical model, whereas the second or developed phase requires additional factors associated with human development and coastal protection. Such approaches for analyzing the morphological evolution of LBI are portable and have the potential to inform best practices for managing coupled barrier-marsh-lagoon systems under different sea-level rise scenarios.

Data availability statement

Historical nautical charts or NOAA T-sheets sheets from 1840, 1897, and 1934 can be accessed as scanned images in digital format at NOAA's "Historical maps and chart collection" database (https://historicalcharts.noaa.gov). The codes and data associated with the GIS analysis can be found on the following GitHub repository: https://github.com/JorgeMSU/LBI_Cross-shore_Barrier-Marsh-Lagoon. Access to the data and code are not restricted, and lie in the public domain.

Author contributions

JL-T, DC, CT, and JM contributed to the conception and design of the study. SN-O, CT and DC performed the GIS analysis. SN-O organized the database of historical maps and images. JL-T and CT developed the numerical model and carried out the simulations. CT and JL-T wrote the first draft of the manuscript. All authors contributed to manuscript revision, read, and approved the submitted version.

Funding

This work was supported by the USGS Coastal and Marine Hazards and Resources Program. Additionally, federal funds as part of the Megalopolitan Coastal Transformation Hub under NSF award ICER-2103754 and the New Jersey Sea Grant Consortium under NOAA grant number NA14OAR4170085 supported CT, JL-T, and SN-O.

Acknowledgments

Any use of trade, firm, or product names is for descriptive purposes only and does not imply endorsement by the US Government. We thank the three reviewers for their constructive feedback, which helped to improve the quality of the manuscript.

Conflict of interest

Publisher's note

Supplementary material

The Supplementary Material for this article can be found online at: https://www.frontiersin.org/articles/10.3389/fmars.2022.958573/full#supplementary-material

References

Anarde, K. A., Kameshwar, S., Irza, J. N., Nittrouer, J. A., Lorenzo-Trueba, J., Padgett, J. E., et al. (2018). Impacts of hurricane storm surge on infrastructure vulnerability for an evolving coastal landscape. *Natural Hazards Rev.* 19 (1), 04017020. doi: 10.1061/(ASCE)NH.1527-6996.0000265

Anderson, W., Lorenzo-Trueba, J., and Voller, V. (2019). A geomorphic enthalpy method: Description and application to the evolution of fluvial-deltas under sea-level cycles. *Comput. Geosci.* 130, 1–10. doi: 10.1016/j.cageo.2019.05.006

Ashton, A. D., and Lorenzo-Trueba, J. (2018). Morphodynamics of Barrier Response to Sea-Level Rise, in Barrier Dynamics and Response to Changing Climate. Cham: Springer International Publishing. 277–304.

Barbier, E. B., Hacker, S. D., Kennedy, C., Koch, E. W., Stier, A. C., and Silliman, B. R. (2011). The value of estuarine and coastal ecosystem services. *Ecol. Monogr.* 81 (2), 169–193. doi: 10.1890/10-1510.1

Bernier, J. C., Miselis, J. L., and Plant, N. G. (2021). Satellite-derived barrier response and recovery following natural and anthropogenic perturbations, northern chandeleur islands, Louisiana. *Remote Sens.* 13, 3779. doi: 10.3390/rs13183779

Boesch, D. F., and Turner, R. E. (1984). Dependence of fishery species on salt marshes: the role of food and refuge. *Estuaries* 7, 460–468. doi: 10.2307/1351627

Cialone, M. A., and Thompson, E. F. (2000). *Wave climate and littoral sediment transport potential, long beach island, new Jersey* (Vicksburg, MS: Engineer Research and Development Center Vicksburg, MS Coastal and Hydraulics Lab). Available at: https://apps.dtic.mil/sti/citations/ADA385444.

Ciarletta, D. J., Shawler, J. L., Tenebruso, C., Hein, C. J., and Lorenzo-Trueba, J. (2019a). Reconstructing coastal sediment budgets from beach-and foredune-ridge morphology: A coupled field and modeling approach. *J. Geophys. Res.: Earth Surf.* 124 (6), 1398–1416. doi: 10.1029/2018JF004908

Ciarletta, D. J., Lorenzo-Trueba, J. , and Ashton, A. D. (2019b). Mechanism for retreating barriers to autogenically form periodic deposits on continental shelves. *Geology* 47 (3), 239–242. doi: 10.1130/G45519.1

Ciarletta, D. J., Lorenzo-Trueba, J. , and Ashton, A. D. (2019c). Interaction of sea-level pulses with periodically retreating barrier islands. *Front. Earth Sci.* 279. doi: 10.3389/feart.2019.00279

Day, J. W., Christian, R. R., Boesch, D. M., Yanez-Arancibia, A., Morris, J., Twilley, R. R., et al. (2008). Consequences of climate change on the ecogeomorphology of coastal wetlands. *Estuaries coasts* 31 (3), 477–491. doi: 10.1007/s12237-008-9047-6

Deaton, C. D., Hein, C. J., and Kirwan, M. L. (2017). Barrier island migration dominates ecogeomorphic feedbacks and drives salt marsh loss along the Virginia Atlantic coast, USA. *Geology* 45 (2), 123–126. doi: 10.1130/G38459.1

Emanuel, K. A. (2005). Increasing destructiveness of tropical cyclones over the past 30 years. *Nature* 436 (7051), 686–688. doi: 10.1038/nature03906

Emanuel, K. A. (2013). Downscaling CMIP5 climate models shows increased tropical cyclone activity over the 21st century. *Proc. Natl. Acad. Sci.* 110 (30), 12219–12224. doi: 10.1073/pnas.1301293110

Erwin, R. M. (1996). Dependence of waterbirds and shorebirds on shallow-water habitats in the mid-Atlantic coastal region: an ecological profile and management recommendations. *Estuaries* 19 (2), 213–219. doi: 10.2307/1352226

Fagherazzi, S., Anisfeld, S. C., Blum, L. K., Long, E. V., Feagin, R. A., Fernandes, A., et al. (2019). Sea Level rise and the dynamics of the marsh-upland boundary. *Front. Environ. Sci.* 7. doi: 10.3389/fenvs.2019.00025

Fagherazzi, S., Mariotti, G., Leonardi, N., Canestrelli, A., Nardin, W., and Kearney, W. S. (2020). Salt marsh dynamics in a period of accelerated sea level rise. *J. Geophys. Res.: Earth Surf.* 125 (8), e2019JF005200. doi: 10.1029/2019JF005200

Ferreira, C. M., Irish, J. L., and Olivera, F. (2014). Quantifying the potential impact of land cover changes due to sea-level rise on storm surge on lower Texas coast bays. *Coast. Eng.* 94, 102–111. doi: 10.1016/j.coastaleng.2014.08.011

FitzGerald, D. M., Hein C., J., Hughes, Z., Kulp, M., Georgiou, I., and Miner, M. (2018). ""Runaway barrier island transgression concept: Global case studies."," in *Barrier dynamics and response to changing climate.* Eds. L. Moore and A Murray (Cham: Springer), 3–56. doi: 10.1007/978-3-319-68086-6_1

Gedan, K. B., Kirwan, M. L., Wolanski, E., Barbier, E. B., and Silliman, B. R. (2011). The present and future role of coastal wetland vegetation in protecting shorelines: answering recent challenges to the paradigm. *Clim. Change* 106 (1), 7–29. doi: 10.1007/s10584-010-0003-7

Hapke, C. J., Kratzmann, M. G., and Himmelstoss, E. A. (2013). Geomorphic and human influence on large-scale coastal change. *Geomorphology* 199, 160–170. doi: 10.1016/j.geomorph.2012.11.025

Hein, C. J., Fenster, M. S., Gedan, K. B., Tabar, J. R., Hein, E. A., and DeMunda, T. (2021). Leveraging the interdependent relationship between barrier islands and backbarrier marshes to enhance resilience to sea-level rise. *Front. Mar. Sci.* 8, 721904. doi: 10.3389/fmars.2021.721904

Houser, C., Hapke, C., and Hamilton, S. (2008). Controls on coastal dune morphology, shoreline erosion and barrier island response to extreme storms. *Geomorphology* 100, 223–240. doi: 10.1016/j.geomorph.2007.12.007

IPCC (2014). *"Sea level change", in climate change 2013 – the physical science basis: Working group I contribution to the fifth assessment report of the intergovernmental panel on climate change* (Cambridge: Cambridge University Press), 1137–1216. doi: 10.1017/CBO9781107415324.026

Janoff, A. (2021). *Community-scale beach nourishment and groin construction decisions along human-modified coasts: The interplay between socioeconomics, coordination, tourism, and shoreline change* (Montclair (NJ: Montclair State University). Available at: https://digitalcommons.montclair.edu/etd/696.

Janoff, A., Lorenzo-Trueba, J., Hoagland, P., Jin, D., and Ashton, A. D. (2020). *From coastal retreat to seaward growth: Emergent behaviors from paired community beach nourishment choices* (Washington DC: Earth and Space Science Open Archive ESSOAr). doi: 10.1002/essoar.10505464.1

Kirshen, P., Borrelli, M., Byrnes, J., Chen, R., Lockwood, L., Watson, C., et al. (2020). Integrated assessment of storm surge barrier systems under present and future climates and comparison to alternatives: A case study of Boston, USA. *Clim. Change* 162 (2), 445–464. doi: 10.1007/s10584-020-02781-8

Kirwan, M. L., and Megonigal, J. P. (2013). Tidal wetland stability in the face of human impacts and sea-level rise. *Nature* 504 (7478), 53–60. doi: 10.1038/nature12856

Kirwan, M. L., and Mudd, S. M. (2012). Response of salt-marsh carbon accumulation to climate change. *Nature* 489 (7417), 550–553. doi: 10.1038/nature11440

Kirwan, M. L., Walters, D. C., Reay, W. G., and Carr, J. A. (2016). Sea Level driven marsh expansion in a coupled model of marsh erosion and migration. *Geophys. Res. Lett.* 43 (9), 4366–4373. doi: 10.1002/2016GL068507

Kolodin, J., Lorenzo-Trueba, J., Hoagland, P., Jin, D., and Ashton, A. (2021). Engineered coastal berm-dune renourishment in New Jersey: Can coastal communities continue to hold the line? *Anthropocene Coasts* 4 (1), 193–209. doi: 10.1139/anc-2020-0024

Komar, P. D. (1998). *Beach processes and sedimentation* (Upper Saddle River, New Jersey: Simon & Schuster), 544 p.

Kopp, R. E., Gilmore, E. A., Little, C. M., Lorenzo-Trueba, J., Ramenzoni, V. C., and Sweet, W. V. (2019). Usable science for managing the risks of sea-level rise. *Earth's Future* 7 (12), 1235–1269. doi: 10.1029/2018EF001145

Lauzon, R., Murray, A. B., Moore, L. J., Walters, D. C., Kirwan, M. L., and Fagherazzi, S. (2018). Effects of marsh edge erosion in coupled barrier island-marsh systems and geometric constraints on marsh evolution. *J. Geophys. Res.: Earth Surf.* 123 (6), 1218–1234. doi: 10.1029/2017JF004530

Lazarus, E. D., and Goldstein, E. B. (2019). Is there a bulldozer in your model? *J. Geophys. Res.: Earth Surf.* 124 (3), 696–699. doi: 10.1029/2018JF004957

Lazarus, E. D., Goldstein, E. B., Taylor, L. A., and Williams, H. E. (2021). Comparing patterns of hurricane washover into built and unbuilt environments. *Earth's Future* 9 (3), e2020EF001818. doi: 10.1029/2020EF001818

Leatherman, S. P. (1979). Migration of assateague island, Maryland, by inlet and overwash processes. *Geology* 7, 104–107. doi: 10.1130/0091-7613(1979)7<104:MOAIMB>2.0.CO;2

Lin, N., Emanuel, K. A., Smith, J. A., and Vanmarcke, E. (2010). Risk assessment of hurricane storm surge for New York city. *J. Geophys. Res.* 115, D18121. doi: 10.1029/2009JD013630

Lin, N., Lane, P., Emanuel, K. A., Sullivan, R. M., and Donnelly, J. P. (2014). Heightened hurricane surge risk in northwest Florida revealed from climatological-hydrodynamic modeling and paleorecord reconstruction. *Journal of Geophysical Research: Atmospheres* 119, 8606–8623. doi: 10.1002/2014JD021584

Lloyd, J. B. (2005). *Two centuries of history on long beach island* (Harvey Cedars, NJ: Down The Shore Publishing Corp).

Lorenzo-Trueba, J., and Ashton, A. D. (2014). Rollover, drowning, and discontinuous retreat: Distinct modes of barrier response to sea-level rise arising from a simple morphodynamic model. *J. Geophys. Res.: Earth Surf.* 119 (4), 779–801. doi: 10.1002/2013JF002941

Lorenzo-Trueba, J., and Mariotti, G. (2017). Chasing boundaries and cascade effects in a coupled barrier-marsh-lagoon system. *Geomorphology* 290, 153–163. doi: 10.1016/j.geomorph.2017.04.019

Lorenzo-Trueba, J., Voller, V. R., Muto, T., Kim, W., Paola, C., and Swenson, J. B. (2009). A similarity solution for a dual moving boundary problem associated with a coastal-plain depositional system. *J. Fluid Mech.* 628, 427–443. doi: 10.1017/S0022112009006715

Lorenzo-Trueba, J., Voller, V. R., and Paola, C. (2013). A geometric model for the dynamics of a fluvially dominated deltaic system under base-level change. *Comput. Geosci.* 53, 39–47. doi: 10.1016/j.cageo.2012.02.010

Marani, M., D'Alpaos, A., Lanzoni, S., and Santalucia, M. (2011). Understanding and predicting wave erosion of marsh edges. *Geophys. Res. Lett.* 38 (21), L21401. doi: 10.1029/2011GL048995

Mariotti, G., and Fagherazzi, S. (2013). Critical width of tidal flats triggers marsh collapse in the absence of sea-level rise. *Natl. Acad. Sci.* 110 (14), 5353–5356. doi: 10.1073/pnas.1219600110

McBride, R. A., Anderson, J. B., Buynevich, I. V., Cleary, W. J., Fenster, M. S., FitzGerald, D. M., et al. (2013). *Morphodynamics of barrier systems: a synthesis, in treatise on geomorphology, v. 10* (San Diego, CA: Academic Press), 166–244. doi: 10.1016/B978-0-12-374739-6.00279-7

Mcleod, E., Chmura, G. L., Bouillon, S., Salm, R., Björk, M., Duarte, C. M., et al. (2011). A blueprint for blue carbon: toward an improved understanding of the role of vegetated coastal habitats in sequestering CO2. *Front. Ecol. Environ.* 9 (10), 552–560. doi: 10.1890/110004

McNamara, D. E., Murray, A. B., and Smith, M. D. (2011). Coastal sustainability depends on how economic and coastline responses to climate change affect each other. *Geophys. Res. Lett.* 38 (7), L07401. doi: 10.1029/2011GL047207

McNamara, D. E., and Werner, B. T. (2008a). Coupled barrier island-resort model: 1. emergent instabilities induced by strong human-landscape interactions. *J. Geophys. Res.* 113, F01016. doi: 10.1029/2007JF000840

McNamara, D. E., and Werner, B. T. (2008b). Coupled barrier island–resort model: 2. tests and predictions along ocean city and assateague island national seashore, Maryland. *J. Geophys. Res.: Earth Surf.* 113, F01017. doi: 10.1029/2007JF000841

Miselis, J. L., Flocks, J. G., Zeigler, S., Passeri, D., Smith, D. R., Bourque, J., et al. (2021). "Impacts of sediment removal from and placement in coastal barrier island systems. United States Geological survey open-file report 2021–1062. Reston, VA: United States Geological Survey," in *Geological survey open-file report 2021–1062*, 94 p. doi: 10.3133/ofr20211062

Miselis, J. L., and Lorenzo-Trueba, J. (2017). Natural and human-induced variability in barrier-island response to sea level rise. *Geophys. Res. Lett.* 44 (23), 11–922. doi: 10.1002/2017GL074811

New Jersey Department of State (1906). *Compendium of censuses 1726-1905, together with the tabulated returns of 1905* (Trenton, NJ: Murphy Publishing Co. Printers).

New Jersey State Data Center (2001) *New Jersey population trends 1790 to 2000; census 2000* (Division of Labor Market and Demographic Research). Available at: http://hdl.handle.net/10929/42812 (Accessed May 30, 2022).

Nienhuis, J. H. , and Lorenzo-Trueba, J. (2019a). Can barrier islands survive sea-level rise? quantifying the relative role of tidal inlets and overwash deposition. *Geophys. Res. Lett.* 46 (24), 14613–14621. doi: 10.1029/2019GL085524

Nienhuis, J. H. , and Lorenzo-Trueba, J. (2019b). Simulating barrier island response to sea level rise with the barrier island and inlet environment (BRIE) model v1. 0. *Geosci. Model. Dev.* 12 (9), 4013–4030. doi: 10.5194/gmd-12-4013-2019

Odezulu, C. I., Lorenzo-Trueba, J., Wallace, D. J., and Anderson, J. B. (2017). *Stratigraphic and sedimentological evidence for unprecedented shoreline migration rate during historic time: Follets island, TX, in barrier island dynamics and response to changing climate* (New York, NY: Springer). doi: 10.1007/978-3-319-68086-6

Orton, P., Vinogradov, S., Georgas, N., Blumberg, A., Lin, N., Gornitz, V., et al. (2015). New York city panel on climate change 2015 report chapter 4: Dynamic coastal flood modeling. *Ann. New York Acad. Sci.* 1336 (1), 56–66. doi: 10.1111/nyas.12589

Passeri, D. L., Bilskie, M. V., Plant, N. G., Long, J. W., and Hagen, S. C. (2018). Dynamic modeling of barrier island response to hurricane storm surge under future sea level rise. *Clim. Change* 149 (3), 413–425. doi: 10.1007/s10584-018-2245-8

Reeves, I. R., Moore, L. J., Goldstein, E. B., Murray, A. B., Carr, J. A., and Kirwan, M. L. (2020). Impacts of seagrass dynamics on the coupled long-term evolution of barrier-marsh-bay systems. *J. Geophys. Res.: Biogeosci.* 125 (2), e2019JG005416. doi: 10.1029/2019JG005416

Roberts, T. M., and Wang, P. (2012). Four-year performance and associated controlling factors of several beach nourishment projects along three adjacent barrier islands, west-central Florida, USA. *Coast. Eng.* 70, 21–39. doi: 10.1016/j.coastaleng.2012.06.003

Roelvink, D., Reniers, A., van Dongeren, A., van Thiel de Vries, J., McCall, R., and Lescinski, J. (2009). Modelling storm impacts on beaches, dunes and barrier islands. *Coast. Eng.* 56 (11-12), 1133–1152. doi: 10.1016/J.COASTALENG.2009.08.006

Rogers, L. J., Moore, L. J., Goldstein, E. B., Hein, C. J., Lorenzo-Trueba, J., and Ashton, A. D. (2015). Anthropogenic controls on overwash deposition: Evidence and consequences. *J. Geophys. Res.: Earth Surf.* 120 (12), 2609–2624. doi: 10.1002/2015JF003634

Shawler, J. L., Ciarletta, D. J., Connell, J. E., Boggs, B. Q., Lorenzo-Trueba, J., and Hein, C. J. (2021). Relative influence of antecedent topography and sea-level rise on barrier-island migration. *Sedimentology* 68 (2), 639–669. doi: 10.1111/sed.12798

Smith, K. E. L., and Terrano, J. F. (2017). "Shorelines for barnegat and great bay, NJ: 1839 to 2012," in *U.S. geological survey data release, ver 1.1, December 2017* St. Petersburg, FL: United States Geological Survey. doi: 10.5066/F75X275C

Stutz, M. L., and Pilkey, O. H. (2005). The relative influence of humans on barrier islands: Humans versus geomorphology. *Rev. Eng. Geol.* 16, 137–147. doi: 10.1130/REG16

Stutz, M. L., and Pilkey, O. H. (2011). Open-ocean barrier islands: global influence of climatic, oceanographic, and depositional settings. *J. Coast. Res.* 27 (2), 207–222. doi: 10.2112/09-1190.1

Swenson, J. B., Voller, V. R., Paola, C., Parker, G., and Marr, J. G. (2000). Fluvio-deltaic sedimentation: A generalized Stefan problem. *Eur. J. Appl. Math.* 11 (5), 433–452. doi: 10.1017/S0956792500004198

Teal, J. M., and Weishar, L. (2005). Ecological engineering, adaptive management, and restoration management in Delaware bay salt marsh restoration. *Ecol. Eng.* 25 (3), 304–314. doi: 10.1016/j.ecoleng.2005.04.009

Theuerkauf, E. J., and Rodriguez, A. B. (2017). Placing barrier-island transgression in a blue-carbon context. *Earth's Future* 5 (7), 789–810. doi: 10.1002/2017EF000568

Titus, J. G., Park, R. A., Leatherman, S. P., Weggel, J. R., Greene, M. S., Mausel, P. W., et al. (1991). Greenhouse effect and sea level rise: the cost of holding back the sea. *Coast. Manage.* 19 (2), 171–204. doi: 10.1080/08920759109362138

Trembanis, A. C., Pilkey, O. H., and Valverde, H. R. (1999). Comparison of beach nourishment along the US Atlantic, great lakes, gulf of Mexico, and new England shorelines. *Coast. Manage.* 27 (4), 329–340. doi: 10.1080/089207599263730

United States Army Corps of Engineers (1999) *Barnegat inlet to little egg inlet, long beach island, ocean county, new Jersey (revised draft feasibility report and integrated environmental impact statement). EPA number: 990228D*. Available at: https://www.sciencebase.gov/catalog/item/5057a80de4b01ad7e02881f6.

United States Bureau of the Census (1912). *Thirteenth census of the united states 1910: Population by counties and minor civil divisions 1900, 1890* (Washington, D.C: Washington Government Print Office).

Uptegrove, J., Waldner, J., Stanford, S., Monteverde, D., Sheridan, R., and Hall, D. (2012). *Geology of the New Jersey offshore in the vicinity of Barnegat Inlet and Long Beach Island. New Jersey Geological and Water survey, Geologic Map Series (GMS). GMS.* 12-2. Available at: https://www.researchgate.net/publication/305809013_Geology_of_the_New_Jersey_offshore_in_the_vicinity_of_Barnegat_Inlet_and_Long_Beach_Island_New_Jersey_Geological_and_Water_Survey_Geological_Map_Series_GMS_12-2

U.S. Army Corps of Engineers (1984). "Shoreline protection manual (*fourth edition*)": in *U.S. Department of the Army, coastal engineering research center technical papers and reports*. Washington DC: Department of the Army Waterways Experiment Station, Corps of Engineers. Available at: https://archive.org/details/shoreprotectionm01unit.

Valverde, H. R., Trembanis, A. C., and Pilkey, O. H. (1999). Summary of beach nourishment episodes on the US east coast barrier islands. *J. Coast. Res.* 15, 1100–1118. Available at: https://www.jstor.org/stable/4299028

Walters, D. C., and Kirwan, M. L. (2016). Optimal hurricane overwash thickness for maximizing marsh resilience to sea level rise. *Ecol. Evol.* 6 (9), 2948–2956. doi: 10.1002/ece3.2024

Walters, D., Moore, L. J., Duran Vinent, O., Fagherazzi, S., and Mariotti, G. (2014). Interactions between barrier islands and backbarrier marshes affect island system response to sea level rise: Insights from a coupled model. *J. Geophys. Res.: Earth Surf.* 119 (9), 2013–2031. doi: 10.1002/2014JF003091

Weinstein, M. P., Teal, J. M., Balletto, J. H., and Strait, K. A. (2001). Restoration principles emerging from one of the world's largest tidal marsh restoration projects. *Wetlands Ecol. Manage.* 9 (5), 387–407. doi: 10.1023/A:1012058713910

Werner, B. T., and Mcnamara, D. E. (2007). Dynamics of coupled human-landscape systems. *Geomorphology* 91 (3-4), 393–407. doi: 10.1016/j.geomorph.2007.04.020

Wolters, M., Garbutt, A., and Bakker, J. P. (2005). Salt-marsh restoration: evaluating the success of de-embankments in north-west Europe. *Biol. Conserv.* 123 (2), 249–268. doi: 10.1016/j.biocon.2004.11.013

Zhang, X., Leonardi, N., Donatelli, C., and Fagherazzi, S. (2020). Divergence of sediment fluxes triggered by sea-level rise will reshape coastal bays. *Geophys. Res. Lett.* 47 (13), e2020GL087862. doi: 10.1029/2020GL087862

frontiers | Frontiers in Marine Science

TYPE Original Research
PUBLISHED 09 November 2022
DOI 10.3389/fmars.2022.1005514

EDITED BY
Amaia Ruiz de Alegría-Arzaburu,
Universidad Autónoma de Baja
California, Mexico

REVIEWED BY
Eduardo Cuevas,
Laboratorio de Ecología Espacial y del
Movimiento, Mexico
Christian M. Appendini,
National Autonomous University of
Mexico, Mexico

*CORRESPONDENCE
Tomás Fernández-Montblanc
tomas.fernandez@uca.es

SPECIALTY SECTION
This article was submitted to
Coastal Ocean Processes,
a section of the journal
Frontiers in Marine Science

RECEIVED 28 July 2022
ACCEPTED 10 October 2022
PUBLISHED 09 November 2022

CITATION
Fernández-Montblanc T,
Bethencourt M and Izquierdo A (2022)
Underwater Cultural heritage risk
assessment methodology for wave-induced hazards: The showcase of the
Bay of Cadiz.
Front. Mar. Sci. 9:1005514.
doi: 10.3389/fmars.2022.1005514

Underwater Cultural heritage risk assessment methodology for wave-induced hazards: The showcase of the Bay of Cadiz

Tomás Fernández-Montblanc[1]*, Manuel Bethencourt[2] and Alfredo Izquierdo[3]

[1]Earth Sciences Department, University of Cadiz INMAR, Puerto Real, Spain, [2]Department of Materials Science, Metallurgy Engineering and Inorganic Chemistry, University of Cadiz INMAR, Puerto Real, Spain, [3]Applied Physics Department, University of Cadiz INMAR, Puerto Real, Spain

Coastal areas are characterized by high energetic conditions associated to the wave transformation process and by numerous underwater cultural heritage (UCH) sites whose preservation is crucial given their cultural and economic value. UCH management requires a decision support system to prioritize UCH interventions and actions for long-term preservation. This paper presents a novel UCH risk assessment methodology to quantitatively assess the impact of wave-induced hazards on UCH in coastal environments at a local level and the screening of UCH sites at risk. The UCH risk is calculated as a function of vulnerability (depending on archaeological materials, slope, and seabed type), hazard (decontextualization, scouring, and erosive wear), and exposure computed for the UCH sites registered in an archaeological database. The procedure was validated at two shipwreck sites, *Bucentaure* and *Fougueux*, in the Bay of Cadiz. An agreement between the risk index value and the *in situ* measurements of the rates of scouring and corrosion (used as a proxy of erosive wear) was observed. The methodology was tested in the Bay of Cadiz using an archaeological database containing 56 UCH sites. It allowed identifying the UCH sites at high risk: six are at risk of decontextualization, four are in peril of scouring erosion, and two are at risk of erosive wear. Two UCH sites at high risk of at least two hazards were also identified. This UCH risk assessment methodology is a stepping stone towards a decision support system that will give priority to research, prospection, management, and protection measures in the UCH sites analyzed to ensure their preservation in a context of climate change in the era of a sustainable blue economy.

KEYWORDS

coastal risk, coastal management, scouring, shipwreck, underwater cultural heritage

1 Introduction

A large number of underwater cultural heritage (UCH) sites are characteristic of coastal areas as a result of the intense use of those areas for human settlement as well as commercial and military purposes for centuries. The concentration of UCH sites is also a direct consequence of coastal sailing and perils such as stormy weather conditions, rocky shoals, or other hazards existing in those areas used for coastal navigation. Shallow coastal waters therefore contain numerous UCH sites. Intensive exploitation of ocean resources, along with the advances in acoustic seafloor mapping, and the expansion of scuba diving in recent decades have contributed to their discovery. Considering the abundance of shipwreck sites and other underwater archaeological structures, an archaeological study or *in situ* protection of all of them is currently unaffordable. Adopting measures to protect underwater archaeological remains, in accordance with the Convention on the Protection of the Underwater Cultural Heritage United Nations Educational, Scientific and Cultural Organization (UNESCO), is challenging when a large number of sites should be managed and considered for interventions with a limited budget.

Furthermore, shallow coastal waters are a very energetic environment where oceanographic agents such as waves, currents, and sediment characteristics determine a dynamic equilibrium. Changes in energetic (*e.g.*, seasonal) conditions can generate the successive burial and exposure of UCH sites (Gregory et al., 2012; Fernández-Montblanc et al., 2016; Fernández-Montblanc et al., 2018), affecting the stability and degradation of UCH materials (Bethencourt et al., 2018; Gregory, 2020). These agents can control the proliferation of harmful organisms for the materials (Ruuskanen et al., 2015; Cámara et al., 2017; González-Duarte et al., 2018), sediment transport, and elimination of concretion layers that act as protective covers of certain archaeological objects (Bethencourt et al., 2018). Therefore, the degradation of UCH sites (Pournou, 2018; Gregory, 2020) may be aggravated in shallow water areas. At the UCH sites located in coastal waters, the degradation rates may experience episodic fluctuations associated with changes in the energetic conditions in the system (Ward et al., 1999). Waves can be considered a major hazard driver for the conservation of UCH sites in wave-exposed coasts. Given the magnitude of the wave force exerted and the sediment transport capacity in shallow water depths, waves contribute to the scattering of archaeological objects and induce scouring or abrasion by displacing sand grains. This results in the loss and degradation of archaeological material.

The scattering of archaeological objects or shipwreck remains caused by waves leads to archaeological decontextualization. It occurs when archaeological objects are transported from their original wreckage location, losing connectivity with their original context and other related archaeological objects. Decontextualization of UCH artefacts occurs when drag forces induced by waves on the seabed are large enough to transport objects located at the UCH site. Additionally, wave forces and wave load can damage and transport part of the structure of a shipwreck, producing the disintegration and decay of the archaeological structure.

Wave-induced oscillatory flow and turbulence may lead to scouring around the shipwreck or other UCH sites (Quinn, 2006; Fernández-Montblanc et al., 2016). Scouring is a key process for the conservation of UCH because it is able to control the sediment budget around UCH sites. It is the result of the intensification of flow velocity by its interaction with near-seabed objects (Whitehouse, 1998). Scouring largely controls the integrity of the UCH sites. A wooden hull structure can collapse if a scour pit is formed around the archaeological remains. It determines the exposure of the archaeological material to the abrasive effect caused by the suspended sediment particles and also produces drastic changes in other environmental variables (*i.e.*, oxygen concentration, benthic communities) governing the deterioration process (Ward et al., 1999; Quinn, 2006; Bethencourt et al., 2018; Gregory, 2020), for example, scour can increase the oxygen concentration that accelerates the microbial degradation process of the wooden remains (Björdal et al., 2000; Björdal and Nilsson, 2008) and increase the corrosion rates of active metals such as copper or iron (Angelini et al., 2013). Scour also controls the composition of the benthic community that affects the conservation of metallic objects (Bethencourt et al., 2018) or the degradation of stone materials (Cámara et al., 2017). The amplification of maximum orbital velocity and the appearance of shear stress and coherent flow structures caused by waves and seabed structure interactions are the main mechanisms in generating scour associated to waves (Sumer and Fredsøe, 2002). Wave-induced scour will vary depending on the structure's size and wave conditions (McNinch et al., 2006; Fernández-Montblanc et al., 2016).

Suspended sediment transported by currents or waves can produce abrasion by impacting on the surface of the archaeological materials [see Thompson et al. (2011)]. Erosive wear, a wave-induced hazard on UCH, is the process of progressively removing material from a surface due to the repeated impacts of solid particles present in the flow. If there is enough energy, each particle re-suspended in the flow can cut or fracture a small amount of material from the surface. If this is repeated over a long period of time, a significant loss of material may occur. The rate of erosive wear depends on several factors. The characteristics of the suspended particle and its shape, hardness, impact velocity, and impact angle are key factors, along with the properties of the surface being eroded (Bitter, 1963).

Hence, given the profusion of UCH sites in coastal areas and the hazardous conditions linked to wave action, the development of tools and methodologies to select and identify sites prone to damage is necessary. This is especially relevant in a context of climate change, given the significant changes in wave energy expected by the end of the century (Mentaschi et al., 2017). These methods will allow the screening of UCHs that are more susceptible to be impacted by waves. It provides UCH managers with a tool for decision support in order to prioritize UCH interventions. This tool gives precedence to UCH sites where special measures must be implemented for *in situ* protection or where excavation and documentation must be a priority, as the loss of archaeological information is highly likely.

The present work therefore aims to develop a risk assessment method that takes into account the impact of wave-induced hazards on underwater cultural heritage. This paper is structured as follows: The Methods section describes the methodology developed and the datasets used to validate the proposed methodology; the Results section outlines the main results, including validation and UCH risk assessment in the case of the Bay of Cadiz; in the Discussion section, the applicability, limitations and potential of the methodology are analyzed based on the achieved results; and, finally, the main findings of this paper are summarized.

2 Methods

2.1 Study area

The Bay of Cadiz is an inlet located in the Gulf of Cadiz (southwest coast of the Iberian Peninsula) extending from Punta Candor to Sancti Petri tidal creek (Figure 1A). The seafloor mainly consists of unconsolidated sediments in which the mean grain size varies from very fine quartz sand to very fine gravel. Exceptions in this general pattern are the bedrock crops in the study area (Figure 1A). Wind waves can be considered the key hydrodynamic agent in the area with regard to UCH preservation. The active sector is defined between NNW and SE, with W being the most frequent and WSW the most energetic direction (Figure 1B). Mean wave climate is characterized by low energy [90% of significant wave height (Hs) is<1 m], although Hs can exceed 3 m for 105 hours in an average year (Figure 1C). The peak wave period (Tp) is rarely over 18 s, and the Hs–Tp joint probability plot shows two peaks from 5 to 9 s, and Hs =1 m, which are representative of mean conditions, whereas for storm wave conditions, it is represented by Tp ~8–12 s and Hs > 3 m (Figure 1D). Tides are semi-diurnal, and the tidal range can be defined as meso-tidal (mean spring range of 2.96 m). Tidal current velocity decreases rapidly in shallow water areas with the exception of the channels and tidal creeks in the Bay of Cadiz.

From a historical and archaeological point of view, because of how old the Bay of Cadiz is as a center of sustained port dominance and the dynamism of the region in terms of maritime cultural activity for millennia, an incredibly large number of UCH sites are observed. Among the existing archaeological sites, two coetaneous shipwrecks were selected to validate the UHC risk assessment methodology: the *Fougueux* and *Bucentaure* shipwreck sites. Both ships sank during a violent storm after the Battle of Trafalgar (1805). The *Bucentaure* represents a scattered shipwreck site including a total of 22 iron guns and the remains of an anchor (Figure 1E) seated at 12-m depth in the outer Bay of Cadiz (Figure 1A). The seafloor is a combination of a rocky seabed and gravelly quartz sand (D50 = 1.095 mm). Meanwhile, the *Fougueux* shipwreck site preserves an important portion of the wooden hull structure along with 31 cannons and an anchor (Figure 1F). *Fougueux* is seated at 7-m depth, and the seabed is mainly composed of unconsolidated sediments, medium and fine quartz sands (D50 = 0.177 mm), and a little rock shoal attached to the hull remains of the shipwreck.

2.2 Environmental and archaeological datasets

2.2.1 Bathymetry and sediment characterization

The present work is based on an eco-cartographic study including bathymetry and sediment characterization performed in 2011 (Spanish Ministry of Agriculture, Food and Environment, 2012). Multibeam-derived bathymetry was used for seafloor characterization in the wave model and to calculate the seabed slope. Seafloor mapping from multibeam backscatter was used to classify the seabed type (rocky/unconsolidated sediment). We used data from a field study in the whole Bay of Cadiz comprising 460 samples collected using a Van Veen grab sampler for sediment grain size characterization. A grain size analysis was conducted using the dry sieving method. The statistics of particle size distributions were calculated using the Folk and Ward method with the GRADISTAT software developed by Blott and Pye (2001).

2.2.2 Archaeological database

We created a dedicated archaeological database (ADB) for the Bay of Cadiz based on a scientific literature review including books, papers, and/or conference proceedings. Several bibliographic sources were employed (Guillemot and Meanteau; Lagostena, 2009; Lakey, 1987; García Rivera and Alonso Villalobos, 2005; Alzaga García et al., 2022). The ADB encompasses the archaeological resources identified and geo-localized in the outer Bay of Cadiz. The geolocation of the different UCH sites was established by georeferencing maps and figures of the scientific data sources in ARCGIS 10.1. The ADB contains relevant information about the main characteristics of the UCH sites including origin or provenance, chronology, composed materials organized into five categories (metallic, stone, glass, ceramic, and wood/organic materials), dominant material, and metadata regarding the data source. Basic

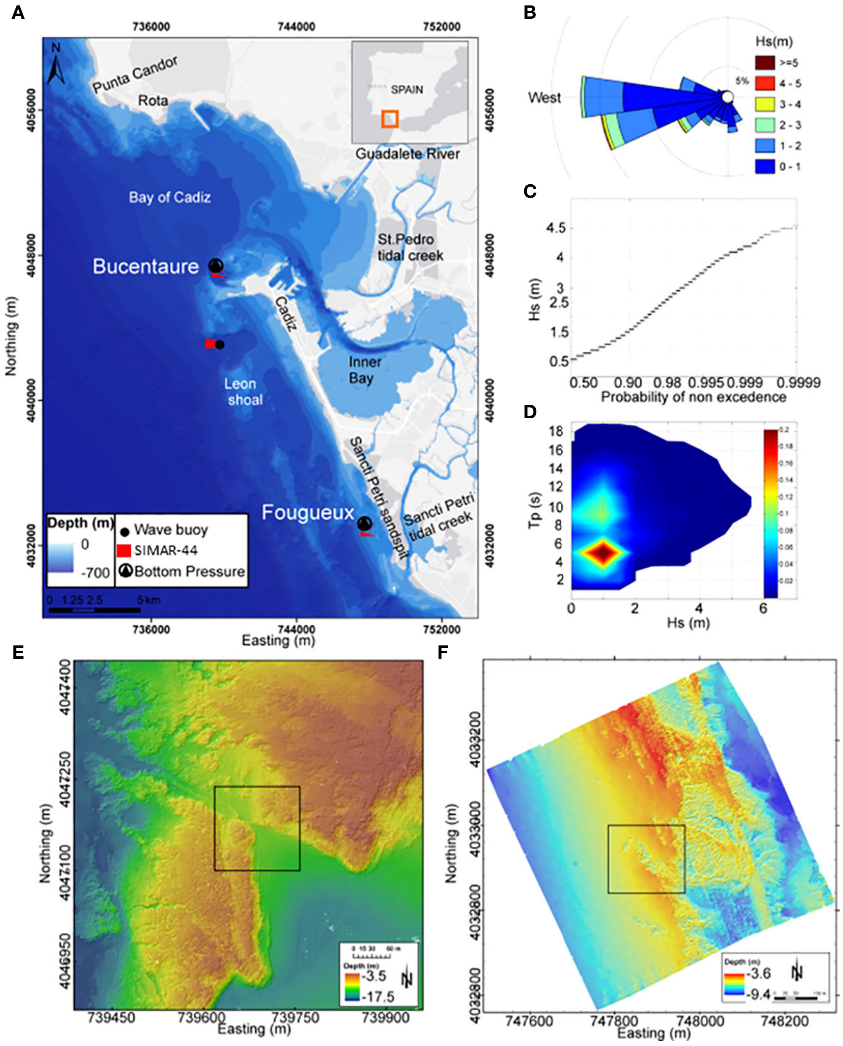

FIGURE 1
(A) Location of the studied sites. **(B)** Wave rose diagram of significant wave-height for directional wave buoy. **(C)** Scalar wave climate of significant wave height. **(D)** Joint distribution of significant wave height (Hs) and peak period (Tp). **(E)** Bathymetry of the Bucentaure site. **(F)** Bathymetry of the Fougeux site (Fernández-Montblanc et al, 2016).

environmental characteristics of the sites (depth and seabed type), when available, were also added.

2.2.3 Wave database

A simplified version of the hybrid downscaling method (Camus et al., 2011; Diaz-Hernandez et al., 2021) was used to propagate the historical wave hindcast (SIMAR-44) in the outer Bay of Cadiz (Figure 1A). At first, a manual selection of a reduced number of sea states representative of the offshore wave hindcast climate was performed. Then, the selected N sea-states were propagated into the outer Bay of Cadiz using the SWAN third-generation wave model (Booij et al., 1999) implemented on a regular mesh (~37-m resolution). Finally, the whole wave hindcast in each cell of the computational domain was reconstructed based on the interpolation in a 3D matrix of propagation coefficients for wave direction, peak period, significant wave height, and maximum near-bottom orbital velocity.

2.3 UCH risk assessment

The present work uses the 2009 UNISDR terminology on disaster risk reduction (https://www.undrr.org/terminology), and risk (R) is calculated as a function of the hazard (H) with a given probability, vulnerability (V), and exposure (E) [R = f(H, V, E)] (Field and Barros, 2014). We developed an UCH risk assessment methodology, whose workflow is schematized in Figure 2. The UCH risk assessment presented here is based on the risk index calculated at each specific location in accordance

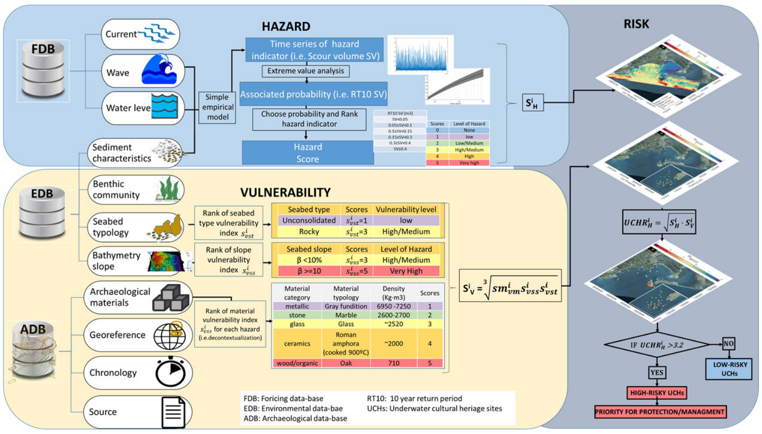

RT10 SV (m3)	Scores	Level of Hazard
SV<0.05	0	None
0.05≥SV<0.1	1	low
0.1≥SV<0.15	2	Low/Medium
0.15≥SV<0.3	3	High/Medium
0.3≥SV<0.4	4	High
SV≥0.4	5	Very high

Seabed type	Scores	Vulnerability level
Unconsolidated	s^i_{vst}=1	low
Rocky	s^i_{vst}=3	High/Medium

Seabed slope	Scores	Level of Hazard
β <10%	s^i_{vss}=3	High/Medium
β >=10	s^i_{vss}=5	Very High

Material category	Material typology	Density (Kg·m3)	Scores
metallic	Gray fundition	6950 -7250	1
stone	Marble	2600-2700	2
glass	Glass	~2520	3
ceramics	Roman amphora (cooked 900ºC)	~2000	4
wood/organic	Oak	710	5

FDB: Foricing data-base
EDB: Environmental data-bae
ADB: Archaeological data-base
RT10: 10 year return period
UCHs: Underwater cultural heriage sites

FIGURE 2
Workflow of the developed underwater cultural heritage risk assessment methodology.

with the main environmental and UCH site characteristics following an object-oriented approach. Each specific site registered in the archaeological database was considered an asset to be potentially damaged by the considered hazard. This paper focuses on the identification and screening of those UCH sites at high risk, where waves may imperil the sites, thus facilitating the loss of archaeological information and the degradation of archaeological materials and hampering the *in situ* preservation of UCH sites considered as a priority option. This conservation approach is included in Rule 1 of the Guidelines to the Annex of the Convention on the Protection of the Underwater Cultural Heritage—UNESCO that establishes *in situ* preservation as the first option for UCH protection. The methodology followed the scheme used in previous studies on coastal risk assessment at the regional scale [*i.e.*, CRAFT1 (Armaroli and Duo, 2018; Ferreira et al., 2018)]. A GIS index and a simple empirical model-based approach were integrated to support decision making and prioritizing the investment in available resources and actions to counteract the effect of wind waves in the UCH sites at high risk.

The methodology was designed to be applied from the local to the regional scale ≈*O* (10–100 km), targeting to avoid the request of very detailed environmental information (*e.g.*, DEM resolution<1 m).

A complete risk assessment would require exposure quantification based on the valuation of UCHsites. This high level of baseline information is rarely available at the local or regional scales. Therefore, we considered a similar market and not market value for all the UCH sites in the database, assuming equal exposure values for all the UCH sites. The risk index was then calculated as the root geometric mean of the hazard multiplied by vulnerability scores according to Eq. 1 (Gornitz, 1990; Viavattene et al., 2018).

$$UCHR^i_H = \sqrt{S^i_H \cdot S^i_V} \qquad \text{Eq. 1}$$

where $UCHR^i_H$ is the UCH risk index for each hazard (*H*) at each specific archaeological site (*i*), S^i_H is the score of the hazard, and S^i_V is the score of the vulnerability at site *i*. $UCHR^i_H$ is an index (integer values from 0 to 5) associated to each UCH site that allows quantitatively comparing different UCH sites located in the region of analysis and showing the UCH sites at high risk of the specific hazards. The S^i_H is a six-class score ranging from 0 to 5 which correspond to none, low, low-medium, medium-high, high, and very high hazard. The level of hazard is defined in accordance with the magnitude of the hazard associated to a given non-exceedance probability expressed as a return period. The S^i_V is a score which ranges from 1 to 5 (low to very high classes) that represents the vulnerability of the UCH sites according to the characteristics of the archaeological material prevalent in the UCH site, its propensity to be affected by a certain hazard, and the environmental factors that increase or reduce the susceptibility of the UCH sites to the impacts produced by the considered hazards.

An UCH site is considered at risk if the risk index $UCHR^i_H$ >3.2. This threshold corresponds to the rounded root square of low (2) and very high (5) classes (Viavattene et al., 2018). UCH sites with higher values are those subject to the combination of medium and very high classes of vulnerability and hazard.

The vulnerability and hazard levels at each UCH site are specified in the sections below and summarized in Tables 1, 2. There is a lack of information relative to the definition of the hazard and vulnerability threshold to define the different categories of hazard and vulnerability levels. Therefore, those levels have been defined by expert judgment with local knowledge in oceanography and UCH conservation. The group of experts includes oceanographers, archaeologists, conservators, biologists, physicists, chemists, and engineers.

TABLE 1 Hazard indicator scores for decontextualization, erosive wear, and scouring.

Critical size of decontextualized object, Dcr (m) RT10	Erosive wear potential, EWP (J/m^3)RT1	Scouring volume, SV (m^3) RT10	Scores	Level of hazard
Dcr< 0.02	-20 ≥ EWP<-18	SV< 0.05	0	None
0.02 ≥ Dcr<0.04	-18 ≥ EWP<-16	0.05 ≥ SV<0.1	1	Low
0.04 ≥ Dcr<0.08	-16 ≥ EWP<-13.5	0.1 ≥ SV<0.15	2	Low/medium
0.08 ≥ Dcr<0.12	-13.5 ≥ EWP<-12.5	0.15 ≥ SV<0.3	3	High/medium
0.12 ≥ Dcr<0.16	-12.5 ≥ EWP<-11.5	0.3 ≥ SV<0.4	4	High
Dcr ≥ 0.16	EWP ≥ -11.5	SV ≥ 0.4	5	Very high

RT10 corresponds to the value of a 10-year return period and RT1 to a 1-year return period.

2.4 Hazard assessment

Previous studies have identified physical factors (Ward et al., 1999) and, more particularly, wind waves to be key in preserving UCH and in the evolution of UCH sites in shallow water sites (Quinn, 2006; Fernández-Montblanc et al., 2016). This work therefore focuses on wave-induced hazards on archaeological sites in shallow water. Three wave-induced hazards were selected considering their impact in the long-term preservation of UCH: archaeological decontextualization), scouring (SC), and erosive wear (EW). For those hazards, risk assessment was performed independently without taking into account multi-hazard interactions.

A simple three-step workflow was applied for the hazard assessment (Ferreira et al., 2018; Viavattene et al., 2018). First, the time series of the hazard indicator was calculated in accordance with bathymetry, sediment, grain size, wave characteristics, and water level. Second, a fit to an extreme value distribution was applied to calculate the associated probability. In this case, the transformed-stationary methodology was applied, including a 72-h time window for storm decluttering and a constant threshold (97th percentile) to select the extreme event. Then, the selected hazard events were fit into the generalized Pareto distribution [see Mentaschi et al. (2016) for further details]. Finally, the hazard scores were defined by ranking the hazard indicator for the selected probabilities.

This methodology followed the so-called response approach (Garrity et al., 2007), which is widely used for coastal storm impact assessment. This approach consists in calculating the probability of occurrence of the hazard (*i.e.*, archaeological decontextualization),

TABLE 2 Vulnerability scores in common materials in underwater cultural heritage sites for decontextualization, erosive wear, and scour hazard.

Material category	Material type	Property: density (kg·cm^3)	Property: Brinel hardness scale	Proxy sensitivity to aerobic biological communities	Vulnerability score
Decontextualization					
Metallic	Gray iron	6.95–7.25			1
Stone	Marble	2.6–2.8			2
Glass	Glass	~2.52			3
Ceramics	Coarse ware	~2.0			4
wood/organic	Oak	0.71			5
Erosive wear					
Glass	Glass		482–550		1
Metallic	Gray iron		140–250		2
Ceramics	Coarse ware		120–125		3
Stone	Marble		35		4
Wood/organic	Oak		4–8		5
Scour					
Stone	Marble			–	1
Metallic	Gray iron			–	2
Ceramics	Coarse ware			+	3
Glass	Glass			++	4
Wood/organic	Oak			+++	5

The increase in sensitivity to biologial degradation is indicated from low sensitivity (–) to very high sensitivity (+++).

but not of the driver, or variables governing the hazard (*i.e.*, water level, wave period and significant wave height).

2.4.1 Archaeological decontextualization hazard

The decontextualization of an UCH artefact occurs when drag forces induced by waves on the seabed are sufficient to transport objects located in the UCH site. Furthermore, wave forces and wave load can damage and transport part of the damaged structure away from the shipwreck site, producing the disintegration and decay of the archaeological structure (Ward et al., 1999). The potential damage of scattering and loss of archaeological artifacts induced by waves was evaluated using Eq. 2 as proposed by Soulsby (1997) for the threshold motion of large-diameter particles, taking into account the sole action of wind waves.

$$Dcr = \left(\frac{97.9 U_b^{3.08}}{Tp_{1.08}\left[g\left(\left(\frac{\rho_s}{\rho}\right) - 1\right)\right]^{2.08}} \right)^{0.5} \qquad \text{Eq. 2}$$

where U_b is the undisturbed near-bed orbital velocity, T_p is the peak wave period, g is the gravitational constant, ρ_s is the density of the grain sediment, and ρ is the seawater density.

The scattering and loss of archaeological objects at UCH sites depends on the material, size, and shape of the archaeological objects. For the sake of simplicity, in the present study, a spherical shape and quartz density (2,600 kg m^{-3}) was assumed based on the shape and density of the material employed to derive the empirical Eq. 2. This assumption does not represent the specific shape and density of the archaeological materials but allows calculating the potential decontextualization comparing the hazard of the different UCH sites without requesting specific and detailed information on the size, shape, or density of the objects or structures in the UCH sites. This information is incorporated into the risk assessment by specifying the vulnerability in accordance with the type of the archaeological material. Table 1 shows the decontextualization hazard scores. In this case, the selected probability corresponds to the 10-year return period, an intermediate value in the extreme distribution. The ranges of the hazard magnitude to score the hazards were defined and compliant with expert judgment based on local knowledge.

2.4.2 Scour hazard

The potential scour was estimated using the equilibrium scour depth. Calculating the equilibrium scour depth was based on Eq. 3 for maximum scour depth and Eq. 4 (Sumer and Fredsøe, 1990) for the maximum scour length for wave-induced scour on pipelines. A constant archaeological object/structure of a cylindrical shape of 1 m in diameter was assumed.

$$S_{max} = D \cdot 0.1 \cdot \sqrt{KC} \qquad \text{Eq. 3}$$

$$L_{Smax} = D \cdot 0.35 \cdot KC^{0.65} \qquad \text{Eq. 4}$$

where $KC = U_b \cdot T_p / D$ is the Keulegan–Carpenter dimensionless number, U_b is the maximum undisturbed near-bed orbital velocity, T_p is the peak wave period, and D is the structure diameter (1 m).

In the of case of breaking or near-breaking wave conditions, the equilibrium scour depth was calculated according to expressions Eq. 5 and Eq. 6 proposed by Young and Testik (2009) for vertical and semicircular breakwaters applied for conditions $0.6 < KC_H = \leq 9.0$ *and* $0.4 < fb = \leq 1.7$,

where KC_H is the Keulegan–Carpenter number expressed as a function of the significant wave height (H_s, $KC_H = H_s \cdot \pi / D$), and *fb* is the ratio of the water depth and structure height $(h - D)/H^s$, h is the water depth, and D is the structure/object diameter:

$$S_{max} = D \cdot 0.125 \cdot KC_H \sqrt{\psi} \qquad \text{Eq. 5}$$

$$L_{Smax} = \begin{cases} D/2 \cdot KC_H, & KC > \pi, \ detached \ scour \\ D \cdot KC, & KC_H \leq \pi \ attached \ scour \end{cases} \qquad \text{Eq. 6}$$

Both equations allow calculating the maximum scour depth and the length of the scour hole. If the scour mark is approximated to a triangular shape, the volume of scour can be calculated (Eq. 7) and used as an indicator of the magnitude of the scour.

$$SCV = \frac{1}{2} S_{max} L_{Smax} \qquad \text{Eq. 7}$$

Table 1 presents the scour hazard scores. In this case, the selected probability corresponds to the 10-year return period, an intermediate value in the extreme distribution.

2.4.3 Wear hazard

Wear hazard refers to the erosive wear caused by solid particle erosion, the process that occurs on archaeological structures/artifacts in the seabed exposed to the impact of suspended sediment particles transported by waves. The optimal approach to evaluate this hazard includes estimating the volume of material eroded by a single grain impact (Vi) according to the impact wear equation proposed by Bitter (1963). However, this approach requires specific measurements and the details of the threshold energy required for impact as well as the kinetic energy necessary to erode a unit of volume of material, depending on the status of the different archaeological materials.

This information is not available at the regional or local scale for all the archaeological sites. Therefore, the erosive wear potential ($EWP = log(KE \cdot IR)$) is used as an erosive wear hazard indicator. It is calculated using the kinetic energy ($KE = \frac{1}{2}(M_{sp} U_i^2)$) (where U_i is the grain velocity and Msp the mass of the particle) of the impacting grain considering the direction that maximizes the erosion (α=90°) multiplied by the impact rate (Thompson et al., 2011) ($IR=C/M_{sp}$ assumed to be proportional to the sediment concentration divided by the mass of the sediment particle.

We can assume $U_i \cong U_b$ considering the low velocity lag between flow and sediment particles in non-concentrated flows (Nian-Sheng, 2004). $M_{sp} = (\frac{4}{3}) \cdot \pi(\frac{D_{50}}{2})^3(\frac{\rho_s}{\rho})$ is calculated assuming spherical particles, quartz density (ρ_s=2600$kg{\cdot}m^{-3}$), and seawater density (ρ=1025$kg{\cdot}m^{-3}$). Sediment concentration was calculated at a reference level of 0.5 m above seabed, assuming a logarithmic profile (van Rijn, 1993).

$$C(z) = C_o\left(\left(h-\frac{z}{z}\right)\left(\frac{a}{h-a}\right)\right)^{\frac{w_s}{ku_\star}} \qquad \text{Eq. 8}$$

where h is the water depth accounting for the tidal variability of the sea surface, z is the height above bed, a is the reference level (a=10D_{50}) (Nielsen, 1986), D_{50} being the median particle size; w_s the particle settling velocity, k the von Karman's constant (0.4), and $u_\star$ the wave friction velocity.

The reference concentration (C_o) is given from equation Eq. 9, and shield entrainment (θ_s) is given from Eq. 10 as proposed by Zyserman and Fredsøe (1994):

$$C_o = \frac{0.331(\theta_s - 0.045)^{1.75}}{1+\frac{0.331}{0.46}(\theta_s - 0.045)^{1.75}} \qquad \text{Eq. 9}$$

$$\theta_s = \frac{f_w U_b}{2g\left(\left(\frac{\rho_s}{\rho}\right)-1\right)} \qquad \text{Eq. 10}$$

and the critical shield parameter for the initiation of motion is given by the expression proposed by Soulsby (1997):

$$\theta_{cr} = \frac{0.3}{1+1.2D_\star} + 0.055\left(1-exp\left(-0.02D_\star\right)\right) \qquad \text{Eq. 11}$$

where $D_\star$ is the dimensionless grain diameter:

$$D_\star = D_{50}\left[\frac{g\left(\left(\frac{\rho_s}{\rho}\right)-1\right)}{\vartheta^2}\right]^{1/3} \qquad \text{Eq. 12}$$

f_w is the wave friction factor for oscillatory flow assuming the sheet flow estimated as follows (van Rijn, 1993):

$$f = \begin{cases} \exp(-6+5.2\left(\frac{A_w}{K_s}\right)^{-0.19}) & \text{rough oscillatory flow} \quad (Re \geq 1e6) \\ 0.09(U_b A_w/\vartheta)^{-0.2} & \text{smooth oscillatory flow} \quad (1.5e5 \leq Re < 1e6) \\ 2(U_b A_w/\vartheta)^{-0.5} & \text{laminar oscillatory flow} \quad (Re \leq 1.5e5) \end{cases} \qquad \text{Eq. 13}$$

$A_w = \frac{Tp}{2\pi}U_b$ is the peak orbital excursion, Tp is the peak wave period, U_b is the undisturbed near-bed orbital velocity, ϑ is the kinematic viscosity (1.075e-6 m^2s^{-1}), K_s=2.5D_{50} is the bed roughness (Soulsby, 1997), and $Re=U_bA_w/\vartheta$ is the Reynolds number.

The settling velocity w_s is calculated in accordance with the equation proposed by Soulsby (1997):

$$w_s = \frac{\vartheta}{D_{50}}\left[(10.36^2 + 1.049D_\star^3)^{0.5} - 10.36\right] \qquad \text{Eq. 14}$$

The friction velocity is estimated in accordance with the equation proposed by van Rijn (1993):

$$u_\star = \sqrt{\frac{1}{4}\ \rho f_w U_b^2/\rho} \qquad \text{Eq. 15}$$

The suspended sediment concentration is calculated for those sea states where the shield number exceeds the critical value (θ_s>θ_{cr}), and friction velocity is larger than settling velocity ($u_\star$>w_s). If any of these conditions is not met, the suspended sediment concentration is assumed to be zero.

Table 1 presents the scores of the erosive wear hazard. In this case, the indicator is based on a high probability event corresponding to a 1-year return period. This high frequency value in the extreme distribution was selected to account for the continuous effect of erosive wear to damage UCH materials rather than the occasional (longer return periods) erosive wear effect that takes place for a limited time in an extreme event.

2.5 Vulnerability assessment

According to the 2009 UNISDR terminology, vulnerability is defined in terms of the *conditions determined by physical, social, economic and environmental factors or processes which increase the susceptibility of an individual, a community, assets, or systems to the impacts of hazards*. In this paper, vulnerability of UCH assets is determined by the characteristics of the archaeological material that prevails in the UCH site (metal, stone, wood, ceramic, and glass) and its tendency to be affected by a certain hazard and the environmental characteristics that increase the susceptibility of the UCH assets to be impacted by a hazard. The vulnerability index for the prevalent materials was established according to the specificity of the UCH site types in the study area and the main characteristics of the archaeological material. Thus, the vulnerability of metallic materials is defined in compliance with the specific properties of gray iron, the most frequent metallic material in the archaeological database of the case study. The ceramic vulnerability was established according to the properties of coarse ware, the type of archaeological artifact most represented in the ADB.

The vulnerability index related to the materials (sm^i_{vm}) is sensitive to the hazard considered. It is therefore defined in conformity with the specific properties of each material to cope with a certain hazard—for instance, stone materials (marble in our ADB) may be more vulnerable to erosive wear hazard than metallic (gray iron) ones, as they stand lower in the Brinell hardness scale or the equivalent hardness scale. However, marble is less vulnerable than gray iron to the impact of the decontextualization hazard based on the higher density property used to define the propensity of materials to be transported by waves.

The vulnerability index related to the materials ranges from 1 to 5 after assigning a score (1 to 5) to the types of materials (metal, stone, wood, ceramic, and glass). The vulnerability assigned by materials and hazards is summarized in Table 2. It includes the categories and types of materials as well as the properties selected to assign the vulnerability.

Regarding the decontextualization hazard, we did not have real data of the objects in each site. We decided to establish the rank based on the density of the main materials that can be found in the sites. The values in Table 2 are commercial, except in the case of ceramics, and obtained from Vila Socias et al. (2007).

With respect to the erosive wear hazard, Table 2 shows the hardness values of the main types of materials located in the sites on the Brinell scale (Vander Voort, 2000). In the case of stone and wood, the value is established by comparison with another material capable of scratching it. Coarse ware is scratched with steel, which has a Brinell hardness number (BHN) of 125, and oak is scratched with copper, which has a BHN of 35.

In the case of scour hazard, Table 2 ranks the material according to its sensitivity of the aerobic biological communities. The scour processes facilitate the increase of dissolved oxygen transforming the anoxic condition of the sediment into well-oxygenated waters. The aerobic biological communities living in this environment produce the deterioration of the different materials depending on their nature (Pearson, 1987), for example, in the waters of the Bay of Cadiz, wood is badly affected by mollusks of the genus *Teredo*.

Moreover, vulnerability was defined accounting for the environmental factors (seabed slope s^i_{vss} and seabed typology s^i_{vst}), which increase or decrease the susceptibility of the UCH sites to the impacts of each assessed hazard. In this case, the vulnerability index related to the environmental factors was considered constant for all the hazards. According to expert judgment, the higher values of vulnerability level (5) were established for those conditions that significantly amplify the vulnerability, the lower value (1) was established for those conditions that significantly decrease the vulnerability, and a neutral value of 3 was established for those conditions that do not modify the vulnerability. Following this approach, the seabed slope increased the vertical and horizontal velocities and the turbulence because of the modification of waves and current velocity fields. These amplifications cannot be addressed properly with the resolution and processes parametrized in commonly used wave propagation models for coastal applications. They could lead to greater susceptibility of the UCH sites located at a sloped seabed to the impact of the decontextualization, erosive wear, and scour hazards. Therefore, a sloped seabed (>10%) was scored as high vulnerability class (s^i_{vss}=5) and a gentle sloped seabed as medium vulnerability class (s^i_{vss}=3). The second environmental factor considered is the type of seabed. In this paper, two categories, rocky and non-consolidated seabed, were established in accordance with the seabed characteristics in the case study. However, they can be adapted to other categories (salt marsh vegetation, seagrass meadows, *etc*.). In this case, the UCH sites lying on a rocky seabed were scored as low vulnerability class (s^i_{vst}=1) and those on a non-consolidated one as medium vulnerability class (s^i_{vst}=3). Although the rocky seabed may house sand patches, the limited quantity of sediment potentially reduces the scour, and erosive wear is limited in comparison with the non-consolidated seabed. The decontextualization hazard is reduced because the irregularities in a rocky seabed may protect the archaeological objects hampering scattering by wave action. Table 3 lists the vulnerability scores according to the slope and the type of seabed.

The final vulnerability index S^i_V was calculated as the geometric mean of all the vulnerability indicators, the material-related vulnerability index (sm^i_{vm}) established from the ADB, and the environmental vulnerability indicator (seabed slope index (s^i_{vss}) and seabed type index (s^i_{vss}). These values were stablished from the DEM dataset and the seabed type dataset. The final value of S^i_V may take values from 1, indicating low-vulnerability class, to 5, for the very-high-vulnerability class.

$$S^i_V = \left[sm^i_{vm} \cdot s^i_{vss} \cdot s^i_{vst}\right]^{1/3} \qquad \text{Eq. 16}$$

2.6 Validation of the UCH risk assessment methodology

The *Fougueux* and *Bucentaure* sites were monitored, and metallic archaeological artifacts from each site were analyzed using archaeometric techniques to evaluate their degree of stability (Bethencourt et al., 2018). The result was used to validate the method for UCH risk assessment presented in this paper, focusing on erosive wear and scour hazards. Unfortunately, there are no data available to evaluate the decontextualization hazard in the study area.

At both sites, several cannons and anchors were selected as targets to establish their current conservation condition and to assess their prospects for *in situ* conservation. First, partial de-concretion was carried out, which allowed performing *in situ* measurements of the pH and corrosion potential of the iron object, E_{corr} [see Bethencourt et al. (2018) for further details]. The conservation status of the cannons was assessed by

TABLE 3 Vulnerability scores by environmental factors in underwater cultural heritage sites.

Slope, β (%)	Vulnerability score	Bed type	Vulnerability score
β< 10	3	Rock	1
β ≥ 10	5	Not consolidated	3

measuring the thickness of the surface corrosion layer. Then, the mean corrosion rate of the archaeological object was estimated by dividing the surface corrosion layer by the number of years since wrecking.

The spatial pattern of the corrosion rates measured in the cannons of the *Fougueux* site was analyzed with regard to the seabed type and slope in order to evaluate the vulnerability index related to environmental factors. The method to estimate the erosive wear risk was also validated by comparing the corrosion rates calculated from *in situ* measurement at both sites as a proxy of the erosive wear at the sites.

The accretion–erosion model derived by subtracting different DEM from time lapsed bathymetric surveys conducted in the *Fougueux* and *Bucentaure* sites [see Fernández-Montblanc et al. (2016) and Bethencourt et al. (2018) for further details] was used to evaluate the UCH risk assessment for the scour hazard.

3 Results

3.1 Archaeological database

The ADB incorporated a total of 56 UCH sites located at the outer Bay of Cadiz. Regarding the archaeological material, ceramic (34%) and metallic (23%) materials are the most commonly prevalent materials in the UCH sites where this information is available. In the ADB, UCH sites are rarely composed of prevalent materials such as wood and stone (~4%). The ADB included 36% of the UCH sites without information relative to the archaeological material corresponding to the modern period (Figure 3A). For that period, metal was the most common material in the rest of the UCH sites included in the database when that information was available in the bibliographic references. Therefore, we assigned the metallic material as prevalent in those UCH sites lacking information relative to the material composition. Most of the sites (~47%) range from 8 to 12 m in depth, and few of them (5%) are in very shallow water (<4 m) (Figure 3B).

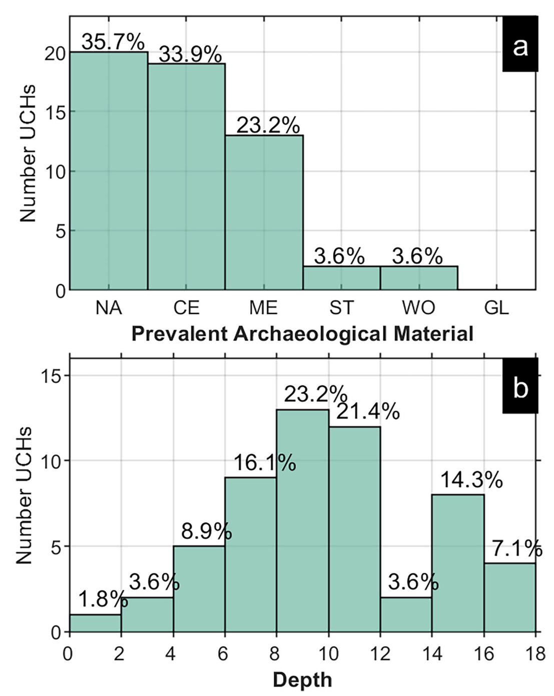

FIGURE 3
Archaeological database. **(A)** Prevalent archaeological material: NA, not assigned; CE, ceramics; ME, metallic; ST, stone; WO, wood/organic; GL, glass. **(B)** Depth of the underwater cultural heritage sites (referring to the mean sea level).

The bibliographic sources used to build the ADB include the main materials present in these sites. We divided them into five categories, each represented by the most common material, namely: metallic (gray iron), stone (marble), glass (glass), ceramics (coarse ware), and wood/organic (oak).

3.2 Hazard assessment in the Bay of Cadiz

3.2.1 Decontextualization hazard

Figure 4A shows the distribution of the maximum critical size of an object that could be moved due to wave action in a 10-year return period (RT10). Overall, the area is characterized by an average value of 0.12 m. Values larger than 0.15 m of critical size were observed in 25% of the outer bay, mostly in shallower regions. Figure 4B relates the number of UCH sites located in areas with the different classes of hazard. Seven UCH sites are located in very-high-hazard areas (Dcr ≥ 0.16 m) and nine in high-hazard areas (0.12 ≤ Dcr< 0.16).

3.2.2 Scour hazard

The spatial pattern of scour hazard represented by the potential scour volume corresponding to RT10 is presented in Figure 5A. A potential scour volume of 0.32 m^3 is observed in most of the area, while values >0.5 m^3 can be observed in the north, central, and southern coastal areas. Most of the UCH sites (~38%) show SC hazard values ranging from 0.3 to 0.4 m^3. Only one UCH site is located in an area with a very high hazard category (>0.7 m^3), while four UCH sites (0.5–0.6 m^3) are in areas categorized as high-hazard areas (Figure 5B).

3.2.3 Erosive wear hazard

The erosive wear hazard ranges from -16 to -12 (Figure 6A). Most of the area is characterized by -13.5. The higher erosion potential (< -12.5) was observed in the mouth of the bay and in the southern areas. These areas combine higher wave bed shear stress and orbital velocity with finer sediment that can be easily resuspended. Most of the sites (~70%) in the central area are located in medium–high hazard areas, whereas only one UCH site was affected by high EW hazard (Figure 6B).

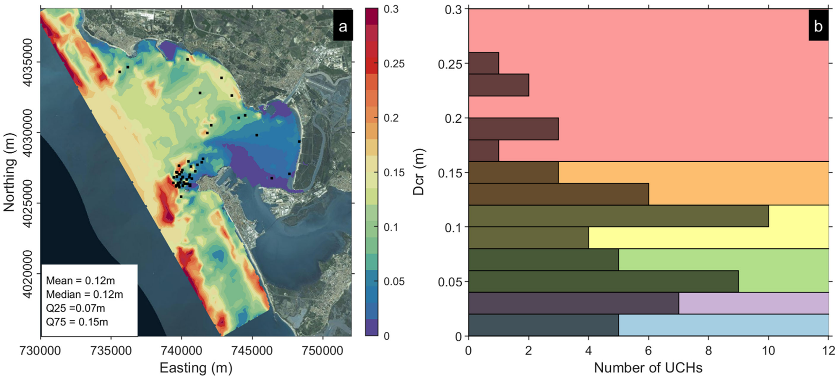

FIGURE 4
(A) Map of decontextualization hazard (critical diameter moved under wave action) in the outer Bay of Cadiz [black dots mark the position of the underwater cultural heritage (UCH) sites]. **(B)** Histogram of the hazard at UCH sites and hazard classes (background color).

3.3 UCH risk assessment in the Bay of Cadiz

3.3.1 Decontextualization risk

The calculated $UCHR_{DE}$ risk indexes are distributed around the median value of 2.5 (Figures 7A, B). The UCH sites with higher $UCHR_{DE}$ values (>3) are located in the southern area of the mouth of the Bay of Cadiz (Figure 8A), where six UCH sites exceeding the threshold of 3.2 are located (Figure 7B). Metallic materials are prevalent in five of them, and only one is a ceramic material site showing a higher $UCHR_{DE}$ value (3.6). The UCHs composed of wood—therefore with a higher vulnerability index related to the prevalent material—are located in a low-energy area at the sandy coast of the inner bay characterized by low-wave orbital velocities.

3.3.2 Scour risk

The $UCHR_{SC}$ index oscillates between low–medium and medium–high values (1.5-2.5) in most of the UCH sites registered in the ADB (Figures 8A, B). A total of four UCH sites were identified as high-risk sites, all of them in the southern side of the mouth of the Bay of Cadiz (Figure 8A). Three of these UCH sites correspond to sites where metallic materials prevail, including the site with a higher $UCHR_{SC}$ (3.94). Only one site is composed of ceramic material ($UCHR_{SC}$ =3.87). The risk index in wooden UCH sites increases compared with the decontextualization hazard, with maximum values of 2.7.

3.3.3 Erosive wear risk

The risk imposed by the erosive wear hazard is depicted in Figure 9. The $UCHWR_{WE}$ index shows the lower spread (Sd = 0.35)

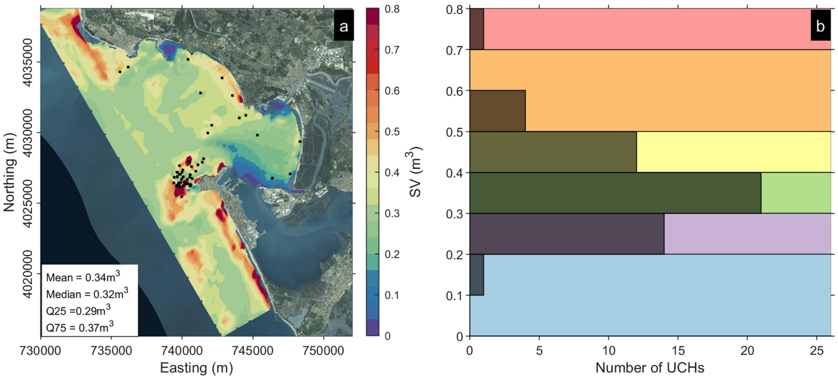

FIGURE 5
(A) Map of scour hazard (scour volume) in the outer Bay of Cadiz. **(B)** Histogram of the hazard at underwater cultural heritage sites and hazard classes (background color).

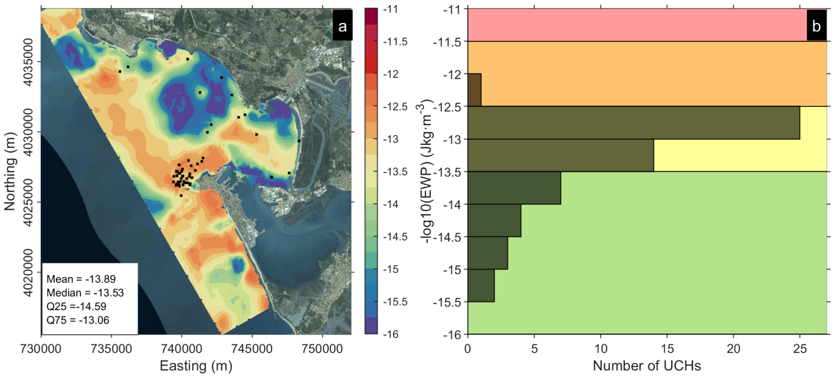

FIGURE 6
(A) Map of erosive wear hazard (log of erosive wear potential) in the outer Bay of Cadiz. **(B)** Histogram of the hazard at underwater cultural heritage sites and hazard classes (background color).

among the hazards analyzed. The most frequent categories of erosive wear risk for the UCH sites in the Bay of Cadiz are medium–high and high (Figures 9A, B). However, only two sites exceed $UCHR_{WE}$ >3.2. As in the previous cases, these sites are located in the area with a higher concentration of UCH sites. Those UCH sites include one site composed of metallic artefacts ($UCHR_{WE}$ = 3.24) and another site where ceramic is the prevailing material ($UCHR_{WE}$ = 3.27).

3.4 Validation of the UCH risk assessment methodology for erosive wear and scour hazards

The qualitative assessment of the vulnerability index related to the environmental factors in comparison with the estimated corrosion rates (CR) of cannons at the *Fougueux* site indicates a good correlation between the higher values of corrosion rates in metallic artefacts and the seabed type and slope. Higher values of CR are associated to cannons located in sandy seabeds and slopes >10% (Figure 10). The statistical significance of the differences in the averages of CR of each group of cannons according to the environmental factor was evaluated through a *t*-test. A comparison between cannons located on a sandy bottom (0.20 mm·year^{-1}) and on a rocky bottom (0.22 mm·year^{-1}) indicates significant differences (*p*-value = 0.03) at 0.05% significance level. No significant differences were found between gentle slope seabeds (<10%) (0.21 mm·year^{-1}) and sloped seabeds (0.24 mm·year^{-1}), although only one cannon was on a sloped seabed, thus reducing the test validity.

Regarding the risk assessment, good agreement was observed between CR, the proxy used to estimate the erosive

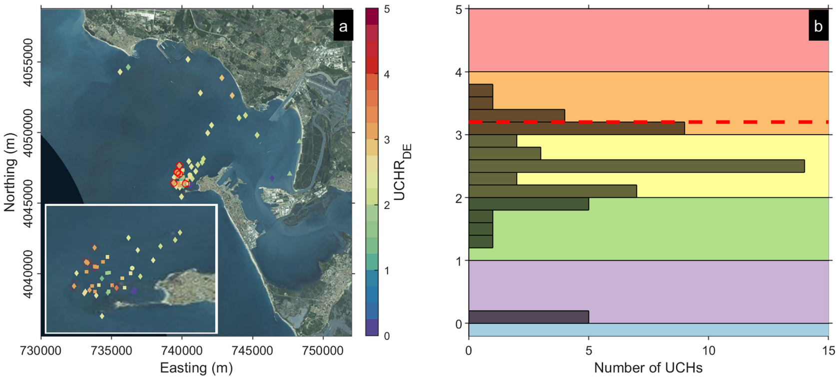

FIGURE 7
(A) Decontextualization risk in the outer Bay of Cadiz. Warm colors indicate a higher risk index, and the different shapes refer to the prevalent material (diamond, metallic; square, ceramics; filled circles, stone; triangles, wood/organic). The red circles represent the underwater cultural heritage (UCH) sites where $UCHR_{DE}$ >3.2. **(B)** Histogram of the decontextualization risk index. The red dashed line shows the threshold (3.2) used to identify UCH sites at risk.

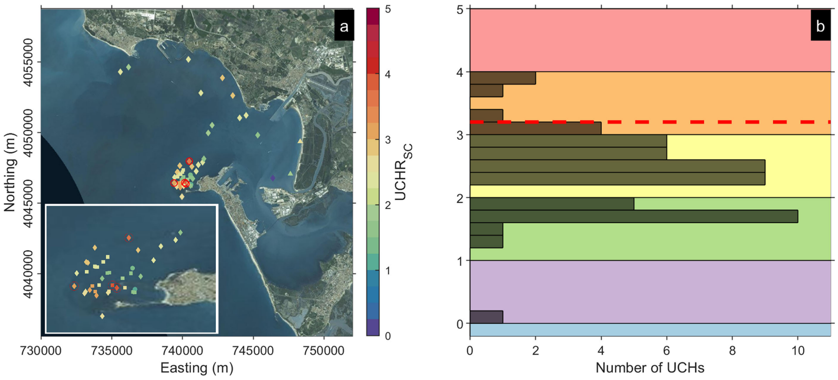

FIGURE 8
(A) Scour risk in the outer Bay of Cadiz. Warm colors indicate a higher risk index, and the different shapes refer to the prevalent material (diamond, metallic; square, ceramics; filled circles, stone; triangles, wood/organic). The red circles represent the underwater cultural heritage (UCH) sites where $UCHR_{SC}$ >3.2. **(B)** Histogram of the scour risk index. The red dashed line shows the threshold (3.2) used to identify UCH sites at risk.

wear impact, and the erosive wear risk index calculated at the *Fougueux* and *Bucentaure* sites (Table 4). The averages of the cannons' CR were 0.11 mm·year^{-1} at the *Bucentaure* site and 0.22 mm·year^{-1} at the *Fougueux* site. The difference is statistically significant according to the *t*-test (*p*-value = 2e-9). These values of corrosion rates correspond to 0 and 3.27 erosive wear risk index, indicating a large difference that marks the *Fougueux* site over the threshold to mark high-risk sites. No re-suspension was observed for the *Bucentaure* site that could lead to erosive wear potential (EWP) (S_H=0), whereas the EWP for RT10 was 9.5e-13 (S_H=4) at the *Fougueux* site. The vulnerability score was similar at both sites (S_V = 2.67), which is the result of gentle slopes (s_{vss}=3) and sandy seabed as the dominant seabed types in the sites (s_{vst}=3) and gray iron as the prevalent material (sm_{vm}=2). Although the corrosion rates provide integrated information of all degradation processes related to the marine conditions, erosive wear was recognized as the key process after completing a meticulous monitoring program in the sites[4].

With respect to the scour risk assessment evaluation, the methodology highlights both sites as UCH sites at risk. The scour risk index presents higher values at the *Fougueux* site (3.65), whereas at the *Bucentaure* site (3.27) it slightly exceeds the threshold (3.2). This classification reflects the observations of the drastic morpho-dynamic changes (Smax = 0.7 m) at the *Fougueux* site compared with those observed at the *Bucentaure* site (Smax = 0.3 m) (Table 4).

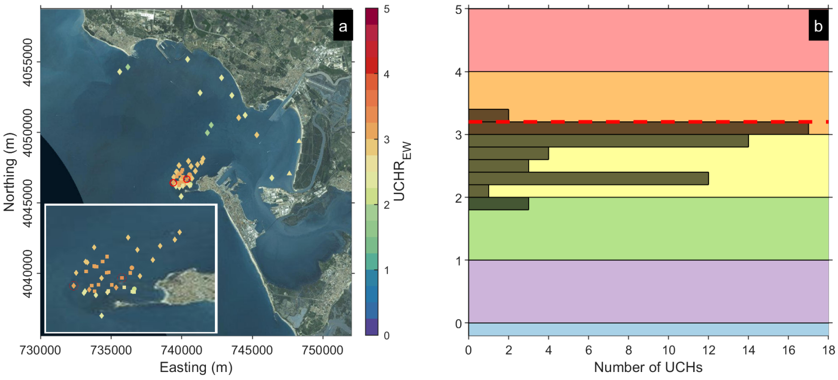

FIGURE 9
(A) Erosive wear risk in the outer Bay of Cadiz. Warm colors indicate a higher risk index, and the different shapes refer to the prevalent material (diamond, metallic; square, ceramics; filled circles, stone; triangles, wood/organic). The red circles represent underwater cultural heritage (UCH) where $UCHR_{SC}$ >3.2. **(B)** Histogram of the erosive wear risk index. The red dashed line shows the threshold (3.2) used to identify UCH sites at risk.

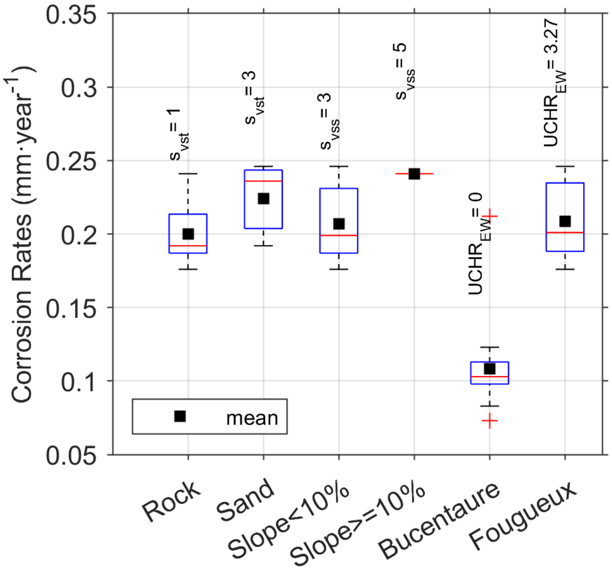

FIGURE 10
Box plot of corrosion rates by group according to the environment factor (vulnerability index assessment at the Fougueux site) and location (erosive wear risk at the Fougueux and Bucentaure sites).

4 Discussion

As a part of maritime cultural heritage, UCH constitutes a non-renewable cultural resource that must be preserved. UCH is only related to tangible assets and resources, while maritime heritage includes intangible assets (Kyvelou et al. 2022). Hence, UCH is a finite resource affected by natural threats (*e.g.*, shipworms, microbiological decay, erosion, natural hazards) or anthropogenic pressures (*e.g.*, pollution, dredging, bottom trawling using a dragnet, pillage). Among the natural threats, wave-induced hazards are a key player for the preservation of UCH in shallow water. This paper adapts the CRAFT1 methodology for coastal risk assessment (Armaroli and Duo, 2018; Ferreira et al., 2018) and presents a new methodology for UCH risk assessment associated to wave-induced hazards. This methodology can be adjusted and expanded to include other natural or anthropogenic-induced hazards. There are some studies that focus on other specific hazards such us ship anchoring damage (Aps et al., 2020) or damage caused by bottom trawling to ancient shipwreck sites (Brennan et al., 2016). To the best of our knowledge, no similar methodological developments have been applied to UCH risk assessment to evaluate wave impact. This risk assessment method includes the quantification of the probability of the hazard and the vulnerability of UCH sites at risk in a systematic and transparent manner that facilitates the adoption of the methodology for UCH managers as well as the adaptation to their necessities.

Identifying UCH sites at risk is the first step in UCH protection and preservation. It requires a concentrated effort and allows optimizing protection measures at specific sites. Additionally, risk assessment enables identifying the threatened UCH sites, which is key to include UCH in maritime spatial planning (Kyvelou et al. 2022; Papageorgiou,

TABLE 4 Qualitative validation of erosive wear risk (average corrosion rates ± standard deviation) and scour risk (maximum scour) measured in the sites.

Site	RT1 E erosive wear potential (J/m^3)	RT10-scouring volume (m^3)	S_H	S_V	Erosive wear risk index	Scour risk index	Corrosion rates (mm·year^{-1})	Smax (m)
Erosive wear								
Bucentaure	0		0	2.67	0		0.11 ± 0.04	
Fougueux	9.5e^{-13}		4	2.67	3.27		0.21 ± 0.03	
Scour								
Bucentaure		0.62	4	2.67		3.27		0.3
Fougueux		1.09	5	2.67		3.65		0.7

2018). This is particularly important in the era of a sustainable blue economy where UCH, beyond its undeniable social and cultural value, can be considered a resource with uses of socio-economic relevance (Papageorgiou, 2019).

The proposed methodology is based on indicators that follow the principles of acceptability, reliability, simplicity of application, and low data requirements (Alexandrakis and Poulos, 2014). The acceptability of this methodology relies on the transparency of the methods for hazard and vulnerability computation as well as on the flexibility to be adapted for a specific coastal environment and the completeness of the ADB—for instance, the protective role of some ecosystems diminishing wave energy such as seagrass meadows (Infantes et al., 2012) can be incorporated by defining new categories in the seabed vulnerability index. Similarly, the ADB could be completed by incorporating other archaeological materials. The expertise and know-how of the managers and decision-makers could also be considered as well as changing the ranks of the hazards and vulnerability or the chosen probabilities (*i.e.*, RT1 for erosive wear or RT10 for scour and decontextualization hazards).

The methodology, built upon simple empirical models for the hazard computation, reduces the uncertainties associated to the many parameters appearing in more complex process-based models. It increases the reliability of the hazard computation methods considering the target of hazard intercomparison between different UCH sites. The reliability of the methodology including hazard and vulnerability components was evaluated for scour and erosive wear showing a good correlation with *in situ* measurements of scour and corrosion rates (used as a proxy of erosive wear). It is difficult to validate the UCH risk assessment for the decontextualization hazard given the lack of field measurements to quantify UCH decontextualization. The validation of UCH risk assessment should be expanded to different coastal environments covering various wave energy conditions and sediment characteristics and UCH sites containing different archaeological materials. The additional advantages of the method are the simplicity of the application and the low amount and availability of the required data. These advantages are related to the use of a simple empirical model and to the fact that the environmental information about depth and seabed type is readily available from nautical charts. The use of process-based models, *i.e.*, hydro-morphodynamic models, would be more accurate from the physical–chemical point of view, but there would be more uncertainties, and the simplicity of the interpretation of results would be reduced. They would also require a large amount of high-quality data for proper regional applications.

4.1 Limitations and challenges for UCH risk assessment

The use of a simple empirical model for hazard quantification overlooks several processes of major relevance for the analyzed hazards, such as flow speed and turbulence enhancement, because of flow–structure interaction (Fernández-Montblanc et al., 2018; Quinn and Smyth, 2018). The inclusion of these processes would request high-resolution bathymetry (<1 m) and an enormous computational effort necessary for computational fluid dynamics. These limitations can be overcome at a later stage when a new risk assessment including these processes is targeted at UCH sites at high risk in order to provide accurate solutions to design protection measures. Other secondary processes such as the enhancement of bed shear stress due to the effect of wave–current interaction (Soulsby and Clarke, 2005) and wave–tide interaction (Kagan et al., 2001), accounting for the influence of bottom mobility (Kagan et al., 2005), sediment load stratification (Kagan et al., 2003), or the modification sediment concentration by the bed forms (Nielsen, 1986), can be incorporated using empirical and theoretical models.

In this paper, risk assessment was conducted for each hazard separately. Nevertheless, Figure 11 illustrates the concurrency of the three analyzed hazards in a single UCH site (Id15) and scour and decontextualization hazard concurrency (Id17). A multi-hazard analysis should be incorporated to evaluate if the hazardous events occur simultaneously in a cascading or cumulative manner over time (UNISDR, 2017)—for example, scour in sites Id15 and Id17 would facilitate the decontextualization of buried archaeological objects in those sites.

Regarding the vulnerability quantification, the limitations are linked to an ADB built upon bibliographic research. Underwater ADBs are very scarce, incomplete, or not publicly available to prevent illicit actions (Papageorgiou, 2019). These databases would allow identifying patterns affecting UCH and taking actions, which is often hampered by the lack of accessible data (Andreou et al., 2022). A more complete ADB in terms of UCH site characterization would allow the improvement of vulnerability quantification, *i.e.*, including chronology or conservation status as an additional vulnerability index. Additionally, it would allow expanding the analysis from a single prevalent material to all the materials that constitute the UCH site, thus providing a more complete UCH risk assessment.

Exposure is considered equal for all the UCH sites included in the ADB because of a lack of information. Quantifying exposure should be addressed through the valuation of UCH. The valuation of UCH includes the cultural capital or non-extractive value and the extractive or market-associated value as well as cultural tourism and recreational activities (Claesson, 2011). This information is key to know if an UCH site is worth being protected. Including this information could change the nine UCH sites at risk identified in the Bay of Cadiz.

Finally, the risk index definition should take the objectives and expertise of the stakeholders involved in UCH management into account by means of a participative process. It has been demonstrated in other disciplines that the involvement of stakeholders in risk assessment for the definition of vulnerability, hazard type, and risk thresholds allows gathering

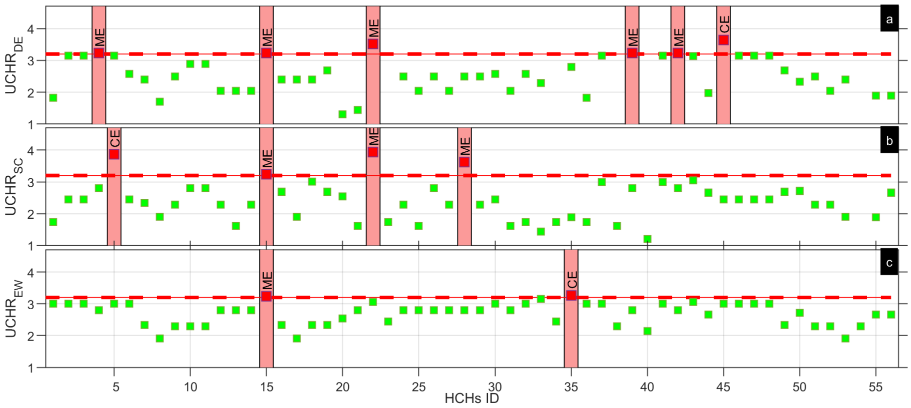

FIGURE 11
Risk index in the underwater cultural heritage sites located at the Bay of Cadiz. **(A)** Decontextualization risk. **(B)** Scour risk. **(C)** Erosive wear risk.

useful information to improve the indicators and to increase confidence in the risk assessment (Meadow et al., 2015; Viavattene et al., 2018).

5 Concluding remark

This paper presents a novel UCH risk assessment methodology to quantitatively assess the impact of wave-induced hazards on UCH in the coastal environment and to give precedence to the UCH sites at high risk. The risk assessment was performed for decontextualization, scour and erosive wear, and major natural hazards threatening the preservation of UCH in shallow water areas.

The methodology was validated at the *Bucentaure* and *Fougueux* sites through a comparative analysis including *in situ* measurements. The validation showed a good correlation between the risk index and the *in situ* measurements of scour and corrosion rates (used as a proxy of erosive wear). The methodology was tested in the Bay of Cadiz using an ADB containing 56 UCH sites, with metallic and ceramic materials being prevalent in most of them. The sites are seated at a depth ranging from 6 to 12 m. The methodology allowed identifying the UCH sites at high risk in the Bay of Cadiz: six are at risk of decontextualization, four are in peril of scour, and two are at risk of erosive wear. Moreover, the UCH risk assessment revealed the concurrency of at least two hazards in two of the UCH sites at high risk.

Even though the methodology has only been validated in a specific coastal environment, showing limitations related to the completeness of the ADB, it is a steppingstone towards a decision support system that will give priority to research, prospection, management, and protection measures in the UCH sites analyzed to ensure their preservation in the context of climate change in the era of a sustainable blue economy.

Data availability statement

The datasets presented in this article are not readily available, as raw data will be available on request with the exception of the archaeological data-base to ensure underwater cultural heritage preservation.Requests to access the datasets should be directed to tomas.fernandez@uca.es.

Author contributions

TF-M: conceptualization, methods, investigation, formal analysis, visualization, writing the original draft, writing, review and editing, management and coordination of the project. MB: methods, writing, review and editing, management and coordination of the project. AI: conceptualization, writing, review and editing. All authors contributed to the article and approved the submitted version.

Funding

This study was partially supported by the Ministry of Science and Innovation thorough the project "Vulnerability of littoralcultural heritage to environmental agents: impact of climate change (VOLICHE)" (PID2020-117812RB-I00 / AEI / 10.13039/501100011033) and CEI MAR thorough the project "Dynamic projections of waves and sea level in the Gulf of Cadiz and the Alboran Sea: Impact of climatechange on coastal vulnerability and coastal cultural heritage"(CEIJ-015).

Conflict of interest

The authors declare that the research was conducted in the absence of any commercial or financial relationships that could be construed as a potential conflict of interest.

Publisher's note

References

Alexandrakis, G., and Poulos, S. E. (2014). An holistic approach to beach erosion vulnerability assessment *Sci. Rep.* 4, 6078. doi: 10.1038/srep06078

Alzaga García, M., Márquez Carmona, L., Rodríguez Mariscal, N., Martí Solano, J., Higueras-Milena Castellano, A., Gallardo Abárzuza, M., et al. (2022). *Shipwrecks of the Iberian tradition in the Bay of Cadiz (Andalucía, Spain) BT - heritage and the Sea: Volume 2: Maritime history and archaeology of the global Iberian world (15th–18th centuries)*. Eds. A. Crespo Solana, F. Castro and N. Nayling (Cham: Springer International Publishing), 145–167. doi: 10.1007/978-3-030-86464-4_6

Andreou, G. M., Nikolaus, J., Westley, K., el Safadi, C., Blue, L., Smith, A., et al. (2022). Big data in maritime archaeology: Challenges and prospects from the middle East and north Africa. *J. F. Archaeol.* 47, 131–148. doi: 10.1080/00934690.2022.2028082

Angelini, E., Grassini, S., Tusa, S.A. B. T.-C. and C. @ of C. H. M. A. Adriaens (2013). "12 - underwater corrosion of metallic heritage artefacts," in *European Federation of corrosion (EFC) series*. Eds. P. Dillmann, D. Watkinson and E. Angelini (Oxford: Woodhead Publishing), 236–259. doi: 10.1533/9781782421573.3.236

Aps, R., Lees, L., Herkül, K., Roio, M., and Tõnismaa, O. (2020). Towards STAMP approach based protection of underwater cultural heritage. *Proc. Int. Semin. Saf. Secur. Auton. Vessel. Eur. STAMP Work. Conf.* 2019, 169–178. doi: 10.2478/9788395669606-014

Armaroli, C., and Duo, E. (2018). Validation of the coastal storm risk assessment framework along the Emilia-romagna coast. *Coast. Eng.* 134, 159–167. doi: 10.1016/J.COASTALENG.2017.08.014

Bethencourt, M., Fernández-Montblanc, T., Izquierdo, A., González-Duarte, M. M., and Muñoz-Mas, C. (2018). Study of the influence of physical, chemical and biological conditions that influence the deterioration and protection of underwater cultural heritage. *Sci. Total Environ.*, 613–614, 98–114. doi: 10.1016/j.scitotenv.2017.09.007

Bitter, J. G. A. (1963). A study of erosion phenomena part I. *Wear* 6, 5–21. doi: 10.1016/0043-1648(63)90003-6

Björdal, C. G., Daniel, G., and Nilsson, T. (2000). Depth of burial, an important factor in controlling bacterial decay of waterlogged archaeological poles. *Int. Biodeterior. Biodegrad.* 45, 15–26. doi: 10.1016/S0964-8305(00)00035-4

Björdal, C. G., and Nilsson, T. (2008). Reburial of shipwrecks in marine sediments: a long-term study on wood degradation. *J. Archaeol. Sci.* 35, 862–872. doi: 10.1016/j.jas.2007.06.005

Blott, S. J., and Pye, K. (2001). GRADISTAT: a grain size distribution and statistics package for the analysis of unconsolidated sediments. *Earth Surf. Process. Landforms* 26, 1237–1248. doi: 10.1002/esp.261

Booij, N., Ris, R. C., and Holthuijsen, L. H. (1999). A third-generation wave model for coastal regions 1. model description and validation. *J. Geophys. Res. Ocean.* 104, 7649–7666. doi: 10.1029/98JC02622

Brennan, M. L., Davis, D., Ballard, R. D., Trembanis, A. C., Vaughn, J. I., Krumholz, J. S., et al. (2016). Quantification of bottom trawl fishing damage to ancient shipwreck sites. *Mar. Geol.* 371, 82–88. doi: 10.1016/j.margeo.2015.11.001

Cámara, B., de Buergo, M. Á., Bethencourt, M., Fernández-Montblanc, T., La Russa, M. F., Ricca, M., et al. (2017). Biodeterioration of marble in an underwater environment. *Sci. Total Environ.* 609, 109–122. doi: 10.1016/j.scitotenv.2017.07.103

Camus, P., Mendez, F. J., Medina, R., and Cofiño, A. S. (2011). Analysis of clustering and selection algorithms for the study of multivariate wave climate. *Coast. Eng.* 58, 453–462. doi: 10.1016/j.coastaleng.2011.02.003

Claesson, S. (2011). The value and valuation of maritime cultural heritage. *Int. J. Cult. Prop.* 18, 61–80. doi: 10.1017/S0940739111000051

Diaz-Hernandez, G., Rodríguez Fernández, B., Romano-Moreno, E., and XXXL. Lara, J. (2021). An improved model for fast and reliable harbour wave agitation assessment. *Coast. Eng.* 170, 104011. doi: 10.1016/J.COASTALENG.2021.104011

Fernández-Montblanc, T., Izquierdo, A., Quinn, R., and Bethencourt, M. (2018). Waves and wrecks: A computational fluid dynamic study in an underwater archaeological site. *Ocean Eng.* 163, 232–250. doi: 10.1016/j.oceaneng.2018.05.062

Fernández-Montblanc, T., Quinn, R., Izquierdo, A., and Bethencourt, M. (2016). Evolution of a shallow water wave-dominated shipwreck site: Fougueux, (1805), Gulf of Cadiz. *Geoarchaeology* 31, 487–505. doi: 10.1002/gea.21565

Ferreira, O., Viavattene, C., Jiménez, J. A., Bolle, A., das Neves, L., Plomaritis, T. A., et al. (2018). Storm-induced risk assessment: Evaluation of two tools at the regional and hotspot scale. *Coast. Eng.* 134, 241–253. doi: 10.1016/J.COASTALENG.2017.10.005

Field, C., and Barros, V. (2014) *Climate change 2014–impacts, adaptation and vulnerability: Regional aspects*. Available at: https://books.google.com/books?hl=es&lr=&id=aJ-TBQAAQBAJ&oi=fnd&pg=PA1142&ots=v2QuHId8HG&sig=aL_w43yxj2tjPCqJRXSKatyJt24 (Accessed May 7, 2022).

García Rivera, C., and Alonso Villalobos, C. (2005). *(16) (PDF) Los naufragios de Trafalgar*. Sevilla: Junta de Andalucía, Consejería de Cultura.

Garrity, N. J., Battalio, R., Hawkes, P. J., and Roupe, D. (2007). Evaluation of event and response approaches to estimate the 100-year coastal flood for pacificcoast sheltered waters. *Coast. Eng. 2006, World Scientific Publishing Company*, 1651–1663. doi: 10.1142/9789812709554_0140

González-Duarte, M. M., Fernández-Montblanc, T., Bethencourt, M., and Izquierdo, A. (2018). Effects of substrata and environmental conditions on ecological succession on historic shipwrecks. *Estuar. Coast. Shelf Sci.* 200, 301–310. doi: 10.1016/j.ecss.2017.11.014

Gornitz, V. (1990). Vulnerability of the East coast, USA to future sea level rise. *J. Coast. Res.* 9(1), 201–237. Available at: http://www.jstor.org/stable/44868636

Gregory, D. (2020). Characterizing the preservation potential of buried marine archaeological sites. *Herit* 3, 838–857. doi: 10.3390/HERITAGE3030046

Gregory, D., Jensen, P., and Strætkvern, K. (2012). Conservation and *in situ* preservation of wooden shipwrecks from marine environments. *J. Cult. Herit.* 13, S139–S148. doi: 10.1016/j.culher.2012.03.005

Guillemot, E., and Meanteau, L. *Mapa fisiográfico del litoral atlántico de Andalucía: 1/50.000 - publicaciones - junta de andalucía*. Available at: https://www.juntadeandalucia.es/servicios/publicaciones/detalle/48731.html (Accessed July 8, 2022).

Infantes, E., Orfila, A., Simarro, G., Terrados, J., Luhar, M., and Nepf, H. M. (2012). Effect of a seagrass (*Posidonia Oceanica*) meadow on wave propagation. *Mar. Ecol. Prog. Ser.* 456, 63–72. doi: 10.3354/meps09754

Kagan, B. A., Alvarez, O., and Izquierdo, A. (2005). Weak wind-wave/tide interaction over fixed and moveable bottoms: a formulation and some preliminary results. *Cont. Shelf Res.* 25, 753–773. doi: 10.1016/j.csr.2004.09.021

Kagan, B. A., Álvarez, O., Izquierdo, A., Mañanes, R., Tejedor, B., and Tejedor, L. (2003). Weak wave/tide interaction in suspended sediment-stratified flow: a case study. *Estuar. Coast. Shelf Sci.* 56, 989–1000. doi: 10.1016/S0272-7714(02)00306-2

Kagan, B. A., Tejedor, L., Álvarez, O., Izquierdo, A., Tejedor, B., and Mañanes, R. (2001). Weak wave–tide interaction formulation and its application to Cádiz bay. *Cont. Shelf Res.* 21, 697–725. doi: 10.1016/S0278-4343(00)00099-6

Kyvelou, S. S., and Henocque, Y.. (2022). How to incorporate underwater cultural heritage into maritime spatial Planning: guidelines and good practices. *EUROPEAN COMMISSION European Climate, Infrastructure and Environment Executive Agency Unit D.3 – Sustainable Blue Economy*. Luxembiurg: Publications Office of the European Union.

Lagostena, L. G. (2009). *Catálogo del Patrimonio Histórico del Parque Metropolitano Los toruños*. Sevilla: Junta de Andalucía.

Lakey, D. C. (1987). *Shipwrecks in the Gulf of Cadiz: a catalog of historically documented wrecks from the fifteenth through the nineteenth centuries, Institute of Nautical Archaeology (U.S.)*. Texas A & M University: United States-Spanish Joint Committee for Cultural and Educational Cooperation.

McNinch, J. E., Wells, J. T., and Trembanis, A. C. (2006). Predicting the fate of artefacts in energetic, shallow marine environments: an approach to site management. *Int. J. Naut. Archaeol.* 35, 290–309. doi: 10.1111/j.1095-9270.2006.00105.x

Meadow, A. M., Ferguson, D. B., Guido, Z., Horangic, A., Owen, G., and Wall, T. (2015). Moving toward the deliberate coproduction of climate science knowledge. *Weather. Clim. Soc* 7, 179–191. doi: 10.1175/WCAS-D-14-00050.1

Mentaschi, L., Vousdoukas, M. I., Voukouvalas, E., Dosio, A., and Feyen, L. (2017). Global changes of extreme coastal wave energy fluxes triggered by intensified teleconnection patterns. *Geophys. Res. Lett.* 44, 2416–2426. doi: 10.1002/2016GL072488

Mentaschi, L., Vousdoukas, M., Voukouvalas, E., Sartini, L., Feyen, L., Besio, G., et al. (2016). The transformed-stationary approach: a generic and simplified methodology for non-stationary extreme value analysis. *Hydrol. Earth Syst. Sci.* 20, 3527–3547. doi: 10.5194/hess-20-3527-2016

Nian-Sheng, C. (2004). Analysis of velocity lag in sediment-laden open channel flows. *J. Hydraul. Eng.* 130, 657–666. doi: 10.1061/(ASCE)0733-9429(2004)130:7(657)

Nielsen, P. (1986). Suspended sediment concentrations under waves. *Coast. Eng.* 10, 23–31. doi: 10.1016/0378-3839(86)90037-2

Papageorgiou, M. (2018). Underwater cultural heritage facing maritime spatial planning: Legislative and technical issues. *Ocean Coast. Manage.* 165, 195–202. doi: 10.1016/j.ocecoaman.2018.08.032

Papageorgiou, M. (2019). Stakes and challenges for underwater cultural heritage in the era of blue growth and the role of spatial planning: Implications and prospects in Greece. *Herit* 2, 1060–1069. doi: 10.3390/HERITAGE2020069

Pearson, C. (1987). *Conservation of marine archaeological objects* (London; Boston: Butterworths).

Pournou, A. (2018). Assessing the long-term efficacy of geotextiles in preserving archaeological wooden shipwrecks in the marine environment. *J. Marit. Archaeol.* 13, 1–14. doi: 10.1007/S11457-017-9176-9

Quinn, R. (2006). The role of scour in shipwreck site formation processes and the preservation of wreck-associated scour signatures in the sedimentary record - evidence from seabed and sub-surface data. *J. Archaeol. Sci.* 33, 1419–1432. doi: 10.1016/J.JAS.2006.01.011

Quinn, R., and Smyth, T. A. G. (2018). Processes and patterns of flow, erosion, and deposition at shipwreck sites: a computational fluid dynamic simulation. *Archaeol. Anthropol. Sci.* 10, 1429–1442. doi: 10.1007/s12520-017-0468-7

Ruuskanen, A. T., Kraufvelin, P., Alvik, R., Díaz, E. R., Honkonen, J., Kanerva, J., et al. (2015). Benthic conditions around a historic shipwreck: Vrouw maria, (1771)) in the northern Baltic proper. *Cont. Shelf Res.* 98, 1–12. doi: 10.1016/j.csr.2015.02.006

Soulsby, R. (1997). *Dynamics of marine sands* (London: Thomas Telford Publishing). doi: 10.1680/doms.25844

Soulsby, R. L., and Clarke, S. (2005). *Bed shear-stresses under combined waves and currents on smooth and rough beds produced within defra project FD1905 Technical Report*. Wallingford: HR Wallingford.

Spanish Ministry of Agriculture, Food and Environment. (2012). *Data from: Plan de Ecocartografías del litoral Español.*

Sumer, B. M., and Fredsøe, J. (1990). Scour below pipelines in waves. *J. Waterw. Port Coastal Ocean Eng.* 116, 307–323. doi: 10.1061/(ASCE)0733-950X(1990)116:3(307

Sumer, B. M., and Fredsøe, J. (2002). The mechanics of scour in the marine environment. *World Sci Sinagpore*. doi: 10.1142/4942

Thompson, C. E. L., Ball, S., Thompson, T. J. U., and Gowland, R. (2011). The abrasion of modern and archaeological bones by mobile sediments: the importance of transport modes. *J. Archaeol. Sci.* 38, 784–793. doi: 10.1016/J.JAS.2010.11.001

UNISDR (2017) *National disaster risk assessment words into action guidelines governance system, methodologies, and use of results*. Available at: https://www.unisdr.org/files/52828_nationaldisasterriskassessmentpart1.pdf (Accessed July 4, 2022).

Vander Voort, G. F. (2000). Microindentation hardness testing. *Mech. Test. Eval.* 8, 0. doi: 10.31399/asm.hb.v08.a0003272

van Rijn, L. C. (1993). *Principles of sediment transport in rivers, estuaries and coastal seas*. Amsterdam: Aqua publications

Viavattene, C., Jiménez, J. A., Ferreira, O., Priest, S., Owen, D., and McCall, R. (2018). Selecting coastal hotspots to storm impacts at the regional scale: a coastal risk assessment framework. *Coast. Eng.* 134, 33–47. doi: 10.1016/J.COASTALENG.2017.09.002

Vila Socias, L., Hein, A., Kilikoglou, V., and Buxeda i Garrigós, J. (2007). Disseny amforal i canvi tecnològic al voltant del canvi d'era: L'aportació de l'Anālisi d'Elements finits. *Empúries* 55, 27–38. Available at: https://raco.cat/index.php/Empuries/article/view/138911

Ward, I. A. K., Larcombe, P., and Veth, P. (1999). A new process-based model for wreck site formation. *J. Archaeol. Sci.* 26, 561–570. doi: 10.1006/JASC.1998.0331

Whitehouse, R. (1998). *Scour at marine structures* (London: Thomas Telford Publishing). doi: 10.1680/sams.26551

Young, D. M., and Testik, F. Y. (2009). Onshore scour characteristics around submerged vertical and semicircular breakwaters. *Coast. Eng.* 56, 868–875. doi: 10.1016/J.COASTALENG.2009.04.003

Zyserman, J. A., and Fredsøe, J. (1994). Data analysis of bed concentration of suspended sediment. *J. Hydraul. Eng.* 120, 1021–1042. doi: 10.1061/(ASCE)0733-9429(1994)120:9(1021

Frontiers in Marine Science

TYPE Original Research
PUBLISHED 01 December 2022
DOI 10.3389/fmars.2022.993644

EDITED BY
Javier Benavente,
University of Cádiz, Spain

REVIEWED BY
Papa Ibnou Ndiaye,
Cheikh Anta Diop University, Senegal
William James Pringle,
Argonne National Laboratory (DOE),
United States

*CORRESPONDENCE
Cheikh Omar Tidjani Cisse
cheikhomartidjaniciss@yahoo.fr

SPECIALTY SECTION
This article was submitted to
Coastal Ocean Processes,
a section of the journal
Frontiers in Marine Science

RECEIVED 13 July 2022
ACCEPTED 15 November 2022
PUBLISHED 01 December 2022

CITATION
Cisse COT, Brempong EK,
Taveneau A, Almar R, Sy BA
and Angnuureng DB (2022)
Extreme coastal water levels
with potential flooding risk at
the low-lying Saint Louis historic
city, Senegal (West Africa).
Front. Mar. Sci. 9:993644.
doi: 10.3389/fmars.2022.993644

Extreme coastal water levels with potential flooding risk at the low-lying Saint Louis historic city, Senegal (West Africa)

Cheikh Omar Tidjani Cisse[1]*,
Emmanuel K. Brempong[2,3,4], Adélaïde Taveneau[4],
Rafael Almar[4], Boubou Aldiouma Sy[1]
and Donatus Bapentire Angnuureng[2]

[1]Laboratory Leïdi "Dynamics of the Territories and Development" Department of Geography, University Gaston Berger, Saint-Louis, Senegal, [2]Africa Centre of Excellence in Coastal Resilience, Centre for Coastal Management, School of Biological Sciences (SBS), University of Cape Coast, Cape Coast, Ghana, [3]Department of Fisheries and Aquatic Sciences (DFAS), University of Cape Coast, Cape Coast, Ghana, [4]Laboratory of Geophysical and Oceanographic Spatial Studies (LEGOS), University of Toulouse/CNRS/IRD/CNES), Toulouse, France

In a context of global warming characterized by a mean sea level rise and extreme meteorological events, the study of the causes for coastal flooding is essential to protect communities and ecosystems. Densely urbanized, and rather unprotected cities in developing countries such as the historic Saint Louis city in Senegal are particularly vulnerable to coastal flooding and sea hazards. From satellite-derived high resolution DEM and global ocean reanalyses, here we quantify the extreme coastal water level in order to identify the neighborhoods and places of particular socio-economical interest of Saint-Louis potentially vulnerable to flooding. The results reveal that the most severe levels have the potential to flood up to almost half of this low-lying river mouth plain. Social, economic and heritage stakes are exposed, and the artisanal fisherman district of Gueth Ndar, is particularly vulnerable to coastal flooding because of its low elevation and situation on the sand barrier. The co-occurrence of high tides and wave-induced runup contributes most to ECWL but they do not present a significant trend over the study period. The results show that over the period 1994-2015, potential flood risk increased by nearly one day per year, primarily due to sea level rise, sounding a warning signal to take countermeasures to protect communities and infrastructure.

KEYWORDS

coastal flooding, extreme coastal water level, satellite-derived DEM, heritages issues, sea level rise, wave runup

Introduction

In a global context marked by global warming leading to an increasing rise in sea level, coastal areas are increasingly threatened by the risks of erosion and coastal flooding (Woodruff and Stults, 2016; Kulp and Strauss, 2019; Almar et al., 2021; Kirezci et al., 2020). Coastal areas are among the most vulnerable ecosystems and will be gradually exposed to the effects of climate change over the course of the century (IPCC report, Oppenheimer et al., 2019). According to recent studies, for instance in Almar et al. (2021), the IPCC RCP8.5 scenario would give 50x increase in coastal overtopping by 2100, worldwide. These hazards occur when strong winds and low atmospheric pressure act on the sea surface to cause a temporary rise in sea level (Wells, 2011; Prime et al., 2016), becoming a real environmental concern for anthropized coastlines (e.g. Le Roy et al., 2015). Knowing that more than 600 million people reside in the low elevation coastal zone (<10 m, Ganguli and Merz, 2020), that the coastal activities expose the population to floods and storms (Dupuis, 2016) and that 3/4 of the world's largest cities are located on those vulnerable areas (Melet et al., 2018), the combination of current massive urban growth and climate change impacts exposes coastal cities to increased and unprecedented coastal risks and environmental issues (Cain et al., 2015; Bongarts Lebbe et al., 2021). Whether riverine or coastal, flooding is one of the most devastating coastal hazards in the world, causing numerous deaths and significant socio-economic consequences each year (Kupfer et al., 2022). According to Vousdoukas et al. (2016), coastal flooding will increase in the context of future storm variability and sea level rise. Nowadays, flooding represent one of the most important issues facing coastal communities (Woodruff et al., 2013).

On the Atlantic coast of Central and West Africa, coastal flooding is one of the greatest threats to the socio-economic and environmental balances of countries south of the Sahara (Tchindjang et al., 2019; Alves et al., 2020; Dada et al., 2021; Vousdoukas et al., 2022). Most West African major cities are exposed to flooding there, and current forecasts show that sub-Saharan Africa and the low elevation, flat deltaic and island coastal regions are among the most affected areas by climate change (Gemenne et al., 2017; Giardino et al., 2018). Extreme Coastal Water Level (ECWL) at the coast results from the combination of several different coastal processes (Eq. 1); the regional sea level anomaly (here referred to as SLA) due to the steric effect, ocean circulation and transfer of mass from the continents (ice sheets, glaciers, land water) to the ocean, storm surge or "Dynamic Atmospheric Correction" (DAC) due to atmospheric pressure and winds, astronomical tide (T) and wave effects here referred to as runup (R) which includes a time-averaged component (setup) and an oscillatory component (swash) (see Melet et al., 2018; Dodet et al., 2019; Almar et al., 2021).

The West Africa coast is generally considered a storm-free environment, dominated by North Atlantic distant swells (Sadio, 2017; Almar et al., 2019; Ndour et al., 2020). The evolution of the sandy coast is controlled by strong longshore sediment drift resulting from oblique waves (Laïbi et al., 2014; Almar et al., 2015; Giardino et al., 2018; Almar et al., 2019; Anthony et al., 2019). Tidal amplitude is typically micro to meso at open stretches of coasts, with the highest amplitudes recorded in deltas and estuaries of Guinea, Guinea-Bissau and Sierra Leone (2.8 - 4.7 m; Diop et al., 2014). Senegalese urban coastal areas, which are low elevated and made of loose or low-strength materials (Weissenberger et al., 2016; Ndour et al., 2018; Ndour et al., 2020) often lying on barrier and at delta, are particularly exposed to marine flooding, which has severe consequences on coastal development (Quiroga et al., 2021). Located at the mouth of the Senegal River, Saint-Louis has a mixed environmental problem with respect to flooding, affected by both coastal flooding and river flooding (Sall, 2006; Wade et al., 2008; Ndour et al., 2018). Although this situation is well known in the history of this city, the situation recently worsened (Durand et al., 2010; Sadio, 2017; Bergsma et al., 2020) due to the rising sea level together with the increase in ocean influence induced by a breach made in the Langue de Barbarie in 2003, a coastal spit that previously protected the city from the Atlantic. When large storm surges occur during rainy periods, when the agitation of the sea hinders the evacuation of river water (Sadio et al. 2017), large-scale events can occur, including those of August 2017 and February 2018, which caused the destruction of 100 houses and the displacement of 2600 people (Diagne, 2020).

In the context of ongoing climate change and the prediction of an increase in climatic instability, the extension of flood-prone areas, in relation to a given climatic hazard, is a scientific concern with strong societal implications (Breilh et al., 2012), but in Senegal, there is almost non- existent work on marine flooding and the anticipation of their impact and mitigation/adaptation (Cisse et al., 2022). In addition, given the gradual artificialization of Saint-Louis coastline, which is reflected in the emergence of numerous coastal protection projects (Alves et al., 2020) such as a riprap built between 2020 and 2022 it is of the essence to study coastal flooding. According to Tebaldi et al. (2012) understanding coastal flooding vulnerability is essential to the decision-making logic and to the protection policies of coastal communities and assets.

Using satellite-derived data and model hindcast data, this paper aims to evidence the vulnerability of the historic Saint-Louis city to potential coastal flooding where it endangers property and people, economic activities, and cultural and religious heritage.

Study area

The city of Saint-Louis is located in northern Senegal (Figure 1). It has the characteristics of an amphibious city, as it is built partly on the mainland, partly on an island in the Senegal River and partly on the Langue de Barbarie (Sall, 2006).

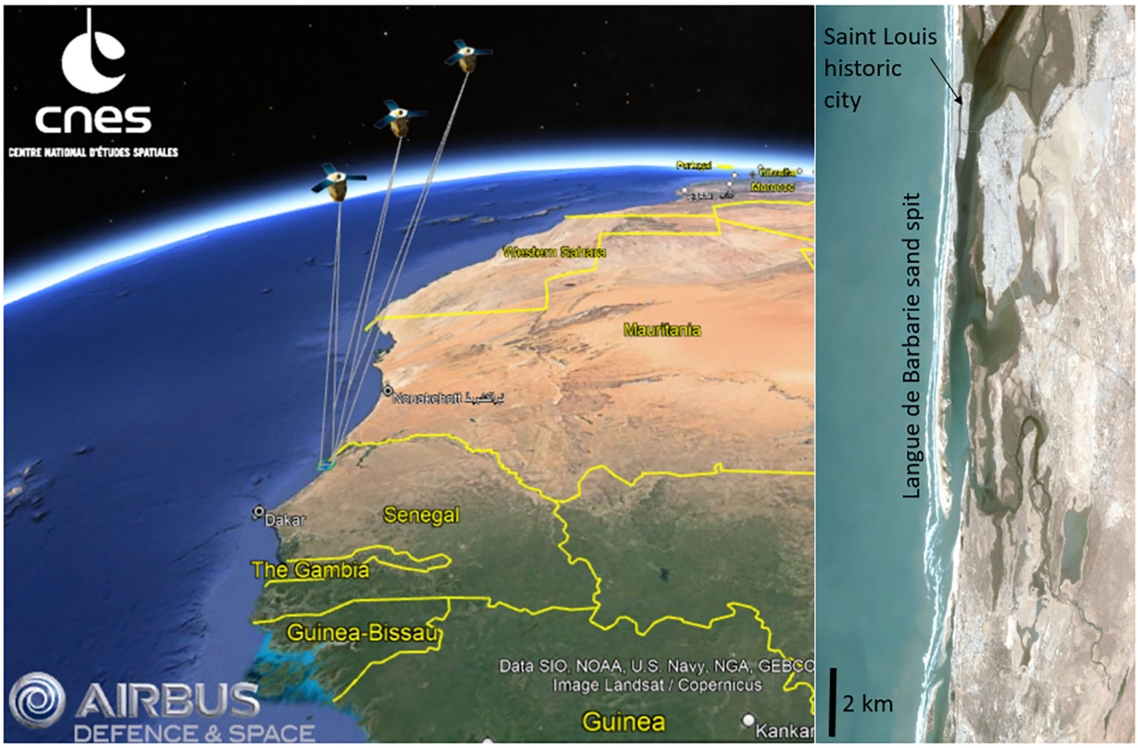

FIGURE 1
Location of the study area and satellite images acquisition. (Left) Pleaides satellite (CNES/Airbus) tri-stereo acquisition (made using Google Earth). (Right) North-oriented Pleiades satellite image of Saint Louis city.

The latter is a sandy coastal spit that extends for 40 km and has a variable width of about 100 m. Bounded by the Atlantic Ocean to the west and the Senegal River to the east, the Langue de Barbarie forms an elongated peninsula running north-south (Kante and Fall, 2019; Brüning, 2022). It is a highly urbanized site with the presence of human settlements, artisanal landing ports, tourist facilities, and a national park of high environmental value. Indeed, like other sections of the Senegalese coastline, the Saint-Louis coastline is among the most vulnerable to flooding and erosion risks. It has a flat topography (most neighborhoods are built less than 2 m above sea level), sandy soil, and a site dominated by water, which exposes the population to many natural hazards, the most recurrent of which are floods (Durand et al., 2010; Sy et al., 2011).

Materials and methods

Topographic data

The Digital Elevation Model (DEM) used in this study is derived from the very high- resolution optical imagery from Pleiades satellite (CNES/Airbus) - see Figure 1. Using Pleiades panchromatic image (0.5 m ground pixel resolution), a tri-stereogrammetry method is performed using the NASA software ASP (Ames Stereo Pipeline; Shean et al., 2016) to extract the topography of the Langue de Barbarie (Almeida et al., 2019; Salameh et al., 2019; Taveneau et al., 2021). The use of tri-stereo method (three images) is preferred over stereo one (two images) as it significantly improves the derived-topography (Almeida et al., 2018; Collin et al., 2018; Taveneau et al., 2021; James et al., 2022). The images selected for this work are 3 acquired in March 2019, and further processed using the method further described by Taveneau et al., 2021. The obtained DEM has a 2 m ground pixel resolution and is map-projected into the UTM 28 coordinates system thanks to the RPC (Rational Polynomial Coefficient) geometric file provided with each Pleiades product.

This satellite-derived DEM-generation method allows a good relative map-projection of the data, but the vertical values "float" in absolute as no elevation information is provided within ASP. Ground control points are essential to give reference points to the DEM and correct the offset. With ground surveys carried out few days apart from the satellite acquisition using a RTK-GPS (Real Time Kinematic - Global Positioning System) with a centimetric-precision (performed by the SHOM, the French Navy Hydrographic and Oceanographic Service) over 13 km of the Langue de Barbarie), the DEM elevation is vertically-corrected (Garlan et al., 2020) thanks to the collected ground control points. Overall, although it depends on the nature of the ground (e.g., buildings, flat terrain, vegetation), sub-metric to metric accuracy is obtained from Pleaides mission-derived DEMs after offset correction (Almeida et al., 2019; Taveneau et al., 2021).

Hydrodynamic data

Quantification of extreme coastal water levels requires the availability of hydrodynamic, meteorological and tidal parameters. Tide data are extracted from the global tide FES2014 model (Finite Element Solution, Carrere et al., 2016) at hourly resolution and gridded worldwide at a 1/16° resolution and produced by Laboratory of Geophysical and Oceanographic Spatial Studies of Toulouse (LEGOS). Atmospheric pressure and winds component (DAC) is produced by the Collecte Localisation Satellites (CLS) Space Oceanography Division using the MOG2D model from LEGOS and distributed by AVISO (Archiving, Validation and Interpretation of Satellite Oceanographic data), with support from Centre National d'Etudes Spatiales (CNES) (http://www.aviso.altimetry.fr/). Altimetric-derived SLA, including global mean level rise, is extracted at the closest altimetry gridded data point from AVISO and it corresponds to offshore regional sea level (Marti et al., 2021). ERA-Interim reanalysis data (global climate and weather data available from 1979 onward) at a 0.5° x 0.5° resolution developed by the European Center for Medium-Range Weather Forecasting (ECMWF) model are used for waves data at a 6-hour resolution over the 1994-2015 period. Wave runup R is computed following the dissipative beach form of Stockdon et al., 2006 (see Almar et al., 2021):

$$R = 0.043\sqrt{H_s L_o}$$

Where H_s and L_o are offshore significant wave height and wavelength. All the above-mentioned parameters are resampled on an hourly basis over the 2013-2015 period. All the hydrodynamic data used in this study are global dataset available worldwide are all extracted at the nearest point from Saint Louis city (latitude 16.23°, longitude -16.21°) in the corresponding grids, which ensures here a maximum distance of 50 km from the coarsest grid. They correspond to off the coast forcing and does not reflect local coastal complex processes that might occur (i.e. interactions between drivers, waves refraction, morphology changes – see Idier et al., 2019; Bergsma et al., 2022).

Quantification of the extreme coastal water level

To quantify the extreme coastal water level at Saint-Louis, we use the formula of Almar et al. (2021) (Eq. 1):

$$\mathbf{ECWL} = \mathbf{SLA} + \mathbf{DAC} + \mathbf{T} + \mathbf{R} \tag{1}$$

The extreme levels are generated following the combination of several parameters, this model incorporates the sea level anomaly (SLA), the height of the storm surge (DAC) due to atmospheric pressure and winds, the level of the astronomical tide (T) and the height of wave breaking (R). In order to physically determine the impact of extreme water level reached by the sea in Saint-Louis, we define the severe water levels corresponding to the top 2%, thus the 98th percentile (following a common definition of extreme storms). The cumulative annual occurrence of the of the time spent over this threshold is computed over the study period.

To compute overtopping and flooding potential, the topographic data in this work are set to a geoidal coordinate system (vertical datum). Here, the ECWL are converted to geodetic data using the vertical datum value (0.981m) of Wöppelmann et al. (2008), so that they can be superimposed with the topographic data. It should be recalled that the vertical datum used is that of the tide gauge in Dakar, because there is no one in Saint-Louis.

To study the trend of evolution of the extremes in Saint-Louis on the basis of annualized data, the regress function of the Matlab software (linear regression) is used. In addition, the statistical test p-value is calculated to determine the level of significance of the trend.

Flood zone and mapping and risk for infrastructures

The methodological approach to flood mapping adopted in this work is based on the calculation of the percentage of potentially floodable surface through the satellite-derived DEM and the raster calculator tool of the Arc Gis software. Then, from the OSM (Open Street Map) databases, the properties (buildings, parcels, etc.) are vectorized in Arc Gis. To identify the infrastructures potentially exposed to flooding, spatial queries similar to the selection by location are made in order to extract the properties that are under the spatial extension of a certain ECWL threshold.

Results

Evolution of extreme coastal level occurrences

The thresholds representing the percentiles of low (30%), moderate (60%) and severe (98%) ECWL correspond to -0.05 m, 0.78 m and 1.98 m, respectively (Figure 2A). Figure 2B shows the evolution of the most severe threshold that presents a strong interannual variability. The maximum temporal occurrence of the 1.98 m level was 180 hours between 1995 and 2000, but since 2005, there are 3 years out of 5 where it does not exceed 100 h, with a minimum value of 54h. By extension, the occurrence of floods has weakened over the sequence 2005-2010. On the other hand, from 2010, there is an increase in the frequency of flooding, with a maximum value of 220h, which reflects an increase in the total annual duration of extreme sea levels, and probably the frequency of coastal flooding in Saint-Louis. Overall, the increasing trend in occurrence (significant at 95% level) is 1h per year which correspond to almost a day spent with flooding over this 23 years period.

Flood-prone areas and associated impacts

To show the potential of extension of the coastal flooding in Saint-Louis, a mapping of flood-prone areas is performed based on the two highest percentiles, 60th and 98th, combined with satellite-based DEM (Figure 3). This because the 30th (-0.05 m) percentile does not generate any risk of flooding in Saint-Louis.

Figure 3 shows a significant variation in the extent of flooding between the 60th and 98th percentiles and highlights a spatial contrast of the Saint-Louis coastline sections submerged by extreme water-levels. The used-approach reveals that 10% of the Saint Louis area would be potentially flooded under the 60th ECWL threshold, in this low-lying river mouth alluvial plain. This surface potentially submerged under the severe 98th ECWL threshold reaches 45% of the area is floodable, reaching key urbanized areas.

The results reveal that some neighborhoods of Saint-Louis are potentially exposed to extreme coastal water levels. Indeed, much of the area covered by the Langue de Barbarie is submersible. Figure 4 shows that the district of Gueth Ndar (the most densely populated of Saint Louis and Senegal; Diop, 2017) is the most exposed to coastal flooding, followed by Ndar Toute and Goxxu Mbacc. On the other hand, important governmental infrastructures located on the island of Saint-Louis appears to be preserved: the spatial extent of the severe water level (98th percentile) does not affect this part of Saint-Louis (north and south island). Moreover, the spatial disparity of the flood extension observed on the Langue de Barbarie is similar to that observed in the Sor suburb. In this part of Saint-Louis, only the neighborhoods located in front of the Senegal River are subject to flooding and the Pikine neighborhood located inside the Sor suburb. From the 10 sites (Goxxu Mbacc, Ndiollofène, Gueth Ndar, North and South Islands, Corniche, Balacos, Diamaguene, Léona and Pikine), Gueth Ndar remains the most vulnerable to coastal flooding. This is explained by its elevation characteristics largely below the hydrodynamic extreme levels (i.e. 1.98 m). In terms of infrastructure, the spatial queries performed reveal that 140 of the 24588 buildings and 452 plots of land (or parcels) on 13796 can be flooded. This means that many social, economic, cultural and religious assets are potentially endangered if not protection is deployed.

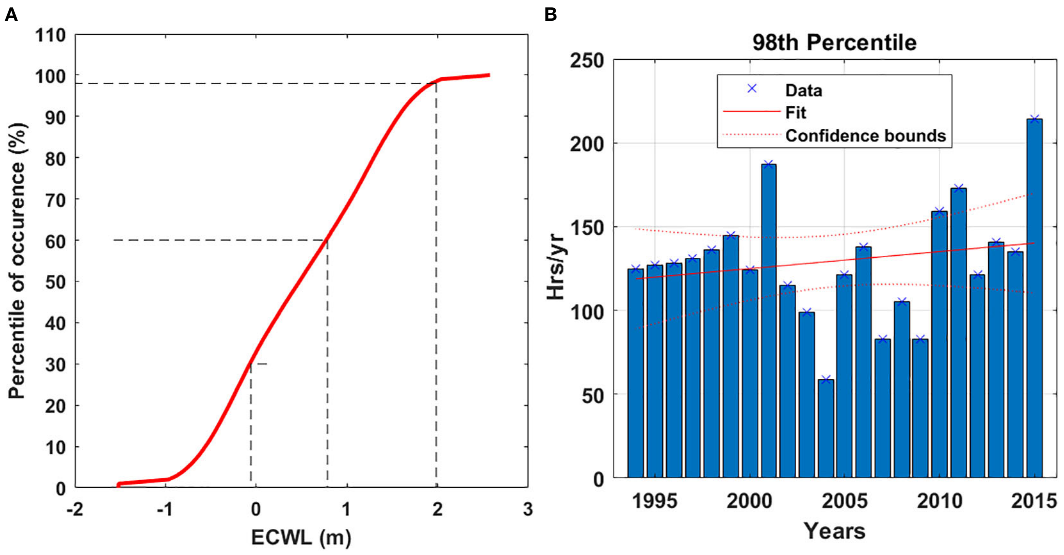

FIGURE 2
(A) Distribution of different percentiles of extreme coastal water level (ECWL), from 1994 to 2015. **(B)** Number of hours per year that coastal sea level at Saint-Louis reaches the 98th percentile (1.98 m).

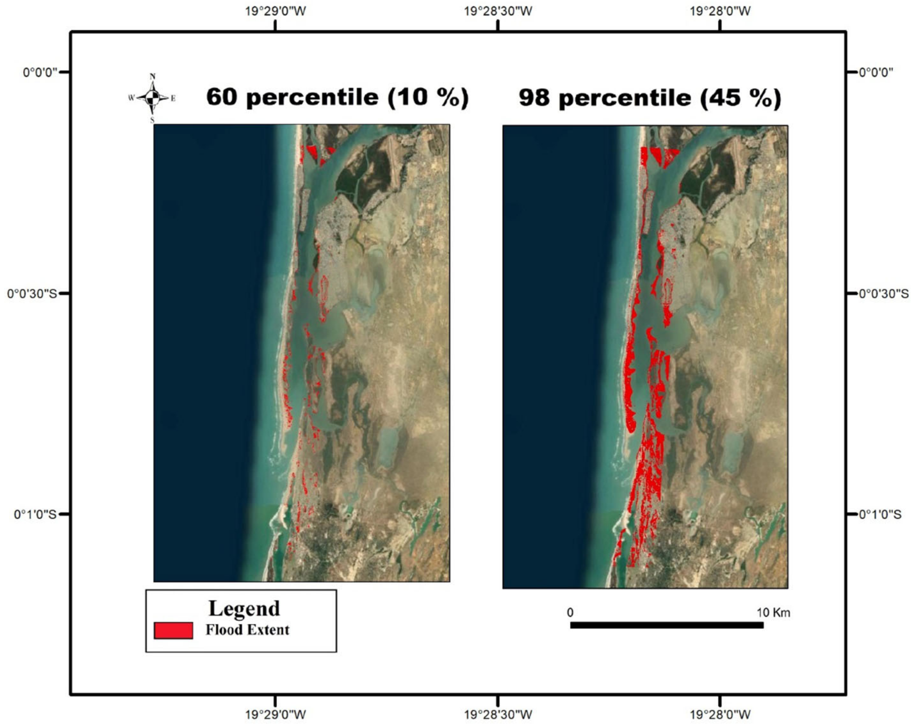

FIGURE 3
Spatial extent (red) of potential flooding for the moderate and severe ECWL scenarios, i.e. the 60th and 98th percentile.

Hydrodynamic factors contributing to coastal flooding

Since the estimation of EWCL from the Almar et al. (2021) model involves four parameters, we estimate here the relative weight of each of them in the 98th percentile for the period 1994-2015. Figures 5A–E shows hourly overall timeseries and annual means of each component. Figure 5F shows the aggregated annual conditions that produced a level above the 98th percentile. The tide (T) contributes the most with 71%, followed by wave run-up (R) with 25%, sea level anomaly (SLA) drives 3%, with a negligible contribution (<1%) of storm surge height due to atmospheric pressure and winds (DAC) in this storm free environment. Noteworthy, while SLA and DAC are dominated by interannual low varying evolutions (i.e. season to years), waves and particularly tide have rapid changes (i.e. hours to days).

The analysis of the evolution of the extreme level of coastal waters in Saint-Louis reveals that despite his minor influence on ECWL events, only SLA shows a significant 3.5 mm/yr trend at the 95% level (pvalue less than 0.05), which contributes to the increase in potential flooding. However, the large variability of wave runup T and R during the events prevent a robust overall trend assessment of ECWL on the study period and is a clear source of uncertainty for coastal flooding risk prediction in Saint Louis and elsewhere. This is due to the combined effect of their large amplitude with high frequency signal with a random phasing: waves randomly reach the coast during neap or spring tides, low or high tides.

Discussion

The estimation of the extreme coastal water level in Saint-Louis reveals that this section of the Senegalese coastline is extremely vulnerable to ocean-induced flooding. Being a highly urbanized site with an urban growth of 5% (Sidibe, 2013), there is no doubt that the shores are highly exposed to coastal flooding. Therefore we cannot talk about risk or vulnerability without the existence of stakes (Pont, 2015): socio-economic or environmental. The potential flood events of the Langue de Barbarie are likely to affect social, cultural, economic, heritage and cultural matters. Flooding in Saint-Louis causes a wide range of impacts (Sall, 2006). From a spatial point of view, the potential impacts manifest themselves in variable geometry. Of the 10 sites (Goxxu Mbacc, Ndiolloféne, Gueth Ndar, North and

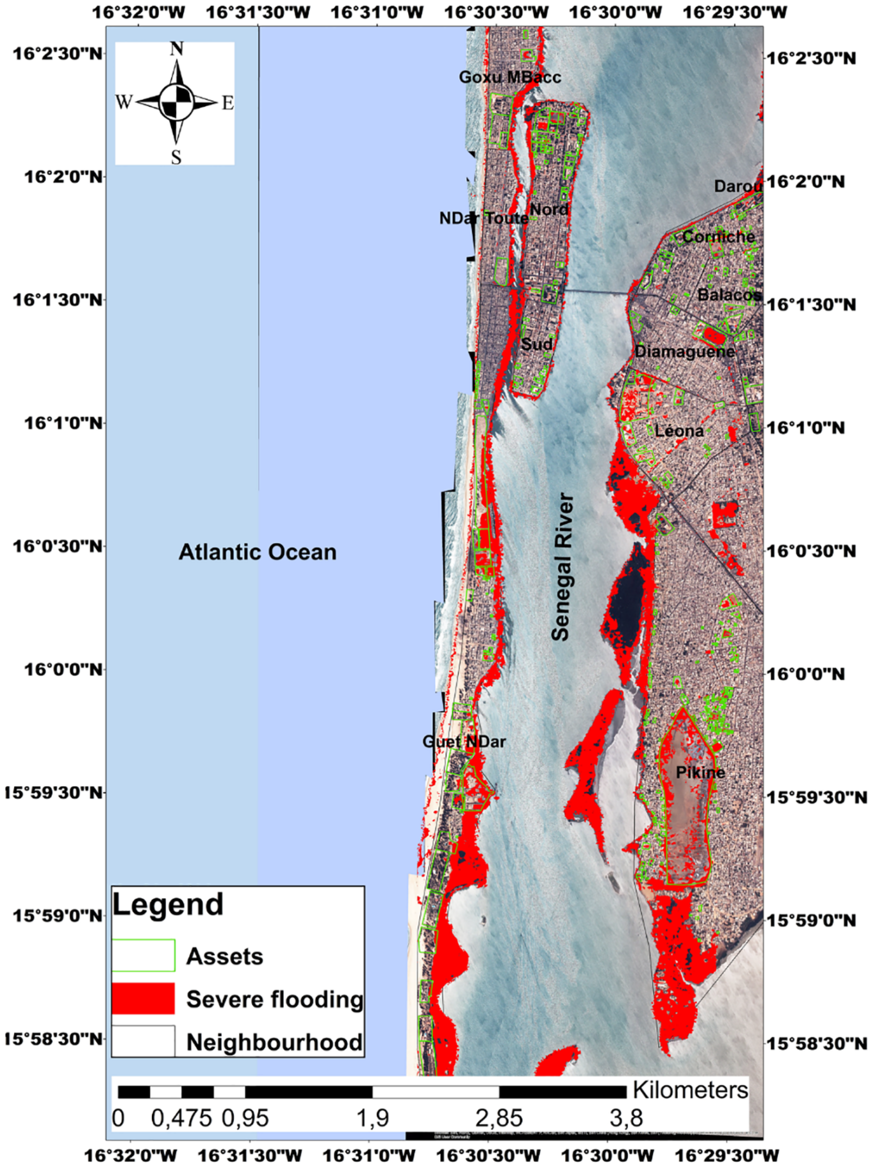

FIGURE 4
Map of infrastructures and assets of Saint Louis likely to be potentially flooded under the 98th ECWL percentile (i.e. 1.98 m).

South Islands, Corniche, Balacos, Diamaguene, Léona and Pikine), the site of Gueth Ndar remains the most vulnerable to coastal flooding. The district of Gueth Ndar is the most exposed to flooding likely to be induced by the 1.98m water level. Given its high human density, it is the most populated neighborhood of the Saint Louis, but also of Senegal and West Africa (Diop, 2017; Brüning, 2022). This high human concentration combined with its sensitivity to flooding, makes it particularly vulnerable. Many of the social assets (including historical cemetery) present in this part of the Langue de Barbarie would be impacted by flooding, which would also have consequences for the population as well as for socio-economic activities, particularly fishing, which is the dominant activity. This situation of vulnerability should incite decision makers and coastal managers to consider the protection of this section of the Saint-Louis coastline. Efforts concerning the protection of coastal communities of the Langue de Barbarie have been made through the construction of a protective dyke of 3m height in 2022. However, beyond the hard methods of coastal protection, other alternatives of protection should be adopted such as soft and nature based solutions (Alves et al.,

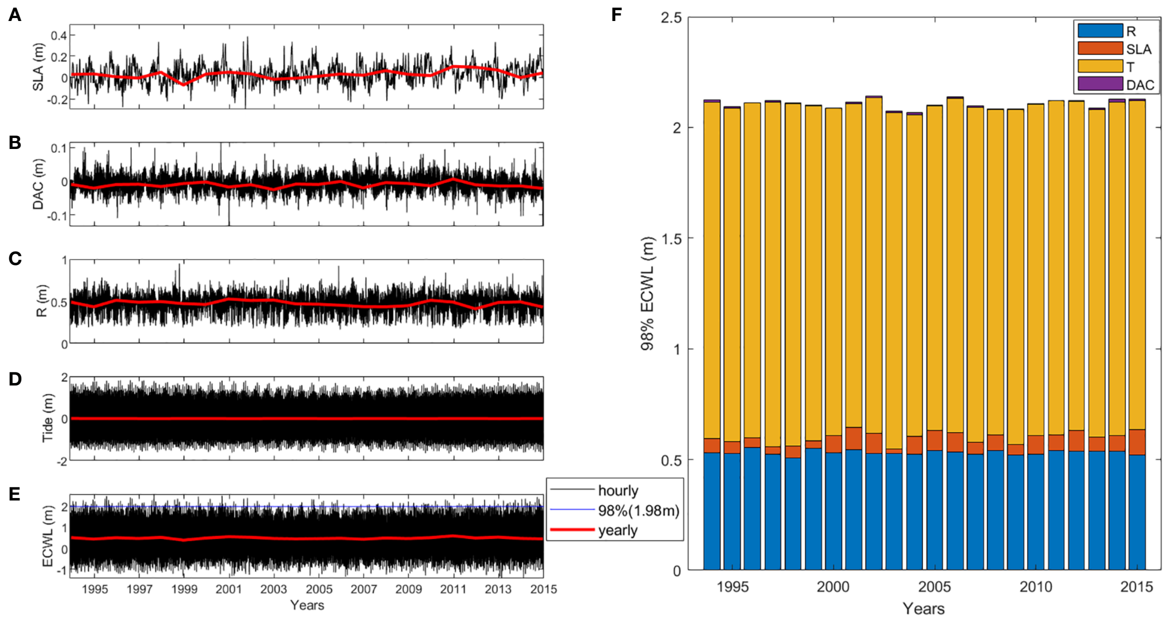

FIGURE 5
(A–E) ECWL components hourly (black) and yearly (red) timeseries and **(F)** contribution of each ECWL component passing the 98 percentile and potentially causing severe flooding in Saint-Louis between 1994 and 2015. In **(F)** the components are aggregated yearly during the moments overpassing the 98 percentile. Blue line in **(E)** stands for the 98th percentile of the ECWL timeseries, and referred to as "severe" value.

2020). Indeed, our results show that more and more extreme coastal water levels are expected and could overtop and overflow the protective dike. To this end, the use of soft development measures would be an effective solution. Soft solutions are less damaging to the environment than hard solutions (Schoones et al., 2019). Moreover, Baldé et al. (2021) showed that beach nourishment in the Langue de Barbarie, in this case the beaches of Pilote Bar, played an important role in that it contributed to beach widening. This method can also be efficient in dealing with coastal flooding. A wide, fattened beach provides good protection against erosion and overwash by decreasing runup propagation, as well as the probability of crossing (Duvat, 2001; Balouin et al., 2012; Itzkin et al., 2021). Moreover, it is likely to encounter the phenomena of land subsidence of this densely populated Gueth Ndar neighborhood. Continued subsidence catalyzes sea level rise, which in turn increases water levels, which exacerbates coastal flooding (Moller et al., 2014). According to Woodruff et al. (2013), the impacts of coastal flooding can be mitigated in part through the implementation of adaptation strategies using conservative sediment management and human-induced subsidence reduction. The protection of this sandy strip (Langue de Barbarie) is of paramount importance, as its disappearance could have significant impacts on the city of Saint-Louis and the Sor suburb. In fine, the relocation of populations may be a possible solution to protect people. Moreover, a relocation project to offer long-term protection to the populations of the Langue of Barbarie in Saint-Louis is underway. A 14-hectare relocation site located in Diougop outside the city of Saint-Louis is being developed. On this site, 600 housing units will be built to accommodate 10,000 people (Brüning, 2022). This relocation project is currently encountering a number of pitfalls related to the issue of social acceptability. The populations of Gueth Ndar, who are mostly fishermen, feel that this policy of relocation inland would take them away from their place of work, the sea. However, a participatory approach should be adopted to facilitate acceptance of the project if their cultural and socio-economic contribution to the identity of Saint-Louis is to be maintained.

Given that the drivers of coastal flooding are varied (Prime et al., 2016), we attempted to separately analyze the factors contributing to coastal flooding in Saint-Louis. Our results show that the tide is the dominant driver of coastal flooding in Saint-Louis. This observation is also made by Durand et al. (2010) on the Langue de Barbarie. This finding is consistent with Almeida et al. (2018) and Dada et al. (2019) works showing at other low-lying coasts exposed to energetic waves that coastal flooding in Nha Trang (Vietnam) and low-lying mud coast in Nigeria Delta (Gulf of Guinea) are due to the interaction between waves and tide. Durand et al. (2010) also points out that the tidal range has significantly increased after the opening in 2003 of a breach in the sandspit and water levels in Saint-Louis lagoon are increasingly aligned with the rhythm of the tides. However, due to the lack of long-term tide gauges in Saint Louis, more generally along the African coast (Abessolo Ondoa et al., 2019; Marti et al., 2021; Almar et al., 2022), our current study is limited by the use of the FES2014 tide data which are harmonic-based, off-shore, and do not reflect change over time (Figure 5D); any trends or changes in local tides in could not be determined. Our results also show interannual variability in the temporal occurrence of extreme water levels at Saint-Louis. Especially since our results reveal that the tide is the main factor contributing to coastal flooding in Saint- Louis, and that in a global context of global warming the sea level is expected to increase. Thus, the impact of flooding in Saint-Louis will strongly impact coastal communities. Due to the presence of the river, the study area is at great risk of flooding as the sea level rises gradually. Sea level rise by 2100 will strengthen coastal flooding in Saint-Louis (Sall, 2006). Our data reveal that waves have a significant impact on the occurrence of ECWL events at Saint-Louis. As a difference with tides, the action of waves on extreme events is likely to take significant proportions especially in a context of climate and climate variability change, it should be remembered. In particular, waves have a strong interannual fluctuation controlled by the North Atlantic Oscillation (Almar et al., 2019). Climate change, - which is reflected in the sea level rise, has the effect of strengthening the action of waves (Costa, 1995; Wang et al., 2003; Melet et al., 2018), and will influence the generation of swells of high intensity at the coast (Sergent et al., 2010; Vitousek et al., 2017). This concern is confirmed by the global simulations of Vitousek et al. (2017) that identify the inter-tropical zone as particularly exposed to future increase in coastal flooding.

In St. Louis, we find that this increase in potentially inundated area with ECWL is rather linear (Table 1). Interestingly, while there is considerable climate-induced variability in waves, model predictions do not indicate clear long-term trends (Melet et al., 2020a), nor does the R runup. While current ECWL maxima are about 2 m, with a 1 m sea level rise offset, as predicted (Oppenheimer et al., 2019) for the late 21st century, the inundated area can be expected to increase by 25% if no protective measures are taken.

TABLE 1 Potential flooded area (%) at Saint Louis for ECWL thresholds.

ECWL (m)	Potential flooded area (%)
0,05	0,29
0,5	4,5
1	15,20
1,5	30,13
2	45,42
2,5	58,30
3	67,43

Lastly, it should be noted that when interpreting the consequences of overtopping on coastal flooding, the occurrence of overtopping does not necessarily imply that the entire low elevation coastal zone is flooded. Rather, overtopping drives localized coastal flooding, immediately adjacent to areas of overtopping, which would likely be both temporally and spatially variable due to the combined effects of temporal and alongshore gradients in breaking wave heights, and alongshore variations in coastal elevation maxima (Almar et al., 2021). Even if a standalone use for coastal studies (e.g. without ground control point) is not yet conceivable at this stage with operational accuracy (Taveneau et al., 2021; Turner et al., 2021), considering the encountered accuracy limitations, satellite-based topography monitoring appears as a breakthrough in decade-old monitoring technological barriers (Benveniste et al., 2019; Melet et al., 2020b), in support of coastal engineering.

Conclusion

By combining satellite-derived DEM with reanalyzes and satellite observations of sea level components, this paper assessed the vulnerability of the Saint-Louis coastline to the potential risk of coastal flooding. Testimonies already reported various impacts on economic, cultural, patrimonial and infrastructural. Our results confirm that this site is extremely vulnerable to coastal flooding potential almost half of this low lying river mouth plain flooded under severe water levels. Spatially, the different neighborhoods of Saint-Louis are unequally affected with the most exposed one, also one of the poorest with vulnerable communities, being located on the Langue of Barbarie sandspit. Sea level rise is the main factor for the trend. However, the fact that on top of rising sea, that the compound influence of waves and tide that is predominant responsible for the events induce a large uncertainty on the prediction of coastal risk. This study documents coastal risk flooding potential and its drivers which is not sufficiently quantified and understood on the Senegalese coasts and West Africa, and whose knowledge is an essential element in the elaboration of coastal development schemes and protection of coastal communities.

Data availability statement

The original contributions presented in the study are included in the article/supplementary material. Further inquiries can be directed to the corresponding author.

Author contributions

All authors contributed to the article and approved the submitted version.

Funding

This article was produced with the support of coastal protection project in Saint-Louis (PPCS) co-financed by French Agency for Development/Municipal Development Agency. Convention n°CSN156102.

Acknowledgments

The authors would want to thank the Senegalese Agence of Development Municipal (ADM), the French Agency Development (AFD) for funding this research and the program DINAMIS for making the satellite Pleiades data available.

Conflict of interest

Publisher's note

References

Abessolo Ondoa, G., Almar, R., Castelle, B., Testut, L., Léger, F., Sohou, Z., et al. (2019). Sea Level at the coast from video-sensed waves: Comparison to tidal gauges and satellite altimetry. *J. Atmospheric Oceanic Technol.* 36 (8), 1591–1603. doi: 10.1175/JTECH-D-18-0203.1

Almar, R., Kestenare, E., Reyns, J., Jouanno, J., Anthony, E. J., Laibi, R., et al. (2015). Response of the bight of Benin (Gulf of Guinea, West Africa) coastline to anthropogenic and natural forcing, Part1: Wave climate variability and impacts on the longshore sediment transport. *Continental Shelf Res.* 110, 48–59.

Almar, R., Kestenare, E., and Boucharel, J. (2019). On the key influence of remote climate variability from tropical cyclones, north and south Atlantic mid-latitude storms on the Senegalese coast (West Africa). *Environ. Res. Commun.* 1 (7), 071001. doi: 10.1088/2515-7620/ab2ec6

Almar, R., Ranasinghe, R., Bergsma, E. ,. W. J., Diaz, H., Melet, A., Papa, F., et al. (2021). A global analysis of extreme coastal water levels with implications for potential coastal overtopping. *Nat. communication* 12, 3775. doi: 10.1038/s41467-021-24008-9

Almar, R., Stieglitz, T., Addo, K. A., Ba, K., Ondoa, G. A., Bergsma, E. W., et al. (2022). Coastal zone changes in West Africa: challenges and opportunities for satellite earth observations. *Surveys Geophysics*, 1–27. doi: 10.1007/s10712-022-09721-4

Almeida, L. P., Almar, R., Bergsma, E. W., Berthier, E., Baptista, P., Garel, E., et al. (2019). Deriving high spatial-resolution coastal topography from sub-meter satellite stereo imagery. *Remote Sens.* 11 (5), 590. doi: 10.3390/rs11050590

Almeida, L. P., Almar, R., Meyssignac, B., and Viet, N. T. (2018). Contributions to coastal flooding events in southeast of Vietnam and their link with global mean sea level rise. *Geosciences* 8, 437. doi: 10.3390/geosciences8120437

Alves, B., Angnuureng, D. B., Morand, P., and Almar, R. (2020). A review on coastal erosion and flooding risks and best management practices in West Africa: what has been done and should be done. *J. Coast. Conserv.* 24 (3), 1–22. doi: 10.1007/s11852-020-00755-7

Anthony, E. J., Besset, M., Dussouillez, P., Goichot, M., and Loisel, H. (2019). Overview of the moonsoon-influenced ayeyarwady river delta, and delta shoreline mobility in response to changing fluvial sediment supply. *Mar. Geology* 417, 106038. doi: 10.1016/j.margeo.2019.106038

Baldé, O., Sakho, I., Diouf, M. ,. B., Bop, M., Tine, D., and Ibouroi, W. (2021). Effectiveness of pilote bar (St. Louis) beach nourishment after a decade of erosion. *Eur. Sci. J.* 1710, 207–231.

Balouin, Y., Belon, R., Stépanian, A., and Bodéré, G. (2012). General study for the protection of the coastline of the eastern plain of Corsica: management recommendations. *Rapport BRGM/ RP 61650-FR*, 52.

Benveniste, J., Cazenave, A., Vignudelli, S., Fenoglio-Marc, L., Shah, R., Almar, R., et al. (2019). Requirements for a coastal hazards observing system. *Front. Mar. Sci.* 6, 348. doi: 10.3389/fmars.2019.00348

Bergsma, E. W., Almar, R., Anthony, E. J., Garlan, T., and Kestenare, E. (2022). Wave variability along the world's continental shelves and coasts: Monitoring opportunities from satellite earth observation. *Adv. Space Res.* 69 (9), 3236–3244. doi: 10.1016/j.asr.2022.02.047

Bergsma, E. W., Sadio, M., Sakho, I., Almar, R., Garlan, T., Gosselin, M., et al. (2020). Sand-spit evolution and inlet dynamics derived from space-borne optical imagery: Is the Senegal-river inlet closing? *J. Coast. Res.* 95 (SI), 372–376. doi: 10.2112/SI95-072.1

Bongarts Lebbe, T., Rey-Valette, H., Chaumillon, É., Camus, G., Almar, R., Cazenave, A., et al. (2021). Designing coastal adaptation strategies to tackle sea level rise. *Front. Mar. Sci.* 1640.

Breilh, J. F., Chaumillon, E., and Bertin, J. (2012). "Improve of a static flooding method and application to the case of the xynthia storm," in *XIIth National Conference on Coastal Engineering*, Cherbourg (Nantes, France: Paralia). doi: 10.5150/jngcgc.2012.100-B

Brüning, L. (2022). *Erosion côtière au nord du sénégal: migrations et stratégies d'adaptation* (these de géographie, instiut: Institut de Géographie, Université de Neuchâtel).

Cain, A., Cisse, O., Abdrabo, M., and Sah Akwen, N. (2015). Climate-responsive planning for angola's coastal cities. *Dev. Workshop*, 4.

Carrere, L., Lyard, F. H., Cancet, M., and Guillot, A. (2016). "Finite element solution FES2014, a new tidal model – validation results and perspectives for improvements," in *ESA Living Planet Conference* (Paris, France: European Space Agency).

Cisse, C. O. T., Sagne, P., Ba, K., Fall, B., Sy, B. A., and Marone, A. (2022). Modelling of extreme water levels on Malibu, gadaye and malika sandy beaches (Dakar, Senegal) following the 19 November. *Eur. Sci. J.* 18 (3), 80–100. doi: 10.19044/esj.2022.v18n3p79

Collin, A., Hench, J. L., Pastol, Y., Planes, S., Thiault, L., Schmitt, R. J., et al. (2018). High resolution topobathymetry using a Pleiades-1 triplet: Moorea island in 3D. *Remote Sens. Environ.* 208, 109–119. doi: 10.1016/j.rse.2018.02.015

Costa, S. (1995). "Sea Level rise and response strategies: the case of the Normandy-picardy coastline," in *Annales de géographie* 107, n°600edition, 179–200.

Dada, O., Almar, R., Morand, P., and Ménard, F. (2021). Towards West African coastal social- ecosystems sustainability: Interdisciplinary approaches. *Ocean Coast. Manage.* 211, 105746. doi: 10.1016/j.ocecoaman.2021.105746

Dada, O. A., Almar, R., and Oladapo, M. I. (2019). Recent coastal sea level variations and flooding events in the Nigerian transgressive mud coast of gulf of Guinea. *J. Afr. Earth Sci.* 161, 103668. doi: 10.1016/j.jafrearsci.2019.103668

Diagne, M. K. (2020). Coastal erosion: The hydra that keeps engulfing the Senegalese coasts, what's green? *Sustain. Dev. bimonthly* 13.

Diop, C. (2017). Water and sanitation in the neighborhood of guet ndar-Senegal cheikh DIOP. *Int. J. Eng. Works* 4 (5), 93–100.

Diop, S., Fabres, J., Pravettoni, R., Barusseau, J. P., Descamps, C., and Ducrotoy, J. P. (2014). The western and central africa land–sea interface: a vulnerable, threatened, and important coastal zone within a changing environment. *land/ocean Interact. Coast. zone west Cent. Afr.*, 1–8.

Dodet, G., Melet, A., Ardhuin, F., Bertin, X., Idier, D., and Almar, R. (2019). The contribution of wind-generated waves to coastal sea-level changes. *Surveys Geophysics* 40 (6), 1563–1601. doi: 10.1007/s10712-019-09557-5

Dupuis, L. (2016). *The erosion of the coves of the city of schoelcher: determination of the dynamics and processes involved* (University of the Antilles), 151.

Durand, P., Anselme, B., and Thomas, Y. F. (2010). The impact of the opening of the breach in the langue de barbarie in saint-Louis, Senegal in 2003: a change in the nature of the flood hazard? *Cybergeo: Eur. J. Geography Environment Nature Landscape* 496. doi: 10.4000/cybergeo.23017

Duvat, C. V. (2001). Evaluation of beach vulnerability to erosion: application to the Seychelles archipelago. *Geomorphology* 7 (1), 31–40.

Ganguli, P., and Merz, B. (2020). *Compounding effects of riverine and coastal floods and its implications for coastal urban flood residence* (EGU General Assembly 2020). doi: 10.5194/egusphere-egu2020-6439

Garlan, T., Almar, R., Gauduin, H., Gosselin, M., Morio, O., and Labarthe, C. (2020). 3D variability of sediment granulometry in two tropical environments: Nha trang (Vietnam) and saint-Louis (Senegal). *J. Coast. Res.* 95 (SI), 495–499. doi: 10.2112/SI95-096.1

Gemenne, F., Blocher, J., De Longueville, F., Telenti, S. V. D., Zickraf, C., Gharbaoui, D., et al. (2017). Climate change, natural disasters and population displacement in West Africa. *Geo-Eco-Trop: Int. J. Trop. Geology* 41 (3).

Giardino, A., Schrijvershof, R., Nederhoff, C. M., De Vroeg, H., Briere, C., Tonnon, P. K., et al. (2018). A quantitative assessment of human interventions and climate change on the West African sediment budget. *Ocean Coast. Manage.* 156, 249–265. doi: 10.1016/j.ocecoaman.2017.11.008

Idier, D., Bertin, X., Thompson, P., and Pickering, M. D. (2019). Interactions between mean sea level, tide, surge, waves and flooding: mechanisms and contributions to sea level variations at the coast. *Surveys Geophysics* 40 (6), 1603–1630. doi: 10.1007/s10712-019-09549-5

Itzkin, M., Moore, L. J., Ruggiero, P., Hacker, S. D., and Biel, R. G. (2021). The relative influence of dune aspect ratio and beach width on dune erosion as a function of storm duration and surge level. *Earth Surf. Dynam.* 9, 12231237.

James, D., Collin, A., Muty, A., and Qin, R. (2022). Satellite–derived topography and morphometry for VHR coastal habitat mapping: The Pleiades–1 tri–stereo enhancement. *Remote Sens.* 14 (1), 219. doi: 10.3390/rs14010219

Kante, F., and Fall, N. A. (2019). 3.3 Érosion côtière et déplacement de populations. Étude de cas du site de recasement des sinistrés de la langue de barbarie dans la ville de saint-Louis du sénégal. *Edité publié avec l'aimable soutien* 51, 51–53.

Kirezci, E., Young, I. R., Ranasinghe, R., Muis, S., Nicholls, R. J., Lincke, D., et al. (2020). Projections of global-scale extreme sea levels and resulting episodic coastal flooding over the 21st century. *Sci. Rep.* 10 (1), 1–12.

Kulp, S. A., and Strauss, B. H. (2019). New elevation data triple estimates of global vulnerability to sea-level rise and coastal flooding. *Nat. Commun.* 10 (1), 1–12.

Kupfer, S., Aguilar, S. S., Niekerk, L. V., Luck-Voger, M., and Vafeidis, A. T. (2022). Investigating the interaction of waves and river discharge during compound flooding at breede estuary, south Africa. *Nat.Hazards Earth Syst.Sci* 22, 187–205. doi: 10.5194/nhess-22-187-2022

Laïbi, R. A., Anthony, E. J., Almar, R., Castelle, B., Senechal, N., and Kestenare, E. (2014). Longshore drift cell development on the human-impacted bight of Benin sand barrier coast, West Africa. *J. Coast. Res.* 70 (10070), 78–83.

Le Roy, S., Pedreros, R., André, C., Paris, F., Lecacheux, S., Marche, F., et al. (2015). Coastal flooding of urban areas by overtopping: Dynamic modelling application to the Johanna storm, (2008) in gâvres (France). *Nat. Hazards Earth Syst. Sci.* 15 (11), 2497–2510. doi: 10.5194/nhess-15-2497-2015

Marti, F., Cazenave, A., Birol, F., Passaro, M., Léger, F., Niño, F., et al. (2021). Altimetry-based sea level trends along the coasts of western Africa. *Adv. Space Res.* 68 (2), 504–522. doi: 10.1016/j.asr.2019.05.033

Melet, A., Almar, R., Hemer, M., Le Cozannet, G., Meyssignac, B., and Ruggiero, P. (2020a). Contribution of wave setup to projected coastal sea level changes. *J. Geophysical Research: Oceans* 125 (8), e2020JC016078. doi: 10.1029/2020JC016078

Melet, A., Meyssignac, B., Almar, R., and Le Gozannet, G. (2018). Under estimate wave contribution to coastal sea-level rise. *Nat. Climate Change* 8, 234–239. doi: 10.1038/s41558-018-0088-y

Melet, A., Teatini, P., Le Cozannet, G., Jamet, C., Conversi, A., Benveniste, J., et al. (2020b). Earth observations for monitoring marine coastal hazards and their drivers. *Surveys Geophysics* 41 (6), 1489–1534. doi: 10.1007/s10712-020-09594-5

Möller, I., Kudella, M., Rupprecht, F., Spencer, T., Paul, M., Wesenbeeck, B. K. V., et al. (2014). Wave attenuation over coastal saltmarshes under storm surge conditions. *Nat. Geosci.* 7. doi: 10.1038/NGEO2251

Ndour, A., Ba, K., Almar, A., Almeida, P., Sall, M., Diedhiou, P. M., et al. (2020). On the natural and anthropogenic drivers of the Senegalese (West Africa) low coast evolution: Saint Louis beach 2016 COASTVAR experiment and 3D modeling of short term coastal protection measures. *J. Coast. Res.* 95 (SI), 583–587. doi: 10.2112/SI95-114.1

Ndour, A., Laïbi, R. A., Sadio, M., Degbe, C. G., Diaw, A. T., Oyédé, L. M., et al. (2018). Management strategies for coastal erosion problems in West Africa: analysis, issues, and constraints drawn from the examples of Senegal and Benin. *Ocean Coast. Manage.* 156, 92–106. doi: 10.1016/j.ocecoaman.2017.09.001

Oppenheimer, M., Glavovic, B., Hinkel, J., van de Wal, R., Magnan, A. K., Abd-Elgawad, A., et al. (2019). Sea Level rise and implications for low lying islands, coasts and communities. *IPCC Spec. Rep. Ocean Cryosph. Change Clim* 355, 126–129.

Pont, C. (2015). *Addressing and characterizing the risk of on Mediterranean sandy coasts: the example of Mediterranean sandy coasts: the example of the commune of leucate, master 1 risks and environment* Vol. 150 (Paris, France: Institute of Geography University of Paris 1 Pantheon-Sorbonne).

Prime, T., Brown, J. M., and Plater, A. J. (2016). Flood inundation uncertainty: the case of a 0.5% annual probablity flood event. *Environ. science&policy* 59, 1–9.

Quiroga, I. A., Elisa Sainz de Murieta, E. S., Losada, I., Toimil, A., Torres, S., Markanday., A., et al. (2021). Coastal flooding and erosion under climate change : risk assessment risk in Dakar. *BC3 Policy Briefs Rep. Res. carried*, 9.

Sadio, M. (2017). Morphodynamics and development of the coastal spits of the Senegal coast. *Journal of Coastal Research* (university Cheikh Anta Diop of Dakar and Aix-Marseille University), 403. thesis in physical geography, speciality: geomorphology.

Sadio, M., Anthony, E. J., Diaw, A. T., Dussouillez, P., Fleury, J. T., Kane, A., Almar, R., and Kestenare, E. (2017). Shoreline changes on the wave-influenced senegal river delta, west africa: The roles of natural processes and human interventions. Water. 9(5):357, 2017.

Salameh, E., Frappart, F., Almar, R., Baptista, P., Heygster, G., Lubac, B., et al. (2019). Monitoring beach topography and nearshore bathymetry using spaceborne remote sensing: A review. *Remote Sens.* 11 (19), 2212.

Sergent, P., Prevot, G., and Trmal, C. (2010). Reinforcement of shallow structures with respect to of the sea level rise, collection of the acts of the days. *impacts Climate Change Coast. risks* (Orleans, France), 147–151.

Sall, M. (2006). *Flooding and sea level rise in saint-Louis of Senegal: potential impacts and adaptation measures* (university of Le Mans), 332. Thesis of geography.

Shean, D., Alexandrov, O., Moratto, Z., Smith, B., Joughin, I., Porter, C., et al. (2016). An automated, open-source pipeline for mass production of digital elevation models (DEMs) from very-high-resolution commercial stereo satellite imagery. *ISPRS J. Photogramm. Remote Sens.* 116, 101–117.

Schoonees, T., Gijón Mancheño, A., Scheres, B., Bouma, T. J., Silva, R., Schlurmann, T., et al. (2019). Hard structures for coastal protection, towards greener designs. *Estuaries Coasts* 42 (7), 1709–1729.

Sidibe, I. (2013). A coastal territory in a political, economic and religious space in Senegal: the case of ouakam bay (Dakar). *spaces populations societies*, 159–176.

Stockdon, H. F., Holman, R. A., Howd, P. A., and Sallenger, A. H.Jr. (2006). Empirical parameterization of setup, swash, and runup. *Coast. Eng.* 53 (7), 573–588. doi: 10.1016/j.coastaleng.2005.12.005

Sy, B. A., Alonso Bilbao, I., Sy, A. A., Perez, I. S., and Valido, S. R. (2011). Results of the 2010-2012 monitoring of the evolution of the open gap on the Langue de Barbarie in Senegal and its consequences. *Physio-Geo* 7, 136. doi: 10.4000/physio-geo.3569

Taveneau, A., Almar, R., Bergsma, E. W., Sy, B. A., Ndour, A., Sadio, M., et al. (2021). Observing and predicting coastal erosion at the langue de barbarie sand spit around saint-Louis (Senegal, West Africa) through satellite-derived digital elevation model and shoreline. *Remote Sens.* 13 (13), 2454. doi: 10.3390/rs13132454

Tchindjang, M., Mbevo, F., and Bodpa, ,. A. (2019). *Building the port city of tomorrow in Atlantic Africa* edition ecm, 30p.

Tebaldi, C., Strass, B. H., and Zervas., C. E. (2012). Modelling sea level rise impacts on storm surges along us coasts. *Envr.Res.Lett* 7, 014032. doi: 10.1088/1748-9326/7/1/014032

Turner, I. L., Harley, M. D., Almar, R., and Bergsma, E. W. (2021). Satellite optical imagery in coastal engineering. *Coast. Eng.* 167, 103919. doi: 10.1016/j.coastaleng.2021.103919

Vitousek, S., Barnard, P. L., Fletcher, C. H., Frazer, N., Erikson., L., and Storlazzi, C. D. (2017). Doubling of coastal flooding frequency within decades due to sea-level rise. *Sci. Rep.* 7, 1399. doi: 10.1038/s41598-017-01362-7

Vousdoukas, M. I, Voukouvalas, E., Mentaschi, L., Dottori, F., Giardino, A., Bouziotas, D., et al. (2016). Developments in large-scale coastal flood hazard mapping. *Nat. Hazards Earth Syst. Sci.* 16, 1841–1853. doi: 10.5194/nhess-16-1841-2016

Vousdoukas, M. I., Clarke, J., Ranasinghe, R., Reimann, L., Khalaf, N., Duong, T. M., et al. (2022). African Heritage sites threatened as sea-level rise accelerates. *Nat. Climate Change* 12 (3), 256–262. doi: 10.1038/s41558-022-01280-1

Wade, S., Rudant, J. P., Ba, K., and Ndoye, B. (2008). Remote sensing and management of natural disasters :application to the study of urban flooding of saint-Louis and gulling due to water erosion in nioro du Rip(Senegal). *Rev. teledetection*, 203–210.

Wang, X. L., Zwiers, F. W., and Swail, V. R. (2003). North Atlantic ocean wave cliamte change scenarios for the twebty first century. *J. Climate* 17, 2368–2383. doi: 10.1175/1520-0442(2004)017<2368:NAOWCC>2.0.CO;2

Weissenberger, S., Noblet, M., Plante, S., Chouinard, O., Guillemot, J., Aube, M., et al. (2016). Climate change, coastal development and vulnerability: a comparison of French, Canadian and Senegalese territories. *VertigO - electronic J. Environ. sciences Volume 16 Issue 3 Environ. vulnerabilities: historical Perspect.*, 2–33. doi: 10.4000/vertigo.18050

Wells, N. C. (2011). “The atmosphere and ocean: a physical introduction,” (John Wiley & Sons).

Woodruff, J. D., Irish, J. L., and Camargo, S. J. (2013). Coastal flooding by tropical cyclones and sea-level rise. *Nature* 504, 44–51. doi: 10.1038/nature12855

Woodruff, S. C., and Stults, M. (2016). Numerous strategies but limited implementation guidance in US local adaptation plans. *Nat. Climate Change* 6 (8), 796–802.

Wöppelmann, G., Miguez, B. L., and et Creach, R. (2008). Tide gauge records at Dakar, Senegal (Africa): Towards a 100-years consistent sea-level time series. (Vienna, Austria: European Geophysical Union, General Assambly).

frontiers | Frontiers in Marine Science

TYPE Original Research
PUBLISHED 22 December 2022
DOI 10.3389/fmars.2022.1012041

OPEN ACCESS

EDITED BY
Amaia Ruiz de Alegría-Arzaburu,
Universidad Autónoma de Baja
California, Mexico

REVIEWED BY
Alejandro López-Ruiz,
University of Seville, Spain
Maurizio D'Anna,
Bureau de Recherches Géologiques et
Minières, France

*CORRESPONDENCE
Raimundo Ibaceta
rai.ibaceta.v@gmail.com

SPECIALTY SECTION
This article was submitted to
Coastal Ocean Processes,
a section of the journal
Frontiers in Marine Science

RECEIVED 05 August 2022
ACCEPTED 29 November 2022
PUBLISHED 22 December 2022

CITATION
Ibaceta R, Splinter KD, Harley MD and
Turner IL (2022) Improving multi-
decadal coastal shoreline change
predictions by including model
parameter non-stationarity.
Front. Mar. Sci. 9:1012041.
doi: 10.3389/fmars.2022.1012041

Improving multi-decadal coastal shoreline change predictions by including model parameter non-stationarity

Raimundo Ibaceta*, Kristen D. Splinter, Mitchell D. Harley and Ian L. Turner

Water Research Laboratory, School of Civil and Environmental Engineering, UNSW Sydney, Sydney, NSW, Australia

Our ability to predict sandy shoreline evolution resulting from future changes in regional wave climates is critical for the sustainable management of coastlines worldwide. To this end, the present generation of simple and efficient semi-empirical shoreline change models have shown good skill at predicting shoreline changes from seasons up to several years at a number of diverse sites around the world. However, a key limitation of these existing approaches is that they rely on time-invariant model parameters, and assume that beaches will evolve within constrained envelopes of variability based on past observations. This raises an interesting challenge because the expected future variability in key meteocean and hydrodynamic drivers of shoreline change are likely to violate this 'stationary' approach to longer-term shoreline change prediction. Using a newly available, multi-decadal (28-year) dataset of satellite-derived shorelines at the Gold Coast, Australia, this contribution presents the first attempt to improve multi-decadal shoreline change predictions by allowing the magnitude of the shoreline model parameters to vary in time. A data assimilation technique (Ensemble Kalman Filter, EnKF) embedded within the well-established *ShoreFor* shoreline change model is first applied to a 14-year training period of approximately fortnightly shoreline observations, to explore temporal variability in model parameters. Then, the magnitudes of these observed non-stationary parameters are modelled as a function of selected wave climate covariates, representing the underlying seasonal to interannual variability in wave forcing. These modelled time-varying parameters are then incorporated into the shoreline change model and tested over the complete 28-year dataset. This new inclusion of non-stationary model parameters that are directly modelled as a function of the underlying wave forcing and corresponding time scales of beach response, is shown to outperform the multi-decadal predictions obtained by applying the conventional stationary approach ($RMSE_{non\text{-}stationary}$ = 11.1 m; $RMSE_{stationary}$ =

254.3 m). Based on these results, it is proposed that a non-stationary approach to shoreline change modelling can reduce the uncertainty associated with the misspecification of physical processes driving shoreline change and should be considered for future shoreline change predictions.

KEYWORDS

ShoreFor, shoreline change model, ensemble kalman filter, Gold Coast, Australia

1 Introduction

Sandy coastlines vary at time scales of individual storms to longer-term variability due to changes in waves, water levels, and sediment supply (Vitousek et al., 2017a; Jackson and Short, 2020). Reliable predictions of shoreline evolution that span this range of time scales, both now and by the end of the century, are required for assessing coastal vulnerability in a changing climate (Ranasinghe, 2020; Toimil et al., 2020). This is particularly important given the uncertainty and possible changes in regional wave climates and/or ocean water levels due to climate variability that have the potential to influence the coast (Wong et al., 2014; Ranasinghe, 2016; Vousdoukas et al., 2020; Odériz et al., 2022). As such, significant research effort has been directed towards the development of relatively simple and efficient semi-empirical shoreline change models to predict shoreline evolution over time scales ranging from seasons to decades (e.g., Miller and Dean, 2004; Castelle et al., 2014; Jaramillo et al., 2020; Roelvink et al., 2020; Yates et al., 2009; Splinter et al., 2014; Vitousek et al., 2017b). These models are now being used to explore shoreline changes that may occur during the 21st century (e.g., Toimil et al., 2017; Vitousek et al., 2017b; D'Anna et al., 2021; D'Anna et al., 2022) assuming that beaches will evolve within constrained envelopes of variability based on past measurements (Luijendijk et al., 2018; Vousdoukas et al., 2020). However, the expected future changes in key meteocean and hydrodynamic drivers of shoreline evolution (e.g., Wong et al., 2014; Morim et al., 2019) suggest that predictive models of longer-term shoreline changes should also include the capability to adapt to changing wave forcing, as well as corresponding time scales of shoreline response (Montaño et al., 2021; Schepper et al., 2021; Splinter and Coco, 2021).

Semi-empirical shoreline change models are simplified representations of the complex sediment transport processes occurring between the shoreface and beach face, and therefore inherit uncertainties from the imprecise representation of physical processes in the model structure and from the forcing inputs (Le Cozannet et al., 2019; Le Cozannet et al., 2016; Kroon et al., 2020; Montaño et al., 2020; D'Anna et al., 2021; Toimil et al., 2021; Vitousek et al., 2021). This misspecification of physical processes is typically addressed *via* site-specific model calibration, whereby a set of stationary (or time-invariant) model parameters are optimized for a specific time period using observed forcing and co-located shoreline data (Long and Plant, 2012; Splinter et al., 2013). For example, Yates et al. (2011, 2009) applied a semi-empirical cross-shore shoreline model to five beaches in California (USA) spanning up to 5 years of data and found inter-site variability in the magnitude of their four model parameters. Splinter et al. (2014) applied a different cross-shore shoreline change model to datasets obtained from seven diverse beaches across the USA, Europe and Australia, each spanning more than 5 years. These authors similarly found large inter-site variability between the magnitude of model parameters.

In addition to site-specific dependencies on model parameter calibration, recent research suggests that the calibration period and associated characteristics of the wave climate may also introduce parameter biases (D'Anna et al., 2022, D'Anna et al., 2020; Ibaceta et al., 2020; Montaño et al., 2020). For instance, Splinter et al. (2017) analysed 8 years of wave and shoreline observations at the Gold Coast, Australia, finding a substantial difference in optimized model parameters between two independently calibrated 4-year time periods. This was shown to be consistent with a relatively subtle difference in the annual distribution of storm wave events during each of the two consecutive 4-year observation periods. More recently, D'Anna et al. (2022) used a climate-based wave emulator to produce ensemble-based past and future projections of shoreline evolution spanning the 21st century at Truc Vert, France. Using two different semi-empirical shoreline change models, it was shown that different wave chronologies produced by the emulator can significantly alter the modelled shoreline response. Based on these findings, the authors advocated for more research into the underlying link(s) between model parameters and wave climate variability.

To achieve this objective, data assimilation techniques offer the possibility to estimate non-stationary (i.e., time-varying) parameters and explore their links to changes in natural forcing (Pathiraja et al., 2018; Deng et al., 2019, Pathiraja et al., 2016a; Xiong et al., 2019; Zeng et al., 2019). More specifically, Kalman filter variants (Kalman, 1960) are data assimilation techniques that are already employed in semi-empirical shoreline change modelling to assist with model calibration (e.g., Long and Plant, 2012; Vitousek et al., 2017b; Muir et al., 2020; Alvarez-Cuesta et al., 2021a). By this approach model parameters are continually adjusted as additional state (i.e., shoreline) observations become available (Evensen, 2009). Optimized shoreline predictions are achieved by efficiently weighting and combining the spread of the shoreline observations (represented by the shoreline measurement accuracy) with the spread of the model simulations (referred to as 'parameter process-noise'). Most commonly, these existing applications have used a Kalman filter to estimate the stationary (i.e., time-invariant) magnitude of shoreline model parameters, by assuming a very low level of parameter process-noise (Vitousek et al., 2017b; Alvarez-Cuesta et al., 2021b; Vitousek et al., 2021). However, Ibaceta et al. (2020) presented a dual state-parameter Ensemble Kalman Filter (EnKF) variant (Pathiraja et al., 2016a, Pathiraja et al., 2016b) and showed its suitability to explore non-stationary, or time-varying parameters within the context of the established cross-shore shoreline change model, *ShoreFor* (Davidson et al., 2013; Splinter et al., 2014). Specifically, it was found that using a sufficiently high magnitude of parameter process-noise, the EnKF was able to track non-stationary parameters as demonstrated by several synthetic scenarios that were designed to emulate differing modes of shoreline behaviour. The method was also applied to an 8-year real-world shoreline dataset presented in Splinter et al. (2017), that – as was previously noted above - exhibited a distinct shift in shoreline behaviour. In this prior work the EnKF technique successfully reproduced the observed shift in shoreline behaviour and revealed that the resulting non-stationary model parameters were related to changing characteristics of the wave forcing. While this application was limited to past periods where shoreline observations were available for data assimilation, the next challenge is to investigate strategies for extrapolating the detected time-varying parameters out of the training period where the EnKF is applied. To this end, the recent availability of longer and publicly available satellite-derived shoreline datasets (Luijendijk et al., 2018; Vos et al., 2019b; Almeida et al., 2021; Castelle et al., 2021) offers for the first time the opportunity to significantly expand the application of the EnKF methodology, with a particular focus on future shoreline change predictions under climate projections where multi-year variability in wave climate forcing is expected (e.g., D'Anna et al., 2021).

In this work, the EnKF technique that was introduced in Ibaceta et al. (2020) is now applied to an extended multi-decadal dataset of satellite-derived shorelines at the Gold Coast, Australia. As described in Section 2 (Methodology), the technique is first used to estimate the magnitude of non-stationary parameters when applied to the established cross-shore shoreline change model, *ShoreFor* (Davidson et al., 2013; Splinter et al., 2014). Importantly, the magnitude of these time-varying parameters is then physically related and numerically parametrized as a function of the multi-year variability in wave forcing. Using these new insights, Section 3 incorporates the results of this EnKF time-varying model parameter estimation to predict nearly three decades of observed shoreline changes at the Gold Coast. A comparison of these newly obtained results to the more common 'stationary' modeling approach is discussed in Section 4, along with a discussion of the physical interpretation of time-varying model parameters.

2 Methodology

2.1 Study site and data

The Gold Coast is located on the east coast of Australia (Figure 1A). This region spans ~30 km of relatively straight, open-coast sandy beaches characterized by energetic intermediate beach states that typically exhibit double-barred morphology (van Enckevort et al., 2004; Price and Ruessink, 2011). Beach sediments have a median grain size of 0.25 mm and tides are microtidal with mean spring tidal range of 1.5 m (Davidson and Turner, 2009; Splinter et al., 2017). The predominant direction of wave incidence is from S to SE directions, with mean offshore significant wave height (H_s) and spectral peak wave periods (T_p) of 1.1 m and 9.4 s, respectively (Davidson and Turner, 2009). The wave climate of this region generally displays a seasonal nature with more easterly (and smaller) waves in the summer and more southerly (larger) waves in the winter (Zarifsanayei et al., 2022). In general, this results in a seasonal response to shoreline variability as well, with more accreted beaches in the summer and more eroded beaches in the winter that are also modulated at interannual time scales by changes in storminess patterns (Splinter et al., 2017). At interannual time scales, the wave climate is also modulated by the El Niño-Southern Oscillation (Phinn and Hastings, 1995; Barnard et al., 2015).

Time series of three-hourly wave data (H_s and T_p) are available from a waverider buoy located approximately 4 km to the north and 2 km offshore of the study site in 17 m water depth (Figure 1C). Gaps in the wave buoy time series were filled using values from the closest grid point of the CAWCR reanalysis dataset (Durrant et al., 2014, see Figure 1C). A comprehensive assessment of this wave dataset quality for the Australian region is presented in Hemer et al. (2017).

The portion of coastline examined in this work coincides with the same stretch of coast that was previously analysed over shorter time periods by Splinter et al. (2017) and Ibaceta et al. (2020). Specifically, a 1 km stretch of sandy beach at Surfers Paradise (Figure 1B) was selected. Previous investigations showed that this stretch of coastline is outside the influence of down-drift engineering interventions (Turner, 2006), including the construction of an artificial reef and the placement of a sand

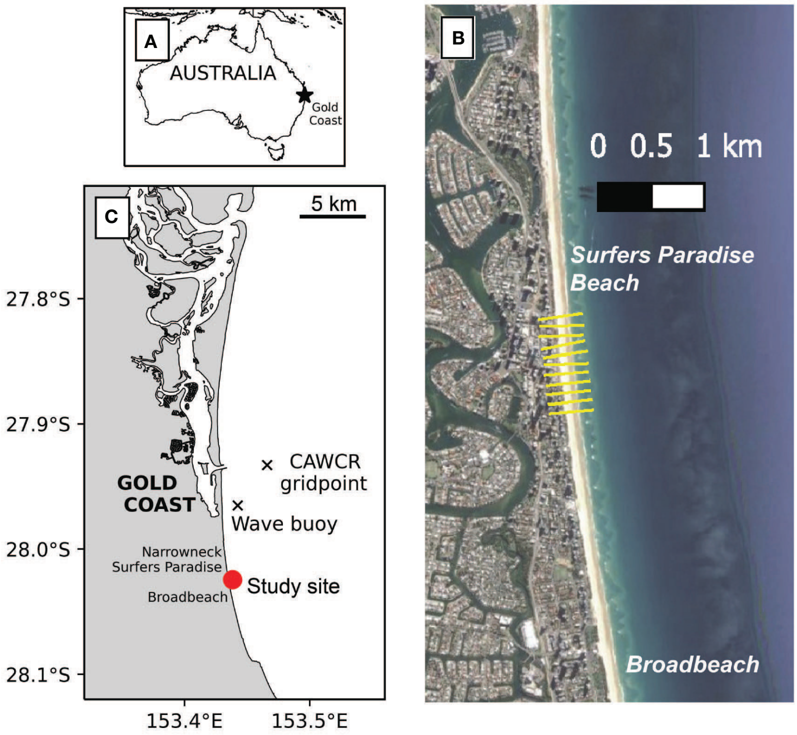

FIGURE 1
Study site and data. **(A)** Location of the Gold Coast on the east coast of Australia. **(B)** Satellite image (source: Google Earth) of the study site and the location of ten shore-normal transects (yellow lines) used for extraction of satellite-derived shoreline time series. **(C)** Map of the Gold Coast location showing specific location of the study site (red point). Black crosses indicate the location of the waverider buoy and the CAWCR gridpoint used to fill gaps in wave measurements.

nourishment (Boak et al., 2000; Black and Mead, 2001; Turner, 2006). And importantly, Splinter et al. (2011) also showed that minimal gradients of alongshore sediment transport have been observed at this location, necessary for the assumptions of the cross-shore shoreline change model used here (Section 2.2).

The *CoastSat* toolbox (Vos et al., 2019b) was used to extract satellite-derived shorelines at ten shore-normal transects spaced every 100 m alongshore (Figure 1B, yellow lines). Briefly, *CoastSat* retrieves time series of cross-shore shoreline position (accuracy ~10-15 m) at any sandy beach from 30+ years of publicly available satellite imagery (Landsat 5,7, 8 and Sentinel 2) at a revisit period of ~2 weeks. At the Gold Coast, 28 years of suitable satellite imagery is available spanning the period 1992-2020. To remove high-frequency shoreline changes related to tidal variations, the resulting time series at each transect were tidally corrected to a fixed datum (MSL) using water levels from a global tide model and an average beach slope (Vos et al., 2020). An average beach slope was used in line with previous studies on satellite-derived shorelines, where using a time-evolving beach slope did not result in better shoreline mapping (Castelle et al., 2021). The reader is referred to Vos et al. (2021) for further details on this dataset.

As the final step in shoreline data pre-processing, the resulting 28-year time series of tidally corrected shorelines were alongshore-averaged over the 1 km long study site, to remove the effect of smaller-scale shoreline features such as beach cusps, commensurate to previous studies at this same site (e.g., Splinter et al., 2017).

Figure 2 summarizes the complete 28-year wave and shoreline Gold Coast dataset. In Figure 2A the wave data is represented by the single parameter dimensionless fall velocity, $\Omega = H_{s,b}/wT_p$, where w is the sediment fall velocity, which in turn is a function of the site-specific median grain size (i.e., d_{50} = 0.25 mm). T_p is the 3-hourly peak wave period measured at the wave buoy, and the significant breaking wave height ($H_{s,b}$) is estimated from the 3-hourly offshore conditions by reverse-shoaling of the inshore (17 m depth) wave buoy data (after Splinter et al., 2014). In summary, a clear seasonality in the Gold Coast wave climate is evident (Figure 2A), and in addition to this, calculation of the 5-year backwards running mean of Ω (i,e., $\bar{\Omega}$) also reveals longer-term interannual wave climate variability (Figure 2B). The corresponding alongshore-averaged shoreline time series is shown in Figure 2C. Of relevance to this work, both seasonal and interannual shoreline changes are evident during

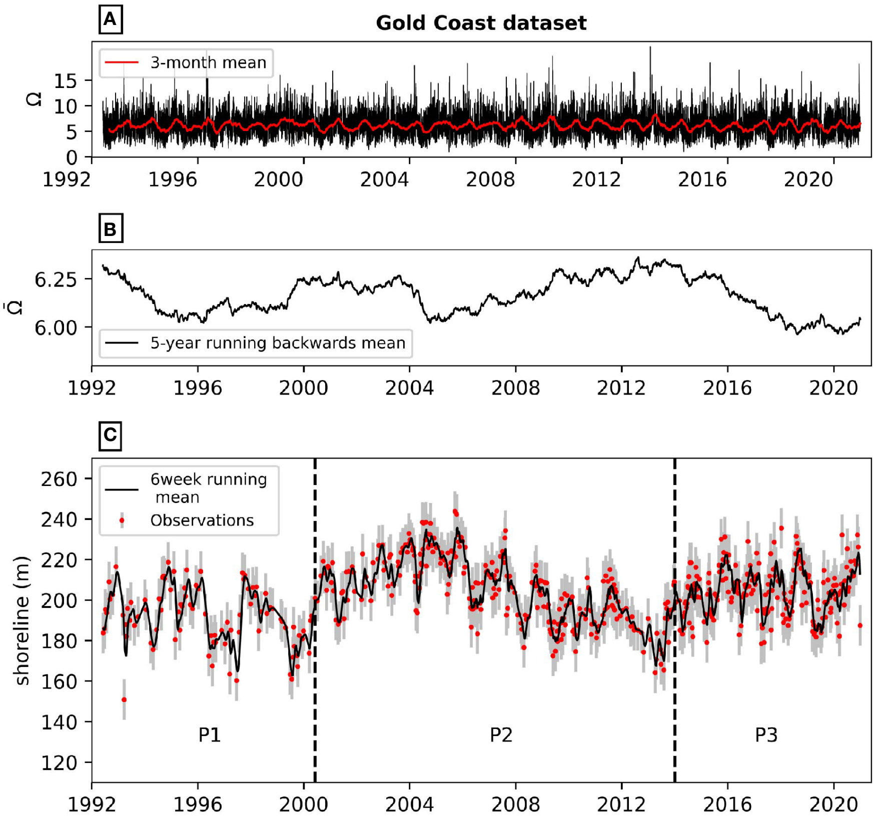

FIGURE 2
Wave and shoreline datasets. **(A)** Time series of dimensionless fall velocity spanning the 1992-2020 period (black line). The red line is the 3-month running mean. **(B)** Interannual variability of the dimensionless fall velocity, here represented by a 5-year running backwards mean. **(C)** Time series of shoreline evolution at the Gold Coast relative to a local datum. This data was obtained from satellite-derived shorelines (red dots with grey error bars representing the accuracy of the satellite-derived shorelines, here given by R =10 m). The black line is the 6-week centered running mean used to facilitate visualization of the seasonal to interannual variability at this study site. The dataset is split into 3 different time periods (P1, P2, P3). P2 is used for training and all three are used for testing purposes.

the 1992-2020 period with the shoreline position negatively correlated with the multi-year wave climate variability $\bar{\Omega}$, (r = - 0.3, p< 0.01). The previously identified links between $\bar{\Omega}$ and model parameters of the *ShoreFor* shoreline change model (Splinter et al., 2014) are now investigated and quantified in the following sections.

2.2 Shoreline change model: *ShoreFor*

The generalized version of the semi-empirical shoreline change model, *ShoreFor* (Splinter et al., 2014) is used in the present study to model cross-shore driven shoreline evolution at the Gold Coast study site. *ShoreFor* is based on the behavioural concept that shorelines continuously evolve towards a time-varying equilibrium position (Davidson et al., 2013), with the cross-shore rate of shoreline change (dx/dt) given by:

$$\frac{dx}{dt} = c^a F^a + c^e F^e + b \tag{1}$$

In this formulation, the forcing term $F^{a,e} = P^{0.5}\Delta\Omega_{a,e}/\sigma_{\Delta\Omega}$ $F^{a,e}$ is a function of the wave power at the breaking point (P) and the disequilibrium dimensionless fall velocity ($\Delta\Omega$). The wave power at the breaking point is calculated as $P = {}^1/_{16}\rho g H_{s,b}^2\sqrt{gh_b}$ assuming a breaking criterion $h_b = H_{s,b}/0.78$ (Splinter et al., 2014). The variables ρ, g are the water density and acceleration due to gravity, respectively. Importantly, the disequilibrium dimensionless fall velocity ($\Delta\Omega$) dictates the potential direction of cross-shore sediment transport as either offshore ($\Delta\Omega_e$,when $\Delta\Omega < 0$) during erosive conditions or onshore ($\Delta\Omega_a$,for $\Delta\Omega > 0$) during accretionary conditions. From this, the disequilibrium component $\Delta\Omega = (\Omega_{eq} - \Omega)$ and its associated standard deviation $\sigma_{\Delta\Omega}$ are computed from the 3-hourly dimensionless fall velocity $\Omega = {}^{H_{s,b}}\!\big/_{T_p w}$ at the wave breaking point, where T_p is the peak wave period and w is the sediment fall velocity. The time-varying equilibrium expression (after Wright et al., 1985) is given by:

$$\Omega_{\mathrm{eq}} = \left[\sum\nolimits_{i=1}^{2\phi} 10^{-i/\phi}\right]^{-1} \sum_{i=1}^{2\phi} \Omega_{\mathrm{i}} 10^{-i/\phi} \tag{2}$$

Of particular relevance to the new work presented here is the physical interpretation of the underlying model parameters in Equation 1. These include three wave-driven cross-shore sediment transport-related parameters c^a, c^e and ϕ that in this study are estimated and permitted to vary independently using the EnKF technique (as described in Section 2.3 below). The two rate parameters c^a and c^e (units: $m^{1.5}s^{-1}W^{-0.5}$) are proxies for the accretion/erosion sediment transport efficiency and the response factor parameter ϕ (in days) represents a beach response time. This model parameter (ϕ) has also been described as a proxy for 'beach memory' as it represents the time length to which predicted shorelines 'remember' antecedent wave conditions (Vitousek et al., 2021).

Based on previous testing of the *ShoreFor* model at a diverse range of seasonal and storm-dominated sandy coastlines in Australia, Europe and the USA, Splinter et al. (2014) showed that the magnitude of these parameters can be related to the mean interannual (≥ 5 years) dimensionless fall velocity $\bar{\Omega}$ (e.g., Figure 2B), consistent with well-established relationships (e.g., Wright and Short, 1984) between modal beach states and cross-shore processes. Conceptually, mild-slope beaches experience slower rates of shoreline changes (i.e., $\phi > 100$ days) and decreased sediment exchange efficiency (lower c^a and c^e values) between the surf zone and beach face. Conversely, the breaker line tends to be closer to the beach face at steeper beaches, enhancing efficient (larger c^a and c^e magnitudes) and rapid (i.e., $\phi < 100$ days) sediment exchange. Note that the additional b term in Equation 1 is a residual term accounting for any unresolved processes. The reader is referred to Splinter et al. (2014) and Davidson et al. (2013) for a full description and formulation of the *ShoreFor* model.

2.3 Shoreline modelling with non-stationary parameters

The new methodology that is developed here for predicting shoreline change using non-stationary parameters is comprised of four steps:

(1) Non-stationary model parameters are estimated using the EnKF methodology presented in Ibaceta et al. (2020). The same EnKF algorithm is also tuned to calculate stationary (i.e., time-invariant) or 'converged' parameters (e.g., Long and Plant, 2012; Vitousek et al., 2017b) to compare with this new non-stationary approach;

(2) Correlation analyses between estimated non-stationary parameters and wave forcing covariates (e.g., $\bar{\Omega}$) are undertaken using the Pearson correlation coefficient (r).;

(3) Linear regression is used to develop expressions of the non-stationary parameters based on the results from (2) and a Pearson correlation coefficient $|r| > 0.7$; and

(4) The performance of the *ShoreFor* model predictions for the full 28-year time period is assessed using the newly modelled non-stationary parametrizations, and compared with the predictions of the conventional stationary approach.

Each of these four steps is outlined in further detail below.

2.3.1 Parameter estimation using the EnKF (Step 1)

The EnKF technique first presented in Pathiraja et al. (2016a) and adapted to the *ShoreFor* model in Ibaceta et al. (2020) is used to estimate model parameters (c^a, c^e, ϕ, b) for the multi-decadal Gold Coast dataset. The EnKF is a Monte Carlo application of the well-known Kalman Filter (Kalman, 1960), which produces optimal state and parameter estimates for Gaussian systems by optimally combining noisy observations and model simulations (Evensen, 2009). Optimized state (e.g., shoreline) predictions are achieved by efficiently weighting the model predictions and shoreline observations, represented by ensembles of simulations (i.e., process-noise) and noisy data characterized by an observational error (R), respectively. In addition, the EnKF provides the best estimate of the (time-varying) model parameters resulting in this optimized shoreline predictions.

While it is possible to define a parameter evolution model within the EnKF (i.e., an equation describing parameter variability in time), this requires some *a priori* knowledge about the parameter non-stationarity (Pathiraja et al., 2016a). Here, no *a priori* knowledge is assumed and thus a random-walk approach is adopted, allowing the model parameters to vary freely in time when observations become available (Deng et al., 2019). In brief, at each 3-hourly time-step corresponding to each new observation of the forcing wave data $H_{s,b}$ and T_p, the shoreline model uses inflated (i.e., process-noise included) background parameter ensembles modelled as a random-walk to estimate shorelines at the next time-step. This procedure continues until a new shoreline observation is available, which in turn is dependent on the particular sampling frequency, here given by the satellite's revisiting period of approximately two weeks (Vos et al., 2019b). At this point, parameter ensembles are updated based on the shoreline observation ensembles (i.e., mean with error statistics representing the measurement accuracy, R). These updated parameters are then used to provide new shoreline estimates that are then state-updated using the same observations of the parameter update step. Importantly, Ibaceta et al. (2020) found that a sufficiently high magnitude of parameter process-noise successfully tracked the magnitude of non-stationary parameters as demonstrated by several synthetic scenarios emulating natural shoreline behaviour. Otherwise, low (or null) process noise magnitudes resulted in updated estimates with lower variance than the previous time-step and time-invariant parameter estimation (e.g., Long and Plant, 2012; Vitousek et al., 2017b).

The EnKF technique was run over 50% of the dataset (P2 time period, 2000-2014, Figure 2C) for model training purposes. This period was selected due to the higher temporal resolution of the satellite-derived shorelines coinciding with the launch of an additional satellite in April 1999 (Landsat 7, Vos et al., 2019a). This higher temporal frequency can improve non-stationary parameter estimation, as demonstrated in Ibaceta et al. (2020). To avoid filter divergence by large differences in the order of magnitude of the different cross-shore driven parameters, the EnKF algorithm was set-up to estimate the magnitude of $\varphi = log_{10}(\phi)$, from which the magnitude and uncertainty of ϕ is then calculated. Initial model parameter estimates (c_o^a, c_o^e, ϕ_o, b_o) were determined from the generalized parametrizations provided in Splinter et al. (2014) applied to the first 4 years of the wave record, along with the initial seed value of $b_o = 0$. Initial parameter ensembles are generated from truncated normal distributions to ensure that parameters fall within their feasible range (Splinter et al., 2014). Following the analyses of Ibaceta et al. (2020), single EnKF experiments (NE=1) are run using n = 500 ensemble members. In addition, a shoreline observation accuracy value of R = 10 m is allocated to each measurement, to represent the expected satellite-derived shoreline position accuracy. This magnitude is consistent with a previous assessment of the accuracy of satellite-derived shorelines along the east coast of Australia (Vos et al., 2019a).

To estimate non-stationary parameters, the EnKF technique was set-up so that $b = 0$ in Equation 1, to align with previous field observations showing that gradients in alongshore transport along this 1 km stretch of coastline are minimal (Splinter et al., 2011). This is arranged in the EnKF algorithm by allocating a null magnitude of process-noise to this term such that the initial seed value ($b_o = 0$) does not vary in time. In contrast, the magnitude of process-noise of the cross-shore driven parameters (c^a, c^e and ϕ) is set sufficiently high enough to track non-stationary parametrizations. By this approach, the contribution of model parameters to the EnKF shoreline time series hindcast is explained by temporal changes in the cross-shore driven parameters (c^a, c^e and ϕ) only.

In addition to the above non-stationary approach to time-varying parameter estimation, the EnKF algorithm was also modified to track stationary (i.e., converged or time-invariant) wave-driven parameters at the end of the P2 training period (e.g., Long and Plant, 2012; Vitousek et al., 2017b; Alvarez-Cuesta et al., 2021a). This was achieved by modifying the magnitude of process-noise for all model parameters. Following previous approaches (e.g., Vitousek et al., 2021), a null magnitude of process-noise for the cross-shore wave driven parameters (c^a, c^e and ϕ) and a finite but sufficiently high magnitude for b is expected to provide time-invariant estimates of c^a, c^e, ϕ and a time-varying estimation of the residual term b representing unresolved model processes (Vitousek et al., 2017b).

2.3.2 Correlation analysis between model parameters and wave climate covariates (Step 2)

Using the results from Step 1 and following the guidance of previous studies in which non-stationary parameter estimation has been undertaken within the context of hydrological models (e.g., Westra et al., 2014; Deng et al., 2019; Xiong et al., 2019; Zeng et al., 2019), the physical links between non-stationary parameters obtained in Step 1 and the underlying variability in natural forcing was explored *via* correlation analysis. This step assumes that the contribution of the underlying wave forcing overwhelms the effect of sea-level changes over this training period (e.g., D'Anna et al., 2021, D'Anna et al., 2020). Furthermore, the effects of sea-level changes over the past three decades are neglected since previous studies suggested that beaches in southeast Australia are unlikely to begin receding by sea-level rise within the present century (Short, 2022).

Consistent with previous research on beach morphodynamics and shoreline change modelling (e.g., Wright and Short, 1984; Davidson and Turner, 2009; Yates et al., 2009; Ludka et al., 2015), three wave climate indicators of coastal change were used to compare to the temporal variability of c^a, c^e and ϕ found from the non-stationary EnKF in Step 1 above. These variables included the dimensionless fall velocity (Ω), the significant wave height at the breaking position, $H_{s,b}$ and its square magnitude $H_{s,b}^2$, the latter a proxy for wave energy. Rather than correlating the three-hourly time series of these variables, the focus here was on lower-frequency seasonal to interannual variability. Therefore, the backwards-calculated running average and standard deviation (*std*) of the three-hourly Ω, $H_{s,b}$ and $H_{s,b}^2$ time series were obtained at varying time window lengths. Given the acknowledged dependence of model parameters on the duration and selection of the calibration period (e.g., Splinter et al., 2013; D'Anna et al., 2020), running-average windows ranging in length from 6 months to 10 years (updated every 3 months) were used for averaging prior to correlation analysis. The Pearson correlation coefficient (r) between the six wave climate indicators and three model parameters was then calculated using values from time steps when shoreline observations were available in the EnKF recursion (Step 1). The statistical significance (95% level) of the correlations was verified using a two-sample Student t-test. To reduce the impact of uncertain initial conditions in Step 1, the first 6 months of model run were disregarded from the correlation analysis and considered as a 'warm-up' period (Deng et al., 2019; Ibaceta et al., 2020).

Modelling non-stationary parameters (Step 3)

Using the results from Step 2, the EnKF non-stationary parameters found during the P2 time period (Figure 2C) were then modelled as linear functions of the identified wave climate indicators:

$$\hat{\theta}_t = \beta Z_t + \delta \tag{3}$$

where $\hat{\theta}_t$ is the modelled non-stationary parameter at time t (i.e., $\hat{c^a}$, $\hat{c^e}$ or $\hat{\varphi}$, where $\varphi = log_{10}(\phi)$ as described in Step 1), Z_t is the running average or standard deviation of a selected wave climate covariate (Ω, $H_{s,b}$ or $H^2_{s,b}$) and β, δ, are the hyperparameters representing the slope and intersect of the regressed linear function, respectively. These hyperparameters are estimated using least squares regression from pairs (θ_t, Z_t) of values obtained from time steps when shoreline observations become available in the EnKF recursion. The assumption here is that the three cross-shore driven parameters can be independently modelled as a function of an external wave climate covariate (Ω, $H_{s,b}$ or $H^2_{s,b}$)

Only correlations at window lengths leading to statistically significant (95% C.I.) and strong correlations (here defined as |r| > 0.7) were used to develop relationships described by Equation 3. This magnitude of correlation is more conservative than previous hydrological studies that used a lower cut-off value (|r| > 0.6) but found better model predictions from the strongest magnitude correlations (Deng et al., 2019; Zeng et al., 2019).

2.3.4 Predicting shoreline change and performance criteria (Step 4)

In this final step to include non-stationary parameters in the modelling of shoreline change, all possible combinations (i.e., |r| > 0.7) of linearly modelled $\hat{c^a}$, $\hat{c^e}$ and $\hat{\varphi}$ relationships determined in Step 3 were used to generate deterministic multi-decadal time series of shoreline evolution using Equation 1, spanning the complete 28-year period. Equation 1 was calculated forward in time at a three-hourly time-step, starting from the first available magnitude of shoreline position in Figure 2C (~ January 1992). The performance of each hindcasted shoreline time series was assessed during P2 to align with the time period used in the previous Steps 1-3. The hyperparameters defining the optimal $\hat{c^a}$, $\hat{c^e}$ and $\hat{\varphi}$ combination resulting in the best *ShoreFor* model prediction during P2 were selected and used for test purposes (i.e., 'blind predictions') during P1 and P3 (Figure 2C). Two different metrics were used to assess the performance of shoreline predictions; the root mean square error (RMSE, Equation 4) and the skill index (Equation 5) between the modelled, s, and observed data, s_m:

$$\text{RMSE} = \sqrt{\sum_1^n \frac{(s - s_m)^2}{n}} \tag{4}$$

$$skill = 1 - \frac{\sum |s - s_m|^2}{\sum (|s - s_m| + |s_m - \overline{s_m}|)^2} \tag{5}$$

where n is the total number of samples, | | indicates absolute value, and an overbar represents the mean of the sample. The skill index (e.g., Jaramillo et al., 2021) is a standardized metric bounded between 0 and 1. A skill value equal to 0 is indicative of complete disagreement between modelled and observed shoreline time series, whereas a maximum skill (1) is indicative of a perfect agreement.

To compare the new non-stationary parameter modelling approach with the existing stationary parameter approach, a long-term stationary prediction was also obtained from Equation 1. The modelled shoreline time series makes use of time-invariant parameters obtained from 'converged' magnitudes of c^a, c^e and ϕ at the end of the stationary EnKF recursion, previously described in Step 1. While b is allowed to vary in time during the shorter 14-year stationary EnKF run of Step 1, note that this longer-term 28-year stationary prediction assumes $b = 0$ during the 28-year period (e.g., Vitousek et al., 2017b), since this parameter represents unresolved processes that can't be explained by the mathematical structure of the employed shoreline model during future predictions.

3 Results

3.1 EnKF parameter estimation (Step 1)

Application of the EnKF algorithm shown in Figure 3 (left panels) to estimate non-stationary parameters for the Gold Coast dataset during the 14-year training period P2 (2000-2014) shows a clear temporal variability in the *ShoreFor* model parameters. Figure 3A indicates shoreline time series obtained from the EnKF, while Figures 3C, E, G show the corresponding values of non-stationary model parameters c^a, c^e, $\phi = 10^{\varphi}$ and b. As was previously observed in Ibaceta et al. (2020) using a shorter (8-year) shoreline dataset derived from more limited video-imagery, the left panels of Figure 3 demonstrate that parameter estimation is sensitive to the study time period. Provided a sufficiently high magnitude of process-noise for the cross-shore driven parameters (c^a, c^e and ϕ) is assumed, the corresponding uncertainty bands remain approximately constant so that the EnKF continuously adjusts the magnitude of the model parameters as shoreline observations become available. On the other hand, a null magnitude of process-noise for the b term results in minimal contribution from this term to the overall shoreline variability ($b \sim 0$, Figure 3G). The rate parameters (c^a and c^e) vary on seasonal to interannual time scales and are approximately proportional to each other over the training period P2. Both parameters remain approximately constant until around 2004, when they rapidly increase and then exhibit a decreasing trend until the end of the training period in 2014. The response parameter ϕ (Figure 3E), here numerically represented as $\phi = 10^{\varphi}$ also varies at interannual time scales with some additional higher frequency variability attributed to the more challenging estimation of this parameter (Ibaceta et al., 2020). Figure 3E shows that ϕ is relatively high (ϕ > 100 days) at the start of P2, and then shifts

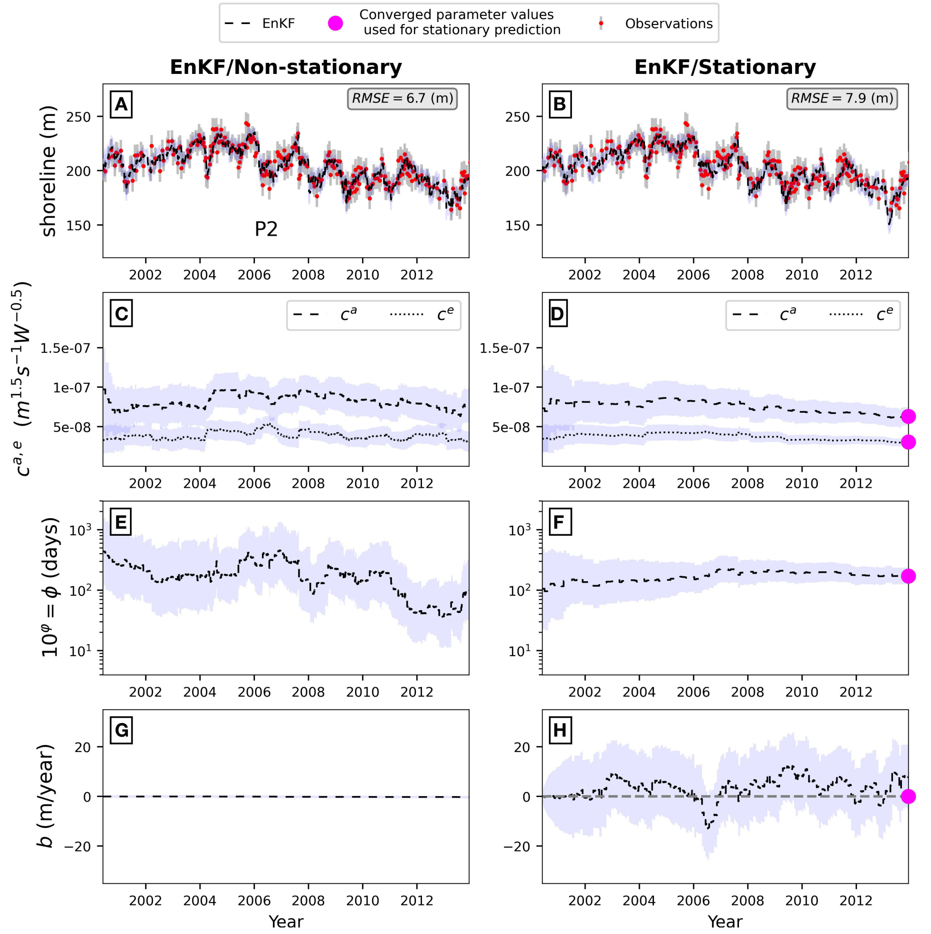

FIGURE 3
EnKF application to a multi-year (2000-2014) portion of the long-term dataset at the Gold Coast. Left and right panels show the non-stationary and stationary approaches, respectively. From top to bottom, each approach shows the shoreline observations and shoreline EnKF estimates (black line), c^a and c^e (dashed and dotted lines, respectively), $\phi = 10^{\varphi}$ and *b*. Blue bands indicate uncertainty, represented by the standard deviation of the ensemble (*n=500*). Magenta dots in the right panels indicate the converged parameters used for predicting shoreline time series with a stationary approach.

towards smaller magnitudes ($\phi < 100$ days) in subsequent years, more indicative of a storm-dominated shoreline behaviour. The time-varying response of these cross-shore driven model parameters suggest that shoreline predictions out of this training period (P2) may be enhanced by allowing these parameters to evolve in response to changes in wave forcing. This is analyzed in the next steps and discussed in Section 4.

Applying the EnKF algorithm using the stationary parameter approach during the same 14-year time period is shown in the right panels of Figure 3. For both the non-stationary and stationary approaches, the EnKF produces a skillful shoreline hindcast because shoreline observations are available for data assimilation (Figures 3A, B). However, in contrast to the non-stationary EnKF results that assumed process-noise in the wave-driven parameters (c^a, c^e and ϕ), the stationary case that assumes negligible process-noise in these same three parameters results in c^a, c^e and ϕ (Figures 3D, F) varying more slowly as their uncertainty bands continuously reduce, leading to parameter convergence and approximately constant parameter magnitudes around ~2013. Additional model parameter contribution to the overall shoreline variability in this stationary approach is given by temporal variability in the residual term *b* (Figure 3H). The variability of this residual term compensates the minimal variability of the cross-shore driven parameters (c^a, c^e and ϕ, Figures 3D, F) and shows seasonal to interannual variability attributed to processes not resolved by the contribution of stationary cross-shore parameters. These unresolved processes contributed up to +/- 10 (m/year) of shoreline change at this site over this period.

The potential to physically relate the time-varying parameters of the nonstationary approach (Figures 3C, E, c^a, c^e

and ϕ) to the underlying changes in wave forcing is now explored in the following section.

3.2 Correlation between estimated model parameters and wave climate covariates (Step 2)

Correlation analyses between non-stationary model parameters and wave climate covariates over the central 14-year time period (P2) are summarized in Figure 4. Panels A, B and C show the magnitude of the Pearson correlation coefficient (r, vertical axes) for c^a, c^e and φ, respectively. These include the correlation with the backwards running-average and standard deviation of Ω, $H_{s,b}$ and $H_{s,b}^2$ (see colour lines in legend) at window lengths varying from 6 months to 10 years (horizontal axes). For c^a and c^e, the strongest negative and statistically significant correlations are given for the running-average dimensionless fall velocity at approximately 5-year time windows ($\bar{\Omega}$, red continuous lines). Other wave climate covariates show similar but weaker correlation patterns. For the φ parameter (ϕ = 10^{φ}), all wave climate covariates show statistically significant and strong correlations for averaging windows larger than ~4-5 years. The existence of strong (|r| > 0.7) and statistically significant correlations enables the creation of linear parametrizations of c^a, c^e and φ as a function of the underlying physical changes in wave forcing.

3.3 Non-stationary parametrizations, model predictions and performance (Step 3-4)

Strong (|r| > 0.7) and significant (95% C.I.) correlations for different wave climate covariates and averaging windows resulted in 744 combinations of non-stationary $\hat{c^a}$, $\hat{c^e}$, $\hat{\varphi}$ parameterizations (i.e., Equation 3) and an equivalent amount of modelled shoreline time series spanning the multi-decadal period. Figures 4D-F shows

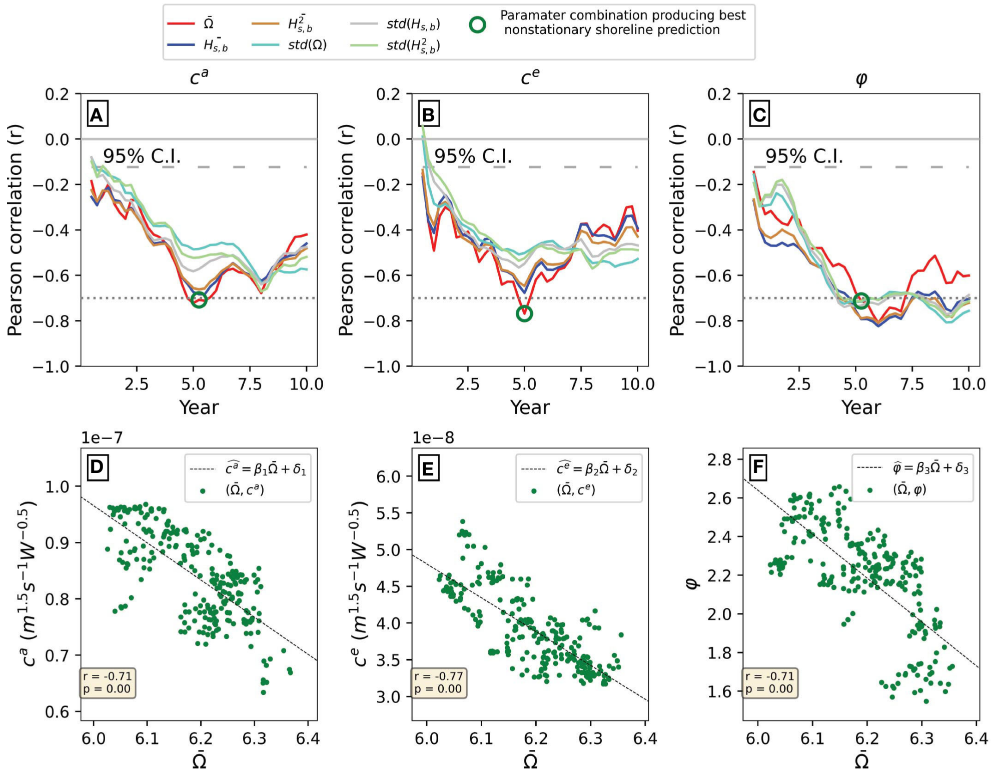

FIGURE 4
Summary results from Step 2 (Correlation analysis) and Step 3 (Parameterization) for each of the three wave-driven parameters (c^a, c^e and φ, left to right). Upper panels **(A-C)** show the Pearson correlation coefficient (vertical axes) for different wave climate covariates (coloured lines, see legend) at different averaging windows (horizontal axes). Horizontal and dotted black lines indicate the cut-off magnitude for strong correlations (|r|>0.7). Green open circles (panels a-c) indicate the time-window and wave climate covariate combination (here Ω at roughly ~5 years for all three parameters) resulting in the best shoreline prediction (using Equation 1) during the P2 period. Lower panels **(D-F)** show the data and linear parametrizations (Equation 3) resulting from the best non-stationary shoreline prediction.

the linear parametrizations ($\widehat{c^a}$, $\widehat{c^e}$, $\hat{\varphi}$) of the combination that produced the optimal shoreline hindcast (minimum RMSE and maximum skill). All three linear expressions are derived from $\bar{\Omega}$ averaged at a ~5-year running window (open green circles in Figures 4A-C). Figure 5 shows the shoreline model hindcast (green continuous line) corresponding to this combination of $\widehat{c^a}$, $\widehat{c^e}$, and $\hat{\varphi}$. Additionally, the shoreline model hindcast using a conventional stationary approach is shown in magenta using the converged values (magenta dots in Figure 3) and $b = 0$ for prediction purposes (e.g., Vitousek et al., 2017b). Setting $b = 0$ is also a reasonable assumption based on previous work that showed alongshore gradients in sediment transports are negligible at portion of the Gold Coast (Splinter et al., 2011) and neither the wave climate, nor the shoreline time series (see Figure 2) show a distinct long-term trend.

Visual inspection of the prediction based on stationary model parameters exhibits a distinct long-term negative trend between 1992-2014 that accumulates in time despite setting $b = 0$. This suggests an overall long-term imbalance in the wave-driven cross-shore processes captured in the *ShoreFor* model using the stationary approach for model calibration. Encouragingly, the new non-stationary model that now enables model parameters to vary as a function of the underlying wave forcing, results in improved shoreline predictions over the full 28-year period, compared to the stationary approach ($RMSE_{non\text{-}stationary}$ = 11.1 m; $RMSE_{stationary}$ = 254.3 m). Performance statistics over the three different periods for both stationary and non-stationary approaches are summarized in Table 1. Notably, the RMSE magnitudes of the non-stationary prediction are on the order of the satellite-derived shorelines accuracy (~10-15 m) used to develop the non-stationary parametrizations, while the skill metric is strong (~>0.7) for all periods.

Of particular interest to this study, the non-stationary prediction is able to reproduce the long-term shoreline behaviour from seasonal to interannual time scales. Interestingly, post-2014 both the stationary and non-stationary approaches predict seasonal oscillations of the shoreline in the absence of any noticeable long-term trend. These results indicate a large difference in model performance and predicted shoreline evolution between both approaches at multi-decadal time scales, including the increasing divergence of the stationary model hindcasts at time scales greater than ~10 years.

4 Discussion

4.1 The non-stationary versus stationary approach

While the assumptions of using stationary parameters to model shoreline change may be valid for shorter-term prediction horizons of seasons to a few years (e.g., Splinter et al., 2013; Splinter et al., 2014; Davidson et al., 2017; D'Anna et al., 2020), the new results presented here demonstrate that improved shoreline predictions at decadal time scales can be achieved through the inclusion of non-stationary model parameters in the *ShoreFor* model. Provided a sufficiently high magnitude of parameter process-noise is defined, the non-stationary EnKF approach (Figure 3, left panels) allows for the time-varying estimation of model parameters (c^a, c^e, ϕ and $b \sim 0$) that best hindcasted the observed shoreline response. While this non-stationary approach has been embraced within the hydrological and water resources modelling communities in recent years (e.g., Milly et al., 2008; Pathiraja et al., 2018), it differs from previous Kalman Filter applications to shoreline modelling (e.g., Alvarez-Cuesta et al., 2021a,b; Long and Plant, 2012; Vitousek et al., 2017b; Vitousek et al., 2021) that assumed negligible magnitudes of process-noise to achieve time-invariant parameter convergence (e.g., stationary approach). While these previous Kalman Filter shoreline applications were based on the Yates et al. (2009) model rather than *ShoreFor*, both models follow the same underlying principles of wave driven equilibrium-based shoreline change and perform similarly from seasonal to interannual time frames (Castelle et al., 2014; Montaño et al., 2020; D'Anna et al., 2021). Although the *ShoreFor* model equilibrium formulation is determined from past wave conditions alone (Equation 2), the Yates et al. (2009) formulation depends on the shoreline observations seen during calibration to relate shoreline position to wave energy. The implication of these two assumptions is that *ShoreFor* shoreline predictions are sensitive to the wave forcing, whereas the Yates et al. (2009) approach tends to result in the modelled shorelines oscillating more persistently around the same long-term position irrespective of the underlying variability in wave forcing (D'Anna et al., 2021). This difference was also discussed by Vitousek et al. (2021), who analytically demonstrated that the *ShoreFor* model

TABLE 1 Summary statistics of the stationary and non-stationary approaches for different time periods.

	Non-stationary		Stationary	
Period	**RMSE (m)**	**skill**	**RMSE (m)**	**skill**
Long-term (1992-2020)	11.1	0.78	254.3	0.08
P1 (1992-2000)	10.3	0.81	210.0	0.1
P2 (2000-2014)	8.4	0.87	246.2	0.1
P3 (2014-2020)	12.9	0.69	271.7	0.07

Reported statistics are all based on a model start date of ~Jan 1992 and using Equation 1 with $b = 0$.

structure has a 'perfect beach memory', such that initial shoreline conditions and subsequent evolution are accumulated in time and 'never forgotten' (see Figure 5, magenta line). If $b = 0$, the stationary version of *ShoreFor* cannot produce a stable (i.e., zero-trend) shoreline hindcast in the absence of a balanced wave climate where erosive and accretive conditions equally contribute to the long-term shoreline behaviour. While both model assumptions are likely to have some merit in long-term equilibrium shoreline behaviour, the present work demonstrates that adjusting the *ShoreFor* model structure in response to the multi-year variability in wave forcing overcomes the issue of perfect beach memory and provides more realistic long-term predictions that are not as sensitive to a particular training period as is evident in the stationary approach (Figure 5).

Both the choice of model and calibration period become important when considering long-term shoreline predictions. Previous studies used stationary cross-shore parameters to explore future shoreline changes (Vitousek et al., 2017b; Alvarez-Cuesta et al., 2021b) without the inclusion of a residual term ($b = 0$). Using stationary model parameters, D'Anna et al. (2022) concluded that *ShoreFor* was sensitive to the chronology of the wave time series at various time scales. When examining the results from the Gold Coast, the stationary model hindcast reproduces the overall magnitude of seasonal and some interannual variability observed in the data, but what is most noticeable is an erroneous long-term erosional trend predicted between 1992-2014 before the model appears to stabilize and oscillate at a seasonal scale around a mean value between 2014-2020 (Figure 5). This clearly demonstrates the sensitivity of the model to variability and/or trends in the wave forcing and that a non-stationary version of *ShoreFor* can improve long-term shoreline predictions when future regional wave climates are expected to change.

4.2 Physical interpretation of model parameters

It is now of interest to physically interpret the observed (Step 1) and modelled (Steps 2 and 3) non-stationary parametrizations at the Gold Coast study site. Correlation analysis of six different wave climate covariates (mean and *std* of Ω, $H_{s,b}$ and $H_{s,b}^2$) at different window lengths revealed strong correlations for the non-stationary parameters during P2 (Figure 4). Specifically, c^a and c^e, which were previously observed to co-vary proportionally (Figure 3C), showed strong negative correlations with $\bar{\Omega}$ at 5-year running average windows. This negative relationship with $\bar{\Omega}$ agrees with previous physical interpretations of these parameters as proxies for sediment transport efficiency (Splinter et al., 2014). Conceptually, this result implies that more/less energetic beach state systems ($\bar{\Omega}$) are less/more efficient (c^a and c^e) at transporting sediment between the surf zone and beach face. For instance, high-energy dissipative beach states typically have a deep offshore sand bar that rarely welds to the beach face. Lower-energy reflective beach states meanwhile are much more vulnerable to erosion and the sediment subsequently returns to the beach face during calmer periods (Phillips et al., 2017).

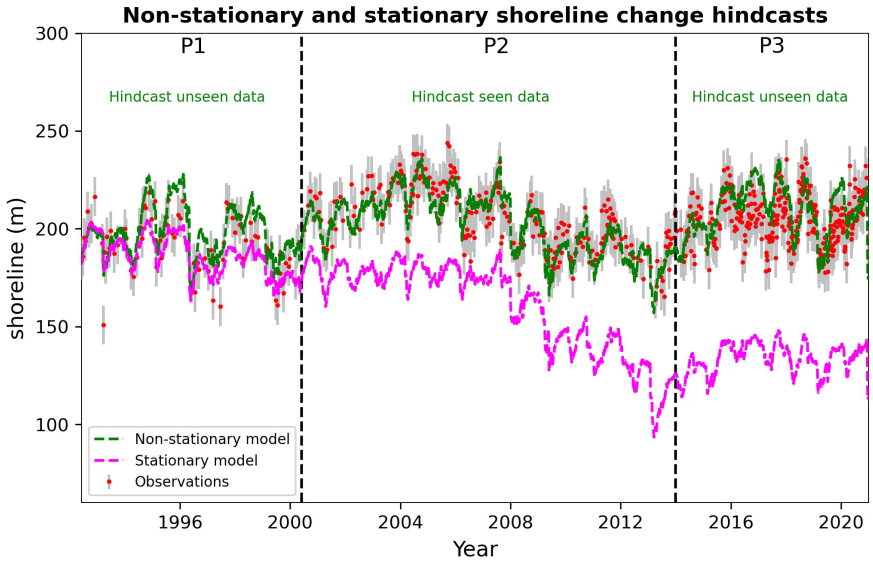

FIGURE 5
Comparison of shoreline predictions using non-stationary (green line) and stationary (magenta line) parameters with the ShoreFor model when $b = 0$. Both hindcasts were initialized from the same shoreline position in ~January 1992 and run forward in time using Equation 1.

Interannual changes in waves and the intra-annual distribution of storminess (e.g., Splinter et al., 2017) may also influence the nearshore morphology (Price and Ruessink, 2011; Price and Ruessink, 2013) and net offshore bar migration events (Ruessink et al., 2009) at this site that all contribute to the observed shoreline dynamics. The observed co-variability and proportionality between c^a and c^e suggests that, in the absence of a residual term (b), multi-year changes in the wave forcing and the *ShoreFor* model parameters can reproduce the observed interannual shoreline variability (See Figure 5). However, over the longer-term spanning several decades, the integrated response of the slowly-varying wave climate produces a zero-trended shoreline response as discussed above.

The response parameter ϕ is used within the *Shorefor* model to low-pass filter the wave forcing to determine the equilibrium response (Equation 2). Incrementally increasing the response parameter for longer time periods has decreasing effect on the resulting filtered time series (see Figure 7 in Davidson et al., 2013). The response parameter ϕ, here represented by φ ($\phi = 10^{\varphi}$) showed strong negative correlations with all wave climate covariates at averaging windows longer than ~4-5 years (Figure 4C). The less distinct peaks (or troughs) in correlation observed for φ compared to c^a and c^e are likely due to the more challenging estimation of this parameter by the EnKF due to the model insensitivity to small changes in ϕ for ϕ > 100 days as demonstrated in Ibaceta et al. (2020). Specifically, the combination of modelled $\hat{c^a}$, $\hat{c^e}$ and $\hat{\varphi}$ (Figures 4D-F) resulting in the best shoreline hindcast during the 14-year time period P2 (Figure 5) did not coincide with the maximum observed individual correlation for φ of approximately ~6 years. Instead, the best shoreline prediction occurred for the parametrization of $\hat{\varphi}$ as a function of the ~5-year averaged $\bar{\Omega}$ (Figures 4A-C). Fortuitously, this 5-year window coincides with the minimum duration identified by Splinter et al. (2013) as optimal to calibrate the same shoreline numerical model used in this study for long-term hindcasts (> 5 years). To explore the negative relationship between $\bar{\Omega}$ and ϕ in further detail, Figure 6 shows the multi-decadal (year to year) and intra-annual (summer and winter) distribution of storm events at the Gold Coast (bar chart, left axis), as well the estimated and modelled ϕ (right axis). In line with previous work exploring the links between ϕ and time scales of shoreline evolution (Splinter et al., 2017; Montaño et al., 2021; Schepper et al., 2021, Splinter et al., 2014), P2 (2000-2014) shows an initial period (~2000-2003) of few (<10), seasonally distributed storms and slow beach response (ϕ > 100 days). Then, the shoreline response shifts towards a more rapid shoreline behaviour (decreasing ϕ) coinciding with more storm events per year (>10, ~2005-2012) that are also more evenly distributed throughout individual years (e.g., Splinter et al., 2017). This increasing number of storm events coincides with slowly varying increases in $\bar{\Omega}$ (Figure 2B) and match with the empirical negative relationship between $\bar{\Omega}$ and ϕ, providing a physically-interpreted approach to adjust the shoreline model structure to periods of varying levels of storminess.

5 Conclusions

This paper presents a new methodology for identifying and incorporating time-varying model parameters to predict shoreline response to changes in regional wave climate forcing, spanning seasonal to multi-year time periods of up to several decades. Extending on the Ensemble Kalman Filter technique developed by Ibaceta et al. (2020), new correlation analysis spanning a ~14-year period at the Gold Coast Australia study

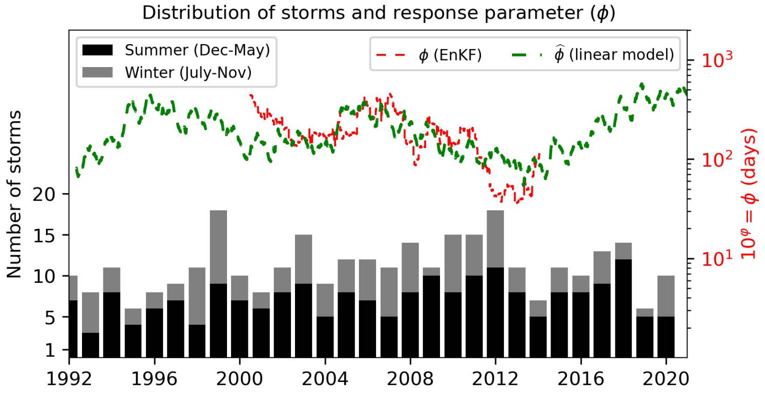

FIGURE 6
Bar chart and left axis: multi-decadal distribution of storm events per year and season (summer and winter). Storm events were obtained using a peak-over-threshold method over the long-term timeseries of significant wave height at the breaking position (i.e., $H_{s,b} > H_{95\%}$ and $H_{s,b} > H_{75\%}$ for at least 24 hours, Masselink et al., 2014). The green and red dashed lines (right axis) show the estimated (EnKF) and modelled magnitude of the ϕ parameter (pearson correlation with total number storms per year = -0.26, pvalue = 0.16).

site, shows that all three cross-shore associated parameters of the *ShoreFor* model were negatively correlated with the mean dimensionless fall velocity, $\overline{\Omega}$, at 5-year running average windows. By expressing this time-variability using simple linear regressions, an enhanced model that incorporates model parameter non-stationarity outperformed the predictions of a more conventional stationary approach over the 28-year period (see Figure 5).

Consistent with the conclusions of two recent review papers (Toimil et al., 2020; Splinter and Coco, 2021), the new analyses presented here demonstrate that adjusting the magnitude of time-varying model parameters at multi-year time scales can be interpreted as a physical adjustment of the shoreline response to changes in multi-year variability in the wave climate represented in the mathematical model structure. This may reduce the bias and uncertainty for future long-term shoreline predictions where the forcings associated with coastline change are expected to change (Morim et al., 2019; D'Anna et al., 2021). As suggested in D'Anna et al. (2022) the wider application of this methodology is now encouraged within different semi-empirical shoreline models and at a broad range of study sites that exhibit a range of differing wave and water level forcing, to further explore model adjustment to multi-year wave climate variability. It is realistic to anticipate that this can lead to the development of more generalized approaches (e.g., Splinter et al., 2014) to shoreline change modelling that are well suited to applications where time-variability of the model parameters is expected. By linking the magnitude of non-stationary model parameters to the underlying variability in wave forcing, this work presented the first effort to enhance multi-decadal shoreline predictions and provides an important step to achieve more reliable future shoreline projections in a changing wave climate.

Data availability statement

Wave data from the Gold Coast were provided by Gold Coast City Council (https://www.data.qld.gov.au/dataset/coastal-data-system-waves-gold-coast). The CAWCR dataset was provided by CSIRO (http://hdl.handle.net/102.100.100/137152? index=1). Satellite data was provided by Kilian Vos from the Water Research Laboratory, UNSW (https://zenodo.org/record/4760145.Ypl3rKhByUk).

Author contributions

RI: conceptualization, methodology, modelling and analyses, writing, reviewing, and editing. KDS: supervision, conceptualization, methodology, writing, reviewing, and editing. MDH: supervision, conceptualization, reviewing and editing. ILT: supervision, conceptualization, reviewing and editing,

Acknowledgments

The authors acknowledge the Queensland Government and the City of Gold Coast for providing the wave buoy data. CSIRO is acknowledged for providing the CAWCR wave hindcast dataset. R.I. was funded by UNSW Faculty of Engineering, the Agencia Nacional de Investigación y Desarrollo (ANID, previously CONICYT), The Commonwealth of Australia through an Australian Government Research Training Program Scholarship and the NSW Environmental Trust Environmental Research Program (RD2015/0128). K.S. is the recipient of an Australian Research Council Australian Future Fellowship (project number FT220100009) funded by the Australian Government.

Conflict of interest

The authors declare that the research was conducted in the absence of any commercial or financial relationships that could be construed as a potential conflict of interest.

Publisher's note

References

Almeida, L. P., Efraim de Oliveira, I., Lyra, R., Scaranto Dazzi, R. L., Martins, V. G., and Henrique da Fontoura Klein, A. (2021). Coastal analyst system from space imagery engine (CASSIE): Shoreline management module. *Environ. Model. Software* 140, 105033. doi: 10.1016/j.envsoft.2021.105033

Alvarez-Cuesta, M., Toimil, A., and Losada, I. J. (2021a). Modelling long-term shoreline evolution in highly anthropized coastal areas. part 1: Model description and validation. *Coast. Eng.* 169, 103960. doi: 10.1016/j.coastaleng.2021.103960

Alvarez-Cuesta, M., Toimil, A., and Losada, I. J. (2021b). Modelling long-term shoreline evolution in highly anthropized coastal areas . part 2 : Assessing the response to climate change. *Coast. Eng.* 168, 103961. doi: 10.1016/j.coastaleng.2021.103961

Barnard, P. L., Short, A. D., Harley, M. D., Splinter, K. D., Vitousek, S., Turner, I. L., et al. (2015). Coastal vulnerability across the pacific dominated by El Niño/Southern oscillation. *Nat. Geosci.* 8, 801–807. doi: 10.1038/ngeo2539

Black, K., and Mead, S. (2001). Design of the gold coast reef for surfing, public amenity and coastal protection: Surfing aspects. *J. Coast. Res.* 29, 115–130. http://www.jstor.org/stable/25736210

Boak, L., McGrath, J., and Jackson L, A. (2000). "IENCE ? a case Study ? the northern gold coast beach protection strategy," in *Coast. Eng. 2000, Proceedings*. ASCE. doi: 10.1061/40549(276)289

Castelle, B., Marieu, V., Bujan, S., Ferreira, S., Parisot, J. P., Capo, S., et al. (2014). Equilibrium shoreline modelling of a high-energy meso-macrotidal multiple-barred beach. *Mar. Geol.* 347, 85–94. doi: 10.1016/j.margeo.2013.11.003

Castelle, B., Masselink, G., Scott, T., Stokes, C., Konstantinou, A., Marieu, V., et al. (2021). Satellite-derived shoreline detection at a high-energy meso-macrotidal beach. *Geomorphology* 383, 107707. doi: 10.1016/j.geomorph.2021.107707

D'Anna, M., Castelle, B., Idier, D., Rohmer, J., Le Cozannet, G., Thieblemont, R., et al. (2021). Uncertainties in shoreline projections to 2100 at truc vert beach (France): Role of Sea-level rise and equilibrium model assumptions. *J. Geophys. Res. Earth Surf.* 126, e2021JF006160. doi: 10.1029/2021JF006160

D'Anna, M., Idier, D., Castelle, B., Le Cozannet, G., Rohmer, J., and Robinet, A. (2020). Impact of model free parameters and sea-level rise uncertainties on 20-years shoreline hindcast: the case of truc vert beach (SW France). *Earth Surf. Process. Landforms.* 45, 1895–1907. doi: 10.1002/esp.4854

D'Anna, M., Idier, D., Castelle, B., Rohmer, J., Cagigal, L., and Mendez, F. J. (2022). Effects of stochastic wave forcing on probabilistic equilibrium shoreline response across the 21st century including sea-level rise. *Coast. Eng.* 175, 104149. doi: 10.1016/j.coastaleng.2022.104149

Davidson, M. A., Splinter, K. D., and Turner, I. L. (2013). A simple equilibrium model for predicting shoreline change. *Coast. Eng.* 73, 191–202. doi: 10.1016/j.coastaleng.2012.11.002

Davidson, M. A., and Turner, I. L. (2009). A behavioral template beach profile model for predicting seasonal to interannual shoreline evolution. *J. Geophys. Res. Earth Surf.* 114. doi: 10.1029/2007JF000888

Davidson, M. A., Turner, I. L., Splinter, K. D., and Harley, M. D. (2017). Annual prediction of shoreline erosion and subsequent recovery. *Coast. Eng.* 130, 14–25. doi: 10.1016/j.coastaleng.2017.09.008

Deng, C., Liu, P., Wang, W., Shao, Q., and Wang, D. (2019). Modelling time-variant parameters of a two-parameter monthly water balance model. *J. Hydrol.* 573, 918–936. doi: 10.1016/j.jhydrol.2019.04.027

Durrant, T., Greenslade, D., Hemer, M., and Trenham, C. (2014). A global wave hindcast focused on the central and South Pacific (Technical Report No. 070). *The Centre for Australian Weather and Climate Research*. https://www.cawcr.gov.au/technical-reports/CTR_070.pdf

Evensen, G. (2009). *Data assimilation: The ensemble kalman filter. 2nd ed* (Heidelberg: Springer Berlin). doi: 10.1007/978-3-540-38301-7

Hemer, M. A., Zieger, S., Durrant, T., O'Grady, J., Hoeke, R. K., McInnes, K. L., et al. (2017). A revised assessment of australia's national wave energy resource. *Renew. Energy* 114, 85–107. doi: 10.1016/j.renene.2016.08.039

Ibaceta, R., Splinter, K. D., Harley, M. D., and Turner, I. L. (2020). Enhanced coastal shoreline modelling using an ensemble kalman filter to include non-stationarity in future wave climates. *Geophys. Res. Lett.* 47, e2020GL090724. doi: 10.1029/2020GL090724

Jackson, D., and Short, A. (2020). "1 - introduction to beach morphodynamics," in *Sandy beach morphodynamics*. Eds. D. W. T. Jackson and A. D. Short (Elsevier), 1–14. doi: 10.1016/B978-0-08-102927-5.00001-1

Jaramillo, C., González, M., Medina, R., and Turki, I. (2021). An equilibrium-based shoreline rotation model. *Coast. Eng.* 163, 103789. doi: 10.1016/j.coastaleng.2020.103789

Jaramillo, C., Jara, M. S., González, M., and Medina, R. (2020). A shoreline evolution model considering the temporal variability of the beach profile sediment volume (sediment gain / loss). *Coast. Eng.* 156, 103612. doi: 10.1016/j.coastaleng.2019.103612

Kalman, R. E. (1960). A new approach to linear filtering and prediction problems. *Trans. ASME–Journal Basic Eng.* 82, 35–45. doi: 10.1115/1.3662552

Kroon, A., de Schipper, M. A., van Gelder, P.H.A.J.M., and Aarninkhof, S. G. J. (2020). Ranking uncertainty: Wave climate variability versus model uncertainty in probabilistic assessment of coastline change. *Coast. Eng.* 158, 103673. doi: 10.1016/j.coastaleng.2020.103673

Le Cozannet, G., Bulteau, T., Castelle, B., Ranasinghe, R., Wöppelmann, G., Rohmer, J., et al. (2019). Quantifying uncertainties of sandy shoreline change projections as sea level rises. *Sci. Rep.* 9, 42. doi: 10.1038/s41598-018-37017-4

Le Cozannet, G., Oliveros, C., Castelle, B., Garcin, M., Idier, D., Pedreros, R., et al. (2016). Uncertainties in sandy shorelines evolution under the bruun rule assumption. *Front. Mar. Sci.* 3. doi: 10.3389/fmars.2016.00049

Long, J. W., and Plant, N. G. (2012). Extended kalman filter framework for forecasting shoreline evolution. *Geophys. Res. Lett.* 39, L13603. doi: 10.1029/2012GL052180

Ludka, B. C., Guza, R. T., O'Reilly, W. C., and Yates, M. L. (2015). Field evidence of beach profile evolution toward equilibrium. *J. Geophys. Res. Ocean.* 120, 7574–7597. doi: 10.1002/2015JC010893

Luijendijk, A., Hagenaars, G., Ranasinghe, R., Baart, F., Donchyts, G., and Aarninkhof, S. (2018). The state of the world's beaches. *Sci. Rep.* 8, 1–11. doi: 10.1038/s41598-018-24630-6

Masselink, G., Austin, M., Scott, T., Poate, T., and Russell, P. (2014). Role of wave forcing, storms and NAO in outer bar dynamics on a high-energy, macro-tidal beach. *Geomorphology* 226, 76–93. doi: 10.1016/j.geomorph.2014.07.025

Miller, J. K., and Dean, R. G. (2004). A simple new shoreline change model. *Coast. Eng.* 51, 531–556. doi: 10.1016/j.coastaleng.2004.05.006

Milly, P. C. D., Betancourt, J., Falkenmark, M., Hirsch, R. M., Kundzewicz, Z. W., Lettenmaier, D. P., et al. (2008). Climate change: Stationarity is dead: Whither water management? *Sci. (80-.).* 319, 573–574. doi: 10.1126/science.1151915

Montaño, J., Coco, G., Antolínez, J. A. A., Beuzen, T., Bryan, K. R., Cagigal, L., et al. (2020). Blind testing of shoreline evolution models. *Sci. Rep.* 10, 1–10. doi: 10.1038/s41598-020-59018-y

Montaño, J., Coco, G., Cagigal, L., Mendez, F., Rueda, A., Bryan, K. R., et al. (2021). A multiscale approach to shoreline prediction. *Geophys. Res. Lett.* 48, 1–11. doi: 10.1029/2020gl090587

Morim, J., Hemer, M., Wang, X. L., Cartwright, N., Trenham, C., Semedo, A., et al. (2019). Robustness and uncertainties in global multivariate wind-wave climate projections. *Nat. Clim. Change* 9, 711–718. doi: 10.1038/s41558-019-0542-5

Muir, F., Hurst, M., Vitousek, S., Hansom, J., Rennie, A., Fitton, J., et al. (2020). "Predicting coastal change in Scotland across decadal-centennial timescales using a process-driven one-line model," in *Coastal Management 2019*. 551–563. doi: 10.1680/cm.65147.551

Odériz, I., Mori, N., Shimura, T., Webb, A., Silva, R., and Mortlock, T. R. (2022). Transitional wave climate regions on continental and polar coasts in a warming world. *Nat. Clim. Change* 12, 662–671. doi: 10.1038/s41558-022-01389-3

Pathiraja, S., Anghileri, D., Burlando, P., Sharma, A., Marshall, L., and Moradkhani, H. (2018). Time-varying parameter models for catchments with land use change: The importance of model structure. *Hydrol. Earth Syst. Sci.* 22, 2903–2919. doi: 10.5194/hess-22-2903-2018

Pathiraja, S., Marshall, L., Sharma, A., and Moradkhani, H. (2016a). Hydrologic modeling in dynamic catchments: A data assimilation approach. *Water Resour. Res.* 52, 3350–3372. doi: 10.1002/2015WR017192

Pathiraja, S., Marshall, L., Sharma, A., and Moradkhani, H. (2016b). Detecting non-stationary hydrologic model parameters in a paired catchment system using data assimilation. *Adv. Water Resour.* 94, 103–119. doi: 10.1016/j.advwatres.2016.04.021

Phillips, M. S., Harley, M. D., Turner, I. L., Splinter, K. D., and Cox, R. J. (2017). Shoreline recovery on wave-dominated sandy coastlines: the role of sandbar morphodynamics and nearshore wave parameters. *Mar. Geol.* 385, 146–159. doi: 10.1016/j.margeo.2017.01.005

Phinn, S. R., and Hastings, P. A. (1995). Southern oscillation influences on the gold coast's summer wave climate. *J. Coast. Res.* 11, 946–958. http://www.jstor.org/stable/4298394

Price, T. D., and Ruessink, B. G. (2011). State dynamics of a double sandbar system. *Cont. Shelf Res.* 31, 659–674. doi: 10.1016/j.csr.2010.12.018

Price, T. D., and Ruessink, B. G. (2013). Observations and conceptual modelling of morphological coupling in a double sandbar system. *Earth Surf. Process. Landforms* 38, 477–489. doi: 10.1002/esp.3293

Ranasinghe, R. (2016). Assessing climate change impacts on open sandy coasts: A review. *Earth-Science Rev.* 160, 320–332. doi: 10.1016/j.earscirev.2016.07.011

Ranasinghe, R. (2020). On the need for a new generation of coastal change models for the 21 st century. *Sci. Rep.* 10, 2010. doi: 10.1038/s41598-020-58376-x

Roelvink, D., Huisman, B., Elghandour, A., and Ghonim, M. (2020). Efficient modeling of complex sandy coastal evolution at monthly to century time scales. *Front. Mar. Sci.* 7, 1–20. doi: 10.3389/fmars.2020.00535

Ruessink, B. G., Pape, L., and Turner, I. L. (2009). Daily to interannual cross-shore sandbar migration: Observations from a multiple sandbar system. *Cont. Shelf Res.* 29, 1663–1677. doi: 10.1016/j.csr.2009.05.011

Schepper, R., Almar, R., Bergsma, E. W. J., de Vries, S., Reniers, A., Davidson, M. A., et al. (2021). Modelling cross-shore shoreline change on multiple timescales and their interactions. *J. Geophys. Res. Earth Surf.* 9(6), 582. doi: 10.3390/jmse9060582

Short, A. D. (2022). Australian Beach systems: Are they at risk to climate change? *Ocean Coast. Manage.* 224, 106180. doi: 10.1016/j.ocecoaman.2022.106180

Splinter, K. D., and Coco, G. (2021). Challenges and opportunities in coastal shoreline prediction. *Front. Mar. Sci.* 8. doi: 10.3389/fmars.2021.788657

Splinter, K. D., Strauss, D. R., and Tomlinson, R. B. (2011). Assessment of post-storm recovery of beaches using video imaging techniques: A case study at gold coast, Australia. *IEEE Trans. Geosci. Remote Sens.* 49, 4704–4716. doi: 10.1109/TGRS.2011.2136351

Splinter, K. D., Turner, I. L., and Davidson, M. A. (2013). How much data is enough? the importance of morphological sampling interval and duration for calibration of empirical shoreline models. *Coast. Eng.* 77, 14–27. doi: 10.1016/j.coastaleng.2013.02.009

Splinter, K. D., Turner, I. L., Davidson, M. A., Barnard, P., Castelle, B., and Oltman-Shay, J. (2014). A generalized equilibrium model for predicting daily to inter-annual shoreline response. *J. Geophys. Res. Earth Surf.* 119, 1936–1958. doi: 10.1002/2014JF003106

Splinter, K. D., Turner, I. L., Reinhardt, M., and Ruessink, G. (2017). Rapid adjustment of shoreline behavior to changing seasonality of storms: observations and modelling at an open-coast beach. *Earth Surf. Process. Landforms* 42, 1186–1194. doi: 10.1002/esp.4088

Toimil, A., Camus, P., Losada, I. J., and Alvarez-Cuesta, M. (2021). Visualising the uncertainty cascade in multi-ensemble probabilistic coastal erosion projections. *Front. Mar. Sci.* 202, 103110. doi: 10.3389/fmars.2021.683535

Toimil, A., Camus, P., Losada, I. J., Le Cozannet, G., Nicholls, R. J., Idier, D., et al. (2020). Climate change-driven coastal erosion modelling in temperate sandy beaches: Methods and uncertainty treatment. *Earth-Science Rev.*, 202, 103110. doi: 10.1016/J.EARSCIREV.2020.103110

Toimil, A., Losada, I. J., Camus, P., and Díaz-simal, P. (2017). Managing coastal erosion under climate change at the regional scale. *Coast. Eng.* 128, 106–122. doi: 10.1016/j.coastaleng.2017.08.004

Turner, I. L. (2006). Discriminating modes of shoreline response to offshore-detached structures. *J. Waterw. Port Coastal Ocean Eng.* 132, 180–191. doi: 10.1061/(ASCE)0733-950X

van Enckevort, I. M. J., Ruessink, B. G., Coco, G., Suzuki, K., Turner, I. L., Plant, N. G., et al. (2004). Observations of nearshore crescentic sandbars. *J. Geophys. Res. Ocean.* 109, 1–17. doi: 10.1029/2003JC002214

Vitousek, S., Barnard, P. L., and Limber, P. (2017a). Can beaches survive climate change? *J. Geophys. Res. Earth Surf.* 122, 1060–1067. doi: 10.1002/2017JF004308

Vitousek, S., Barnard, P. L., Limber, P., Erikson, L., and Cole, B. (2017b). A model integrating longshore and cross-shore processes for predicting long-term shoreline response to climate change. *J. Geophys. Res. Earth Surf.* 122, 782–806. doi: 10.1002/2016JF004065

Vitousek, S., Cagigal, L., Montaño, J., Rueda, A., Mendez, F., Coco, G., et al. (2021). The application of ensemble wave forcing to quantify uncertainty of shoreline change predictions. *J. Geophys. Res. Earth Surf.* 126, e2019JF005506. doi: 10.1029/2019jf005506

Vos, K., Harley, M. D., Splinter, K. D., Simmons, J. A., and Turner, I. L. (2019a). Sub-Annual to multi-decadal shoreline variability from publicly available satellite imagery. *Coast. Eng.* 150, 160–174. doi: 10.1016/j.coastaleng.2019.04.004

Vos, K., Harley, M. D., Splinter, K. D., Walker, A., and Turner, I. L. (2020). Beach slopes from satellite-derived shorelines. *Geophys. Res. Lett.* 47, e2020GL088365. doi: 10.1029/2020GL088365

Vos, K., Harley, M., and Turner, I. (2021). *Large Regional variability in coastal erosion caused by ENSO*. 1–16. doi: 10.21203/rs.3.rs-666160/v1

Vos, K., Splinter, K. D., Harley, M. D., Simmons, J. A., and Turner, I. L. (2019b). CoastSat: A Google earth engine-enabled Python toolkit to extract shorelines from publicly available satellite imagery. *Environ. Model. Software* 122, 104528. doi: 10.1016/j.envsoft.2019.104528

Vousdoukas, M. I., Ranasinghe, R., Mentaschi, L., Plomaritis, T. A., Athanasiou, P., Luijendijk, A., et al. (2020). Sandy coastlines under threat of erosion. *Nat. Clim. Change* 10, 260–263. doi: 10.1038/s41558-020-0697-0

Westra, S., Thyer, M., Leonard, M., Kavetski, D., and Lambert, M. (2014). A strategy for diagnosing and interpreting hydrological model nonstationarity. *Water Resour. Res.* 50, 5090–5113. doi: 10.1002/2013WR014719

Wong, P. P., Losada, I. J., Gatusso, J. P., Hinkel, J., A, K., McInnes, K. L., et al. (2014). “Coastal systems and low-lying areas,” in *Climate change 2014 – impacts, adaptation and vulnerability: Part a: Global and sectoral aspects: Working group II contribution to the IPCC fifth assessment report: Volume 1: Global and sectoral aspects*. Ed. Intergovernmental Panel on Climate Change, (Cambridge: Cambridge University Press), 361–410. doi: 10.1017/CBO9781107415379.010

Wright, L. D., and Short, A. D. (1984). Morphodynamic variability of surf zones and beaches: A synthesis. *Mar. Geol.* 56, 93–118. doi: 10.1016/0025-3227(84)90008-2

Wright, L. D., Short, A. D., and Green, M. O. (1985). Short-term changes in the morphodynamic states of beaches and surf zones: An empirical predictive model. *Mar. Geol.* 62, 339–364. doi: 10.1016/0025-3227(85)90123-9

Xiong, M., Liu, P., Cheng, L., Deng, C., Gui, Z., Zhang, X., et al. (2019). Identifying time-varying hydrological model parameters to improve simulation efficiency by the ensemble kalman filter: A joint assimilation of streamflow and actual evapotranspiration. *J. Hydrol.* 568, 758–768. doi: 10.1016/j.jhydrol.2018.11.038

Yates, M. L., Guza, R. T., and O’Reilly, W. C. (2009). Equilibrium shoreline response: Observations and modeling. *J. Geophys. Res. Ocean.* 114, C09014. doi: 10.1029/2009JC005359

Yates, M. L., Guza, R. T., O’Reilly, W. C., Hansen, J. E., and Barnard, P. L. (2011). Equilibrium shoreline response of a high wave energy beach. *J. Geophys. Res. Ocean.* 116, 1–13. doi: 10.1029/2010JC006681

Zarifsanayei, A. R., Antolínez, J. A. A., Etemad-Shahidi, A., Cartwright, N., and Strauss, D. (2022). A multi-model ensemble to investigate uncertainty in the estimation of wave-driven longshore sediment transport patterns along a non-straight coastline. *Coast. Eng.* 173, 104080. doi: 10.1016/j.coastaleng.2022.104080

Zeng, L., Xiong, L., Liu, D., Chen, J., and Kim, J. S. (2019). Improving parameter transferability of GR4J model under changing environments considering nonstationarity. *Water (Switzerland)* 11(10), 2029. doi: 10.3390/w11102029

frontiers | Frontiers in Marine Science

TYPE Original Research
PUBLISHED 23 March 2023
DOI 10.3389/fmars.2023.1007789

OPEN ACCESS

EDITED BY
Mouncef Sedrati,
Université Bretagne Sud, France

REVIEWED BY
Meredith L. McPherson,
University of Massachusetts Boston,
United States
Zhixuan Feng,
East China Normal University, China

*CORRESPONDENCE
James J. Leichter
✉ jleichter@ucsd.edu

SPECIALTY SECTION
This article was submitted to
Coastal Ocean Processes,
a section of the journal
Frontiers in Marine Science

RECEIVED 30 July 2022
ACCEPTED 14 February 2023
PUBLISHED 23 March 2023

CITATION
Leichter JJ, Ladah LB, Parnell PE,
Stokes MD, Costa MT, Fumo J and
Dayton PK (2023) Persistence of southern
California giant kelp beds and alongshore
variation in nutrient exposure driven by
seasonal upwelling and internal waves.
Front. Mar. Sci. 10:1007789.
doi: 10.3389/fmars.2023.1007789

Persistence of southern California giant kelp beds and alongshore variation in nutrient exposure driven by seasonal upwelling and internal waves

James J. Leichter[1]*, Lydia B. Ladah[2], P. Ed Parnell[1],
M. Dale Stokes[1], Matthew T. Costa[3], James Fumo[4]
and Paul K. Dayton[1]

[1]Scripps Institution of Oceanography, University of California San Diego, La Jolla, CA, United States, [2]Department of Biological Oceanography, Centro de Investigación Científica y de Educación Superior de Ensenada (CICESE), Carretera Ensenada-Tijuana, Ensenada, Baja California, Mexico, [3]Marine Science Center, Northeastern University, Boston, MA, United States, [4]Marine Biology Graduate Program, University of Hawaii, Honolulu, HI, United States

Kelp beds provide significant ecosystem services and socioeconomic benefits globally, and prominently in coastal zones of the California Current. Their distributions and abundance, however, vary greatly over space and time. Here, we describe long-term patterns of Giant Kelp (*Macrocystis pyrifera*) sea surface canopy area off the coast of San Diego County from 1983 through 2019 along with recent patterns of water column nitrate (NO_3^-) exposure inferred from *in situ* temperature data in 2014 and 2015 at sites spanning 30 km of the coastline near San Diego California, USA. Site-specific patterns of kelp persistence and resilience were associated with ocean and climate dynamics, with total sea surface kelp canopy area varying approximately 33-fold over the almost 4 decades (min 0.34 km^2 in 1984; max 11.25 km^2 in 2008, median 4.79 km^2). Site-normalized canopy areas showed that recent kelp persistence since 2014 was greater at Point Loma and La Jolla, the largest kelp beds off California, than at the much smaller kelp bed off Cardiff. NO_3^- exposure was estimated from an 11-month time series of *in situ* water column temperature collected in 2014 and 2015 at 4 kelp beds, using a relationship between temperature and NO_3^- concentration previously established for the region. The vertical position of the 14.5°C isotherm, an indicator of the main thermocline and nutricline, varied across the entire water column at semidiurnal to seasonal frequencies. We use a novel means of quantifying estimated water column NO_3^- exposure integrated through time (mol-days m^{-2}) adapted from degree days approaches commonly used to characterize thermal exposures. Water column integrated NO_3^- exposure binned by quarters of the time series showed strong seasonal differences with highest exposure in Mar - May 2015, lowest exposure in Sep - Dec 2014, with consistently highest exposure off Point Loma. The water column integrated NO_3^- signal was filtered to provide estimates of the contribution to total nitrate exposure from high frequency variability ($f >= 1$ cycle 30 hr^{-1}) associated predominantly with internal waves, and low frequency variability driven predominantly by seasonal upwelling. While seasonal upwelling accounted for > 90% of NO_3^- exposure across the full year, during warm periods when seasonal upwelling was reduced or absent and NO_3^- exposure was low overall, the proportion due to internal waves increased markedly to 84 to 100% of the site-specific total exposure. The high frequency variability associated with internal waves may supply critical nutrient availability during anomalously warm periods. Overall, these analyses support a hypothesis that differences in NO_3^- exposure among sites due to seasonal upwelling and higher frequency internal wave forcing contribute to spatial patterns in Giant Kelp persistence in southern California. The study period includes anomalously warm surface conditions and the marine heatwave associated with the "Pacific Warm Blob" superimposed on the seasonal thermal signal and corresponding to the onset of a multi-year decline in kelp canopy area and marked differences in kelp persistence among sites. Our analysis suggests that, particularly during periods of warm surface conditions, variation in NO_3^- exposure associated with processes occurring at higher frequencies, including internal waves can be a significant source of NO_3^- exposure to kelp beds in this region. The patterns described here also offer a view of the potential roles of seasonal and higher frequency nutrient dynamics for Giant Kelp persistence in southern California under continuing ocean surface warming and increasing frequency and intensity of marine heatwaves.

KEYWORDS

kelp forests, temperature, nutrient dynamics, internal waves, kelp forest ecosystem, *Macrocystis pyrifera*

1 Introduction

The size and abundance of Giant Kelp (*Macrocystis pyrifera*) beds are highly dynamic (e.g. Dayton, 1985; Steneck et al., 2002). Kelps are foundation species (sensu Dayton, 1972) providing high biodiversity habitats in the coastal zone. Kelp forest ecosystems offer valuable contributions to coastal communities including the harvesting of kelp biomass, invertebrates, and fish, as well as non-consumptive activities including recreation and tourism (Wheeler and North, 1980; Dayton, 1985). Because of the ecological and socioeconomic importance of kelp beds, understanding the factors driving the spatiotemporal variation in their distribution and abundance can directly benefit coastal management.

Kelp beds are distributed heterogeneously in space, and exhibit highly variable abundance through time, influenced by both physical and biological factors promoting growth interacting with disturbances that remove biomass and rapidly reset succession (Dayton, 1985). The ability of kelps, especially the Giant Kelp (*Macrocystis pyrifera*) which has a broad distribution in the northern and southern hemispheres, and the Bull Kelp (*Nereocystis luetkeana*) which ranges from the Aleutian Islands to central California, to dominate subtidal habitats and support complex associated species assemblages is dependent on the availability of rocky substrata at suitable depths (generally depths < 25 to 30 m), the quantity and spectral quality of light penetrating the water column (Gerard, 1984; Reed and Foster, 1984), complex species interactions between kelp grazers, particularly urchins, and their predators and pathogens (Steneck et al., 2002; Estes et al., 2004; Feehan and Scheibling, 2014); and the supply of critical nutrients (Jackson, 1977; Gerard 1982a; Jackson, 1983; Zimmerman and Kremer, 1984; Foster and Schiel, 1985; Kinlan et al., 2003). However, despite the complex factors and feedbacks driving the variability in kelp bed distributions and abundance, some locations consistently show long-term ecosystem persistence through multiple disturbances, and thus likely represent hot spots of successful kelp recruitment and growth linked to habitat quality (Parnell et al., 2006; Parnell et al., 2010; Young et al., 2016; Cavanaugh et al., 2019; Bell et al., 2020). For example, some kelp beds contain core areas where rapid post-disturbance recovery consistently occurs due to a combination of seascape structure (Parnell, 2015), depth distributions, competition between surface canopy and understory guilds, and post disturbance nutrient climates (e.g., see Figure 1 in Parnell et al., 2006). Recognizing and protecting core areas of long-term persistence and understanding environmental and habitat drivers of kelp resilience through time can contribute to improved management, conservation, and restoration, as these ecosystems confront increasingly complex challenges of a rapidly changing ocean climate including a deepening thermocline depth in southern California and the increasing frequency of anomalous warm temperatures and marine heatwaves (e.g. Arafeh-Dalmau et al., 2019; Cavanaugh et al., 2019; McPherson et al., 2021).

The exceptional productivity of kelps, especially *M. pyrifera* in California, depends in large part, on availability of dissolved inorganic nutrients which limit primary productivity in coastal environments (Dayton et al., 1992; Dayton et al., 1999). Nitrogen uptake in macroalgae, including kelps, is related to water column concentrations (Harrison and Hurd, 2001), photosynthetic energy, temperature-dependent kinetics, and water motion impacting boundary layer concentrations and dynamics (Hepburn et al., 2007; Gerard 1982b). Biological characteristics such as tissue morphology, type, ontogeny, and nutritional history also impact incorporation of nitrogenous nutrients (Rosenberg and Ramus, 1984; Duke et al., 1989; Lobban and Harrison, 1994; Pedersen, 1994; Pedersen and Borum, 1996; Neori et al., 2004). Importantly, kelps have the ability to translocate nitrogen sources, including amino acids, from blades in deeper water to the surface canopy, and therefore can take advantage of varying nutrient concentrations and availability throughout the water column (Schmitz and Srivastava, 1979; Manley, 1983; Konotchick et al., 2012).

For coastal waters of the California Current, there is a well-established relationship between temperature and forms of biologically available nitrogen, with NO_3^- concentrations inversely related to temperature below approximately 14°C to 15.5°C (Zentara and Kamykowski, 1977; Zimmerman and Kremer, 1986; Dayton et al., 1999), principally because remineralized organic nitrogen mainly in the form of NO_3^- occurs at elevated concentrations in deeper colder waters, typically below the thermocline (Strickland, 1970; Jackson, 1977; Zentara and Kamykowski, 1977; Eppley et al., 1979; Zimmerman and Kremer, 1986; Ladah, 2003; Parnell et al., 2010). Above the threshold temperatures, NO_3^- becomes low to undetectable (i.e. concentrations < 0.1 μmol L^{-1}). Ammonium and urea associated primarily with runoff and biological nitrogen recycling in surface waters (Bray et al., 1986; Smith et al., 2018), and potentially with recycling by epibiont communities (Hurd et al., 1994), may also be relevant and intermittent sources of nitrogen in coastal waters.

A range of oceanographic mechanisms can deliver nitrogenous nutrients to kelp beds (McPhee-Shaw et al., 2007) with strong spatial and temporal variation, including zonal variability in upwelling-favorable winds (Checkley and Barth, 2009), jets associated with coastal headlands (Mooers and Robinson, 1984), proximity to deep-water canyons (Ryan et al., 2005; Walter and Phelan, 2016), and variable exposure in both frequency and intensity to internal wave forcing (Filonov et al., 2014). In southern California kelp beds, ambient nutrient concentrations can vary dramatically on time scales of hours to days, associated with variation in upwelling strength which determines the depth of the thermocline and nutricline, as well as with periods of elevated internal wave activity that deliver pulses of cool, sub-thermocline water to inshore habitats (Jackson, 1977; Jackson and Winant, 1983; Zimmerman and Kremer, 1984; Konotchick et al., 2012). However, the causes and consequences of nutrient variability among kelp forest sites, especially within the same upwelling region, remain largely unexplored, and we have limited understanding of the ways in which local nutrient climates contribute to kelp forest persistence and resilience.

The primary sources of inorganic nitrogen along the coast of California include sub-thermocline NO_3^- transported by wind-driven upwelling as well as higher-frequency pulses associated with internal waves (Jackson, 1977; Zimmerman and Kremer, 1984; McPhee-Shaw et al., 2007; Fram et al., 2008). Upwelling in the Southern California Bight occurs on large scales extending to ~ 200 km off the coast, and on more local scales that are quasi-synchronous, for example in San Diego occurring approximately twice per month in summer lasting approximately 6 to 24 days (Dorman and Palmer, 1981). Additionally, there is long-recognized, extensive internal wave activity in the Southern California Bight (e.g., Ewing, 1950; Jackson, 1977; Jackson and Winant, 1983; Zimmerman and Kremer, 1984; Pineda, 1991; Lucas et al., 2011) with spatial variability in internal wave forcing at relatively smaller scales (Filonov et al., 2014). Internal waves are vertical oscillations generated along density gradients forced by wind or tidal currents as they flow across abrupt landscape features with critical slope contours, such as at the continental shelf break, offshore banks, or sea mounts (Holloway, 1987; Lamb, 1997). The complex bathymetry in the Southern California Bight, combined with persistent vertical water column density stratification during most of the year, and strong barotropic tidal forcing create significant potential for conversion of barotropic to baroclinic energy and resulting shoreward propagating internal waves. For the study region near San Diego, numerical modelling indicates that the large 9 Mile Bank is a zone of high barotropic to baroclinic energy conversion and source of internal wave formation (Ponte and Cornuelle, 2013).

Once formed, depending on slope angle, internal wave energy can propagate shoreward along the wave guide of the greatest density difference, which in arid temperate upwelling regions with little salinity change over depth occurs at the thermocline and associated nutricline. Nonlinear shoaling and breaking of internal waves result in turbulent energy dissipation in shallow waters leading to mixing and cross-shelf transport of sub-thermocline water (Sandstrom and Elliott, 1984; Helfrich and Melville, 2006; Sharples et al., 2007). This process has been estimated to account for up to 25% of annual nitrate contribution on the Mauritanian shelf (Schafstall et al., 2010) and up to 15% in the Santa Barbara channel (McPhee-Shaw et al., 2007). Because tidal forcing is likely to be both semidiurnal and diurnal in nature due to the M2 or O1 tide, and because wind forcing is usually diurnal due to daily warming and cooling affecting the sea breeze and wind forcing patterns, their frequencies and consequences can be distinguished in time series of both temperature and related NO_3^-. Internal waves are biologically relevant in a range of ecosystems, including the coastal shelf of the Southern California Bight. Evidence exists that seaweeds can incorporate nutrients from semidiurnal internal waves (Ladah et al., 2012) and that kelps can take up and store nutrients on time scales of days to months (Wheeler and North, 1980; Gerard, 1982a). Prior inshore oceanographic and ecological work has shown strong physical gradients in temperature and modeled NO_3^- exposure between two sites at North and South La Jolla (Konotchick et al., 2012) as well as large variation in kelp persistence throughout southern California's kelp forest "Region 9" (Parnell et al., 2010).

Here we first examine patterns of kelp canopy abundance through time for the distinct kelp beds in San Diego using the annual maximum canopy area measured from aerial surveys conducted since 1983 (MBC Aquatic Sciences, 2020). There are large differences in the total size among these kelp beds, primarily determined by differences in availability of benthic rocky substrata at suitable depths (i.e. ~5 to 25 m). However, there also are differences in the trajectory of relative canopy cover normalized by maximum cover, suggesting that additional factors that vary alongshore contribute to kelp persistence through time. We hypothesize that differences in high frequency shoaling of the nutricline associated with the impact of internal waves contribute to the variation in persistence among sites and analyze a recent dataset of water column temperature observations at the seaward edge of 4 kelp beds in the San Diego region.

2 Methods

2.1 Long-term kelp canopy survey data

Data on the annual maximum kelp canopy cover from 1983 through 2019 were obtained from a published dataset for the southern California study region (MBC Aquatic Sciences, 2020). The data were collected *via* quarterly infrared aerial imaging surveys covering 24 distinct kelp beds conducted for the Region Nine Kelp Survey Consortium. The data are reported as the annual maximum cover across the quarterly surveys, with annual data available starting in 1983, along with categorization of yearly thermal data from the Multivariate ENSO Index (MBC Aquatic Sciences, 2020). We analyzed the data for 3 sites at Cardiff, La Jolla, and Point Loma (CAR, LJ, PTL) corresponding to locations of our instrument mooring deployments. Although our mooring deployments (see below) included sites at the north and south of the La Jolla kelp bed, the kelp canopy data are reported as one contiguous kelp bed at La Jolla. The dataset was used to construct and plot an annual time series of kelp bed area (km^2) for each site. Because the kelp beds differ greatly in area, with PTL > LJ >> CAR, we also calculated the annual proportional kelp cover for each site normalized by the maximum area observed at each site across the 37-yr time series. The time series of site-normalized cover were used to estimate kelp bed persistence starting in 2014 corresponding to the mooring deployments and for the subsequent 5 years through 2019. Following Cavanaugh et al. (2019), kelp canopy persistence for each site was calculated as the proportional cover in each year relative to a baseline of the site-specific mean kelp cover over the preceding 5 years.

2.2 *In situ* temperature observations

Vertical moorings with affixed recording temperature sensors were deployed on the 36 m isobath approximately 100 to 200 m seaward of established kelp beds at each of 4 sites along the coast of San Diego, CA (Figure 1) . The moorings were deployed from the ship *R/V New Horizon* with ~250 kg anchors, and instruments were subsequently retrieved and re-deployed by scuba divers using standard air and non-decompression diving. The moorings were deployed off the kelp beds at Cardiff (CAR, 33.01503°N, 117.30386° E), North La Jolla (NLJ, 32.85772°N, 117.29111°E), South La Jolla (SLJ, 32.80270,°N, 117.30107°E), and Point Loma (PTL, 32.69866° N, 117.27696°E). To prevent boat strikes, subsurface floats at the tops of the moorings were located approximately 4 m below the sea surface relative to mean low tide. Each mooring was initially instrumented with 5 Seabird Electronics SBE 39 temperature sensors (0.01°C resolution, ~ 10 sec response time) placed at heights of 1, 6, 12, 18, 24 m above the sea floor with an additional Seabird Electronics SBE 39+ temperature/pressure sensor 29 m above the seafloor. The pressure records near the top of the mooring lines were used to assess potential knock-down of the moorings by currents. Depth deviations were less than 2 m at almost all times except in one case at North La Jolla when the mooring had been entangled with lobster trapping gear and the top of the mooring pulled down to a depth of ~8 m for multiple days. After the initial deployment, redeployed instruments included Seabird Electronics SBE 56 temperature sensors (0.01°C resolution, ~10 sec response time) and RBR 1050 temperature sensors (0.01°C resolution, ~30 sec response time). All instruments were factory-calibrated and sampled at 1 min intervals, with deployment durations typically 4 to 6 months. Moorings were deployed on 17 June 2014 with all instruments synchronized to begin sampling at midnight 18 June 2014 (GMT

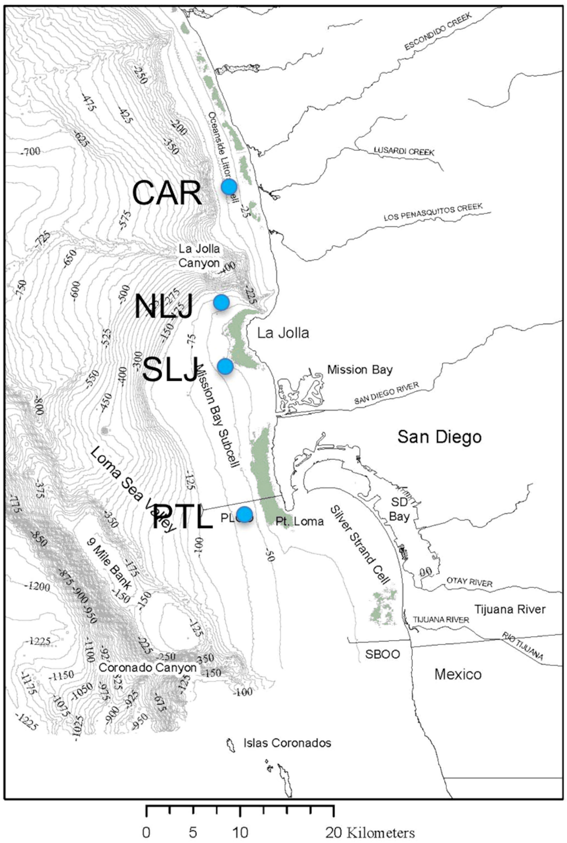

FIGURE 1
Study region along the coast of San Diego, CA, showing locations (blue circles) of recording temperature moorings deployed seaward of kelp beds off Cardiff (CAR), North La Jolla (NLJ), South La Jolla (SLJ), and Point Loma (PTL). Green tinted areas inshore of the study site markers indicate the maximum cover of kelp canopies recorded in aerial surveys 1983 through 2019 (MBC Aquatic Sciences, 2020).

-8). Here we analyze ~11 mo (336 d) of the continuous temperature records from June 2014 through May 2015.

2.3 Temperature and NO_3^- analysis

The raw temperature data were quality controlled, with records from successive deployments at each location trimmed to remove times when instruments were out of the water, and data then spliced together to form continuous time series for each position above the seafloor on each mooring. The data from the individual sensors at 6 m vertical intervals were linearly interpolated to 1 m to create estimated vertical profiles of the water column temperatures for the bottom 24 m at each site. The data from the temperature/pressure sensors 29 m above the bottom (just below the mooring floats) were excluded from this analysis because those records started later at Cardiff and South La Jolla than at North La Jolla and Point Loma. The temperature data were then averaged to 10 min intervals and the height above bottom of the 14.5°C isotherm representing the main thermocline was calculated.

The temperature time series were used to produce records of estimated NO_3^- concentrations using a linear regression equation (NO_3^- = -5.8 x Temperature + 81.7, r^2 = 0.90, per Konotchick et al., 2012). Use of a linear relationship between NO_3^- and temperature below ~14.5°C for southern California nearshore waters has a strong empirical basis (Kamykowski and Zentara, 1986; Zimmerman and Kremer, 1986; Dayton et al., 1999; Lucas et al., 2011; Konotchick et al., 2012), although some periods with greater than expected NO_3^- at warmer temperatures have been documented in the southern part of the range (Ladah, 2003). The linear relationship reported in Konotchick et al. (2012) and applied here was derived from n = 1904 hydrographic bottle samples collected in the California Cooperative Oceanic Fisheries Investigations from 1959 to 2010 for a station offshore of La Jolla, CA at (32°54' N, 117° 23' W). Following Konotchick et al. (2012), we apply the linear relationship to all temperatures less than the y-intercept value 14.2°C, and a constant value of 0.1 µmol L^{-1} NO_3^- for all temperatures greater than 14.2°C. This assumes that the linear relationship between temperature and nitrate measured offshore is consistent inshore, which has been confirmed by Parnell et al. (2010) for a station at 5 m depth off the Scripps Pier, although there is potential for changes associated with diapycnal mixing that could cause transient deviations from this linear relationship. The estimated concentration of NO_3^- for each 1 m bin of the water column was converted from units of umol L^{-1} to mol m^{-3} and summed across the 24 1-m vertical bins, with units of mol m^{-2} representing the estimated total water column integrated NO_3^- in each time step for an idealized 1 m x 1 m x 24 m water column above a 1 m^2 area of seafloor at each site. To characterize total NO_3^- exposures through time we adapted a common approach of quantifying temperature exposure using degree days (°C x days) above or below set thermal thresholds. To our knowledge this is a novel approach to quantifying accumulated nutrient exposure, with the water column integrated NO_3^- values in each time step accumulated through time with units of mol-days m^{-2} (mol x days m^{-2}). Here the threshold value corresponds to zero water column NO_3^-, and positive values multiplied by the time step are then accumulated to daily values and summed across longer time intervals. It is important to note that this approach only estimates concentrations across the water column in each measurement time step without information on transport and fluxes of nutrients which would be present in a moving fluid environment. However, the approach provides a method of comparing environmental conditions through time and quantifying potential differences among sites. The following hypothetical example mat help to clarify the approach and provide a sense of the units and magnitude of accumulated NO_3^- exposure here: From the NO_3^- - Temperature relationship above, NO_3^- = 10 µmol L^{-1} at T ~= 12.36° C. Therefore, if the entire 24 m water column above a 1 m^2 areas of the seafloor had a uniform temperature of 12.36°C in a given time interval, by unit conversion there would be 0.24 mol m^{-2} NO_3^- present. If the temperature were constant for an entire day, there would be 0.24 mol-days m^{-2} of accumulated NO_3^- exposure. By multiplication, a constant 12.36°C water column over 30 and 365 days would then correspond, respectively, to 7.2 and 87.6 mol-days m^{-2} of accumulated NO_3^- exposure.

Here the daily NO_3^- exposure estimated from the water column temperature time series at each site were binned and accumulated by quarters of the time series. We also estimated the nitrate exposure based on temperature time series filtered into two frequency bins to estimate the relative contributions of internal waves and seasonal upwelling relative to the overall total NO_3^- exposure at each site. For each site the water column temperature data were filtered with a low pass filter (pl64t) with a cutoff frequency of f = 1 cycle 30 hr^{-1}, corresponding approximately to the local inertial frequency. The difference between the raw and the low-pass signals provides an estimate of the high-frequency variability primarily associated with diurnal and semidiurnal forcing, while the low-pass signal provides an estimate of the variability associated with seasonal upwelling. The low and high frequency NO_3^- signals were summed by quarters for the time period 24 Jun 2014 through 25 May 2015 (n = 336 d total, n = 84 d per quarter). The quarterly totals associated with the low frequency (seasonal upwelling) and high frequency (internal waves) components were also expressed as percentages of the overall total daily water column integrated NO_3^- exposure.

Power spectra of the temperature and estimated NO_3^- time series for each site were also calculated using Welch's averaged periodogram method for a series of 14-day data segments with application of a Hamming window and 50% overlap, yielding estimates of spectral power with 95% confidence intervals, as a function of frequency (Thomson and Emery, 2014; Trauth, 2015). The power spectra of the NO_3^- time series were calculated on the estimated NO_3^- time series from June 2014 through May 2015.

3 Results

Annual total canopy area of the three kelp beds at Cardiff, La Jolla, and Point Loma varied by ~33 fold across the 37-yr time series, from a minimum of 0.34 km^2 in 1984 to a maximum of 11.25

km^2 in 2008 with the larger kelp beds at La Jolla and Point Loma accounting for the significant majority of the canopy area (Figure 2). Kelp canopy area was generally large or increasing during nominally cold years, and small or decreasing during warm years. Kelp canopy area normalized by site-specific maximum cover across the time series showed large variations through time with the largest proportional changes in the small kelp bed at Cardiff, and more consistent patterns at La Jolla and especially at Point Loma. Notably, the Cardiff kelp bed exhibited very low area and low proportional cover during a multi-year period of warm conditions in the 1990s and again from 2016 through 2019 when canopy area was close to zero. Total canopy area and proportional cover at the Point Loma kelp bed remained closer to its long-term mean throughout the time series and exhibited its maximum cover in 2018. Since 2014, kelp persistence calculated as the annual cover as a proportion of the average cover for the preceding 5 years was lowest at Cardiff (mean 26.4%) and markedly higher at La Jolla (mean 68.7%) and Point Loma (mean 99.9%) (see yearly values in Table 1). The median values of the site-normalized canopy cover differed among sites and among nominally warm versus cold years with the lowest median at Cardiff (9.2% warm years, 37.5% cold years), and more consistent median values at La Jolla (23.5%, 39.6%) and Point Loma (38.3%, 48.0%) between warm years and cold years (Figure 3).

The 11-mo temperature time series exhibited clear seasonal variation with cooler temperatures across the water column dominating from Jun through Aug 2014, and Feb through May 2015, while significantly warmer temperatures persisted from Sep 2014 through Jan 2015 (Figure 4A). Temperature extremes ranged from low of 10.14°C to high of 23.94°C at 1 m and 24 m above the bottom respectively at North La Jolla and temperature extreme values were similar among sites. The minimum and maximum temperatures were comparable across sites (minima 10.14 to 10.27°C, maxima 22.28 to 23.94°C), with the mean temperatures 0.7 to 1.1°C warmer at North La Jolla than at the other sites. The depth of the 14.5°C isotherm varied significantly through time at both seasonal time scales and higher frequencies (Figure 4A **white line**). From Jun through Aug 2014 and Feb through May 2015 the height of the 14.5°C isotherm ranged from ~ 5 to > 24 m above the bottom across the study sites, with isotherm depths at North La Jolla occurring deeper than at other sites, especially during Mar through May 2015. Corresponding to the water column temperature distributions and isotherm depths, the estimated total water column NO_3^- exhibited clear seasonal differences with highest NO_3^- and extensive variability from Jun through Aug 2014 and from Feb through May 2015, and consistently low NO_3^- from Sep 2014 through Jan 2015 associated with anomalous warming and the onset of a marine heatwave during the “Pacific Blob” event

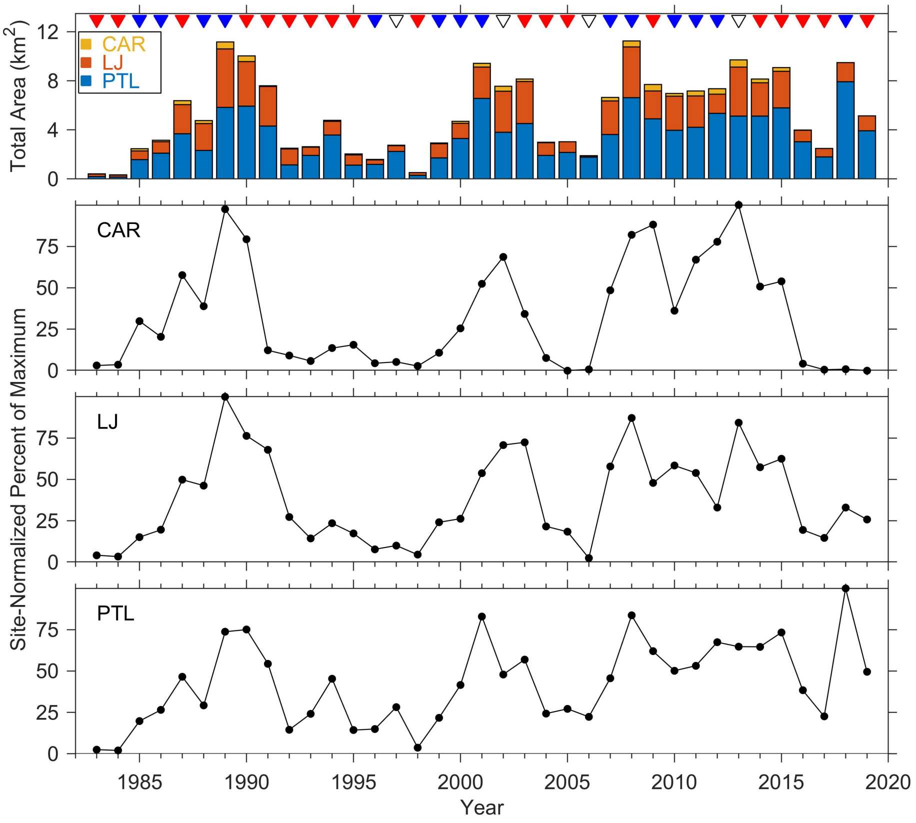

FIGURE 2
Sea surface kelp canopy cover at Cardiff (CAR), La Jolla (LJ), and Point Loma (PTL) kelp beds 1983 through 2019. Top panel shows total canopy area (km^2) color coded by site. Lower three panels show the yearly observations normalized by the maximum value observed across the time series within each site. Triangles at the top indicate years categorized by thermal patterns as warm (red), cold (blue), neutral (black) from the Multivariate ENSO Index; kelp cover are the maximum values recorded annually from quarterly aerial surveys. Data from (MBC Aquatic Sciences, 2020).

TABLE 1 Kelp persistence 2014 through 2019 for sites at Cardiff (CAR), La Jolla (LJ), and Point Loma (PTL).

Year	CAR	LJ	PTL
2014	69	103	109
2015	81	109	122
2016	6	34	59
2017	1	28	37
2018	2	69	190
2019	0	69	83
Mean	26	69	100

Site-specific kelp persistence (%) in each year calculated as 100 x annual maximum canopy cover divided by mean of the annual maximum canopy cover for the preceding 5 years. Kelp cover data from MBC Aquatic Sciences (2020).

(Figure 4B). The total daily water column integrated NO_3^- exposure (mol-days m^{-2}) over the 11-mo time series differed across sites, with maximum values at Point Loma (28.45) followed by South La Jolla (25.06), Cardiff (23.61), and North La Jolla (18.61). For the full study period the high frequency components of NO_3^- exposure associated with internal waves accounted for 4.4 to 8.7% of the totals with greatest contribution at Point Loma, while lower frequency components of NO_3^- exposure associated with seasonal upwelling accounted for 91.3 to 94.9% of the totals, see Table 2.

Associated with the varying presence of water cooler than 14.5°C, the winter and spring seasons were characterized by relatively high NO_3^- concentrations and extensive variability of NO_3^- at high frequencies, while the period from Sep through Jan was characterized by consistently low predicted NO_3^- concentrations, and occasional high frequency pulses of nitrate exposure. The view of the full 11-mo time series in Figure 4 illustrates the major seasonal differences.

A more detailed, expanded view of the temperature and estimated NO_3^- time series for mid Sep through mid-Dec 2014 and Mar through May 2015 reveal additional details of the variability within and among sites (Figures 5A, B). From mid Sep through mid-Dec 2014 temperatures were at their annual warmest, with only intermittent periods when the 14.5°C isotherm was present, corresponding to short-term pulses of NO_3^- exposure which were most evident at Point Loma. By contrast, temperatures were cold and highly variable from Mar through May 2015 with the depth of the 14.5°C isotherm varying throughout the water column and frequently changing depth by as much as 5 to 20 m within tens of minutes to several hours. The variability among sites from Mar through May 2015 is evident in both the water column temperatures and water column integrated

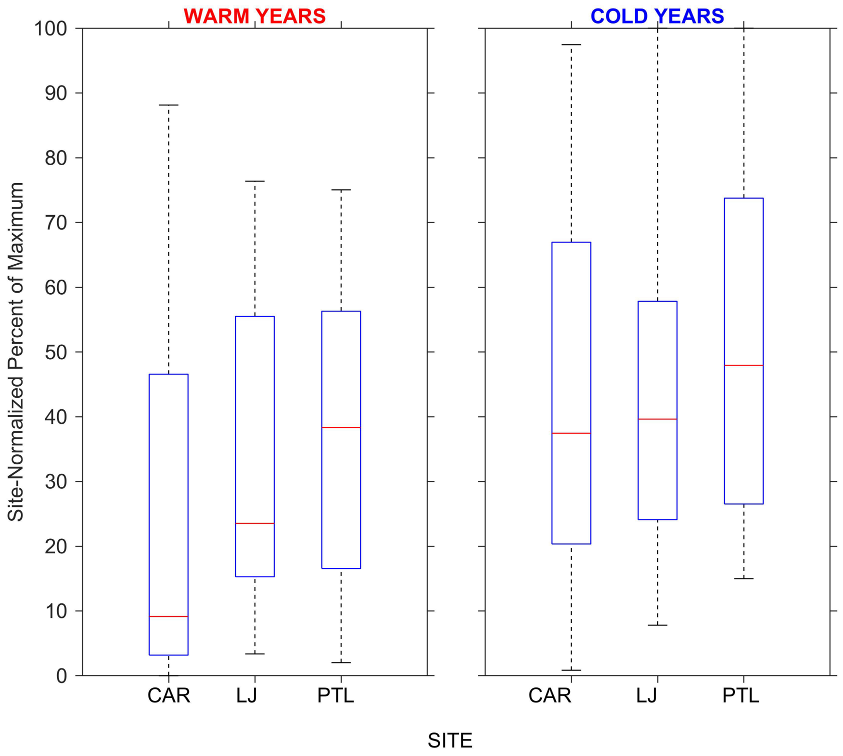

FIGURE 3
Box plot comparing the distributions of site-normalized historical kelp canopy cover at the Cardiff (CAR), La Jolla (LJ), and Point Loma (PTL) sites for the period 1983 through 2019 among nominally warm and cold years. Horizontal red bars indicate median values, blue boxes extend to the 25th and 75th percentiles and whiskers include the extreme values. Median values at CAR, LJ, and PTL were 9.2, 23.5, and 38.4 % in warm years and 37.5, 39.6, and 47.9 % in cold years respectively. Data from MBC Aquatic Sciences, 2020.

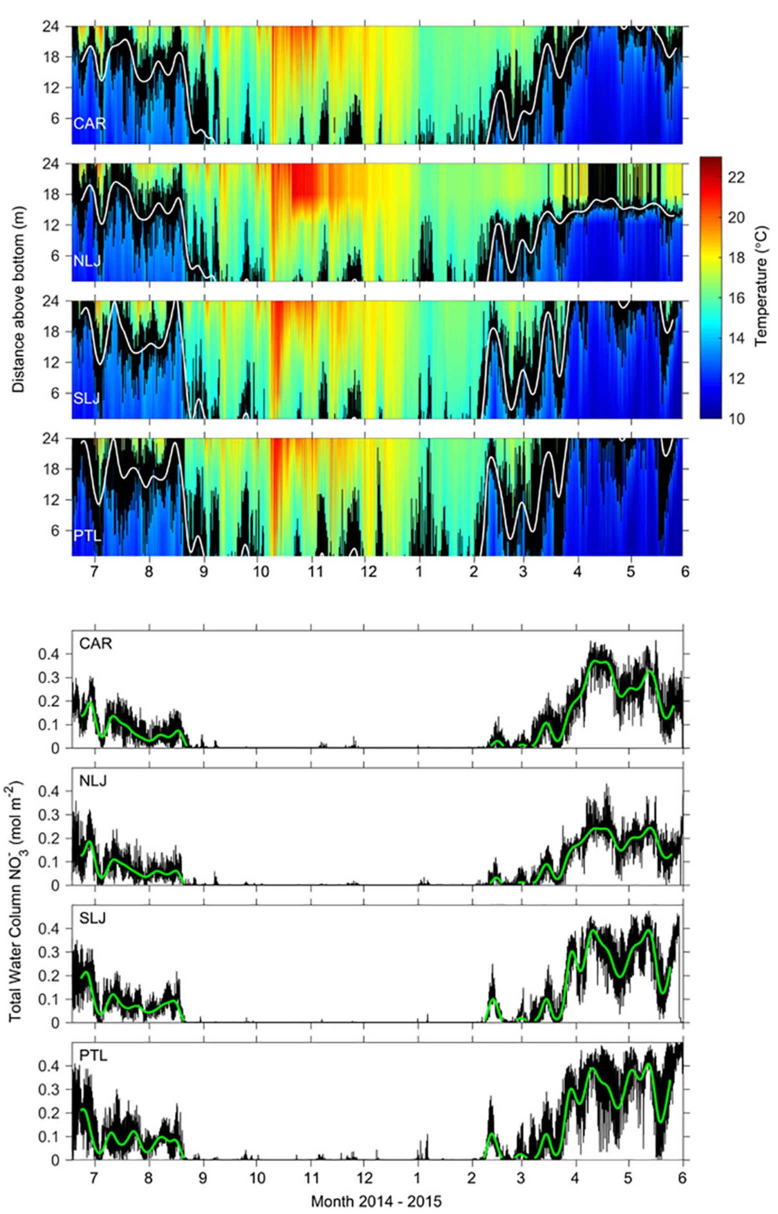

FIGURE 4
(A) Continuous record of water column temperatures June 2014 through May 2015 at 4 coastal study sites at 1 min intervals for the lower 24 m of the water column above the seafloor at 36 m bottom depth. Color shows interpolated temperature indicated by color bar at right. Black lines indicate vertical position of the 14.5 °C isotherm in raw data; white lines indicate vertical position of 14.5 °C isotherm for 10-d filtered data. **(B)** Water column integrated nitrate (NO_3^-) predicted from temperature; black lines show water column NO_3^- based on 1-min temperature data, green lines show water column NO_3^- based on 10-d filtered temperatures.

TABLE 2 Total nutrient exposure (NO_3^- mol-days m^{-2}) across the study year (24 Jun 2014 through 25 May 2015, n = 336 d) for sites at Cardiff (CAR), North La Jolla (NLJ), South La Jolla (SLJ), and Point Loma (PTL).

	Total (NO_3^- mol-days m^{-2}	% Internal Waves	% Upwelling
CAR	23.61	5.1	94.9
NLJ	18.63	6.3	93.7
SLJ	25.06	4.4	95.6
PTL	28.45	8.7	91.3

Totals are broken down as percentages associated with forcing frequencies corresponding to internal waves (f >= 1 cycle 30 hr^{-1}) and upwelling (f < 1 cycle 30 hr^{-1}).

NO_3^- time series, with generally high concentrations of NO_3^- across sites, but with a persistent pool of warmer water evident shallower than 15 m above the bottom at North La Jolla. Corresponding to the differences in water column temperatures, North La Jolla exhibited the lowest total water column NO_3^- among sites during Mar through May 2015, followed by Cardiff, South La Jolla, and Point Loma. The variability in NO_3^- exhibited similar corresponding patterns of differences among sites, lowest at North La Jolla and greatest at Point Loma (Figure 5B).

Power spectra of the NO_3^- time series for each site indicate marked spectral peaks at the semidiurnal frequency, 1.94 cycles per day, and also peaks corresponding to the diurnal frequency

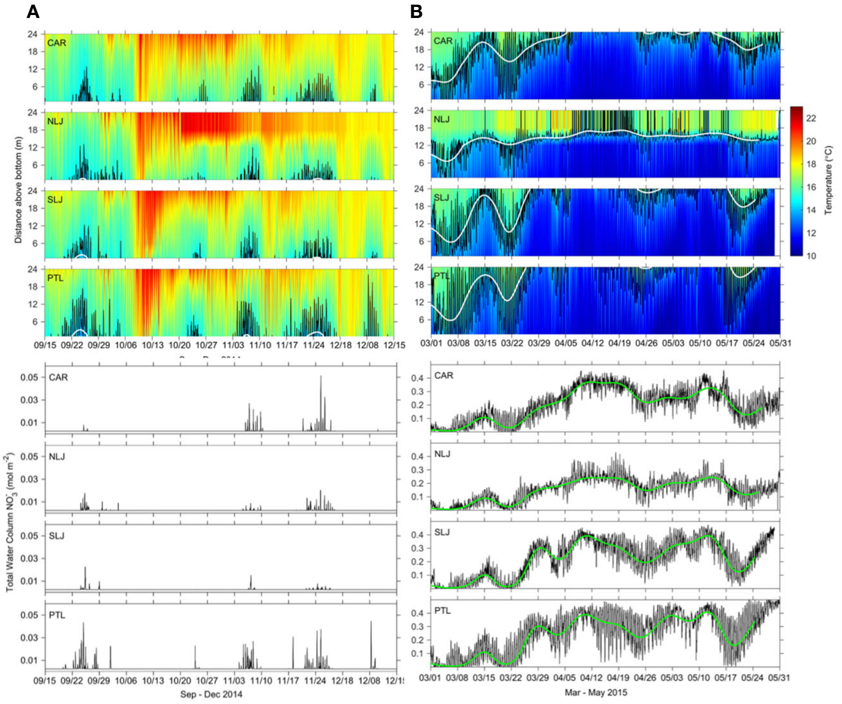

FIGURE 5
Expanded views of data seaward of 4 kelp forest study sites shown in Fig 4 for two time periods: **(A)** 15 Sep - 15 Dec 2014 and **(B)** 1 Mar – 31 May 2015. Upper panels in A and B show temperatures at 1 min intervals for the lower 24 m of the water column measured at 36 m bottom depth. Black lines indicate position of the 14.5 °C isotherm at 1 min intervals, white lines indicate position of the 14.5 °C isotherm for 10-d filtered data. Lower panels show total water column integrated NO_3^- for 1-min data (black lines) and 10-d filtered data (green lines).

(Figure 6). There are also differences among sites in the heights of the peaks at the semidiurnal frequency, indicating greatest semidiurnal variability at Point Loma, followed by South La Jolla, and smaller peaks at Cardiff and North La Jolla.

The total estimated NO_3^-, binned quarterly, further demonstrates the patterns of major variation among seasons as well as differences among sites (Figure 7). There was high NO_3^- exposure in Jun-Sep 2014 and especially in Mar-May 2015, while total NO_3^- was consistently low in Sep-Dec 2014 and low to intermediate in Dec-Mar 2015. There were clear differences among sites in the total estimated NO_3^- with exposure consistently highest at Point Loma and consistently lowest at North La Jolla across quarters and for the full year totals (Figure 7 and Table 2). The relative contribution of high frequency (f >= 1 cycle 30 hr^{-1}) and low frequency variability in NO_3^- exposure as a percentage of the totals varied markedly among quarters of the study period. During the periods of high NO_3^- exposure in Jun-Sep 2014 and Mar-May 2015, seasonal upwelling accounted for 90 to 95% of the total NO_3^- signals across sites. By contrast, during periods of low overall NO_3^- exposure, when water column temperatures were generally warm, short pulses associated with high frequency internal waves accounted for 10% to as much as 100% of the total NO_3^- exposure.

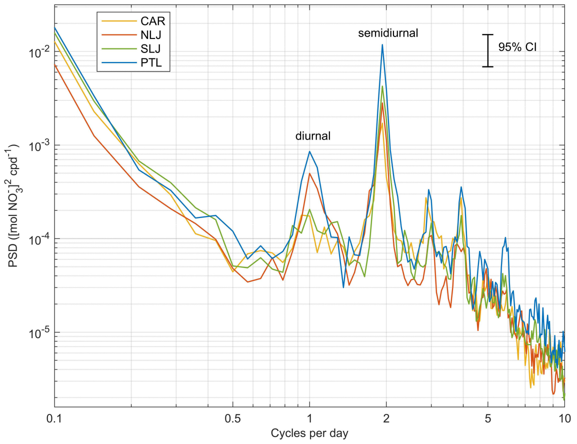

FIGURE 6
Power spectral density of water column integrated NO_3^- at each kelp forest study site for the study period Jun 2014 through May 2015. Error bar shows 95% confidence interval for the spectra calculated on a series of 14-d windows with 50% overlap. Sites indicated by color shown in legend in upper left.

4 Discussion

Variation in kelp bed canopy cover across the nearly 4-decade time series considered here highlights both the highly variable nature of kelp abundance and clear differences among kelp beds with respect to total size and site-normalized persistence through time. The total area of the Point Loma and La Jolla kelp beds far surpass that of the small bed at Cardiff, primarily reflecting marked

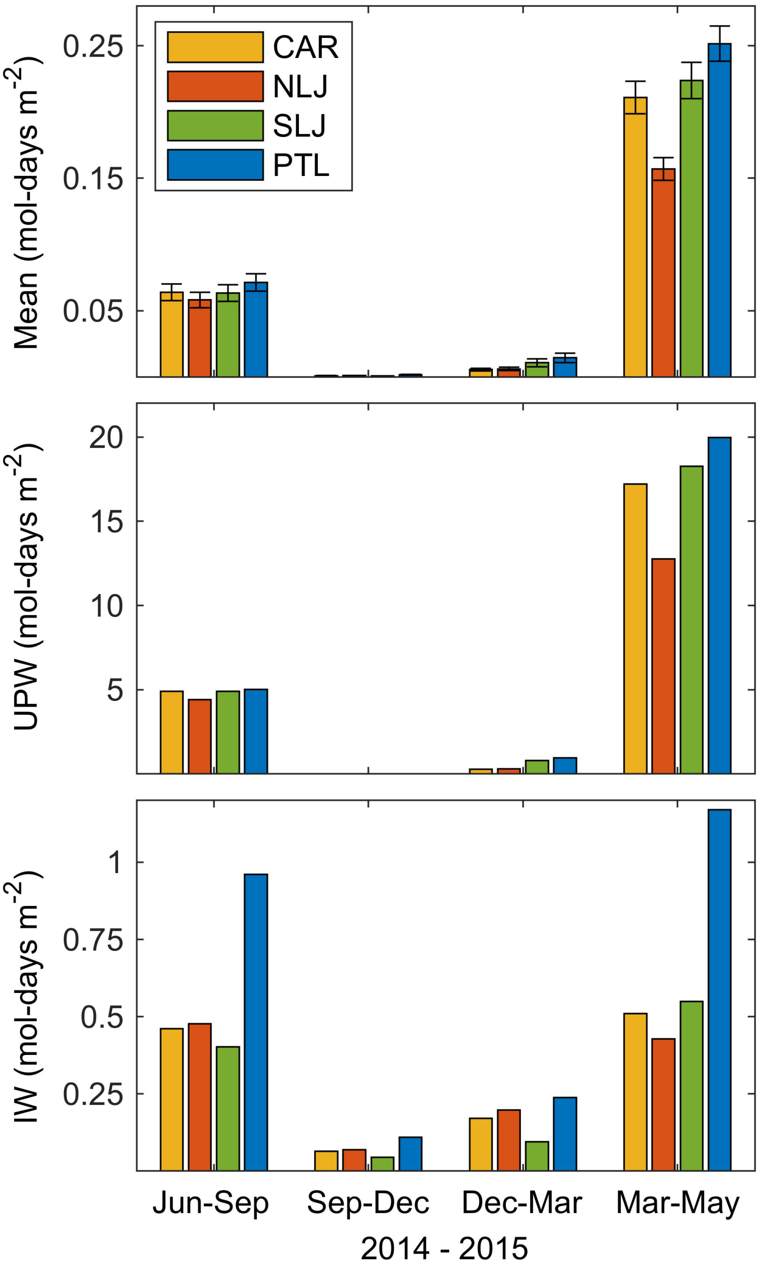

FIGURE 7
Quarterly estimated total nitrate exposure, (NO_3^- mol-days m^{-2}) for each of the study sites for period 24 Jun 2014 through 25 May 2015. Top panel shows quarterly means and standard error of the total NO_3^- exposure. Middle panel show totals for the low-frequency component of exposure corresponding to seasonal upwelling, UPW, (f < 1 cycle 30 hr^{-1}). Lower panel shows totals for the high-frequency component of exposure dominated by diurnal and semidiurnal internal waves, IW, (f >= 1 cycle 30 hr^{-1}). Note differences in y-axis scaling among panels. Sites indicated by color legend in top panel.

differences among sites in the availability of rocky substrata at depths less than ~25 m. Changes in the site-normalized canopy cover, and patterns of persistence since 2014 show clear patterns of Point Loma > La Jolla >> Cardiff. Notable during the recent period is a sharp decline in the Cardiff kelp bed since 2016 while the kelp beds at La Jolla and particularly at Point Loma have persisted and even increased in area. While the aerial survey data analyzed here consider the La Jolla kelp bed as a continuous one, local observations have also shown recent, as well as long-term differences between the south portion which has remained relatively consistent and the north portion, where kelp cover has been very low especially since 2016. It is important to note that canopy cover at the sea surface is only a portion of the total kelp biomass through the water column, and near bottom biomass of kelps, as well as the components of total algal biomass associated with other benthic algae, can remain present even in years when kelp surface canopy is reduced or absent. However, during years of high surface canopy biomass, there is likely to be corresponding high kelp biomass both through the water column and at the seafloor. It is reasonable to expect that variation in kelp bed canopy cover, and site-normalized cover through time are useful indicators of overall kelp dynamics.

The distribution, abundance, persistence and resilience of kelp beds are controlled by a range of interacting environmental and biological processes with complex, stochastic, and non-linear responses. For the study sites here, Cardiff has the smallest area of suitable rocky substrata and the smallest kelp bed size (E. Parnell unpublished observations). At Cardiff the primary mode of the rocky substrate depth distribution (~8 m) is shallower than at La Jolla (~17 m) or Point Loma (~14 m) (E. Parnell unpublished data). The Cardiff kelp bed, along with shallow portions of the North La Jolla kelp bed, are therefore, likely exposed to less frequent intrusions of NO_3^- from deeper water, and longer durations of exposure to warmer surface waters. In addition to effects on mature sporophytes, spatial differences in nutrient exposure associated with the site-specific quantity and depth distribution of rocky substrata may influence spore production, gametophyte growth and reproduction, and subsequent recruitment of early stage sporophytes. It is important to note that individual factors such as nutrient exposure are unlikely to explain complex interactions in kelp ecosystems. However, there is also significant potential for mechanistic links between spatial variation in oceanographic forcing and the dynamics, spatial heterogeneity, and ecology of kelp communities. The observations of spatial differences in kelp persistence, with the greatest persistence at Point Loma, correspond to consistent patterns of variability among sites in the modelled integrated water column NO_3^- exposure among sites, both seasonally and when summed through time. Notably variability in the NO_3^- signal also showed the same spatial pattern and was concentrated at the semidiurnal and to a smaller extent the diurnal frequencies, indicative of internal waves which may play significant roles in alongshore heterogeneity of the kelp beds in San Diego. These observations support the general hypothesis that patterns of kelp persistence within the region map onto, and are influenced by, spatial and temporal patterns of NO_3^- availability, and suggest that differences in nutrient climate can at least partially explain spatial variation in community dynamics of these key foundation species.

Nitrate exposure is clearly not the only driver of kelp bed persistence; however, it is certainly one of the most recognized limiting factors in kelp survival, with the nutrient status of kelp blades being linked to adult survival during periods of suboptimal environmental conditions, such as thermal stress (Gerard, 1997; Ladah and Zertuche-González, 2022). Although the approach used here is based on a well-established relationship between temperature and nitrate (Zimmerman and Kremer, 1984; Konotchick et al., 2012), the integrated water-column NO_3^- model does not include fluxes of water and nutrients over the kelp beds, which could further impact complex feedbacks between boundary layer dynamics and nitrate uptake kinetics beyond our characterization of a static nutrient environment (Hepburn et al., 2007). Nevertheless, the patterns detected were notably different across sites and do coincide with spatial patterns of kelp forest persistence in this region. The approach of characterizing site-specific integrated water-column NO_3^- environments might provide an additional tool for quantifying the physicochemical forcing of sub-thermocline nitrate, which along with light, substrate availability, and disturbance regimes (e.g. storm waves, sand movement, urchins), greatly influence kelp persistence and resilience. The approach of estimating total nitrate exposure from temperature data that are relatively straightforward to collect could be applied in combination with other approaches for reserve planning, restoration efforts, resource management, and potential offshore aquaculture site selection (e.g. Snyder et al., 2020; Zertuche-Gonzales et al., 2022).

Across the full temperature time series from in 2014 and 2015, and during periods of cold water temperatures and high NO_3^- exposure, we observed as much as 1.2 to 1.5 fold differences among sites, with the North La Jolla and Cardiff sites consistently lower than South La Jolla and especially Point Loma which consistently showed the highest integrated water-column NO_3^-. During periods of warm temperatures and low overall NO_3^- exposure, NO_3^- exposure was 2 to 2.7 fold greater at Point Loma than at North La Jolla and Cardiff with South La Jolla intermediate and generally closer to exposures at Point Loma. During the period from Mar through May 2015, although all sites showed similar temperatures in the bottom of the water column, a persistent surface warm-water pool was present at North La Jolla and not at the other sites in. This persistent surface warm pool from Mar through May 2015, with temperatures consistently warmer than the 14.2°C intercept in the temperature-nitrate relationship, essentially removed the top half of the water column at North La Jolla from contributing to total integrated NO_3^- over a significant vertical section of the kelp forest. By contrast, the Point Loma, South La Jolla, and Cardiff sites showed a greater overall integrated NO_3^-, with little to no warm surface pooling, and cooler temperatures throughout the water column during this period.

Of note in the spectral analysis, the Point Loma site also showed the greatest NO_3^- variability at the semidiurnal frequency, and this pattern is also visible as variability in the raw temperature time series. This demonstrates that NO_3^- exposure at this site is strongly influenced by semidiurnal internal tidal forcing, even during typical upwelling periods. Semidiurnal internal waves have been shown to provide sub-thermocline nutrients to the shelf in many regions of the world (e.g. Sandstrom and Elliott, 1984; Leichter et al. 1996; Leichter et al., 2003; Lucas et al., 2011). Pulses of nutrients associated with internal waves can result in an increase in seaweed tissue nitrogen over relatively short periods of time (Pérez-Mayorga et al., 2011; Ladah et al., 2012), and have been suggested to lead to kelp forest persistence at depth during warm periods in the Southern California bight (Ladah and Zertuche-González, 2004). While seasonal upwelling is the dominant mode of nutrient exposure overall, during the warmest water period in this study, internal waves provided virtually all of the cool water and associated NO_3^-, which may be critical for sustaining kelp through nutrient deplete seasons in southern California.

The dynamics and spatial variability of incident internal waves interacting with the continental slope and inshore coastal bathymetry are highly complex. Among the factors influencing these dynamics are changes in the overall mean depth of the thermocline, as well as bottom depth, distance from shore, the strength of forcing, and bottom slope angle (Aghsaee et al., 2010). The mean depth of the thermocline and associated nutricline modulates nutrient provision by high frequency internal waves to the coastal environment due to greater nitrate availability at depth, and the high frequency shoaling transiently makes this pool available to inshore communities in shallow water. At longer seasonal time frames the mean depth of the thermocline is controlled by patterns of seasonal upwelling. The landscape and steepness of the kelp bed area can also influence the amplitude and impact of internal waves. For example, bottom depth, bottom slope, and distance to offshore bathymetric features where internal waves are generated all impact the strength and propagation of internal tidal forcing, all of which can vary over short distances (Ladah et al., 2012; Filonov et al., 2014). These processes might be particularly relevant at a site such as Point Loma where the kelp bed occurs in deeper water closer in horizontal distance to a nutrient source at depth as well as to potential internal wave generation sites. Furthermore, even if the upwards motion of this cooler deeper water does not actually reach the deepest sections of the kelp bed, such as may occur during warmer periods of deeper thermoclines and nutriclines, the non-linear diapycnal mixing of nutrients by internal waves up the slope into the bottom layers of deeper kelp forests might be sufficient to maintain productivity at core areas even during warm years and during marine heatwaves, such as occurs during El Niño events at some sites in the Southern California Bight adjacent to a deep water channel (Ladah and Zertuche- González, 2004). This process has been shown to be highly-spatially variable at scales of only a few kilometers (Filonov et al., 2014) and could certainly result in differences in kelp bed persistence over short distances.

During the period of low NO_3^- exposure during Sep 2014 through Jan 2015, associated with anomalous surface heating and depression of the thermocline at the onset of the "Pacific Warm Blob", the pattern of greater integrated water column nitrate at Point Loma relative to the other kelp forest sites studied here was maintained, although with much lower values and much shorter and smaller nutrient pulses. Kelp survival through the important fall period of higher irradiance aided by episodic nitrate provision could allow for some growth and potentially prevent the dilution of nitrogen reserves in new tissue. The combination of high light and sufficient nutrients could allow kelps at sites with short-term nutrient pulses to maintain biomass and spatial dominance in their environment and reduce fall senescence. The provision of even small amounts of nitrate during this period could provide an advantage and increase survivorship, potentially leading to year-to-year persistence. It is unclear from this analysis, however, whether the small, short-term pulses of NO_3^- would be sufficient for enhanced kelp survivorship, and physiological experiments on nutrient uptake at low concentrations and during periods of nutrient replete conditions would be a valuable next step. Pulse fertilization experiments in culture do suggest that for a smaller kelp (*Ecklonia aborea nee Eisenia*), weekly 2-hr fertilizations could nearly double tissue nitrogen concentrations (Sánchez-Barredo et al., 2011) and allow for extended survivorship under thermal stress, whereas uptake kinetics of giant kelp suggest they can take advantage of even very rapid, small nutrient pulses (Gerard 1982a; Fram et al., 2008).

Prior studies of nutrient availability in kelp forest habitats have relied primarily on environmental sensing of winds, currents, and ocean temperature (e.g. Jackson, 1977; Zimmerman and Kremer, 1984) and in some recent cases deployment of *in situ* NO_3^- sensors (e.g. McPhee-Shaw et al., 2007; Fram et al., 2008). The former studies generally relied on relationships between temperature and nitrate to predict nutrient levels from temperature records, and the latter more recent studies used portions of the study periods when the *in situ* nitrate measurements were successful to generate estimates of the relationship between temperature and nitrate that could then be used to model NO_3^- exposure through time from *in situ* temperature records (e.g. Snyder et al., 2020). There are large variations in total NO_3^- exposure through time (up to 50-fold changes in monthly integrated totals) associated with wind-driven upwelling that can account for up to 70% of total NO_3^- exposure and are largely coherent among sites (McPhee-Shaw et al., 2007; Fram et al., 2008). There can also be significant NO_3^- delivery associated with diurnal, semidiurnal, and higher-frequency internal waves. For a site along the coast of Santa Barbara, NO_3^- delivery associated with high-frequency events has been estimated to supply from 9 to 12% of total annual exposure (McPhee-Shaw et al., 2007; Fram et al., 2008) and in Northern Baja California, about 11% of the days of the year were shown to have biologically relevant high-frequency sub-thermocline nutrient pulses due to internal wave forcing (Ladah et al., 2012).

In southern California, exposure to internal waves is likely to be more important for overall kelp growth than the annual percentages estimated for Santa Barbara suggest. In this region internal wave impacts can be strongest in summer months when reduced wind-driven upwelling and water column stratification typically lead to a significant reduction in surface NO_3^- concentrations and periods of prolonged physiological stress in kelps (Zimmerman and Kremer, 1984). Also, the alongshore variation in internal wave exposure may explain a significant proportion of the differences in nutrient availability among sites, particularly for nearby sites (e.g. < 10 – 30 km apart) where wind-driven upwelling may be largely coherent. In Northern Baja California at a spatial scale of less than 10 km, an order of magnitude difference in variance occurs for current speeds forced at the semidiurnal frequency, with large differences in the dominance of the diurnal versus the semidiurnal signal in temperature over this spatial scale (Filonov et al., 2014). Furthermore, inter-annual variation in stratification associated with the El Niño Southern Oscillation (ENSO) has been shown to affect inter- and intra-specific competition among kelp species, and in seasons and years of low surface nitrate availability, internal waves are again likely to be an important source of sustaining nutrients (Dayton et al., 1999). Similarly, with increasing distance south along the coast (e.g. from Santa Barbara to San Diego), warmer surface temperatures and greater depth of stratification may significantly increase the relative importance of short-term nutrient pulses to overall nutrient availability, particularly in seasons and years when upwelling is reduced.

In this study, *in situ* measurements of variation in temperature with depth and modeled NO_3^- exposure at multiple sites reveal the importance of both seasonal and higher-frequency diurnal and semidiurnal physical forcing that may contribute to the growth and persistence of local kelp beds. Identifying suitable habitat for productive and resilient kelp is necessary to manage and potentially to restore these valuable resources. Our results suggest that previously observed among-site variability in kelp growth and persistence may be explained, at least partially, by variation in high-frequency pulses of nutrients to overcome persistent warm, nutrient-deplete conditions near the surface. The differences in nutrient exposure estimated here for sites along ~30 km of the coastline in San Diego point to the importance of spatial heterogeneity of nutrient availability at a range of scales, particularly within regions. These observations also suggest high frequency variability and intermittent exposure to nutrient pulses may be increasingly important as southern California coastal ecosystems are exposed to continuing warming and deepening of stratification associated with climate change and increasingly frequent marine heatwaves.

Data availability statement

The raw data supporting the conclusions of this article will be made available by the authors, without undue reservation.

Author contributions

JL led the research and developed the analysis. JL and LL wrote the primary text, and all co-authors contributed to the field research, data analysis, manuscript production, and/or editing. All authors contributed to the article and approved the submitted version.

Funding

This work was support by National Science Foundation grants OCE-1535203 and OCE-2022959, as well as funding from the UC San Diego Academic Senate and UC Ship Fund.

Acknowledgments

We thank the NSF funding agency, UC Academic Senate and UC Ship Fund. We thank the Captain and crew of the *R/V New Horizon* for assistance with mooring deployments. We thank the Scripps Institution of Oceanography Diving Program for support.

Conflict of interest

The authors declare that the research was conducted in the absence of any commercial or financial relationships that could be construed as a potential conflict of interest.

Publisher's note

References

Aghsaee, P., Boegman, L., and Lamb, K. G. (2010). Breaking of shoaling internal solitary waves. *J. Fluid Mechanics* 659, 289–317. doi: 10.1017/S002211201000248X

Arafeh-Dalmau, N., Montaño-Moctezuma, G., Martínez, J. A., Beas-Luna, R., Schoeman, D. S., and Torres-Moye, G. (2019). Extreme marine heatwaves alter kelp forest community near its equatorward distribution limit. *Front. Mar. Sci.* 6, 499. doi: 10.3389/fmars.2019.00499

Bell, T. W., Allen, J. G., Cavanaugh, K. C., and Siegel, D. A. (2020). Three decades of variability in california's giant kelp forests from the landsat satellites. *Remote Sens. Environ.* 238, 110811. doi: 10.1016/j.rse.2018.06.039

Bray, R. N., Purcell, L. J., and Miller, A. C. (1986). Ammonium excretion in a temperate-reef community by a planktivorous fish, chromis punctipinnis (Pomacentridae), and potential uptake by young giant kelp, *Macrocystis pyrifera* (Laminariales). *Mar. Biol.* 90 (3), 327–334. doi: 10.1007/BF00428556

Cavanaugh, K. C., Reed, D. C., Bell, T. W., Castorani, M. C., and Beas-Luna, R. (2019). Spatial variability in the resistance and resilience of giant kelp in southern and Baja California to a multiyear heatwave. *Front. Mar. Sci.* 6, 413. doi: 10.3389/fmars.2019.00413

Checkley, J. D. M., and Barth, J. A. (2009). Patterns and processes in the California current system. *Prog. Oceanography* 83 (1-4), 49–64. doi: 10.1016/j.pocean.2009.07.028

Chung, I. K., Oak, J. H., Lee, J. A., Shin, J. A., Kim, J. G., and Park, K. S. (2013). Installing kelp forests/seaweed beds for mitigation and adaptation against global warming: Korean project overview. *ICES J. Mar. Sci.* 70 (5), pp.1038–1044.

Dayton, P. K. (1972). Toward an understanding of community resilience and the potential effects of enrichments to the benthos at McMurdo sound, antarctica. in. *Proc. Colloquium Conserv. Problems Antarctica*, 81–96.

Dayton, P. K. (1985). Ecology of kelp communities. *Annu. Rev. Ecol. System.* 16 (1), 215–245.

Dayton, P. K., Tegner, M. J., Edwards, P. B., and Riser, K. L. (1999). Temporal and spatial scales of kelp demography: The role of oceanographic climate. *Ecol. Monogr.* 69 (2), 219–250. doi: 10.1890/0012-9615(1999)069[0219:TASSOK]2.0.CO;2

Dayton, P. K., Tegner, M. J., Parnell, P. E., and Edwards, P. B. (1992). Temporal and spatial patterns of disturbance and recovery in a kelp forest community. *Ecol. Monogr.* 62 (3), 421–445. doi: 10.2307/2937118

Dorman, C. E., and Palmer, D. P. (1981). Southern California summer coastal upwelling. *Coast. Upwelling* 1, 44–56. doi: 10.1029/CO001p0044

Duke, C. S., Litaker, W., and Ramus, J. (1989). Effect of temperature on nitrogen-limited growth rate and chemical composition of ulva curvata (Ulvales: Chlorophyta). *Mar. Biol.* 100, 143–150. doi: 10.1007/BF00391953

Eppley, R. W., Renger, E. H., and Harrison, W. G. (1979). Nitrate and phytoplankton production in southern California coastal waters 1. *Limnology Oceanography* 24 (3), 483–494. doi: 10.4319/lo.1979.24.3.0483

Estes, J. A., Danner, E. M., Doak, D. F., Konar, B., Springer, A. M., Steinberg, P. D., et al. (2004). Complex trophic interactions in kelp forest ecosystems. *Bull. Mar. Sci.* 74 (3), 621–638.

Ewing, G. C. (1950). Relation between band slicks at the surface and internal waves in the sea. *Science* 111 (2874), 91–94. doi: 10.1126/science.111.2874.91

Feehan, C. J., and Scheibling, R. E. (2014). Effects of sea urchin disease on coastal marine ecosystems. *Mar. Biol.* 161 (7), 1467–1485. doi: 10.1007/s00227-014-2452-4

Filonov, A., Lavín, M. F., Ladah, L. B., and Tereshchenko, I. (2014). Spatial variability of internal waves in an open bay with a narrow steep shelf in the pacific off NW Mexico. *Continental Shelf Res.* 78, 1–15. doi: 10.1016/j.csr.2014.01.015

Foster, M. S., and Schiel, D. R. (1985). The ecology of giant kelp forests in California: A community profile US Fish and Wildlife Service. *Biol. Rep.* 85 (2), 152.

Fram, J. P., Stewart, H. L., Brzezinski, M. A., Gaylord, B., Reed, D. C., Williams, S. L., et al. (2008). Physical pathways and utilization of nitrate supply to the giant kelp, *Macrocystis pyrifera*. *Limnology Oceanography* 53 (4), 1589–1603. doi: 10.4319/lo.2008.53.4.1589

Gerard, V. A. (1982a). Growth and utilization of internal nitrogen reserves by the giant kelp *Macrocystis pyrifera* in a low-nitrogen environment. *Mar. Biol.* 66 (1), 27–35. doi: 10.1007/BF00397251

Gerard, V. A. (1982b). *In situ* water motion and nutrient uptake by the giant kelp *Macrocystis pyrifera*. *Mar. Biol.* 69 (1), 51–54. doi: 10.1007/BF00396960

Gerard, V. A. (1984). The light environment in a giant kelp forest: Influence of *Macrocystis pyrifera* on spatial and temporal variability. *Mar. Biol.* 84 (2), 189–195. doi: 10.1007/BF00393004

Gerard, V. A. (1997). The role of nitrogen nutrition in high-temperuatre tolerance of the kelp laminaria saccharina (Chromophyta). *J. Phycology* 33 (5), 800–810. doi: 10.1111/j.0022-3646.1997.00800.x

Harrison, P. J., and Hurd, C. L. (2001). Nutrient physiology of seaweeds: Application of concepts to aquaculture. *Cahiers biologie Mar.* 42 (1-2), 71–82.

Helfrich, K. R., and Melville, W. K. (2006). Long nonlinear internal waves. *Annu. Rev. Fluid Mech.* 38, 395–425. doi: 10.1146/annurev.fluid.38.050304.092129

Hepburn, C. D., Pritchard, D. W., Cornwall, C. E., McLeod, R. J., Beardall, J., Raven, J. A., et al. (2011). Diversity of carbon use strategies in a kelp forest community: Implications for a high CO2 ocean. *Global Change Biol.* 17 (7), 2488–2497. doi: 10.1111/j.1365-2486.2011.02411.x

Holloway, P. E. (1987). Internal hydraulic jumps and solitons at a shelf break region on the Australian north West shelf. *J. Geophysical Research: Oceans* 92 (C5), 5405–5416. doi: 10.1029/JC092iC05p05405

Hurd, C. L., Durante, K. M., Chia, F. S., and Harrison, P. J. (1994). Effect of bryozoan colonization on inorganic nitrogen acquisition by the kelps agarum fimbriatum and macrocystis integrifolia. *Mar. Biol.* 121 (1), 167–173. doi: 10.1007/BF00349486

Jackson, G. A. (1977). Nutrients and production of giant kelp, *Macrocystis pyrifera*, off southern California. *Limnology Oceanography* 22 (6), 979–995. doi: 10.4319/lo.1977.22.6.0979

Jackson, G. A. (1983). The physical and chemical environment of a kelp community. the effects of waste disposal on kelp communities. *South. California Coast. Water Res. Project Long Beach*, 11–37.

Jackson, G. A., and Winant, C. D. (1983). Effect of a kelp forest on coastal currents. *Continental Shelf Res.* 2 (1), 75–80. doi: 10.1016/0278-4343(83)90023-7

Kamykowski, D., and Zentara, S. J. (1986). Predicting plant nutrient concentrations from temperature and sigma-t in the upper kilometer of the world ocean. *Deep Sea Res. Part A. Oceanographic Res. Papers* 33 (1), 89–105. doi: 10.1016/0198-0149(86)90109-3

Kinlan, B. P., Graham, M. H., Sala, E., and Dayton, P. K. (2003). Arrested development of giant kelp (*Macrocystis pyrifera*, phaeophyceae) embryonic sporophytes: A mechanism for delayed recruitment in perennial kelps? *J. Phycology* 39 (1), 47–57. doi: 10.1046/j.1529-8817.2003.02087.x

Konotchick, T., Parnell, P. E., Dayton, P. K., and Leichter, J. J. (2012). Vertical distribution of *Macrocystis pyrifera* nutrient exposure in southern California. *Estuarine Coast. Shelf Sci.* 106, 85–92. doi: 10.1016/j.ecss.2012.04.026

Ladah, L. B. (2003). The shoaling of nutrient-enriched subsurface waters as a mechanism to sustain primary productivity off central Baja California during El niño winters. *J. Mar. Syst.* 42 (3-4), 145–152. doi: 10.1016/S0924-7963(03)00072-1

Ladah, L. B., Filonov, A., Lavín, M. F., Leichter, J. J., Zertuche-Gonzalez, J. A., and Perez-Mayorga, D. M. (2012). Cross-shelf transport of sub-thermocline nitrate by the internal tide and rapid (3–6 h) incorporation by an inshore macroalga. *Continental Shelf Res.* 42, 10–19. doi: 10.1016/j.csr.2012.03.010

Ladah, L., and Zertuche- González, J. (2004). Giant kelp (*Macrocystis pyrifera*) survival in deep water (25-40m) during El niño of 1997-1998 in Baja California, Mexico. *Botanica Marina* 47, 367–372. doi: 10.1515/BOT.2004.054

Ladah, L. B., and Zertuche-González, J. A. (2022). Local adaptation of juvenile giant kelp, *Macrocystis pyrifera*, from their southern limit in the northern hemisphere explored using reciprocal transplantation. *Eur. J. Phycology*, 1–10. doi: 10.1080/09670262.2021.2007543

Lamb, K. G. (1997). Particle transport by nonbreaking, solitary internal waves. *J. Geophysical Research: Oceans* 102 (C8), 18641–18660. doi: 10.1029/97JC00441

Leichter, J. J., Stewart, H. L., and Miller, S. L. (2003). Episodic nutrient transport to Florida coral reefs. *Limnology Oceanography* 48 (4), 1394–1407. doi: 10.4319/lo.2003.48.4.1394

Leichter, J. J., Wing, S. R., Miller, S. L., and Denny, M. W. (1996). Pulsed delivery of subthermocline water to conch reef (Florida keys) by internal tidal bores. *Limnology Oceanography* 41 (7), 1490–1501. doi: 10.4319/lo.1996.41.7.1490

Lobban, C. S., and Harrison, P. J. (1994). *Seaweed ecology and physiology* (Cambridge UK: Cambridge University Press).

Lucas, A. J., Franks, P. J., and Dupont, C. L. (2011). Horizontal internal-tide fluxes support elevated phytoplankton productivity over the inner continental shelf. *Limnology Oceanography: Fluids Environments* 1 (1), 56–74. doi: 10.1215/21573698-1258185

Manley, S. L. (1983). Composition of sieve tube sap from *Macrocystis pyrifera* (Phaeophyta) with emphasis on the inorganic constituents 1. *J. Phycology* 19 (1), 118–121. doi: 10.1111/j.0022-3646.1983.00118.x

MBC Aquatic Sciences (2020). *Status of the kelp beds in 2019: Orange and San Diego counties* (Costa Mesa, CA, USA: MBC Aquatic Sciences).

McPhee-Shaw, E. E., Siegel, D. A., Washburn, L., Brzezinski, M. A., Jones, J. L., Leydecker, A., et al. (2007). Mechanisms for nutrient delivery to the inner shelf: Observations from the Santa Barbara channel. *Limnology Oceanography* 52 (5), 1748–1766. doi: 10.4319/lo.2007.52.5.1748

McPherson, M. L., Finger, D. J., Houskeeper, H. F., Bell, T. W., Carr, M. H., Rogers-Bennett, L., et al. (2021). Large-Scale shift in the structure of a kelp forest ecosystem co-occurs with an epizootic and marine heatwave. *Commun. Biol.* 4 (1), 298. doi: 10.1038/s42003-021-01827-6

Mooers, C. N., and Robinson, A. R. (1984). Turbulent jets and eddies in the California current and inferred cross-shore transports. *Science* 223 (4631), 51–53. doi: 10.1126/science.223.4631.51

Neori, A., Chopin, T., Troell, M., Buschmann, A. H., Kraemer, G. P., Halling, C., et al. (2004). Integrated aquaculture: Rationale, evolution and state of the art emphasizing seaweed biofiltration in modern mariculture. *Aquaculture* 231 (1-4), 361–391. doi: 10.1016/j.aquaculture.2003.11.015

Parnell, P. E. (2015). The effects of seascape pattern on algal patch structure, sea urchin barrens, and ecological processes. *J. Exp. Mar. Biol. Ecol.* 465, 64–76. doi: 10.1016/j.jembe.2015.01.010

Parnell, P. E., Dayton, P. K., Lennert-Cody, C. E., Rasmussen, L. L., and Leichter, J. J. (2006). Marine reserve design: Optimal size, habitats, species affinities, diversity, and ocean microclimate. *Ecol. Appl.* 16 (3), 945–962. doi: 10.1890/1051-0761(2006)016[0945:MRDOSH]2.0.CO;2

Parnell, P. E., Miller, E. F., Cody, C. E. L., Dayton, P. K., Carter, M. L., and Stebbinsd, T. D. (2010). The response of giant kelp (*Macrocystis pyrifera*) in southern California to low-frequency climate forcing. *Limnology Oceanography* 55 (6), 2686–2702. doi: 10.4319/lo.2010.55.6.2686

Pedersen, M. F. (1994). Transient ammonium uptake in the macroalga ulva lactuca (chlorophyta): Nature, regulation, and the consequences for choice of measuring technique 1. *J. Phycology* 30 (6), 980–986. doi: 10.1111/j.0022-3646.1994.00980.x

Pedersen, M. F., and Borum, J. (1996). Nutrient control of algal growth in estuarine waters. nutrient limitation and the importance of nitrogen requirements and nitrogen storage among phytoplankton and species of macroalgae. *Mar. Ecol. Prog. Ser.* 142, 261–272. doi: 10.3354/meps142261

Pérez-Mayorga, D. M., Ladah, L. B., Zertuche-González, J. A., Leichter, J. J., Filonov, A. E., and Lavín, M. F. (2011). Nitrogen uptake and growth by the opportunistic macroalga ulva lactuca (Linnaeus) during the internal tide. *J. Exp. Mar. Biol. Ecol.* 406 (1-2), 108–115. doi: 10.1016/j.jembe.2011.05.028

Pineda, J. (1991). Predictable upwelling and the shoreward transport of planktonic larvae by internal tidal bores. *Science* 253 (5019), 548–549. doi: 10.1126/science.253.5019.548

Ponte, A. L., and Cornuelle, B. D. (2013). Coastal numerical modelling of tides: Sensitivity to domain size and remotely generated internal tide. *Ocean Model.* 62, 17–26. doi: 10.1016/j.ocemod.2012.11.007

Reed, D. C., and Foster, M. S. (1984). The effects of canopy shadings on algal recruitment and growth in a giant kelp forest. *Ecology* 65 (3), 937–948. doi: 10.2307/1938066

Rosenberg, G., and Ramus, J. (1984). Uptake of inorganic nitrogen and seaweed surface area: Volume ratios. *Aquat. Bot.* 19 (1-2), 65–72. doi: 10.1016/0304-3770(84)90008-1

Ryan, J. P., Chavez, F. P., and Bellingham, J. G. (2005). Physical-biological coupling in Monterey bay, California: Topographic influences on phytoplankton ecology. *Mar. Ecol. Prog. Ser.* 287, 23–32. doi: 10.3354/meps287023

Sánchez-Barredo, M., Ladah, L. B., and Zertuche-González, J. A. (2011). Nitrate uptake and duration of internal nitrogen reserves in the kelp eisenia arborea. *Bot. Marina* 54 (5), 441–446. doi: 10.1515/BOT.2011.058

Sandstrom, H., and Elliott, J. A. (1984). Internal tide and solitons on the scotian shelf: A nutrient pump at work. *J. Geophysical Research: Oceans* 89 (C4), 6415–6426. doi: 10.1029/JC089iC04p06415

Schafstall, J., Dengler, M., Brandt, P., and Bange, H. (2010). Tidal-induced mixing and diapycnal nutrient fluxes in the Mauritanian upwelling region. *J. Geophysical Research: Oceans* 115 (C10).

Schmitz, K., and Srivastava, L. M. (1979). Long distance transport in macrocystis integrifolia: I. translocation of 14C-labeled assimilates. *Plant Physiol.* 63 (6), 995–1002.

Sharples, J., Tweddle, J. F., Mattias Green, J. A., Palmer, M. R., Kim, Y. N., Hickman, A. E., et al. (2007). Spring-neap modulation of internal tide mixing and vertical nitrate fluxes at a shelf edge in summer. *Limnology Oceanography* 52 (5), 1735–1747. doi: 10.4319/lo.2007.52.5.1735

Smith, J. M., Brzezinski, M. A., Melack, J. M., Miller, R. J., and Reed, D. C. (2018). Urea as a source of nitrogen to giant kelp (*Macrocystis pyrifera*). *Limnology Oceanography Lett.* 3 (4), 365–373. doi: 10.1002/lol2.10088

Snyder, J. N., Bell, T. W., Siegel, D. A., Nidzieko, N. J., and Cavanaugh, K. C. (2020). Sea Surface temperature imagery elucidates spatiotemporal nutrient patterns for offshore kelp aquaculture siting in the southern California bight. *Front. Mar. Sci.* 7, 22. doi: 10.3389/fmars.2020.00022

Steneck, R. S., Graham, M. H., Bourque, B. J., Corbett, D., Erlandson, J. M., Estes, J. A., et al. (2002). Kelp forest ecosystems: Biodiversity, stability, resilience and future. *Environ. Conserv.* 29 (4), 436–459. doi: 10.1017/S0376892902000322

Strickland, J. D. (1970). *The ecology of the plankton off la Jolla, California, in the period April through September 1967*. (Berkeley, CA, USA: University of California Press)

Thomson, R. E., and Emery, W. J. (2014). *Data analysis methods in physical oceanography* (Waltham, MA USA: Newnes).

Trauth, M. H. (2015). *MATLAB® recipes for earth sciences* (Berlin/Heidelberg, Germany: Springer), 427.

Walter, R. K., and Phelan, P. J. (2016). Internal bore seasonality and tidal pumping of subthermocline waters at the head of the Monterey submarine canyon. *Continental Shelf Res.* 116, 42–53. doi: 10.1016/j.csr.2016.01.015

Wheeler, P. A., and North, W. J. (1980). Effects of nitrogen supply on nitrogen content and growth rate of juveniles *Macrocystis pyrifera* (Phaeophyta) sporophytes. *J. Phycology* 16 (4), 577–582. doi: 10.1111/j.1529-8817.1980.tb03076.x

Young, M., Cavanaugh, K., Bell, T., Raimondi, P., Edwards, C. A., Drake, P. T., et al. (2016). Environmental controls on spatial patterns in the long-term persistence of giant kelp in central California. *Ecol. Monogr.* 86 (1), 45–60. doi: 10.1890/15-0267.1

Zentara, S. J., and Kamykowski, D. (1977). Latitudinal relationships among temperature and selected plant nutrients along the west coast of north and south America. *J. Mar. Res.* 35 (2), pp.321–pp.337.

Zertuche-Gonzalez, J. A., Gil, J. S., Sanchez-Barredo, M., Altamirano_Gómez, Z., Guzmán-Calderón, J. M., Rangel-Mendoza, L. K., et al. (2022). Eisenia arborea (Areschoung) domestication and mariculture development on the Pacific coast of Baja California, México. *Front. Mar. Sci.* 9, 932534. doi: 10.3389/fmars.2022.932534

Zimmerman, R. C., and Kremer, J. N. (1984). Episodic nutrient supply to a kelp forest ecosystem in southern California. *J. Mar. Res.* 42 (3), 591–604. doi: 10.1357/002224084788506031

Zimmerman, R. C., and Kremer, J. N. (1986). *In situ* growth and chemical composition of the giant kelp, *Macrocystis pyrifera*: Response to temporal changes in ambient nutrient availability. *Mar. Ecol. Prog. Ser.* 27 (2), 277–285. doi: 10.3354/meps027277

Frontiers in
Marine Science

Explores ocean-based solutions for emerging global challenges

The third most-cited marine and freshwater biology journal, advancing our understanding of marine systems and addressing global challenges including overfishing, pollution, and climate change.

Discover the latest Research Topics

See more →

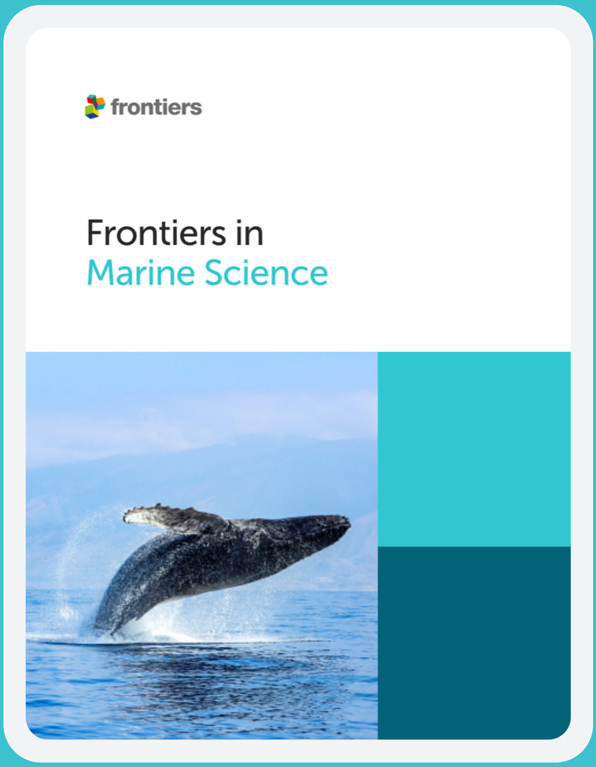
frontiers

Frontiers in
Marine Science

Frontiers

Avenue du Tribunal-Fédéral 34
1005 Lausanne, Switzerland
frontiersin.org

Contact us

+41 (0)21 510 17 00
frontiersin.org/about/contact